Ce $M_{4,5}$ XAS and XMCD as Local Probes for Kondo and Heavy Fermion Materials

– A Study of $CePt_5$/Pt(111) Surface Intermetallics –

Dissertation zur Erlangung des
naturwissenschaftlichen Doktorgrades der
Julius-Maximilians-Universität Würzburg

vorgelegt von

Christian Michael Praetorius

aus Wiesbaden

Würzburg 2015

Eingereicht am: 21.07.2015
bei der Fakultät für Physik und Astronomie

1. Gutachter: PD Dr. Kai Fauth
2. Gutachter: Prof. Dr. Ralph Claessen
3. Gutachter: ....
der Dissertation

Vorsitzende(r): Prof. Dr. Wolfgang Kinzel
1. Prüfer: PD Dr. Kai Fauth
2. Prüfer: Prof. Dr. Ralph Claessen
3. Prüfer: Prof. Dr. Fakher Assaad
des Promotionskolloquiums

Tag des Promotionskolloquiums: 15.04.2016
Doktorurkunde ausgehändigt am: ....

meiner Familie gewidmet

Sunt quasi nanos, gigantum umeris insidentes, ut possimus plura eis et remotiora uidere, non utique proprii uisus acumine, aut eminentia corporis, sed quia in altum subuehimur et extollimur magnitudine gigantea. [3]

BERNARD OF CHARTRES, French scholastic, 12th century

If I have seen further, it is by standing on ye shoulders of giants. [4]

ISAAC NEWTON, British physicist, astronomer and mathematician, 1643-1727

Contact information

The author can be contacted electronically via christian.praetorius(at)gmx.de.

Abstract

The aim of the present thesis is to explore the potential of X-ray magnetic circular dichroism (XMCD) experiments on gaining new insights into Kondo and heavy fermion materials. XMCD, which is derived from X-ray absorption spectroscopy (XAS), allows probing magnetic polarization specific to the different elements in a material and to their atomic orbitals. In particular, at the Ce $M_{4,5}$ edges the method is sensitive to the localized $4f$ level, which provides the magnetic impurity moment responsible for Kondo physics in Ce compounds. Hence, Ce $M_{4,5}$ XMCD is ideally suited to investigate local magnetism in the presence of interaction of impurity and conduction electrons in such materials.

As a model material, $CePt_5/Pt(111)$ surface intermetallics were chosen for the present study. This thin-film material can be prepared by well-defined procedures involving molecular beam epitaxy. Crystalline Ordered samples are obtained by exploiting the single-crystallinity of the Pt(111) substrate. The surface character of thin films ideally matches the probing depth of soft X-ray spectroscopy in the total electron yield mode.

The XMCD and XAS experiments, taking into account dependence on temperature, angle of incidence, sample thickness and external magnetic field, revealed the presence of four relevant energy scales that influence the magnetic response:

1. The $4f$ level in $CePt_5/Pt(111)$ is subject to significant crystal field (CF) splitting, which leads to reorganization of the six $j = 5/2$ sublevels. The hexagonal symmetry of the crystal structure conserves m_j as a good quantum number. The proposed CF scheme, which is derived from measurements of the paramagnetic susceptibility by XMCD as well as linear dichroism in XAS, consists of nearly degenerate $|1/2\rangle$ and $|3/2\rangle$ doublets with the $|5/2\rangle$ doublet excited by $\Delta E_{5/2} = 15 \ldots 25$ meV.

2. Single impurity Kondo interaction significantly couples the magnetic moments of the impurity and conduction electrons. A signature thereof is the $f^0 \to f^1$ contribution to Ce $M_{4,5}$ XAS, the strength of which can be tuned by control of the sample thickness. This finding is in line with the observation of reduced effective $4f$ moments as detected by XMCD.

3. Ruderman-Kittel-Kasuya-Yosida (RKKY) interaction induces ferromagnetic correlations on the impurity lattice, which induces a positive Curie-Weiss temperature in the temperature-dependent inverse susceptibility.

4. Indications for the transition to a coherent heavy fermion state are found in the inverse susceptibility at $T \approx 20$ K; the ferromagnetic ground state is not observed. The field-dependence of the magnetic moment in the coherent state can be interpreted in terms of a metamagnetic transition. This allows studying basic characteristics of the renormalized band structure of a heavy fermion system by XMCD.

The disentanglement of these different contributions to the $4f$ magnetism not only required extensive Ce $M_{4,5}$ XAS and XMCD data, but also a thorough structural characterization of the material, a fundamental study of the Ce $M_{4,5}$ line shape in relation to the degree of $4f$ hybridization and the development of a model for the paramagnetic susceptibility.

The unit cell dimensions and sample morphology of $CePt_5/Pt(111)$ intermetallics were studied by low-energy electron diffraction (LEED) and scanning transmission electron microscopy (STEM). These experiments showed that well-defined intermetallic films form on top of the substrate. This lead to introduction of the film thickness t, measured in unit cells (u.c.), as a key feature to characterize the samples.

Systematic LEED measurements in the thickness range $t \approx 1 \ldots 15$ u.c. allowed identification of six different phases, which could be interpreted as resulting from the same crystal structure with different rotational alignments and lattice constants. An accurate determination of the surface lattice constant at $t \approx 3$ u.c. could be achieved by interpretation of additional superstructure spots as arising from a well-defined combination of substrate and film lattices. The thickness-dependence of the lateral lattice constant could be explained in terms of lattice relaxation.

Confirmation of the $\mathrm{CePt_5}$ stoichiometry and structure was performed by use of thickness-dependent XAS and a representative LEED-IV study. The results of this study indicate that the intermetallic films exhibit hexagonal $\mathrm{CaCu_5}$ structure over the entire range of thicknesses that were studied. The terminating layer consists purely of Pt with one additional Pt atom per unit cell compared to the bulk structure.

The line shape of Ce $\mathrm{M_{4,5}}$ spectra was analyzed with the help of full multiplet calculations. Experimentally, characteristic variations of the line shape were observed with increasing $f^0 \rightarrow f^1$ contribution. The calculations show that these variations are not due to an admixture of $j = 7/2$ character to the ground state, as often stated in the literature. As alternatives, this observation can be explained by either considering an additional contribution to the spectrum or by assumption of an asymmetric lifetime profile.

The model that was developed for the inverse paramagnetic susceptibility contains the hexagonal crystal field, magnetic coupling of the impurity moments in a mean field scheme and Kondo screening. The latter is included phenomenologically by screening factors for the effective moment. Assumption of doublet-specific screening factors, which means that the degree of Kondo interaction depends on the m_j character of the $4f$ sublevels, allows satisfactory reproduction of the experimental data.

Zusammenfassung

Das Ziel der vorliegenden Arbeit ist die Untersuchung der Frage, welche neuen Einsichten in Kondo- und schwere Fermionen-Materialien mittels Röntgenzirkulardichroismus-Experimenten (XMCD) gewonnen werden können. Die Methode XMCD, die sich aus der Röntgenabsorption (XAS) ableitet, detektiert die magnetischen Polarisation gezielt für die verschiedenen Elemente in einem Material und für deren Atomorbitale. Insbesondere an den Ce $\mathrm{M_{4,5}}$ Absorptionskanten bietet die Methode Zugang zum lokalisierte $4f$ Niveau und damit zum magnetische Störstellenmoment in Ce-Verbindungen, welches eine Voraussetzung für Kondo-Physik ist. Ce $\mathrm{M_{4,5}}$ XMCD ist daher bestens geeignet, um lokalen Magnetismus in Gegenwart von Wechselwirkung zwischen Störstellen- und Leitungselektronen zu studieren.

Als Modellmaterial wurde für diese Arbeit $\mathrm{CePt_5/Pt(111)}$, eine oberflächennahe intermetallische Verbindung, gewählt. Die Präparation dieses Dünnfilmmaterials mithilfe von Molekularstrahlepitaxie kann bestens kontrolliert werden. Die Ausnutzung des einkristallinen Pt(111) Substrats liefert kristallin geordnete Proben. Der Oberflächencharakter der Filme ist gut auf die Informationstiefe von Absorptionsspektroskopie im weichen Röntgenbereich abgestimmt, wenn im Modus totaler Elektronenausbeute gemessen wird.

Die XAS- und XMCD-Experimente unter Variation von Temperatur, Einfallswinkel, Probendicke und Magnetfeld lassen die Gegenwart von vier relevanten Energieskalen für das magnetische Verhalten erkennen:

1. Das $4f$ Niveau in $\mathrm{CePt_5/Pt(111)}$ ist einer deutlichen Kristallfeldaufspaltung unterworfen, welche eine Neuordnung der sechs $j = 5/2$ Unterniveaus bewirkt. Dabei erhält die hexagonale Symmetrie der Kristallstruktur m_j als gute Quantenzahl. Basierend auf Messungen der paramagnetischen Suszeptibilität mit XMCD und des Lineardichroismus in XAS wird ein Niveauschema vorgeschlagen, das aus beinahe entarteten $|1/2\rangle$ und $|3/2\rangle$ Dubletts besteht, das $|5/2\rangle$ Dublett folgt bei einer höheren Energie von $\Delta E_{5/2} = 15 \ldots 25$ meV.

2. Einzelstörstellen-Kondowechselwirkung bewirkt eine signifikante Kopplung der magnetis-

chen Momente von Störstellen und Leitungszuständen. Dies ist anhand der $f^0 \rightarrow f^1$-Anteile in Ce $M_{4,5}$ XAS ersichtlich, deren Stärke über die Probendicke kontrolliert werden kann. In Übereinstimmung damit werden reduzierte effektive $4f$-Momente mit XMCD beobachtet.

3. Ruderman-Kittel-Kasuya-Yosida (RKKY) Wechselwirkung erzeugt ferromagnetische Kopplung auf dem Störstellengitter, was zu einer positiven Curie-Weiss-Temperatur in der temperaturabhängigen inversen Suszeptibilität führt.

4. Die inverse Suszeptibilität erlaubt Rückschlüsse auf einen Übergang in den kohärenten schwere-Fermionen-Zustand bei $T \approx 20\,\mathrm{K}$. Ein ferromagnetischer Zustand wurde nicht beobachtet. Die Magnetfeldabhängigkeit des magnetischen Moments in diesem Bereich kann im Sinne eines metamagnetischen Übergangs interpretiert werden. Dies eröffnet die Möglichkeit, grundlegende Charakteristika der renormalisierten Bandstruktur eines schweren Fermionen-Systems mittels XMCD zu erforschen.

Die Entschlüsselung dieser unterschiedlichen Beiträge zum $4f$-Magnetismus erforderte nicht nur umfangreiche Ce $M_{4,5}$ XAS und XMCD Experimente, sondern auch eine gründliche strukturelle Charakterisierung des Materials, eine grundlegende Studie der spektralen Linienform in Abhängigkeit vom Grad der $4f$-Hybridisierung sowie die Entwicklung eines Modells für die paramagnetische Suszeptibilität.

Die Abmessungen der Einheitszelle sowie die Filmmorphologie wurden mit niederenergetischer Elektronenbeugung (LEED) und Rastertransmissionselektronenmikroskopie (STEM) analysiert, wobei sich zeigte, dass die intermetallische Verbindung wohldefinierte Filme auf dem Substrat bildet. Daher wird die Filmdicke t, gemessen in Einheitszellen (u.c.), als Hauptmerkmal zur Charakterisierung der Proben eingeführt.

Mittels systematische LEED-Messungen im Dickenbereich $t \approx 1 \dots 15$ u.c. wurden sechs verschiedene Phasen identifiziert, welche auf eine gemeinsame Kristallstruktur mit unterschiedlichem Drehwinkel zum Substrat und unterschiedlichen Gitterkonstanten zurückgeführt werden. Bei einer Dicke von $t \approx 3$ u.c. konnte eine genaue Bestimmung der Oberflächengitterkonstante durchgeführt werden, indem zusätzliche Überstrukturreflexe als Ergebnis von kombinierter Streuung an Substrat- und Filmgitter gedeutet wurden. Die Dickenabhängigkeit der Gitterkonstante kann als abnehmende Gitterverspannung erklärt werden.

Die angenommene Stöchiometrie $\mathrm{CePt_5}$ und die zugehörige Kristallstruktur konnten mithilfe von dickenabhängigen XAS-Experimenten und einer repräsentativen LEED-IV Studie bestätigt werden. Die Ergebnisse der Letzteren weisen darauf hin dass die Filme im gesamten untersuchten Dickenbereich die $\mathrm{CaCu_5}$-Struktur aufweisen. Die Oberflächenabschlusslage besteht rein aus Pt und besitzt im Vergleich zum Volumengitter ein zusätzliches Pt-Atom pro Einheitszelle.

Die Linienform von Ce $M_{4,5}$ Spektren wurde mittels Gesamtmultiplett-Rechnungen analysiert. die experimentellen Daten zeigen charakteristische Variationen der Linienform in Abhängigkeit des $f^0 \rightarrow f^1$-Gewichts. Mit Rechnungen konnte gezeigt werden, dass diese Variationen nicht durch eine signifikante Beimischung von $j = 7/2$-Charakter zum Grundzustand erklärt werden können, was in der Literatur häufig angeführt wird. Zwei Alternativen wurden als mögliche Erklärungen für die Beobachtungen entwickelt: Die Linienformänderungen können entweder durch einen zusätzlichen Beitrag zum Spektrum oder durch asymmetrische Linienprofile erzeugt werden.

Das Modell für die inverse paramagnetische Suszeptibilität beinhaltet das hexagonale Kristallfeld, magnetische Kopplung auf dem Strörstellengitter in Molekularfeldnäherung und Kondoabschirmung. Letztere ist phänomenologisch durch Abschirmfaktoren für das effektive Moment berücksichtigt. Eine zufriedenstellende Widergabe der experimentellen Daten konnte durch die Einführung von Dublett-spezifischen Abschirmfaktoren erreicht werden, was darauf hindeutet, dass das Ausmaß der Kondowechselwirkung vom m_j-Charakter der $4f$ Unterniveaus abhängt.

Contents

Preface

Strongly correlated electrons and heavy fermions

The physical description of systems with many degrees of freedom is one of the oldest challenges in science, a prominent example being the classical three-body problem. Even more complexity is encountered in many-body systems, like the electronic states in a solid. Although impossible to solve analytically, this problem can be treated within appropriate assumptions: The electronic states are either assumed to be well-localized and derived from atomic, hydrogen-like states, or the nearly-free electron approach is used. Both models rely on single-electron descriptions, with the assumption of independent quasiparticles.

The limit of this approximation is reached in materials with large Coulomb[1] interaction. Despite the considerable computational power that is available today, such strongly correlated electron systems represent a major challenge in modern science. Meeting this challenge is highly rewarding: Apart from fundamental interest, strong correlation can lead to physical properties of high technological relevance like, e.g., superconductivity at high temperature.

In addition to the charge-related Coulomb potential, the electron spin is also responsible for fascinating phenomena in strongly correlated electron systems. For example, the magnetic moments of impurity atoms that are embedded in a metallic host can locally polarize the spin of the conduction electrons. This results in surprising low-temperature characteristics, which is known as the Kondo effect.

Even more intriguing behavior can occur if the impurities are placed on a regular crystalline lattice. At low temperatures, the band structure of such materials can be renormalized due to the formation of coherent quasiparticles, which emerge from the magnetic impurities and their locally polarized conduction electron clouds and form a flat band. These quasiparticles can be described within Fermi[2] liquid theory for particles with a very high effective mass. Hence, such compounds are termed "heavy fermion" materials.

Typically, the ground state of strongly correlated electron systems is influenced by several competing energy scales. In the case of Ce-based heavy fermion compounds, these are the scales of single-impurity Kondo interaction, coherent band formation and Ruderman-Kittel-Kasuya-Yosida (RKKY) interaction, which establishes magnetic order of the impurity moments. Furthermore, the sixfold degenerate Hund's[3] rule $j = 5/2$ ground state is in general subject to crystal field (CF) splitting due to a non-spherical local environment of the Ce ions, whereas spin-orbit coupling (SOC) is the dominant energy scale. The consequence is a variety of phase diagrams in the class of heavy fermion materials, which can even include unconventional superconductivity.

The scope of the present thesis

The development of theoretical concepts always needs input from dedicated experiments. Kondo interaction and heavy fermion formation in a material strongly affect the low-temperature thermodynamical properties, like electric resistivity, specific heat or paramagnetic susceptibility. Experiments probing these properties have provided valuable input to the understanding of these phenomena. However, thermodynamical measurements never give direct access to the

---

[1] Charles Augustin de Coulomb, French physicist, 1736-1806. Life dates that are given throughout the present thesis were taken from the catalog of the German national library [5], if not otherwise stated.

[2] Enrico Fermi, Italian physicist, 1901-1954

[3] Friedrich Hund, German physicist, 1896-1997

driving mechanism: the local interaction of the impurity moment and the conduction electrons. The experimental method of X-ray Magnetic Circular Dichroism (XMCD) provides a probe for local magnetic moments. XMCD exploits differences in the absorption of circularly polarized X-rays at element- and orbital specific absorption edges as a function of the relative orientation of light helicity and sample magnetization. A quantitative evaluation of the detected signal is made possible by dedicated sum rules that allow separation of the contributions from spin and orbital magnetic moment. Hence, XMCD allows separation of the different contributions to the total magnetization of a sample. In many cases, this leads to an immense simplification for the interpretation of such data. Furthermore, it gives access to the interplay of the different contributions.

The impurity magnetic moment in Ce compounds is provided by the Ce $4f$ level. Spectroscopic access to this level is given by x-ray absorption spectroscopy (XAS) at the Ce $M_{4,5}$ edges, which represent the $3d^{10}4f^n \to 3d^9 4f^{n+1}$ transition. Hence, Ce $M_{4,5}$ XMCD is a promising approaches for studying the local magnetism in Ce-based Kondo and heavy fermion compounds. While separate aspects of Ce $M_{4,5}$ XAS and XMCD on Ce compounds have been discussed in the literature, only few XMCD studies that analyze $4f$ magnetism in Kondo and heavy fermion systems can be found. In particular, no study that adequately considers all of the present energy scales by exploiting the immense potential of these techniques is known to the author. This is aimed at in the present thesis.

Absorption spectra of solid samples in the soft X-ray regime are most conveniently recorded in the Total Electron Yield (TEY) mode. This involves an information depth of the order of nanometers and thus makes the method surface-sensitive. The proposed experiments therefore require a sample system that shows heavy fermion behavior at the surface.

The choice was $CePt_5$/Pt(111) surface intermetallics. This material is produced by molecular beam epitaxy of pure Ce onto a Pt(111) single crystal and subsequent alloying using well-established methods of surface preparation. Well-ordered samples can be prepared with high reproducibility, without the need for tedious crystal growth and avoiding the arbitrariness that is often encountered on cleaved surfaces regarding a well-defined termination. Furthermore, the Ce deposit represents a parameter that can be varied during preparation, and which influences the resultant electronic properties of a sample.

The reliable interpretation of the XMCD data requires knowledge of the CF scheme, which in turn depends on the crystal structure. Hence, attempts were made in the present thesis to provide such information. Low-energy electron diffraction (LEED) was primarily used to investigate the crystal structure. Both conventional LEED and LEED-IV were applied.

Even with this characterization done, the parametrization of the CF did not allow unambiguous conclusions from the XMCD data alone. As an alternative approach to CF effects, linear dichroism in Ce $M_{4,5}$ XAS was analyzed in detail. The shape of the XA spectra, which are recorded to produce the XMCD signal, contains valuable information on the CF scheme as well as on the single-impurity Kondo interaction. With full multiplet calculations, a powerful theoretical tool exists to calculate such spectra. However, studies that address the spectra of materials with considerable $4f$-level hybridization are scarce in the literature. The attempt to extract quantitative CF and Kondo related information from such spectra required a combined study of both experimental and theoretical spectra. This study is also reported in the present thesis, along with the results of the spectral shape analysis.

Some of the present results have been published in Physical Review B [1, 2].

Outline of the text

The present work is divided into two parts. Part I covers the theoretical, experimental and methodology-related prerequisites for the experiments, as well as reviews on the state of research. Special attention is paid to methods of recording and evaluating the experimental data, since this aspect strongly affects the data quality and thus the quality of the conclusions. Part II contains the presentation, analysis and interpretation of the experimental results. In the following, an outline of the individual chapters is given.

In chapter 1, basic theoretical concepts of single-impurity Kondo systems, Kondo lattices and heavy fermion materials are presented. The case of Ce compounds is treated in more detail in chapter 2. Section 2.1 deepens the theoretical description, whereas section 2.2 is focused on compounds of Ce and Pt, including a literature review of the $CePt_5/Pt(111)$ sample system.
The experimental methods for the structural characterization of this system are presented in chapter 3, which treats general experimental requirements and auxiliary methods, and chapter 4, which is devoted to LEED.
Chapter 5 introduces the experimental methods of X-ray absorption spectroscopy (XAS) and XMCD. In particular, the experimental setups are described (section 5.4), but also model calculations regarding the TEY signal of a thin film can be found therein (section 5.5).
Chapter 6 is devoted to the application of XAS and XMCD to the Ce $M_{4,5}$ edges. In addition to a detailed review of the available literature, especially regarding Kondo and heavy fermion physics (section 6.1), it includes the data analysis regarding the Ce valence (section 6.2), a treatment of full multiplet calculations (section 6.3) and considerations for application of the XMCD sum rules (section 6.4)
The results of the structural analysis are described in chapter 7 of part II, which also contains the description of the sample preparation procedure. These results provide the background for the determination of the CF level scheme by XAS, which is presented in chapter 9 together with studies of the Ce valence. However, the analysis of the XA spectra also requires a detailed knowledge of their line shape. This issue is addressed by both experiments and calculations in chapter 8.
Finally, the XMCD results are presented in chapter 10 and discussed in the framework of the results of the previous chapters.

Notes on nomenclature

Based on the results presented in chapter 7, the $CePt_5$/Pt(111) samples are regarded as thin films with well-defined thickness on top of a substrate. The film possesses a certain stoichiometry and a crystal structure distinct from the substrate. It thus represents an intermetallic compound [6, 7].
In the literature, $CePt_5$/Pt(111) is often termed a "surface alloy". An alloy is a mixture of two or more substances of which at least one is a metal. In some definitions, an intermetallic compound is a special case of an alloy with stricter requirements, making "surface alloy" an understatement for the $CePt_5$/Pt(111) system. Moreover, alloys are often characterized by one substance representing the host material into which the others are alloyed or dissolved. The crystal structure of the alloy is then the one of the host, with foreign atoms occupying substitutional or interstitial positions. While ordered alloys exist, this description does not meet the properties of the $CePt_5$/Pt(111) system. To avoid this conflict, the material is addressed as "intermetallic compound" rather than "alloy" throughout the present thesis. Nevertheless, the process in which the intermetallic compound is formed represents a mixing of two metals. Hence, it is correctly denoted "alloying".

Concerning the ordering of the elemental symbols in structural formulae of compounds, the recommendation of the International Union of Pure and Applied Chemistry (IUPAC) is to either use alphanumeric ordering or to order the constituents by increasing electronegativity [8]. The second method, which is more commonly applied for binary species, is used here.

The major tool for structural characterization of $CePt_5$/Pt(111) in the present thesis is low-energy electron diffraction (LEED), which provides direct access to the surface unit cell lattice parameters. The variety of observed LEED patterns required detailed studies to obtain a complete phase diagram, which is part of the discussion in chapter 7.
The LEED patterns of the surface compounds are described as superstructures with respect to the pristine substrate lattice. As introduced in section 3.1, the notation after Wood is used to describe these superstructures [9]. If not otherwise stated, relative lattice constants $\mathcal{S}$ and rotational alignment φ are given with respect to the substrate surface lattice. In one case (phase IV in section 7.2), an additional signature of a moiré superstructure with interrelation to both substrate and film lattice was found. The different relations are addressed separately.
The indexing of superstructure spots in LEED is done with respect to the reciprocal lattice of the surface intermetallics (compare fig. 4.2).

For the description of the unit cell of the intermetallic films, lateral and vertical lattice constants are distinguished. Lateral thereby refers to the surface lattice, i.e., the length of the unit cell vectors parallel to the surface is meant. The vertical lattice constant is the length of the unit cell vector perpendicular to the surface (compare section 3.1).

A relative alignment parallel and perpendicular to the hexagonal c-axis, which is the surface normal in the present samples, is distinguished for both the light polarization direction in the discussion of linear dichroism in XAS (see section 5.2), as well as the external magnetic field direction in the analysis of anisotropic paramagnetic susceptibility (see section 2.1.3). In order to avoid confusion, the reader should be aware of the fact that the direction of linear light polarization is perpendicular to the direction of light propagation, whereas the magnetic field is always parallel to the incoming X-rays in the the present experimental setup (see fig. 5.5).

Part I

Prerequisites

Chapter 1

The Kondo effect and heavy fermions

Contents

The electrons in a periodic lattice of magnetic impurities embedded in a metallic host can behave as a Fermi liquid with strongly enhanced effective mass. This "heavy fermion" formation is connected to unconventional low-temperature properties, which are explained by strong correlation of localized and itinerant electrons.

The ongoing process of understanding heavy fermion physics has seen an exciting history, starting from the explanation of the anomalous low-temperature behavior of dilute magnetic alloys by Kondo in 1964 [10]. These anomalies, which are nowadays referred to as the "Kondo effect", had been discovered as early as in 1934 by de Haas *et al.* [11], who investigated the temperature-dependence of the electrical resistance of Au, Cu and Pb down to $T \approx 1$ K . Their samples showed an increase of the resistivity towards low temperature, which contradicts Matthiessen's[1] rule. It was soon discovered that magnetic impurities were responsible for the unexpected behavior. In addition to the resistivity, other thermodynamical quantities like the specific heat and the magnetic susceptibility also showed to be affected by the impurity concentration.

At first glance, an increasing electrical resistivity at a temperature far below ambient working conditions, which is furthermore caused by sample contaminations, appears rather unattractive. Indeed, the prospects for technical applications of the Kondo effect are limited. Nevertheless, high fundamental interest arose in the theoretical concepts that were developed to obtain an understanding of the underlying mechanisms.

Certainly, this is owed to the complexity of the phenomenon, which is reflected by the long time that elapsed between the experimental discovery and the theoretical description of the effect. The most important source of interest, however, is the close relation between the theoretical description of Kondo systems and the so-called high-$T_\mathcal{C}$ superconductors, where $T_\mathcal{C}$ denotes the critical temperature below which superconductivity occurs. Hence, fundamental insights regarding the former might well lead to technically relevant developments in the search for room-temperature superconductors, the technical relevance of which is indisputable.

The scope of the present chapter is to briefly introduce selected concepts of Kondo and heavy fermion physics. On the next pages, a wide range is covered including single impurities (section 1.1) and periodic arrays of impurities, so-called Kondo lattices (section 1.2), which finally leads to the concept of heavy fermions (section 1.3). The presentation is far from being a full review of the subject. It is restricted to the requirements for the interpretation of the experimental data in part II. Comprehensive accounts of the theoretical and experimental achievements in the field of Kondo and heavy fermion physics can be found, e.g., in the books by Hewson [12], Fulde [13] and Fazekas [14] and in several review articles [15–18].

---

[1] Augustus Matthiessen, British chemist, 1831-1870

1.1 The single-impurity Kondo effect

Different models have been developed for the theoretical description of magnetic impurities in a metallic host [12]. One of the most important ones is the single-impurity Anderson model (SIAM), which was introduced by Anderson in 1961 [19].

Anderson considered a single impurity level and a conduction band. The impurity level is twofold degenerate with spin up and spin down. Interaction with the conduction band is accounted for by a hopping matrix element V^{ic}. This allows double occupation of the impurity, which is why a Coulomb potential U_{i} is also included.

With $\hat{n} = \hat{c}^{\dagger}\hat{c}$ denoting the particle number operator in second quantization, the complete Hamiltonian[2] of the SIAM reads

$$H_{\mathrm{SIAM}} = \underbrace{\sum_{\vec{k},\sigma} E_{\vec{k}} \hat{n}_{\vec{k}\sigma}}_{\text{conduction band}} + \underbrace{E_{\mathrm{i}} \left(\hat{n}_{\mathrm{i}+} + \hat{n}_{\mathrm{i}-}\right) + U_{\mathrm{i}} \hat{n}_{\mathrm{i}\uparrow} \hat{n}_{\mathrm{i}\downarrow}}_{\text{impurity level with Coulomb interaction}} + \underbrace{\sum_{\vec{k},\sigma} V^{\mathrm{ic}}_{\vec{k}} \hat{c}^{\dagger}_{\vec{k}\sigma} \hat{c}_{\mathrm{i}\sigma} + V^{\mathrm{ic}*}_{\vec{k}} \hat{c}^{\dagger}_{\mathrm{i}\sigma} \hat{c}_{\vec{k}\sigma}}_{\text{interaction of impurity and conduction band}}. \tag{1.1}$$

In his ground-breaking work, Kondo used the *s*-*d* model [20], which is obtained by integrating out the charge fluctuations in the SIAM [12]. Hence, there is no charge but only a spin degree of freedom. The spins of impurity and conduction electrons are coupled via an exchange parameter J in analogy to Heisenberg's[3] model of ferromagnetism. For assumption of particle-hole symmetry, it is related to the parameters of the SIAM via $J = 8(V^{\mathrm{ic}})^2/U_{\mathrm{i}}$ [15].

In order to calculate the electrical resistivity, Kondo treated the *s*-*d* model perturbatively up to third order in J. This results in a logarithmic term that is consistent with the experimentally observed resistance minimum. For $J < 0$, which corresponds to antiferromagnetic coupling between the impurity and conduction electron spins, the resistivity increases to lower temperature due to spin-flip-scattering of conduction electrons at the impurity. This process is denoted as Kondo interaction.

However, some aspects of the problem remained unresolved. The logarithmic term diverges for $T \to 0$. An exact, non-perturbative solution of the low-T behavior was presented in 1975 by Wilson in his "numerical renormalization group" approach [21]. Wilson's results were confirmed by another exact solution of the *s*-*d* model with the Bethe[4] Ansatz, which was achieved in 1980 independently by Andrei and Wiegmann [22, 23]. This approach received special attention, since it allowed generalization to more realistic models.

Such models were especially needed to describe rare-earth based systems, which received increasing attention at this time. In such materials, the impurity level possesses a high degeneracy compared to the simple SIAM and *s*-*d* model, which had been generalized to the case of Ce and Yb compounds by Coqblin and Schrieffer in 1969 [24].

The high degeneracy can be exploited in the so-called $1/N$ expansion. An important contribution using this approach was given in 1983 by Gunnarsson and Schönhammer [25, 26], who solved an extended SIAM in additional presence of a core-hole for $T = 0$.

As is treated in more detail in section 2.1.5, their results clarified the question of the Ce valence. This was done by connection of the $4f$ occupancy n_f to the relative weights of different contributions that can be observed in various core-level spectroscopies. Such experiments had become possible by previous developments in the field of photoelectron spectroscopy (PES) and the advent of synchrotron radiation facilities (see section 5.4.1).

An extension of the $1/N$ expansion to finite temperatures was achieved in 1987 by Bickers *et al.* using the non-crossing approximation (NCA) [27]. This allowed calculation of the T-dependence of a variety of different properties with a unified temperature scale. As examples, reproduced results for the $4f$ occupancy and the paramagnetic susceptibility are shown in fig. 1.1.

The concept of a characteristic temperature scale is intrinsic to the Kondo problem. In early

---

[2] William Rowan Hamilton, Irish astronomer, mathematician and physicist, 1805-1895

[3] Werner Karl Heisenberg, German physicist, 1901 - 1976

[4] Hans Albrecht Bethe, German-American physicist, 1906-2005

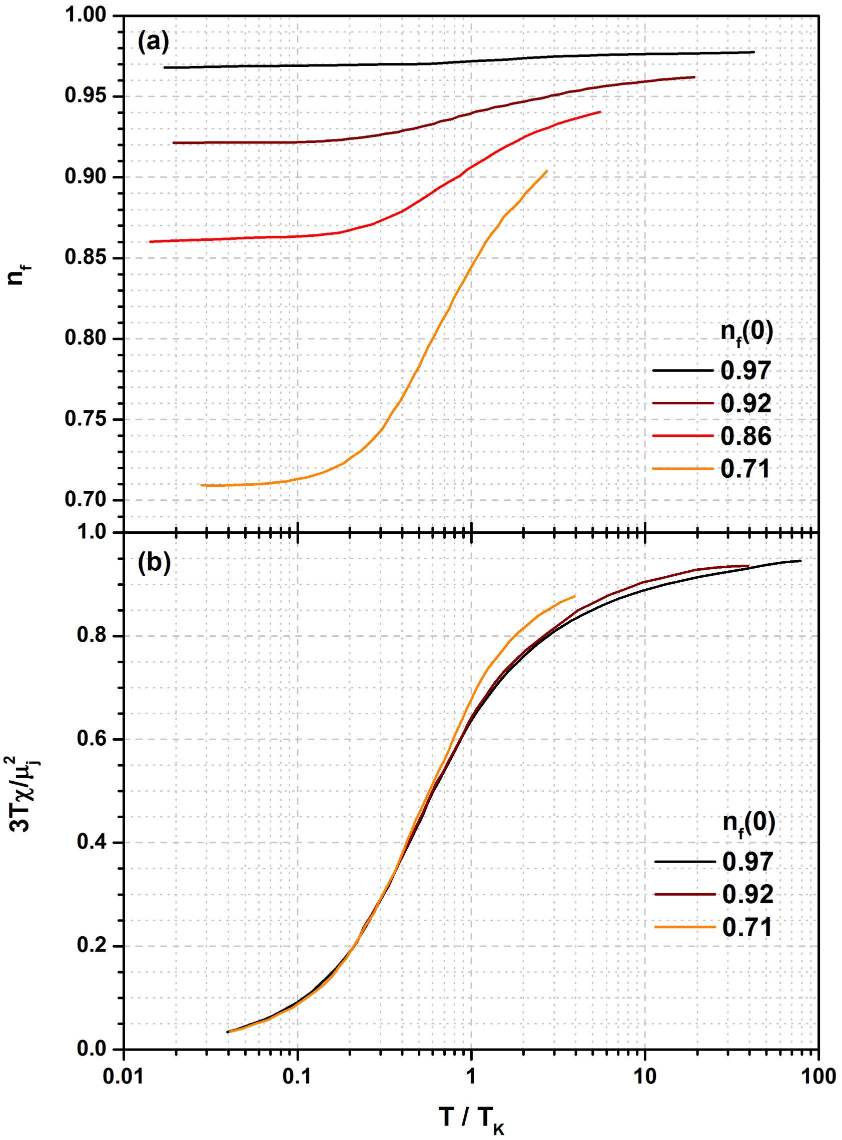

Figure 1.1: Reproduced results of Bickers calculated in NCA for dilute Ce impurities *et al.* [27] (a) T-dependence of the $4f$ occupancy n_f for different zero-temperature values. (b) T-dependence of the effective paramagnetic moment scaled by the value of the free Ce ion.

works, such parameters were used to define boundaries at which certain models lost their validity. In contrast, the temperature scale as introduced by Bickers *et al.* defines an energy scale on which the presence of the magnetic impurity become apparent in different physical properties. It characterizes the cross-over between different regimes rather than a sharp phase transition. Throughout the present thesis, the Kondo temperature T_{K} is used in this sense.

The Kondo temperature scale can be used to characterize the “strength” of the Kondo effect in a material. It mainly reflects the magnitude of V^{ic}, but also depends on the energetic separation of configurations with different impurity occupancies and the conduction bandwidth [27].

The choice of data for fig. 1.1 was made with respect to quantities that were investigated in the present work. Results for $n_f(T)$ obtained by Ce $\mathrm{M}_{4,5}$ XAS are shown in section 9.1.2, where the aim is to estimate T_K from such data.

Measurements of the effective paramagnetic $4f$ moment by means of XMCD are discussed in chapter 10. The experimental results show a significant reduction with respect to the value of the free Ce^{3+} ion, which is also apparent in the calculated data of fig. 1.1 (b). This reduction of the magnetic moment is often referred to as “Kondo screening”. Due to the antiferromagnetic coupling of impurity and conduction electron spins, a spin-polarized electron cloud forms in the vicinity of the impurity. The magnetic moment of this “Kondo cloud” screens the impurity moment, which thus appears reduced. Depending on the temperature, the screening is more or less complete: The effective moment is expected to vanish at $T \to 0$, where only the ground state, a singlet without net magnetic moment [28], is populated.

1.2 Kondo lattices

The single-impurity picture breaks down in concentrated alloys, where the average distance between magnetic impurities is small enough to allow inter-impurity interaction. The theoretically best controlled archetype of such a system is a crystalline lattice with impurity-conduction interaction in each unit cell. Such systems are referred to as "Kondo lattices", a term introduced by Doniach in 1977 [29].

In his pioneering work, Doniach used a periodic version of the *s*-*d* model, the Kondo lattice model, to investigated the competition between different ground states in Kondo lattices. One possibility is a Kondo singlet for each impurity, which arises due to the hybridization matrix element V^{ic} or the exchange parameter J in analogy to the single-impurity problem. Another option is a ground state with magnetically ordered impurity moments.

For an impurity to carry a localized magnetic moment, a partially filled electron shell is required, like the d shells of transition metals or the f shells of Lanthanides and Actinides. Particularly for the latter, the spatial localization leads to no or weak exchange interaction with the conduction bands, which is represented by J. An overlap of the electron shells of neighboring impurities can usually be neglected.

In the absence of direct exchange, the dominant mechanism for inter-impurity interaction is the weaker RKKY interaction [30]. The presence of a localized magnetic moment leads to a local polarization of the spins of the conduction electrons, which oscillates depending on the distance to the impurity. This spin polarization can lead to an indirect coupling of the magnetic moments of different impurities. The inter-impurity coupling is also oscillatory,

$$J_{\mathrm{RKKY}} \propto \frac{\sin x - x\cos x}{x^4}, \tag{1.2}$$

with $x = 2k_{\mathrm{F}}R$ and k_{F} and R being the Fermi wave vector and the inter-impurity distance, respectively. Hence, ferromagnetic or antiferromagnetic alignment is possible depending on R. Furthermore, $J_{\mathrm{RKKY}} \propto 1/R^3$ for large R, which makes RKKY interaction long-ranged compared to other exchange mechanisms. The coupling is not restricted to nearest neighbors only and can also lead to exotic states of magnetic order like frustrated spin glasses.

Since RKKY interaction is mediated by the conduction electrons, it is also governed by the impurity-conduction exchange parameter via $J_{\mathrm{RKKY}} \propto J^2$. Using his well-known diagram, Doniach pointed out that the ground state of a Kondo lattice, being either a Kondo singlet or a magnetically ordered state, depends on the magnitude of J, with a second-order phase transition at a critical value [29]. Since this transition occurs at zero temperature, it produces a quantum critical point in a J-T diagram.

The fact that mutually exclusive ground states can exist in Kondo lattices in dependence of J or V^{ic} illustrates how the delicate balance of localization and delocalization of the impurity levels governs the behavior of such materials. Furthermore, it stresses the importance of experiments that offer controllability of this parameter.

1.3 Heavy fermions

The behavior of many Kondo lattice materials is well explained by the theoretical methods that were developed to describe the effect of non-interacting magnetic impurities. However, the thermodynamical properties of some materials, typically based on Ce, Yb and U, exhibit low-temperature characteristics that are not reproduced by single-impurity theories. Measurements of the Fermi surfaces of such materials indicate Fermi liquid behavior, whereas their specific heat coefficients correspond to a very large effective electron mass. Therefore, these materials

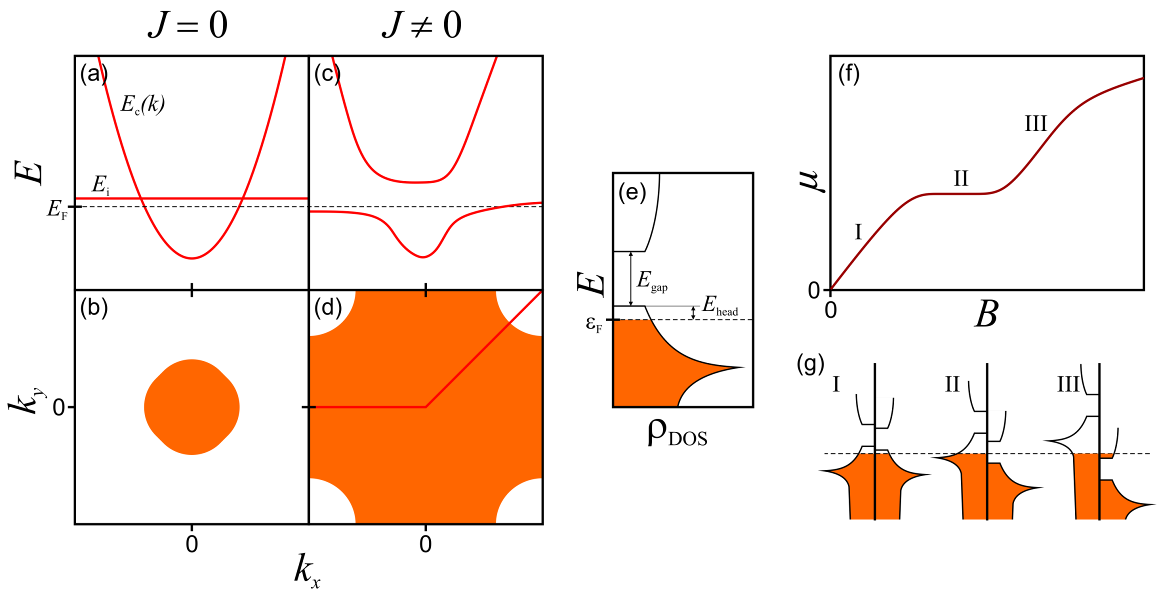

Figure 1.2: Schematic drawings of the effect of band renormalization in heavy fermion compounds. The case of a two-dimensional square impurity lattice at zero temperature is drawn after [33]. (a),(b) band structure and Fermi surface, respectively, without hybridization. (c),(d) The same for the case with hybridization. The red lines in panel (d) indicate the k-direction of the abscissa in panel (c), which is projected to the k_x direction. (e) Close-up of the density of states in the vicinity of the Fermi level ϵ_F in the coherent state. (f) Signature of the resulting metamagnetic transition in $M(B)$. (g) Spin-resolved DOS for the three different magnetic field regimes that are marked in panel (f).

are referred to as "heavy fermion" systems.

In addition to the two cases of antiferromagnetic order and Kondo singlets that were already studied by Doniach for the Kondo lattice [29] (see section 1.2), experiments on heavy fermion compounds revealed further exotic ground states. This includes superconductivity as well as ferromagnetic order. The study of quantum phase transitions between such different ground states in dependence of experimentally controllable parameters has opened the exciting field of quantum criticality research, which is of ongoing interest [16, 18].

The picture of a Fermi liquid with large effective mass can also be derived theoretically from the Kondo lattice model, at least for the paramagnetic, metallic ground state [31]. The fermions that constitute the Fermi liquid are quasiparticles, which can be imagined to derive from the impurity and conduction electrons that constitute the Kondo cloud. Electronic bands emerge if these quasiparticles coherently form Bloch[5] waves in the periodic impurity lattice. Consequently, with the coherence temperature T^* of the heavy Fermi liquid an additional temperature scale can arise in heavy fermion compounds [32]. It is expected to be considerably smaller than the single-impurity Kondo temperature in a certain material.

The f-level occupancy in Ce compounds is close to, but smaller than unity (compare section 2.1.5). This means that the $4f$-level and thus the $4f$ band are located slightly above the Fermi level ϵ_F. Mean field calculation allow derivation of the quasiparticle band structure by renormalization of the impurity and conduction bands. They predict the opening of a hybridization gap and a transition from a small to a large Fermi surface that includes the additional f electrons. This is schematically shown in fig. 1.2 for the case of a parabolic conduction band and a two-dimensional square impurity lattice at zero temperature, following [33]. Panel (a),(b) and (c),(d) represent the cases without and with hybridization, respectively. The directional dependence of the band structure is included to panel (c) by showing two different k directions, as is indicated by the red lines in panel (d). Panel (e) represents the resulting density of states (DOS). At appropriate choice of parameters, the indirect gap of magnitude E_gap in the DOS is located slightly above the Fermi level, which leaves a small headroom E_head in the lower hybridized band.

---

[5] Felix Bloch, Swiss-American physicist, 1905-1983

The consequences of this renormalization for the paramagnetic response of heavy fermion systems has been studied theoretically by Beach and Assaad in 2008 [33]. The expectation for a band-induced Pauli[6] paramagnet is a linear relation of magnetic moment μ and external field B accompanied by a temperature-independent susceptibility χ. In contrast, the results of Beach and Assaad indicate a metamagnetic Lifshitz[7]-transition. It can be explained in the picture of rigid, hybridized bands, whose spin-resolved DOS is relatively shifted due to Zeeman[8] energy E_Z in the presence of an external field B (compare eq. 2.15).

As is illustrated in fig. 1.2 (f) and (g), this strongly influences the field-dependence of the magnetic moment μ. For small magnetic field, $\mu(B)$ is linear as for a normal paramagnet (I). If E_Z exceeds the head room of the majority band, the Fermi level is within the gap. Consequently, no more free majority states become available by increasing the magnetic field, which leads to a plateau at intermediate moment in $\mu(B)$ (II). Only if E_Z suffices to overcome the gap in addition to the headroom, which eventually happens upon further increasing B, $\mu(B)$ increases again and the plateau ends (III).

Hence, the upper and lower field limits of the plateau in $\mu(B)$ give access to the relevant energy scales of the renormalized band structure. Furthermore, the plateau moment is directly related to the fraction of the Brillouin[9] zone volume that is outside the Fermi surface. Hence, $\mu(B)$ measurements can address the size of the Fermi surface and track respective changes under variation of control parameters.

The magnitudes of band gap and head room are expected to be of the order of millielectronvolt. Zeeman splitting that large can only be achieved with high external fields of some to some ten tesla, which represents a serious experimental challenge. Results of such experiments on $\mathrm{CePt_5}$/ Pt(111) films are presented in section 10.5.

---

[6] Wolfgang Ernst Pauli, Austrian-Swiss-American physicist, 1900-1958

[7] Evgeny Mikhailovich Lifshitz, Soviet physicist, 1915-1985

[8] Pieter Zeeman, Dutch physicist, 1865-1943

[9] Léon Nicolas Brillouin, French-American physicist, 1889-1969

Chapter 2

Cerium compounds

Contents

In 1803, Berzelius[1] and Hisinger[2] as well as Klaproth[3] independently discovered a new element. It was named Cerium after the celestial object Ceres [34].

Two years earlier, the twofold discovery of Ceres had caused considerable sensation among scientists. By that time, it was regarded as a new planet[4], being located in between the orbits of Mars and Jupiter. It was first sighted by Piazzi[5], who chose the name with reference to the Roman goddess of agriculture [36].

Shortly thereafter, Ceres was lost from sight. The prediction of its position from the scarce data that was available was a task beyond the state of the art of that time. The spectacular rediscovery of Ceres is owed to Gauß[6], who introduced two important techniques in this course: The iterative computation of Keplerian[7] orbit elements and the method of least squares. The latter was also applied for all curve fitting procedures in the present thesis.

After the discovery of Cerium, several attempts were made by different chemists to isolate the rare earth metal. Pure Cerium was first obtained by Hillebrand and Norton in 1875 [34]. Cerium has the symbol Ce and the atomic number $Z = 58$. Its atomic mass is $m_{\mathrm{Ce}} = 140.1$ u [37]. In the periodic system of elements (PSE), Ce is the first element after La in the lanthanide group, which means that it should have a $4f$ shell that is occupied by a single electron.

The $4f$ electrons are responsible the interesting physical properties of the Lanthanides concerning magnetism and correlation effects (see chapter 1). Ce does not only provide an ideal model system with its nominally single $4f$ electron, but also shows a prominent complexity in its behavior. The structural and magnetic phase diagrams of metallic Ce are among the most intriguing of all elements in the PSE [38]

---

[1] Jöns Jakob Berzelius, Swedish Chemist, 1779-1848

[2] Wilhelm von Hisinger, Swedish Chemist, Physicist and Geologist, 1766-1852

[3] Martin Heinrich Klaproth, German Pharmacist and Chemist, 1743-1817

[4] After being categorized as an asteroid later on, Ceres is a dwarf planet since 2006 [35]

[5] Giuseppe Piazzi, Italian astronomer, 1746-1826

[6] Carl Friedrich Gauß, German mathematician, astronomer, physicist and geodesist, 1777-1855

[7] Johannes Kepler, German astronomer, astrologist and mathematician, 1571-1630

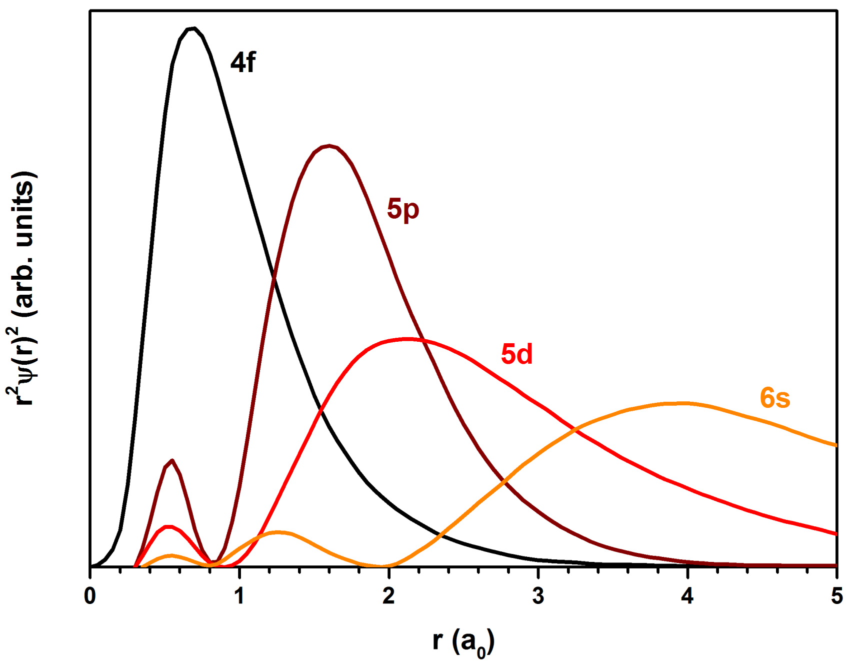

Figure 2.1: Radial probability density for some of the atomic wavefunctions of Ce, calculated in local density approximation (LDA) for the configuration [Xe]$4f^1 5d^1 6s^2$. The data are reproduced from [39]. For $r < 0.3\,\mathrm{a}_0$, where a_0 denotes the Bohr radius, the nodes of the functions are not shown.

In the following section, a more specific account is given for the properties of the Ce $4f$ electron. Section 2.2 is devoted to compounds of Ce and Pt. This material class includes the CePt_5/Pt(111) sample system that was primary investigated in the present thesis.

2.1 Electronic and magnetic properties of Ce and its compounds

Due to their high angular momentum, the probability density of $4f$ electrons has its maximum closer to the nucleus than neighboring electron shells. Thus, there is a discrepancy between the energetic and spatial ordering of the electron shells in Cerium and the other rare earths. While the $4f$ binding energy is rather low, the shell is located rather deep in the atom.

This is illustrated in fig. 2.1, where the probability densities of the Ce $4f$ shell as well as for the $5d$ and $6s$ valence electrons and the $5p$ core electrons are shown as a function of the radial distance in units of Bohr[8] radii. All of the latter electron shells are significantly more extended than the $4f$ shell. Hence, while the valence electrons form the metallic bond in a solid state system, the completely filled $5p$ shell as well as the filled $5s$ shell, which is not shown in fig. 2.1, shield the $4f$ electron from the other constituents of the crystal. This results in small overlap integrals with neighboring electron states, which means that the $4f$ electron is highly localized at its atomic site [39].

Partial filling of a localized electron shell following Hund's rules leads to a localized magnetic moment due to unpaired electrons. If “localized” is understood as “completely independent of its environment”, the embedding of Ce atoms into a solid-state crystal produces a simple paramagnet. The Ce $4f$ electron is then expected to be in the spin-orbit coupled, sixfold degenerate $J = 5/2$ ground state.

The exact degree of independence determines to which extent this simple picture is applicable. This, in turn, depends on the details of the chemical environment. Along with the complex phase diagrams of pure Ce metal, different Ce compounds therefore show a variety of different behaviors.

There are mainly three mechanisms by which the environment influences the $4f$ electron in

---

[8] Niels Henrik David Bohr, Danish physicist, 1885-1962

a more or less drastic way: the electrostatic potential of the crystal, RKKY interaction and hybridization with conduction states.

The electrostatic interaction is contained in crystal field or ligand field theory. The terms are equivalently used with the ionic and covalent part, respectively, of the crystal field. The crystal field leads to a rearrangement of the atomic states and to a lifting of degeneracies, which is perturbative. To first order, only states within the $j = 5/2$ multiplet are coupled in Ce. The details of the coupling are governed by the local symmetry that is experienced by the Ce ions, whereas the lattice parameters influence the magnitude of the effect. The crystal field is treated in more detail in section 2.1.2.

RKKY interaction is a coupling mechanism for localized magnetic moments in metals. It is mediated by the spin of the conduction electrons and is the primary coupling mechanism for magnetic moments of rare earths, since direct exchange is suppressed due to the localization of the $4f$ electrons. RKKY interaction can establish a magnetically ordered state and can thus lift the degeneracy between spin up and spin down states. The concept is introduced in section 1.2, whereas its consequences for the paramagnetic susceptibility are described in section 2.1.4.

Hybridization between the $4f$ level and the conduction states means the presence of a hopping matrix element V^{ic}, which would be zero in the case of complete localization. The balance of localization and itinerancy in Ce is reflected by the Ce valence v. It was realized early that the low binding energy of the Ce $4f$ electron can lead to fluctuations of v [40]. Many Ce compounds show a dependence of v on external pressure [41, 42], and a broad range of valencies is observed for different Ce compounds [43]. This reflects that v is strongly influenced by the environment of the Ce ions.

Furthermore, V^{ic} is an essential ingredient of the SIAM. Hybridization is closely connected to all the peculiarities of Kondo and heavy fermion systems that are introduced in chapter 1. A more detailed account of hybridization and mixed valence in Ce compounds is given in section 2.1.5.

Each of the three mentioned mechanisms can lead to deviations from the picture of a simple paramagnet. In particular, hybridization can induce completely different ground states. Furthermore, the three interaction mechanisms can coexist. This increases the complexity of theoretical description of a Ce compound, for example if the hybridization strength is assumed to be different for the crystal field split energy levels. On the contrary, if the hybridization leads to a coherent heavy fermion state with formation of a $4f$ band, this excludes the application of RKKY theory. In this case, it is certainly interesting to study the transition regimes between different states, since this gives access to the complex interplay of the differnet energy scales. Such considerations are at the basis of the interpretation of the results presented in chapter 10.

2.1.1 Ionic description of the $4f^1$ configuration

The delicate balance of localization and itinerancy is characteristic for the $4f$ shell of Cerium atoms in various compounds. It gives rise to interesting effects, which require dedicated theoretical description. In contrast, the special case of complete localization of the $4f$ shell can be fully described by the well-established concepts of atomic physics (see, e.g., [44, 45]). When embedded into a solid, the three outer $5d$ and $6s$ valence electrons of Ce usually contribute to the metallic bond. Hence, they can be regarded as part of the "environment" and are consequently neglected in a description of the localized $4f$ shell. Thus, the $4f$ shell of a Ce^{3+} ion represents a single electron in a central field, one of the prime examples of quantum mechanics.

Since a small hybridization can be introduced as a perturbation to the localized $4f$ shell, it is a basic requirement for a description of Ce compounds to study the Ce^{3+} ion. The fundamental concepts are introduced in the following.

The $4f^1$ state is most conveniently described in terms of atomic, hydrogen-like wave functions that are separable into radial and angular parts,

$$\Psi(r, \theta, \phi) = R_{nl}(r) Y_{lm}(\theta, \phi). \tag{2.1}$$

The radial part $R_{nl}(r)$ depends on the main quantum number n and the details of the central field. A procedure to treat the radial part for full multiplet calculations of XA spectra is outlined in section 6.3. In the present section, the focus is on the angular momentum properties, which are included in the angular part of the wave functions. It is usually expressed in spherical harmonics $Y_{lm}(\theta, \phi)$, which are the Eigenfunctions of the angular momentum operator [45].
Since the orbital and spin angular momentum quantum number of $4f$ electrons $l = 3$ and $s = 1/2$, respectively, there are $(2l+1)(2s+1) = 14$ different states. In Ce, the dominant coupling mechanism for the angular momenta is spin-orbit coupling (SOC). Since the spin is a relativistic quantity, the description of SOC has to be derived from the Dirac[9] equation. The corresponding term in the Hamiltonian for a single electron with mass m_e and charge e and with the magnetic constant μ_0 reads [45]

$$\hat{H}_\mathrm{SOC} = \frac{Ze^2\mu_0}{8\pi m_\mathrm{e}^2 r^3}\,\hat{\vec{l}}\cdot\hat{\vec{s}}. \tag{2.2}$$

As a consequence of the introduction of SOC to the ionic model, the pure orbital and spin states $|l, m_l\rangle$ and $|s, m_s\rangle$, respectively, are no longer eigenfunctions of the Hamiltonian and the corresponding quantum numbers are no longer good ones. Instead, the eigenstates are characterized by the total angular momentum operator $\hat{\vec{j}} = \hat{\vec{l}} \pm \hat{\vec{s}}$. Since $\hat{\vec{j}}$ is also a quantum mechanical angular momentum operator, a set of eigenfunctions $|j, m_j\rangle$ can be found with the quantum numbers j and m_j. Those are defined by the expectation values

$$\langle\hat{\vec{j}}^2\rangle = \langle j, m_j|\,\hat{\vec{j}}^2\,|j, m_j\rangle = j(j+1)\hbar^2\,\langle j, m_j|j, m_j\rangle = j(j+1)\hbar^2 \quad \text{and}$$

$$\langle\hat{j}_z\rangle = \langle j, m_j|\,\hat{j}_z\,|j, m_j\rangle = m_j\hbar\,\langle j, m_j|j, m_j\rangle = m_j\hbar. \tag{2.3}$$

Here, $\hbar$ is Planck's[10] constant h divided by 2π. The quantum number j is representative of the magnitude of the total angular momentum, while m_j characterizes the z-component, which is arbitrarily chosen from the three coordinates in accordance with common practice. With this choice made, the other two components are indeterminate.
The quantum numbers can have the values $j = l \pm s$ and $m_j \in \{-j, -j+1, \ldots, j\}$. The separation into states with two different j values is accompanied by an energy splitting ΔE_SOC. Hence, the 14-fold degenerate $4f$ level is split into a sixfold degenerate $j = 5/2$ and an eightfold degenerate $j = 7/2$ state. According to Hund's rules, $j = 5/2$ is the ground state. The energy splitting between the two states has been measured to $\Delta E^{4f}_\mathrm{SOC} \approx 260$ meV by neutron scattering [46]. Atomic multiplet calculations that are presented in section 6.3 yield $\Delta E^{4f}_\mathrm{SOC} \approx 300$ meV.
The coupling of spin and orbital angular momenta to a total angular momentum can be visualized in a vector model. This is shown in fig. 2.2 for the $j = 7/2$ (a) and $j = 5/2$ (b) substates of an f electron. The total angular momentum is represented by a vector with length $|\vec{j}| = \sqrt{j(j+1)}\hbar$ and z-component $j_z = m_j\hbar$. Since only the z-component is well-defined and the vector is not aligned along the z-axis, $\vec{j}$ must be regarded as precessing around the z-axis. In the figure, a representative projection of this precession is shown.
For orbital and spin angular momentum, only the vector lengths are defined by $l = 3$ and $s = 1/2$. Hence, possible combinations of the two that produce the desired $\vec{j}$ can be found at the intersections of two circles with respective radii. The uncertainty in the individual components of the vectors is connected to a precession of $\vec{l}$ and $\vec{s}$ around the direction of $\vec{j}$, which is represented by two possible combinations in the projection plane of the figure.
The exemplary constructions that are shown in fig. 2.2 allow derivation of the general relation between $\langle l_z\rangle$, $\langle s_z\rangle$ and $\langle j_z\rangle$. It should be noted that the expectation values can be negative, thus $\langle j_z\rangle = \langle l_z\rangle + \langle s_z\rangle$ for both possible combinations of $\vec{l} \pm \vec{s}$.
For a determination of $\langle l_z\rangle$, $\vec{l}$ first has to be projected to the direction of $\vec{j}$ and then to the z-axis

---

[9] Paul Adrien Maurice Dirac, British physicist, 1902-1984

[10] Max Karl Ernst Ludwig Planck, German physicist, 1858-1947

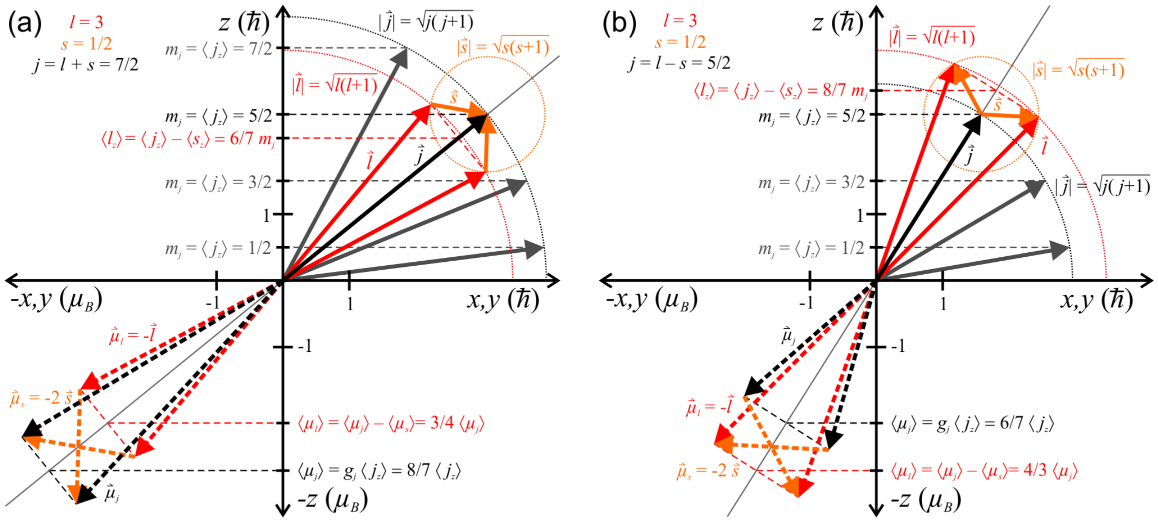

Figure 2.2: Vector model for the total angular momentum ($\vec{j}$, black) obtained by addition of orbital ($\vec{l}$, red) and spin ($\vec{s}$, orange) angular momenta of a single f electron (solid arrows, upper right quadrants) and construction of the resulting magnetic moments $\vec{\mu}$ (dashed arrows, lower left quadrants) for (a) $\vec{j} = \vec{l} + \vec{s}$, $j = l + s = 7/2$ and (b) $\vec{j} = \vec{l} - \vec{s}$, $j = l - s = 5/2$. Note the different units of the axes for $\vec{j}$ and $\vec{\mu}$. The possible total angular momentum vector alignments are drawn for $m_j > 0$. The construction is exemplarily shown for $m_j = 5/2$ in both cases.

in order to account for the two precessions. Hence,

$$\langle l_z \rangle = \left(\frac{\vec{l} \cdot \vec{j}}{|\vec{j}|} \right) \frac{\vec{j}}{|\vec{j}|}\ \vec{e}_z = \frac{\vec{l} \cdot \vec{j}}{|\vec{j}|^2}\ \langle j_z \rangle = \frac{\vec{l} \cdot (\vec{l} \pm \vec{s})}{|\vec{j}|^2}\ \langle j_z \rangle = \frac{|\vec{l}|^2 \pm \vec{l} \cdot \vec{s}}{|\vec{j}|^2}\ \langle j_z \rangle$$

$$= \frac{|\vec{l}|^2 - \frac{1}{2}(|\vec{l}|^2 + |\vec{s}|^2 - |\vec{j}|^2)}{|\vec{j}|^2}\ \langle j_z \rangle = \frac{l(l+1) - \frac{1}{2}(l(l+1) + s(s+1) - j(j+1))}{j(j+1)}\ \langle j_z \rangle$$

$$= \begin{cases} \frac{6}{7}\ \langle j_z \rangle = 6\ \langle s_z \rangle & \text{for } j = 7/2 \\ \frac{8}{7}\ \langle j_z \rangle = -8\ \langle s_z \rangle & \text{for } j = 5/2 \end{cases} \tag{2.4}$$

with application of the law of cosines to substitute $\pm\vec{l} \cdot \vec{s} = -1/2\ (|\vec{l}|^2 + |\vec{s}|^2 - |\vec{j}|^2)$.
A charged particle with a finite angular momentum exhibits a magnetic moment. Quantum mechanically, this magnetic moment is connected to the angular momentum operator via the Landé[11] factor g_j,

$$\vec{\mu}_j = -\frac{g_j \mu_\mathrm{B}}{\hbar} \vec{j} \quad \text{and} \quad \langle \mu_j \rangle = -\frac{g_j \mu_\mathrm{B}}{\hbar} \langle j_z \rangle = -g_j \mu_\mathrm{B} m_j, \tag{2.5}$$

where μ_B is the Bohr magneton. The last identity is of course only valid if the expectation value is evaluated in a basis of eigenfunctions to $\hat{j}_z$.
For electrons, $g_l = 1$ and $g_s \approx 2$. As a consequence, the vector construction for the magnetic moment of the total angular momentum yields a non-collinear alignment of $\vec{\mu}_j = \vec{\mu}_l \pm \vec{\mu}_s$ and $\vec{j} = \vec{l} \pm \vec{s}$, as is shown in the lower left quadrants in fig. 2.2. This result again has to be interpreted as a precession. The definition of the g-factor as given in eq. 2.5 then refers to the projection of these precessing vectors to the direction of $\vec{j}$.
The Landé factor of the total angular momentum can be determined similar to eq. 2.4:

---

[11] Alfred Landé, German-American physicist, 1888-1976

j	g_j	$\lvert\vec{\mu}_j\rvert$ (μ_B)	$\langle\mu_j\rangle$ (μ_B) $m_j = \pm 1/2$	$\pm 3/2$	$\pm 5/2$	$\pm 7/2$
7/2	8/7	4.536	∓ 0.571	∓ 1.714	∓ 2.857	∓ 4.000
5/2	6/7	2.535	∓ 0.429	∓ 1.286	∓ 2.143	

Table 2.1: Landé factors and expectation values of the magnetic moment for the possible states of a $4f$ electron.

$$\langle\mu_j\rangle = \left(\frac{\vec{\mu}_j\cdot\vec{j}}{|\vec{j}|}\right)\frac{\vec{j}}{|\vec{j}|}\,\vec{e}_z = -\frac{\mu_\mathrm{B}}{\hbar}\frac{(\vec{l}\pm 2\vec{s})(\vec{l}\pm\vec{s})}{|\vec{j}|^2}\,\hbar m_j = -\mu_\mathrm{B} m_j \frac{|\vec{l}|^2 + 2|\vec{s}|^2 \pm 3\vec{l}\cdot\vec{s}}{|\vec{j}|^2}$$

$$= -\mu_\mathrm{B} m_j\left(1 + \frac{j(j+1) - l(l+1) + s(s+1)}{2j(j+1)}\right). \tag{2.6}$$

This result yields the values that are given in tab. 2.1 together with the expectation values of the magnetic moment according to eq. 2.5.

The macroscopic magnetic behavior of a material is governed by the total magnetic moment. With XMCD (see section 5.3), an experimental tool is available to address spin and orbital contributions to the total moment independently. The connection of $\langle\mu_j\rangle$, $\langle\mu_l\rangle$ and $\langle\mu_s\rangle$ in the present ionic model can be derived by application of eqs. 2.5 and 2.4:

$$\frac{\langle\mu_l\rangle}{\langle\mu_s\rangle} = \frac{\langle l_z\rangle}{2\langle s_z\rangle} = \begin{cases} 3 & \text{for } j = 7/2 \\ -4 & \text{for } j = 5/2 \end{cases} \quad \text{and hence} \tag{2.7}$$

$$\langle\mu_j\rangle = \begin{cases} \frac{4}{3}\langle\mu_l\rangle & \text{for } j = 7/2 \\ \frac{3}{4}\langle\mu_l\rangle & \text{for } j = 5/2. \end{cases} \tag{2.8}$$

Finally, the understanding of the coupling of the angular momenta can be used to construct the eigenfunctions $|j, m_j\rangle$. Those are most conveniently expressed by the spin and orbital eigenfunctions $|l, m_l\rangle$ and $|s, m_s\rangle$, respectively.

For the spin-orbit coupled f electron, the state with highest m_j is $|j = 7/2, m_j = 7/2\rangle$. Application of eq. 2.4 yields that for this state, $\langle l_z\rangle = 3$ and $\langle s_z\rangle = 1/2$, which reflects that it can only be obtained if $|l = 3, m_l = 3\rangle$ and $|s = 1/2, m_s = 1/2\rangle$ are coupled. The states with next smaller m_j are $|j = 7/2, m_j = 5/2\rangle$ and $|j = 5/2, m_j = 5/2\rangle$. A total angular momentum with $m_j = 5/2$ can be constructed from the combinations $|l = 3, m_l = 3\rangle\,|s = 1/2, m_s = -1/2\rangle$ and $|l = 3, m_l = 2\rangle\,|s = 1/2, m_s = 1/2\rangle$. The ratio in which these two states have to be mixed in order to produce the correct spin-orbit coupled states can in principle also be obtained from eq. 2.4. For example, for $|j = 7/2, m_j = 5/2\rangle$, $\langle l_z\rangle = 30/14 = 6/7\cdot 2 + 1/7\cdot 3$.

More generally, these considerations lead to the Clebsh[12]-Gordan[13] coefficients. Those can most elegantly be derived by step-up and step-down operators in a given j manifold [44],

$$\hat{j}^{\pm}\,|j, m_j\rangle = (\hat{j}_x \pm i\hat{j}_y)\,|j, m_j\rangle = \hbar\sqrt{(j \mp m_j)(j \pm m_j + 1)}\,|j, m_j \pm 1\rangle \tag{2.9}$$

The coefficients are, however, only defined up to a complex phase factor. If the choice is made in favor of real coefficients, their signs are still arbitrary, although the relative signs of the coefficients in a given j subspace are defined by the $\hat{j}^{\pm}$ operators.

In the present thesis, the following $4f^1$ states are used in accordance with most literature:

---

[12] Rudolf Friedrich Alfred Clebsh, German mathematician, 1833-1872

[13] Paul Albert Gordan, German-Polish mathematician, 1837-1912

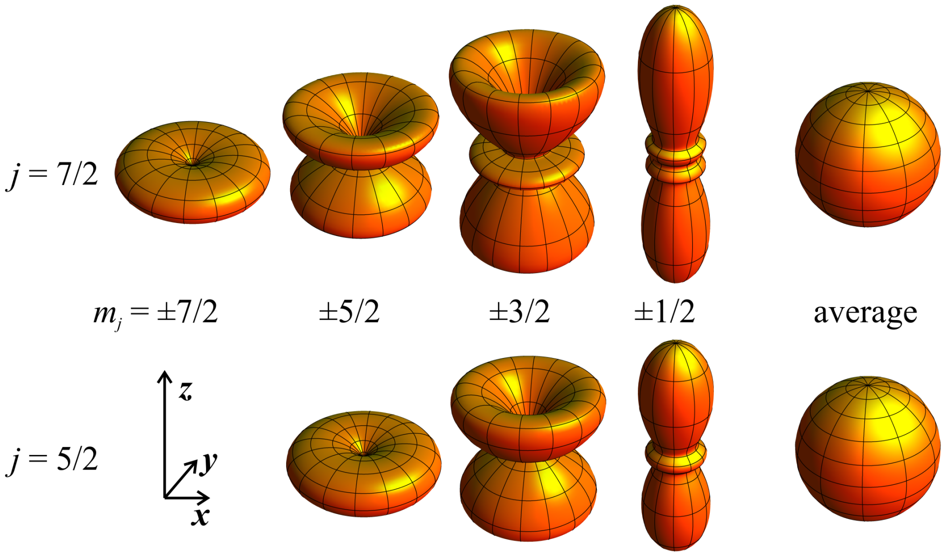

Figure 2.3: Spatial electron distribution of the different $|j, m_j\rangle$ states produced by spin-orbit coupling of a $4f$ electron, as given in eq. 2.10. Furthermore, the averages of all states are shown for both j subspaces, which are spherical symmetric.

$$\begin{aligned}
|7/2, \pm 7/2\rangle &= \quad |3, \pm 3\rangle\,|1/2, \pm 1/2\rangle \\
|7/2, \pm 5/2\rangle &= \sqrt{\frac{1}{7}}\,|3, \pm 3\rangle\,|1/2, \mp 1/2\rangle + \sqrt{\frac{6}{7}}\,|3, \pm 2\rangle\,|1/2, \pm 1/2\rangle \\
|7/2, \pm 3/2\rangle &= \sqrt{\frac{2}{7}}\,|3, \pm 2\rangle\,|1/2, \mp 1/2\rangle + \sqrt{\frac{5}{7}}\,|3, \pm 1\rangle\,|1/2, \pm 1/2\rangle \\
|7/2, \pm 1/2\rangle &= \sqrt{\frac{3}{7}}\,|3, \pm 1\rangle\,|1/2, \mp 1/2\rangle + \sqrt{\frac{4}{7}}\,|3, 0\rangle\,|1/2, \pm 1/2\rangle
\end{aligned}$$

$$\begin{aligned}
|5/2, \pm 5/2\rangle &= \sqrt{\frac{6}{7}}\,|3, \pm 3\rangle\,|1/2, \mp 1/2\rangle - \sqrt{\frac{1}{7}}\,|3, \pm 2\rangle\,|1/2, \pm 1/2\rangle \\
|5/2, \pm 3/2\rangle &= \sqrt{\frac{5}{7}}\,|3, \pm 2\rangle\,|1/2, \mp 1/2\rangle - \sqrt{\frac{2}{7}}\,|3, \pm 1\rangle\,|1/2, \pm 1/2\rangle \\
|5/2, \pm 1/2\rangle &= \sqrt{\frac{4}{7}}\,|3, \pm 1\rangle\,|1/2, \mp 1/2\rangle - \sqrt{\frac{3}{7}}\,|3, 0\rangle\,|1/2, \pm 1/2\rangle \qquad (2.10)
\end{aligned}$$

The spatial distribution of these orbitals can be visualized by their angular probability density, which is shown in fig. 2.3. Since the spin eigenfunctions have no spatial dependence, it is governed by the squared absolute values of spherical harmonics $Y_{lm_l}(\theta, \phi)$, which are weighted and added according to eqs. 2.10.
This visualization clearly shows that the individual m_j states are highly anisotropic. However, as long as only spin-orbit coupling is present, the states in the two j subspaces are degenerate and the wave function of a $4f$ electron will appear as the spherical symmetric average of all m_j states.

2.1.2 The crystal field

The considerations that are presented in section 2.1.1 are valid for a free Ce^{3+} ion. In this case, the Hund's rule ground state consists of degenerate $|j, m_j\rangle$ states for each j. Their equal

population is expressed by their average, which is spherical symmetric as shown in fig. 2.3.
The spherical symmetry of a Ce ion is usually lifted when it is embedded into a solid crystal. As a consequence, the $4f$ electron has to adapt to the symmetry of the environment, which leads to the formation of a new ground state. This is referred to as "Crystal field effect". As in most rare earth material, the crystal field (CF) potential in Ce can usually be treated as a perturbation on the spin-orbit coupled $4f$ states[14,15].
The sixfold degeneracy of the $j = 5/2$ states is lifted by the crystal field. The resulting states are always Kramers[16] doublets, since the electron spin operator is independent of spatial coordinates. As can be seen in fig. 2.3, the different $|j, m_j\rangle$ eigenstates exhibit very different spatial distributions. The new ground state is the mixture of these states that is best adapted to the symmetry of the CF potential, whereas the higher-lying doublets mainly derive from the eigenstates with less favorable symmetry.
Hence, while j remains a good quantum number, this is not necessarily true for m_j. In general, the CF mixes and energetically shifts the different $|j = 5/2, m_j\rangle$ states, which results in three separate doublets. The resulting level diagram is referred to as the crystal field scheme.
Determination of the CF scheme is a basic part of the characterization of a Ce compound, since the new ground state sensitively affects electronic and magnetic properties of the material. The relative population of the nth level with energy E_n follows Boltzmann[17] statistics and is determined by

$$\mathcal{P}_n(T) = \frac{e^{-\frac{E_n}{k_\mathrm{B}T}}}{\sum_i e^{-\frac{E_i}{k_\mathrm{B}T}}}. \tag{2.11}$$

Here, k_B is Boltzmann's constant and e is Euler's[18] number.
The consequences of the CF effect for electronic and magnetic properties of a material are most drastic if the CF split $j = 5/2$ doublets are unequally populated. In most Ce compounds, the energetic splitting is not larger than $\Delta E = 10 \ldots 20$ meV. This means that temperatures well below room temperature are required for the CF effect to become visible, although certain characteristics, like an anisotropic paramagnetic response, can also persist at higher temperature [48].
The potential of Ce compounds to show electron correlation effects (see chapter 1) is directly connected to the ground state of the $4f$ electron. Its symmetry and degeneracy are important parameters of different theoretical approaches to Kondo and heavy fermion physics, like, e.g., the large-N expansion. This provides another source of interest in the characterization of the CF ground state of such materials.
Regarding the mechanism that drives the CF effect, two contributions can be identified. In the ionic picture, the electrostatic interaction of neighboring ions with the localized state leads to the rearrangement of the eigenstates of the free ion. Equivalent coupling can also be mediated by ligand states that hybridize with the state of interest, which leads to the covalent CF or ligand field effect. Both contributions can be described analogously by a CF potential. For the $4f$ electrons of rare earth ions, the ionic part of the CF is usually dominant, whereas the covalent part is more important in molecules. Nevertheless, both contributions in general coexist [49]. In strongly correlated materials, the relative contributions certainly depend on the impurity-conduction exchange parameter J.
The theoretical description of the CF is based on the separability of the electronic wave function into radial and angular parts according to eq. 2.1. Expansion of the CF potential in spherical harmonics then produces matrix elements that are composed of series of analytically solvable

---

[14] In most transition metal compounds with localized but partially filled d shells, the hierarchy of the two effects is reversed.

[15] $\mathrm{CeRh_3B_2}$ is an example for a Ce compound where the perturbative treatment fails due to the large crystal field potential (see, e.g., [47] and the references therein)

[16] Hendrik Anthony Kramers, Dutch physicist, 1894-1952

[17] Ludwig Eduard Boltzmann, Austrian physicist and philosopher, 1844-1906

[18] Leonhard Euler, Swiss mathematician and physicist, 1707-1783

integrals over spherical harmonics and integrals of the radial parts. The latter are usually determined experimentally, which means that they act as model parameters in the simulation of experimental data.

In the case of a periodic lattice, the symmetry of the CF potential acting on the ions is defined by the symmetry of the lattice. This is reflected by the local point group of the lattice site. For each point group, only certain terms have to be considered in the expansion of the potential. Hence, the complexity of the problem can be reduced by symmetry considerations.

The theoretical treatment can be further simplified by a formalism that was presented in 1952 by Stevens [50]. In the approximation that the CF acts as perturbation on the spin-orbit split $4f$ level, Stevens introduced so-called operator equivalents $\hat{O}_k^q$ that can be constructed from the components of the total angular momentum operator. The matrix elements of the $\hat{O}_k^q$ can be connected to the ones of the respective spherical harmonics Y_kq in a simple way. In the notation introduced by Hutchings [51], the CF Hamiltonian for f electrons is then written as

$$H_{CF} = \sum_{k=0,2,4,6} \sum_{q=0}^{k} B_k^q \hat{O}_k^q. \tag{2.12}$$

The CF intensity parameters B_k^q include the lattice sum, the radial integral and the so-called Stevens factor. This factor can be calculated for a given symmetry, which is of special interest if it is zero.

The $\mathrm{CePt_5}$/Pt(111) surface intermetallics of the present experiments possess the hexagonal $\mathrm{CaCu_5}$ structure, which means that the local symmetry of the $\mathrm{Ce^{3+}}$ ions is represented by the D_{6h} or $P6/mmm$ point group. In hexagonal symmetry, the quantization (z) axis is adequately defined parallel to the hexagonal c axis, which is the axis of highest symmetry. Generally, H_{CF} then has the form [52]

$$H_{CF} = B_0^0\hat{O}_0^0 + B_2^0\hat{O}_2^0 + B_4^0\hat{O}_4^0 + B_6^0\hat{O}_6^0 + B_6^6\hat{O}_6^6. \tag{2.13}$$

The term for $k = 0$ does not contribute to an energetic splitting of the states. Furthermore, the Stevens factors for the terms with $k = 6$ are zero in the case of Ce with $j = 5/2$ [50, 53–55]. These terms do not have to be considered in the present treatment, which leaves only two free parameters, B_2^0 and B_4^0.

Thus, the consequences of a hexagonal crystal field for the $j = 5/2$ states are much less drastic than in most other cases. The two relevant operator equivalents do not mix the $|j = 5/2, m_j\rangle$ doublets. They remain eigenstates of the Hamiltonian and m_j is conserved as a good quantum number. This allows abbreviation of the denotation of the Kramers doublets as $|m_j\rangle$ in the following.

The CF scheme is then fully characterized by the sign and magnitude of two relative splitting energies. In the present work, the energetic distance of the $|\pm3/2\rangle$ and $|\pm5/2\rangle$ doublets with respect to the $|\pm1/2\rangle$ doublet are used and denoted as $\Delta E_{3/2}$ and $\Delta E_{5/2}$, respectively. The conversion between CF intensity parameters and energy splittings is [55]

$$\begin{aligned} \Delta E_{3/2} &= 6B_2^0 - 300B_4^0 \\ \Delta E_{5/2} &= 18B_2^0 - 60B_4^0. \end{aligned} \tag{2.14}$$

Exemplary CF level schemes for the Ce $4f$ state in a hexagonal CF are shown in fig. 2.4 in the following section, where the consequences of the CF for the paramagnetic susceptibility are discussed.

2.1.3 The paramagnetic susceptibility of Ce in a hexagonal crystal field

The $\mathrm{Ce^{3+}}$ ion as treated in section 2.1.1 possesses an uncompensated magnetic moment, which is usually conserved in Ce compounds due to the strong localization of the $4f$ shell. The

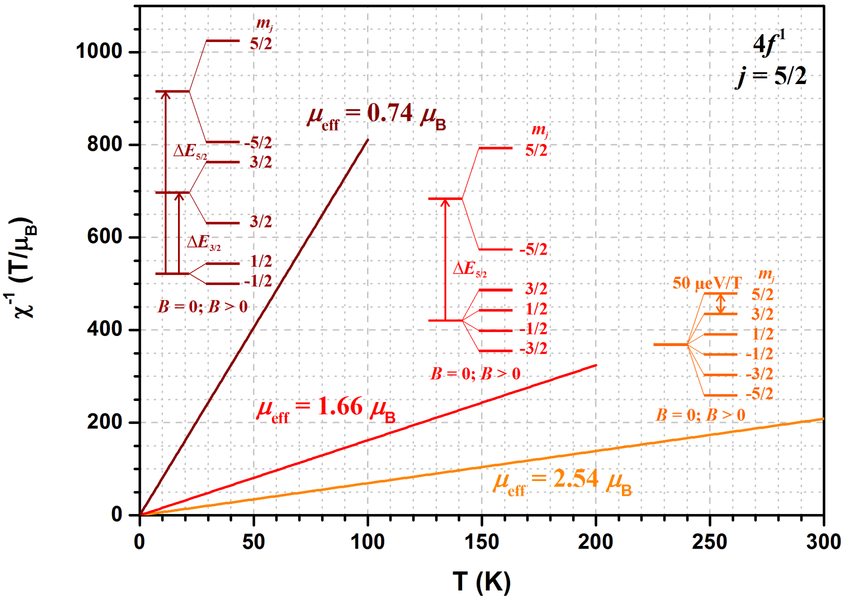

Figure 2.4: Energy level schemes and calculated $\chi^{-1}(T)$ curves for three scenarios in a $4f^1$, $j = 5/2$ configuration and for a hexagonal crystal field. Orange: no CF splitting, sixfold degeneracy of the ground state without magnetic field. Red: The $|\pm5/2\rangle$ doublet is lifted in energy by the CF. Dark red: All three doublets are energetically separated. The $\chi^{-1}(T)$ curves for the latter two configurations represent the low-temperature limits.

localization also prevents direct exchange interaction between different lattice sites. Hence, the only magnetic interaction channel is RKKY interaction, which is described in section 1.2. This mechanism is usually weak, and common Ce compounds are paramagnetic in a large temperature range. The present section provides a theoretical description of the paramagnetic susceptibility of a Ce^{3+} ion in a hexagonal crystal field. Analytic expressions are derived based on perturbation theory, which are used in chapter 10 for fitting of experimental data.

Paramagnetism describes the reaction of a system of N preexisting magnetic moments to an external field. The sum of these vector moments $\vec{\mu}$ constitutes the sample magnetization $\vec{M}$. In the absence of an external field, the moments are statistically distributed in space. In this case, there is no macroscopic magnetization and thus no net magnetic moment per atom $\mu = |\vec{M}|/N$. Application of an external field leads to an energetic preference of moments that are aligned parallel to the field. The gain in energy is the Zeeman energy. The quantization (z) axis is adequately defined by the external magnetic field direction. Consequently, the expectation value of the z component of each moment can be positive or negative, which corresponds to parallel and antiparallel alignment of the moment with respect to the field. The two configurations become separated in energy by the Zeeman splitting. Under restriction to a single j multiplet, the corresponding contribution to the Hamiltonian then reads

$$\hat{H}^{\mathrm{Z}} = -\frac{g_j \mu_{\mathrm{B}} B}{\hbar}\, \hat{j}_z \mathrel{\hat{=}} -\langle \mu_j \rangle \cdot B = g_j \mu_{\mathrm{B}} m_j B, \tag{2.15}$$

which includes the relation between field-dependence of the energy and magnetic moment,

$$\langle \mu_j \rangle = -\frac{\partial E}{\partial B}. \tag{2.16}$$

Hence, the energy gain is largest for the level with largest negative m_j. The resulting energy level scheme for a $4f$ electron in a free Ce^{3+} ion is shown in orange in fig. 2.4. The sixfold degeneracy of the $j = 5/2$ level is lifted by a magnetic field and the ground state is characterized by $m_j = -5/2$.

The red and dark red level schemes in fig. 2.4 represent two possible configurations for the same electron in presence of a hexagonal crystal field with collinear c axis and magnetic field directions, which then also define the quantization (z) axis. As introduced in section 2.1.2, the hexagonal CF does not mix states within the $j = 5/2$ multiplet, but it separates the three $m_j = \pm 1/2, \pm 3/2, \pm 5/2$ doublets in energy. Hence, the energy of the nth m_j level has the form

$$E_n = E_n^{\mathrm{CF}} + E_n^{\mathrm{Z}}. \tag{2.17}$$

The CF energies E_n^{CF} are expressed by the relative energy shifts $\Delta E_{3/2}$ and $\Delta E_{5/2}$ as defined in section 2.1.2.

The character of the ground state now depends on the signs of the CF energies and on their magnitude compared to the Zeeman energies. This already illustrates that the magnetic properties of a sample can significantly be altered by the CF.

The relative population of the separated levels is determined by thermal excitations (see eq. 2.11). Hence, the magnetic moment μ depends on the ratio of magnetic field and temperature. For the simple example without crystal field potential (orange part of fig. 2.4), the Zeeman splitting amounts to $\Delta E^{\mathrm{Z}}/B = g_j \mu_{\mathrm{B}} \approx 50\ \mu\mathrm{eV/T}$. This corresponds to only $T \approx 580\ \mathrm{mK/T}$. Consequently, very low temperatures or very high magnetic fields are required to achieve maximum magnetization, i.e., exclusive population of the lowest level, in this case.

An expression for $\mu(B,T)$ can be derived by application of eqs. 2.11 and 2.15 to 2.17 as follows:

$$\begin{aligned}\mu(B,T) = \sum_{n=1}^{2j+1} -\frac{dE_n}{dB}\mathcal{P}_n &= \frac{\sum_{m_j=-j}^{j} -g_j\mu_{\mathrm{B}} m_j\ e^{-\frac{E_{m_j}^{CF}+g_j\mu_{\mathrm{B}} m_j B}{k_{\mathrm{B}}T}}}{\sum_{m_j=-j}^{j} e^{-\frac{E_{m_j}^{CF}+g_j\mu_{\mathrm{B}} m_j B}{k_{\mathrm{B}}T}}} \\ &= \frac{\sum_{m_j>0} g_j\mu_{\mathrm{B}} m_j \sinh\left(\frac{g_j\mu_{\mathrm{B}} m_j B}{k_{\mathrm{B}}T}\right)\ e^{-\frac{E_{m_j}^{\mathrm{CF}}}{k_{\mathrm{B}}T}}}{\sum_{m_j>0} \cosh\left(\frac{g_j\mu_{\mathrm{B}} m_j B}{k_{\mathrm{B}}T}\right)\ e^{-\frac{E_{m_j}^{\mathrm{CF}}}{k_{\mathrm{B}}T}}}.\end{aligned} \tag{2.18}$$

For the case without crystal field ($E_{m_j}^{\mathrm{CF}} = 0\ \forall m_j$), this equation can be simplified to (see, e.g., [56])

$$\mu(B,T) = g_j\mu_{\mathrm{B}} j\ \mathcal{B}_j\left(\frac{g_j\mu_{\mathrm{B}} jB}{k_{\mathrm{B}}T}\right) \tag{2.19}$$

with the Brillouin function

$$\mathcal{B}_j(x) = \frac{2j+1}{2j}\coth\left(\frac{2j+1}{2j}\ x\right) - \frac{1}{2j}\coth\left(\frac{1}{2j}\ x\right). \tag{2.20}$$

As mentioned above, low temperatures and high magnetic fields are required to magnetically saturate a typical paramagnet. Under normal conditions, the argument of the Brillouin function in eq. 2.19 is much smaller than unity. This limit allows the approximation

$$\coth(x) \approx \frac{1}{x} + \frac{x}{3}, \quad \mathcal{B}_j(x) \approx \frac{j+1}{3j}\ x \quad \text{and} \quad \mu(B,T) \approx \frac{g_j^2\mu_{\mathrm{B}}^2 j(j+1)B}{3k_{\mathrm{B}}T}. \tag{2.21}$$

With the definition of the magnetic susceptibility,

$$\chi(T) = \left.\frac{d\mu(B,T)}{dB}\right|_{B=0}, \tag{2.22}$$

this yields the well-known Curie[19] law

$$\chi^{-1}(T) = \frac{3k_{\mathrm{B}}T}{g_j^2\mu_{\mathrm{B}}^2 j(j+1)} = \frac{3k_{\mathrm{B}}}{\mu_{\mathrm{eff},j}^2}\ T, \tag{2.23}$$

which is shown as the orange line in fig. 2.4. The effective moment $\mu_{\mathrm{eff},j}$ is not to be mixed

---

[19] Pierre Curie, French physicist, 1859-1906

up with the expectation value of the magnetic moment $\langle \mu_j \rangle$. In the vector picture as applied in section 2.1.1, it measures the length of the moment vector $\vec{\mu}_j$, whereas $\langle \mu_j \rangle$ measures the z component. Hence, $\mu_{\text{eff},5/2} = 2.54\ \mu_\text{B}$ is larger than the values given in tab. 2.1.

The concept of the effective moment can also be applied to the more complicated case including the crystal field. For this purpose, a general definition can be written as

$$\mu_\text{eff}(T) = \sqrt{\frac{3k_\text{B}}{d\chi^{-1}(T)/dT}}. \tag{2.24}$$

With this, effective moments can be evaluated from any experimental $\chi^{-1}(T)$ curve and compared to other data or calculated $\mu_{\text{eff},j}$ values.

In presence of a hexagonal crystal field, there are two special cases for which the calculation of the effective moment is straightforward. These are (1) a ground state that consists of the degenerate $|\pm 1/2\rangle$ and $|\pm 3/2\rangle$ doublets, as drawn in red in fig. 2.4, and (2) the $|\pm 1/2\rangle$ ground state, as drawn in dark red. In both cases it is assumed that the non-ground state levels are well-separated in energy and can be neglected at low temperatures.

In both of these scenarios, the maximum m_j and the number and m_j values of the participating levels match a case with $j = m_j^\text{max}$. Hence, the definition of $\mu_{\text{eff},j}$ as derived in eq. 2.23 can directly be applied, but with the Landé factor for $j = 5/2$. Hence, the effective moments amount to $\mu^1_\text{eff} = \sqrt{15/4} \cdot g_{5/2}\mu_\text{B} = 1.66\ \mu_\text{B}$ and $\mu^2_\text{eff} = \sqrt{3/4} \cdot g_{5/2}\mu_\text{B} = 0.74\ \mu_\text{B}$. The low-temperature limits of the $\chi^{-1}(T)$ curves of these two scenarios are shown in the respective coloring in fig. 2.4.

By chance, these two simple configurations are of relevance for the interpretation of the experimental results of the present thesis. Furthermore, μ^2_eff is the smallest effective moment that can be obtained for a $j = 5/2$ electron in a hexagonal crystal field without further modifications to the model.

For any other configuration of the crystal field splitting as well as for a description at higher temperatures, a more general calculation has to be performed starting from eq. 2.18:

$$\mu(B,T) = \frac{g_j\mu_\text{B}\left(\frac{1}{2}\sinh\left(\frac{g_j\mu_\text{B}B}{2k_\text{B}T}\right) + \frac{3}{2}\ e^{-\frac{\Delta E_{3/2}}{k_\text{B}T}} \sinh\left(\frac{3g_j\mu_\text{B}B}{2k_\text{B}T}\right) + \frac{5}{2}\ e^{-\frac{\Delta E_{5/2}}{k_\text{B}T}} \sinh\left(\frac{5g_j\mu_\text{B}B}{2k_\text{B}T}\right)\right)}{\cosh\left(\frac{g_j\mu_\text{B}B}{2k_\text{B}T}\right) + e^{-\frac{\Delta E_{3/2}}{k_\text{B}T}} \cosh\left(\frac{3g_j\mu_\text{B}B}{2k_\text{B}T}\right) + e^{-\frac{\Delta E_{5/2}}{k_\text{B}T}} \cosh\left(\frac{5g_j\mu_\text{B}B}{2k_\text{B}T}\right)}. \tag{2.25}$$

With eq. 2.22, it follows that

$$\chi_\parallel(T) = \frac{\frac{g_j^2\mu_\text{B}^2}{4k_\text{B}T}\left(1 + 9\ e^{-\frac{\Delta E_{3/2}}{k_\text{B}T}} + 25\ e^{-\frac{\Delta E_{5/2}}{k_\text{B}T}}\right)}{1 + e^{-\frac{\Delta E_{3/2}}{k_\text{B}T}} + e^{-\frac{\Delta E_{5/2}}{k_\text{B}T}}}. \tag{2.26}$$

The index of $\chi_\parallel(T)$ is chosen to recall the fact that the above considerations are only valid for the case with collinearity of the hexagonal c axis and the magnetic field. The other extreme is a perpendicular alignment, with the azimuthal rotation in the ab plane being degenerate in hexagonal symmetry.

For the description of the perpendicular case, some complexity is introduced by the fact that the quantization axes that are defined by the crystal field and the magnetic field do not coincide. Consequently, the Zeeman and the crystal field Hamiltonians do not share the same set of eigenfunctions in their natural representation, and one of the two has to be transformed.

Keeping the z axis as the quantization direction that is defined by the crystal field, the Zeeman operator with a field applied in the x direction can be expressed by step-up and step-down operators according to eq. 2.9,

$$\hat{H}^\text{Z}_x = -\frac{g_j\mu_\text{B}B}{\hbar}\ \hat{j}_x = -\frac{g_j\mu_\text{B}B}{2\hbar}\ (\hat{j}^+ + \hat{j}^-) \tag{2.27}$$

In a matrix representation with the basis

$$\vec{\psi} = \begin{pmatrix} |-5/2\rangle \\ |-3/2\rangle \\ |-1/2\rangle \\ |+1/2\rangle \\ |+3/2\rangle \\ |+5/2\rangle \end{pmatrix}, \tag{2.28}$$

the Hamiltonian then reads

$$\begin{aligned} \hat{H} &= \hat{H}^{\mathrm{CF}} + \hat{H}^{\mathrm{Z}}_x \\ &= \begin{pmatrix} \Delta E_{\frac{5}{2}} & 0 & 0 & 0 & 0 & 0 \\ 0 & \Delta E_{\frac{3}{2}} & 0 & 0 & 0 & 0 \\ 0 & 0 & 0 & 0 & 0 & 0 \\ 0 & 0 & 0 & 0 & 0 & 0 \\ 0 & 0 & 0 & 0 & \Delta E_{\frac{3}{2}} & 0 \\ 0 & 0 & 0 & 0 & 0 & \Delta E_{\frac{5}{2}} \end{pmatrix} - \frac{g_j \mu_{\mathrm{B}} B}{2} \begin{pmatrix} 0 & \sqrt{5} & 0 & 0 & 0 & 0 \\ \sqrt{5} & 0 & 2\sqrt{2} & 0 & 0 & 0 \\ 0 & 2\sqrt{2} & 0 & 3 & 0 & 0 \\ 0 & 0 & 3 & 0 & 2\sqrt{2} & 0 \\ 0 & 0 & 0 & 2\sqrt{2} & 0 & \sqrt{5} \\ 0 & 0 & 0 & 0 & \sqrt{5} & 0 \end{pmatrix}. \end{aligned} \tag{2.29}$$

In order to solve the problem exactly, the Hamiltonian has to be diagonalized, which can be done numerically. Alternatively, a perturbation treatment can be applied to the Zeeman term. This has the advantage of producing an analytical expression that facilitates numerical fitting of experimental data.

The perturbation treatment is justified if the crystal field energies are large compared to the Zeeman energy. As long as $\Delta E_{3/2}, \Delta E_{5/2} \neq 0$, this is always true in the limit $B \to 0$, as applied in eq. 2.22. This limit is used in the theoretical derivation, but the experimental data are of course obtained at finite magnetic field. Hence, the validity of the approach has to be tested for the energy scales that are encountered in the experiments. For the present results, this is done in appendix A.5 by comparison to results of numerical diagonalization.

In perturbation theory up to second order, the energy values of the unperturbed eigenstates are slightly modified by the small off-diagonal elements according to [45]

$$E_n = E_n^0 + \hat{H}^{\mathrm{pert}}_{n,n} + \sum_{m \neq n} \frac{|\hat{H}^{\mathrm{pert}}_{n,m}|^2}{E_n^0 - E_m^0}. \tag{2.30}$$

This prerequires that states, which are connected via off-diagonal elements up to the given order, are not degenerate in energy. In the present case, this situation occurs for the $|\pm 1/2\rangle$ doublet in second order. Hence, non-degenerate states have to be produced by a basis transformation. An adequate basis for the given Hamiltonian is a symmetric mixture of states with equal $|m_j|$, $\psi' = 1/\sqrt{2}\,(|m_j\rangle \pm |-m_j\rangle$. The basis transformation is represented by

$$\vec{\psi}' = \hat{\mathcal{T}}\vec{\psi} = \frac{1}{\sqrt{2}} \begin{pmatrix} 1 & 0 & 0 & 0 & 0 & 1 \\ 0 & 1 & 0 & 0 & 1 & 0 \\ 0 & 0 & 1 & 1 & 0 & 0 \\ 0 & 0 & 1 & -1 & 0 & 0 \\ 0 & 1 & 0 & 0 & -1 & 0 \\ 1 & 0 & 0 & 0 & 0 & -1 \end{pmatrix} \begin{pmatrix} |-5/2\rangle \\ |-3/2\rangle \\ |-1/2\rangle \\ |+1/2\rangle \\ |+3/2\rangle \\ |+5/2\rangle \end{pmatrix} = \frac{1}{\sqrt{2}} \begin{pmatrix} |-5/2\rangle + |+5/2\rangle \\ |-3/2\rangle + |+3/2\rangle \\ |-1/2\rangle + |+1/2\rangle \\ |-1/2\rangle - |+1/2\rangle \\ |-3/2\rangle - |+3/2\rangle \\ |-5/2\rangle - |+5/2\rangle \end{pmatrix} \tag{2.31}$$

The crystal field Hamiltonian is unaffected by this transformation, as is the part concerning the $|\pm 3/2\rangle$ and $|\pm 5/2\rangle$ doublets in the Zeeman term. This reflects that both operators do not lift the degeneracy of these m_j and $-m_j$ states up to second order perturbation theory. For the

$|\pm 1/2\rangle$ doublet, the transformation diagonalizes the respective part of the Zeeman term and provides the basis for the perturbation treatment. The transformed Zeeman operator reads

$$\hat{H}_x^{\mathrm{Z}\prime} = \hat{\mathcal{T}}^t \hat{H}_x^{\mathrm{Z}} \hat{\mathcal{T}} = -\frac{g_j \mu_\mathrm{B} B}{2} \begin{pmatrix} 0 & \sqrt{5} & 0 & 0 & 0 & 0 \\ \sqrt{5} & 0 & 2\sqrt{2} & 0 & 0 & 0 \\ 0 & 2\sqrt{2} & 3 & 0 & 0 & 0 \\ 0 & 0 & 0 & -3 & 2\sqrt{2} & 0 \\ 0 & 0 & 0 & 2\sqrt{2} & 0 & \sqrt{5} \\ 0 & 0 & 0 & 0 & \sqrt{5} & 0 \end{pmatrix}. \tag{2.32}$$

According to eq. 2.30, the perturbation treatment then yields the energy values

$$\begin{aligned} E_1 = E_6 &= \Delta E_{5/2} + \frac{5 g_j^2 \mu_\mathrm{B}^2 B^2}{4(\Delta E_{5/2} - \Delta E_{3/2})} \\ E_2 = E_5 &= \Delta E_{3/2} + \frac{g_j^2 \mu_\mathrm{B}^2 B^2}{4} \left(\frac{8}{\Delta E_{3/2}} + \frac{5}{\Delta E_{5/2} - \Delta E_{3/2}} \right) \\ E_3 &= -\frac{3 g_j \mu_\mathrm{B} B}{2} - \frac{2 g_j^2 \mu_\mathrm{B}^2 B^2}{\Delta E_{3/2}} \\ E_4 &= \frac{3 g_j \mu_\mathrm{B} B}{2} - \frac{2 g_j^2 \mu_\mathrm{B}^2 B^2}{\Delta E_{3/2}}. \end{aligned} \tag{2.33}$$

With this, the susceptibility for $B \perp c$ can be calculated via the first identity in eq. 2.18, eq. 2.11 and eq. 2.22, which yields

$$\chi_\perp(T) = \frac{\frac{g_j^2 \mu_\mathrm{B}^2}{4 k_\mathrm{B} T} \left(9 + \frac{16 k_\mathrm{B} T}{\Delta E_{3/2}} - \left(\frac{16 k_\mathrm{B} T}{\Delta E_{3/2}} - \frac{10 k_\mathrm{B} T}{\Delta E_{5/2} - \Delta E_{3/2}} \right) e^{-\frac{\Delta E_{3/2}}{k_\mathrm{B} T}} - \frac{10 k_\mathrm{B} T}{\Delta E_{5/2} - \Delta E_{3/2}} \, e^{-\frac{\Delta E_{5/2}}{k_\mathrm{B} T}} \right)}{1 + e^{-\frac{\Delta E_{3/2}}{k_\mathrm{B} T}} + e^{-\frac{\Delta E_{5/2}}{k_\mathrm{B} T}}}. \tag{2.34}$$

The such derived results for $\chi_\parallel(T)$ and $\chi_\perp(T)$ are in line with previous calculations [53, 55, 57]. Exemplary $\chi^{-1}(T)$ curves for different sets of $\Delta E_{3/2}, \Delta E_{5/2}$ and for parallel and perpendicular alignment of B and the c axis according to eqs. 2.26 and 2.34, respectively, are shown in fig. 2.5. The total crystal field splitting for all calculations was chosen to $\Delta E = 20$ meV, which is a realistic value for the samples investigated in the present thesis. Degeneracy of the m_j levels was approximated by very small crystal field splitting $\Delta E \leq 1$ µeV in the calculations. For exact degeneracy, the perturbational expression for $\chi_\perp$ is not defined. For theoretical calculations, the pertrubation approximation is valid even for arbitrarily small splitting energies, since the susceptibility is calculated by the zero-field slope of $\mu(B)$ according to eq. 2.22. This is different for experimental data obtained at finite field, which is discussed in appendix mA.5.

The energy level schemes that have been chosen for these calculations produce different representative types of curves. Variation of the ratio of the two energy splittings influences certain details of the curves, but not their general appearance. Further calculated curves based on the model with only minor modification are shown in fig. 10.5.

The calculated curves show that the crystal field has significant impact on the paramagnetic susceptibility. The capability of the CF-split system to respond to an external magnetic field is highly anisotropic regarding the field direction. Whether the paramagnetic moments are more easily aligned parallel or perpendicular to the c axis depends on the energetic ordering of the levels and, in cases with a $|\pm 3/2\rangle$ ground state (orange lines), even on the temperature.

An interesting feature is the finite, temperature-independent susceptibility that is obtained at low temperatures for $B \perp c$ in the cases of $|\pm 3/2\rangle$ or $|\pm 5/2\rangle$ ground states. It represents a contribution to the susceptibility that is not connected to an effective moment according to

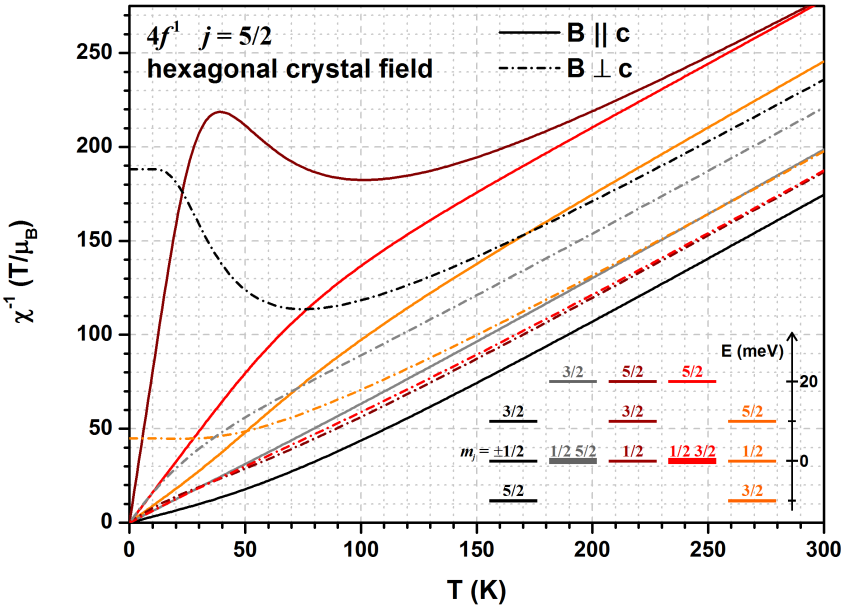

Figure 2.5: Inverse susceptibility of a Ce $4f$ electron in a hexagonal crystal field. Curves are shown for parallel and perpendicular alignment of c axis and magnetic field direction for selected, representative sets of energy splitting parameters. The corresponding energy level schemes with a total splitting of $\Delta E = 20$ meV are shown in the lower right. Note that the ordinate is stretched by a factor of 4 compared to fig. 2.4.

eq. 2.24. This finding is explained by the fact that the degeneracy of the respective levels with opposite signs in m_j is not lifted by the Zeeman term up to second order perturbation theory. The observed behavior is called Van Vleck[20]-paramagnetism [58]. It should not be mixed up with signatures of Kondo interaction (compare fig. 1.1 (b)), which have similar characteristics. Furthermore, fig. 2.5 demonstrates that the inspection of $\chi^{-1}(T)$ data can yield valuable information on the crystal field scheme, especially when measured direction-dependent on single-crystalline samples. The most prominent features are the direction and magnitude of the anisotropy, which is indicative of the ground state, and changes in slope in $\chi_{\|}^{-1}(T)$, which indicate the onset of significant population of higher-lying states and the accompanying change in the effective moment (see eq. 2.24 and fig. 2.4).

Reversely, the examples also underline the necessity to consider crystal field effects in the interpretation of magnetic measurements. For quantitative analyses, the CF induced energy level scheme has to be known. This becomes even more crucial for symmetries other than hexagonal. In general, the theoretical description is by far more complicated than in the given example, since the $|j, m_j\rangle$ states are not only split in energy, but can also be mixed.

2.1.4 Magnetic coupling in the paramagnetic regime

As a consequence of the high localization of the $4f$ orbitals in Ce and other rare earths (compare fig.2.1), the overlap of $4f$ wave functions of neighboring sites is negligible. Hence, no direct exchange interaction is present. Nevertheless, magnetic coupling can occur by RKKY interaction, which describes indirect coupling with participation of conduction states. The concept is introduced in section 1.2.

Irrespective of the detailed coupling mechanism, the effect of magnetic coupling in the paramagnetic regime can be described by a molecular mean field. This approach expands the Curie-law given in eq. 2.23 to the Curie-Weiss[21] law. The idea was introduced in 1926 by Weiss and Forrer [56].

In this phenomenological treatment, the external magnetic field B_{ext} is augmented by the internal

---

[20] John Hasbrouck Van Vleck, American physicist, 1899-1980

[21] Pierre Ernest Weiss, French physicist, 1865-1940

molecular field B_{mol}, which is assumed to be proportional to the sample magnetization. In the picture of individual moments of average magnitude as used in section 2.1.3, the proportionality constant λ can be understood as the sum of all coupling constants between neighboring moments. The sign of λ reflects the sign of the exchange constant and thus indicates if the coupling is ferromagnetic or antiferromagnetic. The effective magnetic field can then be written as

$$B_{\text{eff}} = B_{\text{ext}} + B_{\text{mol}} = B_{\text{ext}} + \lambda\mu \tag{2.35}$$

The paramagnetic susceptibility is the proportionality constant between magnetic moment μ and external field B for $B \to 0$ (see eqs. 2.21 and 2.22). Introducing the effective magnetic field, it follows that

$$\mu = \chi B_{\text{eff}} = \chi(B_{\text{ext}} + \lambda\mu). \tag{2.36}$$

Hence,

$$\mu = \frac{\chi}{1 - \chi\lambda} B_{\text{ext}} = \chi^{\lambda} B_{\text{ext}}. \tag{2.37}$$

The susceptibility in the presence of a molecular field as measured experimentally is usually χ^{λ}. The effect of λ is best seen for the inverse susceptibility, since

$$\frac{1}{\chi^{\lambda}} = \frac{1}{\chi} - \lambda. \tag{2.38}$$

This provides a convenient way to introduce magnetic coupling to a model for the paramagnetic susceptibility. In doing so, the $\chi^{-1}(T)$ curve as calculated without coupling is simply vertically shifted by the coupling constant. This does not affect the slope of the curve and thus conserves the effective moment (see eq. 2.24). The presentation of susceptibility data as $\chi^{-1}(T)$ curves is commonly referred to as Curie-Weiss plot.

If μ_{eff} is finite at low temperatures, the shift of $\chi^{-1}(T)$ causes the T-axis intercept to deviate from $T = 0$. Depending on the sign of λ, this leads to a positive, paramagnetic Curie temperature Θ_C in the case of ferromagnetic coupling, or to a negative paramagnetic Néel[22] temperature Θ_N, which indicates antiferromagnetic coupling. While the approach of Θ_C in the ferromagnetic case leads to a direct breakdown of the model, Θ_N can never be reached. Instead, the system exhibits a finite, positive Néel temperature T_N, which cannot be directly included to the model. Below T_N, the model also breaks down due to the onset of antiferromagnetic order.

2.1.5 The Cerium valence

The valence of Ce is variable and strongly depends on the environment. Probably the best example for this effect is the α-γ transition in pure Ce metal [38, 40, 41]. At ambient conditions, the γ phase is stable. It has a valence close to three, which means that the three $5d$ and $6s$ electrons form a metallic bond and the $4f$ electron is nearly completely localized. The α phase exists at low temperature or high pressure. It possesses a significantly increased valence, which means that the $4f$ electrons are partly delocalized. Due to this observation, Ce compounds are often classified as γ- or α-like depending on their valence.

The degree of delocalization in α-Ce was the subject of a long-standing debate. The earliest interpretation of the α-γ transition was based on the complete promotion of the $4f$ electron to the conduction band [38]. Hence, the valence of α-Ce was assumed to be four[23]. Doubts on this interpretation were caused by several experimental findings, which lead to the proposal of a variety of different models. In this course, the concept of mixed or intermediate valence was introduced, which means that the average valence is non-integer. Whether the different

---

[22] Louis Eugène Felix Néel, French physicist, 1904-2000

[23] An integer valence of four would also be expected for CeO_2 from simple electron counting. The interesting issue of CeO_2 is beyond the scope of the present thesis and is not treated here. An account can be found in [59] and the references therein.

atoms in an ensemble possess different valencies or the valence of each atom fluctuates over time is not distinguishable in a statistical quantum mechanical interpretation. Both scenarios are equivalently used in the following.

The valence debate was resolved in the early 1980s, when theories were developed that applied Kondo physics via the SIAM Ansatz to Ce compounds. The interaction between the f level and the conduction states is thereby included as a hopping matrix element V^{ic}, the size of which is governed by the energy separation between the two states. Furthermore, the Coulomb interaction U_f between multiple f electrons at one atomic site is considered.

In this framework, the α-γ transition was qualitatively explained by Allen and Martin in 1982 [60]. In 1983, Gunnarsson and Schönhammer advanced the SIAM Ansatz by introduction of a realistic basis set that allowed application of the $1/N$ expansion [25, 26][24]. N is the degeneracy of the impurity level, which is 14 for a completely degenerate f-level and 6 and 8 for the spin-orbit split $j = 5/2$ and $j = 7/2$ multiplets, respectively. In any case, N is large enough in rare-earth systems to yield excellent results with this approach.

Gunnarsson and Schönhammer were primarily interested in electron spectroscopy. Hence, they had to consider the presence of a core-hole. The complete Hamiltonian of their model reads (compare to the SIAM in eq. 1.1)

$$\begin{aligned} H = \; & \overbrace{\sum_{\vec{k},\sigma} E_{\vec{k}} \hat{n}_{\vec{k}\sigma}}^{\text{conduction band}} + \overbrace{E_{\mathrm{i}} \sum_{m,\sigma} \hat{n}_{m\sigma}}^{\text{impurity } f\text{-level}} + \overbrace{U_{\mathrm{i}} \sum_{m,m',\sigma,\sigma'} \hat{n}_{m\sigma} \hat{n}_{m'\sigma'}}^{\text{Coulomb interaction of } f \text{ electrons}} \\ & + \underbrace{\sum_{m,\vec{k},\sigma} V^{\mathrm{ic}}_{m\vec{k}} \hat{c}^{\dagger}_{m\sigma} \hat{c}_{\vec{k}\sigma} + V^{\mathrm{ic}*}_{m\vec{k}} \hat{c}^{\dagger}_{\vec{k}\sigma} \hat{c}_{m\sigma}}_{\text{interaction of } f\text{-level and conduction band}} + \underbrace{E_{\mathrm{h}} \hat{n}_{\mathrm{h}}}_{\text{core-hole}} - \underbrace{U_{\mathrm{ih}} \left(1 - \hat{n}_{\mathrm{h}}\right) \sum_{m,\sigma} \hat{n}_{m\sigma}}_{\text{interaction of } f\text{-level and core-hole}} \end{aligned} \tag{2.39}$$

In order to address the Ce valence with spectroscopy, it is instructive to investigate the energetic ordering of states with variable number of f electrons. The large Coulomb repulsion allows neglect of $4f$ occupancy with more than two electrons in the ground state. The relevant terms in the Hamiltonian are the f-f Coulomb interaction and the f-h interaction. The removal of a core electron significantly reduces the screening of the positive charge of the nucleus, which attractively acts on the f electrons. Consequently, the energies of states with f electrons are reduced by the presence of a core-hole with respect to the state with empty f-shell. This is depicted in fig. 2.6.

In the initial state without a core-hole, the energy separation is small, especially for the $4f^1$ and $4f^0$ configurations. As a consequence, the states mix and the ground state Ψ of the Ce atom has contributions from states with zero, one and two f electrons,

$$\Psi = \sqrt{c_{f^0}}\ \psi^0 + \sqrt{c_{f^1}}\ \psi^1 + \sqrt{c_{f^2}}\ \psi^2. \tag{2.40}$$

In the final state, the presence of the core-hole leads to an increased energy separation. Mixing of the states can thus be neglected, and the relative weights of different contributions in a spectrum can be connected to the mixing coefficients of the initial state.

The mixing coefficients can be summarized in the average f-level occupancy n_f, which is related to the valence via $v = 4 - n_f$. Regarding the level ordering in the ground state without a core-hole, one can conclude that $c_{f^1} > c_{f^0}$ and that c_{f^2} is rather small. This conclusion is supported by experimental data [43, 61]. If c_{f^2} can be neglected, $n_f \approx c_{f^1}$ and $v \geq 3$. This definition of n_f is used throughout the present thesis, although the analysis presented in section 8.4.1 might indicate that c_{f^2} should be considered in the evaluation.

The second important parameter in the Gunnarsson-Schönhammer (GS) theory is the hybridization strength Δ, which derives from the hopping matrix element V^{ic}. The connection of n_f and Δ

---

[24] This theory is also reviewed in many textbooks, see e.g. [12, 39, 59]

is not straightforward since it involves further model parameters, like the DOS of the conduction band at the Fermi energy [43].

In order to compare their results to experimental spectroscopic data, Gunnarsson and Schönhammer performed model calculations for various parameter combinations. They considered valence-band, core-level and inverse photoemission spectroscopy as well as X-ray absorption spectroscopy [39]. The model spectra allowed identification of the spectral contributions from the three different valencies in the ground state and to determine the values of the model parameters.

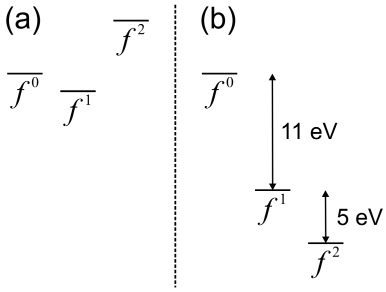

Figure 2.6: relative ordering of energy levels with variable f occupancy in absence (a) and presence (b) of a core-hole in the limit of zero conduction bandwidth, after [39]

While the GS theory was later also used to investigate the α-γ transition [62], the most important results were of higher generality. It was shown that it is possible to consistently reproduce the results of different electron spectroscopies within the SIAM, using the same set of parameters for a certain material.

In this course, the GS theory allowed determination of values for Δ and n_f for various Ce compounds [43, 63]. Contrary to earlier estimates, it turned out that typically $\Delta \approx 100$ meV and that n_f is not smaller than 0.7 for all Ce compounds that were investigated. Furthermore, it was also possible to reproduce the results of "traditional" thermodynamic experiments with the parameters that were obtained from spectroscopy.

Apart from the success of helping to resolve the historical valence debate, the GS theory provides a tool to obtain the Ce valence and the hybridization strength from spectroscopic experiments. This directly gives access to quantities that reflect electron correlation effects. For example, the Kondo energy scale can be determined by analyzing the temperature-dependence of n_f. This is a result of the NCA calculations by Bickers *et al.* [27], who improved the zero-temperature Ansatz of Gunnarsson and Schönhammer by consideration of finite temperatures.

The different spectroscopic techniques that are covered by the work of Gunnarsson and Schönhammer yield n_f with different reliability. This is caused by the fundamental differences in the resulting final states. Generally speaking, in PES an electron is removed, in inverse PES an electron is added, and in XAS an electron is removed and added somewhere else. In any case, the final state is also a mixture of the states ψ^n in analogy to eq. 2.40, but the character of the mixing depends on the technique. As a consequence, inverse PES overestimates n_f and XAS underestimates it. The most reliable results can be obtained with PES [39].

Furthermore, the different final states have a consequence on the nature of the spectroscopic signatures that are used to determine n_f. Core-level PES measures the spectral function of the $3d^{3/2}$ and $3d^{5/2}$ electrons. Since the resulting core-hole interacts with the $4f$ electrons, separated peaks are observed that can be attributed to f^0, f^1 and f^2 ground states [26]. The f count is thereby not different in the final state, which makes a labeling of the peaks as f^n meaningful. The same is valid for $L_{2,3}$ XAS, where essentially the $2p \to 5d$ transition is studied. Different peaks arise that can be attributed to different f^n contributions in both ground and final state [64, 65].

The situation is different for $M_{4,5}$ XAS, which is extensively applied in the present work. Here, the transition $3d^{10}4f^n \to 3d^9 4f^{n+1}$ is studied and the f-count increases by one in the process. For the sake of consistency with the other techniques, one could label the contributions in the spectrum by the initial-state f-count, but the spectrum is largely influenced by the final state. In order to avoid confusion, the spectral features are denoted by the full respective transition $f^n \to f^{n+1}$ in the present thesis.

The procedures that were developed to obtain absolute n_f values from Ce $M_{4,5}$ spectra and especially to track relative changes in n_f under variation of the sample temperature and thickness are described in section 6.2. Experimental results of the Ce valence in $CePt_5$/Pt(111) surface intermetallics are presented in chapter 9.

2.2 Binary compounds of Ce and Pt

In the previous section, it is shown that the magnetic properties of Ce compounds strongly depend on the chemical environment and thus on the crystal structure. The symmetry of the environment influences the paramagnetic susceptibility via the crystal field, whereas the magnetic coupling of Ce moments depends on their distance due to the oscillating nature of the RKKY interaction.

Hence, knowledge of the crystal structure of the investigated compound is required for the correct interpretation of experimental findings concerning those properties. Since this is the central issue of the present thesis, considerable effort was spent to increase the available amount of crystallographic information about the $CePt_5$/Pt(111) surface intermetallics.

The successful structure determination, which is presented in chapter 7, is based on systematic evaluation of all information that could be gathered. In this course, the relation of the known properties of the Ce-Pt bulk phases to crystallographic results of the surface system allowed identification of consistencies. Hence, section 2.2.1 is devoted to the detailed investigation of the binary Ce-Pt phase diagram.

The surface compounds were subject of a considerable number of studies prior to the present thesis, which were of course considered in the discussion of the present experimental results. A review of the literature on Ce-Pt(111) is given in section 2.2.2.

The following treatment is not restricted to crystallographic properties. The literature review covers all publications concerning Ce-Pt(111) surface compounds that are presently known to the author, which includes the works that lead to the identification as a heavy fermion system. The discussion of the bulk material also includes results concerning magnetic properties and Kondo physics for the different compounds. This information is valuable for comparison to the present results for the surface compound, which can lead to the identification of effects of the reduced dimension.

2.2.1 The binary Ce-Pt phase diagram: Properties of bulk material

The Landolt-Börnstein database lists eight[25] different intermetallic Ce-Pt phases, which are collected from a variety of publications [67]. These data were the basis for considerations on the structure of the Ce-Pt(111) surface compounds in the literature up to date.

However, the level of information has recently been increased by a publication by Janghorban *et al.* [68]. These authors present a detailed experimental investigation of the complete Ce-Pt phase diagram in a single study. Most of the known phases were reproduced and refined lattice parameters were obtained. Additionally, three new phases were found.

Tab. 2.2 lists the crystallographic data of the phases reported by Janghorban *et al.* In addition, $CePt_3$ in the $AuCu_3$ structure is included, which was not observed by these authors but has been mentioned by Moriarty *et al.* [69].

For Pt concentrations in between $CePt_2$ and $CePt_3$, a homogeneity domain exists. In this regime, a crystal structure called C15 with the prototype $MgCu_2$ is observed independent of the stoichiometry. This explains why the Landolt-Börnstein database also assigns this structure to $CePt_3$ despite the misfit in Pt concentration. In a work that is concerned with the Ce-Pt(111) system, Essen *et al.* list the $CeNi_3$ structure for $CePt_3$ instead [70] (see section 2.2.2). However, it is not clear where this assignment comes from, since these authors also refer to the Landolt-Börnstein database.

Lawrence *et al.* propose the C15b or Be_5Au structure for $CePt_3$ [71]. This statement is again confusing due to the misfit in stoichiometry, but the Be_5Au structure can be obtained from $MgCu_2$ by replacement of some of the large (Mg/Au/Ce) atoms by small ones (Cu/Be/Pt) [72]. The $CePt_{2(+x)}$ homogeneity domain most likely represents a part of this process, which probably takes place in a disordered way.

The $MgCu_2$ structure is one of the so-called Laves[26] phases. This term summarizes crystal

---

[25] The mentioned orthorhombic $CePt_5$ phase is just an alternative notation of the hexagonal $CaCu_5$ phase [66]

[26] Fritz Laves, German mineralogist, 1906-1978

Compound	Structure	Prototype	a_1 (nm)	a_2 (nm)	a_3 (nm)
Ce_7Pt_3	hexagonal	Th_7Fe_3	1.210	-	0.6403
Ce_5Pt_3	tetragonal	Pu_5Rh_3	1.1405	-	0.6648
Ce_3Pt_2	hexagonal	Er_3Ni_2	0.8962	-	1.7119
Ce_5Pt_4	orthorhombic	Sm_5Ge_4	0.7665	1.5066	0.7616
CePt	orthorhombic	CrB	0.391	1.091	0.450
Ce_3Pt_4	hexagonal	Pu_3Pd_4	1.3683	-	0.5796
$CePt_2$	cubic	$MgCu_2$	0.7741	-	-
$CePt_3$	cubic	"$MgCu_2$"	0.7650	-	-
$CePt_3$	cubic	$AuCu_3$	0.4162	-	-
$CePt_{x\approx4.5}$	?	?	?	?	?
$CePt_5$	hexagonal	$CaCu_5$	0.5367	-	0.4391

Table 2.2: Crystallographic information on intermetallic Ce-Pt phases. Lattice constants (a_1, a_2, a_3) were taken from [68] except for the $CePt_3$ phases, for which they were taken from [67]. Redundant values are omitted.

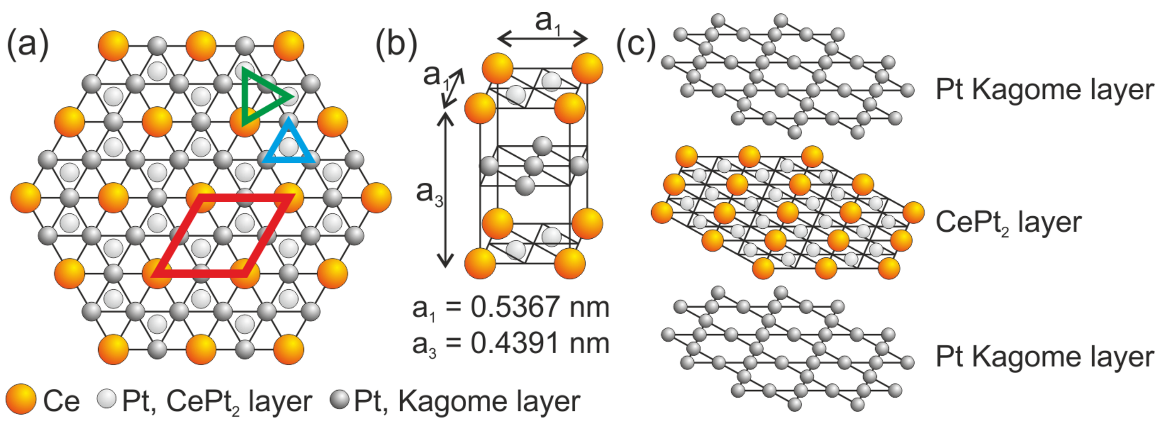

Figure 2.7: Sketch of $CePt_5$ in the $CaCu_5$ structure consisting of $CePt_2$ layers alternating with Pt Kagome layers. (a) Top view of the (001) surface. The surface unit cell is shown in red. Basic building blocks of the triangular lattices of Kagome and $CePt_2$ layers are shown in blue and green, respectively. (b) Hexagonal unit cell with lattice parameters for bulk $CePt_5$ [68]. (c) Schematic of the layered structure.

structures that represent a possibility for dense packaging of atoms with different radii [7, 73]. They are typically found for intermetallic compounds that contain rare earths. Next to the three original Laves-phases, a number of related structures exist, like the $CaCu_5$ structure. This structure is found for $CePt_5$ and is shown in fig. 2.7.

The characteristic building element of the Laves phases is a Kagome[27] lattice of the smaller atoms, as can be seen in the figure. All lattice points in a Kagome lattice are equivalent and possess four neighboring points [74]. It is a regular arrangement of hexagons and triangles that resembles Stars of David. Hence, an atomic Kagome layer has hexagonal and triangular holes. The larger atoms in the Laves phases reside in layers between the Kagome nets, with a hexagonal hole on at least one side. The occupation of the triangular holes and the stacking sequence of the Kagome layers determine the exact phase.

The $CaCu_5$ structure has a hexagonal unit cell and consists of alternating layers of $CePt_2$ and pure Pt Kagome nets. All Kagome layers share the same rotational alignment, which leads to a rather small unit cell volume compared to other Laves phases.

Concerning the magnetic properties and signatures of Kondo physics in the bulk Ce-Pt compounds, only investigations of CePt, $CePt_{2+x}$ and $CePt_5$ are currently known to the author. $CePt_5$ is known to feature a magnetic moment close to the one expected for Ce^{3+} ions [66]. The

---

[27] "Kagome" derives from Japanese, referring to traditional baskets woven from bamboo

paramagnetic susceptibility can be described on the basis of a crystal field split $J = 5/2$ state [55]. It orders antiferromagnetically at $T_N = 1$ K and shows no heavy-fermion behavior [75]. However, a minimum in the electric resistivity at $T \approx 9$ K can be interpreted as a signature of the Kondo effect [76].

$CePt_2$ is also an antiferromagnet with a Néel Temperature of $T_N = 1.6$ K, which can also be described by Ce^{3+} ions in the corresponding crystal field [77]. Samples from the homogeneity domain show no magnetic ordering and a Kondo Temperature of $T_K \approx 2$ K, estimated from specific heat measurements [71]. In contrast, the equatomic compound CePt displays ferromagnetic order below $T_C = 6$ K and features a quantum critical point at a pressure of $p = 12.1$ GPa, as derived from measurements of the *ac* susceptibility and electrical resistivity [78].

These findings show that due to the oscillatory nature of RKKY interaction as well as the variable degree of localization of the Ce $4f$ electron, very different ground states can exist in Ce-Pt intermetallics. Hence, predictions are not easily done. Classification of a material in the phase diagram of mixed valence, magnetic ordering, Kondo- and heavy-fermion behavior requires dedicated experiments.

2.2.2 Previous work on Ce-Pt(111) surface compounds

Surface sensitive experimental methods such as photoemission spectroscopy (PES) or scanning tunneling microscopy (STM) profit from specimen with a well-controlled surface. Furthermore, studying anisotropic or k-dependent effects necessitates ordered single crystals. The desire to have access to such samples of rare earth intermetallics was the motivation for the first study of Ce-based surface compounds on Pt(111). It was published in 1993 by Tang *et al.* [79], who chose the combination of Ce and a transition metal in search for a heavy fermion material.

Ordered compounds were obtained by evaporation of Ce onto clean Pt(111) and subsequent annealing. Characterization with low-energy electron diffraction (LEED) and core-level PES revealed considerable dependence of the investigated properties on the amount of Ce available for compound formation. LEED patterns[28] are reported to show (1.94×1.94) and (1.96×1.96) reconstructions with respect to the substrate. At low Ce deposit, additional satellite spots were observed, while at intermediate initial coverage coexistence of an unrotated structure and one rotated by 30° with varying relative intensities of the two is reported. Although visible in their LEED images, Tang *et al.* do not mention the fact that the patterns at high and low coverage have different orientations.

The stoichiometry of the compound[29] was determined between $CePt_{2.23}$ and $CePt_3$ by PES, that is in the homogeneity domain. The Ce valence was found to lie between 3.07 and 3.12. Adsorption experiments indicated a very low reactivity of the compound surface, which the authors took as a hint towards Pt termination. Hence, this detailed study already addressed three aspects that caused considerable interest in the Ce-Pt(111) compounds in the following: Kondo and heavy fermion physics, the question of catalytic behavior and the determination of the crystal structure.

Photoemission measurements of the spectral function near the Fermi edge of equivalently prepared surface compounds were published in 1995 with participation of the same group [80]. The valence determined at room temperature suggests that the $4f$ electrons are not fully localized. Nevertheless, the authors assumed a rather low Kondo temperature equal to the one of bulk $CePt_2$, i.e., $T_K < 20$ K. Against this background, the finding of a spectral feature resembling a Kondo resonance at $T = 120$ K, which seemed to show amplitude modulations with the probing angle, appeared puzzling and made the authors search for alternative explanations of this signature.

In subsequent studies by Garnier *et al.*, PES with higher energy resolution was applied to the Ce-Pt(111) as well as to the similar La-Pt(111) system. The Kondo resonance in Ce-Pt(111) was clearly identified [81, 82]. LEED patterns for the two systems were also analyzed.

---

[28] examples for most of the LEED patterns mentioned in literature are shown in fig. 7.3

[29] Different stoichiometries have been assumed for the sample system in literature, which is why it is denoted Ce-Pt(111) in the present section

While La-Pt(111) is reported to exhibit a (2×2) superstructure, for Ce-Pt(111) a pattern of $(1.1\sqrt{3} \times 1.1\sqrt{3})R30^\circ$ was observed.

This superstructure appearing without superimposed patterns was neither mentioned in the work of Tang *et al.* nor in a study of the structural and catalytic properties of the system by Baddeley *et al.* [83]. Amongst other experimental techniques, these authors applied LEED and STM to investigate Ce-Pt(111) compounds, which again resulted from different amounts of Ce that were deposited on Pt(111). Four different LEED patterns are shown in this work. The two patterns attributed to higher Ce coverages can be brought in line with the low- and intermediate coverage images of Tang *et al.* For low coverages, a $(5.6 \times 5.6)R30^\circ$ superstructure is reported, followed by a (2×2) structure superimposed on a very complicated pattern. The latter might be identical to the (1.94×1.94) phase reported but not shown by Tang *et al.*, if the superimposed structure is disregarded.

Baddeley *et al.* argue that the sixfold symmetry of all the LEED patterns indicate that the crystal structure corresponds to $CePt_5$ in the $CaCu_5$ structure. This phase is the only one that exhibits hexagonal symmetry and has a lattice constant in line with the observations. This statement has to be regarded with caution, since the formation of domains is to be expected. Two domains with threefold symmetry and rotated by 180° relative to each other would also lead to observation of sixfold symmetry with a technique that averages over rather large surface areas, such as LEED (see section 4.1.4).

Nevertheless, the STM results of Baddeley *et al.* support the assumption that the surface compounds exhibit the $CePt_5$ structure. Although at first glance a variety of surface phases was observed, all of them are consistent with the $CePt_5$ structure, which is schematically shown in fig. 2.7. The manifold phases seen in STM are attributed to different lattice parameters, different orientations of the compound and to the two possible bulk terminations of the structure.

The lattice parameters appear contracted for samples produced from low Ce deposit. They approach the $CePt_5$ bulk values for higher initial Ce coverage. This supports the obvious assumption that compound films with increasing thickness are grown when more Ce is available. Thicker films then have the possibility of releasing the strain imposed by the lattice mismatch between film and substrate.

The fact that the lattice is compressed rather than dilated is understandable if the compound structure is rotated by 30° with respect to the substrate, thus having to adapt to a $(\sqrt{3} \times \sqrt{3})R30^\circ$ reconstruction. Indeed, the non-relaxed phases investigated by Baddeley *et al.* were all rotated except for one. This phase is assigned to $CePt_2$ termination, which is however reported to appear on terraces between rotated Kagome layers. It is possible that the assignment of the rotational alignment was based on the underlying triangular lattices. These are rotated with respect to each other for the two layer types (see green and blue triangles in fig. 2.7). If the Kagome lattice is regarded as a continuation of the substrate with every fourth atom missing, thus representing a non-rotated (2×2) reconstruction, a non-rotated $CePt_2$ layer would belong to a rotated superstructure.

It should be noted that the stoichiometry, which contradicts the result of Tang *et al.*, was not determined independently in this work. Furthermore, STM is, in principle, not capable of providing insight into the structure below the surface. As major support for the $CePt_5$ structure, an STM image is presented that shows terraces of a compound surface after long exposure to the residual gas of the vacuum recipient. Only every second terrace is subject to considerable contamination. This finding is interpreted as resulting from alternating layers in the structure, with Ce residing in every second layer. These layers are expected to be more sensitive to adsorption than the pure Pt layers in between.

The phase corresponding to the reactive terraces is denoted as a minority phase when annealing Ce films deposited at room temperature, but represents the majority of the surface when Ce is evaporated onto a heated substrate. Hence, with the former preparation method, most of the surface is Pt terminated and relatively inert against contamination.

Despite this inertness, Schierbaum showed in 1998 that Ce-Pt(111) compounds can be oxidized under controlled conditions at elevated temperatures, leading to the formation of ordered CeO_2

films [84]. Since CeO_2 as well as Pt surfaces play central roles in three-way car exhaust catalysts, this model system caused considerable interest. Consequently, a number of application-oriented surface science studies on oxidized Ce-Pt(111) have been published, which also treat the pure surface compound [85–88].

The increasing interest in the Ce-Pt(111) system also enhanced the focus on structural properties. In a 1999 publication by Pillo *et al.*, primarily showing Fermi surface maps of a Ce-Pt(111) compound, the authors mention photoelectron diffraction results that reveal a sixfold symmetric local environment of the Ce ions [89]. On the basis of the known Ce-Pt bulk phases, this finding is interpreted as either resulting from hexagonal $CePt_5$ or two domains of cubic $CePt_2$ possessing threefold symmetry. Results obtained with the same method on La-Pt(111), which is assumed to be isostructural to Ce-Pt(111), were published by Ramstad *et al.* in 2000 [90]. The data measured for both constituents were interpreted as not fully conclusive, but consistent with the $CaCu_5$ structure. Concerning the terminating surface layer, strong support for the assumption of a pure Pt termination of the Ce-Pt(111) compounds was found in CO adsorption experiments by Vermang *et al.* in 2006 [91].

An elaborate study by Essen *et al.* regarding the structural and adsorption properties of Ce-Pt(111) surface compounds for a wide range of initial Ce coverage was published in 2009 [70]. Pt termination is again confirmed, independent of the amount of Ce deposited.

The authors present a phase diagram for LEED patterns as a function of annealing temperature and Ce coverage. Five different phases are distinguished. Next to a simple (1×1) reconstruction at very low coverage, a more precise distinction of the low-coverage phases with and without satellite spots reported by Tang *et al.* is given by correctly assigning the rotation with respect to the substrate. At higher coverage, the phase resembling a $(\sqrt{3} \times \sqrt{3})R30^\circ$ superstructure as reported by Garnier *et al.* is included, followed by the phase with superposition of rotated and non-rotated (2×2) patterns which had previously been reported by Tang *et al.*, Baddeley *et al.* and Schierbaum. The lowest-coverage $(5.6 \times 5.6)R30^\circ$ phase reported by Baddeley *et al.* is not mentioned. It would be expected in a coverage range that is designated by Essen *et al.* to show a (1×1) pattern. The (1.96×1.96) phase reported by Tang *et al.* for their highest Ce coverage is also missing. Apparently, such high coverages were not attained by the authors.

In their LEED images, Essen *et al.* discriminate two lattice parameters, namely 2 and 1.98 times the Pt(111) surface lattice constant. The order of appearance of the individual phases with increasing initial Ce coverage in their phase diagram is (1×1), (2×2), $(2 \times 2) + (1.98 \times 1.98)R30^\circ$, $(1.98 \times 1.98)R30^\circ$ and $(1.98 \times 1.98)R30^\circ + (1.98 \times 1.98)$. As an explanation for the pattern with satellite spots appearing in the third phase, multiple scattering processes between the two designated structures are proposed. The decrease of the lattice constant is again explained with lattice relaxation, which in this case starts from a dilated lattice, opposite to the results of Baddeley *et al.*

The observed lattice constant progression with increasing Ce coverage is interpreted as a transition from a "surface-like" to a more "bulk-like alloy". Since all relevant $CePt_x$ phases possess separate Pt Kagome nets and Ce containing layers as a common building element, the topmost layers of a compound film can always be constructed from these elements. Therefore, different stoichiometries cannot be distinguished for very thin compounds, especially if the film thickness is less than one unit cell. It is furthermore argued that, for adsorption studies, the exact nature of the underlying Laves phase does not actually matter. While in principle true, this approach is not adequate when applying spectroscopic methods which are surface sensitive, but have a probing depth of several atomic layers.

While spectroscopic investigations were the main topic of the PhD thesis of M. Klein finished in 2009, structural aspects of the Ce-Pt(111) surface intermetallics were also touched upon in this work [92]. Most importantly, results of theoretical modeling using local density approximations (LDA+U) regarding the surface structure are reported. Meanwhile, these calculation have been published by Tereshchuk *et al.* [93]. They yield an energy optimum for surface termination with a Pt Kagome layer modified by additional Pt atoms placed in the holes, i.e., on top of the first Ce atoms. The resulting densely closed Pt surface layer provides a natural explanation for the strong inertness of the samples.

The spectroscopic experiments of Klein addressed Ce $4f$ electrons by PES. In the Ce-Pt(111) compounds, these do not only exhibit signatures of single impurity Kondo behavior, but also indicate a transition to a coherent heavy fermion state. As published in 2011 by Klein *et al.* [94], angle resolved PES measurements with very high resolution were performed to measure the k-resolved spectral function for temperatures down to $T = 13$ K. While $4f$ related contributions were identified by resonant PES, an optimized evaluation procedure of the low-temperature data revealed the opening of a small energy gap of the size of $E_{\text{gap}} \approx 2$ meV. This finding is interpreted as the hybridization gap due to renormalization of the band structure, as the system undergoes the transition to a coherent heavy fermion state (see section 1.3). The interpretation is supported by theoretical modeling.

In another publication of the same group, Schwab *et al.* addresses the question of hybridization strength and Kondo temperature for Ce-Pt(111) in comparison to the similar material Ce-Ag(111) [95]. LEED images of a non-rotated and a rotated (2×2) reconstruction are shown for the Pt-based system.

The publications that are presented in the present section provided the background for the present work. The identification of the surface compounds as heavy fermion system, which was only possible on a single crystalline sample with a well-controlled surface, qualified the Ce-Pt(111) system as an ideal starting point for XMCD investigations of Kondo and heavy fermion systems.

In advance of the present thesis, a Master's thesis covering first LEED, XAS and XMCD investigations on Ce-Pt(111) surface compounds was completed in the workgroup by A. Köhl [96]. Her results provided a valuable basis for the present work. Two further works on Ce-Pt(111) were completed in the workgroup in the course of the present thesis: The Bachelor's thesis by S. Götz [97] treats some aspects of the results presented in chapter 10. The Diploma thesis by M. Zinner primarily treats the related material Ce-Ag(111), which is referred to in appendix A.4, and compares it to Ce-Pt(111) [98].

Chapter 3

Basic requirements of sample preparation and characterization

Contents

The present chapter provides a basis for sample preparation and characterization, the results of which are presented in chapter 7. Section 3.1 treats basic concepts of crystallography and introduces the required nomenclature. In section 3.2, the necessity of ultra high vacuum for most of the present experiments is accounted for.

In addition, several auxiliary experimental techniques are briefly introduced: Deposition control with a quartz microbalance (section 3.3), Auger[1] electron spectroscopy (section 3.4) and scanning transmission electron microscopy (section 3.5).

The methods of most importance for the present work, low-energy electron diffraction, X-ray absorption spectroscopy and X-ray magnetic circular dichroism, are treated in detail in separate chapters.

3.1 Crystallographic issues

In solid-state physics, certain concepts for the description of crystals are established. It is the aim of the present section to introduce a number of definitions, nomenclatures and notation styles that are used in the present thesis. Further information can be found in the literature, e.g. in the book by Kittel [99].

The crystal lattice

Solid-state crystals are characterized by a high degree of order. Disregarding the finite size and the defects of real samples, the atomic arrangement can be described by infinite translational repetition of a unit cell. The underlying translational operations and the unit cell volume are defined by the same set of linearly independent vectors $\vec{a}_1, \vec{a}_2, \vec{a}_3$, called unit cell vectors in the following. The choice of the unit cell is not unique, which is why conventions for its construction exist.

---

[1] Pierre Auger, French physicist, 1899-1993

One approach is to find a unit cell with a volume as small as possible, which is called the primitive unit cell. Amongst other techniques, this can be achieved by the Wigner[2]-Seitz[3] construction. The primitive unit cell vectors then define a point lattice, which reflects the symmetry of the crystal. In three dimensions, 14 symmetry-inequivalent point or Bravais[4] lattices exist. Most of them are invariant under more symmetry operations than just translation. In particular, rotational symmetry is of importance.

In many cases, the primitive unit cell does not directly exhibit the symmetry of the point lattice. In this case, larger unit cells are commonly chosen to represent the point lattice type. For example, the cubic unit cell of the face-centered cubic (fcc) lattice contains four lattice points.

A lattice point can represent more than one atom in the crystal structure, which equivalently means that the primitive unit cell contains more than one atom. This is apparently the case for crystals composed of several elements, since each unit cell has to contain at least one formula unit. For a full description of the crystal lattice, a so-called basis is therefore needed in addition to the point lattice. The basis is a list of the atoms in the primitive unit cell along with their coordinates.

The local symmetry of an atom can be governed rather by the atomic arrangement in the basis than by the point lattice. For example, if the primitive unit cell contains a tetrahedron of atoms A with a single atom B in the center, the local symmetry of atom B is defined by the tetrahedron, independent of the Bravais lattice. Such considerations are of importance for the description of crystal field effects (see section 2.1.2), which are governed by the local symmetry.

The reciprocal lattice

Many quantum mechanical problems are best formulated in momentum space, which is the Fourier[5] transform of direct space. Fourier transformation of a Bravais lattice yields the so-called reciprocal lattice, which is again a Bravais lattice. The reciprocal unit cell vectors $\vec{a}_j^*$ are defined by

$$\vec{a}_i \cdot \vec{a}_j^* = 2\pi\delta_{ij}. \tag{3.1}$$

Hence, the reciprocal of $\vec{a}_j$ is always perpendicular to the other direct unit cell vectors. It is only parallel to $\vec{a}_j$ if the lattice is cubic, tetragonal or orthorhombic. The magnitude of reciprocal lattice vectors has the dimension reciprocal length.

Miller indices

Directions and planes in crystals are commonly expressed by sets of three Miller[6] indices. The direction [uvw] is defined by the vector $\vec{v} = u\vec{a}_1 + v\vec{a}_2 + w\vec{a}_3$, while the symmetry plane (hkl) is defined perpendicular to the reciprocal lattice vector $\vec{g} = h\vec{a}_1^* + k\vec{a}_2^* + l\vec{a}_3^*$. By definition, the Miller indices are integers written as such that their greatest common divisor is 1. Negative values are expressed by an overbar instead of a minus sign.

The surface lattice

The surface is a very special part of a crystal, since it breaks the translational symmetry. Therefore, unit cell vectors directly at the surface are commonly chosen in a different way than in the bulk. It is convenient to define a surface unit cell by two vectors parallel to the surface, which are complemented by a third vector perpendicular to the surface. This construction is consistent with the bulk Bravais lattice if the surface plane can be characterized by Miller

---

[2] Eugene Paul Wigner, Hungarian-American physicist, 1902-1995

[3] Frederick Seitz, American physicist, 1911-2008

[4] Auguste Bravais, French physicist, 1811-1863

[5] Jean Baptiste Joseph Fourier, French mathematician and physicist, 1768-1830

[6] William Hallowes Miller, British crystallographer, 1801-1880

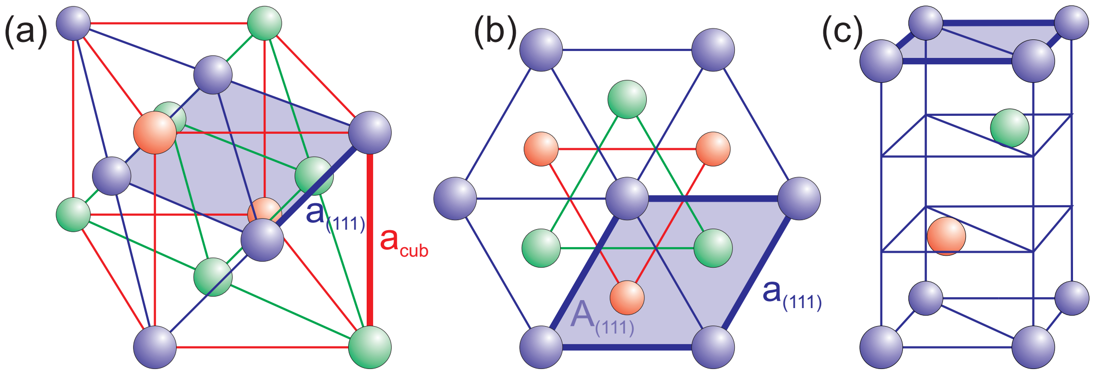

Figure 3.1: (a) Sketch of the cubic unit cell of the *fcc* lattice. Circles represent lattice points or atoms for the case of a monoatomic basis. Red: Outline of the cubic unit cell. Purple and green: Exemplary (111) planes. Shaded purple: Area of the (111) surface unit cell. (b) Top view of the purple surface layer illustrating the hexagonal character of the (111) surface lattice. The green and red circles correspond to atoms in deeper layers. (c) Three-dimensional primitive unit cell of the *fcc* structure in hexagonal representation.

indices. This is normally the case, since termination at a high-symmetry plane with low indices is usually most energy-efficient, making those planes the natural growth and cleavage surfaces or locally stabilizing them by refacetting.

The two-dimensional lattice defined by the surface unit vectors can again be categorized as one of the five existing two-dimensional Bravais lattices. The point lattices of bulk and surface can belong to completely different classes. Fig. 3.1 illustrates the situation for the (111) surface of an *fcc* lattice.

A representative of this example is the Pt(111) surface, which was used as substrate in the present work. Pt crystallizes in the *fcc* structure with a monoatomic basis (cubic unit cell shown in panel (a)). The two-dimensional surface unit cell is hexagonal, also with a monoatomic basis (panel (b)). Its continuation into the bulk yields a three-dimensional hexagonal cell. However, in order to obtain the *fcc* structure in hexagonal representation, a basis including three lattice points (or atoms) has to be chosen (panel c). Therefore, the fundamental Bravais lattice of the structure is *fcc*, not hexagonal. Furthermore, the sixfold rotational symmetry inherent to the hexagonal point lattice of the surface layer is reduced to a threefold symmetry due to the arrangement of atoms in the three-dimensional unit cell (see panel (b)).

Superstructures and domains at surfaces

Surface reconstructions, adlayer or thin film deposition and surface alloying can alter the surface structure. Consequently, the surface unit cell can be different from simple bulk truncation. In the present work, the notation after Wood is used to characterize such superstructures at surfaces [9]. The Notation $(\mathcal{S}_1 \times \mathcal{S}_2)R\varphi$ corresponds to a superstructure unit cell with vectors $\vec{a}_i^{\mathrm{ss}} = \mathcal{S}_i \cdot \vec{a}_i^{\mathrm{sub}}$, which is furthermore rotated by φ with respect to the substrate surface lattice. The angle notation is omitted for unrotated superstructures.

The symmetries of superstructure and substrate surface lattice can be quite different. This is especially the case if $\mathcal{S}_1 \neq \mathcal{S}_2$. As a consequence, domains of the superstructure can be formed. Returning to the example of the (111) surface of an *fcc* lattice, the hexagonal representation shown in fig. 3.1 (b) and (c) has threefold rotational symmetry. Hence, it has two different options to register onto a sixfold symmetric hexagonal surface lattice: as shown and rotated by $\varphi = 60°$. In a real system, both orientations will most likely be degenerate in energy and will therefore coexist with uniform distribution.

3.2 The Ultra High Vacuum setups

The experiments of the present thesis were almost exclusively performed under ultrahigh vacuum (UHV) conditions. Three different setups were applied:

Setup A: Most experiments were performed in this mobile vacuum system. The preparation unit and a superconducting 3 T magnet were mounted on a shared frame which could be moved and transported by truck. The measurement unit was optimized for XAS and XMCD measurements at the PM3 beamline at BESSY II[7], Berlin, and is described in section 5.4.3. Setup A was used for LEED characterization and for the experiments at BESSY.

Setup B: This vacuum chamber was stationary in Würzburg. Unlike setup A, it was equipped with an Auger electron spectrometer and was used for characterization of a series of samples. The specimen for the STEM investigation was also prepared here.

Setup C: The third vacuum system belonged to the DEIMOS[8] beamline at SOLEIL[9]. Similar to the BESSY setup, it primarily consisted of the preparation chamber and a measurement unit for XAS and XMCD. The latter is also described in section 5.4.3.

All three preparation units were equipped with a sample manipulator, which allowed translation and rotation of the sample as well as sample heating by electron bombardment. Furthermore, an Ar^+ ion gun for sputtering, a quartz microbalance and LEED optics were present in all setups. The LEED instruments were retractable, which allows more flexible usage of the available space and prevents contamination during other activities in the chamber. The device in setup C was additionally equipped with a shutter for that purpose.

The two main reasons for the necessity of an evacuated sample environment are best characterized by physical scales: The time scale of sample surface aging is determined by the monolayer formation time τ_{ML}. The mean free path λ_{MF} in the residual gas describes the inelastic length scale for particles that are sent to interact with the sample during the experiments.

The monolayer formation time is defined as the time until a surface free of adsorbants is covered by a complete monolayer of such. It strongly depends on the ambient pressure. During preparation of surface systems, the presence of adsorbates has to be prevented in order to avoid contamination and defects in the sample. Furthermore, contact with physi- or chemisorbed residual gas molecules can sensitively affect the physical properties of surface materials. For the $\mathrm{CePt_5/Pt(111)}$ surface intermetallics investigated in the present work, these aspects are addressed in section 7.1 and chapter 9, as well as in appendix A.3.

The mean free path of a gas is defined as the length that a particle in a gas can in average travel before interacting with another particle. It affects virtually all the experimental techniques that were applied in the present thesis, including sample sputtering, electron-beam annealing, molecular beam epitaxy of thin films and the analysis methods of AES, LEED, STEM and XAS/XMCD (see following sections). In all these techniques, electrons, ions, atoms or photons travel from their respective sources to the sample or from the sample to a detector. For the methods to work, λ_{MF} for the respective particles has to be considerably larger than the distances to overcome.

Nowadays, the techniques for vacuum generation are on a high standard. Hence, commercially available instruments were applied in the present work, which provide high quality and high reliability.

The vacuum recipients consisted of stainless steel chambers sealed with copper gaskets. For evacuation, turbo molecular pumps with additional roughing pumps, ion getter pumps and titanium sublimation pumps were applied. Furthermore, in the spectroscopic units of setups A and C the pumping effects of cryogenic parts were utilized, which were present for cooling

---

[7] Berliner ElektronenSpeicherring-gesellschaft für SYnchrotronstrahlung. The number II is omitted in the following.

[8] Dichroism Experimental Installation for Magneto-Optical Spectroscopy. Deimos is, next to Phobos, one of the two moons of Mars. In ancient Greek and Roman mythology, the twin brothers Deimos and Phobos were sons and companions of Ares or Mars, the god of war. Their names mean “dread” and “fear”, respectively

[9] Source optimisée de lumière d’énergie intermédiaire du LURE (Laboratoire pour l’utilisation du rayonnement électromagnétique)

of the sample and the superconducting magnets in first line. The pressure was monitored applying Bayard-Alpert ionization gauges as well as quadrupole mass spectrometers for residual gas analysis. For detailed descriptions of these instruments, the reader is referred to the literature [100–102].

After bake-out, base pressure values of $p \lesssim 5 \cdot 10^{-10}$ mbar were obtained, with lower values for the chambers hosting cryogenic parts. In this regime, the mean free path of gas molecules is already beyond 100 km, which exceeds the dimensions of the applied vacuum recipients by far. However, pressure that low is necessary to obtain monolayer formation times in the order of hours, when a sticking coefficient of unity is assumed as an upper border [101]. With the exception of the X-ray absorption measurements, this is a typical time scale for the present experiments. Even more importantly, the sample preparation procedure can be performed considerably faster than that. Hence, a solid basis for the experiments was provided by the vacuum chambers.

3.3 The quartz microbalance

A commonly applied technique to determine the growth rate of a deposition experiment is the so-called quartz microbalance, which was introduced by Sauerbrey in 1959 [103]. The term “balance” refers to the fact that the mass of the deposited material m_d is measured. This is done by monitoring the change of the eigenfrequency f_0 of a quartz crystal with time during deposition onto the crystal surface and concluding towards a change of the crystal mass.

Commonly, quartz crystals cut along a plane tilted by $\theta = 35°$ with respect to the c-axis are used (AT crystals). They possess a small temperature dependence of f_0 near room temperature and have a broad technical application in time measurement. The eigenfrequency is measured by using the crystal as the capacitor in an oscillatory circuit.

The relevant crystal oscillation is a shear vibrational mode. Hence, the wavelength and the frequency of the fundamental oscillation depend on the crystal thickness d_Q via the relation $f_0 = v_\mathrm{Q}/2d_\mathrm{Q}$, with the elastic wave velocity v_Q. Expressing d_Q by mass m_Q, area A_Q and density ρ_Q of the crystal, the frequency can be written as

$$f_0 = \frac{v_\mathrm{Q} \rho_\mathrm{Q} A_\mathrm{Q}}{2 m_\mathrm{Q}}. \tag{3.2}$$

The change of frequency with mass change is then

$$\frac{df}{dm_\mathrm{Q}} = -\frac{v_\mathrm{Q} \rho_\mathrm{Q} A_\mathrm{Q}}{2 m_\mathrm{Q}^2} = -\frac{2 f_0^2}{v_\mathrm{Q} \rho_\mathrm{Q} A_\mathrm{Q}}. \tag{3.3}$$

This relation is valid if the additional material has the same elastic wave velocity and density as quartz. In general, this is not the case. Nevertheless, as long as the deposited mass is small compared to the mass of the quartz crystal, that is, if the frequency shift relative to the initial eigenfrequency amounts to less than a few percent, eq. 3.3 is a good approximation. Hence, $dm_\mathrm{d}/df \approx dm_\mathrm{Q}/df$.

In principle, it is possible to derive a more accurate description that also holds for crystals with thick overlayers of foreign material. However, this requires knowledge of the elastic properties of the overlayer material. The balances of the present work were also used for other deposition experiments with material different from Ce, which complicates the exact calculation. Furthermore, the total amount of deposited material was small. Therefore, the practical approach was to work with the approximation and rather exchange the crystal if the frequency deviation became too large. This did not happen during the work on the present thesis.

A possible error source for microbalance measurements is the temperature of the quartz crystal. It usually increases as material is evaporated onto the microbalance, due to radiant heat from the evaporation source and thermal energy transported by the deposited molecules. A change of temperature induces a change of the eigenfrequency and can thus resemble a change of mass. Therefore, the measurements have to be performed in thermal equilibrium, which is obtained after appropriate standby time. To better control this aspect, the microbalance can be equipped with water cooling facilities.

The experimental geometry is another aspect to be considered when the mass gradient of the microbalance is interpreted as a growth rate on the sample. Microbalances are often used to monitor the evaporation rate during deposition. Consequently, the balance is at a different position and in general subject to a different rate than the sample. In the present experiments, the microbalance was moved to the sample position. The high stability of the electron beam evaporator allowed performing a reliable rate measurement prior to deposition onto the sample, such that a correction of geometric aspects was not necessary.

With these considerations in mind, the gradient of the frequency over time τ can directly be translated to a rate of mass deposit per area via the relation

$$\frac{dm_{\mathrm{d}}}{d\tau A_{\mathrm{Q}}} = -\frac{v_{\mathrm{Q}}\rho_{\mathrm{Q}}}{2f_0^2}\,\frac{df}{d\tau} = -C_{\mathrm{Q}}\,\frac{df}{d\tau}. \tag{3.4}$$

The quartz parameters can be summarized in a constant with value $C_{\mathrm{Q}} = 12.181$ ng/cm^2 Hz for a quartz crystal with an initial eigenfrequency of $f_0 = 6$ MHz, as used in the present work.

Most commercial devices readily calculate the measured mass per area to a film thickness for a given film density. For the present experiments, it is more meaningful to calculate the number of deposited atoms per substrate surface unit cell (compare section 7.3). The substrate is the (111) surface of an *fcc* Pt crystal as depicted in fig. 3.1. The cubic lattice constant of Pt is $a_{\mathrm{cub}} = 0.3924$ nm at room temperature [104]. Hence, the (111) surface lattice constant amounts to $a_{(111)} = a_{\mathrm{cub}}/\sqrt{2} = 0.2775$ nm and the area of the surface unit cell is $A_{(111)} = \sqrt{3}/2\ a^2_{(111)} = 0.0667$ nm^2.

Hence, the Pt(111) surface contains 15 atoms per square nanometer. A hypothetical, pseudomorphously grown layer of Ce atoms then weighs $m_{\mathrm{pseudo}} = 15$ at/nm$^2 \cdot 140.1$ u/at $= 348.58$ ng/cm^2. In section 7.3 it is shown that annealing a Ce coverage equivalent to one such layer leads to a surface alloy with a thickness of approximately four unit cells CePt$_5$. Hence, the measured frequency change with time can be calculated to a deposition rate $\mathcal{R}$ via

$$\mathcal{R} \;=\; -\frac{C_{\mathrm{Q}}}{m_{\mathrm{pseudo}}} \cdot \frac{df}{d\tau} \;=\; -0.0349\ \mathrm{layers/Hz} \cdot \frac{df}{d\tau} \;=\; -0.1396\ \mathrm{u.c./Hz} \cdot \frac{df}{d\tau}. \tag{3.5}$$

This allows the calculation of a deposition time for a measured frequency gradient and a desired amount of Ce deposit (see section 7.1). In fig. 3.2, exemplary frequency measurements are shown, which were obtained during Ce evaporation for three different evaporator settings. The linearity of the frequency over time is indicative of constant evaporation rates. The given rate values were calculated using eq. 3.5 for the slope results of linear fits.

3.4 Auger Electron Spectroscopy

Atoms that have been excited by creation of a core-hole emit electrons that show an element-specific energy distribution. This distribution is hardly altered when the atoms are embedded into a solid crystal, since processes in core-near electron shells are rather insensitive to the details of the valence electrons. Since furthermore the inelastic mean free path of electrons in solids is usually of the order $\lambda_{\mathrm{MF}} \leq 1$ nm for kinetic energies in the range $\Delta E = 10 - 1000$ eV [105], spectroscopy of these electrons yields a method for the analysis of the chemical composition near a sample surface.

The underlying process is the Auger-Meitner[10]-effect [106, 107]. It is a special case of autoionization, which is addressed in section 8.2.4. For ions with a core-hole, this effect represents one of the two options for relaxation, next to X-ray emission.

In both cases, an electron from an orbital higher in energy recombines with the core-hole. In

---

[10] Lise Meitner, Austrian physicist, 1878-1958

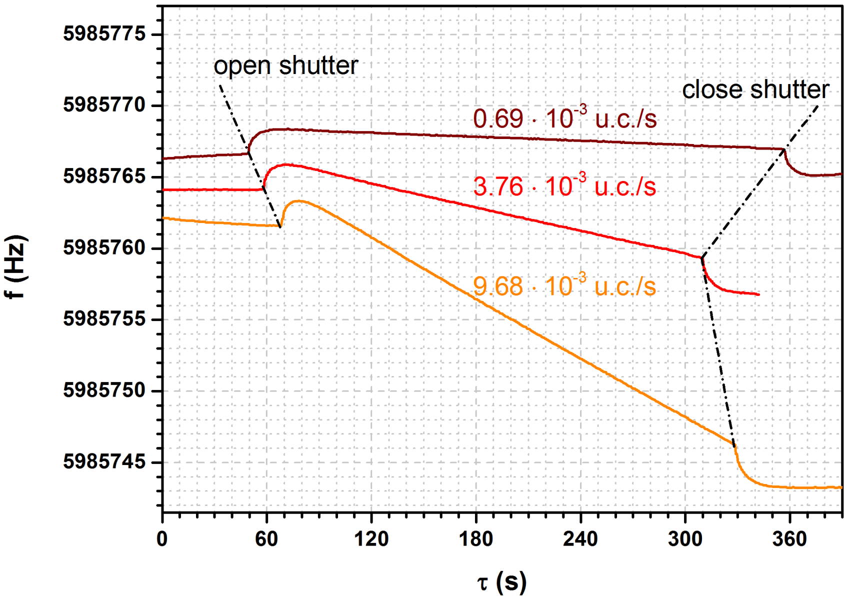

Figure 3.2: Exemplary quartz microbalance measurements during Ce evaporation for evaporator emission current settings of 75 , 85 and 100 mA (dark red, red and orange curve, respectively). The measured frequency is plotted versus time. Growth rates are given, which were calculated from fit results for the slopes according to eq. 3.5. The measurements were performed in the preparation unit of setup C.

this course, energy is left over which can either be released by emitting a photon or another electron. The efficiency of the two competing processes depends on the atomic number Z, Auger electron emission predominates for lighter elements. Whether the initial ionization occurs by X-ray absorption or electron bombardment makes no difference.

The energy that is gained by the recombination of the core-hole, E_{rec}, is transferred to the Auger electron. Since the work function E_{WF} has to be overcome to escape into vacuum, the kinetic energy of an Auger electron is $E_{\mathrm{kin}}^{\mathrm{Auger}} = E_{\mathrm{rec}} - E_{\mathrm{WF}}$. Depending on the number of electrons in a given atom, the core-hole, the recombining electron and the Auger electron can originate from different orbitals. Orbital energies strongly depend on the core potential and thus on the proton number, which gives rise to the element-specificity of $E_{\mathrm{kin}}^{\mathrm{Auger}}$.

Measurement of the electron count rate $N(E_{\mathrm{kin}}^{\mathrm{Auger}})$ yields peaks at the discrete energies belonging to the possible transitions in the given elements and is called Auger electron spectroscopy (AES). A detailed account of this technique is, e.g., given in the book by Ertl [100].

In the present work, AES was applied to confirm the absence of contaminations and to highlight the change in chemical composition at the specimen surface during several steps of sample preparation. These results are presented in section 7.1

For the experiments, a commercial Auger spectrometer was used. Electrons that were produced and accelerated in an electron gun[11] were directed towards the sample for excitation. The returning Auger electrons were detected after passing a cylindrical mirror analyzer for kinetic energy filtering. To obtain higher sensitivity, the detection was performed with Lock-In technique under variation of the potentials in the analyzer. Hence, the derivative $dN(E)/dE$ of the spectrum was measured. The experimental UHV setup that was used (setup B as described in section 3.2) allows very fast recording of high-quality spectra without the need to transfer the sample from the preparation position. Thus, it was also possible to characterize samples in intermediate preparation states that are sensitive to contamination, which necessitates short standby times even in UHV.

---

[11] This is similar in LEED devices, see section 4.1.4

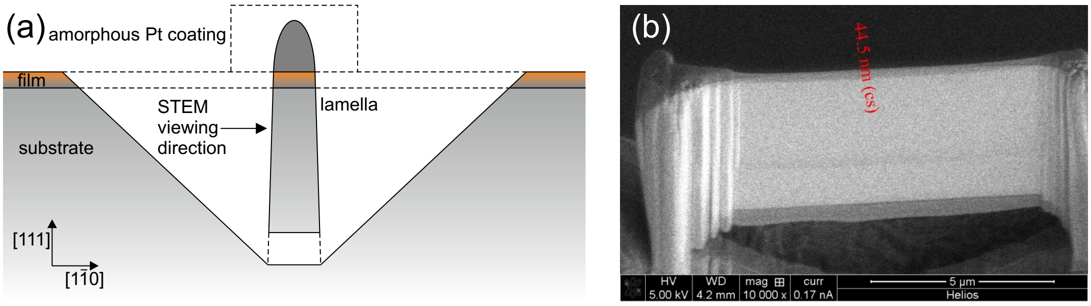

Figure 3.3: (a) Schematic of cross-sectional STEM lamella preparation with a FIB, not drawn to scale. The coordinate system is given with respect to the Pt(111) substrate. (b) Scanning electron micrograph of the finalized lamella attached to the STEM sample holder. The cross-sectional measurement (red) gives the approximate width of the lamella at the upper edge.

3.5 Scanning Transmission Electron Microscopy

The quartz microbalance (see section 3.3) allows calibration of the amount of material per area that is deposited to a surface. Assuming a homogeneous film, this quantity is directly connected to the film thickness as well as to the material density, which in turn depends on the crystal structure. Hence, one of the other two quantities has to be independently determined to obtain the complete picture.

For the $CePt_5$/Pt(111) intermetallic films of the present work, neither the crystal structure nor the film thickness resulting from a certain amount of deposited material were definitely known. In order to close this gap, cross-sectional Scanning Transmission Electron Microscopy (STEM) images of a lamella cut from a sample with nominal thickness of $t = 10$ u.c. were recorded. The results of this investigation are presented in section 7.3.

STEM provides real-space images with atomic resolution. Electrons from a high brightness cold emission gun are focused on the sample, yielding a scanning electron probe of sub-nanometer diameter. Accelerated by high voltages of $V = 300$ kV, the electrons possess an inelastic mean free path of $\lambda_{\mathrm{MF}} \approx 100$ nm in the sample. This allows detection of a bulk-sensitive signal in transmission mode behind a sufficiently thin sample.

The experimental facilities, a FEI Titan 80-300 (S)TEM and a FEI Helios Nanolab dual-beam system, were provided by the Wilhelm Conrad Röntgen[12]-Center for Complex Material Systems. Lamella preparation and microscopic imaging were performed by M. Kamp.

The following description of sample preparation and image formation is aimed at an understanding of the present data. A detailed treatment of the applied techniques can be found in the literature [108–111].

Sample preparation

Transmission electron microscopy requires specimen with a thickness in the order of λ_{MF}. For solid-state crystals, this makes high demands on sample preparation, especially when imaging of the cross-section of a thin film is desired. The method of choice for this task is focused ion beam (FIB) milling. It has the further advantage of destroying only a small portion of the sample, namely a few hundred μm^2 of surface area.

The sample used for STEM investigations was prepared in the standard way as described in section 7.1 in the UHV setup C. The crystal was then removed from the vacuum chamber and brought to the dual beam facility. This transfer as well as the one of the final lamella from the dual beam system to the microscope was done under ambient conditions.

The dual beam facility represents a scanning electron microscope with an additional Ga ion source. The ion beam can be used for imaging, material abrasion and ion-induced deposition of material from process gas. The cross-section lamella was prepared in a standard way. First, the sample was aligned with respect to the orientation of the LEED pattern observed after

---

[12] Wilhelm Conrad Röntgen, German physicist, 1845-1923

preparation. Then an amorphous Pt coating was locally deposited onto the sample surface to protect the surface-near structure during ion bombardment and later lift-off. The lamella was excavated and subsequently thinned by repeated ion milling from both sides. The resulting geometry is schematically drawn in fig. 3.3 (a).

The lamella was then welded to an OmniProbe transfer tip by ion-induced Pt deposition and cut from the crystal. The tip was used to transfer the lamella to a STEM sample holder, where it was attached and finally thinned down to electron transparency. As can be seen in the electron micrograph of fig. 3.3 (b), this resulted in a cross-sectional thickness of $t \approx 44.5$ nm.

Image formation and interpretation

The spatial information of the image is given by the position of the electron probe, while the image intensity is obtained from the detector signal. In the present work, the microscope was operated with a High Angle Annular Dark Field (HAADF) detector. This means that, essentially, electrons are detected that have experienced Rutherford[13] scattering in the sample. The directly transmitted beam is excluded. Since the efficiency of Rutherford scattering sensitively depends on the atomic number Z, large material contrast is obtained by HAADF detectors.

The usage of a dark field detector leads to low intensity at high transmission and to high intensity if the electron beam encounters an obstacle, like, e.g., an atom. For solid-state samples, usually more than a single atomic layer is penetrated. Hence, after proper alignment of the electron beam with respect to the crystal structure, rows of atoms can be visualized as bright spots.

Consequently, STEM images provide the option to locally measure lattice parameters, like layer spacings. For this purpose, the following procedure was performed in the present work: The positions of atomic row projections were determined by an automated intensity peak finder algorithm in the image processing software ImageJ. The obtained positions were then assigned to layers, the data for each layer were linearly fitted. The average distance between layers was calculated from these fits. This evaluation was performed for as many layers as possible in each image to reduce statistical errors.

---

[13] Ernest Rutherford, British physicist and chemist, 1871-1937

Chapter 4

Low-Energy Electron Diffraction

Contents

Low-Energy electron diffraction (LEED) is among the most important techniques for surface crystallography. Certainly, one reason for its large impact is its flexible broad-range application. In addition to quick control of sample preparation, LEED was used for quantitative analysis of surface unit cell properties and even dedicated structure determination in the present thesis. The method largely contributed to the solving of the crystal structure of the $\mathrm{CePt_5/Pt(111)}$ surface intermetallics.

This chapter is divided into two parts: First, the geometric aspects of diffraction of electrons on crystals are discussed, which are required to understand and quantitatively interpret the observed LEED pattern as a projection of the reciprocal surface lattice. The second part concerns the method of LEED IV crystallography, where the energy-dependence of spot intensities is used to obtain a model for the surface-near crystal structure of a sample.

LEED IV is the more powerful usage of electron diffraction and the results of a mere geometric analysis, e.g., concerning the lateral unit cell dimensions, are more accurately obtained from LEED IV. In contrast, the experimental demands for sample alignment are much stricter for a geometric LEED analysis. In LEED IV, misalignment is a minor problem and can even be applied by purpose to enlarge the amount of information in a single experiment.

However, a comprehensive LEED IV analysis requires high computational effort due to the underlying trial-and error-procedure. This effort can significantly be reduced by any information that is available concerning the crystal structure under investigation. The required information can be obtained from various experiments, which have to be chosen with respect to the material under investigation. Since the valuable information of the LEED pattern regarding structural symmetry and length scales is in any case available when performing LEED crystallography, the benefit of its careful inspection is self-evident. This justifies a detailed treatment of geometric pattern analysis.

The scope of the present text is to provide the background for interpretation of the experimental results of chapter 7. It is based on the books by Ertl and Küppers [100] and van Hove, Weinberg and Chan [112], as well as on the review of Heinz [113] and the PhD thesis of G. Held [114].

4.1 Geometric treatment of LEED

The most basic result of a LEED experiment is the two-dimensional diffraction pattern, which is a projection of the reciprocal surface lattice. Modern devices provide easy visualization of this pattern, which allows quick checks of sample quality. Furthermore, important quantitative information regarding the symmetry and length scales of the surface unit cell of a sample can be obtained from the pattern.

Such evaluations can be accurately performed on the basis of a simple geometric description, which is presented in the following. Principles of diffraction are discussed as well as the LEED pattern formation, which leads to the ideal design of a LEED experiment. Finally, possible experimental uncertainties, which have to be controlled for a quantitative interpretation, are analyzed and an optimized working scheme for image evaluation in the present experiments is derived.

4.1.1 Principles of diffraction on crystals

A wave that encounters an object is scattered at the edges. Consequently, wave intensity can be detected in the "shadow" behind the object, where a classical particle beam would be blocked by the object. This allows observation of interference effects, which become manifest as a spatially modulated intensity distribution, the diffraction pattern, in the case of a monochromatic wave. It arises from interference of waves that are scattered at different spatial coordinates and have thus traveled different distances. One of the best-known examples for diffraction is Young's[1] double slit experiment, which was first described in 1804 [115].

A maximum in the diffraction pattern is obtained for constructive interference, which occurs if the path difference between elastically scattered waves equals an integer multiple of the wavelength λ. This mechanism is depicted in fig. 4.1. It shows the two-dimensional Huygens[2] construction for a plane wave with wavevector $\vec{k}_\mathrm{i}$ and angle of incidence ϑ_i that is diffracted by two point scatterers of distance $a = |\vec{a}|$.

In the Huygens picture, the plane wave is scattered into spherical elemental waves by the scatterers. If only elastic scattering is considered, the wavelength is conserved. This allows constructing the wavefronts of the scattered waves from tangents to the wavefronts of the scattered spherical waves. This construction is equivalent to an approach where the time-evolution of the spatial coordinates with constructive interference, represented by points where two spherical wavefronts intersect, is analyzed.

The angle ϑ_n, under which a diffracted beam is observed, can be related to ϑ_i, λ and a. As depicted in fig. 4.1 (c) and (d), the auxiliary length ξ allows derivation of the expression

$$a\left(\sin\vartheta_n - \sin\vartheta_\mathrm{i}\right) = n\lambda \qquad \text{with } n \in \mathbb{Z}. \tag{4.1}$$

Apart from the trivial zero order beams (direct transmission and reflection), this interference condition can only be met if $\lambda \leq a$. Furthermore, different wavelengths lead to different diffraction angles. This is easily rationalized since $\vartheta_1' = \vartheta_2$ for $\lambda' = 2\lambda$. Hence, a polychromatic wave can be spatially monochromatized by diffraction.

Eq. 4.1 can be generalized to more complicated distributions of multiple scatterers. While diffraction on a string of equidistant scatterers does not change the condition, an ordered array

---

[1] Thomas Young, English polymath, 1773-1829

[2] Christiaan Huygens, Dutch mathematician, physicist and astronomer, 1629-1695

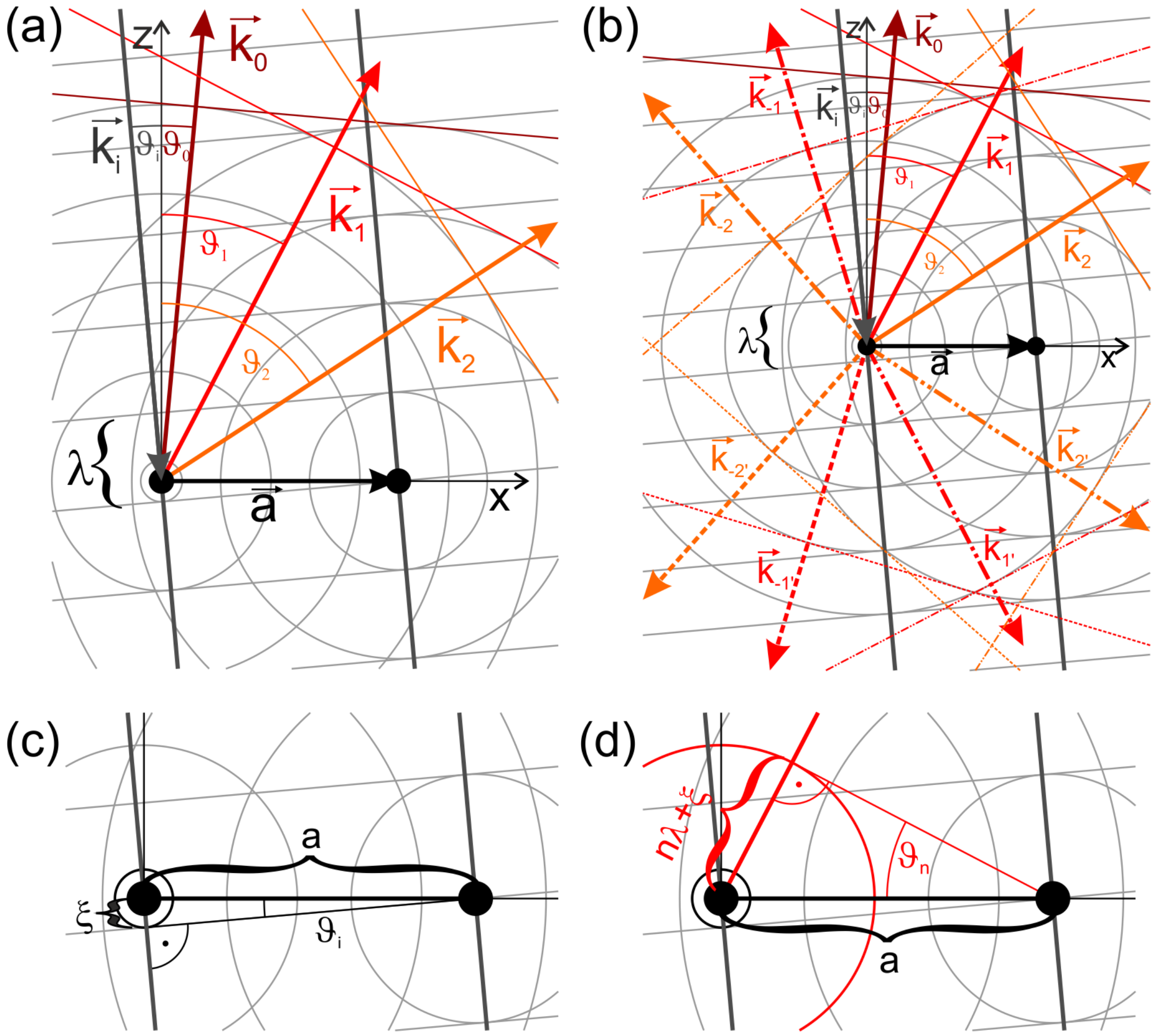

Figure 4.1: (a) Two-dimensional Huygens construction of diffraction of a planar wave with wavelength λ and wave vector $\vec{k}_\mathrm{i}$ by two point scatterers of distance $a = |\vec{a}|$. The angle of incidence is defined with respect to the z-axis, the general case of non-normal incidence $\vartheta_\mathrm{i} \neq 0°$ is shown. Zero, first and second order diffraction are constructed in directions $\vec{k}_n$ from the tangents to the wavefronts of the scattered elementary waves. For clarity, panel (a) only shows the case $\vartheta_n < 90°$. Panel (b) shows the construction for all four quadrants. Panels (c) and (d) show a zoom-in of the scatterer region. The auxiliary length ξ is defined and the relation of λ and ϑ_n is illustrated.

in two or three dimensions yields equivalent relations for the different Cartesian[3] directions. These conditions have to be fulfilled simultaneously to obtain a diffraction maximum. Hence, the diffraction pattern includes information about the symmetry of the diffracting object (e.g. circle, square, slit or regular array) as well as about the relation between the wavelength and the object's length scales.

In condensed matter physics, diffraction plays a central role in conjunction with X-rays, the wavelengths of which are of the order of interatomic distances in solid state crystals. This means that on one hand single crystals can serve as monochromator gratings for X-rays, while on the other hand diffraction of monochromatic X-rays on crystals can be used for determination of lattice constants. Even full crystal structures can be solved, if spot intensities are taken into account. This method has been pioneered in early 20th century by the works of von Laue[4] and father and son Bragg[5]. X-ray diffraction (XRD) is nowadays the fundamental technique of bulk crystallography.

---

[3] René Descartes, French philosopher, 1596-1650

[4] Max von Laue, German physicist, 1879-1960

[5] William Henry Bragg, 1862-1942 and his son William Lawrence Bragg, 1890-1971, British physicists

4.1.2 Diffraction of electrons

In accordance with the quantum mechanical wave description, diffraction can be observed for beams of photons, electrons, neutrons, atoms etc. Electrons that are directed towards a solid material interact with its electrons via Coulomb repulsion. Hence, the diffraction primarily takes place at the electron density distribution, which reflects the atomic lattice.

The kinetic energy E_{kin} that is needed to obtain electron wavelengths of the magnitude of interatomic distances can be calculated by the well-known de Broglie[6] equation [116]

$$\lambda = \frac{h}{mv} = \frac{h}{\sqrt{2m_{\mathrm{e}}E_{\mathrm{kin}}}} \approx \sqrt{\frac{1.5\ \mathrm{eV}}{E_{\mathrm{kin}}\ (\text{in eV})}} \quad \text{in nm.} \tag{4.2}$$

Here, m_{e} and v denote mass and velocity of the electron, respectively. Low kinetic energies of some electronvolts are sufficient to allow diffraction of electrons on single crystals with lattice constants of the order of $a \lesssim 1$ nm.

The experimental realization of low-energy electron diffraction was serendipitously discovered by Davisson and Germer in 1927 [117, 118], while Thomson and Reid verified diffraction of high-energy electrons in the same year [119].

As a consequence of the small electron wavelength, LEED can be applied for crystallographic investigations in analogy to X-ray diffraction. However, the interaction with matter is much stronger for electrons, which has important consequences. The resulting high rate of inelastic scattering leads to a penetration depth of a few nanometers only for electrons in solids, compared to micrometers for X-rays. Hence, the information obtained by LEED originates from the first few atomic layers only, which contribute very little to normal XRD. If one's interest lies in the crystal structure at a surface, LEED is therefore the method of choice.

Another consequence of the strong electron-matter-interaction is a significant probability for an electron to be scattered more than once. Hence, the scattering problem has to be formulated in a multiple-scattering description (so-called dynamical scattering theory). This introduces considerable complexity compared to the single-scattering description (kinematic scattering theory) that is applicable for XRD.

This results in higher computational effort and in the necessity of trial-and-error approaches for LEED crystallography, which is discussed in more detail in section 4.2. The geometric treatment of LEED is independent of multiple-scattering effects [112], which means that a considerable amount of information, especially regarding geometry and symmetry of the surface unit cell, can be deduced from LEED experiments without performing full dynamical calculations.

It should be noted that there are successful approaches to enhance the surface sensitivity of XRD [120]. However, these techniques require the use of synchrotron radiation. The smaller computational effort in evaluation is thus counterweighted by high experimental demands. In contrast, the facilities needed for LEED experiments are available in most surface science laboratories. Therefore, LEED was chosen to investigate the structure of the $\mathrm{CePt_5/Pt(111)}$ surface intermetallics in the present thesis.

4.1.3 Ewald sphere and diffraction pattern

An alternative formulation of eq. 4.1, which represents a form of the Bragg-condition, is the equivalent Laue-condition. It is deduced by using the incident and scattered wave vectors $\vec{k}_{\mathrm{i}}, \vec{k}_n$ and the relation $\vec{a} \cdot \vec{k} = -a \cdot k \cdot \sin(90° - \sphericalangle \vec{a}, \vec{k})$. For a three-dimensional lattice that is characterized by the unit cell vectors $\vec{a}_1, \vec{a}_2, \vec{a}_3$, three conditions arise, which read

$$\frac{\vec{k}_{\mathrm{i}} \cdot \vec{a}_j}{k_{\mathrm{i}}} - \frac{\vec{k}_{n_j} \cdot \vec{a}_j}{k_{n_j}} = n_j \lambda \quad \text{for } j = 1, 2, 3 \text{ and } n_j \in \mathbb{Z}. \tag{4.3}$$

If only elastic scattering with $k_{n_j} = k_{\mathrm{i}} = 2\pi/\lambda$ is regarded and with the abbreviation $\vec{k}_{\mathrm{i}} - \vec{k}_{n_j} =$

---

[6] Louis Victor Pierre Raymond de Broglie, French physicist, 1892-1987. Brother of Louis César Victor Maurice de Broglie.

$\Delta\vec{k}$, this simplifies to

$$\Delta\vec{k}\cdot\vec{a}_j = \Delta k^x a_j^x + \Delta k^y a_j^y + \Delta k^z a_j^z = 2\pi n_j \quad \text{for } j = 1, 2, 3. \tag{4.4}$$

Choosing the coordinate system and the unit cell in a way that $\vec{a}_1$ and $\vec{a}_2$ define the surface unit cell in the x-y-plane and $\vec{a}_3$ points perpendicular to the surface, the condition for n_3 becomes independent of the other two. Eq. 4.4 can then be divided into separate conditions for $\Delta\vec{k}_{||}$ and $\Delta k_\perp = \Delta k^z$:

$$\Delta\vec{k}_{||}\cdot\vec{a}_1 = \Delta k^x a_1^x + \Delta k^y a_1^y = 2\pi n_1 \quad \text{and} \quad \Delta\vec{k}_{||}\cdot\vec{a}_2 = \Delta k^x a_2^x + \Delta k^y a_2^y = 2\pi n_2, \tag{4.5}$$

$$\Delta k_\perp a_3^z = 2\pi n_3. \tag{4.6}$$

The two conditions in eq. 4.5 are fulfilled if $\Delta\vec{k}_{||} = \vec{g} = n_1\vec{a}_1^* + n_2\vec{a}_2^*$ by notice of eq. 3.1. This means that the momentum transfer in the surface plane equals a vector of the reciprocal lattice with respect to the two-dimensional surface lattice. An equivalent argument can be applied to eq. 4.6, but perpendicular to the surface another important aspect has to be considered: Due to the strong inelastic interaction of low-energy electrons in solids, the intensity of the electron wave is already considerably reduced after passing the first atomic layer. Hence, destructive interference of waves that are scattered in different layers does not generally lead to complete extinction. As a consequence, diffracted beams can be observed independent of the momentum transfer perpendicular to the surface.

A convenient way to picture the diffraction process is the so-called Ewald[7] sphere construction, which is exemplarily shown in fig. 4.2. A sphere with radius $k_\mathrm{i} = 2\pi/\lambda$ is drawn around a point where the crystal is thought to be. The direction of the incoming wave is defined by $\vec{k}_\mathrm{i}$, which originates in the sphere center. Then the reciprocal lattice $\{\vec{g}\}$[8] is drawn with its origin at the intersection of $\vec{k}_\mathrm{i}$ and the sphere. The relative orientation of $\{\vec{g}\}$ and $\vec{k}_\mathrm{i}$ is constructed via the real space lattice. It has a well-defined orientation relative to both and is therefore appropriate to define the Cartesian and spherical coordinate system.

For the case of a three-dimensional lattice, a diffracted beam is observed if a point of the reciprocal lattice lies on the surface of the sphere. This condition is equivalent to eq. 4.4. The direction of a diffracted beam can then be constructed by connecting the sphere center with the reciprocal lattice point. This condition is rarely met for a given crystal if λ and ϑ_i are fixed. Therefore, ϑ_i is commonly varied in XRD by rotating the crystal or using powdered or polycrystalline samples. Varying λ requires the use of synchrotron radiation (compare section 5.4.1) and is thus less practical.

The independence of LEED spot visibility of the momentum transfer perpendicular to the surface is represented by so-called diffraction rods in the Ewald picture. Those rods connect the reciprocal lattice points in the $k_\perp$ direction. A diffracted beam is then in general observed whenever a rod intersects with the sphere surface. Its direction is defined by connecting the sphere center with this intersection, as shown in fig. 4.2 (b). The intersections can then be projected onto a plane parallel to the crystal surface as drawn in fig. 4.2 (c). The such obtained diffraction pattern is a direct reproduction of the reciprocal surface lattice, containing valuable information on dimensions and symmetry of the surface unit cell.

In LEED, diffracted beams are present for most angles of incidences and wavelengths, which are both experimentally accessible degrees of freedom. The radius of the Ewald sphere increases with increasing E_kin, i.e., decreasing λ. As soon as the conditions in eq. 4.5 are met for $n \neq 0$, i.e., $\lambda \geq a$, the first diffraction rods intersect with the sphere, giving rise to diffracted beams. Their number increases when E_kin is further increased, the diffraction angle of a certain beam thereby gets smaller.

In the kinematic picture of electron diffraction, a diffracted beam has maximum intensity if the intersection of its diffraction rod with the Ewald sphere coincides with a reciprocal lattice point,

---

[7] Paul Peter Ewald, German-American physicist,1888-1985

[8] $\{\vec{g}\}$ denotes the set of all reciprocal lattice vectors, i.e., the reciprocal lattice

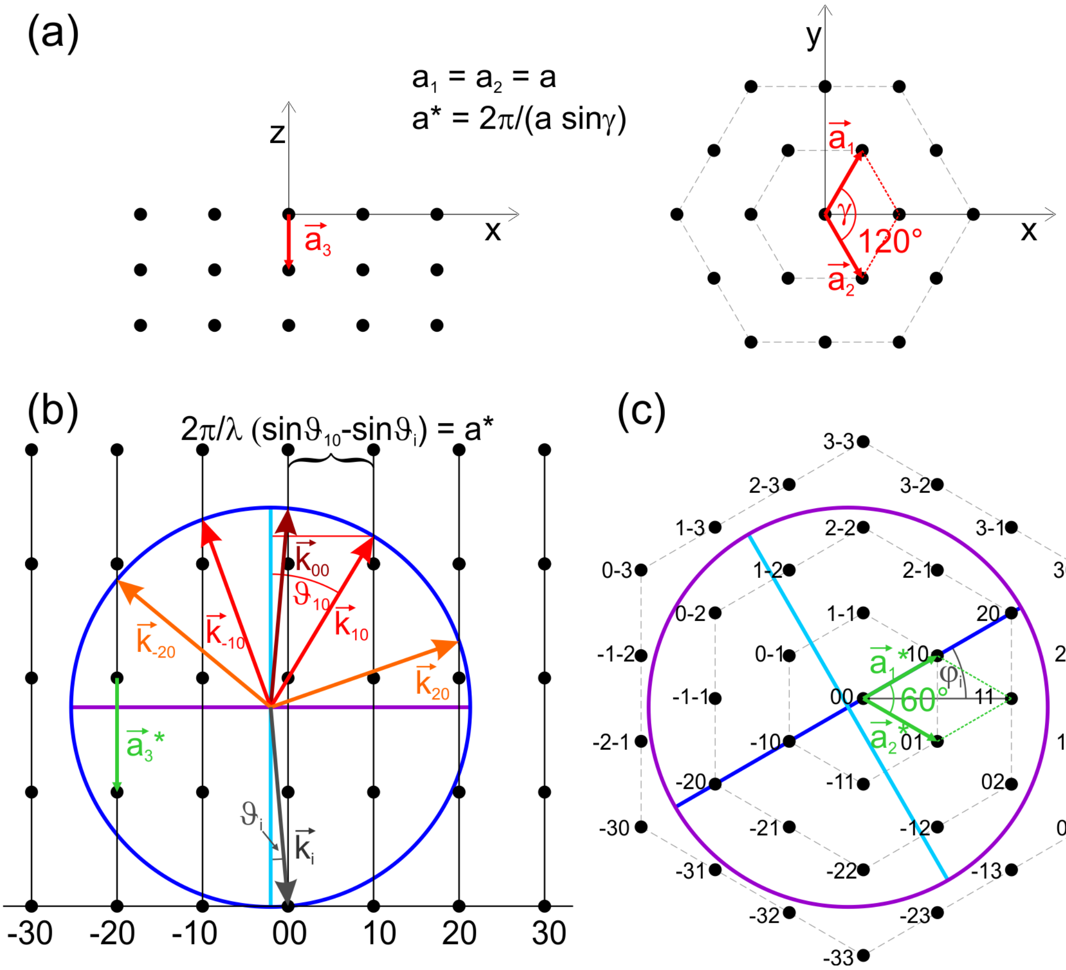

Figure 4.2: Ewald sphere construction for LEED at the example of the (001) surface of a simple hexagonal lattice. Cartesian (x,y,z) and spherical (ϑ,φ) coordinate systems are defined. In analogy to fig. 4.1, the general case of non-normal incidence ($\vartheta_\mathrm{i} \neq 0°$) is shown, which prepares for the discussion of sample misalignment in section 4.1.5. (a) Real space lattice with definition of the unit cell. Unit cell vectors are drawn in red, while reciprocal unit cell vectors are drawn in green in the following. The relation of real and reciprocal lattice vector lengths as a function of their angle γ is given according to eq. 3.1. (b) Reciprocal lattice viewed perpendicular to $\vec{a}_3^*$ and $\vec{a}_2^*$. The Ewald sphere projection and diffraction rods are shown. Directions of diffraction in the plane shown ($\vec{k}_{n0}$) are constructed as described in the text. (c) Reciprocal lattice viewed parallel to $\vec{a}_3^*$. The Ewald sphere projection is shown and diffraction beam indices are given.

i.e., if eq. 4.6 is additionally fulfilled. The beam intensity is thus connected to the position where the rod intersects with the sphere. Consequently, it changes as E_kin or ϑ_i are varied. For normal incidence ($\vartheta_\mathrm{i} = 0°$), all diffraction rods of the same order intersect at the same point. Hence, the intensity of the beams are expected to be equal, which is not the case for non-normal incidence. The simple picture of broadened Bragg peaks is strongly modified by complete dynamical LEED theory. Nevertheless, the concept of probing intensity profiles for individual beams by variation of energy or angle of incidence stays valid. These intensity profiles contain information about the complete crystal structure of the first atomic layers and thus provides the basis for LEED IV crystallography, which is addressed in section 4.2.

As a consequence, the beam intensities reflect the symmetry of the three-dimensional unit cell rather than the one of the two-dimensional surface unit cell. In a mathematic description of diffraction intensity, this is accounted for by the structure factor. Again, this is well pictured at the example of the (111) surface of an *fcc* crystal. As introduced in section 3.1, the three-dimensional continuation of the surface unit cell is simple hexagonal with a three-atomic basis. The diffraction pattern is hexagonal, as shown for a simple hexagonal unit cell in fig. 4.2. It exhibits sixfold rotational symmetry in accordance with the topmost atomic layer. However, the intensity profiles of the diffracted beams reveal the threefold rotational symmetry of the complete unit cell (see fig. 3.1 (b)): For example, in normal incidence the intensity profiles of the (1,0),(0,-1),(-1,1) and (0,1),(1,-1),(-1,0) beams (as labeled in fig. 4.2 (c)) are equal within the two groups, but differ between the groups. To account for this effect, the spots in each group are termed as symmetrically equivalent, whereas the two groups are inequivalent.

4.1.4 The LEED experiment

The three LEED apparatuses that were used in the present work (compare section 3.2) were four-grid standard display-type devices. The vast majority of LEED data was obtained with the instrument in setup A, which was of the ErLEED type, manufactured by SPECS GmbH, Berlin [121]. This design, which is schematically drawn in fig. 4.3 (a), is therefore at the basis of the following description.

In order to map the reciprocal lattice of an appropriate sample, the experimental setup should mimic the Ewald construction. This is achieved by a spherical detector with a radially incident electron beam, if the sample is placed in the center of the arrangement. These three key aspects, pattern detection, electron beam control and sample mounting, are discussed in detail in the following.

LEED pattern detection

The spherical detector is a glass screen, which is homogeneously coated with the transparent conductor indium tin oxide and phosphor. The latter fluoresces when hit by electrons, making the diffracted beams appear as luminous spots. To construct the spot positions, the Ewald sphere can be drawn with the radius of the screen sphere. The relative scaling of the reciprocal lattice with respect to the fixed sphere radius then depends on E_{kin}. Hence, the diffraction spots move towards the zero order spot as E_{kin} is increased, while more and more higher-order spots appear at the edge of the screen.

In order to produce bright spots, the electrons have to be post-accelerated to the screen, which is achieved by applying a high voltage of several kilovolts. The screen has an inner radius of $R = 66$ mm at a thickness of $t \approx 2$ mm and a maximal opening angle of $2\vartheta_{\mathrm{max}} = 100°$. The diffraction pattern is visible on both sides of the screen and most conveniently looked at trough a viewport in the vacuum recipient at the side facing away from the sample.

The diffraction pattern on the fluorescent screen has to be projected onto a plane in order to allow interpretation as the reciprocal lattice. This is directly evident from the Ewald construction shown in fig. 4.2 (b). Furthermore, the pattern has to be stored for quantitative analysis. Both, projection and storage, are obtained by photographic imaging of the screen[9].

In the present work, diffraction patterns were photographed with a commercial digital camera (Panasonic DMC-FZ28) by exclusion of any stray light. The camera was manually adjusted as such that the detector plane was parallel to the flat surface of the LEED viewport, which is assumed to be perpendicular to the incident electron beam. Angular uncertainties are estimated to $\Delta\vartheta_{\mathrm{Cam}} = 2°$ (see fig. A.1), the distance between screen and object lens was $d_{\mathrm{OS}} \approx 300$ mm (see fig. 4.4). Both angular misalignment of the camera and the finite d_{OS} lead to distortions of the photographed pattern with respect to the reciprocal surface lattice of the sample, which is discussed in detail in section 4.1.5.

For the photographs, the camera aperture was opened to the maximum at a value of F3.6. This allowed short exposure times, which were adjusted to obtain sufficient intensity without saturation of the detector. Typically, several seconds were chosen. The focus was manually adjusted to a spot on the screen halfway between electron gun and screen edge. For energy series, a picture was taken at each energy step, starting from low values and without changing any parameter except for E_{kin}. The images were stored in the jpg file format. This has the disadvantage of a possible loss of information, which was accounted for in experiments subsequent

---

[9] Early LEED optics were equipped with movable Faraday (Michael Faraday, English physicist and bookbinder, 1791-1867) cups for current measurement.

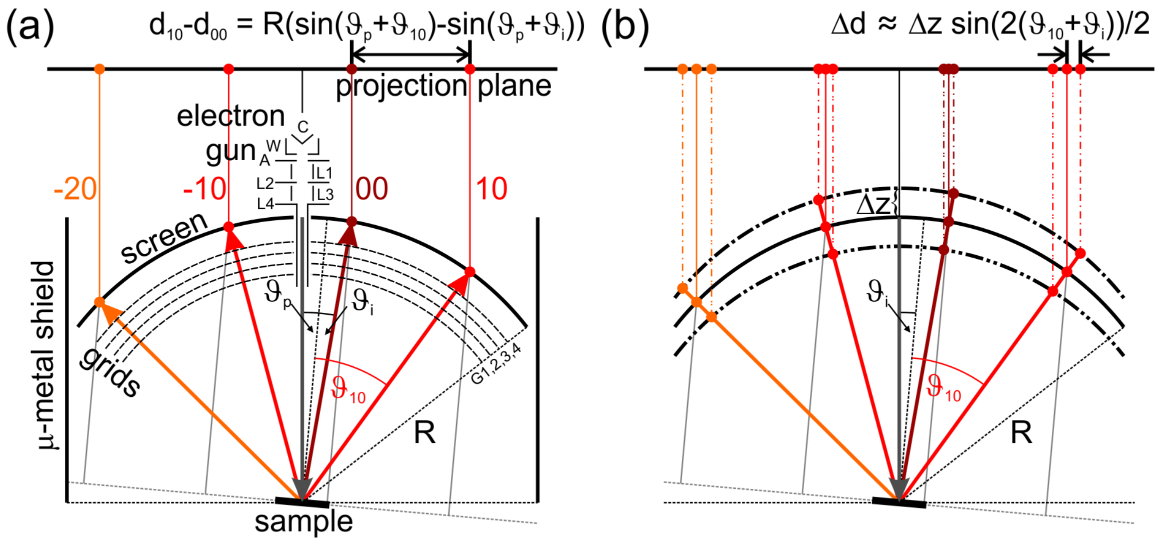

Figure 4.3: (a) Schematic of a LEED instrument as used in the present work, with reproduction of the Ewald sphere construction from fig. 4.2 (b). Additionally, the imaging at a projection plane perpendicular to the electron beam and with angle ϑ_p to the sample surface is constructed for non-normal incidence on the sample. (b) Geometric construction of the pattern distortion if the sample is placed out of the screen center. For derivation of the expression given for the spot displacement see appendix A.1.2.

to the present ones by using a raw image format [122, 123]. For the present analysis, no significant drawbacks are expected from using jpg images (compare section 4.2.6).

Electron beam control

The incident electron beam is produced in the electron gun, which is placed in the center of the screen calotte and aligned to emit radial to the screen sphere. It is designed very compact to obscure as little of the screen as possible and to emanate as little light as possible. The diameter of the electron beam at the sample that is produced by such electron guns is typically of the order of $2R \approx 1$ mm [100].

The beam is formed of free electrons that are created by thermal emission from a cathode (C in fig. 4.3). In the present experiments, cathodes made of $\mathrm{LaB_6}$ were used. The electrons are accelerated to their final kinetic energy E_kin by a negative potential that is applied to the cathode with respect to the electrically grounded sample.

The electron gun further consists of a number of electrostatic lens elements, namely the Wehnelt[10] cylinder (W), the Anode (A) and lenses L1/3 and L2. Different potentials relative to the acceleration voltage are applied to those elements in order to allow focusing of the diffracted beams on the detector screen. In order to account for energy-dependence of the focal conditions, most of the potentials can be scaled linearly with the energy. Offset and gain for these potentials were optimized for a given experiment by the benchmark of sharp spots and low background on the detector screen.

For successful experiments, field-free propagation of the electrons in the vacuum between electron gun, sample and detector is required. Hence, electrical charging of any components must be avoided. Furthermore, the electron trajectories have to be shielded from existing fields. For the earth's magnetic field, this is done by a thin sheet of μ-metal that encloses the setup.

Electric fields are present in the electron gun and at the detector screen.The former is shielded by the drift tube (L4), which is set to the potential of the sample. The spherical screen is accompanied with four concentric grids (G1-4) made of thin gold-coated molybdenum wire. G1 is set to the sample potential for shielding purpose, while G2 and G3 act as suppressor for inelastically scattered electrons. Those are reflected by a negative bias applied here, with

---

[10] Arthur Wehnelt, German physicist, 1871-1944

a magnitude slightly smaller than the kinetic energy. Two grids are used to counteract the electrostatic potential inhomogeneities produced by the mesh width of a single grid.

G4 is also grounded in the LEED measurement mode. It is of further importance when the instrument is operated as retarding field analyzer, which allows performing Auger electron spectroscopy. Due to the availability of a much faster and more sophisticated Auger spectrometer, this mode was not used throughout the work on the present thesis.

Sample mounting

The purpose of the sample mounting for LEED experiments is mainly to allow exact rotational and translational positioning. Additionally, a variable sample temperature can be desirable, which however requires special instrumentation. The LEED experiments presented in this work were all performed near room temperature.

The diffraction pattern of a misaligned sample is not a direct reproduction of the reciprocal surface lattice, but is subject to distortion. This is introduced in the following and quantitatively discussed in section 4.1.5.

The effect of angular misalignment can be understood in comparison of figs. 4.2 (b) and 4.3 (a). In the former, the projection plane is parallel to the sample surface. The projected pattern as shown in panel (c) reproduces the reciprocal surface lattice, while off-normal incidence merely causes the whole pattern to shift. Fig. 4.3 (a) shows the case for a non-zero angle ϑ_p between sample surface and projection plane. Consequently, the distance of two projected spots depends on ϑ_p and is not directly proportional to the reciprocal lattice constant.

It is in principle possible to align the camera with respect to the sample surface independent of the LEED instrument and ϑ_i. However, in practice it is much more convenient to work in the laboratory system with the vacuum chamber as reference. For the observation of undistorted patterns, both the optical axis of the camera and the sample surface normal have to be brought to coincidence with the fixed direction of the incident electron beam.

Hence, such experiments are best performed at normal incidence, which has the further advantage of producing symmetric spot intensities. However, the angular dependence of spot intensities yields structural information, which makes systematic off-normal incidence an important tool to access additional crystallographic data ina LEED IV study. Furthermore, in some materials certain diffraction spots exhibit zero intensity at normal incidence [124]. This can lead to a misinterpretation of the diffraction pattern if ϑ_i is not varied. Hence, all available degrees of freedom should be systematically tested in an experiment.

If the sample surface is translated out of the screen sphere center, the Ewald sphere does not coincide with the screen. Consequently, the observed pattern again appears distorted with respect to the reciprocal lattice, which is illustrated in fig. 4.3 (b). Translation of the sample parallel to the projection plane has no effect on the diffraction geometry. It can be used to scan the sample with the electron beam, which allows studying the homogeneity of the sample surface.

In summary, an ideal projection of the reciprocal lattice is obtained for sample positioning in the screen sphere center and alignment to normal incidence. For angular alignment in the present experiments, first of all the zero order spot was identified and roughly moved to the screen center. Since it is the only spot with an energy-independent position on the screen, this identification was done by varying E_kin. The energy was then chosen to produce spots near the screen edge and the angle was adjusted by eye to obtain a symmetrical image. This procedure is relatively sensitive, since rotation of the sample around a polar axis by a certain angle causes the diffracted beams to be displaced by twice that angle.

The precision in alignment could be enhanced, e.g., by laser-based methods. However, in the present experiments this would not have eliminated the major source of uncertainty: The design of the sample manipulator only allowed controlling the sample tilt in one direction *in situ*. The rotation perpendicular to this axis could not be fine-tuned in a given experiment, which usually prohibited to exploit the full potential of the applied alignment procedure. The remaining uncertainty in angular alignment is estimated to amount to $\Delta\vartheta_\mathrm{i} = 1^\circ$.

The translational positioning of the sample causes homogeneous pattern distortion, but no asymmetries as the angular alignment. Such distortions only become manifest in deviations of the absolute spot distance values, which cannot be identified easily during alignment. Hence, a procedure to optimize the position equivalent to the one for angular alignment is not available. Furthermore, the design of the experimental setups prevented that the sample was moved close enough to the instrument to be in the screen sphere center. Hence, it was moved as close as possible during the experiments. While the uncertainty in reproduction of this position is estimated to $\Delta z_{\mathrm{rel}} = 1$ mm, the systematic error is expected to be $\Delta z_{\mathrm{tot}} \approx 5$ mm.

4.1.5 Interpretation and analysis of experimental LEED patterns

In sections 4.1.1 to 4.1.3, the diffraction process is described in an ideal picture. However, many of the underlying assumptions are only approximatively met in real experiments. This affects the observed LEED pattern in two ways: First, imperfections of the electron gun have to be considered in the interpretation of the LEED pattern, especially in the case of complex sample surfaces including, e.g., different domains of finite size and defects. This is accounted for by the instrumental response function.

Second, misalignment of the experimental setup, as is discussed in section 4.1.4, lead to distortions of the observed pattern. Since the present experiments aim at a quantitative evaluation of lattice parameters, an estimate of the given uncertainties is presented in the following. The result of this analysis is that these uncertainties are too large to allow reliable determination of absolute lattice constants. Consequently, a working scheme for relative evaluations was developed, which is described at the end of the present section.

The instrumental response function

In a real LEED experiment, the incident electron beam is never a perfect plane wave. This is described by the instrumental response function of the electron gun. It has, amongst others, contributions from the energy uncertainty, the finite dimensions of the electron source and the beam diameter. The source extension has the largest impact [112].

The instrumental response function is one of the two main reasons for the diffraction spots to have finite width. Its knowledge allows separation of the other contribution, which is the imperfection of the crystal surface due to, e.g., steps and domain boundaries. This is utilized in the technique spot-profile analysis LEED, which requires special instrumentation that was not available for the present experiments.

Another consequence of the instrumental response function is a finite coherence length l_{c} of the incoming wave. This means that waves that are scattered at atoms at distance $a \gg l_{\mathrm{c}}$ cannot be considered coherent. The resulting phase shift prohibits simple interference as assumed for the derivation of eq. 4.1. For standard LEED instruments as used in the present work, the coherence length is typically of the order of $l_{\mathrm{c}} \approx 10$ nm [113].

The importance of l_{c} becomes apparent when simultaneous diffraction on structural domains with different reciprocal surface lattices $\{\vec{g}_1\}$ and $\{\vec{g}_2\}$ is considered. If the average domain size is larger than l_{c}, interference of waves that are scattered at the different structures can be neglected. The observed pattern is dominated by a mere superposition of $\{\vec{g}_1\}$ and $\{\vec{g}_2\}$. If the domain size is of the order of l_{c} or smaller, coherent multiple scattering between the two structures can occur. Consequently, diffracted beams are also observed if $\Delta\vec{k}_{\parallel} = \vec{g}_1 + \vec{g}_2$. This can give rise to additional spots.

Geometric pattern distortions

As introduced in section 4.1.4, the observed diffraction pattern only reproduces the reciprocal surface lattice if the experimental setup reflects the Ewald construction. This is achieved for normal incidence and if the sample surface is located in the screen sphere center. Experimental conditions can lead to deviations of this ideal geometry. Furthermore, the spots on the spherical screen have to be projected to a plane, which is only approximatively achieved by photographic imaging.

All of these aspects can produce distortion of the observed pattern and thus lead to errors in the measurement of lattice parameters. In the following, these errors are discussed and their expected magnitude is determined for the setup used in the present work.

The length scales of the projected pattern are represented by spot positions, which are measured as the distance d between a projected spot and the projected intersection of surface normal and screen (K as marked in fig. A.1). The choice of the reference point, which is not visible on the screen, arises from the fact that the surface normal defines the alignment of the reciprocal lattice, which makes the coordinate system of the sample the most convenient reference system.

For comparison of the different sources of distortion, the relative deviation of the spot position, $\Delta d/d$, is calculated for each of them and related to the polar diffraction angle ϑ_n of the spot.

If the projection plane is non-parallel to the surface, the projected pattern is distorted, which is introduced in fig. 4.3 (a). The distortion only occurs perpendicular to the tilt axis. Since sample and camera are aligned individually with respect to the instrument, two tilt axes with different tilt angles can exist. In the worst case, both effects add up. In order to estimate an upper border for the error, the total angular uncertainty of the present experiments is assumed as $\Delta\vartheta_\mathrm{p} = \Delta\vartheta_\mathrm{i} + \Delta\vartheta_\mathrm{Cam} = 3°$.

The relative spot displacement in dependence of ϑ_n in the small-angle approximation for ϑ_p is derived in appendix A.1.1 and reads

$$\frac{\Delta d}{d} \approx \frac{\cos\vartheta_n - 1}{\sin\vartheta_n}\,\vartheta'_\mathrm{p} \quad \text{with } \vartheta'_\mathrm{p} = \frac{2\pi\ \vartheta_\mathrm{p}}{360°}. \tag{4.7}$$

The resulting distortion is zero for $\vartheta_n = 0°$ and largest for $\vartheta_n = \vartheta_{max}$, where it amounts to $|\Delta d/d| \approx 2.4\ \%$ for the given geometry and uncertainty. Spot positions on one side of the screen appear enlarged, while they are underestimated on the other side. Hence, the error can be compensated by averaging results for d from measurements that are distributed homogeneously over the whole screen.

Translational misplacement Δz of the sample perpendicular to the projection plane is illustrated in fig. 4.3 (b). The magnitude of the resulting spot displacement Δd depends on the polar angle ϑ independently of the azimuthal angle φ. Hence the projected pattern appears radially distorted around the sample normal. A circle thus appears with an altered radius, while a square is subject to pincushion or barrel distortion. The relative displacement can be calculated via

$$\frac{\Delta d}{d} \approx \frac{\Delta z\ \cos\vartheta_n}{R} \tag{4.8}$$

as derived in appendix A.1.2. The basic assumption of the approximation applied there (see eq. A.11) is most critical for large angles and large displacement, but is well met for ϑ_{max}, R and Δz as assumed in the present work. $\Delta d/d$ is smallest for large ϑ_n, i.e., for spots near the screen edge. For the given geometry and the systematic sample misplacement, the relative spot displacement amounts to $\Delta d/d \approx 5 \ldots 7.6\ \%$. Since the distance between sample and screen was rather too large in the experiments, reciprocal lattice spacings would tend to be overestimated. The relative spot displacement due to alignment inaccuracy is smaller and amounts to $\Delta d/d \approx 1 \ldots 1.5\ \%$.

Another effect of translational sample misalignment is a further deflection of the diffracted beam between the grids and the screen. It occurs since the beam direction is not parallel to the radial electric field applied for post-acceleration. This effect counteracts the geometric distortion but is smaller by an order of magnitude [114]. Hence, it is not further considered here.

In addition to the effects of experimental misalignment, additional systematic pattern distortion occurs at photographic imaging of the fluorescent screen [114, 125]. The distance d_OS between screen and objective lens is usually not large compared to the screen radius R. Hence, the curvature of the screen, i.e., the ϑ_n-dependent object distance, cannot be neglected when interpreting the photographic image. Consequently, the photograph does not represent a projection to a plane, which is illustrated in fig. 4.4.

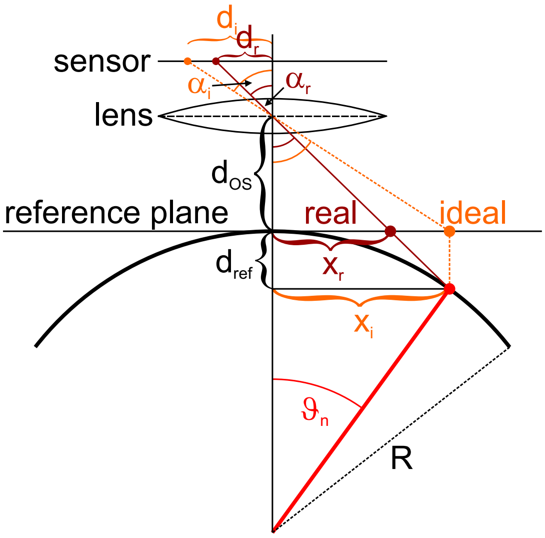

Figure 4.4: Illustration of the pattern distortion caused by photographic imaging of the curved screen.

An expression for the relative spot displacement between real and ideal image is derived in appendix A.1.3 and reads

$$\frac{\Delta d}{d} = \frac{1}{\frac{d_{\mathrm{OS}}}{R(\cos\vartheta_n - 1)} - 1}. \tag{4.9}$$

The arising distortion is again radial around the surface normal projection. While the effect vanishes for small ϑ_n, it is maximal at the screen edge where it amounts to $\Delta d/d = 7.3$ % for the given geometry. Spot distances thereby always appear curtate.

Fig. 4.5 summarizes the magnitudes of pattern distortion for the effects that were discussed above. Relative spot displacements are given in dependence of ϑ_n for eqs. 4.7, 4.8 and 4.9 and the expected uncertainties. Additionally, the sum of the three curves is shown. Under these conditions, an absolute evaluation of lattice constants from a LEED image would not be supposed to be exact within less than 7 %. However, the relative lattice relaxation of the $\mathrm{CePt_5}$/ Pt(111) surface intermetallics with increasing thickness (see chapter 7) amounts to only 4 %, which is far below the expected accuracy.

Working scheme for quantitative pattern analysis

Several strategies exist to address the problem of large pattern distortions. First of all, the accuracy in alignment could be improved. However, in the present work this would have required fundamental modification of the available experimental setup. Furthermore, the distortion that is caused by the screen curvature cannot be avoided by more precise alignment.

Since the major errors that are discussed here are of systematic nature, images could be corrected by applying correction algorithms. Such an algorithm, which is calibrated on a reference image of a known pattern, has recently been presented [126]. This method also covers possible sources of distortion that are not discussed here, such as, e.g., abberation of the camera's object lens.

A less sophisticated approach that aims into the same direction is to evaluate relative changes in spot positions for images that were taken under identical conditions. Especially when surface reconstructions are investigated, which are related to a well-known substrate pattern, this is a promising strategy. However, statistical uncertainties in obtaining these identical conditions remain, as is the case when applying correction algorithms. The relative spot position uncertainties due to statistical errors still amount to a few percent in the present setups. These uncertainties can be eliminated only by comparison of spots in one and the same image.

This approach requires samples that simultaneously exhibit several phases in the LEED pattern. This situation is given for overlayers that are thinner than the LEED information depth. In this

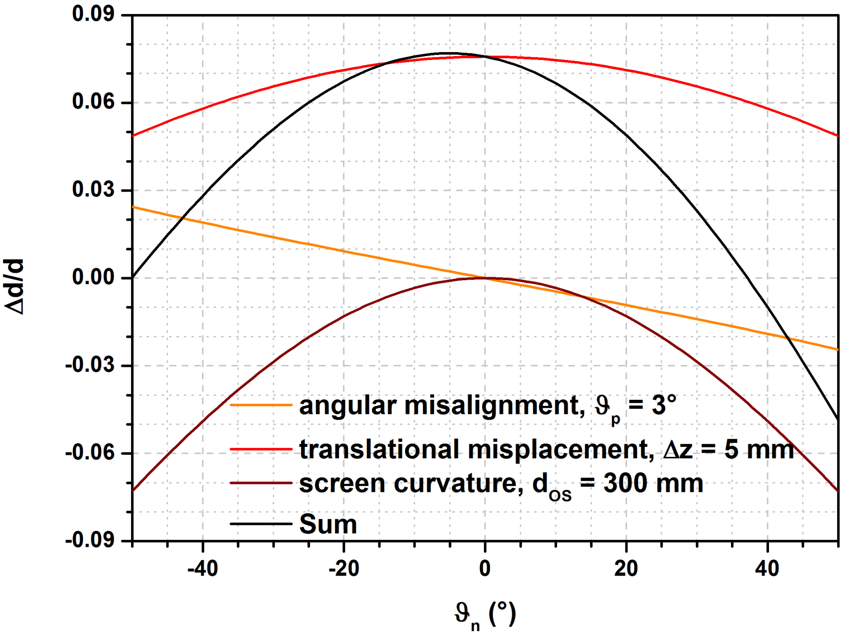

Figure 4.5: Relative spot displacement in dependence of the diffraction angle ϑ_n due to angular misalignment (eq. 4.7), translational sample misplacement (eq. 4.8) and screen curvature (eq. 4.9) for the given geometry and estimated uncertainties, as well as the sum of the three contributions.

case, the LEED pattern exhibits spots from both the overlayer as well as from the substrate, which can thus directly be compared. A very comfortable situation arises if thereby multiple-scattering spots appear. Those provide a large number of spots that can be related to each other, which allows a relative lattice constant determination with very high precision.

For the $CePt_5$/Pt(111) surface intermetallics of the present work, the described situations occurs for samples with different thicknesses. As is presented in section 7.2, this allowed a reliable lattice constant determination despite the high experimental uncertainties.

Due to the reasons stated above, the evaluation of lattice constants was restricted to relative measurements of patterns belonging to different phases but appearing in the same image. In order to control statistical errors, several measures were taken, which are described in the following.

Translational and rotational sample and camera alignment was performed as described in section 4.1.4. For photographing, the kinetic energy was then adjusted to produce the spots of interest with high intensity at a position approximately half way between electron gun and screen edge. For spot position evaluation, preferably spots with similar ϑ_n were chosen. As many symmetrically equivalent spots as possible were included and the results were averaged to reduce measurement errors. Spots that were uniformly distributed over the whole screen were chosen to account for asymmetric distortions caused by angular misalignment.

Distances between spots were determined by approximating the bright spot areas with ellipses in an image processing software and measuring the distance between the ellipse centers. This procedure was performed for as many different samples as were available and for different kinetic energy settings. For the different LEED patterns presented in section 7.2, at least three images were evaluated each, the results were averaged.

4.2 LEED IV crystallography

The previous sections were focused on the formation, measurement and interpretation of the LEED pattern, which represents the reciprocal lattice of the crystal surface under investigation. Its analysis yields valuable information on dimension and symmetry of the surface lattice. However, this information is not sufficient for determination of the full crystal structure in most cases. This is especially true for crystals with more than one atom in the basis, since only the

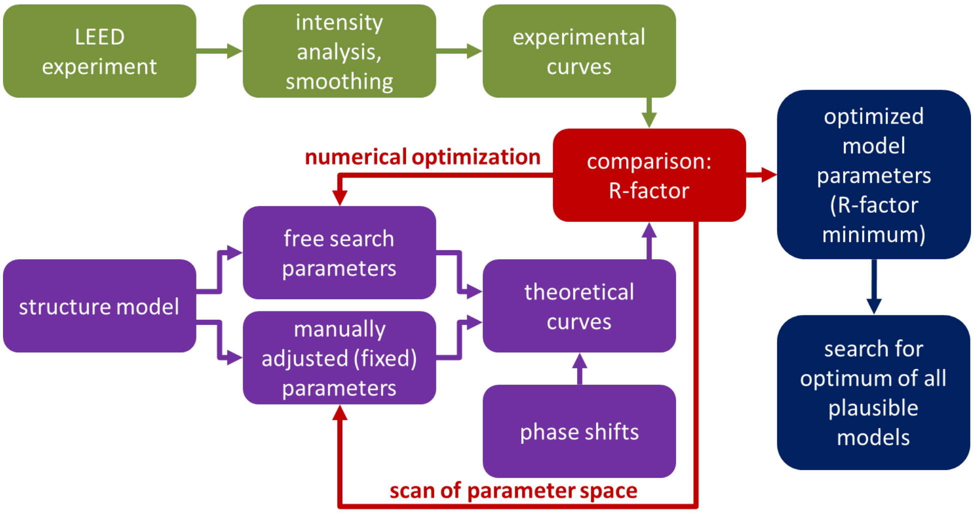

Figure 4.6: Workflow diagram of LEED IV crystallography. Experimental data (green) are compared to calculations based on a certain structure model and separately calculated phase shifts (purple). Model parameters are optimized to obtain the best agreement to the experimental data, which is measured by the R-factor (red). Comparison of the optimized R-factor values of all plausible structure models allows identification of the most probable crystal structure.

Bravais lattice is probed. Furthermore, the vertical dimension of the unit cell is not represented in the LEED pattern.

Nevertheless, LEED provides the possibility of crystallography, at least for the first few atomic layers. The strong interaction of low-energy electrons with solid matter causes the information depth to be low, but finite. While this allows observation of diffraction spots over large energy intervals (compare section 4.1.3), the diffracted intensity depends on the position where the diffraction rod intersects with the Ewald sphere, which is described by the structure factor. Consequently, the intensity profiles of LEED spots contain important structural information.

The profiles can be addressed by variation of the angle of incidence ϑ_i or the kinetic energy E_kin of the incident electrons. In the present work, the intensity I was recorded at a fixed angle of incidence as a function of E_kin, i.e., the electron acceleration voltage V. This method is called LEED IV and represents the most common approach.

Another consequence of the strong electron-matter interaction is the occurrence of a significant rate of multiple scattering, which has to be included into theory. The complexity of the thus required formalism prevents direct inversion procedures to extract the structural information from experimental data. Hence, a trial-and-error approach has to be applied for structure determination. In principle, intensity curves for all plausible structures have to be calculated and compared to the experiment. The result with the best agreement is then assumed to represent the real structure.

The workflow diagram of such an analysis is drawn in fig. 4.6. Experimental curves are obtained by extracting intensity data from a LEED experiment that has been performed on an appropriate sample (green). The experimental data are simulated by calculations that rely on a certain structure model and separately calculated phase shifts (purple). The agreement is quantified by an R-factor (red). This allows optimization of the model parameters to obtain best agreement with the experiment, which is either done automatically by an optimization algorithm or manually by scanning of the parameter space. The optimized R-factors of all plausible structure models are then compared to determine the most probable crystal structure.

The choice of the structure models to be tested is an important issue, since their number strongly governs the computational effort of a given LEED IV study. Hence, as much information as possible should be collected prior to starting the structure determination in order to narrow down the plausible structure models as well as the plausible parameter values.

The calculation of theoretical curves, the R-factor comparison and the structure model optimization in the present work were done with the CLEED package, which thus covers the purple and red parts in fig. 4.6. Access to this software and considerable support was provided by G. Held (University of Reading). This cooperation was started during the course of the present thesis and promoted three Diploma theses by work group members in advance of the present work [98, 122, 123].

CLEED represents a very powerful tool for LEED crystallography with a multitude of functions. The description that is given here is restricted to the aspects that concern the LEED IV analysis of a $CePt_5/Pt(111)$ sample, which is presented in section 7.6. The derivation of experimental $I(E)$ curves from a LEED experiment is described in section 4.2.1. The construction of the structure model and the parameter categories are discussed in section 4.2.2. Basic concepts of $I(E)$ curve calculation are presented in sections 4.2.3, 4.2.4 and 4.2.5. The central aspect of the method, the quantification of the agreement between experimental and theoretical curves, is described in section 4.2.6. Finally, the applied parameter optimization procedure is treated in section 4.2.7.

4.2.1 Extraction of experimental LEED IV curves

Since display-type LEED apparatuses were used in the present work, the LEED spot intensity at a certain energy had to be extracted from photographic images of the fluorescent screen. The photographs were taken as described in section 4.1.4 for an energy range $\Delta E = 35 \ldots 120$ eV in steps of $1 \ldots 2$ eV. The prolonged sample exposition time of more than an hour during image recording showed to be uncritical for the samples investigated here.

The experiments were performed at a fixed, but non-zero angle of incidence. This enhances the amount of information, since ϑ_i affects the direction-dependence of the multiple scattering mechanism. Consequently, symmetry-equivalent spots obtain different $I(E)$ curves. A total of 16 different spots was visible in substantial parts of the recorded energy range, five, six and five spots of (1,0), (2,0) and (1,1) type, respectively. The two missing spots were hidden by the electron gun assembly.

For the purpose of intensity curve extraction from digital photographs, the LIVe software programmed by R. Fradczyk was used [123]. After converting the color pictures to 8 bit grayscale, the intensity of each spot was extracted by integration of the brightness level of the image pixels in a circle with radius R_int including the spot. For background normalization, the integrated intensity in a ring between this circle and one with radius $R_\mathrm{bg} = \sqrt{2}\ R_\mathrm{int}$, thus possessing the same area and number of pixels as the inner circle, was used.

Due to the energy-dependence of LEED spot positions on the screen, a tracking procedure was applied. The spot positions can in principle be predicted for the whole pattern and all kinetic energies if the lattice symmetry and positions of three spots at a certain energy are known. However, one has to deal with the pattern distortions discussed in section 4.1.5. Those do not affect the relation of spot intensity and energy, but can complicate spot position prediction.

Therefore a different, more independent approach was used. The approximate pixel coordinates of spot centers were manually determined for the images at some selected kinetic energy values by using the agf_leed program written by K. Fauth. The program allows position determination and management of coordinates and energy values for large numbers of spots.

The such obtained energy-dependent coordinates were interpolated by fitting the measured data with one of the two empirical functions

$$x_i(E) = c_1\,(E - E_0)^{\pm 1/2} + c_2 \cdot E + c_3. \tag{4.10}$$

The choice depended on whether the values increased or decreased with energy. E_0 and $c_{1,2,3}$ are fit parameters [122].

The obtained $x_i(E)$ functions served as a starting point for an automated intensity maximum search, which was performed by the LIVe software. For this purpose, the cross-correlation of the image and a reference, called peak finder matrix, was calculated within a predefined search radius around the assumed spot position [123]. The applied peak finder matrix was designed

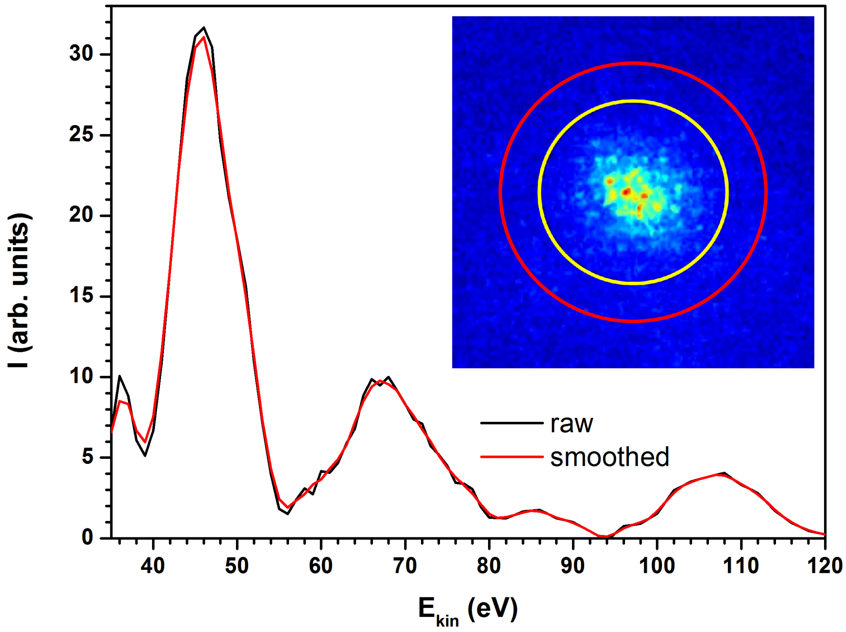

Figure 4.7: Raw and smoothed $I(E)$ curves of the (-1,0) Spot of a $CePt_5$/Pt(111) sample with nominal thickness $t \approx 4$ u.c. Inset: LIVe spot finding image for the same spot at $E_{\text{kin}} = 46$ eV. The spot intensity is integrated in the yellow circle with radius R_{int}, the background intensity in the ring between yellow and red circle.

to resemble an idealized spot. The position of highest cross-correlation was used as the spot position and the integration circles for peak and background were centered around it. Since the spot size decreases with energy, the integration radius R_{int} was accordingly adjusted.

For control purpose, the LIVe software generates images of each spot at each energy including the integration circle, which is exemplarily shown in the inset of fig. 4.7. The procedure has shown to yield reliable results[11], at the cost of being rather time-consuming. The manual spot position determination and interpolation for each spot requires high effort, while an automated spot finding procedure is still necessary to correct deviations from the interpolated positions.

One could also think of an algorithm that automatically tracks the spots when the kinetic energy is changed in small steps. As input, it would only require initial spot positions at the smallest energy value. Such programs are indeed commercially available[12]. However, difficulties arise if the spot intensity is very low over an extended energy range. In this case, the spot position has to be predicted from the preceding positions, which is subject to errors.

Such programs are valuable tools for quick checks of the $I(E)$ curves during the experiment. However, for thorough and detailed structure analysis, it is more advisable to invest the time for manual spot position determination. The effort for curve extraction is usually negligible compared to the computation time that is expended for the structure determination based on the obtained curves. A combination of both manual and automated spot position determination might be the ideal approach, but this option was not available in the present work.

As a last step, the curves that were produced by the intensity analysis were smoothed to reduce experimental noise. A simple three-point adjacent averaging algorithm was used, which replaces the nth data point by

$$I'(E_n) = \frac{I(E_{n-1}) + I(E_n) + I(E_{n+1})}{3}. \tag{4.11}$$

This procedure is similar to the one proposed by van Hove *et al.* [112]. Raw and smoothed data for an exemplary measurement are shown in fig. 4.7.

---

[11] Low R-factor values were obtained for clean single crystal surfaces [123, 127].

[12] see, e.g., the Safire program by Specs Surface Nano Analysis GmbH

	geometric	non-geometric
free	$\vec{x}_i$ (overlayer)	ϑ_i, φ_i
fixed	a, c	$V_\mathrm{o,i}$, Δr

Table 4.1: Overview of model parameters and their classification as (non-)geometric, fixed and free. See text for details.

4.2.2 The structure model and parameter categories

The construction of an adequate structure model is one of the major challenges of surface crystallography with LEED IV. It has to allow modeling of the experimental data with parameters that have physical meaning, while the number of free parameters should be kept as small as possible. In the following, the general construction of a structure model suitable for CLEED is described and the different parameters are introduced, whereas the concrete structure models for the present LEED IV study are presented in section 7.6.1.

The structure model for $I(E)$ curve computation is basically a list of the atoms in the structure along with their Cartesian coordinates $\vec{x}_i$ and a reference to the associated phase shift data (see section 4.2.5). Of course, lattice periodicity is exploited to keep the model manageable, which means that the list only includes atoms in a single unit cell and is complemented by the lattice vectors $\vec{a}$. These are the so-called geometric parameters of the model, as summarized in tab. 4.1. In principle, the atomic radii used to calculate the phase shifts could also be added to this list. They were not varied in the present work as discussed in section 4.2.5.

For the present structure model, the lateral lattice constants of overlayer and bulk are equal and only one length parameter a is needed for the hexagonal unit cell. The vertical lattice constant of the bulk is denoted c. Furthermore, the positions of the atoms in the bulk unit cell are directly given by the lattice parameters, which is why no $\vec{x}_i$ for the bulk appears in tab. 4.1.

The set of model parameters is completed by non-geometric parameters: The polar and azimuthal angles ϑ_i and φ_i, respectively, which define the direction of incidence (see fig. 4.2), the imaginary part of the optical potential $V_\mathrm{o,i}$ (see section 4.2.3) and the temperature-induced average displacement of the atoms Δr (see section 4.2.4).

The structure model that CLEED accepts as input can be divided into a bulk and an overlayer part. The overlayer part describes the surface-near region, its unit cell is only repeated laterally. The bulk is placed below the overlayer, its unit cell is repeated laterally and vertically in the direction away from the surface. This allows treating the scattering on the bulk lattice within the framework of layer doubling and the combined-space method (see section 4.2.3).

The design of the overlayer allows to model all kinds of surface structures, including relaxed top layers, surface reconstructions and adsorbate layers. Since arbitrary and complicated arrangements of atoms are thus possible, scattering in the overlayer cannot be treated layer-wise but has to be calculated for the complete arrangement. The number of atoms in the overlayer unit cell is often much larger than in the bulk, which causes it to yield the most substantial contribution to computation time.

As indicated in fig. 4.6, the model parameters are divided into such that are automatically optimized by CLEED and such that require a manually defined scan of the parameter space for their optimization. This leads to the classification as free and fixed parameters, as given in tab. 4.1. The former category includes the angles of incidence and the coordinates of atoms in the overlayer. The number of truly free parameters can be reduced by definition of restrictions that account for existing symmetries in the given crystal structure. They are formulated as dependencies of several coordinates and thus prevent numeric results that break these symmetries.

4.2.3 Concepts of LEED IV curve computation

The calculation of theoretical LEED IV curves presupposes the solution of the quantum mechanical diffraction problem of electrons at a crystal surface. In the present section, the basic concepts for this task and the approximations that are used in the CLEED package are briefly introduced. The description follows the book by van Hove, Weinberg and Chan [112], which is warmly recommended to the reader interested in a more comprehensive treatment.

In its full complexity, the LEED problem requires the consideration of interactions between the incident LEED electrons and all crystal electrons and nuclei in the probed sample region. Consequently, the Schrödinger[13] equation has terms for Coulomb and exchange interaction. Screening of the LEED electrons by conduction electrons is usually neglected.

Following the Bloch theorem, assumption of incident plane waves and lattice periodicity provide a basis for the resolvability of this problem in the Hartree[14]-Fock[15] formalism. However, the many-body character necessitates iterative self-consistent solution with high computational effort.

The exchange term can be simplified by Slater's[16] Xα approximation [128], which introduces the statistical exchange parameter α. Optimized values for α have been tabulated by Schwarz for most elements [129, 130]. The values for free atoms are commonly transferred to molecular and solid-state calculations.

The crystal structure of the sample is represented in the Schrödinger equation by its elastic scattering potential. It is commonly treated in the so-called “muffin-tin” approximation, which provides an adequate compromise between the required exactness and the computational effort that is maintainable for an iterative method like LEED IV. It relies on the idea that the atoms in the crystal can be modeled as non-overlapping spheres with radius R_{mt}, which separates the potential into regions “inside” and “outside” the atom. Outside, the potential of the nuclei is screened by the crystal electrons, which leads to a constant scattering potential. Inside the atoms, the screening is not complete, since significant probability density of core electrons is located further outward. Hence, a spherically symmetric potential is assumed. At the transition between spheres and region with constant potential, the wave functions are continuously matched.

The muffin-tin model is certainly a drastic simplification. In particular, atoms directly at the surface generally experience a highly non-spherical environment. Nonetheless, various crystallographic studies have shown its practicability, which can be justified by the fact that LEED electrons possess energies significantly above the Fermi level. Hence, they mainly interact with the inner electrons and the nuclei of the crystal atoms, which possess spherical symmetry [113].

The muffin-tin model has two major advantages: First, the complexity of the problem is reduced by allowing separation into radial and angular parts. Second, the problem is divided into scattering inside and outside the muffin-tin spheres, which can be solved independent of each other. As an important consequence, the scattering inside the spheres only has to be solved once per atomic species. It represents scattering at a single atomic site, which includes, in fact, multiple scattering with the various core electrons. Multiple scattering between different atoms is treated in the region outside the spheres.

The assumption of spherical symmetry allows description of the scattering inside the spheres in terms of sums over phase shifts δ_l, where l is the angular momentum quantum number when representing the problem in spherical coordinates. The magnitude of δ_l in general decreases with increasing l, which is why the summation is truncated at some value l_{max}. The choice of l_{max} depends on R_{mt} and E_{kin} via $l_{\text{max}} \approx k \cdot R_{\text{mt}}$. As a practical value for LEED, $l_{\text{max}} = 9$ can be estimated from simple considerations [112]. The calculation of phase shifts, especially the procedure applied in the present work, is described separately in section 4.2.5.

For the scattering of spherical waves on a single atom, a matrix operator $\hat{t}$ in the angular momentum basis can be constructed from the δ_l. Since $0 \leq l \leq l_{\text{max}}$ and $-l \leq m \leq l$, $\hat{t}$ has dimension $D = (l_{\text{max}} + 1)^2$. At proper choice of the coordinate system, the (l, m) representation of $\hat{t}$ is degenerate in m and it is furthermore diagonal due to angular momentum conservation [114]. The coefficients are defined by

---

[13] Erwin Schrödinger, Austrian physicist, 1887-1961

[14] Douglas Rayner Hartree, British mathematician and physicist, 1897-1958

[15] Wladimir Alexandrowitsch Fock, Soviet physicist, 1898-1974

[16] John Clarke Slater, American physicist and Chemist, 1900-1976

$$t_l = -\frac{\hbar^2}{2m_\mathrm{e}k}\sin\delta_l\, e^{i\delta_l}. \tag{4.12}$$

The calculation of the phase shifts includes the finite atomic dimensions. For the further treatment of scattering on the muffin-tin potential, the atoms can equivalently be regarded as point scatterers producing this phase shift. The potential in between these point scatterers is the constant muffin-tin background, also called the optical potential V_o. In principle, different potential values can be assigned to different regions in the sample, e.g., for substrate and adsorbates, which gives rise to potential steps. In the present calculations, only a single potential step at the surface was considered.

A constant potential adds to the kinetic energy of the incident electrons. Hence, it produces a shift of the energy axes of the $I(E)$ curves. In order to remove one dimension from the parameter space, CLEED automatically shifts the calculated curves to obtain the best fit to the experimental data. V_o is then manually adjusted to compensate this shift. As a side effect of this procedure, a possible experimental offset of E_kin due to, e.g., miscalibration of the electron gun, is also compensated or rather transferred to an uncertainty of the resulting value of the real part of the optical potential, $V_\mathrm{o,r}$.

In order to include the strong inelastic interaction of LEED electrons in a solid and the resulting surface-sensitivity, the optical potential also has an imaginary part $V_\mathrm{o,i}$. Consequently, the wave number of an electron traveling in the crystal also becomes complex, leading to a length scale for damping of the wave amplitude.

The LEED penetration depth corresponds to the inelastic mean free path λ_IMF of electrons in solids. It is in general energy-dependent, since the processes leading to energy loss, like plasmon excitation, are energy-dependent. However, $\lambda_\mathrm{IMF}(E)$ can be described by a universal curve that exhibits a broad minimum at the typical LEED energies [105]. Hence, the variation of the penetration depth is small in LEED, which justifies the approximation by a constant.

In principle, $V_\mathrm{o,i}$ is directly present in the $I(E)$ curves. In the kinematic picture, the exponential damping of the incident electron wave leads to a broadening of the Bragg peaks. The line shape of the broadened $I(E)$ peaks is determined by the square of the Laplace[17] transform of the exponentially damped, harmonic electron wave, which leads to a Lorentzian[18] profile[19] in $I(\Delta k_\perp)$ [45].

Consequently, translating $I(E)$ to $I(\Delta k_\perp)$ and fitting of kinematic peaks with a Lorentzian yields $V_\mathrm{o,i}$ as the half width at half maximum, which is typically of the order of $V_\mathrm{o,i} \approx 4\ldots5$ eV [113, 114]. However, this procedure only gives an estimate, since purely kinematic peaks are not easily identified. In the present work, $V_\mathrm{o,i}$ was therefore optimized for the calculated curves to obtain the best agreement with experiment.

The remaining problem consists of multiple scattering of electrons on a lattice of point scatterers, with the wave amplitude being damped as the waves proceed in the crystal. The effect of the point scatterers can be expressed by the atomic scattering operators $\hat{t}$ in angular momentum representation. Hence, the electron wave functions are best expanded in spherical waves.

In order to include multiple scattering, spherical waves emerging from some atom i have to be expanded in spherical waves with respect to the position of another atom j. This leads to the introduction of propagators or Green's[20] functions $\hat{G}^{ji}$. Representing the propagators in the same basis as the $\hat{t}$-matrices for single atom scattering, multiple scattering paths can be expressed by matrix multiplication chains of alternating scattering and propagation events.

The full problem can be solved self-consistently considering multiple-scattering up to infinite order. Denoting the sum of all scattering paths ending at atom n as $\hat{T}^n$, for N atoms the following set of N equations can be written:

---

[17] Pierre-Simon de Laplace, French mathematician and astronomer, 1749-1827

[18] Hendrik Antoon Lorentz, Dutch physicist and mathematician, 1853-1928

[19] see eq. 6.4 for the analytic expression and compare section 5.1.3, where the Lorentzian profile is introduced for lifetime widths in XAS

[20] George Green, British mathematician, physicist and miller, 1793-1841

$$\begin{array}{lllllll}\hat{T}^1 & = & \hat{t}^1 & + & \hat{t}^1\hat{G}^{12}\hat{T}^2 & + \ \dots \ + & \hat{t}^1\hat{G}^{1N}\hat{T}^N \\ \hat{T}^2 & = & \hat{t}^2\hat{G}^{21}\hat{T}^1 & + & \hat{t}^2 & + \ \dots \ + & \hat{t}^2\hat{G}^{2N}\hat{T}^N \\ \vdots & & \vdots & & \vdots & & \vdots \\ \hat{T}^N & = & \hat{t}^N\hat{G}^{N1}\hat{T}^1 & + & \hat{t}^N\hat{G}^{N2}\hat{T}^2 & + \ \dots \ + & \hat{t}^N \end{array} . \tag{4.13}$$

It should be noted that one atom can appear several times in a multiple scattering path, but not multiple times in a row. This would correspond to multiple scattering within a single atom, which is already included in the atomic scattering operators $\hat{t}$.

The total scattering amplitude can be obtained from the complete set of $\hat{T}^n$ matrices. Denoting unit matrices as $\hat{I}$, eqs. 4.13 are solved by

$$\begin{pmatrix}\hat{T}^1 \\ \hat{T}^2 \\ \vdots \\ \hat{T}^N\end{pmatrix} = \begin{pmatrix}\hat{I} & -\hat{t}^1\hat{G}^{12} & \dots & -t^1\hat{G}^{1N} \\ -\hat{t}^2\hat{G}^{21} & \hat{I} & \dots & -t^2\hat{G}^{2N} \\ \vdots & \vdots & & \vdots \\ -\hat{t}^N\hat{G}^{N1} & -\hat{t}^N\hat{G}^{N2} & \dots & \hat{I}\end{pmatrix}^{-1} \begin{pmatrix}\hat{t}^1 \\ \hat{t}^2 \\ \vdots \\ \hat{t}^N\end{pmatrix} . \tag{4.14}$$

The matrix on the right hand side of eq. 4.14 can be constructed for any given structure model. The chemical composition is included in the atomic scattering operators $\hat{t}^n$, while the structural arrangement determines the propagators $\hat{G}^{ji}$.

The inversion of this scattering matrix is the main computational challenge in dynamical scattering theory. It has to be performed for each trial structure at each energy step. In order to reduce computer time at a given number of trial structures, it is therefore desirable to have a large energy stepwidth for the calculated curves. As a rule of thumb, structural information is not contained in steps smaller than the peak width, which is given by the imaginary part of the optical potential. In the present work, a stepwidth of $\delta E = 3$ eV was chosen.

Since the dimension of the scattering matrix amounts to $D = N(l_{\max} + 1)^2$, the computational effort is directly related to the number of atoms in the structure model. Lattice periodicity can of course be exploited, which makes the number of atoms in a unit cell the relevant quantity. For structures consisting of repetitive stacks of layers, like single-crystals, the computation can be further simplified by dividing the problem into intra- and inter-layer scattering. This especially has the advantage that the intra-layer scattering only has to be computed once per occurring layer type, in analogy to the intra- and inter-atomic scattering. The scattering on a single layer is calculated in analogy to eq. 4.14 and is represented by a layer diffraction matrix.

To compute the inter-layer scattering, different approaches exist. CLEED uses so-called layer doubling [114], which represents a method to iteratively construct scattering matrices for large stacks of identical layers. Due to the finite information depth, the construction can be terminated at some point, which means that the surface-near region is modeled as a finite slab.

Furthermore, inter-layer scattering can be computed most time-efficiently in plane wave representation, as long as the layer spacing is not too small. Since in real structures often different layer spacings occur, especially if the unit cell contains more than one atom, it is desirable to combine the virtues of both spherical and plane wave representation. This is achieved in the so-called combined space method, which is also implemented in CLEED [114].

It should be noted that it is also possible to apply perturbation methods to the LEED problem, the most common implementation is Tensor-LEED [131]. In this approach, small geometric deviation from a reference geometry, which is calculated exactly, are treated as perturbations. While this method can significantly reduce the computation time, the validity of the approximation is only given close to the reference geometry. In CLEED, the diffraction problem is solved exactly in the framework of the muffin-tin approximation without perturbation treatment. The computation times for the models that were tested in the present work remained reasonable on a modern workstation (see section 4.2.7).

Element	Z	Configuration	α	R_{mt} (nm)
Ce	58	[Xe]$4\mathrm{f}^1 5\mathrm{d}^1 6\mathrm{s}^2$	0.69845	0.175
Pt	78	[Xe]$4\mathrm{f}^{14} 5\mathrm{d}^9 6\mathrm{s}^1$	0.69306	0.095

Table 4.2: Input that was used for calculation of phase shifts in the muffin-tin model. Values for the statistical exchange parameter α were taken from [130]. The choice of muffin-tin radii R_{mt} is motivated in the text.

4.2.4 Effects of temperature

For the discussion so far, a rigid lattice was assumed. However, the atoms in a crystal are subject to lattice vibrations, the amplitude of which strongly depends on temperature. For the diffraction on atoms that are displaced from their equilibrium positions, different phase relations apply. Hence, vibrations induce a phase uncertainty, which leads to a damping of the wave amplitude [112].

This effect can be described by a Debye[21]-Waller[22] factor F_{DW} in kinematic as well as dynamical scattering theory. The intensity is reduced as $I = F_{\mathrm{DW}} I_0$. With momentum transfer $\Delta\vec{k}$ and for small average root mean square displacement of the atoms $\left\langle \Delta \left|\vec{r}\right|^2 \right\rangle$, the factor can be written as

$$F_{\mathrm{DW}} = \exp\left(- \left|\Delta\vec{k}\right|^2 \left\langle \Delta \left|\vec{r}\right|^2 \right\rangle \right). \tag{4.15}$$

The isotropic average displacement, which is also used in CLEED [114], can be expressed by separate displacements for the three Cartesian coordinates,

$$\left\langle \Delta \left|\vec{r}\right|^2 \right\rangle = \sqrt{\Delta x^2 + \Delta y^2 + \Delta z^2} = \sqrt{3\ \Delta r^2}. \tag{4.16}$$

This representation is used in the present work. Different elements were given distinct displacements, but no further discrimination of atoms at inequivalent positions in the crystal structure was done. The parameters Δr, which are typically in the magnitude of $\Delta r \approx 0.005$ nm [133], were then optimized to obtain the best agreement with experiment.

4.2.5 Parameters for phase shift calculation

For the calculation of phase shifts δ_l, the phase shift package by Barbieri and van Hove was used in the present work [134][23]. The package is operated in four steps, which are described in the following.

First, a self-consistent calculation of atomic orbitals is performed for each element of interest, which yields the radial charge density distribution. Only basic information regarding the atomic number Z and the electronic configuration are required. For the present calculations, the input given in tab. 4.2 was used. While this step is commonly done without approximations for exchange interaction in a Hartree-Fock (HF) scheme, the program reported a failure for Ce due to strong mixing of the $4f$ levels. Hence, an alternative option of the program was used, a Local Density Approximation (LDA) scheme. In order to estimate the impact of this approximation, phase shifts were calculated for La, representative for Ce without a $4f$ electron, with both methods. Comparison of HF and LDA results showed only minor differences, which mainly occurred at energies below $E = 30$ eV. This energy range was not needed for the calculations in the present work.

The second step represents the construction of the complete muffin-tin potential, which includes a structure model, a value for the parameter α of the Xα exchange potential and muffin-tin radii

---

[21] Peter Debye, Dutch-American physicist and chemist, 1884-1966

[22] Ivar Waller, Swedish physicist, 1898-1991 [132]

[23] The phase shift package was downloaded from `http://www.icts.hkbu.edu.hk/vanhove/VanHove_files/leed/leedpack.html` on 5. August 2013

R_{mt} for each element. The structure models that were tested in the present LEED IV study were all based on the CePt$_5$ structure (see fig. 2.7), with different surface terminations and modified lattice constants. A detailed description is given in section 7.6.1. Furthermore, test calculations confirmed the known fact that the influence of the exact structure model on the resulting phase shifts is rather small [134], in contrast to the impact of R_{mt}. Hence, the CePt$_5$ structure with Pt Kagome bulk termination and bulk lattice constants was chosen for the calculation of one set of phase shifts for each element. These data were used for all structure models in the LEED IV analysis.

The α parameters for the two elements were taken from the calculations by Schwarz [130] and are given in tab. 4.2. The phase shift package only accepts a single value as input for the complete structure. Hence, the values for Ce and Pt were averaged with weights according to the sample stoichiometry 1:5. This is not expected to produce significant errors, since the values for the two elements are comparable.

Concerning the muffin-tin radii, the simplest approach for single crystals is to choose half the interatomic nearest-neighbor distance d_{nn}. If the lattice parameters are unknown and their determination is part of the study, this simple rule yields difficulties: For every trial structure, new phase shifts with an adjusted muffin-tin radius have to be calculated. Since the radii and the muffin-tin constant cannot be determined experimentally, they can be seen as empiric model parameters to be adjusted to fit the experiment. It is therefore reasonable to choose a radius smaller than the one for touching spheres. In contrast, a larger radius is hardly justified.

For the bulk lattice constants of CePt$_5$, the Pt atoms locally form tetrahedra with an interatomic distance of $d_{\mathrm{nn}}^{Pt} \approx 0.268$ nm. Assigning half that value to the radius of the Pt spheres, $R_{\mathrm{mt}}^{Pt} = 0.134$ nm, the remaining space for the Ce atoms defines a radius of $R_{\mathrm{mt}}^{Ce} = 0.175$ nm.

In a detailed study of the clean Pt(111) surface in terms of LEED IV, Materer *et al.* found the best agreement with experiment for $R_{\mathrm{mt}}^{\mathrm{Pt}} = 0.095$ nm, in contrast to $0.5\, d_{\mathrm{nn}}^{\mathrm{Pt(111)}} = 0.139$ nm [135]. This result was confirmed by an independent study of the well-characterized Pt(111) surface yielding an excellent R-factor for the reduced value [123, 127]. Since this value is furthermore small enough to prevent overlapping of the muffin-tin spheres even for a strongly compressed CePt$_5$ lattice, it was also used in the present calculations.

For Ce, the radius was set to $R_{\mathrm{mt}}^{\mathrm{Ce}} = 0.175$ nm, the value derived by the method described above. An independent test of this value on a Ce-containing sample with well-known structure was not possible, but would be highly desirable to independently benchmark the reliability of dynamical scattering theory for this element. Regarding the literature, no LEED IV studies involving Ce are presently known to the author.

In the third step, relativistic phase shifts δ_l are calculated for the muffin-tin potential obtained in step 2. The program solves the Schrödinger equation inside the muffin-tin spheres and matches the radial wave functions to the solution in the region with constant potential between the spheres. The resulting curves can possess discontinuities arising from the fact that the δ_l are defined modulo π. Such discontinuities are removed in the fourth step, which then yields data suitable as input for CLEED.

4.2.6 Reliability factors

For structure determination with LEED IV, a plethora of calculated curves have to be compared to experimental data in order to determine the model that produces the optimum agreement with experiment. The best way to process large amounts of data with a maximum of objectivity is provided by computer-based algorithms. This requires to project the quality of agreement between two curves onto a single number, which can be optimized by the program. Such numbers are called reliability factors (R-factors) and can be defined in manifold ways.

In the present work, the R-factor defined by Pendry was used [136]. The main idea of this approach is that the structural information is contained in the extrema of the $I(E)$ curves. The emphasis is laid on the number and existence of both dynamical and kinematic peaks, regardless of the peak height.

Mathematically, the sensitivity to peak and minimum positions and insensitivity to intensity is achieved by using the logarithmic derivative,

$$L(E) = \frac{\frac{dI(E)}{dE}}{I(E)}. \tag{4.17}$$

For $I = 0$, L diverges, which is taken into account by definition of the function

$$Y(E) = \frac{L(E)}{1 + V_{\mathrm{o,i}}^2 L(E)^2}. \tag{4.18}$$

The Pendry R-factor then reads

$$R_{\mathrm{P}} = \frac{\int \left(Y_{\mathrm{e}}(E) - Y_{\mathrm{t}}(E)\right)^2 dE}{\int \left(Y_{\mathrm{e}}(E)^2 + Y_{\mathrm{t}}(E)^2\right) dE}, \tag{4.19}$$

with indices e and t denoting experimental and theoretical data, respectively. For perfect agreement, $R_{\mathrm{P}} = 0$, while for uncorrelated curves it tends to unity.

The insensitivity of R_{P} to peak heights accounts for the fact that absolute intensities are harder to reproduce by dynamical scattering theory than the qualitative curve shape. Furthermore, experimental uncertainties are compensated as well. Those can arise due to inhomogeneities of the fluorescent screen or during data processing, especially when working with jpg files or other lossy image formats.

The calculation of R_{P} is highly susceptible to noise-induced errors. This stresses the need for smoothing of the experimental data (see section 4.2.1).

For reliable structure determination, a maximum of information should be included in the analysis. This means that $I(E)$ curves for as many inequivalent spots as possible should be recorded in an energy range as large as possible. A total R-factor for a certain dataset and model geometry is obtained by averaging the R-factors for the individual spot curves, R_{P}^n. In this respect, the individual energy ranges ΔE^n are a good measure for weighting of the different spots. Hence, the total R-factor for a dataset of N inequivalent curves is calculated by

$$R_{\mathrm{P}}^{\mathrm{tot}} = \frac{\sum_{n=1}^{N} \Delta E^n R_{\mathrm{P}}^n}{\sum_{n=1}^{N} \Delta E^n}. \tag{4.20}$$

Additionally, Pendry proposed a method to estimate the statistical significance of an R-factor result [136]. This especially allows distinguishing a minimum that is caused by geometry optimization from random fluctuations of uncorrelated data with a mean R-factor of $\langle R_{\mathrm{P}} \rangle = 1$. Furthermore, a range can be given in which similar R-factor results are not significantly distinguishable.

For this purpose, the so-called double reliability factor is defined as

$$R_{\mathrm{R}} = \frac{\mathrm{var}(R_{\mathrm{P}})}{R_{\mathrm{P}}} \approx \sqrt{\frac{8V_{\mathrm{o,i}}}{\sum_{n=1}^{N} \Delta E^n}}. \tag{4.21}$$

The approximate expression for the variance is based on an $I(E)$ model curve that is constructed from several Lorentz peaks [136]. It is said to rather overestimate the real errors [114, 137]. This definition is thus regarded to represent an upper limit for uncertainties.

The probability for a result R_{P} to be caused by random fluctuations from the true value R_{P}' in a range $R_{\mathrm{P}}(1 \pm R_{\mathrm{R}})$ amounts to $P = 68\ \%$. The probability reaches $P = 90\ \%$ for a range of $R_{\mathrm{P}}(1 \pm 1.96 R_{\mathrm{R}})$. This allows derivation of a criterion when comparing a series of simulations based on different structure models. A model is regarded as unlikely and sorted out if

$$R_{\mathrm{P}} > (1 + R_{\mathrm{R}}) R_{\mathrm{P}}^{\mathrm{min}}, \tag{4.22}$$

where $R_{\mathrm{P}}^{\mathrm{min}}$ is the smallest R-factor result obtained for the complete series [114].

The criterion given in eq. 4.22 can also be used to estimate error bars for the model parameters [136]. For this purpose, R_{P} is calculated as a function of the parameter value in the vicinity of the optimized result with all other model parameters fixed. The uncertainty then corresponds to the width of the minimum around $R_\mathrm{P}^\mathrm{min}$ at $(1 + R_\mathrm{R})R_\mathrm{P}^\mathrm{min}$.

Based on this consideration, CLEED provides error bars for the free search parameters. For their calculation, a method introduced by Held *et al.* is used [138], assuming that the R-factor varies quadratic in the vicinity of its minimum. The error bars given with the results in section 7.6.2 were obtained by this procedure.

Finally, it should be noted that application of the R-factor is not restricted to comparison of experimental and theoretical data. It can of course be used to quantify the agreement between any two curves. In section 7.2, experimental $I(E)$ curves for $\mathrm{CePt_5/Pt(111)}$ samples with different thicknesses are compared this way to investigate if the crystal structure varies with the thickness.

4.2.7 Parameter optimization

The optimization of the model parameters aims at a minimization of the R-factor, which is equivalent to finding the best possible agreement of theory and experiment for the given model. The procedure is divided into two parts, the automated optimization procedure and the search strategy, which accounts for the differences of free and fixed parameters (see tab. 4.1).

The automated optimization procedure in CLEED includes three actions in a single optimization run: Computation of theoretical $I(E)$ curves, R-factor quantification of the agreement between theory and experiment and management of a downhill simplex algorithm. The latter is applied to vary the free parameters, repeat the first two steps and finally find the nearest minimum of the total R-factor in the parameter space. The parameter set of this local minimum and the calculated curves including their individual R-factors are returned as output.

The global R-factor minimum is searched for by repetition of such optimization runs under systematic variation of the fixed parameters and adjustment of the start values of the free parameters. This is called the search strategy.

For the LEED IV study of section 7.6, more than 2000 optimization runs were performed in CLEED, not counting preliminary attempts. The computation time for a single run was of the order of $\tau = 15 \dots 30$ min, which means that approximately one month of computer time was consumed. Without an automated search strategy, this study would not have been possible.

The automated optimization procedure

The computation time for dynamical electron scattering theory is dominated by the giant matrix inversion which has to be performed at each energy step for each set of trial parameters. The methods that are implemented in CLEED for simplification of the matrix inversion are introduced in section 4.2.3. The second challenge, to find the R-factor minimum in a high-dimensional parameter space, can be met by numerical optimization procedures [137, 139].

Such procedures can be divided into methods that are designed to find the global minimum in the parameter space and methods that search for the local minimum nearest to the starting point. The downhill simplex algorithm, as implemented in CLEED, represents one of the latter, "direct" methods [114, 139, 140]. It is known to be slower, but more robust than other direct algorithms. Since no calculation of derivatives is necessary, it can easily be adapted to the requirements of LEED IV crystallography [114].

For an optimization problem with N parameters, the simplex that is referred to in the algorithm's name represents an N-dimensional non-degenerate polytope which is defined by $N + 1$ points in the parameter space. The initial simplex in CLEED is constructed from the starting geometry and N geometries that are produced by variation of each free parameter by a certain value. In the following steps, the geometry with the worst R-factor result is replaced by a trial structure with a better result, which is searched for in a number of iterative steps. In this process, the simplex adapts to the parameter space landscape and finally contracts around an R-factor minimum. The algorithm terminates when a predefined criterion is fulfilled for all R-factor values of the simplex, which is typically set to a maximum relative deviation of $R_\mathrm{P}^n / R_\mathrm{P}^\mathrm{min} - 1 \leq 0.01$ with respect to the optimum that was found.

Using a direct optimization method has the advantage that a single optimization run is performed much faster than for a global method like, e.g., simulated annealing [137]. This is especially true for complex problems with a high-dimensional parameter space. However, one has to assure that the global minimum is really found, which means that optimization runs have to be started from different points in the parameter space. Hence, a direct optimization method provides a compromise between a completely automated optimization and a systematic scan of the parameter space, which can effectively be performed on a much wider grid.

The search strategy

The choice of an appropriate search strategy is another challenge in LEED crystallography. Most importantly, the specifics of the structure model that is tested have to be considered. In the present work, the model optimizations were performed by iterative series of optimization runs. In the initial scan, a starting geometry was chosen that was characterized by a single parameter, the vertical layer spacing. This parameter was then systematically varied in a series of optimization runs. The starting values of the fixed parameters thereby had to be guessed.

In the following, further series of optimization runs were calculated by systematical variation of the fixed parameters. The parameter values of the best R_P result of the preceding series were used as the starting geometry for each new scan. Furthermore, the energy shift, which is introduced by CLEED to match experimental and theoretical curves, was always kept near zero by adjustment of $V_{\mathrm{o,r}}$, since the R-factor seemed to depend on its value.

The two fixed geometric parameters, the lateral lattice constant and the vertical one of the bulk, were scanned in dependence of each other. This means that two-dimensional R-factor maps were created as a function of a and c. The same was done for the atomic displacement of Ce and Pt atoms, which however showed not much dependency. For the imaginary part of the optical potential, only one-dimensional scans were performed. It mainly characterizes the peak width in the $I(E)$ curve and should not strongly depend on other parameters.

It is a common assumption that the non-geometric parameters influence the quantitative R_P result, but have only minor impact on the geometry of the optimized structure [133]. Hence, a possible dependency between geometric and non-geometric parameters was only considered by repeating the two-dimensional scan for the geometric parameters after optimizing the non-geometric ones.

In a final step, the calculation that had yielded the best R-factor result was restarted from its free parameter results. This is recommended for the simplex algorithm to assure correct termination. The result of this final run was taken as the optimized geometry for each tested model.

Chapter 5

X-ray Absorption Spectroscopy and X-ray Magnetic Circular Dichroism

Contents

The interaction of light with matter has intrigued scientists since ancient Greece, when the question of the nature of light as a wave or a particle first arose. The following debate found its climax in the 17th century, when Newton and Huygens developed their contradictory theories [4]. In the following, the wave theory of light became generally accepted after Young's double slit experiment in 1804 [115] (see section 4.1.1) and the derivation of Maxwell's[1] equations for electromagnetic waves in 1865 [141]. Finally, the debate was resolved in 1905, when Einstein[2] explained the photoelectric effect by proposal of particle-wave-duality [142]. This concept is the basis for the modern, quantum mechanical point of view of light-matter interaction.

This interaction leads to different processes depending on the photon energy E. Well-known examples are the photoelectric effect, which involves the absorption of photons by atoms, Compton[3] scattering and pair production. Absorption predominates in the energy range $\Delta E = 10 \dots 10000$ eV. This involves the ultraviolet, soft- and hard X-ray regions of the electromagnetic spectrum. As a rule of thumb, the soft X-ray region in the middle of the three represents the range $\Delta E = 100 \dots 2000$ eV.

X-rays were discovered in 1895 by Röntgen in Würzburg [143]. In 1913, de Broglie[4] reported the

---

[1] James Clerk Maxwell, British physicist, 1831-1879

[2] Albert Einstein, German-Swiss-American physicist, 1879-1955

[3] Arthur Holly Compton, American physicist, 1892-1962

[4] Louis César Victor Maurice de Broglie, French physicist, 1875-1960. Brother of Louis Victor Pierre Raymond de Broglie [144]

observation of an X-ray absorption spectrum[5] [145, 146]. However, the success story of X-ray spectroscopy[6] (XAS) had to wait until the 1980s, when intense, monochromatized X-rays became available at synchrotron facilities. Since then, XAS has been applied to answer a multitude of questions [59, 145, 147].

As is discussed in the following sections, XAS is an element-specific technique and thus qualifies for chemical analysis. It can be applied to solid-state samples as well as small particles, molecular complexes, gases or liquids. Depending on the detection mode, bulk or surface-sensitivity can be chosen. Furthermore, XAS allows addressing the electronic energy scales of the atoms under investigation.

The absorption experiments of the present work focus on the Ce $\mathrm{M}_{4,5}$ edges, which represent the resonant transition $3d^{10}4f^n \rightarrow 3d^9 4f^{n+1}$. The spectra give access to the $3d$ electron binding energy $E_\mathrm{b} \approx 900$ eV and the $3d$ spin-orbit splitting $\Delta E_\mathrm{SOC} \approx 20$ eV. The Ce valence can be studied due to the difference in absorption energy for states with different $4f$ count, $\Delta E \approx 5$ eV. Furthermore, investigation of temperature-dependent effects can give access to very small energy scales in the order of millielectronvolts, like crystal field splitting or the Kondo temperature. Hence, energy scales within several orders of magnitude can be studied by XAS despite the large excitation energy.

An important enhancement of standard XAS was made when it was recognized that the absorption signal at resonant edges depends on the magnetization direction, if the incident X-rays are circularly polarized. This was proposed in 1975 by Erskine and Stern [148], the first experimental realization of the effect was reported in 1987 by Schütz *et al.* [149]. The usefulness of the so-called X-ray Magnetic Circular Dichroism (XMCD) effect was further increased by the theoretical work of Thole[7], Carra and coworkers. In 1992 and 1993, they published methods to quantitatively determine spin and orbital magnetic moments from XMCD experiments by application of sum rules [151, 152].

Certainly, the XMCD sum rules largely contributed to the success of the technique. Soon after their theoretical derivation, the validity of the sum rules was experimentally confirmed for the $\mathrm{L}_{2,3}$ edges of Fe and Co metal by Chen *et al.* [153]. Another direct test by Lee *et al.* confirmed their accurateness for Ni films [154]. By today, the two publications of Thole, Carra *et al.* have been cited far more than a thousand times each.

With these theoretical tools and appropriate experimental facilities, very small magnetic moments down to $\mu = 10^{-5}\,\mu_\mathrm{B}$ can be detected [155]. Hence, XMCD complements the features of XAS by a quantitative, highly sensitive probe for magnetization, which opened new fields of research [155, 156]. Probably the best indicator for the growing importance of this technique is the increasing number of high-performance beamlines at synchrotron facilities around the world that are equipped with dedicated experimental setups.

The present chapter covers the general background of XAS and XMCD (sections 5.1 to 5.3) as well as a description of the experimental requirements and their realization in the present work (section 5.4). Finally, section 5.5 provides a model description for the XAS signal of thin film samples, which is required for quantitative analysis of the present data. The aspects of the techniques that are specific to their application to the Ce $\mathrm{M}_{4,5}$ edges are addressed separately in chapter 6

5.1 Concepts of X-ray Absorption Spectroscopy

When Röntgen discovered the X-rays in 1895, he characterized this “new kind of rays” primarily by the absorption in solids. He already pointed out that the thickness as well as the density of an absorber determine the magnitude of absorption.

---

[5] Latin: image. A spectrum in its physical meaning is the dependence of a quantity on the energy of an excitation. This is often electromagnetic radiation, but one also speaks of the mass spectrum of a gas, e.g.

[6] Hybrid from Latin “spectrum” and Greek “skopein”, which means “to look at”.

[7] Bernard Theo Thole, Dutch physicist, 1950-1996. The memory of Theo Thole, who died as a consequence of a tragic accident, is kept alive in his scientific legacy. A review of his work along with a number of texts that vividly describe the circumstances of its development is collected in the “Theo Thole Memorial Issue” [150]

Concerning the absorber thickness, X-ray absorption (XA) follows the Bouguer[8]-Lambert[9]-Beer[10] law, as is the case for all electromagnetic waves. It states that the decrease of intensity I of radiation that propagates along the z-direction in a medium is proportional to the incoming intensity,

$$dI(E,z) = -\mu_{\mathrm{x}}(E)\ I(E,z)\ dz. \tag{5.1}$$

Equivalently, the z-dependence of the intensity can be formulated as an exponential law,

$$I(E,z) = I_0\ e^{-\mu_{\mathrm{x}}(E)z}. \tag{5.2}$$

The proportionality constant μ_{x} in eq. 5.1, which is called the linear absorption coefficient, is connected to a characteristic length scale, the X-ray penetration length $l_x = 1/\mu_{\mathrm{x}}$. In general, μ_{x} depends on the photon energy $E = \hbar\omega$ and it is a material-specific quantity.

The material-specificity is mainly, but not only governed by the density of the material, as Röntgen already stated. This reflects the fact that the absorption is a local process, it takes place at individual atomic sites. For a certain material that is homogeneously composed of N different elements, the absorption coefficient can be written as

$$\mu_{\mathrm{x}}(E) = \sum_{n=1}^{N} \rho_n^{\mathrm{at}} \sigma_n(E). \tag{5.3}$$

Here, σ_n is the atomic absorption cross-section of the nth element, while ρ_n^{at} is its atomic density. Consequently, σ has the dimension area per atom. It is defined as the number of absorbed photons per atom divided by the number of incident photons per area. In a semiclassical picture, the atoms in a sample can be imagined as hard spheres with a cross-section area that equals σ. A point-shaped photon is then absorbed if it hits a sphere.

In a quantum mechanical treatment, the absorption process is described in terms of transition probabilities T_{if} between an initial state $|i\rangle$ and a final state $|f\rangle$ with energies E_i and E_f, respectively. Both states are many-body states: The initial state is the thermal state of the undisturbed atom or ion. In the final state, a hole is created by excitation of an electron.

If the photon energy exceeds the electron binding energy E_{b}, the final state includes an electron that is excited to a continuum state with $E_{\mathrm{kin}} = E - E_{\mathrm{b}}$. In a solid, the continuum is synonymous with empty valence states. If the photon energy suffices for the continuum electron to reach the sample surface and overcome the workfunction, it leaves the sample as a direct photoelectron. This is the aforementioned photoelectric effect.

At photon energies slightly below E_{b}, excitation to a higher-lying bound state in the same atom can occur. In the following, this excitation is referred to as resonant absorption, in contrast to the continuum absorption described above. A main difference is that resonant absorption only occurs at well-defined energies, whereas continuum absorption can be observed independent of E as soon as the threshold energy is exceeded. An illustration of the two processes is given in fig. 5.1.

The transition from $|i\rangle$ to $|f\rangle$ is induced by the temporally oscillating electromagnetic field of the incoming X-rays, which is expressed by the interaction Hamiltonian $\hat{H}_{\mathrm{int}} = \hat{H}' e^{-i\omega\tau}$. A treatment in perturbation theory up to first order leads to the well-known equation called "Fermi's golden rule", which was first derived by Dirac in 1927 [157]:

$$T_{if}(E) = \frac{2\pi}{\hbar} \left| \langle f | \, \hat{H}' \, | i \rangle \right|^2 \delta(E_f - E_i - E)\ \rho_{\mathrm{DOS}}(E_f). \tag{5.4}$$

Here, $\rho_{\mathrm{DOS}}(E_f)$ is the DOS of the final state and the delta-function assures energy conservation. The absorption cross-section σ of the transition to a certain final state is obtained from T_{if}

---

[8] Pierre Bouguer, French astronomer, geodesist and physicist, 1698-1758

[9] Johann Heinrich Lambert, French-Swiss-German book-keeper, private tutor, mathematician, physicist, astronomer and philosopher, 1728-1777

[10] August Beer, German physicist and mathematician, 1825-1863

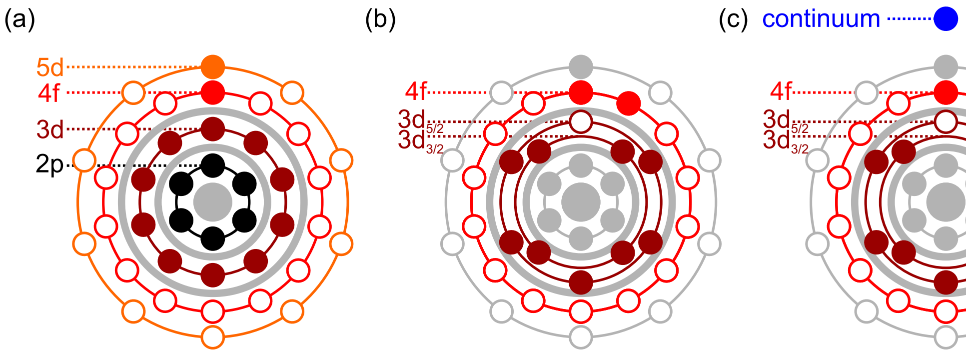

Figure 5.1: Illustration of resonant and continuum absorption at the M_5 edge for a Ce atom in an electron shell model. (a) Initial state $|i\rangle$, the undisturbed atom. Gray sections represent the electron shells that are not explicitly drawn. The arrangement of the shells reflects the energetic ordering rather than the spatial distribution (compare fig. 2.1). (b) Final state $|f\rangle$ for resonant absorption. At a certain photon energy below the electron binding energy E_b, an electron from the $3d$ shell is excited to a bound state, which is the $4f$ shell in this case. (c) Final state $|f\rangle$ for continuum absorption. For $E \geq E_\mathrm{b}$, the $3d$ electron is removed from the atom and excited to a continuum state.

by normalization to the incoming photon flux Φ_0. Summation over all transitions that can be reached with the given photon energy yields the total atomic absorption cross-section,

$$\sigma(E) = \sum_{E_f - E_i \leq E} \frac{T_{if}(E)}{\Phi_0}. \tag{5.5}$$

Consequently, variation of the photon energy can be used to select which transitions contribute to the signal. This allows identification of the different transitions and discern between resonant and continuum absorption, due to their fundamentally different characters. Study of $\sigma(E)$, usually via the absorption coefficient $\mu_\mathrm{x}(E)$, is called X-ray absorption spectroscopy (XAS).

In the following, the transitions that can be studied with XAS are discussed, with a focus on the experiments presented in part II. Basic considerations with respect to eq. 5.4 lead to the so-called dipole selection rules, which allow assignment of well-defined final states to features that are observed in a spectrum. This is presented in section 5.1.1. Thereafter, continuum (section 5.1.2) and resonant (section 5.1.3) absorption are treated in more detail.

5.1.1 Dipole Selection rules

Important conclusions concerning the allowed final states can be drawn by a closer inspection of the transition matrix elements $M_{if} = \langle f|\, \hat{H}' \,|i\rangle$ in eq. 5.4. The interaction Hamiltonian $\hat{H}_\mathrm{int} = \hat{H}' e^{-i\omega\tau}$ can be derived via canonical quantization from the classical expression. The non-relativistic Lagrange[11] function L for an electron with charge $-e$ and mass m_e in an electromagnetic field reads [158]

$$L = E_\mathrm{kin} - E_\mathrm{pot} = \frac{m_\mathrm{e}}{2}\dot{\vec{x}}^2 + e\left(\Phi(t,\vec{x}) - \dot{\vec{x}} \cdot \vec{A}(t,\vec{x})\right). \tag{5.6}$$

Here, the relation between the electric field $\vec{E}$ and the electromagnetic potentials $\vec{A}$ and Φ is used,

$$\vec{E}(t,\vec{x}) = -\vec{\nabla}\Phi(t,\vec{x}) - \frac{\partial}{\partial t}\vec{A}(t,\vec{x}), \tag{5.7}$$

which derives from the Maxwell equations after the vector potential has been defined.

The Hamilton function is obtained from L by calculation of the canonical momentum, $\vec{p} = \partial L / \partial \dot{\vec{x}}$. It reads

---

[11] Joseph Louis de Lagrange, Italian mathematician and astronomer, 1736-1813

$$H = \vec{p} \cdot \dot{\vec{x}} - L = \frac{1}{2m_\mathrm{e}} \left(\vec{p} + e\vec{A}(t,\vec{x})\right)^2 - e\Phi(t,\vec{x}). \tag{5.8}$$

When transforming the Hamilton function H to the Hamiltonian $\hat{H}$, non-commutability of operators has to be considered. Hence,

$$\hat{H} = \frac{1}{2m_\mathrm{e}} \left(\hat{\vec{p}}^2 + e^2\hat{\vec{A}}^2 + e\hat{\vec{p}}\hat{\vec{A}} + e\hat{\vec{A}}\hat{\vec{p}}\right) - e\hat{\Phi}. \tag{5.9}$$

For most X-ray absorption experiments including the ones of the present thesis, the magnitude of $\hat{\vec{A}}$ is in a range that allows neglect of the $\hat{\vec{A}}^2$ term. Furthermore, with $\hat{\vec{p}} = \hbar/i\vec{\nabla}$, it follows that $\hat{\vec{p}}\hat{\vec{A}} = \hbar/i((\vec{\nabla}\hat{\vec{A}}) + \hat{\vec{A}}\vec{\nabla})$. When working in the Coulomb gauge, $\vec{\nabla}\hat{\vec{A}} = 0$ and $\hat{\Phi} = 0$. Consequently, the interaction Hamiltonian reduces to

$$\hat{H}_\mathrm{int} = \hat{H} - \frac{\hat{\vec{p}}^2}{2m_\mathrm{e}} = \frac{e\hat{\vec{A}}\hat{\vec{p}}}{m_\mathrm{e}}. \tag{5.10}$$

The electric field of incoming X-rays is commonly described as a plane wave with wave number $k = |\vec{k}| = 2\pi/\lambda$ and frequency $\omega = E/\hbar$. According to eq. 5.7, the vector potential and the electric field are collinear in space. Hence,

$$\hat{\vec{A}} = A_0 \; \vec{\epsilon} \; e^{i(\vec{k}\vec{x} - \omega\tau)}, \tag{5.11}$$

where $\vec{\epsilon}$ is the unit polarization vector of the electric field. The transition matrix element can then be written as

$$M_{if} \propto \langle f | \, e^{i\vec{k}\vec{x}} \; \vec{\epsilon}e\hat{\vec{p}} | i \rangle = \langle f | \left(1 + i\vec{k}\vec{x} + \ldots\right) \vec{\epsilon}e\hat{\vec{p}} | i \rangle \, . \tag{5.12}$$

In order to identify the term at which the expansion can be terminated, the magnitudes of $1/k$ and x have to be compared. While k derives from the photon energy, the relevant quantity for an estimate of x is the extension of the electron shell in which the core-hole is created.

At the Ce $\mathrm{M}_{4,5}$ edges near $E = 900$ eV (compare fig. 5.1), $1/k \approx 0.219$ nm. The extension of the Ce $3d$ shell can be estimated from the Bohr model via $2 \; r_{n,Z} = 2 \; n^2 \; a_0/Z$ to amount to $x \approx 0.016$ nm. Hence, $kx \approx 0.073$.

While this value is slightly larger than equivalent estimates for the O K edge [147] or the L edges of transition metals [156], it is still small enough to reasonably neglect all k-dependent terms in eq. 5.12 for the Ce $\mathrm{M}_{4,5}$ transitions. By doing this, the electric field is regarded as constant over the extension of the electron shell, which is called the dipole approximation.

In this approximation and by application of the commutator relation $[\hat{H}, \hat{\vec{x}}] = -i\hbar/m_\mathrm{e} \; \hat{\vec{p}}$, the transition matrix element can be rewritten to contain the dipole operator $e\hat{\vec{x}}$ as

$$M_{if} \propto \langle f | \, \vec{\epsilon}e\hat{\vec{p}} \, | i \rangle = i m_\mathrm{e} \omega_{if} \, \langle f | \, \vec{\epsilon}e\hat{\vec{x}} \, | i \rangle \, , \tag{5.13}$$

where $\omega_{if} = (E_f - E_i)/\hbar$ derives from the energy eigenvalues of the initial and the final state. Hence, M_{if} represents a spatial integral over the product of two wavefunctions and the polarization-dependent dipole operator $\vec{\epsilon}e\vec{x}$.

Even for complicated solid-state systems, the wavefunctions $|i\rangle$ and $|f\rangle$ can be written as linear combinations of atomic functions within reasonable approximations. Hence, the following treatment of the matrix element is reduced to such atomic functions, which can be separated into radial and angular parts (see eq. 2.1) and have a well-defined parity.

Furthermore, the initial and final state are considered in a one-electron picture, since this allows formulation of the dipole selection rules. The relevant quantities then are the sets of angular momentum quantum numbers l, m and l', m' of the core electron in the initial and the excited electron in the final state, respectively. The spin is not affected by the dipole operator and is therefore conserved during the transition.

It is now interesting to investigate the conditions at which $M_{if} \neq 0$, since only such transitions can occur. Concerning the radial part, the integral vanishes if the integrand has odd parity along the polarization direction. Hence, a non-vanishing transition matrix element is only obtained if $|i\rangle$ and $|f\rangle$ have different parity. This is the case for $\Delta l = l' - l = \pm 1$.

Concerning the magnetic angular momentum quantum number m, it is most elegant to apply Racah's[12] spherical tensor algebra [44, 156] to the polarization-dependent dipole operator. This is based on the angular momentum of the X-rays, which is written as $l^{\mathrm{ph}} = q\hbar$, with $q = 0$ and $q = \pm 1$ for linearly and circularly polarized light, respectively. In accordance with Stöhr and Siegmann [156], $q = +1$ is attributed to right dircularly polarized light in the present thesis. The dipole operator is then expressed by spherical harmonics. Consequently, the φ-dependent integrand in eq. 5.13 is of the form $e^{i(m_l - m_l' + q)\varphi}$. Hence, for a non-vanishing integral $m_l - m_l' + q = 0$ is required, which translates to $\Delta m_l = m_l' - m_l = q$.

For spin-orbit coupled states, the dipole selection rules can be formulated in terms of the total angular momentum. Allowed transitions are $\Delta j = 0, \pm 1$, but not $j = 0 \rightarrow j = 0$. Since the dipole operator does not act on the spin, the rule for Δm_l directly translates to Δm_j.

The main quantum number n is not restricted by the dipole selection rules. However, the number of nodes in the atomic functions increases with n. Integration over products of wavefunctions with many nodes at different positions tends to yield small integral values, which is why the matrix elements become negligible for transitions to high-n states.

The fact that X-ray absorption is governed by the rather simple dipole selection rules simplifies the interpretation of experimental results. Certainly, the usefulness and success of XAS is largely owed to this simplicity. However, the dipole selection rules also provide a limit for the sensitivity of XAS. An example is the in-plane orientation of the ground state orbital of Ce in tetragonal compounds. which cannot be determined unambiguously by XAS [159].

5.1.2 Continuum absorption

Continuum absorption involves the excitation of a core electron to a continuum or valence state, as is illustrated in fig. 5.1 (c). In order to illustrate the signatures of continuum absorption in the energy-dependent atomic absorption cross-section $\sigma(E)$, fig. 5.2 exemplary shows the continuum part of $\sigma(E)$ for Ce and Pt for photon energies up to $E = 15$ keV. The curves are taken from Henke *et al.* [160][13], who semi-empirically computed $\sigma(E)$ data for nearly all elements and for a wide range of photon energies.

The general shape of $\sigma(E)$ is governed by a decrease with energy on the one hand and by abrupt, stepwise increases at certain energies on the other hand. The former is a consequence of the decreasing wavelength of the excited continuum electron in the final state. This reduces the overlap integral $\langle f | H' | i \rangle$ in eq. 5.4 and thus σ.

The steps, which are often called “absorption edges”, appear whenever the photon energy becomes large enough to create a hole in a deeper-lying electron shell. This opens a new excitation channel, which gives rise to a new term in eq. 5.5.

The absorption edges directly reflect the electronic shell structure of the atom under investigation. The edge energy corresponds to the shell-specific binding energy. Furthermore, most absorption edges appear as pairs, with the exception of core-hole creation in the s shells. This reflects the fact that the final state in the absorption process involves a single core-hole, while higher-order effects with multiple holes can be neglected.

In analogy to a single-electron system, the angular momenta of a core-hole are dominantly coupled by spin-orbit coupling (see eq. 2.2). The resulting total angular momentum can be $j = m \pm s$, which leads to two energetically split levels with $j = m - s$ being lower in energy according to Hund's rules. Each of these states produces a distinct absorption edge in $\sigma(E)$, their energy difference reflects the magnitude of the spin-orbit-splitting ΔE_{SOC}. For a core-hole in an s shell, no SOC and thus only single edges are observed since $l = 0$.

---

[12] Giulio Racah, Italian-Israeli mathematician and physicist, 1909-1965. Cousin of Ugo Fano.

[13] These data are accessible via a web interface, `http://henke.lbl.gov/optical_constants/`, last accessed in April 2015

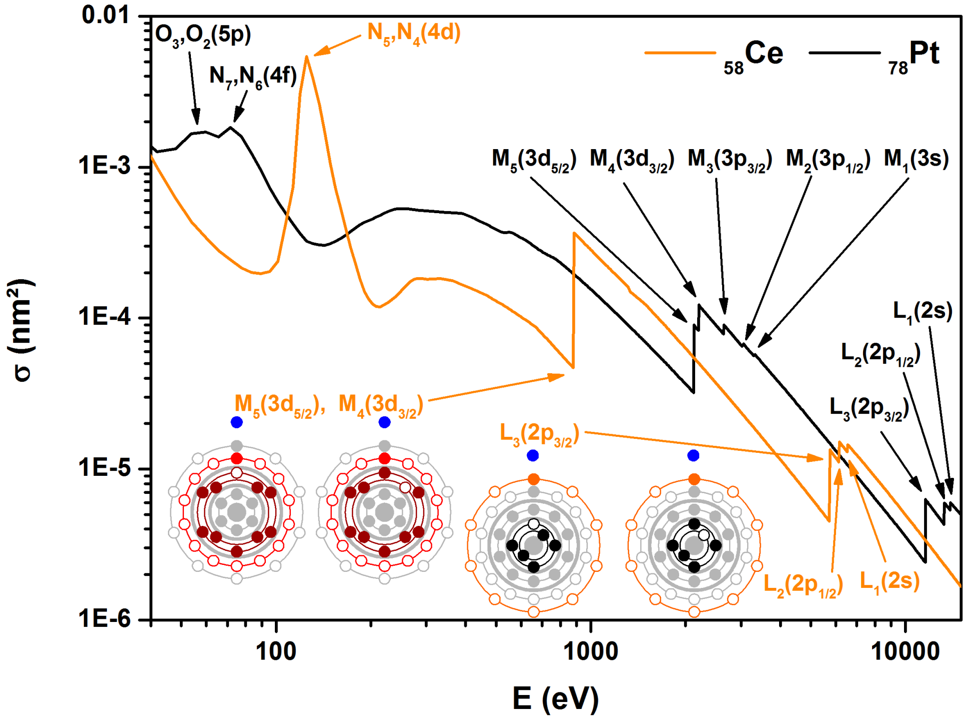

Figure 5.2: Contribution of continuum absorption to the atomic absorption cross-section $\sigma(E)$ for Ce and Pt on a logarithmic scale [160]. Visible absorption edges are labeled. For Ce, atomic shell models of the final states at the M_5, M_4, L_3 and L_2 edges are shown in analogy to fig. 5.1.

A nomenclature for the absorption edges was introduced by Barkla[14] [59], who was the first to describe characteristic X-rays. The atomic shell, in which the core-hole is produced, is denoted by a capital letter. A number index describes the spin-orbit split subshell. In fig. 5.2, the edges that are visible in the data are labeled. Furthermore, shell models of spin-orbit split final states are exemplary drawn for the Ce M_5, M_4, L_3 and L_2 edges.

As can be seen from the comparison of the data for Ce and Pt, the edge energies are not only shell-specific but also element-specific.This reflects the fact that the electron binding energy of a certain shell increases with the positive charge of the nucleus. Hence, it depends on the atomic number Z. Consequently, XAS is an element-specific technique and can be applied for chemical analysis of a sample, if the observed absorption edge energies are compared to E_b values that are tabulated in the literature [161]. With proper reference data, the chemical analysis can even be done quantitatively. An attempt to determine the stoichiometry of Ce-Pt(111) films by XAS is presented in section 7.4.

It has to be kept in mind that resonant absorption is neglected by Henke *et al.* Yet, resonant effects can strongly dominate the absorption in the direct vicinity of the edges, which is why the Henke data shown in fig. 5.2 are generally not directly comparable to experimental results in these regions. The disentanglement of contributions from resonant and continuum absorption is of importance for quantitative analysis of XA spectra. For the present Ce $M_{4,5}$ data, it is therefore addressed in detail in section 8.2.3.

5.1.3 Resonant absorption

In X-ray absorption, the electromagnetic field of the incoming X-rays can be regarded as a periodic driving force acting on the oscillatory system of the undisturbed atom. In this simple picture, resonances in the reaction of the system appear at its eigenfrequencies, which are met if the photon energy matches the transition of a core electron to an unoccupied bound state (see fig. 5.1 (b)). Indeed, peaking of the absorption cross-section is usually observed near the continuum steps, often exceeding them in magnitude. In the following, the term “edge” is used

---

[14] Charles Glover Barkla, British physicist, 1877-1944

to describe the combination of both the resonance and the step.

As a consequence of the dipole selection rules, the resonant absorption cross-section at a given edge is usually characterized by the transition of the core electron to a certain excited state, which is a multiplet in the general case: The lowest unoccupied state that complies with the dipole selection rules. For example, the Ce $M_{4,5}$ edges represent the transition $3d^{10}4f^n \rightarrow 3d^9 4f^{n+1}$. A detailed discussion of Ce $M_{4,5}$ XAS is presented in chapter 6.

For a quantitative treatment of X-ray absorption spectroscopy, it is necessary to quantify the intensity or strength of a resonant transition. Resonant transitions only contribute to the spectrum in a narrow energy range close to their discrete transition energy. While theoretical calculations simply yield paired values of T_{if} and E for each transition, line broadening has to be considered for experimentally observed spectra.

The broadening is caused by the finite lifetime of the excited state as well as by the finite experimental resolution. The latter is caused by deficiencies in the projection of the light source to the exit slit of the monochromator. It is commonly expressed by a Gaussian broadening (see eq. 6.3) with FWHM[15] Γ_{exp}. The resolutions of the setups that were used in the present thesis are addressed in section 5.4.3.

The excited state produced by X-ray absorption can usually relax by the time-reversed process under emission of a photon. Hence, the excitation has finite lifetime, which leads to an uncertainty in the excitation energy due to Heisenberg's energy-time uncertainty,

$$\Delta E \cdot \Delta \tau \gtrsim \hbar. \tag{5.14}$$

There are different additional relaxation processes, which are addressed in section 5.4.2. All of these processes produce a combined lifetime. In order to determine the resulting line shape in an XA spectrum, it is most demonstrative to concentrate on the direct time-reversed absorption process. For the other mechanisms, equivalent considerations can be made.

The light that is emitted by an ensemble of atoms that were excited at $\tau = 0$ can be represented by a harmonic oscillation with exponential damping. The frequency spectrum is determined by the Laplace transform of this wave, which is a Lorentzian[16] [45]. Due to time-reversal symmetry, the same spectral shape appears in absorption spectra. Modifications to this simple picture due to autoionization processes are discussed in section 8.2.4.

As a consequence of the two broadening mechanisms, the peak amplitude, which is readily evaluated from an experimental spectrum, is only a good measure for the transition strength if experimental resolution and lifetime of the excited state do not change. A better characterization of a certain transition is given by the integral of the part of the spectrum associated with the transition, which is referred to as the oscillator strength or the spectral weight w. This quantity is independent of broadening, which is mathematically described by convolution of a transition profile with a normalized kernel and conserves the integral of the spectrum.

5.2 Polarization-dependence of X-ray absorption

The transition matrix element in the dipole approximation as given by eq. 5.13 depends on the polarization vector of the X-rays. Hence, the absorption signal can significantly be influenced by the details of light polarization. For example, this is reflected by the Δm selection rule given in section 5.1.1, which depends on the light helicity via q.

The light helicity also influences the oscillator strengths of the different transition in a spectrum. This leads to the observation of dichroism[17], which denotes a finite difference in two absorption spectra obtained for different polarization states. A prerequisite for the observability of this effect is the presence of anisotropy in the electronic states that are involved in the transition. In the central field of an atom, the spatial distribution of the charge is closely connected to

---

[15] Full Width at Half Maximum

[16] see eq. 6.4 for the analytic expression and compare section 4.2.3, where the Lorentz profile is introduced for intensity profiles of LEED spots

[17] Greek: two-coloredness

angular momenta, which are related to magnetic moments. Hence, dichroism occurs for spatial anisotropy as well as for the presence of magnetic polarization. Accordingly, a discrimination of natural and magnetic dichroism (ND and MD, respectively) is often made.

Furthermore, a classification of dichroism can be made with respect to the light polarization. Circular dichroism (CD) refers to the difference in spectra measured with left and right circularly polarized light (CPL). Linear dichroism (LD) is the difference of spectra measured with linearly polarized light (LPL) of different polarization directions.

The term circular dichroism was coined by Cotton[18], who reported on the phenomenon in 1895 [162]. A spatial origin of CD can be found in chiral and gyrotropic substances [163, 164], which is not of concern in the present work. The difference in absorption of left and right CPL is closely connected to the rotation of the polarization direction of LPL. For magnetic materials, such rotation has been known since the mid of the 19th century as the Faraday and Kerr[19] effects in transmission and reflection, respectively. Hence, it comes as no surprise that a magnetized sample also shows CD.

Regarding XAS, magnetic circular dichroism becomes apparent at the resonant edges. This has been theoretically predicted in 1975 by Erskine and Stern [148], who transferred considerations on magnetooptical properties to the X-ray region, more precisely to the $M_{2,3}$ edges of Ni. The first experimental realization was achieved in 1987 by Schütz *et al.*, who detected a small but unambiguous dichroic signal at the K edge of Fe. The effect is nowadays referred to as X-ray magnetic circular dichroism (XMCD)[20].

One year prior to the pioneering experimental work on XMCD in the hard X-ray region, magnetic linear dichroism was experimentally discovered in XAS by van der Laan *et al.* at the $M_{4,5}$ edges of a rare earth material [165]. The same group had theoretically proposed the XMLD effect in 1985 [166].

Nowadays, XMCD and XMLD are understood on the same basis. The choice between the experimental techniques depends on the material under investigation. For ferro-, ferri-and paramagnetic samples, XMCD is usually preferred. It has the advantage that the application of the magnetic sum rules (see section 5.3) allows a simple but quantitative evaluation of spin and orbital magnetic moments. The fact that CPL is more easily provided and manipulated by bending magnets, which were the basis for the first synchrotron experiments (see section 5.4.1), might also have contributed to the historical preference towards XMCD.

In general, the XMCD signal vanishes in antiferromagnets. However, XMLD can still be observed if there is a well-defined magnetization axis, even if the net magnetization is zero. Hence, it is the method of choice for such samples.

The samples of the present thesis are paramagnets in the accessed temperature range and the magnetic investigations were performed by means of XMCD. Since it thus is among the major experimental techniques of the present work, the underlying mechanism is described in more detail in section 5.3.

The occurrence of non-magnetic XNLD is connected to the polarization vector $\vec{\epsilon}$ in the dipole matrix element in eq. 5.13, since it projects the initial state $|i\rangle$ to the polarization direction. Hence, a deviation of $|i\rangle$ from spherical symmetry leads to differences in the transitions strengths for different orientations of the sample with respect to $\vec{\epsilon}$.

The initial state is anisotropic for the $4f$ electron in Ce^{3+} if the degeneracy of the $j = 5/2$ ground state is lifted, e.g., by a crystal field (see section 2.1.2). The spatial distributions of the different $\hat{j}_z$ eigenstates are shown in fig. 2.3. A uniaxial CF conserves the uniaxial symmetry of these states, but can mix them to three doublets that are shifted in energy. In the special case of a hexagonal CF as present in $CePt_5$/Pt(111), no mixing occurs and the m_j wavefunctions remain the eigenstates. One of the doublets constitutes the ground state, the others are separated by their respective energy splittings.

As a consequence of the such produced anisotropic spatial distribution of the $4f$ charge dis-

---

[18] Aimé Auguste Cotton, French physicist, 1869-1951

[19] John Kerr, Scottish theologian and physicist

[20] In early publications, nearly all possible permutations of the first three characters in this abbreviation can be found.

tribution, the Ce $M_{4,5}$ XA spectra with LPL differ for the two cases $\vec{\epsilon} \parallel c$ and $\vec{\epsilon} \perp c$. The resulting XNLD and its temperature dependence can be used to identify the states that are produced by the CF, as was demonstrated by Hansmann *et al.* in 2008 [167]. Such experiments require single-crystalline samples, since they rely on proper alignment of light polarization and well-defined crystallographic directions. The application of this technique to the $\mathrm{CePt_5/Pt(111)}$ samples of the present thesis is discussed in section 9.2.

It is important to note that in the present experimental conditions, i.e., for uniaxial crystal symmetry with the c-axis perpendicular to the surface, it is possible to measure XNLD with circularly polarized light. This can be done by variation of the angle of incidence θ with respect to the surface normal (see fig. 5.5). As is derived in appendix A.2, the spectrum for CPL can be expressed by the spectra for LPL according to

$$\mu_{\mathrm{x}}(\theta, E) = (\cos^2\theta + 1)\ \mu_{\mathrm{x}}^{\perp}(E) + \sin^2\theta\ \mu_{\mathrm{x}}^{\parallel}(E). \tag{5.15}$$

Hence, for normal incidence ($\theta = 0°$), the spectrum for CPL resembles the case $\vec{\epsilon} \perp c$. The case $\vec{\epsilon} \parallel c$ cannot be achieved, but $\theta = 54.7°$ represents a special situation where $\mu_{\mathrm{x}}^{\perp}$ and $\mu_{\mathrm{x}}^{\parallel}$ contribute in the ratio 2:1. Hence, the spectrum taken at this angle represents the isotropic average over all spatial polarization directions,

$$\mu_{\mathrm{x}}^{\mathrm{iso}}(E) = \frac{1}{3}\left(\mu_{\mathrm{x}}^{x}(E) + \mu_{\mathrm{x}}^{y}(E) + \mu_{\mathrm{x}}^{z}(E)\right). \tag{5.16}$$

The result is the isotropic spectrum[21], which is an important reference. It corresponds to the spectrum of a state with spherical symmetry, as for a nondegenerate $j = 5/2$ state, and thus also equals the average of the three $\hat{j}_z$ eigenstates.

One of the features of the isotropic spectrum is summarized in the so-called charge sum rule. It states that the total oscillator strength of the polarization-averaged, isotropic spectrum of a transition $c^n v^m \rightarrow c^{n-1} v^{m+1}$ is proportional to the number of holes N_h in the v shell in the initial state [168, 169]. In simple terms, an excitation is the stronger the more free final states are available. The charge sum rule does not only allow experimentally addressing N_h, but also qualifies the integral of the isotropic spectrum for normalization of further sum rules (see section 5.3).

In the present work, most of the non-normal incidence data were taken at $\theta = 60°$. The deviations in the mixture of the parallel and perpendicular spectra from the isotropic case are of the order of 10 %. This is sufficiently small to regard those spectra as isotropic. During later experiments, datasets at $\theta = 54.7°$ were also recorded.

5.3 Principles of X-ray Magnetic Circular Dichroism

As is introduced in section 5.2, the X-ray absorption spectrum in many cases depends on the light polarization. A special case is the resonant absorption of circularly polarized light on magnetized samples. The difference between the spectra measured with left and right CPL is called X-ray magnetic circular dichroism. Its analysis yields valuable and quantitative information on element- and orbital specific magnetic moments of the material under investigation.

The element- and orbital specificity of XMCD are inherited from the underlying X-ray absorption process, as is the applicability of the dipole selection rules. As derived in section 5.1.1 in a one-electron picture, conservation of angular momentum during the excitation process introduces a change of the magnetic quantum number of the excited electron by $\Delta m \pm 1$ for CPL.

In general, the excitation thus leads to a preferential population of orbital states with the respective alignment of the corresponding magnetic moments. For example, in the $3d^{10}4f^1 \rightarrow 3d^9 4f^2$ excitation at the Ce $M_{4,5}$ edges, $3d$ core electrons with $m_l \in \{-2, -1, 0, 1, 2\}$ are excited to $4f$ states with $m_l \in \{-3, -2, -1, 0, 1, 2, 3\}$. With CPL, the dipole allowed final states are restricted to $m_l \in \{-3, -2, -1, 0, 1\}$ and $m_l \in \{-1, 0, 1, 2, 3\}$ for left and right CPL, respectively.

---

[21] This requires the assumption that the crystal symmetry is not rhombohedral, monoclinic or triclinic.

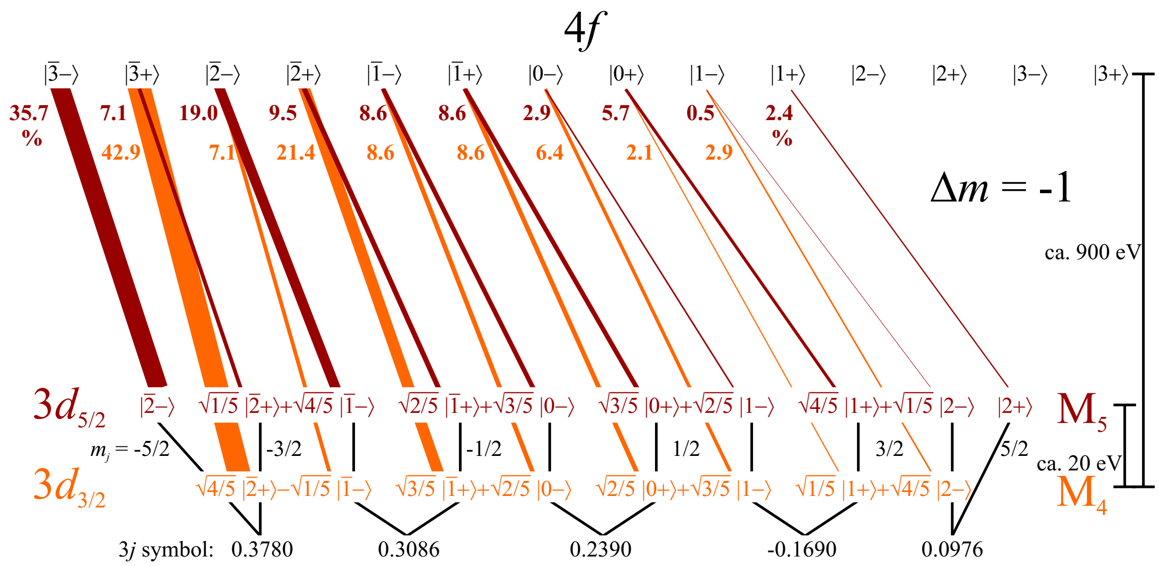

Figure 5.3: One-electron transition probabilities from the spin-orbit split $3d$ core shell to the $4f$ valence shell (Ce $M_{4,5}$ edges) in a $|l, m_l\rangle\,|s, m_s\rangle$ basis for left CPL ($\Delta m_l = -1$). The states are given in a shortened notation $|m_l, m_s\rangle$. For $m_s = \pm 1/2$ only the sign is given and $\overline{m_l}$ denotes a negative value. The transition probabilities for each edge are given in percent and are also reflected by the width of the lines connecting the states. Furthermore, the numeric values of the $3j$ symbols that are needed for the calculation of the transition strengths are given in the lower part. The picture for right CPL ($\Delta m_l = +1$) can be constructed by reversing the signs of all m quantum numbers.

For core shells with non-zero orbital angular momentum, the core-hole that is created during the absorption process is subject to spin-orbit coupling (compare section 5.1.2). As a consequence, the preference in orbital polarization that is induced by the CPL also leads to a preferential alignment of the spin moment.

This effect is illustrated in fig. 5.3 for the example of the Ce $M_{4,5}$ edges. In the lower part, the spin-orbit coupled $3d_{5/2}$ and $3d_{3/2}$ states are written in a $|l = 2, m_l\rangle\,|s = 1/2, m_s\rangle$ basis with the respective Clebsh-Gordan coefficients. In the upper part, the $4f$ level is represented by the 14 possible $|l = 3, m_l\rangle\,|s = 1/2, m_s\rangle$ combinations.

These states represent a basis set for the $4f$ level, but they are not eigenfunctions of the Hamiltonian. However, the relevant conclusions regarding the preferred orbital and spin polarization of the excited electron can be drawn from the sum over all transitions. This sum is conserved independent of the basis set that is chosen for the description of the $4f$ level and can thus also be obtained in a simple one-electron representation.

The lines that connect the $3d$ to the $4f$ states in fig. 5.3 mark the transitions that are allowed according to the dipole selection rules for left CPL ($\Delta m_l = -1$). The transition probabilities can be calculated most elegantly by usage of Wigner's $3j$ symbols [44], which are given in the lower part of fig. 5.3. According to eq. 5.4, the given percentage values for each transition are then obtained by the squares of the $3j$ symbol and the Clebsh-Gordan coefficient of the core state, normalized to the sum of all transition strengths for each of the $3d_{5/2}$ and $3d_{3/2}$ subshells. With this information, the quantities of interest are the expectation values for the z-components of the orbital and spin angular momentum operators, $\langle \hat{l}_z \rangle$ and $\langle \hat{s}_z \rangle$, respectively (see eq. 2.3). The average orbital angular momentum that is obtained by the excitation amounts to $\langle \hat{l}_z \rangle = -2\hbar$ for both $3d$ subshells. Regarding the spin moment, the polarization is different at the two edges. The probability to obtain a core electron with $m_s = +1/2$ is 75 % for the M_4 edge, but only 33 % for M_5. Hence, $\langle \hat{s}_z \rangle_{M_4} = 1/4\ \hbar$ and $\langle \hat{s}_z \rangle_{M_5} = -1/6\ \hbar$. For right CPL, the symmetry of the formulation leads to a mere reversal of the signs of all m quantum numbers in fig. 5.3. Hence, for the expectation values also only the signs change.

The such obtained preferences in spin and orbital polarization of the excited state for the two light polarization directions do not automatically lead to a difference in the observed XAS intensities. The spectra for excitations to final states with opposite signs of m_l are equal, since the magnetic quantum number only affects the angular part of the wavefunction as a phase factor $e^{im_l\varphi}$. Hence, it does not contribute to the squared absolute value of the matrix element in eq. 5.4.

However, a difference in intensity occurs if there already is a preferential population of states with one sign of m_l. This is the situation of a magnetized sample, where states with a magnetic moment aligned parallel to the magnetization direction are reduced in energy due to the Zeeman term of the Hamiltonian (see eq. 2.15). In that case, the number of holes in the initial state differs for the configurations with opposite signs of m_l. This leads to different intensities in analogy to the charge sum rule (see section 5.2).

As a consequence, XMCD can only occur if the resonant transition involves a partially filled valence shell. This indicates that the effect allows probing the magnetic properties of this valence shell in the initial state. Furthermore, this means that the effect can never be observed for the excitation of a core electron to an empty valence shell, e.g., for the $3d^{10}4f^0 \rightarrow 3d^9 4f^1$ contribution at the Ce $M_{4,5}$ edges.

The explanation of XMCD as a combination of excitation of polarized electrons and their momentum-selective "detection" by the partially filled valence states is often referred to as the two-step model in the literature. The "detector" can be visualized in the Stoner[22] band picture or as sharp, Zeeman-split atomic states, depending on the system under investigation. An expansion in the $|l=2,m_l\rangle\,|s=1/2,m_s\rangle$ basis, as applied in fig. 5.3, is always possible. As discussed above, conclusions from the sum over all transitions to the dipole-allowed final state are unaffected by the choice of the basis. This sum can be addressed experimentally by the integral of the total XMCD signal.

The maximum XMCD signal is obtained for collinear alignment of photon angular momentum direction, which corresponds to the propagation direction of the incoming light, and magnetization direction, since the XMCD magnitude depends on the cosine of the angle between the two axes [156]. Hence, this configuration is usually chosen for experiments. For left and right CPL and opposite signs of the external magnetic field, four different relative orientations of photon momentum and sample magnetization exist. Since those are pairwise equivalent in the symmetric situation of the present experiments, a distinction of parallel and antiparallel orientation is sufficient. Under normal conditions, it is of no concern whether the light polarization or the sample magnetization is reversed for measurement of the XMCD[23]. The two spectra are denoted as $\mu_{\mathrm{x}}^{+}(E)$ and $\mu_{\mathrm{x}}^{-}(E)$ for parallel and antiparallel orientation, respectively.

In addition to the qualitative understanding of the mechanism behind the XMCD effect, the considerations made so far can be developed further to connect the integrated XMCD signal to the expectation values $\langle \hat{l}_z \rangle$ and $\langle \hat{s}_z \rangle$ and thus to the respective magnetic moments $\langle \mu \rangle$ of the valence shell in the initial state (see eq. 2.5). This is done by the so-called orbital and spin moment sum rules [151, 152].

While the theoretical derivation of the magnetic sum rules in a general way is sophisticated and is thus not reproduced here, their application and the resulting formulae are rather simple. For the $M_{4,5}$ edges they read

$$\langle \mu_l \rangle = -\frac{\int_{(M_5+M_4)} \; \Delta\mu_{\mathrm{x}}(E)\; dE}{\int_{(M_5+M_4)} \; \mu_{\mathrm{x}}^{iso}(E)\; dE} \; N_h \; \mu_B \tag{5.17}$$

$$\langle \mu_s \rangle = -\left(\frac{\int_{M_5} \; \Delta\mu_{\mathrm{x}}(E)\; dE - \frac{3}{2}\int_{M_4} \; \Delta\mu_{\mathrm{x}}(E)\; dE}{\int_{(M_5+M_4)} \; \mu_{\mathrm{x}}^{iso}(E)\; dE} \; N_h + 6\langle \hat{T}_z \rangle \right) \; \mu_B \tag{5.18}$$

The spin sum rule contains a contribution from the magnetic dipole term $\langle \hat{T}_z \rangle$, which describes a possible aspheric spin contribution and cannot be separated from $\langle \hat{s}_z \rangle$.

---

[22] Edmund Clifton Stoner, British physicist, 1899-1968 [144]

[23] The presence of uncompensated magnetic moments at an ferromagnet/antiferromagnet interface is an example where this is not the case for an experimental signal [170].

For different absorption edges, the sum rules exhibit different numerical factors, whereas the general structure of the equations is always the same. The orbital moment is proportional to the integral of the total XMCD spectrum of a certain transition. The spin moment is obtained from the difference of the integrated signals of two separated, spin-orbit split edges. This reflects that the orbital polarization of the excited core electron has the same sign for the two edges, while the signs are different for the spin polarization. This observation was also made in conjunction with fig. 5.3.

In the sum rules as given above, the integrated XMCD intensities are normalized to the integral of the isotropic spectrum. This is done in order to eliminate prefactors from the calculation, which are unknown in practice. According to the charge sum rule (see section 5.2), this introduces the number of holes in the initial state N_h to the equations.

The sum rules yield the magnetic moment per atom. Results of the application of the sum rules to experimental data in the present thesis are given in units of Bohr magnetons (μ_B), the additional unit “per atom” (at), as often used, is not explicitly given.

The present XMCD experiments were primarily performed at the Ce $\mathrm{M}_{4,5}$ edges. The applicability of the sum rules as well as details on the evaluation procedure in this special context are treated in section 6.4.3

5.4 Experimental requirements for XAS and XMCD

In order to utilize the features of XAS and XMCD as presented in the previous sections, the photon energy-dependent absorption coefficient $\mu_\mathrm{x}(E)$ has to be measured with polarized X-rays. The present section is devoted to the realization of the experimental techniques.

First of all, an appropriate light source is required, which is treated in section 5.4.1. Then, the absorption coefficient has to be measured. Different options on doing so are presented in section 5.4.2. The present experimental setups are described in detail in section 5.4.3, whereas section 5.4.4 is devoted to the particular measurement and signal processing techniques that were applied to reliably detect small XMCD signals. Section 5.4.5 provides information on the way the experimental data are presented in part II.

5.4.1 Light sources

The measurement of X-ray absorption spectra requires an X-ray source with tunable photon energy. For dichroic experiments, the light polarization has to be controlled in addition.

The experiment that lead to the first observation of an absorption edge was performed by monochromatization of the Bremsstrahlung of cathode rays [146]. However, the continuous background of X-ray tubes provide only little light intensity, which is superimposed by intense characteristic lines at certain energies. Furthermore, a well-defined polarization state is hard to accomplish.

Therefore, sensitive XAS and XMCD experiments as the ones of the present work are usually performed at synchrotron radiation sources. In such large-scale facilities, bunches of electrons are accelerated to nearly the speed of light and then injected into a storage ring. Here, the electrons are guided on a stable orbit by bending magnets.

The deflection of the electrons in the magnetic field of a bending magnet leads to the emission of radiation. In the case of relativistic electrons, this synchrotron radiation forms a narrow cone tangential to the orbit. Therefore, experiments that use this radiation have to be placed at the end of a tangential connection to the light-emitting device. This connection is the so-called “beamline”, while the experiment is performed in the “endstation”. The beamline can be separated from the storage ring by the “beamshutter”.

The radiation emitted at a bending magnet is characterized by a broad spectral distribution, the details of which mainly depend on the kinetic energy of the electrons and the magnetic field strength. Higher photon energy can be reached by increasing any of the two parameters [171]. For XAS experiments, the electron binding energies of the absorption edges under investigation define the energy range of interest. In the present work, these primarily are the Ce $\mathrm{M}_{4,5}$ edges

Facility	period	E_{el} (GeV)	injection mode	Beamline	E_{ph} (keV)
BESSY II	2010 to 2011	1.7	decay	PM3 (BM)	0.02-1.9
SOLEIL	2012	2.75	top-up	DEIMOS (U)	0.35-2.5

Table 5.1: Characteristics of the Synchrotron facilities and beamlines that were used for the present XAS and XMCD experiments. The names of the three synchrotron facilities are given along with the time period of the present experiments, electron energy E_{el}, the injection mode, the name of the beamline and the available photon energy E_{ph} range. BM: bending magnet, U: undulator.

at $E_{\mathrm{b}} \approx 900\,\mathrm{keV}$ (see fig. 5.2). This energy lies in the soft X-ray region, which is provided by synchrotron facilities that operate at electron energies of some GeV.

The present experiments were performed at BESSY in Berlin, Germany at the PM3 beamline and at SOLEIL in Saint-Aubin, France at the DEIMOS beamline. Relevant parameters for the two synchrotron facilities and beamlines are summarized in tab. 5.1. Both facilities are generally open to external users. Time slots for experiments, so-called “beamtimes”, can be received following an experimental proposal, which has to pass a reviewing process.

In the time period of the present experiments, BESSY was operated in decay mode, which means that the storage ring is filled with electrons and then operated for several hours before the next injection is performed. In this eight-hour interval, the electron bunches in the ring decay on a characteristic time scale. During injection, the beamshutter is closed for radiation protection reasons. Consequently, the thermal equilibrium of the beamline optics is disturbed, which can affect the quality of data measured directly after an injection (see section 5.4.5). SOLEIL was operated in top-up mode, which means that smaller electron bunches are injected on a shorter time scale. As a result, the filling of the ring and thus the light intensity are virtually constant. Due to their high frequency, the injections have to be performed without closure of the beamshutter in top-up mode.

The polarization of the light emitted at a bending magnet depends on the viewing angle with respect to the electron orbit plane. For visualization, one can imagine the circular electron orbit viewed parallel to the plane or perpendicular to it from above or below the plane. In the plane, an oscillatory linear motion is observed, while it contains a circular component out of plane. If the direction of this motion is clockwise above the plane, it is counter-clockwise when viewed from below. Equalizing the observed electron motion with the polarization of the emitted light, linearly polarized emission is observed in-plane, while circularly polarized light is obtained by moving the direction of viewing out of plane. The direction of the circular polarization depends on the direction of the angle displacement, and the degree of circular polarization depends on the magnitude of displacement. Due to the relativistic emission cone in a synchrotron, a high polarization rate can already be obtained for small angle displacements.

The storage ring of a synchrotron is usually not strictly circular, but consists of straight sections alternating with the curved bending magnets. These straight sections can contain more complicated insertion devices like undulators. An undulator consists of two periodic arrays of permanent magnets with alternating polarity, which are separated by a small gap in which the synchrotron electrons travel.

Due to the periodic magnetic field, the electrons follow an oscillatory track when passing through the device. Each pair of poles acts like a small bending magnet. Hence, radiation is again emitted tangential to the electron orbit. Undulators are designed in a way that interference of the cones emitted at the opposite turning points of the electron track occurs. Hence, light emission with high intensity can be obtained at a certain photon energy and its higher harmonics. This energy is adjusted by variation of the gap size.

The observed polarization again depends on the viewing angle, but also on the relative lateral displacement of the two magnetic arrays. It is linear in the synchrotron orbit plane, if the poles are adjusted directly above each other. Circular polarization can be obtained by relatively shifting the arrays.

The high controllability and the generally better performance make undulators superior to simple

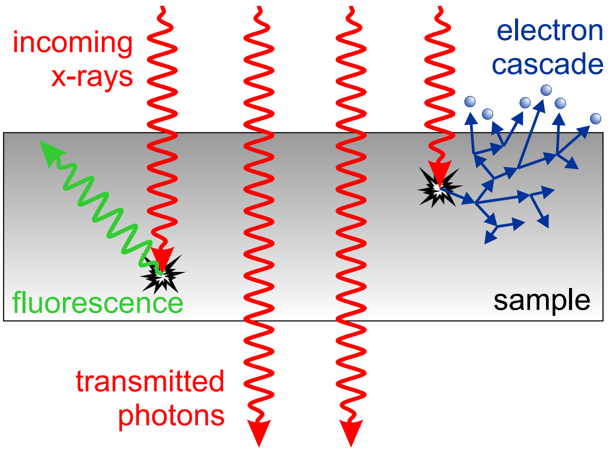

Figure 5.4: Illustration of the three detection modes for $\mu_\mathrm{x}(E)$ that are described in the text: transmission, electron yield and fluorescence yield. X-ray photons that penetrate a sample are either absorbed or transmitted. The reduced number of transmitted photons is a measure of the amount of absorption, as well as the numbers of photons and electrons that are created as a consequence of absorption events.

bending magnets. However, if these advantages are not needed for a given experiment, a bending magnet provides a more cost-efficient and, due to the "parasitic" character[24], more readily available alternative. The experiments at BESSY were done at a bending magnet, while at SOLEIL an undulator was used.

To finally utilize the synchrotron radiation in an experiment, a series of X-ray optics is needed. Next to simple apertures, the X-ray beam has to be guided, focused and monochromatized. Since the refractive index for X-rays is close to and slightly below unity for all common materials, lenses and prisms are not available and the optical elements solely consist of mirrors.

Consequently, rotatable gratings have to be applied for monochromatization by diffraction (compare section 4.1). Both of the used beamlines were equipped with plane grating monochromators (PGM). The PGM was designed by Peterson [172] and is often applied, since it combines good performance with high robustness.

In order to yield reproducible results, the photon energy setting of a monochromator has to be calibrated. For the experiments at BESSY, a calibration procedure was performed at the beginning of each beamtime that involved the recording of the position of a strong XA resonance and its replica at higher harmonics, i.e., at integer fractions of the first order energy. This yielded high reproducibility for the energy axes of Ce $\mathrm{M}_{4,5}$ spectra recorded at different beamtimes. For the experiments at SOLEIL, the monochromators were used as provided by the beamline staff. The resulting energy positions of the spectra did not coincide with the ones obtained at BESSY, which required correction of the energy axis (see section 5.4.5).

5.4.2 Detection modes for the linear absorption coefficient

A direct way to determine the linear absorption coefficient $\mu_\mathrm{x}(E)$ of a sample is to relate the transmitted to the incoming light intensity according to eq. 5.2. Loss of X-ray intensity due to reflection at the sample surfaces is usually negligible if the angle of incidence with respect to the surface normal is not too large. However, in order to obtain a measurable signal in transmission, the sample thickness t has to be of the order of the X-ray penetration length $l_x = 1/\mu_\mathrm{x}$, which is typically of the order of ten to hundred nanometers in metals [160]. While a number of techniques exists to prepare such samples[25], this approach is not practicable for the surface intermetallics investigated in the present thesis.

---

[24] This refers to the fact that historically, synchrotron facilities were initially constructed to address questions of particle physics, while the light emission was regarded as an annoying energy loss. After the realization of the opportunities offered by the radiation, experiments utilizing it were attached to the existing facilities.

[25] The demand is similar for (S)TEM samples, compare section 3.5.

Alternatively, $\mu_\mathrm{x}(E)$ can be addressed via secondary effects, as illustrated in fig. 5.4. The absorption of X-ray photons (see section 5.1) produces excited atomic states containing core-holes. The two main channels to release the additional energy are radiant relaxation by emission of a photon, which is called fluorescence, and Auger electron production (compare section 3.4), which leave the atom in addition to direct photoelectrons that are produced by continuum absorption. The detection of photons and electrons as a measure of $\mu_\mathrm{x}(E)$ is called fluorescence and electron yield, respectively.

The two relaxation processes are competitive, their relative strength depends on the atomic number Z for a given edge [171]. This indirectly leads to a dependence on the photon energy, since a certain edge appears at higher E with increasing Z.

For Ce and Pt with $Z = 58$ and 78, respectively, fluorescence predominates. Nevertheless, electron detection can be successfully applied in the soft X-ray regime, since high sensitivity can be achieved with comparably low experimental effort. Both electron and fluorescent detection techniques were applied in the present thesis. In the following, the different measurement modes are described.

Electron yield

A prerequisite for the detectability of the electrons that are created by X-ray absorption is that these electrons can leave the sample. Hence, only electrons can be detected that have sufficient energy to overcome the work function. However, the energy of the direct and Auger electrons is quickly dissipated by inelastic scattering processes in a solid. Such processes occur on the length scale of the inelastic mean free path λ_IMF [105] (compare sections 3.4 and 4.2.3), which is typically of the order of nanometers.

On one hand, this gives rise to the surface-sensitivity of electron yield techniques, since only electrons that originate from surface-near absorption processes can leave the sample. On the other hand, the scattering again produces secondary electrons. The resulting electron cascade (as depicted in fig 5.4) can facilitate the measurement, since a single absorption event contributes with more than one electron.

Hence, the most practicable approach for electron yield detection of $\mu_\mathrm{x}(E)$ is to measure all electrons that leave the sample, independent of their energy. This is most conveniently done by measurement of the drain current $Y(E)$ at the sample and is called total electron yield (TEY). In particular, this is the method of choice for XMCD experiments, since the high magnetic fields would strongly complicate a direct detection of free electrons[26].

Primary electrons contribute to the smallest part to the TEY signal, which is dominated by secondary electrons with low kinetic energy left. While the information depth for primary electrons is of the order of λ_IMF, a larger information depth can be assumed for the secondary electrons. The TEY escape depth is commonly modeled by a single, energy averaged parameter λ_e [147]. This effective quantity is typically of the order of $\lambda_\mathrm{e} \approx 1 \ldots 2$ nm. In general, it has to be determined experimentally for a given material. Respective experiments for the present CePt$_5$/Pt(111) samples are described in section 7.4.

In order to obtain $\mu_\mathrm{x}(E)$ from the TEY current $Y(E)$, the relation between the two quantities has to be known. The relation depends on different length scales inherent to the sample system and on the measurement geometry. Deviations from direct proportionality, so-called saturation effects, can be a serious problem. This issue is addressed in detail in section 5.5, where a model is developed to describe the TEY signal generated by a thin film on top of a substrate.

In the absence of saturation effects, the proportionality factor between $Y(E)$ and $\mu_\mathrm{x}(E)$ depends on the conversion rate of the number of absorbed photons to the number of electrons that contribute to the measured current. This parameter, and hence the efficiency of the measurement, is strongly affected by electric and magnetic fields in the vicinity of the sample surface. A magnetic

---

[26] Without a magnetic field, energy-resolved analysis of photoelectrons in dependence of the photon energy is of course possible and furthermore very interesting. This technique, which is called resonant photoemission spectroscopy, combines the advantages of normal PES with the element-specificity of XAS. The identification of CePt$_5$/Pt(111) as a heavy fermion system is mainly owed to such experiments [94]

Facility	Detection	B_{max} (T)	T_{b} (K)
BESSY II	TEY	3	12
SOLEIL	TEY, TFY	6.5	2

Table 5.2: Basic parameters of the different XAS and XMCD setups used for the present experiments. For both synchrotron facilities (see section 5.4.1, especially tab. 5.1) the applied detection modes, the maximum magnetic field B_{max} and the base temperature T_{b} are given.

field reduces the signal, which can be explained by electrons that return into the sample due to the Lorentz force. This effect is observed to be asymmetric with the field direction and depends on geometric aspects like surface roughness, angle of incidence and details of the experimental setup [173]. In contrast, a negative bias at the sample creates an electric field that accelerates the electrons away from the surface. Hence, it counteracts the reduction of the signal by the magnetic field and is thus a reasonable feature in an XMCD setup working in TEY mode.

Fluorescence yield

Due to the time-reversal symmetry of the process, the radiant relaxation of an atom that has been excited by X-ray absorption can be described analogous to the excitation. Hence, the dipole selection rules, which are presented in section 5.1.1, also apply and restrict the number of possible final states. Direct reversal is usually the main channel, the photons produced in this process carry the total excitation energy. Depending on the electronic configuration, other recombinations are possible that lead to partial relaxation of the atom. The energy spectrum of the fluorescence features the well-known characteristic lines.

The fluorescence yield is usually measured with a photodiode. In analogy to TEY, detection insensitive to the photon energy is called Total Fluorescence Yield (TFY). Energy-selective detection of single characteristic lines allows enhancement of the signal from certain elements in the sample.

In contrast to TEY detection, secondary photons are not expected for TFY, since inelastic interaction of photons with matter can be neglected[27] [147]. Hence, the length scale, on which the fluorescent X-rays are damped in the sample, is the same as for the incoming light, $l_x(E) = 1/\mu_{\mathrm{x}}(E)$. For metals, it is typically of the order of ten to hundred nanometers, which is why TFY detection is regarded as a bulk-sensitive technique.

A problem with TFY signals is the so-called self-absorption. This means that the fluorescent photons are again absorbed by sample atoms on their way to the detector, which leads to a reduction of the recorded signal. Since this absorption follows the same line profile as the spectrum itself, damping is stronger at energies with large μ_{x}. Qualitatively, this leads to an overdamping of absorption peaks, which complicates the quantitative evaluation of FY spectra. Since the penetration lengths of incident and outgoing light are comparable, the effect is usually more critical than TEY saturation. A correction is laborious and has not been performed in the present thesis.

In general, one can expect that the efficiency for secondary processes is different in resonant and continuum absorption. Furthermore, the efficiencies are different for TFY and TEY detection. Therefore, complementary measurement of both electron and fluorescence yield can be used to disentangle resonant and continuum contributions to a spectrum. Such an analysis for the Ce $\mathrm{M}_{4,5}$ edges is presented in sections 8.2.3 and 8.2.4.

5.4.3 Description of the experimental setups

The basic elements of the present experimental setups for XAS and XMCD measurements are schematically shown in fig. 5.5. This includes the monochromatic, circularly polarized X-ray

---

[27] At this stage, there is an analogy between the discussion of LEED in contrast to XRD and electron yield in contrast to fluorescence yield in XAS, compare section 4.1.2.

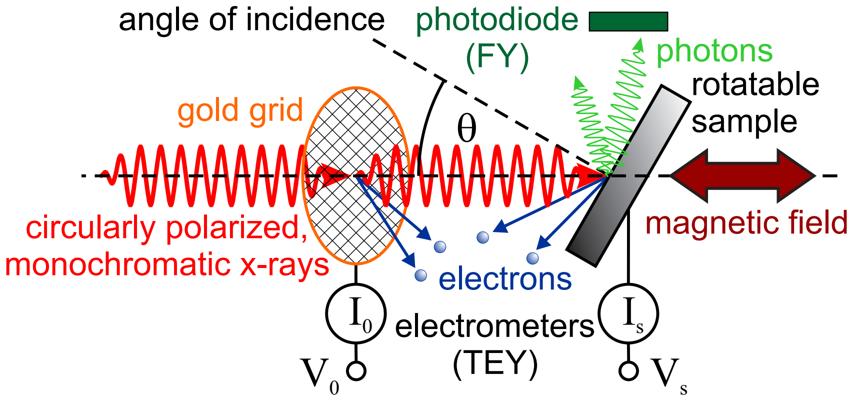

Figure 5.5: Schematic Drawing of the experimental setups used for XAS and XMCD measurements with definition of the angle of incidence θ. A photodiodes for TFY detection was only installed at SOLEIL.

beam provided by the beamline (see section 5.4.1), the rotatable and coolable sample in a variable magnetic field, electrometers and photodiodes for TEY and TFY detection, respectively, and the possibility to measure the light intensity I_0 of the beamline.

Tab. 5.2 summarizes the available detection modes, the maximum magnetic field strength and the lowest sample temperature of the two setups that were used in the present work. In both setups, the magnetic field direction was collinear to the incoming photon beam in order to assure a maximum XMCD signal (see section 5.3).

The recording of I_0 is needed for normalization of the sample signal. Alternatively, the storage ring current I_r can be used. It accounts for intensity variations caused by the electron filling, but does not include the characteristics of the beamline. For example, most beamlines suffer from C and O contamination of the optical components, which are commonly made of Cr. In the vicinity of the absorption edges of these elements, strong intensity modulations can occur. In limited energy ranges free from such effects, I_r normalization can also be used for relative evaluations. In particular, it avoids the introduction of additional noise to the normalized signal.

In the following, the individual characteristics and parameters of the two different setups are described in more detail.

BESSY, PM3

Experiments at BESSY were performed with a custom-built mobile XMCD unit. This unit already had a long tradition at the PM3 bending magnet beamline prior to the present thesis and is optimized for operation at this site.

The XMCD unit is dedicated to the detection of small signals from low-dimensional, surface-near sample systems in the soft X-ray range. For such experiments, TEY is the method of first choice. This is due to the surface-sensitivity of the technique, which even outbalances the higher efficiency for fluorescence yield for heavy elements like Ce and Pt.

As the results of the present thesis show, the lower photon flux at a bending magnet compared to an undulator does not prevent the acquisition of high-quality data. Furthermore, the possibility to use an own setup at a synchrotron allows ideal preparation and optimization of the experiment. The drawbacks of this approach are very high requirements concerning (wo)manpower and logistics.

The complete XMCD unit was transported to Berlin for each beamtime and attached to the beamline, which has no stationary endstation. Great care was taken to correctly align the measurement chamber with respect to the beamline. For this purpose, a theodolite and an optical leveling instrument were applied.

The beamline is optimized for circular light polarization, which is adjusted by changing the viewing angle with a mirror. In addition to the monochromator calibration described in section 5.4.1, a calibration procedure for the mirror angle was performed at the beginning of each beamtime. For this purpose, the XMCD signal of a permalloy foil was measured for various mirror angles with both polarization directions. The nominal point of linear polarization was then set to the interpolated axis intercept. The procedure mainly accounts for step motor deficiencies.

Since inversion of the polarization by mirror rotation is time-consuming and imprecise, the experiments were performed at fixed polarization direction by reversal of the magnetic field.The degree of polarization is reported to amount to 93% at $E = 700$ eV. This value is also assumed to be valid at the Ce $M_{4,5}$ edges near $E = 900$ eV. The finite degree of polarization has to be corrected for when measurements with circularly polarized light are quantitatively discussed, as in the sum rule evaluation of XMCD (see section 5.3).

The energy resolution in the Ce $M_{4,5}$ energy range is specified as $\Delta E \approx 100$ meV for the beamline settings used in the present experiments (fixed focus constant setting $c_{ff} = 2.25$ and standard exit slit setting). The spot size at the sample position amounts to $A = 500 \times 500\ \mu\text{m}^2$. The characteristics of the beamline are summarized in an information sheet [174].

The mobile XMCD unit primarily consists of a sample preparation unit (setup A, see section 3.2), a superconducting magnet with a cryogenic sample stage for the X-ray experiments and a gold grid for I_0 normalization. Sample transfer facilities complete the unit. It can furthermore be complemented by additional devices like a cluster source [175] or a glove box for nanoparticle preparation [176].

The magnet consists of a pair of superconducting Helmholtz[28] coils cooled with liquid helium. The maximum field strength is $|B| = 3$ T, the field is homogeneous in the vicinity of the sample. The magnet is operated with a Lake Shore Model 622 Power supply that allows short standby times of $\tau \lesssim 23$ s between acquisition of two data points with $B = \pm 1.5$ T. With this high sweeping rate, XMCD spectra can be recorded in a measurement mode that is optimized to reduce artifacts. For this purpose, $Y(E)$ is recorded for both field directions at each energy step while progressively scanning E through the spectrum. This approach and the data evaluation procedures connected to it are described in more detail in section 5.4.4. The acquisition time for an XMCD spectrum with 200 energy steps at $|B| = 1.5$ T, a typical configuration for a full Ce $M_{4,5}$ spectrum, amounted to $\tau \approx 90$ min.

The sample stage has threefold purpose: Sample positioning and rotation, control of the sample temperature and measurement of the sample drain current as the TEY signal.

For positioning, the sample stage is mounted on a standard UHV manipulator with a differentially pumped rotation stage. It allows scanning most of a typical sample crystal surface with the X-ray beam. The angle of incidence (see fig. 5.5) can be adjusted in the full range $\theta = 0 \ldots 90°$. The azimuthal orientation of the sample with respect to the surface normal has to be chosen during sample transfer and cannot be adjusted during the experiment.

The sample temperature can be adjusted in the range $T = 12 \ldots 400$ K by the combination of a liquid helium continuous flow cryostat and a thermal resistor. For adjustment and stabilization of the sample temperature, a proportional-integral-derivative (PID) controller is applied (Lake Shore 331 Temperature Controller). The upper temperature limit is set by sensitive material in the vicinity of the heater. In principle, the lower limit could be decreased by a dedicated design of the sample stage. However, this would happen at cost of flexibility of the unit, which is designed to meet the requirements of various experiments. An attempt to find a technical solution to reach lower temperatures was started during the work on the present thesis, but this project is not finished yet.

The temperature is measured with a calibrated GaAlAs diode (TG-120-SD, Lake Shore Cryotronics Inc.), which is placed in the direct vicinity of the transferable sample holder. Comparative measurements with an additional diode mounted to the sample holder showed that the deviation between the two amounts to $\Delta T/T \lesssim 5$ %, with the true sample temperature being higher at low temperatures. Since no complete calibration was performed, the values measured with the fixed sensor are taken as the sample temperature throughout the present thesis. Error bars that are given for the temperature only reflect variations of the sensor reading during the

---

[28] Hermann Ludwig Ferdinand von Helmholtz, German physicist and physiologist, 1821-1894

respective measurements, and not systematic errors.

For measurement of the TEY current, highly sensitive Keithley 6517A electrometers are used. In order to minimize noise, the measurement cable possesses two coaxial shields. The outer shield is grounded and connected to the vacuum chamber. The inner shield is set to the sample potential and is continued inside the chamber as close to the sample as possible.

The sample potential can directly be controlled with the electrometer. It is usually set to $V_\mathrm{s} = -100$ V with respect to the ground level in order to counteract the reduction of the TEY signal due to the magnetic field (see section 5.4.2).

The gold-coated grid that is used for measurement of the normalization current I_0 is placed between the exit slit of the beamline and the sample. The absorption coefficient was measured in TEY mode analogous to the sample signal, with a bias of $V_0 = -100$ V. Gold was chosen as reference material since $\sigma_\mathrm{Au}(E)$ exhibits no sharp features in the soft X-ray regime. A problem arises if the grid material is contaminated with other elements, which occurred during the present experiments. For reasons of manufacturing, signatures of the Ni $L_{2,3}$ edges were visible close to the Ce $M_{4,5}$ edges. This problem was addressed by the installation of a gold evaporator, which produces a clean gold coating whenever needed.

Admittedly, the supplementary recording of an absorption signal with distinct peaks in the energy range of interest has the advantage of providing a sample-independent energy reference. For this reason, the chamber that hosts the I_0 grid was additionally equipped with a mounting for reference wires, which can be moved into the X-ray beam to record their absorption signal parallel to the gold grid and the sample. For the present experiments, one of these wires was coated with Ce and oxidized at ambient air. Ce oxide shows a rich multiplet structure at the Ce $M_{4,5}$ edges and is therefore ideally suited as energy reference. An exemplary spectrum is shown in fig. A.3 (b).

SOLEIL, DEIMOS

With the DEIMOS beamline, SOLEIL provides a modern undulator soft X-ray beamline dedicated to XMCD experiments at high magnetic field and low sample temperature. Those last two aspects, and especially the combination of both, were the main reasons to apply for beamtime to investigate the $\mathrm{CePt_5/Pt(111)}$ surface intermetallics. Facilities for *in situ* preparation of samples are available (setup C, see section 3.2), only the substrate crystal and the Ce evaporator were brought to SOLEIL and inserted into the UHV system.

Many aspects of the DEIMOS setup are designed similar to the mobile XMCD unit described in the previous paragraph, although the technical realization differs at many points. The relevant differences are described in the following.

The beamline is installed at an undulator, which means that full circular polarization is available and inversion of the polarization is much faster and more reproducible than at a bending magnet. Hence, for measurement of XMCD spectra, the magnetization can be kept constant. This allows using high magnetic fields, which cannot be switched readily.

However, a measurement mode with polarization switching at each energy step in analogy to the mode applied at BESSY was not available at the beamtimes of the present thesis. Hence, XMCD spectra were recorded by subsequent scans of the complete spectrum with alternating polarization. Four spectra with a polarization sequence left-right-right-left were usually measured. This sequence minimizes the risk of time-dependent beamline-induced artifacts that resemble dichroism.

The data acquisition time for an XMCD spectrum with 250 energy steps recorded that way amounted to $\tau \approx 60$ min. Hence, spectra were recorded faster than at BESSY. However, the quality of the XMCD measurements regarding the signal-to-noise ratio showed to be worse. Despite the high magnetic field, no usable XMCD signal was resolvable above $T = 50$ K.

The measurement mode could be significantly improved if spectra could be recorded by a continuous scan of the monochromator, since no other parameter is changed during one scan. This would allow recording more spectra for better statistics in less time. Although possible from the technical point of view, this mode was not implemented to the computer control of the monochromator at the present beamtimes.

The energy resolution is not known exactly, but comparison of spectra to PM3 data indicates a slightly better resolution at DEIMOS.

The measurement chamber is equipped with a photodiode that allows TFY detection. The TEY detection is done with electrometers. Regrettably, the option of a negative sample potential is not provided with these devices. Addition of this possibility would surely improve the data quality.

The superconducting magnet allows magnetic fields up to $|B| = 6.5$ T. The sample stage is cooled with a liquid helium continuous flow supplied from the magnet dewar. The heat exchanger can be pumped, which allows reduction of its temperature down to $T \approx 2$ K. The temperature at the sample, which is attached directly to the exchanger, is not known exactly, but it is assumed to be within $\Delta T \leq 1$ K. of the exchanger temperature. In addition to the pumping, the efficient cooling shroud design is responsible for the low temperatures. With these parameters, the available XMCD data for CePt$_5$/Pt(111) were expanded into a regime of very high interest for heavy fermion systems.

5.4.4 Detection of XMCD

The XMCD signal is obtained by the subtraction of two XA spectra measured with parallel and antiparallel alignment of circular light polarization vector and sample magnetization ($\mu_\mathrm{x}^+(E)$ and $\mu_\mathrm{x}^-(E)$, respectively, as introduced in section 5.3). As with all experimental quantities, the detection of small signals is difficult. In the case of XMCD, "smallness" can become manifest in two ways: The initial absorption spectra can have low intensity compared to the noise level of the detection setup and their difference can be small compared to their average intensity.

The intensity of the XA spectra, which is defined as the height of the resonant peak over the continuum background for a given experimental resolution, depends on the photon flux, the absorption cross-section of the element under investigation (see section 5.1) and the fraction of relevant material in the sample volume that is probed with the given detection method (see section 5.4.2). The photon flux is given by the beamline and is not a critical quantity for the present experiments, even at a bending magnet. For the Ce M$_{4,5}$ edges investigated in the present work, the resonant absorption cross-section is known to be comparably high. Furthermore, the small information depth of XAS in TEY mode ideally matches the distribution of material in the present thin-film samples. Hence, the noise level in XAS was of no serious concern in the present work.

However, the resolution of small differences of such intense spectra was a challenge to be met. The magnitude of the XMCD signal relative to the intensity of the isotropic spectrum depends on the magnitude of sample magnetization and the degree of circular polarization. The latter is usually no variable parameter, since the maximum polarization that is provided by the beamline is used (see section 5.4.1).

The present CePt$_5$/Pt(111) samples are paramagnetic, which means that either a high external magnetic field or a low sample temperature are required to produce a high magnetization, the optimum being a combination of both. Furthermore, strong magnetic anisotropy is induced by the crystal field in the single-crystalline intermetallic films, which causes a strong dependence of the magnetization on the angle between the magnetic field direction and the hexagonal c-axis. Beautifully large and noise-free XMCD signals were recorded at $B = 6.5$ T, $T \approx 2$ K and $\theta = 60°$ at SOLEIL, as can be seen in fig. 6.1 (b).

While the maximum magnetic field strength is again limited by the experimental setup, the sample temperature as well as the angle of incidence are important parameters in the present experiments. Many conclusions can only be drawn from analyzing the paramagnetic response in dependence of both parameters, which means that both θ and T were varied. Hence, small XMCD signals had to be detected at high temperatures and normal incidence.

Alignment of the two spectra

In the case of small sample magnetization, the present XMCD signals represent small differences of two intense spectra. In this case, the relative alignment of the two $\mu_\mathrm{x}^+(E)$ and $\mu_\mathrm{x}^-(E)$ spectra crucially affects their difference. A relatively small misalignment can produce an artificial difference signal that is large compared to the true XMCD effect. Three relevant sources of misalignment can be identified: additive relative shifts in energy and intensity, as well as a multiplicative scaling between the two spectra.

If the two spectra are shifted against each other in energy, a derivative-like difference is artificially produced. In Particular, this happens at steep flanks of the resonant XAS peaks. A shift in energy can occur if the two spectra are recorded subsequent to each other and, e.g., the reproducibility of the monochromator position is not perfect, or if thermal drifts have altered the characteristics of the beamline in the meantime. In order to address the problem of monochromator irreproducibility, the energy value returned by the monochromator, and not the initial setting, was used for the energy axis. Apart from that, a shift in energy can best be corrected if an independent reference spectrum is recorded simultaneous with the sample signal. It is avoided from the start if the $\mu_\mathrm{x}^+(E)$ and $\mu_\mathrm{x}^-(E)$ spectra are recorded simultaneously.

At SOLEIL, this option was not available, and no reference spectrum could be measured. Hence, energy shifts are a source of uncertainties here. The good performance of the beamline and the stable beam conditions in the top-up mode (see section 5.4.1) minimized this problem, which might nevertheless provide a main source of noise in the XMCD data. At BESSY, a dedicated measurement mode for simultaneous detection of $\mu_\mathrm{x}^+(E)$ and $\mu_\mathrm{x}^-(E)$ was applied, which is described further below.

If the intensities of the two spectra are additively offset against each other, this produces a constant difference signal that is superimposed to the true XMCD. For XA spectra measured in TEY mode, an offset can be caused by a leak current. However, this should not depend on the light polarization or magnetization direction and should therefore not produce an artificial difference signal for the two spectra. Another source for an additive offset are adsorbates that contribute to the absorption signal by a constant continuum background. If such contaminations are successively collected on the sample surface, this produces a time-dependent change of the background intensity and results in a relative offset for subsequently recorded spectra. The acquisition of spectra in the sequence $\mu_\mathrm{x}^-(E)$, $\mu_\mathrm{x}^+(E)$, $\mu_\mathrm{x}^+(E)$, $\mu_\mathrm{x}^-(E)$ can help to identify and average out such effects, which was therefore performed at SOLEIL. For the experiments at BESSY, such effects are again prevented by the optimized measurement mode.

A multiplicative disparity of the two spectra can occur since the TEY conversion factor is asymmetric under reversal of the magnetic field, as is discussed in section 5.4.2. The difference of two spectra without true XMCD but measured with reversed magnetic field would resemble their average. In order to correct this effect, the multiplicative relation between the two spectra has to be found. Since XMCD only occurs at resonant energies (compare section 5.3), the $\mu_\mathrm{x}^+(E)/\mu_\mathrm{x}^-(E)$ ratio at energies lower and higher than the resonances was used to determine the correction factor. Energy-dependence of this factor was considered by performing a linear fit to the ratio values of the two energy regions.

This procedure can have the reverse effect that one artificially defines photon energies at which the XMCD is zero. In particular, if the experimentally recorded spectrum ends before the XMCD drops to zero behind the edge, there is only little chance to notice the remaining small XMCD signal. It is then forced to zero at a point which depends on the measurement range. While the XMCD intensity in the part of the spectrum that is missed that way might be small, it could nevertheless give a significant contribution to the integral and thus to the sum rule result (see section 5.3), if the energy interval in which it occurs is large. For the present data, this problem is addressed in section 6.4.3.

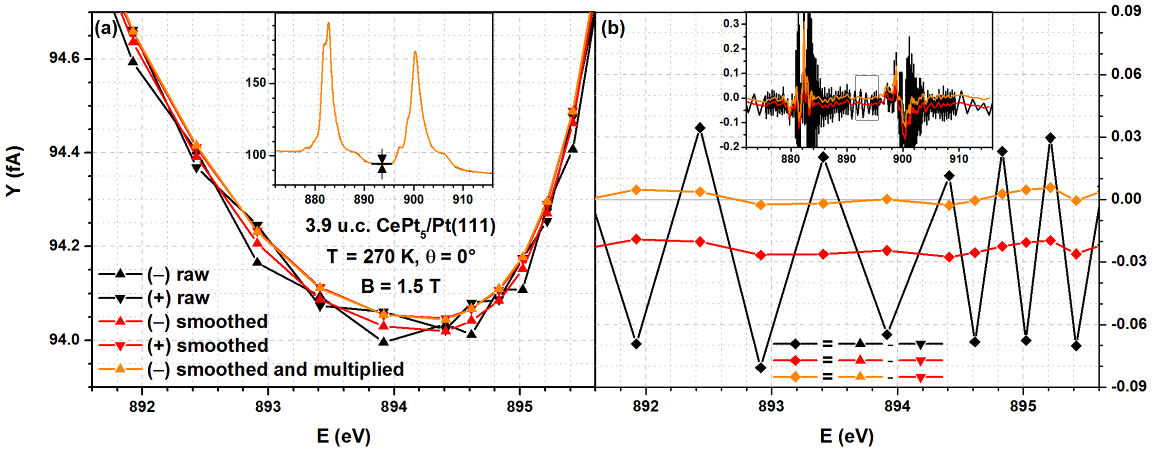

Figure 5.6: Visualization of the correction procedures applied to Ce $M_{4,5}$ XMCD data measured at BESSY for 3.9 u.c. $CePt_5$/Pt(111) at $T = 270$ K and $\theta = 0°$. The magnetic field was switched between $B = \pm 1.5$ T at each energy step as described in the text. (a) Sample current data without normalization for a region of the spectrum with negligible true XMCD. Raw data are shown as well as smoothed and multiplicatively corrected data. The inset shows the complete spectrum with marks for the enlarged part. (b) Differences of the spectra shown in (a).

The XMCD measurement mode at BESSY

As is introduced in the previous paragraph, the problems of additive offsets in energy and spectral intensity, which can prevent reliable detection of small XMCD signals, were addressed by a dedicated measurement mode at BESSY. Both $\mu_\mathrm{x}^+(E)$ and $\mu_\mathrm{x}^-(E)$ spectra were recorded during one scan of the energy by reversing the magnetic field direction at each energy step. Switching of the light helicity, which is an alternative option for such measurements, is not practical at a bending magnet.

Switching of the magnetic field requires a dedicated power supply and magnet design in order to be fast. In any case, the possible switching frequency drastically decreases with the magnetic field strength. Hence, a compromise has to be found between the improvement in data quality due to field switching at each step and the increase in measurement time due to a high magnetic field, which in turn enhances the XMCD magnitude in paramagnets. Due to such considerations, the spectra at BESSY were recorded with $|B| = 1.5$ T only.

Time-dependent changes of the sample signal, which are not accompanied by alteration of the magnetic characteristics, doe not affect the such measured XMCD signal, since the pairs of values that are subtracted are recorded on a short time scale of some seconds to minutes. A shift in the energy is also eliminated. The asymmetry in the TEY efficiency with the magnetic field is still present and has to be corrected as described above.

In the applied measurement mode, the sequence of energy δE and field ΔB setting and current recording Y is of the form $Y^-(E_1)$, ΔB, $Y^+(E_1)$, δE_1, $Y^+(E_2)$, $-\Delta B$, $Y^-(E_2)$, δE_2, $Y^-(E_3)$, ΔB, $Y^+(E_3)$, … This leads to a zig-zag-like modulation with each energy step in the raw data. This can be seen in the black curves of fig. 5.6, where the evaluation procedure is illustrated for an exemplary spectrum with very small XMCD magnitude.

The source of the zig-zag modulation is not fully understood. The magnitude of the effect is largest at energies with large slopes in the spectrum and for short standby times between setting of field or energy and current recording. It is possibly a result of a tiny but finite time-dependent creep of the monochromator. In any case, the modulation can be corrected by a smoothing procedure according to

$$Y'(E_n) = 0.25\ Y(E_{n-1}) + 0.5\ Y(E_n) + 0.25\ Y(E_{n+1}). \tag{5.19}$$

This is illustrated by the red curves in fig. 5.6. It should be noted that this correction produces artifacts if the energy stepwidth is changed, i.e., if $\delta E_{n-1} \neq \delta E_n$, in a region where the spectrum is not constant. The orange curves additionally visualize the benefit of the multiplicative TEY

asymmetry correction, which leads to a zero XMCD signal in the spectral region shown.
The orbital magnetic moment of the spectrum shown in fig. 5.6 has been evaluated to $\langle\mu_l\rangle \approx 0.002\ \mu_\mathrm{B}$ by relative adjustment to a less noisy reference spectrum, which was analyzed according to the orbital sum rule (for details see section 6.4).
The zig-zag-correction also has to be applied to the current measurements of the reference gold grid prior to normalization of the sample signal. The TEY asymmetry correction is best applied to the normalized signal in order to assure that the XMCD is really zero at the specified energies.

Measurement of XMCD magnetization curves at SOLEIL

The weight of the XMCD spectrum is connected to the sample magnetization via the sum rules (see section 5.3). Hence, its dependence on the magnetic field strength allows derivation of magnetization curves. In the present experiments, this was especially interesting for low temperatures and high magnetic fields, which is why this technique was only applied at SOLEIL. Results for $\mathrm{CePt_5/Pt(111)}$ are discussed in section 10.5.
It is reasonable to assume that neither the isotropic XAS nor the XMCD line shape change under variation of the magnetic field in the experimental regime of the present thesis, and no indications for line shape variations have been found experimentally. Hence, the construction of a magnetization curve can be done from the B-dependence of the absorption signal measured with circularly polarized light at two specified energy values. One measurement is done in the pre-edge region where no XMCD is present for normalization, the other preferably at an energy where the XMCD is maximum. The magnetic field-dependent progression of their difference normalized to the pre-edge value then represents the relative progression of the sample magnetization.
The quality and reliability of the data is improved by repeating the measurement with the other polarization direction. Furthermore, the magnetic field is usually scanned in both directions to account for hysteresis effects. Such effects are not expected for paramagnets, and no indications were found in the present data. Hence, point symmetry of the curves around the origin was assumed and the collected data for all combinations of CPL direction, field sign and field scan direction were averaged to produce a symmetrized curve. A calibration of the relative curve to absolute units was done by sum rule analysis of a full reference spectrum at the highest magnetic field (see section 6.4).

5.4.5 Presentation of experimental XA spectra

The experimental XA spectra that are shown in the present thesis are indicated as $\mu_\mathrm{x}(E)$ curves. The dimension of μ_x is inverse length, but the spectra are displayed with arbitrary scaling. The μ_x signal is obtained from electric current readings of the electrometers used for TEY or TFY detection. Hence, proportionality between the two quantities is assumed, which can be misleading in the presence of saturation effects (see sections 5.4.2 and 5.5). For the TEY data, a detailed study of the expected magnitude of such effects is presented in section 8.1, which leads to the conclusion that the such introduced relative errors are smaller than 7 %. For the TFY data, no estimation or correction was performed in the present work, but the only spectra that are shown (see fig. 8.5) are not used for quantitative evaluations.
The presented data are always normalized to the incoming photon flux, usually by the simultaneously measured spectrum of the gold grid reference. Spectra that were recorded in the XMCD mode at BESSY were treated as described in section 5.4.4. Furthermore, the spectra are often background-corrected, usually by subtraction of a straight but not necessarily constant line, and vertically scaled by multiplication with a constant factor.
For the photon energy axes, the monochromator position feedback was used. For the presentation, the $\mathrm{M_4}$ maximum was set to $E \approx 900\mathrm{eV}$ by a constant shift, if this was not the case in the raw data. This value is in accordance with most literature and was automatically obtained at BESSY after performing the energy calibration procedure that is described in section 5.4.1. The spectra that were taken at SOLEIL had to be shifted systematically by $\Delta E \approx 6$ eV.
In cases where multiple spectra are shown in comparison, the energy axes of individual measure-

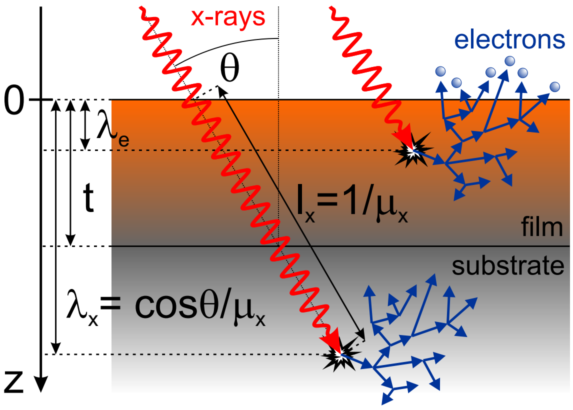

Figure 5.7: Illustration of the length scales involved in the TEY detection of the linear absorption coefficient $\mu_{\mathrm{x}}(E)$ of a thin film on top of a semi-infinite substrate: film thickness t, electron escape depth λ_{e}, X-ray penetration length $l_x(E) = 1/\mu_{\mathrm{x}}(E)$ and X-ray penetration depth $\lambda_{\mathrm{x}}(E,\theta) = l_x(E)\cos\theta$.

ments sometimes had to be linearly stretched in order to obtain equal positions of the maxima of both M_4 and M_5 lines. The resulting corrections in energy position were never larger than $\Delta E = 0.1$ eV. For the comparison of spectra taken at SOLEIL and BESSY, this accounts for differences in the monochromators. The correction was also necessary for some spectra that were taken at BESSY directly after an injection or an otherwise caused measurement pause with closed beamshutter. In these cases, the deformation of the spectra was most probably caused by instabilities of the beamline optics, which were subject to radiation heating after the beam intermission (see section 5.4.1).

Furthermore, all XA spectra that are shown were measured with circularly polarized light. Many of the nonmagnetic XA spectra were obtained by averaging spectra that were taken for magnetized samples with different polarization or magnetization directions.

The XMCD signals shown were calculated as $\Delta\mu_{\mathrm{x}}(E) = \mu_{\mathrm{x}}^{-}(E) - \mu_{\mathrm{x}}^{+}(E)$, with $\mu_{\mathrm{x}}^{-}(E)$ and $\mu_{\mathrm{x}}^{+}(E)$ as introduced in section 5.3). The sign of $\Delta\mu_{\mathrm{x}}$ follows a convention that is established in the community [156].

5.5 Total Electron Yield spectroscopy of thin films

For quantitative evaluations of XAS and XMCD data obtained in the TEY mode, the relation between the linear absorption coefficient $\mu_{\mathrm{x}}(E)$, as defined by eq. 5.1, and the recorded TEY current $Y(E)$ has to be known (see section 5.4.2). In the following, a model for this relation is developed for a sample that consist of a thin film on top of a semi-infinite substrate. The modeling follows Nakajima *et al.* [177] and the book by Stöhr [147] and is applied to the present $\mathrm{CePt}_5/\mathrm{Pt}(111)$ samples in sections 7.4 and 8.1.

Fig. 5.7 gives a sketch of the experimental configuration and introduces the relevant parameters. X-rays with intensity I_0 arrive at the sample surface with the angle of incidence θ, which is measured with respect to the surface normal. The sample consists of a thin film and a substrate. The film at the sample surface is considered to be homogeneous with constant thickness t. The substrate is assumed to be semi-infinite, which implicates that it is much thicker than the X-ray penetration *depth* $\lambda_{\mathrm{x}}(E,\theta)$. This quantity is measured along the z-direction perpendicular to the sample surface. It is connected to $\mu_{\mathrm{x}}(E)$ via the X-ray penetration *length* $l_x(E)$ as $\lambda_{\mathrm{x}}(E,\theta) = l_x(E)\cos\theta = \cos\theta/\mu_{\mathrm{x}}(E)$. The last relevant length scale is the effective, energy-averaged electron escape depth λ_{e}, which is introduced in section 5.4.2.

According to eq. 5.1, the absorption at a depth z in the sample can be described by a decrease of photon intensity $dI(E,z)$ in the depth interval dz. It reads

$$dI(E,z) = -I_0\,\frac{\mu_{\mathrm{x}}(E)}{\cos\theta}\,e^{-\frac{\mu_{\mathrm{x}}(E)}{\cos\theta}z}\,dz. \tag{5.20}$$

The resulting contribution to the current depends on λ_e and is written as

$$dY(E,z) = -C^Y(E)\; dI(E,z)\; e^{-\frac{z}{\lambda_\mathrm{e}}}. \tag{5.21}$$

The minus sign reflects that the current increases as intensity decreases, i.e. absorption increases. The factor $C^Y(E)$ describes the conversion of absorbed intensity to the number of electrons that leave the sample and contribute to the detectable current. It includes the average number of primary electrons that are produced by an absorption event as well as the number of resulting secondary electrons per primary electron. In general, it depends on the photon energy E.
The total current that is obtained from a sample with thickness t is calculated by substituting eq. 5.20 into eq. 5.21 and integrating z from 0 to t,

$$\begin{aligned} Y(E) &= \int_0^t C^Y(E)\; I_0\; \frac{\mu_\mathrm{x}(E)}{\cos\theta}\; e^{-(\mu_\mathrm{x}(E)/\cos\theta + 1/\lambda_\mathrm{e})z}\; dz \\ &= C^Y(E)\; I_0\; \frac{\mu_\mathrm{x}(E)}{\cos\theta}\; \frac{1}{\frac{\mu_\mathrm{x}(E)}{\cos\theta} + \frac{1}{\lambda_\mathrm{e}}}\; \left(1 - e^{-\left(\frac{\mu_\mathrm{x}(E)}{\cos\theta} + \frac{1}{\lambda_\mathrm{e}}\right)t}\right) \\ &= C^Y(E)\; I_0\; \frac{1}{1 + \frac{\lambda_\mathrm{x}(E,\theta)}{\lambda_\mathrm{e}}}\; \left(1 - e^{-\left(1 + \frac{\lambda_\mathrm{e}}{\lambda_\mathrm{x}(E,\theta)}\right)\frac{t}{\lambda_\mathrm{e}}}\right). \end{aligned} \tag{5.22}$$

Hence, the relation between $Y(E)$ and $\mu_\mathrm{x}(E)$ is governed by the ratio of $\lambda_\mathrm{x}(E,\theta)$ and λ_e. For a better understanding, it is helpful to investigate two extreme cases:

1. In the limit $\lambda_\mathrm{x}(E,\theta) \ll \lambda_\mathrm{e}$, $Y(E) \approx C^Y(E)\; I_0$. The signal that is obtained by TEY detection has no relation to $\mu_\mathrm{x}(E)$, since all photons are absorbed directly at the surface and contribute to the maximum possible extent to the measured signal.

2. In the other extreme, $\lambda_\mathrm{x}(E,\theta) \gg \lambda_\mathrm{e}$, $Y(E)$ and $\mu_\mathrm{x}(E)$ are proportional to each other, since eq. 5.22 can be simplified to

$$Y(E) \approx \frac{C^Y(E)\; I_0\; \lambda_\mathrm{e}}{\cos\theta}\; \left(1 - e^{-t/\lambda_\mathrm{e}}\right)\; \mu_\mathrm{x}(E). \tag{5.23}$$

For a quantitative evaluation of XAS data, this is the ideal case. However, the validity of case 2 has to be tested thoroughly for a given experiment. The Ce $\mathrm{M}_{4,5}$ edges can serve as an example: The variation in the X-ray penetration depth for Ce metal ranges from $\lambda_\mathrm{x}(870\text{ eV}) \approx 700$ nm in the pre-edge region to $\lambda_\mathrm{x}(900\text{ eV}) \approx 27$ nm at the M_4 peak. The numbers were obtained from transmission results for $\mu_\mathrm{x}(E)$ of pure Ce films by Fernández-Perea *et al.* [178]. Typically, λ_e is of the order of some nanometers. Hence, while the preconditions for eq. 5.23 are fulfilled for the background, a correction is expected for the peak, especially for spectra taken in grazing incidence.
As a consequence, a Ce $\mathrm{M}_{4,5}$ spectrum obtained for Ce metal in the TEY mode will appear distorted, with damped peaks. This so-called saturation effect is enhanced for large angles of incidence θ. With the knowledge of eq. 5.22, correction procedures can be developed. It has been shown in the literature that correctly accounting for saturation effects is crucial for application of the XMCD sum rules in many cases (e.g. , [177, 179] and references therein). The main problem here is that saturation for $\mu_\mathrm{x}^+(E)$ and $\mu_\mathrm{x}^-(E)$ can be very different due to the different peak heights. Hence, the XMCD signal calculated by subtraction is not only reduced, but can be distorted in a complicated way: The magnitude of reduction does not only depend on the magnitude of the XMCD, but also on the intensity of the averaged XA spectrum at the given energy position.
the present thesis, thin intermetallic films on top of a substrate were investigated. The film thickness t is a variable parameter, its determination and control are described in section 7.3. It

is of the same magnitude as λ_e. Hence, for a correct description of the data, eq. 5.22 has to be expanded to include the contribution from the substrate. Since the thickness of the substrate amounts to several millimeters, far more than λ_e and $\lambda_\mathrm{x}(E,\theta)$, it can be regarded as semi-infinite. Film and substrate in general possess different absorption coefficients $\mu_\mathrm{x}^\mathrm{f}(E)$ and $\mu_\mathrm{x}^\mathrm{s}(E)$ and electron escape depths $\lambda_\mathrm{e}^\mathrm{f}$ and $\lambda_\mathrm{e}^\mathrm{s}$, respectively. In principle, the contribution from the substrate can simply be added to the film contribution, which is described by eq. 5.22. However, it has to be considered that the light that arrives at the substrate has already experienced absorption in the film. Furthermore, the electrons that leave the substrate also have to pass the film before they can contribute to the TEY signal. This leads to the conditions

$$I_0^\mathrm{s} = I_0\; e^{-\frac{\mu_\mathrm{x}^\mathrm{f}(E)}{\cos\theta}t} \qquad \text{and} \qquad dY^\mathrm{s}(E,z) = -C^{TEY}\; dI^\mathrm{s}(E,z)\; e^{-\left(\frac{z-t}{\lambda_\mathrm{e}^\mathrm{s}}+\frac{t}{\lambda_\mathrm{e}^\mathrm{f}}\right)}. \tag{5.24}$$

The total TEY current then reads

$$\begin{aligned} Y(E) &= \int_0^t C^Y(E)\; I_0\; \frac{\mu_\mathrm{x}^\mathrm{f}(E)}{\cos\theta}\; e^{-\left(\frac{\mu_\mathrm{x}^\mathrm{f}(E)}{\cos\theta}+\frac{1}{\lambda_\mathrm{e}^\mathrm{f}}\right)z}\; dz \\ &\quad + \int_t^\infty C^Y(E)\; I_0\; e^{-\left(\frac{\mu_\mathrm{x}^\mathrm{f}(E)}{\cos\theta}\right)t}\; \frac{\mu_\mathrm{x}^\mathrm{s}(E)}{\cos\theta}\; e^{-\left(\frac{\mu_\mathrm{x}^\mathrm{s}(E)}{\cos\theta}+\frac{1}{\lambda_\mathrm{e}^\mathrm{s}}\right)(z-t)}\; e^{-t/\lambda_\mathrm{e}^\mathrm{f}}\; dz \\ &= \frac{C^Y(E)\; I_0}{\cos\theta}\left(\underbrace{\frac{\mu_\mathrm{x}^\mathrm{f}(E)}{\frac{\mu_\mathrm{x}^\mathrm{f}(E)}{\cos\theta}+\frac{1}{\lambda_\mathrm{e}^\mathrm{f}}}\left(1-e^{-\left(\frac{\mu_\mathrm{x}^\mathrm{f}(E)}{\cos\theta}+\frac{1}{\lambda_\mathrm{e}^\mathrm{f}}\right)t}\right)}_{\text{film}} + \underbrace{\frac{\mu_\mathrm{x}^\mathrm{s}(E)}{\frac{\mu_\mathrm{x}^\mathrm{s}(E)}{\cos\theta}+\frac{1}{\lambda_\mathrm{e}^\mathrm{s}}}\; e^{-\left(\frac{\mu_\mathrm{x}^\mathrm{f}(E)}{\cos\theta}+\frac{1}{\lambda_\mathrm{e}^\mathrm{f}}\right)t}}_{\text{substrate}}\right). \end{aligned} \tag{5.25}$$

Quantitative modeling of experimental data with eq. 5.25 is complicated by the prefactor $C^Y(E)$, which is in general unknown. It depends on various factors (see section 5.4.2) and in general differs for different samples. This provides a problem if data as a function of sample thickness are modeled.

One could think of an experimental determination of $C^Y(E)$ by measurement of $Y(E)$ for $\theta \lesssim 90°$, which would result in case 1 of the discussion of eq. 5.22. However, reflection at the sample surface becomes important for angles of incidence that large, which in turn complicates the determination of I_0. Simultaneous measurement of XAS in TEY and transmission mode would of course yield $C^Y(E)$, but for the CePt$_5$/Pt(111) intermetallics, the required investments in sample preparation exceed the benefit of such experiments by far.

A better approach is to eliminate $C^Y(E)$ from the model by proper normalization of the data. A meaningful parameter is defined by the ratio of TEY signals of a resonant peak and the continuum background in one and the same spectrum. This addresses the full range of $\mu_\mathrm{x}(E)$ in that spectrum. Furthermore, it is assured that uncontrollable variations of the prefactor between different spectra are kept small. However, since values for different photon energy E are used, the energy-dependence of $C^Y(E)$ has to be known.

According to Stöhr, the number of secondary electrons linearly increases with E [147], which results in $C^Y(E) \propto E$. In the present thesis, the Ce M$_{4,5}$ edges represent the spectral region of largest interest. With a linear energy dependence of $C^Y(E)$, the electron yield at the Ce M$_4$ peak at $E_1 = 900$ eV would be 3.5 % higher than in the non-resonant pre-edge region at $E_2 = 870$ eV. The pre-edge region was chosen for the continuum background due to uncertainties concerning the continuum steps, which are discussed in section 8.2.3.

As a confirmation, the TEY signals $Y(E)$ measured for Pt and Au at these energies, where both metals exhibit no resonant absorption, were divided by the respective $\mu_\mathrm{x}(E)$ values tabulated by Henke *et al.* [160]. The data were taken for a Pt(111) single crystal at $\theta = 0°$ and for the I_0 gold grid and normalized to the ring current I_r. For both metals, the ratio Y/μ_x was reduced at $E_1 = 900$ eV compared to $E_2 = 870$ eV. The reduction amounted to 3.2 % for Pt and 0.5 % for Au.

These results contradict the assumption of Stöhr. This might reflect that general uncertainties exist that are larger than the effect that is looked for. Since the measured deviations are in the order of a few percent only, the energy-dependence of $C^Y(E)$ is neglected for the purposes of the present thesis.

With this assumption, the peak-to-background ratio of a TEY spectrum can be written as

$$\frac{Y(E_1)}{Y(E_2)} = \frac{\overbrace{\frac{\mu_\mathrm{x}^\mathrm{f}(E_1)}{\frac{\mu_\mathrm{x}^\mathrm{f}(E_1)}{\cos\theta}+\frac{1}{\lambda_\mathrm{e}^\mathrm{f}}}\left(1-e^{-\left(\frac{\mu_\mathrm{x}^\mathrm{f}(E_1)}{\cos\theta}+\frac{1}{\lambda_\mathrm{e}^\mathrm{f}}\right)t}\right)}^{\text{film, }E_1} + \overbrace{\frac{\mu_\mathrm{x}^\mathrm{s}(E_1)}{\frac{\mu_\mathrm{x}^\mathrm{s}(E_1)}{\cos\theta}+\frac{1}{\lambda_\mathrm{e}^\mathrm{s}}}\,e^{-\left(\frac{\mu_\mathrm{x}^\mathrm{f}(E_1)}{\cos\theta}+\frac{1}{\lambda_\mathrm{e}^\mathrm{f}}\right)t}}^{\text{substrate, }E_1}}{\underbrace{\frac{\mu_\mathrm{x}^\mathrm{f}(E_2)}{\frac{\mu_\mathrm{x}^\mathrm{f}(E_2)}{\cos\theta}+\frac{1}{\lambda_\mathrm{e}^\mathrm{f}}}\left(1-e^{-\left(\frac{\mu_\mathrm{x}^\mathrm{f}(E_2)}{\cos\theta}+\frac{1}{\lambda_\mathrm{e}^\mathrm{f}}\right)t}\right)}_{\text{film, }E_2} + \underbrace{\frac{\mu_\mathrm{x}^\mathrm{s}(E_2)}{\frac{\mu_\mathrm{x}^\mathrm{s}(E_2)}{\cos\theta}+\frac{1}{\lambda_\mathrm{e}^\mathrm{s}}}\,e^{-\left(\frac{\mu_\mathrm{x}^\mathrm{f}(E_2)}{\cos\theta}+\frac{1}{\lambda_\mathrm{e}^\mathrm{f}}\right)t}}_{\text{substrate, }E_2}}. \tag{5.26}$$

In total, this model has eight parameters. The film thickness t and the angle of incidence θ are regarded as controllable. Data in dependence of one of the two can be modeled by least-square fits of eq. 5.26 to determine the unknown parameters.

Knowledge of λ_e is required to estimate the magnitude of saturation in XA and XMCD spectra and to develop correction procedures. Furthermore, λ_e determines the degree of surface-sensitivity of XAS and XMCD. Since it is a TEY-specific quantity, it can only be obtained from TEY experiments.

Attempts were made to obtain $\lambda_\mathrm{e}^\mathrm{s}$ of the Pt(111) substrate by θ-dependent measurements of $Y(E)$. However, it turned out that the precision in angular alignment of the experimental setup was not sufficient to allow a reliable result. An offset of $\Delta\theta = 1°$, which is within realistic assumptions for the misalignment of normal incidence, produced variations of $\Delta\lambda_\mathrm{e} = 1.5$ nm. This is the expected order of magnitude for λ_e and hence yields a very large relative error.

An alternative to obtain λ_e for Pt would be to prepare thin films and analyze the thickness dependence of the TEY signal. Such experiments were not in the scope of the present thesis. Regarding the literature, no results for Pt are known to the author. However, a value of $\lambda_\mathrm{e} \approx 2$ nm in the relevant energy range has been determined for Au by Henneken *et al.* [180]. Since Au and Pt are adjacent in the PSE and they share the same crystal structure with comparable lattice constants, it is reasonable to adapt this value for Pt.

Based on this experience with angle-dependent measurements, the further modeling was performed for data in dependence of the thickness of the intermetallic films. In section 7.4, this approach is used to address $\lambda_\mathrm{e}^\mathrm{f}$ and the stoichiometry of $\mathrm{CePt_5}$/Pt(111) surface intermetallics by analysis of Ce $\mathrm{M}_{4,5}$ spectra.

The stoichiometry of the CePt films can be introduced to eq. 5.26 by consideration of eq. 5.3, $\mu_\mathrm{x}^\mathrm{f}(E) = \rho_\mathrm{Ce}^\mathrm{at}\sigma_\mathrm{Ce}(E) + \rho_\mathrm{Pt}^\mathrm{at}\sigma_\mathrm{Pt}(E)$. For the atomic absorption cross-sections σ of the two elements, the values provided by Henke *et al.* [160] can be used (see fig. 5.2), if no resonant absorption is present. This is the case for Ce and Pt in the pre-edge region at $E_2 = 870$ eV and for the Pt substrate also at $E_1 = 900$ eV. regarding the cross-section of Ce at the M_4 resonance, transmission data have been published by Fernández-Perea *et al.* [178].

Since the atomic density of Ce in the film could be determined from STEM images, only two free parameters remained in the model. Furthermore, those two have no dependency: While the electron escape depth governs the scaling of the model curve along the t-axis, the absorption coefficients $\mu_\mathrm{x}(E)$, and hence the interplay of $\rho\check{\sigma}(E)$, do the same for the axis of ordinates.

Chapter 6

Ce $M_{4,5}$ XAS and XMCD

Contents

The many interesting physical properties of Ce compounds derive from the localized $4f$ shell with an electron occupancy close to unity, as discussed in chapters 1 and 2. XAS at the Ce $M_{4,5}$ edges reflects the transition of a $3d$ core electron to the $4f$ shell (see section 5.1.3). Hence, Ce $M_{4,5}$ XAS and XMCD provide direct and local access to the $4f$ states and its electronic and magnetic properties.

Considerable information is contained in the details of Ce $M_{4,5}$ spectra. Fig. 6.1 (a) shows an exemplary experimental Ce $M_{4,5}$ X-ray absorption spectrum of $CePt_5$/Pt(111). It is dominated by two distinct lines[1], which at closer inspection appear as groups of multiple peaks. The distinct features in the substructure of the spectrum are alphabetically labeled A-K for future reference. The details of the spectral shape arise from the characteristics of initial and final state in the resonant absorption process (see eq. 5.4), which are schematically drawn for the M_5 edge in fig. 5.1 (a) and (b), respectively. The initial state is an atomic-like configuration with a single $4f$ electron (compare section 2.1.1), although valence fluctuations can cause deviations from this assumption (compare section 2.1.5). The relevant parameters for the $4f^1$ configuration are SOC of the $4f$ level and an optional crystal field (see section 2.1.2). In contrast, the resulting final state is an excitonic many-particle state with a $3d$ core-hole and two $4f$ electrons, which is additionally subject to SOC of the $3d$ level and $4f$-$4f$ as well as $4f$-$3d$ Coulomb interaction.

---

[1] The expression "(white) line"' for an intensive feature in an absorption spectrum has been coined in a time when spectra were recorded in transmission mode with photographic techniques.

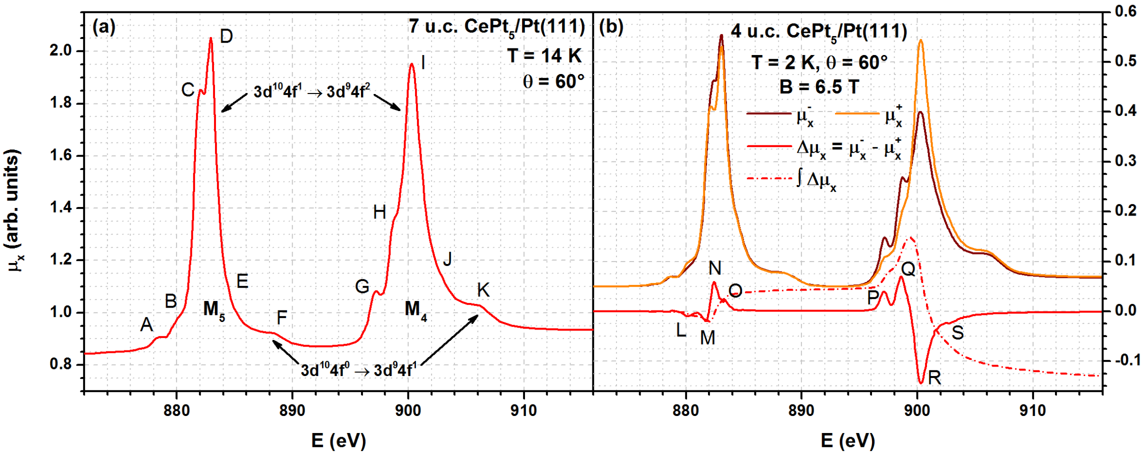

Figure 6.1: Exemplary Ce $M_{4,5}$ XA and XMCD spectra. Distinct features are alphabetically labeled for future reference. (a) Isotropic XA spectrum taken at BESSY in TEY mode for a CePt$_5$/Pt(111) sample with $t = 7$ uc at $T = 14$ K and $\theta = 60°$. (b) XMCD spectrum obtained as the difference of two spectra with antiparallel (μ_x^-) and parallel (μ_x^+) alignment of light polarization and sample magnetization vectors, as well as the integrated XMCD intensity. The spectra were taken at SOLEIL in TEY mode for a CePt$_5$/Pt(111) sample with $t = 4$ uc at $T = 2$ K and $\theta = 60°$. A magnetic field of $B = 6.5$ T was applied to the sample. Note that the unit of the integrated intensity is eV/µm.

As the most obvious feature of the Ce M$_{4,5}$ spectrum, the energy separation of the two main lines reflects the $3d$ spin-orbit coupling $\Delta E_{\mathrm{SOC}}^{3d} = 18.6$ eV [161]. This suggests that the two lines belong to different final states with the total angular momentum of the core-hole being $j = 5/2$ or $3/2$, as depicted in fig. 5.1. Hence, they are commonly referred to as M$_5$ and M$_4$ lines or edges, as given in fig. 6.1 (a).

However, the strong Coulomb interaction in the final state gives rise to considerable configuration interaction between $4f$ and $3d$ states, which couples the angular momenta of these configurations in addition to the SOC in each of them and requires a description in intermediate coupling. As a consequence, the spectrum does not reflect the single-particle DOS of the final state [59]. The single-particle picture is invalid in intermediate coupling.

Furthermore, spectral weight is transferred between the two lines. The ratio of their oscillator strengths is $w(M_5)/w(M_4) \approx 0.85$ in the exemplary spectrum of fig. 6.1 (a). This is far from the ratio of the numbers of levels for the core-hole in the two configurations, 3:2, which would have been expected for the case without configuration interaction [44]. Despite this redistribution of weight and the deviations from the simple SOC picture, the denotation of the two lines as M$_5$ and M$_4$ is kept throughout the present thesis for convenience and in accordance with the literature.

The $4f$-$4f$ Coulomb interaction is responsible for the different sub-peaks that are present in the two main lines and which are called the multiplet structure. Despite the complicated final state, Ce M$_{4,5}$ XAS is a good probe for the Ce ground state, which is owed to the details of the $4f$ multiplet and the selection rules associated with the transition operator in eq. 5.4. Consequently, analysis of the multiplet structure can yield valuable information on the angular momentum character of the $4f^1$ state. Furthermore, the presence of XNLD (see section 5.2) can give access to the ground state symmetry.

In addition to the multiplet structure of the $3d^{10}4f^1 \rightarrow 3d^9 4f^2$ transition, both lines have contributions from the $3d^{10}4f^0 \rightarrow 3d^9 4f^1$ transition, which reflects the variable Ce valence. The features labeled F and K in fig. 6.1 (a) are commonly assigned to this contribution. Since only one $4f$ electron is present in the final state, the $f^0 \rightarrow f^1$ contribution lacks the rich multiplet structure of the $f^1 \rightarrow f^2$ part. The only characteristic is its energetic position and its weight relative to the $f^1 \rightarrow f^2$ part. The latter is an indicator for the Ce valence in the initial state (see section 2.1.5).

The partly filled $4f$ shell exhibits an uncompensated magnetic moment. To first order, this moment can be treated in terms of atomic theory, as is presented in section 2.1.1. Consequently, most Ce compounds are paramagnetic over wide temperature ranges. Application of an external magnetic field then leads to an alignment of the localized magnetic moments. Hence, the prerequisites for the observation of XMCD as discussed in section 5.3 are fulfilled. Application of the magnetic sum rules given in eqs. 5.17 and 5.18 should give quantitative access to the orbital and spin moments of the initial state.

Fig. 6.1 (b) shows XA spectra of a $CePt_5/Pt(111)$ sample measured with circularly polarized light and a magnetic field applied to the sample. The obvious XMCD effect is visualized by the difference of the two spectra, the XMCD signal (solid red curve)[2]. Characteristic features in the XMCD are alphabetically labeled L-S for future reference. The dash-dotted line represents the integrated XMCD intensity. It clearly shows that the application of the XMCD sum rules is technically possible. The orbital moment is positive according to eq. 5.17, which reflects the paramagnetic orientation of the sample magnetization.

The aspects that are touched in this brief introduction reveal the various opportunities that are offered by Ce $M_{4,5}$ XAS and XMCD. Both electronic and magnetic properties of Ce compounds with their potential for intriguing correlation effects can be addressed. The present chapter is devoted to such experiments, which are a key issue of the present thesis.

In the following, a review of the current state of research is given as well as a summary of the procedures that were developed in the present work to evaluate and simulate Ce $M_{4,5}$ XAS and XMCD. These considerations provide a deliberate background to produce experimental results with high quality. Such results are presented and discussed in chapter 8.

6.1 Previous studies of Ce $M_{4,5}$ XAS and XMCD

The earliest reports of rare earth $M_{4,5}$ XAS date back to 1931 [181]. Investigations of Ce $M_{4,5}$ spectra with monochromatized bremsstrahlung were reported in the 1970s [182, 183]. Remarkably, the work by Bonnelle, Karnatak and Sugar already contains a calculated spectrum.

In the 1980s, the availability of synchrotron sources (compare section 5.4.1) permitted experimental XAS data of much higher quality. On the theoretical side, the studies of Gunnarsson and Schönhammer and Thole, van der Laan and Sawatzky established two working directions, that largely improved the understanding of the measured spectra: The GS theory and application of full multiplet calculations, respectively.

The GS theory was presented in 1983 [25, 26]. It allowed addressing the signatures of the f-level occupation in the spectra and clarified the issue of the Ce valence (see section 2.1.5). This was achieved by a consistent description of the results of a variety of electron spectroscopies in terms of the SIAM. Regarding Ce $M_{4,5}$ XAS, the main focus is on the $f^0 \rightarrow f^1$ transition. Hence, multiplet effects, which characterize the $f^1 \rightarrow f^2$ transition, were not discussed by Gunnarsson and Schönhammer. Those can be calculated in full multiplet theory. The excellent agreement between such calculated $f^1 \rightarrow f^2$ spectra and experimental data was shown in 1985 by Thole *et al.* for the whole rare earth series [184].

In the following two sections, studies that were performed along these two working directions are reviewed. It can be seen as a logical consequence that attempts were made to combine both approaches. This was successfully done by Jo and Kotani in 1988 [185, 186] and is accounted for in section 6.1.3. The extension of Ce $M_{4,5}$ XAS by additional investigation of the XMCD started in the 1990s. The respective literature is addressed in section 6.1.4.

---

[2] It should be noted that this XMCD signal is among the largest that have been obtained in the present thesis. The sample is paramagnetic, but the low temperature and the high magnetic field lead to the large magnetic polarization. While instructive to show, such datasets rather represent the exception. In most cases, the difference of the two spectra is smaller than the linewidth that is used in the figure. The meaningful evaluation of the difference spectra under such conditions was one of the major challenges in the present thesis and is addressed in sections 5.4.4 and 6.4.3.

6.1.1 Studies of the Ce valence in XAS

In the framework of the GS theory, contributions from different $4f$ occupancies are expected in the Ce $M_{4,5}$ spectra of mixed-valent Ce compounds. Assuming that the $4f$-$4f$ Coulomb interaction renders configurations with more than two $4f$ electrons irrelevant for the ground state, contributions from the $3d^{10}4f^0 \to 3d^9 4f^1$, $3d^{10}4f^1 \to 3d^9 4f^2$ and $3d^{10}4f^2 \to 3d^9 4f^3$ transitions can appear in the spectrum.

Soon after the initial paper series, the application of the GS theory to Ce $M_{4,5}$ XAS was reported by Fuggle *et al.* [61], who identified and quantified the contributions of the $f^0 \to f^1$ and $f^1 \to f^2$ transitions to the spectrum. Regarding a possible $f^2 \to f^3$ transition, these authors only mention that it should appear at higher energy than the $f^1 \to f^2$ contribution and that it should be weak. No identification of this contribution in a Ce $M_{4,5}$ spectrum is known to the author.

The identification of the $f^0 \to f^1$ and $f^1 \to f^2$ contributions was achieved by comparison of spectra of various Ce compounds. An ideal reference is γ-Ce, which is known to have a valence close to three and should therefore only show a weak $f^0 \to f^1$ contribution. Hence, its $M_{4,5}$ spectrum is representative of the $f^1 \to f^2$ transition, which shows a rich multiplet structure in both lines.

In contrast, the $4f^1$ final state should mainly produce single peaks at both lines that resemble the spectrum of La, since only one $4f$ electron and thus no Coulomb interaction is present in the final state. The energy separation between $f^1 \to f^2$ and $f^0 \to f^1$ contribution is expected to amount to $\Delta E \approx 5$ eV (compare Fig. 2.6). Due to this rather large separation, mixing of the different final states is expected to be small. Consequently, the complete spectrum can reasonably be described by a simple sum of the two separate spectra.

In their systematic study, Fuggle *et al.* showed that Ce $M_{4,5}$ spectra of mixed-valent Ce compounds exhibit peaks at the high-energy side of both main lines that are absent in the spectrum of γ-Ce. Hence, these peaks can be assigned to the $f^0 \to f^1$ transition, as is done in fig. 6.1 (a). Shortly after their publication, the interpretation of Fuggle *et al.* was confirmed in similar studies by Kaindl *et al.* [187, 188] and has been accepted by all other Ce $M_{4,5}$ investigations addressing the valence of different Ce compounds that are known to the author [65, 184, 189–197].

A quantitative evaluation of the relative weights of the two contributions provides access to the $4f$ occupancy n_f and the valence $v = 4 - n_f$ (see section 2.1.5). However, this evaluation from experimental data is subject to two major problems. First, the observed relative $f^0 \to f^1$ weight does not equal the mixing coefficient c_{f^0} in the Ce ground state as written in eq. 2.40. This reflects interaction of the different final state configurations.

From their model calculations, Fuggle *et al.* constructed a calibration curve to correct for this deviation [39, 61]. This curve was constructed from the peak intensities of the two contributions in calculated spectra. While it is intrinsic to XAS that c_{f^0} is underestimated by the observed spectral weight, the magnitude of the deviation depends on the parameters of the Gunnarsson-Schönhammer model. In particular, the hybridization strength Δ influences the result.

Determination of this parameter can be done experimentally by core-level PES, which requires additional experimental effort. Incidentally, such measurements also allow determination of n_f with fewer uncertainties compared to XAS [39]. Hence, if the parameters needed to correct the XAS result for n_f are known, there is actually no further need to perform an analysis of the relative $f^0 \to f^1$ weight, except for a confirmation of consistency.

The second source of uncertainties is the extraction of the experimental values for the spectral weight. In contrast to the model calculations of Fuggle *et al.*, the true spectrum features the complicated multiplet structure in the $f^1 \to f^2$ part, which partly overlaps with the $f^0 \to f^1$ contribution.

In such a situation, the peak intensity is not the ideal measure of a spectral contribution,as argued in section 5.1.3. The oscillator strength should be used instead. In the case of Ce $M_{4,5}$ spectra, the concept of a $f^1 \to f^2$ intensity is additionally obscured by the rich multiplet structure, which prohibits the representation of the two edges as single peaks. Furthermore, usage of the intensities requires the assumption that the lifetime widths of the $f^1 \to f^2$ and $f^0 \to f^1$ contributions are equal. This is not necessarily true. The calibration curve of Fuggle *et* *al.* remains valid for the oscillator strength ratio, since their model calculation produced well-separated, single peaks with equal widths and thus guarantees direct proportionality between the intensities and areas of the peaks.

The extraction of the oscillator strengths from experiment is complex, since the two overlapping contributions and the continuum step have to be disentangled. It might be due to this arduousness that detailed accounts in the literature are scarce. While Fuggle *et al.* use the intensities as already discussed [61], Münzenberg *et al.* show a fit with two Lorentzians at the M_5 edge only [193]. Willers *et al.* subtract a linear background below the $f^0 \rightarrow f^1$ peak to isolate this contribution [195]. Okane *et al.* fit the whole spectrum with a total of 14 peaks with variable widths, two of which are interpreted as the $f^0 \rightarrow f^1$ contribution [196].

There are further studies that include quantitative n_f results without giving details of the evaluation procedure [198–200]. Certainly, each of these methods allows the comparison of different spectra and to draw conclusions about relative progression of n_f with high precision. However, the absolute values remain error-prone. Fuggle *et al.* quantify their relative uncertainty by a factor of two.

Against this background, it comes as no surprise that most authors that address the valence with Ce $M_{4,5}$ XAS restrict themselves to a qualitative comparison of their spectra. Apart from the already mentioned studies that compare different materials, this especially concerns the temperature-dependence. The investigation of $n_f(T)$ is highly interesting since it allows addressing a manifestation of the Kondo temperature. While the GS theory is restricted to zero temperature, this is a result of the NCA solution of the SIAM that was published by Bickers *et al.* in 1987 [27] (see fig. 1.1).

The main interest in this case is on the temperature scale. Hence, a high accuracy in the determination of absolute n_f values is of lesser importance compared to a profound evaluation of relative changes.

An early account of the connection of Kondo scale and temperature dependent valence in the interpretation of XAS data was given in 1988 by Liang *et al.* [201] by means of Ce $L_{2,3}$ XAS. Their work was followed by several explicit, systematic studies of $n_f(T)$ with $L_{2,3}$ XAS [64, 202, 203]. Regarding Ce $M_{4,5}$ XAS, the earliest $n_f(T)$ reports that are known to the author date to 1999. Delobbe *et al.* as well as Rothman *et al.* measured the temperature dependence of the relative $f^0 \rightarrow f^1$ weight for CeRh [198] and thin Ce films [200] and directly compared their results to the NCA results. For some reason, both works received very little attention, although the approach to examine $n_f(T)$ with Ce $M_{4,5}$ XAS has been continued [195, 196, 204–206]. A special role in this context is played by the work of Dallera *et al.* [65], since those authors were primarily interested in the temperature-induced α-γ-transition of Ce and not in the Kondo temperature scale.

6.1.2 Studies of the $f^1 \rightarrow f^2$ multiplet in XAS

In 1985, Thole *et al.* published experimental and calculated $M_{4,5}$ spectra for the complete rare earth series including different ground-state valencies [184]. The calculations were performed in full multiplet theory. While this approach had already been applied before [183, 188], the work by Thole *et al.* significantly led to the acceptance of full multiplet theory as the ideal tool to describe such XA spectra.

This is certainly owed to the completeness of the study, as well as to the fact that the representation of the calculated spectra resembles experimental ones instead of being bar diagrams. The individual transition lines are broadened under assumption of line shapes and widths and added. This representation is ideal for visualization of the high agreement between theory and experiment.

Furthermore, the publication is marked by a high transparency of the ingredients that were used for the calculation and representation of the spectra, without going into too much detail regarding the concrete theoretical formulation. It is well-suited as a guideline for the application of the underlying computer code by experimentalists. Although both theory and experiment have been further developed in the meantime, the 1985 publication is still a very useful reference.

The theoretical approach to XAS that was pursued by Thole *et al.* is remarkable in the respect that it completely disregards the translational symmetry that is usually the basis of solid-state physics. Hence, no bandstructure appears in these calculations. In contrast, the full theoretical arsenal of atomic physics is applied in order to reproduce effects that arise from the atomic $4f$ multiplet, configuration interaction and the excitonic interaction of the core-hole and the excited electron in the final state. The excellent agreement of this approach with experimental data once again reflects the local character of the $4f$ shell.

Thole *et al.* introduced the well-established concepts of atomic physics to their computer code on the basis of a program written by Cowan to calculate atomic spectra [207]. Since the initial publication, the Thole-code has extensively been used to interpret experimental data and for further calculations [150]. In special, XMLD was predicted on this basis [166]. A comprehensive account of this effect for the whole rare earth series was given by Goedkoop *et al.* in 1988 [208], following the spirit of the 1985 publication. The extended understanding of XAS involving partially filled inner shells that was generated through the study by Thole *et al.* was carried on in succeeding theoretical works, especially regarding the XMCD sum rules [151, 152, 169] (see section 5.3).

Hybridization of the $4f$ level with conduction states, which is the main aspect of the GS theory, was considered by Thole *et al.* only as such that they calculated spectra for different f counts in the initial state. If the hybridization is not too strong, it is reasonable to assume that it only affects the f occupancy, but not the character of the atomic wave functions. In this limit, the complete spectrum can be described as the weighted sum of the spectra obtained for the individual transitions. Studies that address the regime with higher hybridization, where this assumption becomes invalid, are presented in section 6.1.3.

The $M_{4,5}$ spectra of materials that can be described in the atomic limit of a single localized $4f$ electron are well represented by full multiplet calculations considering only the Hund's rule ground state. However, the presence of a crystal field can lift its degeneracy and lead to an anisotropic ground state wave function, (compare fig. 2.3). This leads to linear dichroism in XAS on single-crystalline samples, as described in section 5.2.

An early account of this effect was given by Sacchi *et al.* in 1991 for $M_{4,5}$ XAS of Dy/Si(111) [209]. These authors already supported their experimental results with full multiplet calculations [210]. For $CeRh_3B_2$, a somewhat unusual Ce compound due to its high Curie temperature and large CF splitting, LD in Ce $M_{4,5}$ XAS was theoretically predicted in 1990 by Jo [211]. Experimental reports were given in 1993 by Nakai *et al.* [212] and in 2007 by Imada *et al.* [213]. It was shown in 2008 by Hansmann *et al.* that a combination of temperature-dependent XNLD measurements and full multiplet calculations under consideration of the crystal field allows quantitative clarification of the ground state and the CF scheme of Ce compounds [167]. This had been a long-standing issue, especially in cases where the crystal field mixes the states in the $J = 5/2$ multiplet. In this study, the CF splitting energies were taken from inelastic neutron scattering experiments. This reduces the free parameters of the modeling, which then yields the mixing coefficients.

The pioneering work was followed by a comprehensive series of studies from the same group under the direction of Tjeng [47, 194, 195, 197, 214–217]. In these publications, the method was further improved in its application to various sample systems. The compounds that were investigated all exhibit a rather small $f^0 \to f^1$ contribution and the Kondo energy scale is said to be much smaller than the crystal field splitting. This justifies an ionic approach for the calculations, which means the neglect of hybridization.

6.1.3 Studies of the interplay of valence and multiplet structure in XAS

In the original model calculations by Gunnarsson and Schönhammer, only the relative weights of the $f^0 \to f^1$ and $f^1 \to f^2$ contributions to Ce $M_{4,5}$ XAS were analyzed (see section 6.1.1). The multiplet structure of the $f^1 \to f^2$ transition was neglected. It can be calculated in full multiplet theory and can be used to study crystal field effects for systems with small hybridization (see section 6.1.2).

It was realized early that an increasing hybridization does not only change the relative weight of $f^0 \rightarrow f^1$ and $f^1 \rightarrow f^2$ contributions, but also has an impact on the details of the $f^1 \rightarrow f^2$ part. The most systematic studies of experimental spectra for different degrees of hybridization that are known to the author were performed by Kaindl [187, 188], van der Laan [189], Schillé [190] and Finazzi *et al.* [191, 192]. The spectral changes with increasing hybridization that are reported by these authors can be summarized as follows[3]:

1. The $f^1 \rightarrow f^2$ multiplet substructure is smeared out (particularly visible at features A-C and G,H in fig. 6.1) [187–192].
2. The M_5/M_4 weight ratio decreases [189, 191, 192].
3. The energy separation between the M_5 and M_4 main peaks increases [191, 192].
4. At the M_4 line, additional intensity arises at the high-energy side (feature J in fig. 6.1) [189].

The first attempt at an explanation of the hybridization-induced line shape changes was given by van der Laan *et al.* [189]. They argue that the local character of the atomic $4f$ level is transformed to a more band-like character with a finite width by the hybridization. If the band width approaches the spin-orbit splitting, j is not a good quantum number any more and the $j = 5/2$ and $j = 7/2$ states are mixed.

This scenario is supported by full multiplet calculations with varying degree of mixture of the two states. Indeed, the admixture of $j = 7/2$ states to the initial state yields the right trend for the decreasing intensities of the multiplet subpeaks (1) and the decrease of the M_5/M_4 weight ratio (2). As a central result, van der Laan *et al.* underline the importance of an interference term, which causes the mixed spectra to differ from simple weighted sums of the pure $j = 5/2$ and $j = 7/2$ spectra.

The approach by van der Laan *et al.* represents a way to construct spectra in the presence of hybridization without including a hopping matrix element and conduction states to the calculations. This extended approach would mean to combine the GS theory with full multiplet theory. Such calculations were first published in 1988 by Jo and Kotani [185, 186]. These authors explain the smearing out of the multiplet substructure with increasing hybridization by a compression of the atomic multiplet. In a following study of 1990 [218], an analysis of the angular momentum character of the hybridized $4f$ ground state revealed the admixture of $j = 7/2$ states and thus confirmed the interpretation of van der Laan *et al.*

In 1994, Schillé *et al.* published XAS and XMCD spectra of three different Ce compounds with varying degree of hybridization: CeCuSi, $CeRh_3B_2$ and $CeFe_2$ [190]. The data are of higher quality than in the previous works and confirm the observed line shape changes. Apparently, these authors tried to simulate their spectra with full multiplet calculations referring to the study of van der Laan *et al.* [189]. They refrained from presenting these results since the agreement between the calculated spectra and the experimental data was unsatisfactory. It is interesting to note that Schillé *et al.* argue that no interference term is present in the spectrum of a mixed $j = 5/2$ and $j = 7/2$ initial state in the case of a nonmagnetically oriented powder, i.e., in the truly isotropic case without magnetic or structural order.

Several of the authors of [190] also contributed to the succeeding works by Finazzi *et al.* [191, 192]. In these studies, the scenario of an admixture of $j = 7/2$ states to the initial state is further consolidated by analysis of the XAS and XMCD line shape of a series of samples that covers a wide range of hybridization strengths. The experimental spectra are qualitatively compared to the calculated pure $j = 5/2$ and $j = 7/2$ spectra, but a simulation with a weighted sum is omitted due to the interference term. Instead, Finazzi *et al.* present a theoretical Ce $M_{4,5}$ spectrum calculated with the model of Jo and Kotani [185, 186].

---

[3] Regarding the experimental data of the present work, spectral changes are discussed in section 9.1.1. Exemplary spectra with varying degree of hybridization are shown in fig. 8.3 (c)

This spectrum represents the case of rather strong hybridization judged by the $f^0 \rightarrow f^1$ weight. The agreement between the calculation and the experimental data could most likely be improved by assuming a longer lifetime width at the M_4 edge (compare section 6.3.2). In general, the smearing out of the multiplet structure is reproduced by this calculation, but the systematics cannot be judged from the single, extreme spectrum. Furthermore, the calculated XMCD spectrum suffers from an unphysical artifact, which is said to be a consequence of the representation of the conduction band in the model.

A more systematic study of SIAM calculations of Ce $M_{4,5}$ spectra is included in a study by Nakamura *et al.* [205]. Regrettably, these authors are rather sparing with details of the theoretical treatment and do not discuss their results regarding an admixture of $j = 7/2$ states to the ground state. Since only the M4 edge is shown for the theoretical spectra, no conclusions about the relative M_5/M_4 weight (2) are possible. However, the results clearly show that the intensity of the small low-energy peaks are reduced with increasing hybridization intensity (1) and that the absolute energy position of the M_4 edge shifts to higher values. Since the M_5 edge is not shown, it cannot be said if this is connected to an increasing energy separation of the two main lines (3). In the experimental data of this study, a rather large energy shift of the M_4 peak is visible, which is non-monotonous with the $f^0 \rightarrow f^1$ weight of their spectra from different samples. It is not apparent from the text if instabilities in the beamline optics can be excluded as the reason of this shift.

The broadening of the high-energy flank (4) does not occur in the calculations of Nakamura *et al.*, and it is also clearly absent in the calculated spectrum of Finazzi *et al.* [191].

In summary, the admixture of $j = 7/2$ character to the ground state seems to be a reasonable explanation for at least some of the characteristic changes that occur in Ce $M_{4,5}$ spectra of compounds with higher hybridization. The plain assumption of this admixture in the calculation of the spectrum, as performed by van der Laan *et al.* [189], might be a practical approach without the need to perform more extensive SIAM calculations.

For the calculation of mixed spectra, the role of the interference term remains somewhat unclear. The most recent publication on the topic that is known to the author is a 2012 study by Okane *et al.* [196]. These authors present a detailed Ce $M_{4,5}$ XAS and XMCD line shape analysis of $CeRu_2Si_2$ and $CeRu_2Ge_2$, two related compounds with quite different properties, including their $f^0 \rightarrow f^1$ weights.

Okane *et al.* simulate their data by simple weighted sums of pure $j = 5/2$ and $j = 7/2$ spectra without an interference term, but also without to comment on that neglect. Furthermore, they did not consider that the presence of a crystal field influences the Ce $M_{4,5}$ spectral shape (see section 6.1.2). However, their spectra do not represent the isotropic case. This assumption is supported by comparison to the isotropic $CeRu_2Si_2$ spectrum shown by Willers *et al.* [195] and by their observation of a temperature-dependent line shape. Since CF-induced LD is not included in the interpretation of Okane *et al.*, some of their conclusions have to be questioned. In particular, this concerns the $j = 7/2$ admixture.

Regarding the results of the present thesis, the issue of $j = 7/2$ admixture to the ground state and the resulting interference term in Ce $M_{4,5}$ XAS is discussed in section 8.3.2.

6.1.4 XMCD Studies

Historically, the pioneering XMCD works in the late 1980s by Schütz *et al.* were performed in the hard X-ray range [149, 219, 220]. However, a strong interest was shown in the $M_{4,5}$ edges of rare earths materials by the group of Thole, van der Laan and Sawatzky, who investigated XMLD around the same time [165, 166, 184].

XMCD was transferred to the soft X-ray region by Chen *et al.* in 1990, who investigated the $L_{2,3}$ edges of Ni [221]. In the same year, two theoretical works were published by Jo and Imada that cover XMCD at the Ce $M_{4,5}$ edges [218, 222]. The first experimental reports of Ce $M_{4,5}$ XMCD that are known to the author were published in 1994 by Schillé *et al.* [190, 223]. Since then, such measurements have been applied to investigate the local $4f$ magnetism in various Ce-containing materials [191, 192, 196, 199, 200, 205, 213, 224–234].

An important issue for the quantitative evaluation of Ce $M_{4,5}$ XMCD is the validity of the sum rules, which are introduced in section 5.3. As was pointed out by Schillé *et al.* [190], the configuration interaction-induced transfer of spectral weight between the spin-orbit split partners in the Ce $M_{4,5}$ spectrum (see the discussion of fig. 6.1) prohibits the application of the spin sum rule. Therefore, these authors, as well as the ones of several later studies, only used the orbital sum rule. Assuming that the $4f$ electron is in the $j = 5/2$ ground state and fully localized, the total magnetic moment can be calculated from the orbital moment according to eq. 2.7.

The deviation of the spin sum rule result from the true operator expectation value was examined theoretically for the $M_{4,5}$ edges of rare earths by Teramura, Jo *et al.* [235, 236]. For Ce, the overestimation of the sum rules approximately amounts to a factor of 1.6. This factor was used by Tolinski *et al.* to correct their spin sum rule result [233]. However, the spin sum rule additionally requires assumptions about the magnetic dipole term $\langle \hat{T}_z \rangle$ in order to yield the pure spin moment. This quantity was experimentally addressed by Okane *et al.* [196], who, however, did not consider the weight transfer between the two edges in their analysis. Hence, this effect is intermixed to their quantification of $\langle \hat{T}_z \rangle$.

In order to test the results of sum rule evaluations, several attempts have been reported. For strongly hybridized compounds, the comparison of XMCD results to those of band structure calculations and neutron scattering experiments caused some debate [224, 237, 238].

An often used reference is the expected magnetic moment of the free Ce^{3+} ion (see section 2.1.1). However, as is discussed in section 2.1.2, the crystal field scheme has to be known in order to correctly interpret a measurement at a given temperature. Experimental studies that quantitatively include the CF in the analysis of Ce $M_{4,5}$ XMCD are not known to the author.

The comparability of XMCD and Spin QUantum Interference Device (SQUID) results for various Ce compounds was investigated in a comprehensive series of publications by Miyahara *et al.* [205, 227–231]. In these works, temperature-dependent XMCD results are evaluated by a combination of the orbital sum rule and a procedure that assures the relative comparability of the data points for each sample. The results for the magnetic moment are transferred to units of the magnetic susceptibility, which can be compared to the SQUID results.

It is remarkable that for all of the studied Ce compounds the XMCD and SQUID results show significant differences. The SQUID measurements all show typical anomalies, which are interpreted as signatures of Kondo interaction. The XMCD data deviate from these curves in a way that generates the impression of a different, in some cases even inexistent Kondo temperature scale.

One argument in the interpretation of this finding is the site-specificity of XMCD, meaning that the pure $4f$ moment is probed by spectroscopy in contrast to magnetometry, which probes the total moment of the sample. In addition, Miyahara and Shiozawa in 2004 presented a model that reflects different time constants of relaxation for the two techniques [231], coming to the conclusion that this effect could explain an effectively lesser degree of hybridization observed by XMCD.

Several concerns can be raised over the conclusions in these works. Regarding the samples, single- and polycrystals were investigated. The possible effect of a crystal field, which can lead to strongly varying susceptibility curves depending on the alignment of the magnetic field and the crystallographic directions (compare section 2.1.3), is not considered in detail and it is not described whether it was made sure that the geometry in the SQUID and XMCD experiments was equivalent. This of course only concerns the single-crystalline samples.

The quality of the XMCD data regarding the noise level is not very high for many of the examples that are shown by Miyahara *et al.*, in particular at temperatures above $T = 50\,\mathrm{K}$. This is understandable for paramagnetic samples. The description of the measurement and evaluation procedures reflect that the authors were aware of this challenge and met it with caution and accurateness. Nevertheless, the reliability of the data points at high temperature are questionable. In most of the graphs, no error bars are given, but the scatter of the data indicates considerable uncertainties even at the lower temperatures.

In particular, these uncertainties become apparent for the measurements of CeNi. This material has been investigated twice, the first time in 2003 [230] and again in 2006 [205]. While the SQUID curves in both cases agree well, the XMCD data drastically differ at the higher temperatures. Under the assumption that the later experiments profited from advanced knowledge in both experiment and evaluation, this discrepancy indicates that the earlier data have to be treated with caution.

In the study by Nakamura *et al.* [205], the comparison of SQUID and XMCD susceptibility data appears as if both techniques would agree in the temperature range $T = 100 - 150$ K. For higher temperature, no XMCD data are shown. For lower temperatures, the XMCD susceptibility is larger than the SQUID result.

The data point density in the plot of Nakamura *et al.* is considerably higher than in the earlier publications, which also makes this work the most reliable. The studied samples were polycrystalline. Hence, the susceptibility curve does not depend on the direction of the magnetic field and this aspect needs not to be considered in the comparison of different experiments.

The XMCD susceptibility data show some modulation with temperature. Nevertheless, Nakamura *et al.* interpret them in terms of a Curie-Weiss law. A fit is presented that is not in conflict with the error bars shown, but it is not obvious why this should be the valid interpretation. The effect these authors were actually looking for is a Kondo-induced anomaly. Nevertheless, such effects were not included in the interpretation of the experimental data.

Apparently, Nakamura *et al.* were not aware of the fact that the single impurity Kondo energy scale can be probed by Ce $M_{4,5}$ XAS via the temperature dependence of the $f^0 \rightarrow f^1$ weight (see section 6.1.1). They show respective data and even theoretical calculations that reproduce the effect, but state that to their knowledge this effect had not been reported before. Since only three spectra for $T \approx 25 - 100$ K are shown, it is not possible to unambiguously determine the Kondo temperature from these data. There is considerable variation in the $f^0 \rightarrow f^1$ weight in these spectra, which indicates that T_K, as probed by XAS, is not far from this range in CeNi. Hence, it is not unreasonable to expect signatures of the Kondo effect in the XMCD data.

In spite of these concerns over the interpretation of the XMCD data, the deviation between the SQUID and XMCD data of Nakamure *et al.* is obvious. These authors explain their observation with the aforementioned model by Miyahara and Shiozawa. To the opinion of the author of the present thesis, a very important aspect has been disregarded in this analysis, which is the surface sensitivity of XAS and XMCD in TEY mode.

Nakamura *et al.* estimate the information depth of their experiments to $\lambda_e \approx 6$ nm and argue that the XMCD data thus represent the bulk susceptibility. However, this estimate is not very well-founded. Experimental determination of the TEY electron escape depth in the present work yielded $\lambda_e \approx 1$ nm for $CePt_5$/Pt(111) samples, a much smaller value which is in line with other experimentally obtained values for rare-earth materials (see section 7.4). Furthermore, even for $\lambda_e = 6$ nm, a considerable fraction of the signal is generated in the first few layers of the sample. While nothing can be said about the reliability of the SQUID evaluation of Nakamura *et al.*, the comparison to the XMCD data suffers from the surface-sensitivity of the TEY mode. If the surface-nearest layers exhibit electronic and magnetic properties that are different from the sample bulk, this would certainly be visible in the XAS and XMCD data. Examples for the identification of such surface- and interface effects can be found in the literature[199, 239–241]. The results of the present thesis also indicate that such effects can have significant impact on TEY data.

In summary, it can be said that the approach to investigate Kondo and heavy fermion systems with Ce $M_{4,5}$ XMCD has not been exploited to its full potential yet. The studies by Miyahara *et al.* indicate difficulties in the interpretation of such experiments, which can, however, be circumvented if an appropriate material is chosen for the study. For surface-sensitive TEY experiments, the requirements are ideally fulfilled by thin-film materials like $CePt_5$/Pt(111).

Another difficulty in the interpretation of Ce $M_{4,5}$ XMCD experiments on Ce compounds is the presence of different energy scales. Particularly, in order to extract the desired information regarding electronic correlation effects, those have to be separated from crystal field effects.

As is described in sections 6.1.1 to 6.1.3, Ce $M_{4,5}$ XA spectra, which are a component of the respective XMCD data, provide additional access to both the single-impurity Kondo scale and CF splitting via the relative $f^0 \to f^1$ weight and the presence of linear dichroism, respectively. As can be seen from the preceding literature review, these aspects have often been addressed in the past in separate studies. Some attempts have been published to combine the benefits of both Ce $M_{4,5}$ XAS and XMCD, like the work of Okane *et al.* [196]. However, no study that adequately considers all of the required aspects by exploiting the full potential of these techniques is known to the author. At this point, the present thesis ties in with the summarized state of research.

6.2 Determination of the Ce valence from Ce $M_{4,5}$ XA spectra

As is introduced in section 6.1.1, separate contributions for the $f^0 \to f^1$ and $f^1 \to f^2$ transitions can be identified in Ce $M_{4,5}$ XA spectra. Their relative weights provide a signature of the Ce valence v, which is connected to the $4f$ occupancy via $v = 4-n_f$. In the following, the procedures that were developed to extract these information from the experimentally obtained spectra of $CePt_5$/Pt(111) surface intermetallics in the present thesis are introduced.

The determination of absolute n_f values from experimental Ce $M_{4,5}$ XAS is difficult since the two spectral contributions overlap and since the $f^0 \to f^1$ weight is non-linearly related to the f^0 admixture coefficient (see section 6.1.1). A further source of complexity is the fact that the line shapes of the $f^1 \to f^2$ contributions of spectra with different degrees of hybridization differs, which means that peak intensities cannot necessarily be compared directly (see section 6.1.3).

Nevertheless, important conclusions can be drawn from an analysis of relative changes in the $f^0 \to f^1$ weight under variation of experimental parameters. In order to reliably track such trends with the possibility to adapt to different methods for determination of the absolute values, the two purposes were separately addressed.

For a comparison of a series of spectra in dependence of a parameter x (in practice film thickness t or temperature T), a reference spectrum was chosen. This spectrum was analyzed regarding the oscillator strengths of the $f^1 \to f^2$ and $f^0 \to f^1$ transitions, $w^{1\to 2}$ and $w^{0\to 1}$, respectively. In order to achieve the best possible result, this was done by application of full multiplet calculations for both contributions. The procedure is described in section 6.3.2.

The relative oscillator strengths in every other spectrum of the series was determined by least square fits of the reference to the spectrum under investigation. A multiplicative amplitude, an energy shift and a linear background were allowed in the fit. Separate fits were performed for the $f^1 \to f^2$ and for the $f^0 \to f^1$ parts of the spectrum.

The energy ranges that were used for the fits are indicated in fig. 6.2. The $f^1 \to f^2$ fits covered the pre-edge region and the low-energy flanks of the lines, including the peak (features A-D and G-I in fig. 6.1). The $f^0 \to f^1$ fit was performed for the high-energy flank of the respective features (F and K). The cross-over regimes (E and J) were omitted in the analysis, since they cannot be assigned to any of the two contributions alone.

For most samples, the XAS data were extracted from series of XMCD measurements that aimed at a determination of $\chi(T)$ (see chapter 10). For reasons of efficiency, only the M_4 line was recorded in many cases. The choice was made in favor of M_4 since the displays the most pronounced XMCD effect. The $f^0 \to f^1$ contribution is also larger than at the M_5 edge.

The relative change of the signal at one of the two edge can be regarded as representative of the whole spectrum, if no changes in line shape are present. Only a single complete spectrum is then required as the reference for determination of absolute values.

For series with mainly single-edge spectra, the fits were only performed for the M_4 edge. In cases were both edges were measured with sufficient point density, the results of the two fits for each contribution were averaged in order to reduce statistical errors.

The full computer-control of the experimental setup at the DEIMOS beamline at SOLEIL allowed development of the so-called "$n_f(T)$ fast scan mode". This experiment is explicitly designed to efficiently provide $n_f(T)$ data with high point density. Starting from low temperatures,

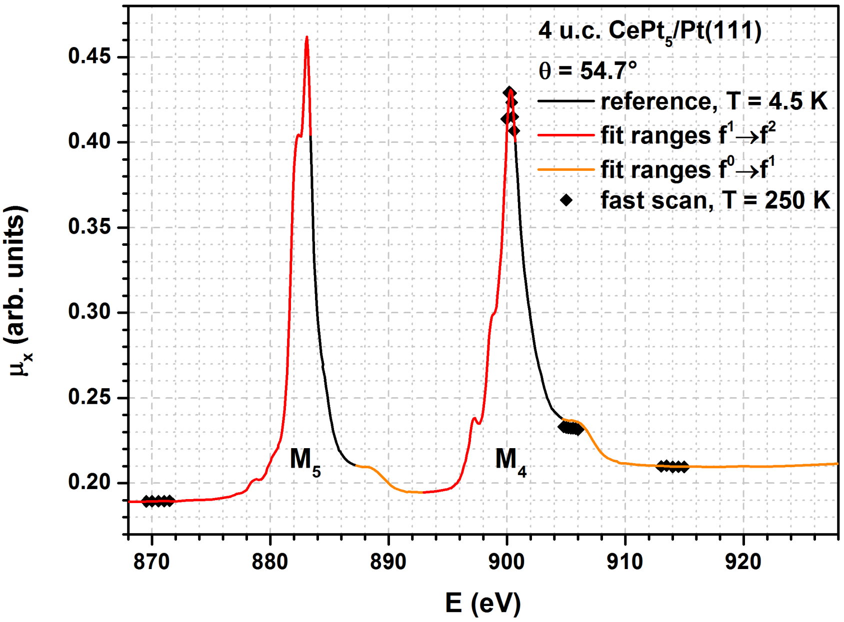

Figure 6.2: Visualization of the fitting procedure applied to track relative changes in n_f. An exemplary isotropic low-temperature reference spectrum is shown with color-coded fit ranges: Red corresponds to the $f^1 \rightarrow f^2$ contributions, orange to the $f^0 \rightarrow f^1$ contributions. The symbols represent a single “fast scan” spectrum at high temperature. The data were recorded in TEY mode at SOLEIL.

the sample is continuously warmed-up. The sample temperature is recorded and used as a trigger to quickly measure the relevant portions of the Ce $M_{4,5}$ spectrum at each $\Delta T = 5$ K step. Only a few points of the spectrum are recorded in the pre-edge region, at the M_4 $f^1 \rightarrow f^2$ maximum, on the M_4 $f^0 \rightarrow f^1$ shoulder and in the post-edge region. An exemplary scan is shown in fig. 6.2 (black symbols).

In order to address $n_f(T)$, the recorded data points of the fast scan spectra were again fitted with a low-temperature reference. The pre- and post-edge data were used as baseline for both contributions. The peak and shoulder points were used for the $f^1 \rightarrow f^2$ and $f^0 \rightarrow f^1$ fit, respectively.

Due to the continuous warm-up during measurement of the spectra, the uncertainty in the temperature for a single data point is of the order of $\Delta T \approx 1 - 2$ K. Since the warm-up is faster for low temperatures, the error is largest there. This uncertainty is not relevant regarding the scale of the effect that is searched for. Furthermore, an even larger error is most likely induced by the fact that the temperature sensor lags behind the real sample temperature. This can especially lead to artifacts when the warm-up is paused for a complete control spectrum and a readjustment of the sample manipulator to compensate for thermal expansion.

For all the procedures described above, the parameter-dependent fit amplitudes $\mathcal{A}^{n\rightarrow n+1}(x)$ represent a measure of the relative change of intensity. This is equivalent to the relative change of spectral weight $w^{n\rightarrow n+1}(x)/w_{\text{ref}}^{n\rightarrow n+1}$ if the linewidths and spectral shapes of the two transitions do not change under variation of x and if the two contributions do not overlap.

In order to fulfill the first requirement for the temperature-dependent measurements, isotropic spectra that are free from crystal field effects were evaluated (compare section 6.3). Since changes in the spectral shape are clearly present for the thickness-dependent data, the relative evaluation suffers from uncertainties here. These are addressed in the discussion of the experimental result in section 9.1.1.

The second requirement is not strictly fulfilled in the Ce $M_{4,5}$ spectra. However, an overlap of two peaks does not affect the presence and character of a relative change of the integrated intensity, as long as the two peaks do not completely coincide. Hence, uncertainties in the magnitude of the relative change have to be expected, whereas qualitative results are unaffected.

With these restrictions in mind, the evaluated amplitudes together with the weights of the reference spectrum can be summarized in the parameter-dependent relative $f^0 \rightarrow f^1$ weight according to

$$w_{\mathrm{rel}}^{0\rightarrow 1}(x) = \frac{w^{0\rightarrow 1}(x)}{w^{1\rightarrow 2}(x)} = \frac{\mathcal{A}^{0\rightarrow 1}(x)}{\mathcal{A}^{1\rightarrow 2}(x)} \cdot \frac{w_{\mathrm{ref}}^{0\rightarrow 1}}{w_{\mathrm{ref}}^{1\rightarrow 2}}. \tag{6.1}$$

The error bars that are given with the experimental data in chapter 9 are calculated from the statistical errors of the fit amplitudes as returned by the fitting algorithm with application of simple error propagation to eq. 6.1.

The translation of $w_{\mathrm{rel}}^{0\rightarrow 1}$ to the valence v or the $4f$ occupancy n_f requires knowledge of the GS-model parameter Δ for the material under investigation (see section 6.1.1). Since the valence changes with the sample thickness, a change in Δ can also be expected, which would require thickness-dependent measurement of this parameter. Core-level PES experiments on $CePt_5$/Pt(111) that are suited for a determination of Δ have been performed by H. Schwab in the course of his PhD thesis [242], but the evaluation was not completed during completion of the present section.

Even without a quantitative access to the GS-model correction, a close connection between $w_{rel}^{0\rightarrow 1}$ and n_f or v can be expected. In any case, the results for $w_{rel}^{0\rightarrow 1}$ allow a qualitative discussion of n_f and v, which can be valuable in comparison to results from other studies. Under neglect of the GS-model corrections, their connection can simply be formulated as

$$v = 4 - n_f = 4 - \frac{1}{1 + \frac{13}{14} w_{\mathrm{rel}}^{0\rightarrow 1}}. \tag{6.2}$$

The factor 13/14 normalizes the spectral weights of the $f^0 \rightarrow f^1$ and $f^1 \rightarrow f^2$ contributions according to the different numbers of holes in the initial state. It thus reflects the charge sum rule (see section 5.2).

Eq. 6.2 allows more or less equivalent usage of valence, $4f$ occupancy and relative $f^0 \rightarrow f^1$ weight. However, it has to be kept in mind that they show a qualitatively different behavior: $w_{\mathrm{rel}}^{0\rightarrow 1}$ behaves like the valence, which means that it increases if n_f decreases.

6.3 Full multiplet calculation of Ce $M_{4,5}$ spectra

Since the ground-breaking 1985 work of Thole *et al.* [184], the capability of full multiplet calculations to reproduce experimental $M_{4,5}$ spectra of rare earths is generally accepted. As is highlighted in section 6.1, the approach of Thole *et al.* and their computer code found broad application. In 1988, Jo and Kotani presented first results that combined full multiplet theory with the SIAM [185, 186].

Another milestone in the usage of calculated Ce $M_{4,5}$ spectra is the work of Hansmann *et al.* [167], which is the first in a series of publications by the group of Tjeng [47, 194, 195, 197, 214–217]. In these studies, full multiplet calculations are applied to determine the crystal field schemes of Ce compounds by exploiting the CF induced XNLD (see section 5.2). The calculations in all of these studies were performed with the XTLS8.3 code by Tanaka [243]. Furthermore, a Mathematica package by Haverkort was frequently used for supporting calculations regarding the CF.

The work on this package started during Haverkort's PhD thesis in the group of Tjeng [244]. In the following, it was further developed to the Solid State Physics Mathematica Package (SSPMP)[4], which is also capable of solving model Hamiltonians and of calculating spectra [245]. In the course of the present thesis, a cooperation with M.W. Haverkort and P. Hansmann was started with the aim to investigate the Ce $M_{4,5}$ XAS line shape of $CePt_5$/Pt(111) samples by comparison to calculated spectra. SSPMP was used in versions 2013.1.17 and 2014.3.6 in

---

[4] SSPMP is represented on a web page, `http://www.solstatphys.org/solid_state_physics/index.php`. Furthermore, it has merged into the Quanty project in the meantime (`http://www.quanty.org`)

conjunction with Mathematica 8.0.4.0. The current state of results of this endeavor is presented in chapter 8.
The range of application of SSPMP is broad, as can be seen from the list of related publications that is collected on the package web page[4]. A full account of the theory and especially the computational realization is far beyond the scope of the present thesis. A well-arranged description of full multiplet theory can be found in a text by van der Laan [246]. In section 6.3.1, a qualitative description of the approach and the single steps in the calculation is given for the example of the $f^1 \rightarrow f^2$ transition. In order to compare the calculated spectra to experimental data, assumptions concerning the line shape and width have to be made. These considerations are presented in section 6.3.2. Finally, section 6.3.3 is devoted to the procedure that was applied to adjust the theoretical spectra to the experimental ones.

6.3.1 Calculation of the spectra

The calculation of Ce $M_{4,5}$ spectra in the present work follows the route of Thole *et al.* [184]. The absorption process on a single Ce ion was treated in terms of atomic multiplet theory. This involves a description of initial and final states and the transition between the two.
The initial state is the ground state of the ion. For Ce^{3+}, all shells are completely filled except for $4f$. The single $4f$ electron is subject to spin-orbit coupling, the crystal field and a potential magnetic field. In most materials and under normal experimental conditions, SOC (see eq. 2.2) introduces the largest energy scale $\Delta E_{\mathrm{SOC}}^{4f} \approx 300$ meV. It is followed by the crystal field, which typically induces a level splitting of $\Delta E_{\mathrm{CF}} \approx 10 \dots 20$ meV. In the present thesis, magnetic fields of $B \leq 7$ T were used, which means that the Zeeman splitting $\Delta E_{\mathrm{Z}} \approx 400$ µeV (see eq. 2.15) is the smallest energy scale.
The Hund's rule ground state of the $4f$ electron is characterized by $j = 5/2$, its sixfold degeneracy can be modified by the CF. To first order, the CF only mixes the states in the $j = 5/2$ manifold (see section 2.1.2).
The excited state has two $4f$ electrons and a $3d$ core-hole. Consequently, SOC of the $3d$ state as well as Coulomb interaction in the $4f$ shell and between $4f$ and $3d$ electrons have to be considered. The number of different final state configurations is $10 \cdot 13 \cdot 14/2 = 910$[5]. The dipole selection rules (see section 5.1.1) prohibit the transition to most of these states, leading to 53 allowed final state configurations [184]. Each of these transitions contributes to the spectrum as a single line with a certain oscillator strength at a certain energy. In principle, a list of these values is the result of the calculation of a spectrum.
In order to come to this end, the Schrödinger equations of the ion in the initial and final state have to be solved. This is equivalent to diagonalization of the Hamiltonian matrix, which yields the eigenvalues and eigenfunctions. If this is achieved for both initial and final state, the transition matrix elements can be calculated according to eq. 5.4. The details of the dipole transition operator are chosen according to the light polarization.
For the matrix representation of the Hamiltonian, a many-electron basis is built from atomic one-electron wave functions. Since Hund's rules apply, a $|j, m_j\rangle$ basis is most conveniently chosen for this task (compare section 2.1.1). In order to define a quantization axis and to assure that the numerically found eigenstates represent pure $|j, m_j\rangle$ states, the calculations are performed with a small magnetic field applied in z direction.
The atomic wave functions can be expressed as the product of a radial and an angular part (see eq. 2.1). The latter is usually expressed in spherical harmonics, which are also chosen as the basis to construct the Hamiltonian. Its effects on the radial and angular parts can then be treated independently.
For a free Ce^{3+} ion, the Hamiltonian includes terms for spin-orbit coupling, Coulomb interaction and a magnetic field. The calculation of both the SOC and the Coulomb terms profits from the factorization into radial and angular parts. While the angular parts can be calculated analytically, the radial parts are commonly treated in a Hartree-Fock Scheme (compare the

---

[5] The division by 2 respects the indistinguishability of the two $4f$ electrons.

configuration	F^2_{ff}	F^4_{ff}	F^6_{ff}	ζ_{4f}	F^2_{df}	F^4_{df}	G^1_{df}	G^3_{df}	G^5_{df}	ζ_{3d}
$3d^{10}4f^0$	0.0	0.0	0.0	0.0						
$3d^94f^1$	0.0	0.0	0.0	0.119	8.200	3.750	5.663	3.313	2.288	7.44
$3d^{10}4f^1$	0.0	0.0	0.0	0.087						
$3d^94f^2$	12.630	7.941	5.718	0.107	7.484	3.383	5.071	2.966	2.047	7.44
$3d^{10}4f^2$	10.245	6.354	4.558	0.075						
$3d^94f^3$	11.388	7.102	5.102	0.095	6.721	2.993	4.470	2.612	1.810	7.45

Table 6.1: Values of the Hartree-Fock parameters for the initial ($3d^{10}4f^n$) and final states ($3d^94f^{n+1}$) that were used for the calculation of XA spectra. F and G are Slater integrals, ζ denotes the SOC constants. All values are given in eV.

theoretical treatment of LEED IV, especially the calculation of the phase shifts, in section 4.2). This leads to the SOC parameter ζ and to the so-called Slater integrals (SIs), which represent momenta of the Coulomb interaction in the expansion in spherical harmonics.

The HF parameters can be computed with Cowan's RCN code [44]. Values for the $f^0 \rightarrow f^1$ transition can be found in the work by Thole *et al.* [184], the $f^1 \rightarrow f^2$ transition is covered there and in the diploma thesis of Hansmann [214]. The parameters for the $f^2 \rightarrow f^3$ transition were kindly computed by P. Hansmann. Tab. 6.1 summarizes the values that were used in the present calculations.

Although translational symmetry can completely be disregarded in the theoretical treatment of Ce $M_{4,5}$ XAS, some account has to be given to the fact that the ion is embedded into a solid crystal. This was done in three ways: First, the HF parameters were reduced. This is meant to account for configuration interaction with covalent configurations that are not included in the HF scheme. Hence, it reflects the altered spatial and electronic situation in a solid compared to the free ion.

The SI reduction is common practice in the adjustment of XA spectra to experimental data. Thole *et al.* reduced all SIs to 80 % of the HF values [184]. While those authors argue that more fully optimized parameters would be artificial and unphysical due to uncertainties in experiment and theory, a significantly higher agreement can be obtained if different reductions are allowed for the $4f$-$4f$ and $3d$-$4f$ SIs. The $4f$ electrons are much more influenced by the environment than the $3d$ core-hole. Hence, it is reasonable to expect that the $4f$-$4f$ SIs are stronger reduced than the $3d$-$4f$ parameters. In the studies of the group of Tjeng, reductions to $60 \dots 65$ % and $75 \dots 80$ % were applied, respectively [167, 194, 195, 197, 215–217].

The second account for the environment in the present calculations is the crystal field. As described in section 2.1.2, the hexagonal symmetry that is present in $CePt_5$ does not mix the states in the $J = 5/2$ manifold, but only leads to an energetic splitting of the three $\pm m_j$ doublets. Consequently, it is not necessary to include the CF in the Hamiltonian. The choice of the ground state and a summation of states weighted with Boltzmann factors for temperature-dependent spectra can conveniently be done manually.

The third spectral signature of the environment of the ion is hybridization with conduction states. A full account of hybridization would require to include a conduction band and a hopping matrix element to the Hamiltonian, in analogy to eq. 2.39. This would lead to a description similar to the model by Jo and Kotani [185, 186].

In the present thesis, a simpler approach was chosen. As is discussed in sections 6.1.1 and 6.1.3, the effect of hybridization can qualitatively be included to the calculations by considering two aspects: First, the relative weight of the $f^0 \rightarrow f^1$ contribution increases. This is simply achieved by adding the calculated $f^0 \rightarrow f^1$ spectrum with variable amplitude. Second, an admixture of states with $j = 7/2$ character to the initial state has to be considered. The $j = 7/2$ subspace is automatically included to full multiplet calculations, as the name indicates. Hence, spectra for mixed states can be calculated by appropriate choice of the ground states. This approach avoids the complications of an additional conduction level in the calculations, but should represent a reasonable representation of the experimentally obtained spectra.

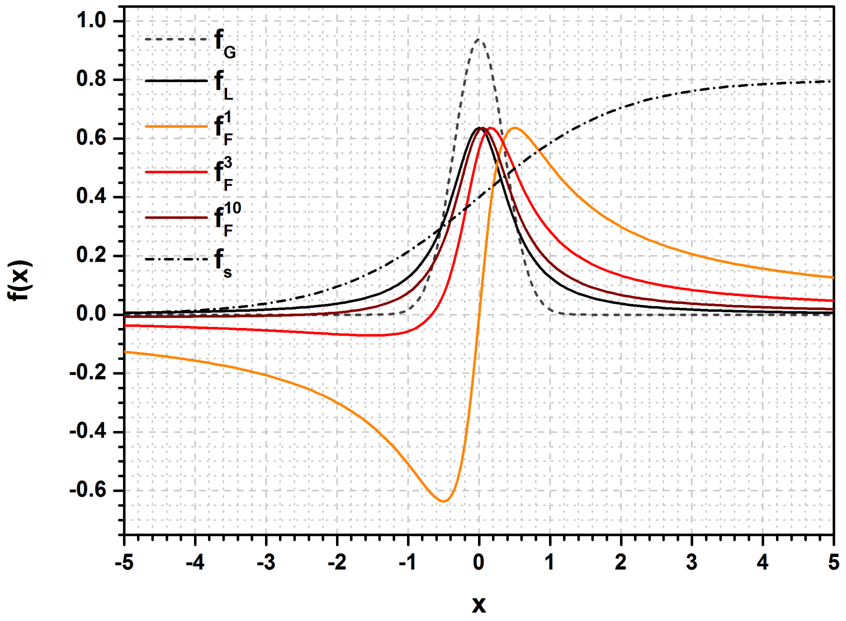

Figure 6.3: Examples for Gauß, Lorentz and Fano profiles, the latter with different asymmetry factors q, as well as for the assumed continuum step profile. For all curves, $\Gamma = 1$.

6.3.2 Representation of calculated XA spectra

The result of a multiplet calculation as described in section 6.3.1 is a list of values of the energy position and the strength of each allowed transition. A direct comparison of calculated and measured spectra requires a graphical representation of this result. The various transitions can be represented by delta-peaks. Those can be broadened and added according to the experiment. As is argued in section 5.1.3, the broadening of the transition lines is twofold. The finite experimental energy resolution is represented by a Gaussian broadening, while the lifetime broadening introduces a Lorentzian shape. In section 8.2.4, it is argued that autoionization effects lead to interference of the resonant M_4 line and an underlying continuum step in the TEY data. Hence, the Lorentzian shape of the lifetime broadening is modified to an asymmetric Fano[6] profile.

The broadening of the transition lines is done by convolution of the spectrum with the respective kernels. All three peak profiles are characterized by the FWHM Γ, the Fano profile has an additional asymmetry parameter q. The kernel function has to be normalized in a way that its integral does not change under variation of these parameters. A modified form of the Fano profile was used [247], since the original function [248] does not meet this requirement.

The functions of the Gauß, Lorentz and Fano profiles that were applied for broadening in the present work are given in the following. Examples for the three profiles are shown in fig. 6.3.

$$f_{\mathrm{G}}(E,\Gamma) = \sqrt{\frac{4\ln 2}{\pi\Gamma^2}}\; e^{-\frac{4E^2}{\Gamma^2}} \tag{6.3}$$

$$f_{\mathrm{L}}(E,\Gamma) = \frac{1}{\pi}\,\frac{\frac{\Gamma}{2}}{E^2 + \left(\frac{\Gamma}{2}\right)^2} \tag{6.4}$$

$$f_{\mathrm{F}}^{q}(E,\Gamma) = \frac{2}{q^2\pi\Gamma}\left(\frac{\left(q+\frac{2E}{\Gamma}\right)^2}{1+\left(\frac{2E}{\Gamma}\right)^2} - 1\right) \tag{6.5}$$

The normalized kernels have the property that repeated convolution with widths Γ_i resembles a single convolution with $\Gamma = \sum_i \Gamma_i$. Furthermore, it is irrelevant in which sequence multiple

---

[6] Ugo Fano, Italian-American physicist, 1912-2001 [144]. Cousin of Giulio Racah.

broadenings are performed.

The asymmetries in the experimental line shape that require the application of a Fano profile are only present at the M_4 edge, but not for M_5. Furthermore, the spectral width is different at the two edges, with broader features at M_4. In general, the lifetime of an excited state is inversely proportional to the Einstein A coefficient of spontaneous emission, which is proportional to the cube of the wavenumber of the emitted light [44]. Hence, $\Delta E \propto E^3$ according to Heisenberg's energy-time uncertainty (see eq. 5.14). While for a complete atomic multiplet with multiple relaxation channels the situation is not as simple as assumed for these arguments, it can be understood that the spectral broadening increases with increasing transition energy.

The different peak profiles and broadenings required a separate treatment of the two edges in the processing of the calculated spectra. For a smooth assembly of the two parts, a gradual averaging was performed in an energy range of $\Delta E = 4\,\mathrm{eV}$ between the edges, where the spectrum is featureless.

The dependence of the lifetime broadening on the transition energy implies different broadenings not only for the two edges, but for each single transition. These individual widths can be convincingly calculated by the t-matrix approach including resonant Auger decay to the photoemission continuum [249, 250]. In this treatment, an artificial broadening becomes unnecessary.

Since this method was not available in the present work, transition-specific lifetime broadening was approximated by energy-dependent broadening. This concept has also been applied in the more recent works of the Tjeng group [251] and leads to a high agreement of theory and experiment. In order to keep the number of parameters low, a linear relationship of lifetime broadening and photon energy was assumed in the present thesis. For each edge, two FWHM parameters were introduced via the relation

$$\Gamma(E) = \Gamma_B(E_{\mathrm{ref}}) + \Gamma_A * (E - E_{\mathrm{ref}}). \tag{6.6}$$

For the results that are presented in section 8.3, E_{ref} was chosen as the position of the peak maximum of the respective edge (features D and I in fig. 6.1).

The energy-dependent broadening required the development of a dedicated routine. Normally, the convolution operation is applied for a certain kernel peak function on the complete spectrum. In the present treatment, the spectrum was divided into delta-like peaks for each point on the given energy mesh. These "slices" of the spectrum were individually convoluted with a kernel of energy-dependent width and then added up again. The Fano profile was used as the kernel. For the M_5 edge, the asymmetry parameter was set to $q = 100$. This is sufficiently large to resemble the case $q \to \infty$, where the Fano profile is a Lorentzian.

The numerical effort of this procedure increases at least quadratic with the number of points in the energy mesh. This critically influences the response of the graphical Mathematica interface that was used to fit the calculations to experimental data. The applied real-time based parameter adjustment requires a quick feedback of the interface, which thus prohibits a too dense energy mesh. In contrast, large increments can lead to a loss of information. The compromise that was found was a mesh with $\delta E = 0.1$ eV on an energy range of $\Delta E = 46$ eV.

Another consequence of the discrete energy mesh is that it restricts the accuracy in the transition energy, if the transitions are represented as delta peaks. This problem can be addressed by an initial broadening of the delta peaks with a width that is sufficiently larger than the mesh increment. However, application of the procedure for the energy-dependent broadening on peaks with finite width leads to artifacts, since the peaks become asymmetric. This effect increases with increasing initial width. A practical compromise was found with $\Gamma_{\mathrm{ini}} = 0.5$ eV.

Furthermore, the increment of the energy mesh sets the scale for the minimum width with which a convolution can be performed in a meaningful way. The main problem is that the normalization of the kernel integral is lost for small widths, which leads to a mis-scaling of the convoluted spectrum. As a consequence, the experimental resolution was set to a slightly larger value than actually assumed, $\Gamma_{\mathrm{exp}} = 0.13$ eV. This was also used as the minimum value in the function for the energy-dependent broadening.

For the complete spectrum, different contributions with indivdual broadening parameters, like the $f^1 \to f^2$ and $f^0 \to f^1$ transitions, were usually added with a relative amplitude scaling and energy shift. The experimental Gaussian broadening with universal Γ_{exp} was applied to the result. Finally, the continuum step was added.

An example for the function that was used to represent the continuum step underneath the M_4 edge is shown in fig. 6.3 as the black dash-dotted line. Detailed considerations on the number and presence of continuum steps in Ce $\mathrm{M}_{4,5}$ spectra are presented in section 8.2.3. Since no theoretical treatment of continuum steps in XA spectra is known to the author, the step was approximated by the function

$$f_{\mathrm{s}}(E) = \mu_{\mathrm{x}}^1 - \frac{\mu_{\mathrm{x}}^0 - \mu_{\mathrm{x}}^1}{2} \tanh\left(\frac{E - E_{\mathrm{st}}}{2\Gamma_{\mathrm{st}}}\right) = \mu_{\mathrm{x}}^1 + \frac{\mu_{\mathrm{x}}^0 - \mu_{\mathrm{x}}^1}{1 + e^{\frac{E - E_{\mathrm{st}}}{\Gamma_{\mathrm{st}}}}}. \tag{6.7}$$

Here, Γ_{st} is not a FWHM, but it controls the energy range over which the step extends. It was adjusted along with the step center E_{st} to produce a smooth crossover from the background μ_{x}^0 at the low-energy side to the one μ_{x}^1 at high-energy side of the resonant M_4 line. The details of the true experimental background are unknown, but there are indications that it is rather extended for the heavier rare earths [184]. Concerning quantitative evaluation, the appearance of the step can have significant influence on the attribution of spectral weight to the $f^1 \to f^2$ and $f^0 \to f^1$ contributions. In order to reduce the uncertainties, a smooth background is the best compromise.

6.3.3 Simulation of experimental XAS data

In the present modeling of Ce $\mathrm{M}_{4,5}$ XAS as described in the preceding sections, the agreement between calculation and experiment can be controlled by several parameters. The Slater Integrals and SOC constants are parameters of the calculation itself. Their variation leads to a different spectrum. In contrast, the parameters for the broadening control the appearance of the spectrum but do not change existence, relative energy position or oscillator strength of the individual transition lines.

The absolute energy position of the calculated spectrum has to be adjusted to experiment. This has to be done individually for each contribution from different f counts, since absolute energies are not correctly treated in the calculation scheme. The relative amplitude of the different contributions are additional parameters. They are a direct measure of the relative oscillator strengths and can therefore be used to determine the $4f$ occupancy (see section 6.2). Finally, a stepped background with additional parameters accounts for continuum absorption. In principle, TEY saturation could be considered, but this has not been done in the present thesis for the reasons given in section 8.1.

If furthermore the light polarization, the CF parameters and the temperature are included to the model, it cannot be controlled any more. Therefore, as a first step the isotropic spectrum has to be modeled in order to obtain the parameters of the multiplet calculation and the spectral representation [167]. With the knowledge of these, the CF-induced LD can be modeled in a meaningful way. The present considerations are focused on the isotropic spectrum.

The adjustment of the calculated spectra to experimental data was done in Mathematica. For the parameters that control the appearance of the spectrum, a “Manipulate” environment was used, which allows variation of the parameters of a graph on a real-time basis. The adjustment was done by eye, no numerical fitting routine has been implemented yet.

Even for the isotropic spectrum, the full model has a rather large number of parameters. Considering only the $f^1 \to f^2$ contribution to the spectrum, these are a total of eleven: Reduction factors for two sets of SIs ($\beta_{\mathrm{SI}}^{4f\text{-}4f/3d\text{-}4f}$) and for the $3d$ and $4f$ SOC constants ($\beta_{\mathrm{SOC}}^{3d/4f}$), two parameters that control the lifetime broadening Γ at each of the two edges according to eq. 6.6 and an additional asymmetry parameter q for M_4. Furthermore, the energy axis has to be shifted by ΔE and the absorption signal has to be scaled to the units of the experiment by an overall amplitude $\mathcal{A}$.

The consideration of the $f^0 \to f^1$ contribution introduces four more parameters. Those are

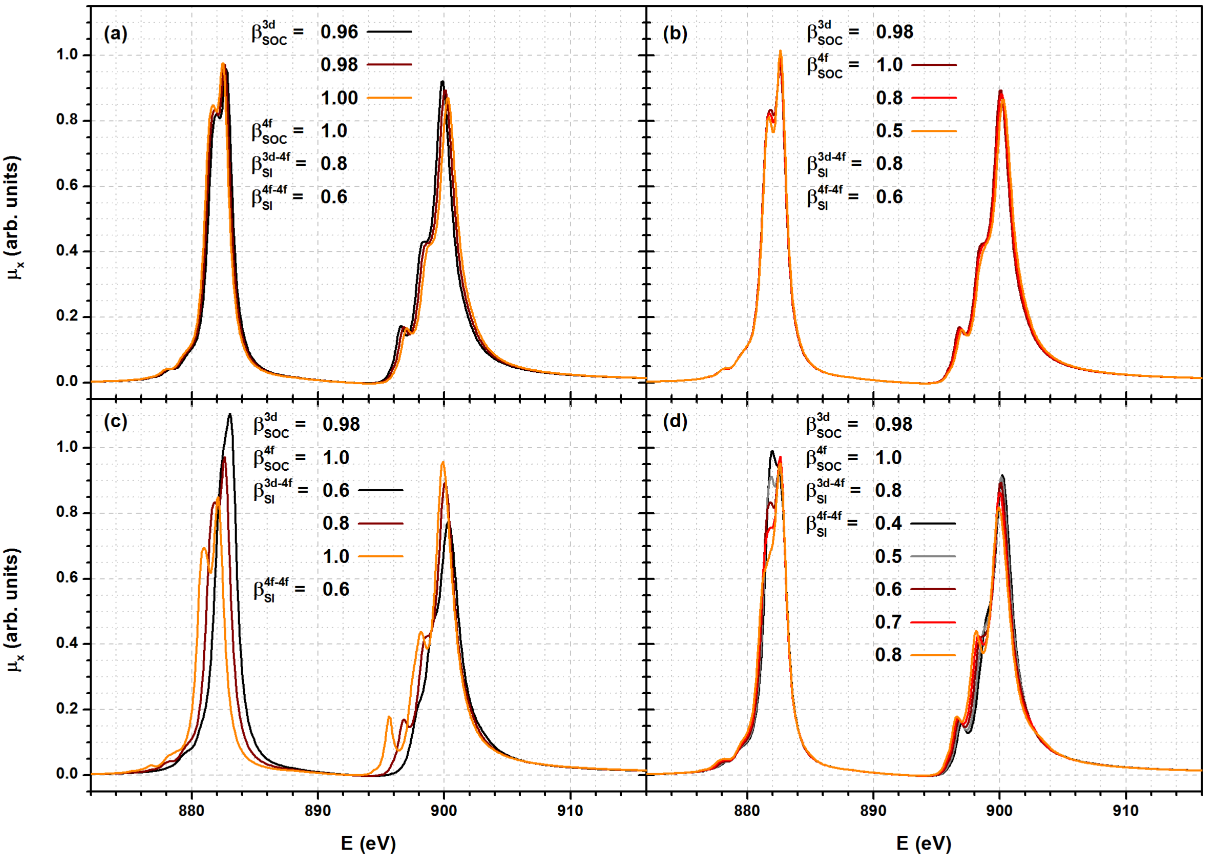

Figure 6.4: Calculated isotropic Ce $M_{4,5}$ $f^1 \rightarrow f^2$ spectra with systematic variation of the four HF reduction factors, as indicated in the individual panels. The broadening parameters were chosen as presented in tab. 8.1.

the relative amplitude $\mathcal{A}_{f^0 \rightarrow f^1}$ and relative energy shift $\Delta E_{f^0 \rightarrow f^1}$ with respect to the $f^1 \rightarrow f^2$ part and the lifetime widths at both edges. Since the $f^0 \rightarrow f^1$ contribution mainly consists of a single transition at each edge, the lifetime broadening was considered as a simple Lorentzian broadening with edge-specific FWHM.

Nevertheless, the model is controllable due to the high amount of information that is found in the rich multiplet structure and since the effects of the parameters are sufficiently distinct. For the reduction factors of the HF parameters and the $f^1 \rightarrow f^2$ transition, this is demonstrated in fig. 6.4. Here, the starting point is the pure $f^1 \rightarrow f^2$ part of the spectrum that was adjusted to the experimental data in fig. 8.7. This spectrum is the dark red line in each of the four panels (a)-(d), where the effects of the variation of the four HF reduction factors on the spectrum are shown.

For the simulation of the experimental data, the following procedure was developed. The first parameter to be optimized was $\beta^{3d}_{\mathrm{SOC}}$ (a). It controls the energy distance of the two edges, which is given by the experiment. The variation of $\beta^{4f}_{\mathrm{SOC}}$ (b) only has a small effect, even if it is set to unreasonably small values. Thus, it was set to unity and not modified in the optimization.

The reduction factor for the $3d$-$4f$-SIs $\beta^{3d\text{-}4f}_{\mathrm{SI}}$ (c) is also directly determined by the appearance of the experimental spectrum, since it controls the energy spread of the multiplet substructure at each edge. The variation of $\beta^{4f\text{-}4f}_{\mathrm{SI}}$ (d) only affects the relative heights of the distinct features (see the labeling in fig. 6.1). Since it does so in a different manner than the assumed linearly energy-dependent lifetime broadening, it can be adjusted along with these parameters in order to yield a convincing appearance of the spectrum.

The remaining parameters like the overall amplitude and the energy shift are self explaining. For the continuum step, the considerations made above only leave the step height as a free parameter. It was adjusted along with the M_4 asymmetry factor q in order to reproduce the background at the high-energy side of the spectrum.

Since the $f^1 \to f^2$ part convincingly defines the HF parameters, the same results were used to calculate the $f^0 \to f^1$ spectrum. The clear separation of the two spectral contributions then allowed adjustment of the $f^0 \to f^1$ parameters independent of the $f^1 \to f^2$ results.

6.4 Evaluation of Ce $M_{4,5}$ XMCD data

The XMCD sum rules contribute a large portion to the usefulness of experimental XMCD data. These rules relate the integrated XMCD signal to the expectation values of the z-components of the orbital and spin angular momentum operators and thus to the expectation values of the respective magnetic moments. Their derivation is discussed in section 5.3, where also the concrete equations 5.17 and 5.18 are given for the application of the orbital and spin sum rule, respectively, to the $M_{4,5}$ edges.

The reliability of the XMCD sum rules in general and at the Ce $M_{4,5}$ edges in particular has been discussed in the literature since their publication by Thole, Carra *et al.* [151, 152] (see section 6.1.4). In this discussion, several aspects have to be discriminated: the validity of the theoretical derivation, the applicability of the underlying assumptions to a certain material and the reliability of the extracted experimental values. These aspects are treated in the following three sections. In this course, the procedures that were applied in the evaluation of the present results are described. Section 6.4.4 is devoted to the conversion of the sum rule results to units of the inverse susceptibility, which is the quantity of primary interest in chapter 10. Finally, section 6.4.5 treats the measurement of an anisotropic susceptibility in dependence of the angle of incidence θ.

6.4.1 Theoretical robustness of the XMCD sum rules at the Ce $M_{4,5}$ edges

The reliability of th XMCD sum rules is affected by assumptions that are made in their derivation, like neglecting relativistic corrections. The resulting uncertainties of this neglect are said to be of the order of some percent only [169]. No further assumptions are made for the orbital sum rule, which includes the integral over the complete spectrum. Hence, it is independent of the details of the spectrum and is even valid in the presence of hybridization. For $4f$ magnetism, the orbital moment represents the most part of the total moment[7]. Hence, the orbital sum rule provides a solid basis for the interpretation of Ce $M_{4,5}$ XMCD data.

Application of the spin sum rule presupposes that the spectral weight can be separated into contributions from the two spin-orbit split core levels. As is discussed in the introduction to the present chapter, this is not possible at the Ce $M_{4,5}$ edges due to strong configuration interaction. The overestimation of the magnetic moment by a plain application of the spin sum rule has been quantified to a factor of 1.6 by Teramura, Jo *et al.* [235, 236].

Additionally, the spin sum rule requires assumptions about the magnetic dipole term $\langle \hat{T}_z \rangle$ in order to yield the pure spin moment. In principle, $\langle \hat{T}_z \rangle$ can be calculated analytically for the $M_{4,5}$ edges of rare earths under the assumption of a simple Hund's rule ground state [152]. However, under the same assumption $\langle \mu_s \rangle$ can directly be calculated from $\langle \mu_l \rangle$ according to eq. 2.7, as pointed out by Schillé *et al.* [190]. The total $4f$ magnetic moment in dependence of the orbital moment for a $j = 5/2$ initial state then reads

$$\mu = \langle \mu_j^{4f} \rangle = \frac{3}{4} \langle \mu_l^{4f} \rangle \tag{6.8}$$

This approach was pursued in the present thesis, an application of the spin sum rule was omitted. The validity of the assumption of a pure $j = 5/2$ ground state is discussed in section 8.3

---

[7] This is in contrast to the $3d$ moment of most transition metals, where the orbital part is usually very small.

6.4.2 Application of the orbital sum rule to experimental data

Application of the orbital sum rule only requires the total spectral weight of the transition under study for both XMCD and isotropic XAS. However, the application of this seemingly simple instruction to experimental Ce $\mathrm{M}_{4,5}$ data is subject to several difficulties. The following discussion is based on the assumption that the detected spectrum represents the energy-dependence of the linear absorption coefficient $\mu_{\mathrm{x}}(E)$. This presupposes that potentially present saturation effects (see section 5.4.2) are accounted for in the evaluation of the data. For the present experiments, this aspect is addressed in section 8.1.

The isotropic spectrum

The first obstacle is the measurement of the isotropic spectrum. As is discussed in section 5.2, the crystal field can lead to strong variations of the XAS line shape depending on the experimental geometry. In the present thesis, two different geometries were used by setting the angle of incidence to $\theta = 0°$ or $60°$.

For circularly polarized light, $\theta = 60°$ nearly corresponds to the isotropic case in the uniaxial crystal structure of $\mathrm{CePt}_5/\mathrm{Pt}(111)$. Hence, the non-magnetic spectrum as obtained by averaging $\mu_{\mathrm{x}}^{-}(E)$ and $\mu_{\mathrm{x}}^{+}(E)$ taken at $\theta = 60°$ is best suited for the sum rule analysis.

For $\theta = 0°$ and CPL, the polarization is perpendicular to the c-axis. Analysis of calculated spectra (see fig. 9.3) showed that in this configuration, the maximum deviation of the spectral weight from the isotropic case amounts to 3.5 %. The deviation is even smaller for the present $\mathrm{CePt}_5/\mathrm{Pt}(111)$ samples, since the measured spectra do not represent the ones of a single m_J state in the experimentally accessible temperature range. In the given crystal field scheme, ignoring the deviation from the isotropic case underestimates the magnetic moment. Due to the acceptable smallness of the uncertainty, an extensive correction for each spectrum was omitted.

Isolation of the transition of interest

Another intricacy is the identification of the part of the spectrum that represents the transition of interest, which is $3d^{10}4f^{1} \rightarrow 3d^{9}4f^{2}$ in the present case. This transition is expected to be the dominant contribution to the Ce $\mathrm{M}_{4,5}$ spectrum based on the dipole selection rules (see section 5.1.1). There are several aspects that have to be considered in this interpretation: The presence of transitions that are not considered in the dipole approximation, excitations to the continuum and contributions from different initial states.

The presence of dipole-forbidden transitions has been addressed by Thole *et al.* [184], who calculated Ce $\mathrm{M}_{4,5}$ $f^{1} \rightarrow f^{2}$ spectra with and without restriction to the dipole selection rules. The dipole-forbidden transitions occur mainly at energies below the main peaks of the dipole-allowed ones. Comparison of experimental data to these results strongly indicates that dipole-forbidden transitions can be neglected in Ce $\mathrm{M}_{4,5}$ XAS.

In principle, transitions could contribute to the spectrum that are dipole-allowed but do not include excitation to the $4f$ shell but, e.g., to the $6p$ shell. For the reasons given in section 5.1.1, transitions to states with higher n should be much weaker than the dominant one. Furthermore, they should occur at higher photon energy and should be broader, due to a higher lifetime compared to the $f^{1} \rightarrow f^{2}$ contribution. The neglect of high-n dipole transitions is again supported by the high agreement between pure $f^{1} \rightarrow f^{2}$ calculations and experimental results. Most likely, such contributions cannot be discriminated from the continuum background, which already produces a larger uncertainty.

The insecurity of the continuum background is maybe the most often heard objective to the application of the XMCD sum rules. For the $\mathrm{L}_{2,3}$ edges of $3d$ transition metals, a procedure for its subtraction has been established that has shown to yield satisfactory results [153, 154], although theoretical considerations can raise concerns against this method [252].

For the Ce $\mathrm{M}_{4,5}$ edges, no well-established procedures exists. Although the impact of the continuum background on the complete spectrum is smaller than for $\mathrm{L}_{2,3}$ spectra, it nevertheless provides a source of uncertainty in the evaluation. For the present experiments, this issue is addressed separately in section 8.2.3.

The valence fluctuations that are present in most Ce compounds give rise to a contribution from the $f^0 \rightarrow f^1$ transition in addition to $f^1 \rightarrow f^2$ (see sections 6.1.1 and 6.2). Accoring to the two-step model (see section 5.3), the $f^0 \rightarrow f^1$ spectrum displays no XMCD. Hence, only the $f^1 \rightarrow f^2$ part should be used for the sum rule evaluation and the number of holes in eq. 5.17 has to be adjusted according to $n_h = 14 - n_f$. This approach is complicated by difficulties in the separation of the two contributions.

Alternatively, assuming that the total weight of the spectrum is conserved when the $f^0 \rightarrow f^1$ weight increases due to hybridization, it is reasonable to use the integral over the total spectrum and the corresponding number of holes $n_h = 13$ for the normalization of the sum rule. This approach was applied in the present thesis.

The energy range of the total spectrum

Since integrals of the total XA and XMCD spectra are required for the sum rules, it has to be clear where the resonant spectrum starts and where it ends. Regarding XAS, this question is again influenced by the uncertainties in the identification of the superimposed continuum background.

Since XMCD is only present in the resonant part of the spectrum, its energy range should be easier to determine. The signal is expected to be zero before and behind the edge. However, experimental difficulties often produce small offsets in the XMCD signal, which requires the definition of a cut-off point for the integration. For the present TEY spectra, this is addressed in section 5.4.4.

For the Ce $M_{4,5}$ XMCD experiments of the present thesis, this cut-off point was set to $E \approx 23$ eV behind the M_4 maximum. For most of the recorded spectra, the measurement was stopped at this point for reasons of beamtime efficiency. However, evaluation of test spectra with a measurement range extended to $E \approx 45$ eV indicated that the XMCD integral could be 15 % larger than obtained with the shorter range.

This is somewhat puzzling, since XMCD resulting from $4f$ magnetism can only be observed at photon energies where the resonant $3d^{10}4f^1 \rightarrow 3d^9 4f^2$ spectrum also has intensity. The $f^1 \rightarrow f^2$ spectrum is composed of sharp lines, and no indications were found that it extends to such a large energy range.

Whether or not there is a mechanism that can explain the transfer of spectral weight to higher photon energies, the respective weight in the isotropic spectrum would also have to be considered in the normalization of the sum rules. Since for the integral of the isotropic spectrum the same short integration range was used, it would be underestimated as well, which reduces the uncertainty in the sum rule evaluation compared to the XMCD integral alone.

Possible explanations for an extended spectral weight could be that it belongs to an aforementioned dipole-allowed transition with higher n. Hybridization of the $4f$ level with conduction states could also be a scenario. The XMCD calculated in the framework of the Jo-Kotani model by Finazzi *et al.* for a highly hybridized Ce compound exhibits an additional feature at the energy position of the $f^0 \rightarrow f^1$ peak [191]. These authors argue that the sharpness of the structure is an artifact of the model, in which the conduction band is represented by a sharp energy level. The feature should be much broader for hybridization with a true band, which might explain the observation. Finally, the asymmetric line shape of the M_4 edge, which is interpreted to arise from autoionization effects (see section 8.2.4), strongly complicates the separation of resonant and continuum absorption behind the edge. The transfer of spectral weight to higher energies due to the Fano profile might provide a mechanism to explain the extended XMCD signal.

It is not clear for all of these scenarios whether or not the possible additional XMCD weight should be included to the sum rule evaluation, and how the continuum background of the isotropic spectrum would have to be constructed. The cut-off energy that was chosen in the present work is a compromise regarding the available data and the current state of knowledge. Future studies that further clarify the details of the Ce $M_{4,5}$ XA spectrum are therefore highly desirable.

6.4.3 Absolute and relative determination of the magnetic moment

With all these considerations and the respective data processing made, the application of the orbital sum rule reduces to the numerical evaluation of two integrals and calculation of the magnetic moment according to eq. 5.17. For noise-free high-quality data like the spectrum shown in fig. 6.1 (b), the procedure is straight forward. For spectra with very small XMCD magnitude, like the one shown in fig. 5.6, the poor signal-to-noise-ratio in the XMCD spectrum makes the numerical integral unreliable.

Nevertheless, the orbital moment of such data can be quantified with high precision by comparison of the XMCD magnitude to a reference spectrum with known magnetic moment. In the present thesis, this comparison was done by numerical least square fits of the isotropic reference XA and XMCD spectrum to the noisier data. For the isotropic spectrum, the amplitude, an energy shift and a linear but not necessarily constant offset was allowed for. For the XMCD, in principle only energy shift and amplitude should be necessary, and the energy shift should equal the value of the isotropic fit. In practice, the same free parameters were allowed as for the isotropic fit. This was meant to account for imperfect baseline correction (see section 5.4.4), the quality of which then can be measured by the magnitude of the offset parameters.

The reliability of the XMCD fit can be significantly improved by a thorough analysis of the line shape with the aim to identify regions in the spectrum that are less susceptible to noise than others. Such regions can then be preferred in the fit. The XMCD is calculated as the difference of two XA spectra. Most of the noise is produced by uncertainties in the relative energy positions of these spectra, which becomes most apparent in regions where the XA spectrum is steep (compare section 5.4.4).

This is especially the case at the M_5 edge, where the lifetime width is smaller than at M_4. Consequently, the high-energy side of the positive peak (feature O in fig. 6.1) is typically the noisiest part of the spectrum. Furthermore, the XMCD at the M_5 edge generally suffers from its smaller magnitude. The negative features (L and M) are particularly problematic. The maximum of the positive peak (N) is the most reliable feature of the M_5 XMCD, if it can be identified in the surrounding noise, since it comes from the plateau between the M_5 double peaks.

The situation at the M_4 edge is better due to the aforementioned larger dichroism and lifetime width. The problematic regions here are the second positive feature (Q) and the flanks of the negative main feature (R), again due to the slopes in the XA spectrum. The XMCD values at the smaller positive peak (P) and near the main minimum (R) provide a solid basis for interpretation.

Under the assumption that the line shape of neither the XMCD nor the isotropic spectrum changes, the relative factor between the orbital moments can be determined by dividing the fit amplitudes. Furthermore, in this case the evaluation can also be performed for the M_4 edge only. Due to the characteristics of the M_5 edge, especially the smaller lifetime width (see section 6.3.2), the XMCD signal is much more susceptible to noise here. This makes a fit less reliable than for the larger dichroism at M_4 edge. Furthermore, this allows saving measurement time by leaving the M_5 region out in the scans. In some of the present datasets, such reduced spectra are included.

Several experimental parameters with possible influence on the line shape were varied in the present experiments: The experimental resolution was different at BESSY and SOLEIL, and the intermetallic film thickness was varied as well as the angle of incidence and the sample temperature. An overview of the line shape variations that are produced by the last three parameters is presented in fig 8.3. Regarding the sample temperature, relatively small variations occur mainly at the $f^0 \rightarrow f^1$ peak. For the angle of incidence, the errors that are induced by ignoring the change in spectral weight are also small, as is discussed in section 6.4.2. However, the differences in the line shape of samples with different film thickness can be drastic. In the comparison of spectra from such different samples, an adjustment of the XAS fit amplitude to equal peak heights can misjudge the spectral weight by more than 10 %.

Since the film thickness is constant for a given sample, the first step towards a consistent sum

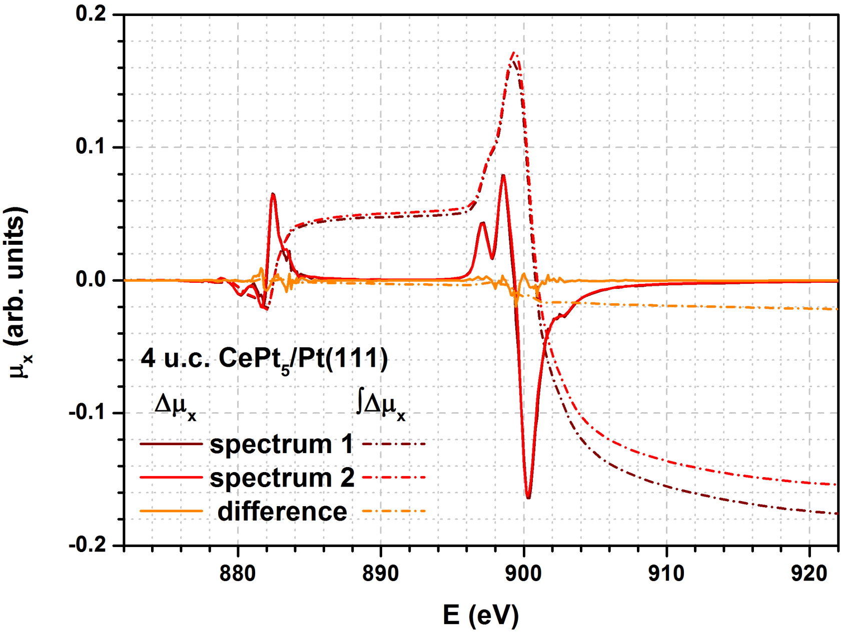

Figure 6.5: Comparison of the total integrals of two Ce $M_{4,5}$ XMCD measurements. The spectra were taken at different beamtimes at SOLEIL for samples with $t = 4$ u.c. at $\theta = 60°$, $T \approx 2$ K and $B \approx 6$ T and adjusted to equal magnitude. Note that the unit of the integrated intensity is eV/µm.

rule evaluation of the complete dataset was to perform a relative evaluation of the data of each sample. For this purpose, individual reference spectra were chosen. This was usually a measurement at $\theta = 60°$ and at the lowest temperature accessible, since in this configuration the averaged XA spectrum can be regarded as isotropic and the XMCD magnitude is largest compared to the other available data. This reference was fitted to the other spectra of the sample under variation of temperature and angle of incidence. The relative progression of the orbital moment was then calculated from the ratio of the fit amplitudes,

$$\langle \mu_{\mathrm{rel}}(T, \theta) \rangle = \frac{\langle \mu(T, \theta) \rangle}{\langle \mu_{\mathrm{ref}} \rangle} = \frac{\mathcal{A}_{\mathrm{XMCD}}}{\mathcal{A}_{\mathrm{XAS}}}, \tag{6.9}$$

without consideration of additional corrections. Error bars that are given in the presentation of respective series in chapter 10 were obtained by error propagation of the standard deviations of the fit amplitudes as returned by the fitting algorithm. Hence, they only reflect uncertainties in the relative adjustment, and not in the absolute values.

The absolute values were multiplicatively included to the datasets after determination of the orbital moment of the reference spectrum. In order to assure equal treatment of all spectra to a maximum extent, the orbital moments of the individual reference spectra of all samples were again related to each other by relative fits with a universal reference spectrum.

The described relative method assures a maximum of comparability for the different measurements. As was revealed by close inspection of the complete set of Ce $M_{4,5}$ XMCD spectra of the present work, the XMCD integral is extremely sensitive to small details of the underlying XA spectrum. This can leads to highly inconsistent results for spectra that were recorded under similar conditions, but in presence of experimental instabilities. These can occur in, e.g., the synchrotron performance, the beamline optics or the sample temperature during recording of the individual spectra, and result in differences in the adjustment of $\mu_{\mathrm{x}}^{-}(E)$ and $\mu_{\mathrm{x}}^{+}(E)$ (see section 5.4.4).

As an example, fig. 6.5 shows the comparison of two XMCD measurements. The XMCD data were adjusted to each other and seem to agree very well. However, the integrals at $E = 922$ eV differ by 15 %. The origin of this difference can be identified by inspecting the integral of the difference of the two datasets. The discrepancy is produced under the M_5 edge, and arises from a drift in the sample temperature in one of the measurements.

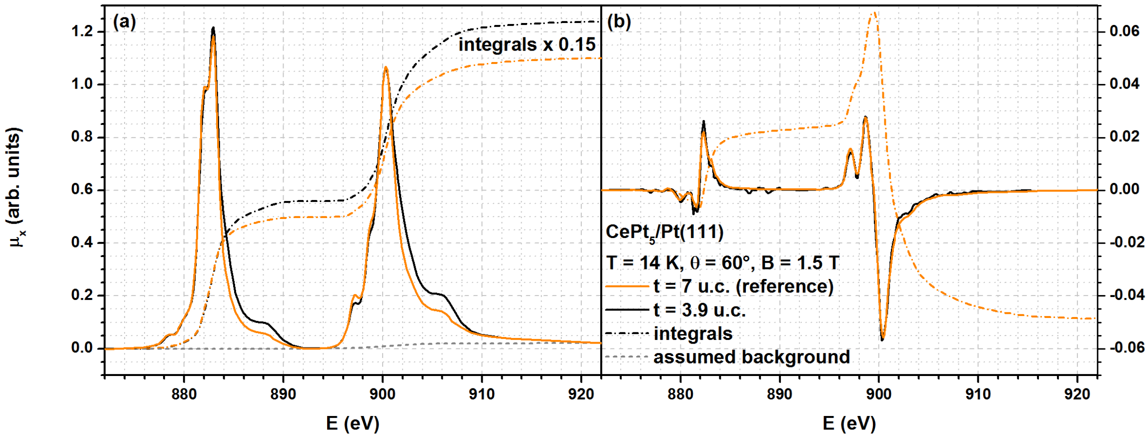

Figure 6.6: Demonstration of the procedure applied for relative sum rule evaluation. (a) Fit of the universal reference XA spectrum to the one of a $t = 7$ u.c. sample taken at BESSY. The assumed continuum background is shown as well as the integrals of the two spectra. (b) Fit of the XMCD spectra and integral of the reference data. Note that the unit of the integrated intensity is eV/µm.

The main reason for the high sensitivity of the XMCD integral to experimental instabilities is the alternating sign of the XMCD signal. The total integral is thus calculated as the difference of the weights of two contributions with opposite signs, but similar magnitude. Hence, uncertainties that are irrelevant for the absolute weight can be significant for the total integral.

The observation of differences in the XMCD integral as illustrated in fig. 6.5 poses the challenge to identify a reliable spectrum that can be used as the universal reference for sum rule evaluation. The absolute values of the complete dataset depend on this single measurement, which necessitates great care in its choice. In the present work, the spectrum of a $\mathrm{CePt_5/Pt(111)}$ sample with $t \approx 7$ u.c. taken at $T = 14$ K, $\theta = 60°$ and $B = 1.5$ T at BESSY was chosen by inspection of the total integrals of the XMCD of more than 20 measurements. It is regarded as the most representative dataset of high quality without obvious peculiarities.

The XA and XMCD spectra of the universal reference are shown in fig. 6.6. Application of the orbital sum rule to this dataset yielded $\langle \mu_l \rangle = 0.08582\ \mu_\mathrm{B}$. This assignment is made without to correct for the finite polarization. For the BESSY data, this correction is done by dividing the sum rule result by 0.93. For the data taken at SOLEIL, the degree of polarization is assumed to be 1.0. Hence, no correction of the moment obtained relative to the reference value is necessary.

Fig. 6.6 demonstrates exemplary fits of the reference to a noisier spectrum for both XA and XMCD, the assumed continuum background and the integrals of the spectra. For normalization of the sum rule (panel (a)), the reference and sample XA spectra were adjusted to match in the pre-, intermediate- and post-edge region as well as at the M_4 peak. Then, the integrals of the background-corrected spectra were compared. This allows accounting for the strong line shape variations with the film thickness.

For subtraction of the continuum background, the same step function was used for all spectra. This provides the further advantage that uncertainties that are induced to the evaluation by the necessary background correction are kept small and, most importantly, equal for the complete dataset. A single continuum step, as given by eq. 6.7, was assumed under the M_4 edge in accordance with the considerations presented in section 8.2.3. Exemplary evaluations with a different background featuring steps at each edge yielded results within 3 % to this method.

For the determination of the XMCD integral (panel (b)), the relative fit amplitude of reference and sample signals and only the integral of the reference were used for the sum rule evaluation. This accounts for the unreliability of the XMCD integral in presence of high noise.

Fig. 6.6 includes data from both BESSY and SOLEIL. The effect of the different experimental resolutions is visible, but small, and partly compensated by the peak amplitude fit. Hence, no explicit correction was made.

The aim of the given detailed description of the evaluation procedure is to produce transparency regarding the data shown in the following chapters on one hand, and to underline the care that has to be taken in order to produce reliable results on the other. The question of the reliability of the experimental technique and the applied evaluation procedure always has to be asked. While comparable results in one and the same dataset can be reliably achieved by consistent application of a well-designed procedure, the interpretation of absolute values in principle requires an external calibration.

As reported in section 6.1.4, previous attempts to independently calibrate the orbital sum rule for the Ce $\mathrm{M}_{4,5}$ edges by comparison to SQUID data failed. A validation of the procedure of the present thesis could be achieved with data of Ce-Ag(111) surface intermetallics. In comparison to CePt_5/Pt(111), this material shows a negligible f level hybridization and only small crystal field effects, which facilitates the interpretation of the magnetic susceptibility. The results, which allow identification of an upper border for the uncertainties, are presented in appendix A.4.

In summary, the relative method with a universal reference combines the disadvantage of a high dependence on the choice of the reference with the advantage of a maximized comparability of the results for different samples. If errors might be discovered in the reference evaluation based on an increased knowledge at a later point, a universal correction factor can be introduced to account for this progress.

6.4.4 Calculation of the paramagnetic susceptibility from the sum rule result

The absolute and relative sum rule evaluation as described in section 6.4.3 allows assignment of an orbital magnetic moment to each measured spectrum at the given sample thickness t, temperature T, angle of incidence θ and magnetic field B. By application of eq. 6.8, this can be transferred to a total moment.

In order to reduce the dimensionality of the parameter space, the magnetic field-dependence is usually treated separately. For a discussion of the angle and temperature dependence of the magnetic properties of paramagnetic samples, a meaningful quantity is the zero-field susceptibility χ as introduced in eq. 2.22.

The definition given there is based on the average magnetic moment per atom, which is exactly the quantity that is addressed by XMCD. Sum rule results are usually presented in units of μ_B for convenience. Analogously, the unit $\mu_\mathrm{B}/\mathrm{T}$ is used for the susceptibility in the present thesis. In order to produce this unit, the equations that are given for χ in section 2.1.3 have to be divided by μ_B.

For low magnetic field and high temperature, the field-dependence of the magnetic moment can be approximated by a linear relation (see eq. 2.21). For the experiments at BESSY with $B = 1.5$ T and $T \geq 12$ K, the validity of this assumption was confirmed by the analysis of exemplary recorded field-dependent XMCD data. Hence, for the BESSY data the susceptibility was calculated according to $\chi = \mu(B)/B$.

At SOLEIL, XMCD data were also recorded beyond the linear regime (see fig. 10.1). In these cases, $\mu(B)$ curves were recorded in addition to the XMCD spectra, as is described in section 5.4.4. These data allowed determination of the zero-field susceptibility by extraction of the zero-field slope from fits with a Langevin[8] function, which is the classical limit of the Brillouin function, $\lim_{j\to\infty} \mathcal{B}_j(x)$ (see eq. 2.20).

6.4.5 Anisotropic susceptibility measurements at arbitrary angle of incidence

In the presence of significant crystal field splitting, the paramagnetic susceptibility of Ce as probed by Ce $\mathrm{M}_{4,5}$ XMCD can be highly anisotropic, as is discussed in section 2.1.3. For a theoretical treatment, the cases with external magnetic field parallel and perpendicular to the c axis have to be discriminated. Regarding the present XMCD experiments on CePt_5/Pt(111) surface intermetallics, $B \parallel c$ is achieved for $\theta = 0°$.

The case $B \perp c$ corresponds to $\theta = 90°$, which is not a practicable geometry for the given intermetallic films. In the present thesis, the maximum angle of incidence amounts to $\theta = 60°$.

---

[8] Paul Langevin, French physicist, 1872-1946

For an interpretation of the data taken in this geometry, a general expression for the anisotropic susceptibility as measured by XMCD for arbitrary angle of incidence has to be derived.
For this purpose and under consideration of possible magnetic coupling, eq. 2.36 is written in a vector notation as

$$\vec{\mu} = \begin{pmatrix} \mu_\parallel \\ \mu_\perp \end{pmatrix} = \begin{pmatrix} \chi_\parallel & 0 \\ 0 & \chi_\perp \end{pmatrix} \left\{ B\ \vec{e}_\theta + \lambda \begin{pmatrix} \mu_\parallel \\ \mu_\perp \end{pmatrix} \right\}, \quad \text{with} \quad \vec{e}_\theta = \begin{pmatrix} \cos\theta \\ \sin\theta \end{pmatrix}. \tag{6.10}$$

This equation is solved for each component separately,

$$\begin{aligned} \mu_i &= \chi_i B\ e_{\theta,i} + \lambda \chi_i \mu_i \\ \mu_i &= \frac{\chi_i}{1-\lambda\chi_i} B\ e_{\theta,i} \end{aligned} \tag{6.11}$$

The quantity that is measured by XMCD is the projection of the moment vector $\vec{\mu}$ to the direction of the incoming light,

$$\mu = \vec{\mu} \cdot \vec{e}_\theta = \sum_{i=\parallel,\perp} e_{\theta,i}^2\ \frac{1}{\chi_i^{-1} - \lambda}\ B \tag{6.12}$$

The susceptibility is then readily calculated by dividing by the magnetic field and reads

$$\chi_\theta(T) = \frac{\cos^2\theta}{\chi_\parallel^{-1}(T) - \lambda} + \frac{\sin^2\theta}{\chi_\perp^{-1}(T) - \lambda}. \tag{6.13}$$

Part II

Experimental Results

Chapter 7

Preparation, stoichiometry and structure of $CePt_5$/Pt(111)

Contents

The interpretation of experimental results that address electronic and magnetic properties of Ce compounds strongly rely on assumptions regarding the crystal structure, as is argued in chapter 2. Hence, detailed structural characterization of the samples under investigation is required. The present chapter provides this background for the $CePt_5$/Pt(111) surface intermetallics.

These ordered surface compounds are produced by alloying of variable amounts of Ce on a Pt(111) substrate. The material is the subject of a considerable number of studies (see section 2.2.2), which is owed to the interest in strong electronic correlations as well as catalytic properties. The crystal structure was addressed in several works, revealing a complex structural phase diagram in LEED and STM. Based on different arguments, the consensus in the recent literature is that the structure corresponds to $CePt_5$.

Prior to the results of the present work, two concerns could be raised over this assumption: First, the only published evaluation of the stoichiometry claims something different from $CePt_5$ [79]. Second, previous structure determinations are primarily based on adsorption experiments and STM, while geometric evaluation of LEED patterns provided supporting arguments [70, 83]. These studies essentially address the topmost surface layer and not the structure of the underlying material.

In the present thesis, the electronic and magnetic properties of the surface compounds were studied with XAS and XMCD in the TEY mode (see section 5.4.2). Although a surface-sensitive technique, the probed sample volume extends over several atomic layers. Therefore, a number of attempts were made to gain insight into the crystal structure of this region, which is required for the interpretation of the spectroscopic results.

The material poses the challenge that it exists between the extremes of bulk material and real surface systems. On one hand, strictly surface-sensitive methods are insufficient for complete structure determination, as stated above. On the other hand, the sample volume is too small to allow application of the powerful standard-techniques for bulk crystallography, like XRD. To meet this challenge, the techniques of choice in the present thesis were LEED IV and cross-sectional STEM, which are both sensitive to the relevant sample region.

The contributions of the present thesis to the successful solution of the crystal structure are described in the following. Since the first step for all experiments are high-quality samples, a procedure was developed that allowed reliable, clean and reproducible surface compound preparation with variable amount of Ce deposit (section 7.1). This deposit strongly affects the appearance of the LEED pattern that is obtained after sample preparation. The resulting phase diagram[1] is studied in great detail in section 7.2, including a quantitative evaluation of lattice constants. A consistent interpretation of the growth of Ce-Pt(111) compounds is provided.

The LEED phase diagram is discussed first, since it represents the most striking characteristic of the surface intermetallics. Its interpretation relies on additional experiments, the results of which are partly anticipated in section 7.2. As mentioned before, the amount of Ce deposit is an important preparation parameter. A combination of LEED, STEM and quartz microbalance measurements showed that this value can be calculated to a film thickness, which describes the sample system in a meaningful way (section 7.3). This result provides the basis to determine the compound stoichiometry by means of thickness-dependent XAS (section 7.4), which allows conclusion on $\mathrm{CePt_5}$ for the whole thickness range that was investigated (section 7.5). Finally, a quantitative LEED IV study is presented in section 7.6. The $\mathrm{CePt_5}$ structure is confirmed and a modification of the surface layer with respect to simple bulk truncation is revealed.

7.1 Sample preparation

Different methods for preparation of $\mathrm{CePt_5}$/Pt(111) surface compounds are described in the literature, including post-annealing of Ce films deposited at room temperature [70, 79, 82, 83], Ce deposition onto a heated substrate [83] and decomposition of CeO clusters deposited under oxygen atmosphere [84]. Evaporation onto a heated substrate leads to Ce rich termination of the surface. Hence, samples most probably will be subject to considerable surface contamination on time scale of several hours, which were necessary for the present spectroscopic studies. Deposition in oxygen atmosphere, which seems to have initially been applied to grow $\mathrm{CeO_2}$ films, does not yield additional benefits. Since experiments are best performed under conditions as controlled, clean and simple as possible, annealing of pure Ce films deposited at room temperature is the method of choice in most studies of $\mathrm{CePt_5}$/Pt(111). It has therefore also been applied in the present work.

During the course of the present thesis, nearly 100 $\mathrm{CePt_5}$/Pt(111) samples were prepared in the three different UHV systems described in section 3.2. Most samples were prepared in setup A, including all specimens investigated at BESSY. Thirteen preparations were performed in setup B and characterized by LEED and AES, including the sample used for the STEM measurements. For the experiments at SOLEIL, samples were prepared in the local preparation setup C. A list of the samples that are relevant for the present results is given in appendix A.6. Specimen were usually freshly prepared *in situ*, earlier preparations were destroyed in this process.

The substrate for all preparations was a Pt single crystal (purity 99.999 %, MaTeck GmbH) with a usable surface diameter of $2R = 8$ mm, cut within $\vartheta = 0.1^\circ$ of the (111) surface. The surface was treated by repeated cycles of Ar^+ ion sputtering with $E_{\mathrm{kin}} = 1$ keV, the duration depending on the sample state, and subsequent annealing to $T \approx 1100\,\mathrm{K}$ for several minutes. While the bombardment with energetic ions dissipates the topmost surface layers and thus removes contaminants and earlier thin film preparations, annealing of the crystal afterwards produces a flat and defect-free surface.

The sample temperature was measured at the molybdenum sample holder using a pyrometer with the emissivity set to 0.3, which was the smallest possible value for the device used. In addition, the annealing color was monitored by eye to ensure that the temperature gradient between the sample holder and the sample was small and to give an approximate cross-calibration of the temperature.

---

[1] In the present usage, this refers to the dependence of the observed LEED phases on the sample thickness

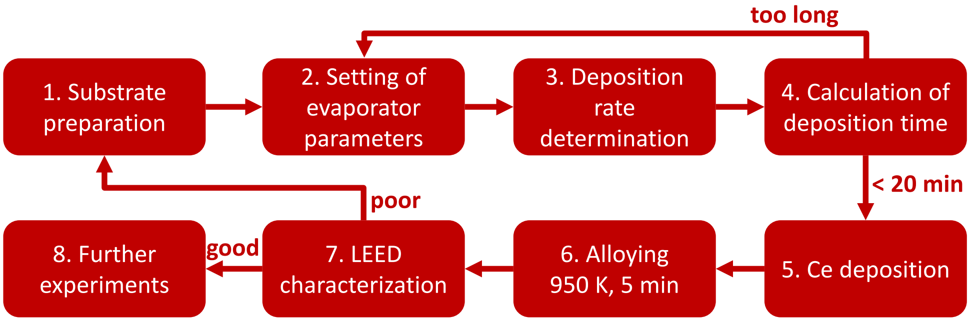

Figure 7.1: Workflow diagram of the procedure that was developed for the preparation of $CePt_5$/ Pt(111) samples.

For preparation of the Pt(111) surface, some authors anneal the crystal under oxygen atmosphere to remove Carbon contamination [84]. This step was not performed in the present work, since the vacuum chambers used for substrate preparation also hosted the pure Ce evaporant.

The cleanliness of the substrate surface was confirmed by evaluation of representative Auger electron spectra, which showed no signatures of contaminants above the detection threshold (see fig. 7.2). LEED patterns of substrate preparations that were regarded as successful featured low level background and sharp (1×1) diffraction spots with threefold symmetry. An exemplary image is shown in fig. 7.3.

Cerium with a purity of 99.95 % (MaTeck GmbH) was evaporated from a tungsten crucible mounted to a commercial FOCUS EFM3i electron beam evaporator. Early experiments with a molybdenum crucible lead to alloying of crucible and evaporant material. The evaporator basically consists of a high-voltage feedthrough for the crucible, a filament and a water-cooled radiation shield. This shield has an aperture followed by a shutter and an electrostatic lens. A positive voltage of $V = 1$ kV is applied to the lens in order to deflect evaporated ions. Hence, damage to the substrate surface by ion bombardment is avoided. In addition, the ions that reach a sensor located next to the deflector are detected by an amperemeter[2]. The such obtained ion flux can be used as a measure of the evaporation rate.

The Cerium used for evaporation was stored under inert atmosphere to avoid oxidation. Exposure to air, especially during crucible refill, was kept as short as possible. Oxidized Cerium, visible as a yellowish or black color of the otherwise silvery-white evaporant, was removed by thorough heating of the crucible *in situ*.

For evaporation, the crucible was heated by bombardment with electrons. Thermal electrons were created from a tungsten filament, which was heated with a current of $\mathcal{I} = 1 \ldots 2$ A, and accelerated by a constant high voltage of $V = 1$ kV. The emission current was regulated in the range $\mathcal{I}_{\text{emis}} = 60 \ldots 100$ mA to adjust the deposition rate. The rate was measured with a quartz microbalance, as described in section 3.3.

Cross-calibration of the quartz microbalance, the ion flux of the evaporator and the LEED patterns of resulting samples showed that the absolute value of the ion flux, typical up to several microamperes, was not a good measure of the evaporation rate. It seemed to be very sensitive to the exact crucible and filament positions and to the amount and oxidation state of the material already deposited to the evaporator walls. This became apparent when changes in the setup were made, especially involving venting of the vacuum recipient. Hence, the ion flux was only monitored as a control parameter for the stability of the evaporator during a single sample preparation cycle under constant conditions.

The pressure during Ce deposition was usually below $p = 1 \cdot 10^{-9}$ mbar after degassing of the evaporator. Apparently, Ce deposited onto the vacuum chamber walls can improve the pressure since it serves as a getter coating.

Based on the gathered experience, a procedure for sample preparation was developed, which is summarized in fig 7.1. First of all, the Pt(111) substrate was prepared. Prior to Ce deposition

---

[2] André-Marie Ampère, French physicist and mathematician, 1775-1836

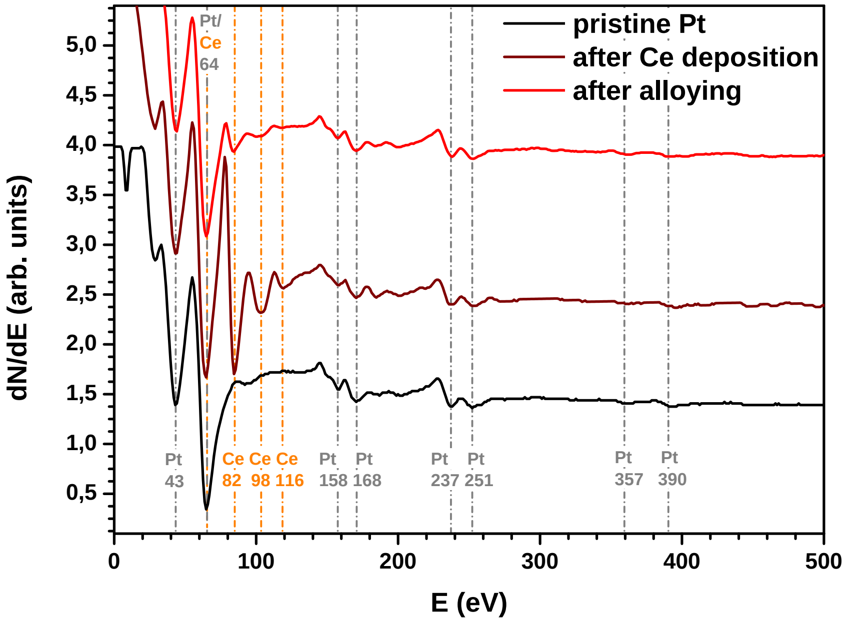

Figure 7.2: Auger electron spectra (derivative of the signal versus kinetic energy of the electrons) of three steps during a sample preparation cycle: after substrate cleaning, after Ce deposition and after alloying (t = 10 u.c.). Energies of characteristic Auger peaks are given for Ce and Pt. The kinetic energy of the primary electron beam was $E_{\mathrm{prim}} = 3$ keV. The spectra are scaled to equal size of the Pt line at $E = 237$ eV.

onto the substrate, the evaporation rate was then measured with the quartz microbalance. Depending on the desired amount of Ce, the deposition time was calculated from the frequency gradient by use of eq. 3.5. If neccessary, the heating power of the evaporator was adjusted to obtain growth rates allowing deposition times below $\tau = 20$ min. Longer time intervals were avoided to reduce the risk of surface contamination during growth.

The prepared substrate was then moved in front of the evaporator, which was opened for the calculated time. Immediately after closure of the shutter, the sample was heated to $T \approx 950$ K and held at this temperature for $\tau = 5$ min.

After cooling down the sample, a characterization of the compound film was done with LEED. If the desired phase was satisfactory achieved with good quality, it was used for further experiments. Otherwise, a new preparation cycle was started. Several features for benchmarking the success of sample preparation are presented in appendix A.3.

Fig. 7.2 shows Auger electron spectra (see section 3.4) after substrate cleaning, after Ce deposition and after alloying during a sample preparation cycle. Element-specific lines were identified by comparison to reference data [253]. Two aspects should be emphasized here: First, no signatures of contaminations from carbon (main line at $E = 272$ eV) and oxygen (lines at $E = 475 \ldots 510$ eV) are visible above the detection threshold. Second, the progression of the intensity of the Ce lines clearly illustrates the alloying process. While after substrate cleaning no signatures of Ce are observed, a large signal arises after deposition, which is reduced by alloying. This observation indicates the change of Ce percentage at the surface during the process and hints at the Pt-termination of the alloyed sample.

The fact that Pt lines are clearly visible in the pre-alloyed state despite the rather large amount of Ce deposited indicates that no closed Ce film is grown. This prevents a straightforward determination of the Ce deposit by evaluation of AES data.

7.2 The LEED phase diagram

Many different LEED patterns have been reported for CePt$_5$/Pt(111) surface compounds in the literature (see section 2.2.2). Apparently, the appearance of the different phases strongly depends on the Ce coverage prior to alloying. The most detailed phase diagram so far has been presented by Essen *et al.* [70]. Their results clearly indicate this connection and they reproduce most of the phases reported so far.

Essen *et al.* discriminate two surface lattice constants, 2 and 1.98 times the one of the Pt(111) surface, while other authors report $s = 1.94, 1.96$ (Tang *et al.* [79]) and 1.91 (Garnier *et al.* [82]). Baddeley *et al.* were able to assign the LEED phases they observed to structures seen in STM, where they measured relative lattice constants between $s = 1.82$ and 1.93 [83]. The latter is close to the relaxed bulk $CePt_5$ value.

While all authors agree that some sort of lattice relaxation takes place with increasing initial Ce coverage, both relaxations to smaller and larger values have been observed. Furthermore, different absolute lattice constants have been reported for apparently equal LEED phases. This might reflect the uncertainties of the evaluation, the main sources of which are discussed in section 4.1.5. As argued there, lattice constant evaluation from diffraction patterns is highly sensitive to the geometrical alignment of the LEED setup. The accuracy that was obtained in the present setups is insufficient to distinguish lattice constant changes within a few percent, unless a relative evaluation is performed. In the following, the strategies described in section 4.1.5 are applied to the LEED data obtained in the present work.

This leads to a reliable determination of lattice constants from information found in LEED images. The interpretations could consistently be augmented by STM data from the group of M. Bode in the framework of a cooperation that was started in the course of the present thesis. The combined results have been published in Physical Review B [1].

Fig. 7.3 shows examples of the different LEED patterns that were observed for $CePt_5/Pt(111)$ surface compounds in the present work. The patterns were classified into seven different phases numbered I to VII with increasing initial Ce deposit, including the (1×1) reconstruction of the pristine Pt(111) substrate. All images were recorded using the same experimental setup (A, see section 3.2). Hence, the relative orientations of the patterns directly reflect the orientation of the surface compound structure. The observed superstructures all feature sixfold symmetry when varying the electron beam energy.

The substrate spots, clearly distinguishable from the compound spots due to their threefold symmetry, are only visible for compounds produced from the smallest Ce deposit. Hence, it is concluded that the compounds form closed films on top of the substrate. Samples usually showed a homogeneous pattern over the whole single crystal surface area after proper alignment of the evaporator. The compound films are therefore regarded as homogeneous on the sample. The average compound film thickness t can thus be used to specify the different phases. It is measured in unit cells (u.c.) and can be calculated from the initial Ce coverage, a procedure which is described in section 7.3. In the following, the seven different phases are described and analyzed in detail. The present section concludes with the presentation of a consistent interpretation for the complete phase diagram.

I (1×1): pristine Pt(111)

The LEED pattern of the pristine substrate crystal features sharp (1×1) spots against a background with low intensity. Threefold symmetry of the spot intensities is observed upon varying the electron beam energy, as expected for the (111) surface of a *fcc* lattice (compare fig. 3.1 and section 4.1.3). The main reason for showing the pattern here is to define the rotational alignment of the substrate lattice.

II $(1 \times 1) + (2 \times 2)$: 1 u.c. $CePt_5/Pt(111)$

Upon annealing small amounts of Ce deposit, weak and broad superstructure spots are observed, which are superimposed to the spots of the substrate. Hence, the lattice constant of the superstructure can be obtained from direct comparison, which is however complicated by the weakness of the spots. It is assigned twice the value of the substrate surface lattice constant within the given uncertainties.

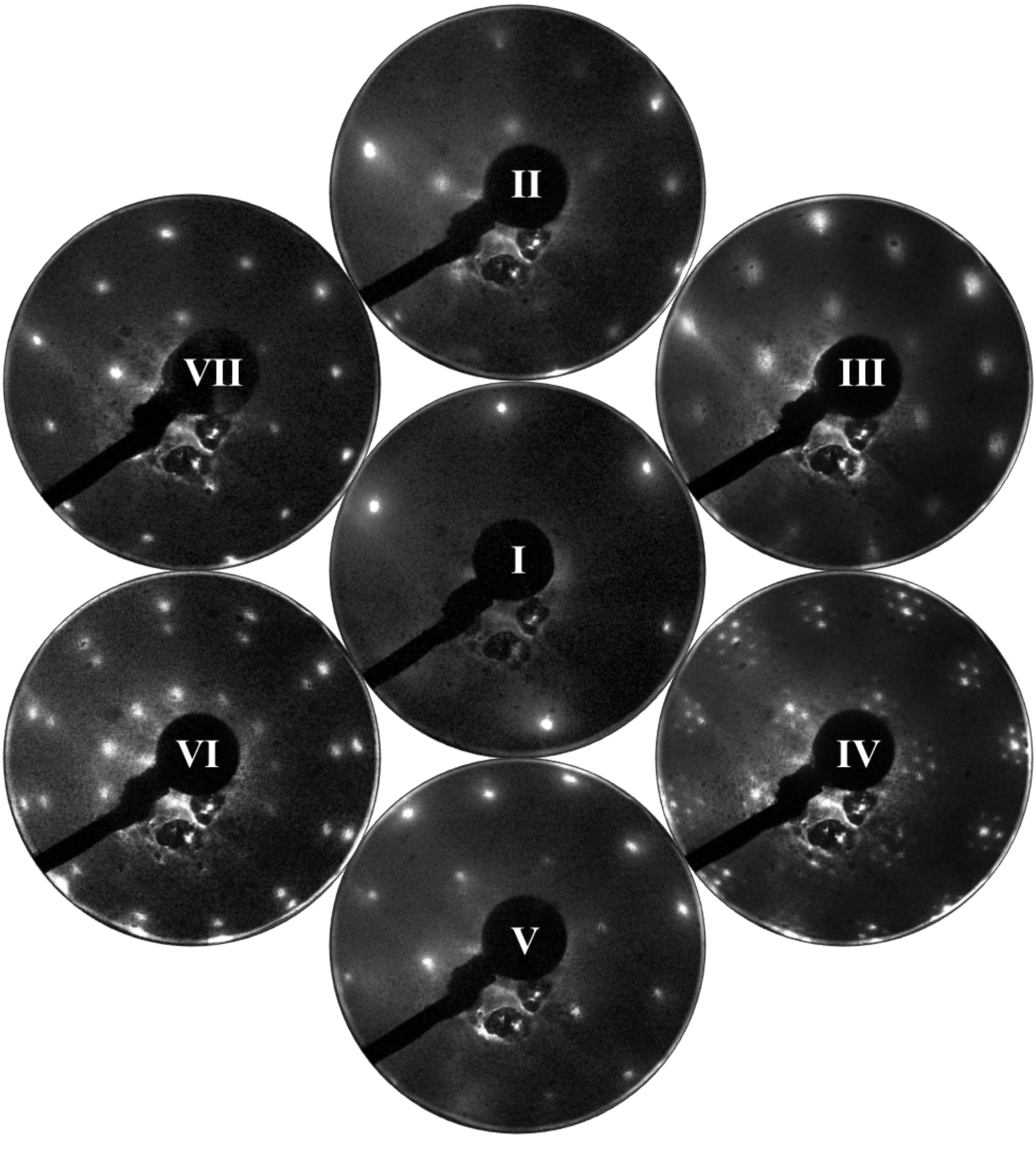

Figure 7.3: Exemplary LEED images of $CePt_5/Pt(111)$ classified into seven phases. All images were taken under identical experimental conditions with an electron beam energy of $E_{\text{kin}} = 63$ eV. The structure that is present in all images directly underneath the electron gun is caused by damage of the suppressor grids of the LEED optics. **I** (1×1) reconstruction of the pristine Pt(111) surface. **II** $(1 \times 1) + (2 \times 2)$ pattern at $t \approx 1$ u.c. **III** (1.98×1.98) superstructure at $t \approx 2$ u.c. **IV** $(\frac{10}{9}\sqrt{3} \times \frac{10}{9}\sqrt{3})R30^\circ$ reconstruction with additional (10×10) satellite spots observed for surface compounds with $t \approx 3$ u.c. **V** The $(1.92 \times 1.92)R30^\circ$ pattern evolving near $t = 4$ u.c. **VI** Superposition of (1.93×1.93) and $(1.93 \times 1.93)R30^\circ$ superstructures in the range $t = 5 \dots 10$ u.c. **VII** The pure unrotated (1.93×1.93) phase as seen at $t = 10 \dots 15$ u.c., the thickest films investigated in the present work.

III (1.98 × 1.98): 2 u.c. CePt$_5$/Pt(111)

Upon increasing the initial Ce coverage, the superstructure spots become brighter. Substrate spots are still visible at high electron beam energy, i.e., at larger penetration depth. They appear within the much broader superstructure spots but not with the same center, which indicates that the lattice has partly relaxed. The relative lattice constant of $\mathcal{S} = 1.98$ has been determined from direct comparison with phase IV. Details of the evaluation are given there.

Non-rotated LEED patterns with similarly broad spots, resulting from low Ce coverage, are reported as "(1.94 × 1.94)" by Tang *et al.* [79] and as "(2 × 2)" by Essen *et al.* [70] and Schwab *et al.* [95]. Baddeley *et al.* show a (2×2)-like pattern with a complicated superimposed structure [83].

This superimposed structure, as well as a (5.6 × 5.6) superstructure also shown by Baddeley *et al.* for the low-coverage regime, was not observed in the present work, nor in the work by Essen *et al.* The latter superstructure resembles a diffraction pattern shown by Luches *et al.* for CeO$_2$ films on Pt(111) [254], who observed a (6 × 6) superstructure. The images shown by Baddeley *et al.* might not belong to clean Ce-Pt compounds.

A distinction of two different phases (II and III) with possibly different lattice constants in this thickness regime has not been made in the previous literature known to the author. The increasing lattice relaxation from phase II to III is best visible at high electron energies, where the substrate spots become more clearly visible in phase III. Furthermore, the scenario of two different phases is supported by the Ce M$_{4,5}$ XAS data shown in fig. 8.3 (c). Samples from the two phases exhibit clearly different fingerprints in XAS, which would not be the case if only the relative portion of surface area covered by the film would change.

The apparent broadness of the diffraction spots does not reflect disorder of the film structure (compare section 4.1.5). It can be understood in comparison to STM results for films in this thickness range, which exhibit long-range superstructures with periodicity of the order of $a = 9$ nm in addition to the film unit cell [1],[83]. This gives rise to a very dense pattern of superstructure spots in reciprocal space and thus in the diffraction pattern. These spots are not resolved with the present LEED setups, but nevertheless appear as broadly distributed intensity around the main diffraction spots.

IV $(\frac{10}{9}\sqrt{3} \times \frac{10}{9}\sqrt{3})R30^\circ$ + (10 × 10) satellites: 3 u.c. CePt$_5$/Pt(111)

For compound films with larger thickness $t \gtrsim 3$ u.c., the appearance of the LEED pattern changes quite abruptly. The superstructure is then rotated by $\varphi = 30^\circ$ and shows additional satellite spots. Such LEED patterns are shown by Tang *et al.* ("1.96 × 1.96 plus satellites") [79], Baddeley *et al.* [83] and Essen *et al.* ("$(2 \times 2) + (1.98 \times 1.98)R30^\circ$") [70].

Occasionally, sample preparation in this thickness regime lead to LEED patterns showing superpositions of phases III and IV. An exemplary image is shown in fig. 7.4 (a). Such findings allow the direct comparison of lattice constants, evaluation yielded $a_{\mathrm{IV}} \approx 0.97 \pm 0.03\ a_{\mathrm{III}}$. An equivalent evaluation has been reported by Essen *et al.* [70], who obtained $a_{\mathrm{IV}}/a_{\mathrm{III}} = 0.99$.

As an explanation of the occurrence of the satellite spots, Essen *et al.* propose a multiple scattering mechanism. They assume the coexistence of a non-rotated (2 × 2) and a rotated $(1.98 \times 1.98)R30^\circ$ compound structure (phases II/III and V in the present work) and argue that multiple scattering with these two reciprocal vectors can explain the observed pattern. In this case, diffraction spots are expected at positions that can be reached by linear combinations of reciprocal vectors from the two sets of basis vectors, which of course includes the two base lattices. Higher-order effects are expected to lead to spots with lesser intensity.

Coherent multiple scattering on different structures can only contribute significantly to the pattern if ordered neighboring domains exist that are smaller than the LEED coherence length of $l_{\mathrm{c}} \approx 10$ nm (compare section 4.1.5). However, larger domain sizes are indicated by the STM data[1],[83]. Furthermore, single-scattering spots of both lattices should be visible in the diffraction pattern. This might be the case in the image in fig. 7.4 (a), but not in the one shown in fig. 7.3, which is a typical pattern. Here, the first order spots of a non-rotated (2 × 2)

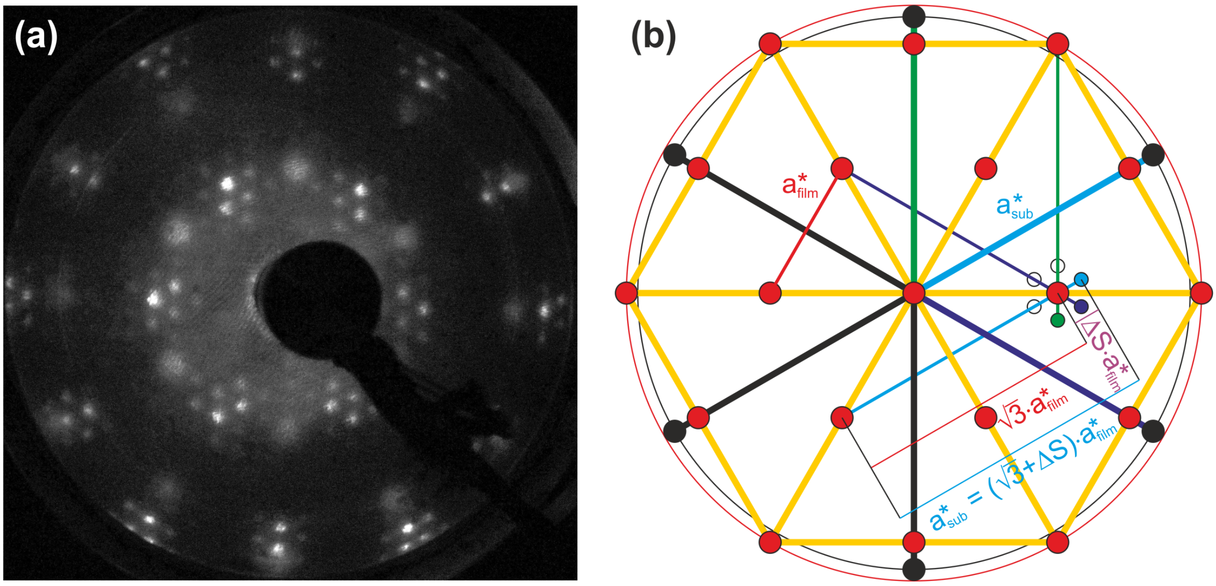

Figure 7.4: (a) LEED image of a preparation showing a superposition of phases III and IV. The picture was taken at $E_{\mathrm{kin}} = 63$ eV and was used for a relative lattice constant determination. (b) Schematic illustration of the diffraction pattern resulting from multiple scattering between a hexagonal reciprocal lattice (black circles) and an incommensurate $(1.92 \times 1.92)R30°$ superstructure (red circles). Combination of reciprocal lattice vectors of the base lattice a^*_{sub} and the superstructure a^*_{film} leads to the green, blue and light blue satellite spots. Measurement of the distance between the main and the satellite spots allows evaluation of $\Delta\mathcal{S} = a_{\mathrm{film}}/a_{\mathrm{sub}} - \sqrt{3}$.

superstructure would be missing. Hence, the explanation by Essen *et al.* is not consistent with the data.

As a further development of the approach by Essen *et al.*, multiple scattering on a single-domain rotated compound film and the substrate can be assumed. This can explain the observed geometric pattern. However, one would expect that the substrate spots exhibit the threefold symmetry of the *fcc* lattice, if more than one layer contributes to the signal. This contradicts the observation of a sixfold symmetric pattern. It can be argued that the given film thickness of $t \approx 3$ u.c. $\hat{\approx}$ 1.3 nm is of the order of the LEED information depth and deeper-lying substrate layers thus do not contributes to the signal.

A simpler explanation is to consider the existence of a moiré[3] structure at the surface, which is supported by the available STM data [1],[83]. The moiré pattern represents a long-ranged modulation of the sample surface as a consequence of a non-integer relation between substrate and film lattice constants. The geometrical construction of the resulting diffraction pattern equals the one for multiple scattering at the two lattices.

Based on this interpretation, the lattice constant of the superstructure can be determined with high precision. A construction of the diffraction pattern of the combination of the substrate lattice and a film lattices that is rotated by $\varphi = 30°$ and exhibits a non-integer lattice constant relation with respect to the former is drawn in fig. 7.4 (b). As can be seen there, no satellite spots occur for $\mathcal{S} = a_{\mathrm{film}}/a_{\mathrm{sub}} = \sqrt{3}$, where a_{sub} and a_{film} are the lattice constants of the substrate and the rotated superstructure, respectively. In this case, the lattices would be commensurate. Consequently, the appearance of satellite spots indicates a deviation Δs of the lattice constant ratio from $\mathcal{S} = \sqrt{3}$, which can directly be measured from the distance of main and satellite spots, $a^*_{\mathrm{sat}} = \Delta\mathcal{S} \cdot a^*_{\mathrm{film}}$.

Evaluation of this quantity yielded $\Delta\mathcal{S} = a_{\mathrm{film}}/a_{\mathrm{sub}} - \sqrt{3} = 0.187$. Within 3 %, this matches $\Delta\mathcal{S} = 1/3\sqrt{3}$, which would mean that the satellite pattern would be related to the film lattice as a $(3\sqrt{3} \times 3\sqrt{3})R30°$ superstructure. Indeed, evaluation of Fourier-transformed STM images allowed unambiguous confirmation of this relation [1].

This allows precise determination of the relations between the three lattices of substrate, film

---

[3] Francois Alfonse Moiré, French mathematician, physicist, philosopher and jester, 1865-1998

and satellites. The formation of a moiré pattern, which leads to the satellite spots, requires an integer relation between the respective lattice constant and the ones of the two base lattices, $a_{\text{sat}} = n_i a_i$ with $i =$ sub,film. Since the film lattice is rotated by $\varphi = 30°$ with respect to the others, the $\sqrt{3}$-fold value of a_{film} has to be used, and $n_{\text{film}} = 3$, as argued above. Since furthermore both LEED and STM data indicate that $\sqrt{3}a_{\text{sub}} < a_{\text{film}} < 2a_{\text{sub}}$, it follows that $n_{\text{sub}} = 10$.

Consequently, the film and satellite patterns can exactly be determined as $(\frac{10}{9}\sqrt{3} \times \frac{10}{9}\sqrt{3})R30°$ and (10×10) superstructures with respect to the substrate, respectively. Assuming that the substrate lattice constant is unchanged from the Pt bulk value, this translates to a film lattice constant of $a_{\text{film}} = 0.534$ nm.

V (1.93 × 1.93)*R*30°: 4 u.c. CePt$_5$/Pt(111)

The characteristic satellite spots of phase IV vanish upon further increasing the film thickness to $t \approx 4$ u.c. A simple hexagonal pattern remains, which is rotated by $\varphi = 30°$ with respect to the substrate and has a lattice constant close to twice the one of the substrate.

Such pure rotated phases are also described by Garnier *et al.* as "$(1.1\sqrt{3} \times 1.1\sqrt{3})R30°$" [82], by Essen *et al.* as "$(1.98 \times 1.98)R30°$" [70] and by Klein *et al.* as well as Schwab *et al.* as "$(2 \times 2)R30°$" [94, 95].

An explanation for the transition from phase IV to V in LEED can be found in STM data [1]. Two surface structures are primarily found in this thickness regime, which exhibit comparable periodicity, particularly regarding the long-range moiré pattern that produces the satellite spots of phase IV. However, the structure that successively covers the majority of the surface when increasing the average film thickness t exhibits significantly lower corrugation of this moiré structure. The LEED result of vanishing satellites spots is a natural consequence thereof, and the STM observations could be explained by a consistent structure model that proposes different local film thicknesses of the two structures.

The superstructure is assigned the same lattice constant as phase IV here. However, further lattice relaxation may take place. The LEED IV study presented in section 7.6 was performed for a sample exhibiting phase V. The surface lattice constant result amounts to $a_{\text{film}} = 0.535$ nm.

VI (1.94 × 1.94) + (1.94 × 1.94)*R*30°: 5 . . . 10 u.c. CePt$_5$/Pt(111)

Starting at a thickness of $t \approx 5$ u.c., a non-rotated structure appears in the LEED images, superimposed to the rotated structure of phase V. With increasing t, the non-rotated pattern gains intensity while the rotated one becomes weaker. This is shown in fig. 7.5 for three exemplary thicknesses.

Images of this phase are shown by Tang *et al.* [79], Baddeley *et al.* [83], Schierbaum [84] and Essen *et al.* [70]. While Tang *et al.* already reported on varying intensities of the two patterns, the clear trend with the compound thickness is not described in these studies.

The most probable explanation of this finding is a gradient of the relative surface coverage of the two domains when increasing t. Whether or not the two domains thereby have the same thickness cannot be decided from LEED experiments. Beyond the intensity difference and the different rotational alignment, the two sublattices appear to produce equal diffraction patterns. No difference in lattice constant could be identified and both show the same relative intensity variation with the electron beam energy.

The relative lattice constant of phase VI cannot be determined precisely from the LEED images, since signatures of the substrate, as utilized for phase IV, are missing. Moreover, this fact along with the coexistence of both rotational alignments with apparently equal lattice constants indicates that the film lattice is essentially relaxed at this thickness. If significant impact of the substrate periodicity would still be present, the rotated domains would have to adapt to an integer multiple of $\sqrt{3}$ times the substrate lattice constant a_{sub}, in contrast to a bare integer multiple of a_{sub} for the non-rotated structure. Both conditions cannot be fulfilled simultaneously. Since it is unlikely that the two coexisting phases experience different amounts of strain but

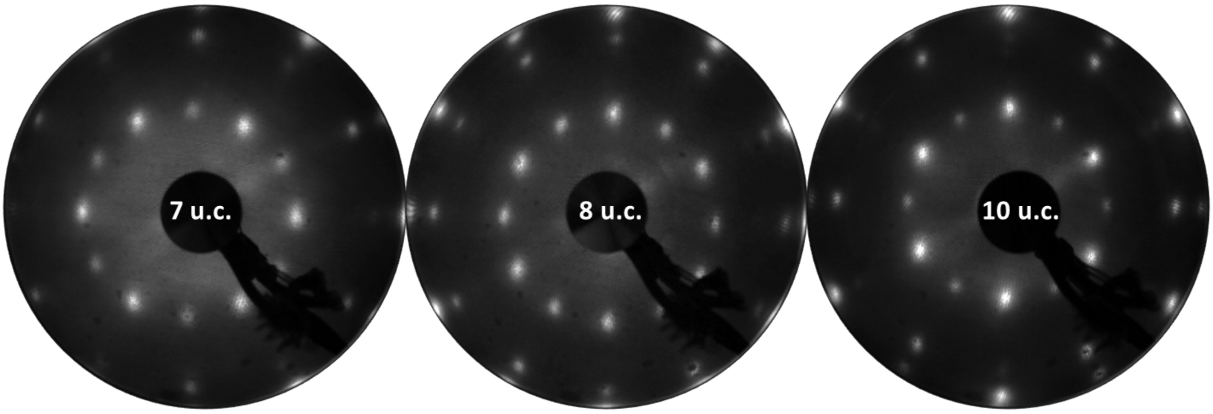

Figure 7.5: LEED images of three preparations featuring phase VI at thicknesses of 7, 8 and 10 u.c. Images were taken at $E_{\mathrm{kin}} = 50$ eV.

feature the same lattice constant, it might well be that the strain is completely transferred to the substrate at this thickness.

For assignment of a relative lattice constant, it is assumed that the films relax to the $\mathrm{CePt_5}$ bulk value, $a = 0.5367$ nm [68], at this thickness. This value is close to the experimentally determined lattice constants for lower t, and assumption of this structure is supported by the results presented in the following sections.

VII (1.94 × 1.94): 10 . . . 15 u.c. $\mathrm{CePt_5}$/Pt(111)

The change of intensities in phase VI already suggests that a transition between the pure rotated phase V and a pure non-rotated phase takes place. LEED patterns of the latter are obtained at thicknesses above 10 u.c. and persist up to $t \approx 15$ u.c., the largest thickness investigated in the present work. Concerning the literature, a pure non-rotated phase at a thickness above the superimposed patterns of phase VI only appears in the work by Tang *et al.* [79].

A consistent interpretation of the complete phase diagram

In the previous paragraphs, LEED patterns of $\mathrm{CePt_5}$/Pt(111) surface intermetallics are systematically analyzed over a wide range of thickness and assembled into a LEED phase diagram. Most phases reported in the literature to date were recognized and set into context. The patterns presented by Essen *et al.* [70] in their comprehensive phase diagram are all reproduced. At low thickness, a refinement of their phase is introduced (II and III) and an additional phase (VII) is added at higher thickness.

The LEED patterns are dominated by superstructures that exhibit surface lattice constants close to twice the one of the Pt(111) substrate. Variations thereof of the order of some percent with increasing film thickness could be resolved. At low thickness, signatures of moiré patterns as resolved in STM [1],[83] are visible as a broadening of the spots in phases II and III and as satellite spots in phase IV.

The rotational alignment of the film lattice with respect to the substrate repeatedly changes when increasing the film thickness, which allows a classification of the patterns: The non-rotated phase at low t is replaced by a rotated pattern ($\varphi = 30°$) for $t \approx 3$ u.c. Above $t \approx 5$ u.c., a non-rotated pattern emerges in coexistence to the rotated one. It successively dominates the diffraction pattern and remains as the only visible phase above $t \approx 10$ u.c. .

These structural changes with t might indicate that the crystal structure of the compound changes. This question can be addressed by an inspection of the energy-dependence of LEED spot intensities, which is sensitive to the atomic arrangement at the surface (see section 4.2). Representative $I(E)$ curves are shown in fig. 7.6. The data were obtained by averaging the curves for the visible (1,0)-type spots of the film lattice (compare fig. 4.2 (c)). Samples showing three different LEED patterns were evaluated: Phase III (the non-rotated superstructure at

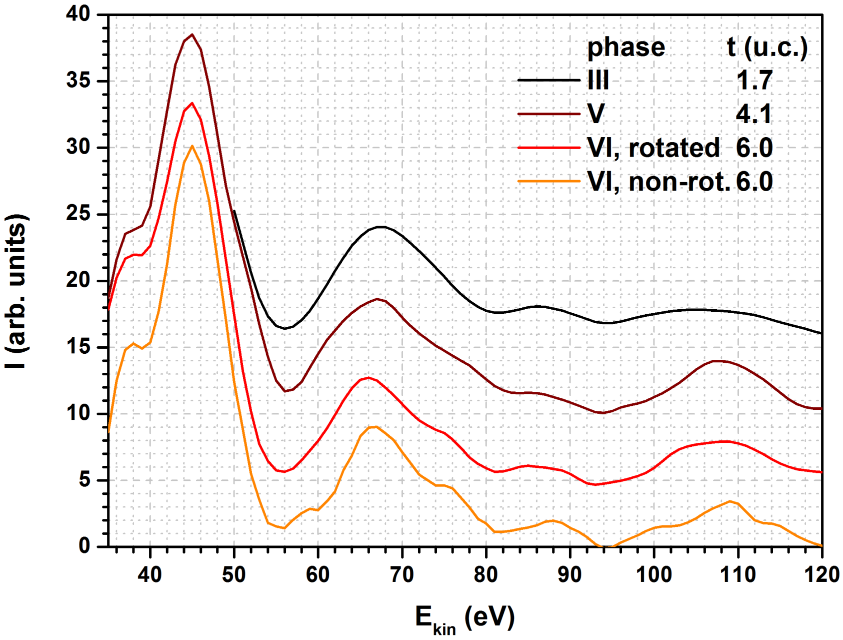

Figure 7.6: Averaged LEED IV curves of first-order spots for three different samples featuring LEED phases III, V and VI. For phase VI, curves for both rotated and non-rotated superstructures are shown separately. For presentation, the curves are successively offset by 5 vertical scaling units.

low t), phase V (the rotated superstructure at intermediate t) and phase VI (superposition of the rotated structure at intermediate t and the non-rotated structure at high t). Hence, all occurring classes of superstructures are covered in this comparison. The choice of the (1,0)-type spots assures that no intensity from the substrate spots contributes to the $I(E)$ curves.

The four $I(E)$ curves show high similarity when compared by eye. In order to quantify this observation, the Pendry R-factors R_P (see section 4.2.6) were calculated for all possible combinations of curves. The obtained values are all below $R_\mathrm{P} \lesssim 0.2$, which reflects the good agreement of the curves. It should be noted that the comparison is complicated by the fact that the experiments were performed under non-normal incidence of the electron beam. Consequently, the intensity profile of a spot depends on the azimuthal angle at which it appears on the screen. Rotation of a crystal structure then changes the $I(E)$ curve of each spot, which is why some degree of inequality has to be expected for the superstructures with different rotational alignment. Averaging of several spots distributed over the screen does not completely balance this effect either.

The similarity of the $I(E)$ curves allows the conclusion that the crystal structure does not change over the whole thickness range that has been investigated. Differences of the structures leading to the different LEED phases then only involve the rotational alignment, the variations in the surface lattice constant can be interpreted as lattice relaxation.

Regarding the lattice constant determination, a key role is played by phase IV. Interpretation of the satellite spots as resulting from a well-defined moiré pattern allowed precise determination of the relation between substrate and film lattice constants as $\mathcal{S}_\mathrm{IV} = \frac{10}{9}\sqrt{3} \approx 1.92$. Furthermore, the occasional coexistence of phases III and IV allowed determination of their relative lattice constant ratio as $a_\mathrm{IV}/a_\mathrm{III} = 0.97$, which translates to $\mathcal{S}_\mathrm{III} \approx 1.98$. Hence, this phase already exhibits relaxation compared to the (2×2) superstructure at the lowest thickness investigated. The relative lattice constant at the high-thickness end of the phase diagram could not reliably be measured from the LEED images, but it can be argued that full relaxation of the film has taken place. Hence, one can expect that the lattice constant of the corresponding Ce-Pt bulk phase is adapted. While the LEED patterns alone do not provide the opportunity to determine stoichiometry or structure of the film, the experimentally determined result for phase IV is very close to the bulk value of $CePt_5$: It corresponds to a compression of 0.5 % only. Furthermore, the assumption of the bulk value for phases VI and VII is not only in line with the stoichiometry

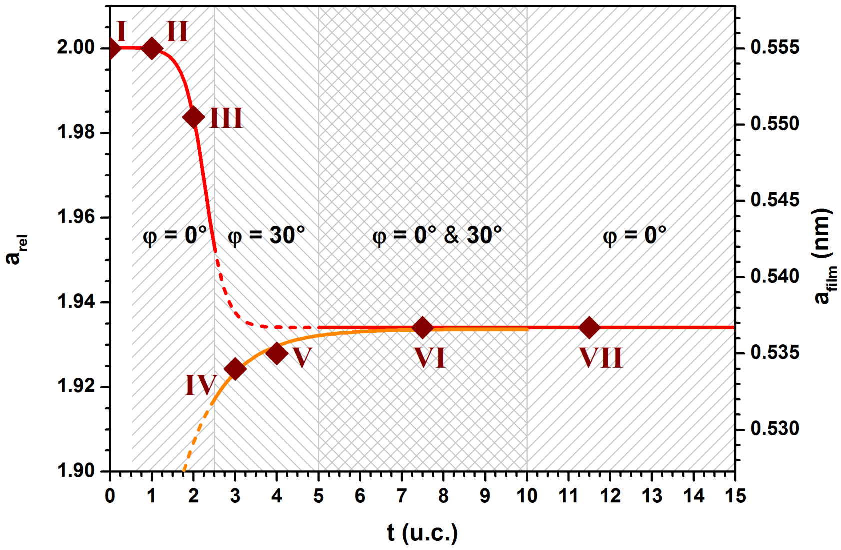

Figure 7.7: Illustration of the film lattice constants of the seven LEED phases observed for $CePt_5$/Pt(111) in the thickness range $t = 0 \ldots 15$ u.c. The relative surface lattice constant is measured with respect to the pristine Pt(111) surface, which is assigned a value of 2 for convenience. Lines are guides to the eye for the progressive lattice relaxation of the alternating non-rotated ($\varphi = 0°$, background hatching bottom left to top right, red line) and rotated ($\varphi = 30°$ background hatching top left to bottom right, orange line) phases.

and structure determinations presented in the following sections, it also allows construction of a consistent scenario for the thickness-dependence of the lattice constants.

As can be seen in fig. 7.7, the resulting progression of the surface lattice constant with the film thickness then features both dilation and compression with respect to the relaxed value, which resides in between $\sqrt{3}$ and 2. Hence, for thin films the substrate periodicity would force a rotated film to adapt to $\sqrt{3}a_{\mathrm{sub}}$, but a non-rotated film to $2a_{\mathrm{sub}}$. Indeed, dilation is observed for the thin non-rotated phases and compression is present in the rotated ones. The direction of the strain is indicated by the solid lines in fig. 7.7. The described scenario yields a consistent picture of the growth of Ce-Pt(111) surface compounds, including the apparently contradictory observations of dilate and compressed lattices in the literature (see section 2.2.2).

7.3 Thickness of the compound films

The $CePt_5$/Pt(111) surface compounds display a rich variety of LEED patterns, which appear in a fixed order depending on the amount of Ce deposited prior to alloying. This finding, along with the observation of a relaxing lattice constant, indicates that the thickness of the compound film increases with the initial Ce deposit.

In the literature, samples are commonly characterized by a number of monolayers (ML) for the initial Ce deposit, which is determined from AES or PES characteristics prior to alloying (see section 2.2.2). However, this quantity does not describe the sample in its final alloyed state, which is the one of interest here. Therefore, attempts were made to classify the compound films by their thickness t, which is conveniently measured in numbers of unit cells (u.c.). This approach is described in the present section.

The initial Ce coverage is experimentally accessible during sample preparation. Therefore, it qualifies as starting point to introduce the compound film thickness. An illustration is given in fig. 7.8. Since the supply of Pt atoms from the substrate is virtually infinite, the number of Ce atoms per Pt(111) surface unit cell, N_{Ce}, governs the thickness of the compound. If the density of Ce atoms in the deposited overlayer is known, N_{Ce} can directly be calculated from the number of monolayers N_{ML}. According to Baddeley *et al.*, the interatomic distance of Ce deposited on Pt(111) is 40 % higher than the Pt-Pt distance of the (111) surface [83]. Consequently, the atomic density in a Ce overlayer is approximately half the one of the substrate surface layer and

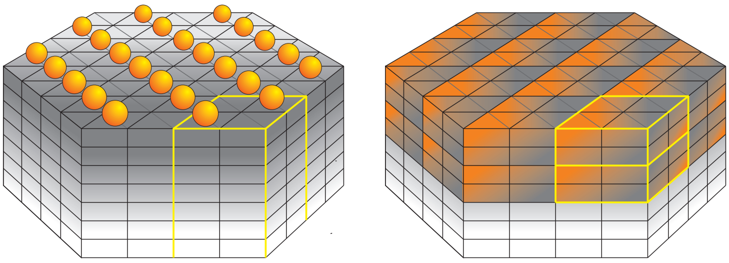

Figure 7.8: Illustration of the conversion from Ce coverage to compound thickness. A coverage of $N_{\text{Ce}} = 0.5$ Ce atoms per Pt(111) surface unit cell (black lines), which is supposed to represent $t_{\text{ol}} = 1$ ML overlayer thickness (left), transforms to a compound with thickness $t = 2$ u.c., if a (2×2) superstructure (yellow) and one Ce atom per compound unit cell is assumed (right).

$N_{\text{Ce}} = 0.5\ N_{\text{ML}}$.

LEED patterns of alloyed samples indicate a superstructure close to (2×2), meaning that the surface unit cell area is approximately four times as large as for Pt(111). Hence, the number of Ce atoms per compound surface unit cell is $N_{\text{Ce}}^{2\times2} \approx 4\ N_{\text{Ce}} \approx 2\ N_{\text{ML}}$. Finally, the film thickness measured in unit cells is calculated by $t = N_{\text{Ce}}^{2\times2}/N_{\text{Ce}}^{\text{u.c.}}$. In the case of $CePt_5$, the number of Ce atoms per three-dimensional compound unit cell is $N_{\text{Ce}}^{\text{u.c.}} = 1$.

The thickness in length units can be calculated from t and the vertical lattice constant. The derived relation between the initial coverage as used in most literature and the thickness in unit cells as used here is consistent when comparing LEED patterns, which are very sensitive to the film thickness.

With a quartz microbalance, N_{Ce} and thus t can directly be measured from the frequency shift during the deposition time by application of eq. 3.5. In order to obtain an independent calibration of the quartz microbalance and a characterization of the surface compounds, a STEM experiment was performed, as described in section 3.5. For this purpose, a suitable lamella was prepared from a sample with a nominal thickness of $t = 10$ u.c.

An image of the LEED pattern of this sample is shown in fig. 7.5. It exhibits phase VI, a superposition of a rotated and an unrotated superstructure with relaxed surface lattice constants. This has the advantage that both structures should be visible in the STEM images. Assuming that both domains possess the same crystal structure, this means that views from two different directions onto the lattice are expected. The disadvantage is that domain boundaries can exist in the lamella, meaning that the electrons have to pass both crystal structures. This will in general not lead to an ordered pattern, since the atoms may not be aligned along rows across the boundary.

Two exemplary micrographs of the lamella are shown in fig. 7.9. In the lower parts, the pattern expected for the substrate is clearly visible. In between this well-ordered part and the dark signature of the amorphous capping layer, a region is visible that shows ordered patterns different from the substrate, at least in some parts. Two different patterns of atomic rows were found on the lamella, as shown in panels (a) and (b) and schematically drawn in panel (c).

Although the interfaces of the different vertically stacked sample regions are not defined by monoatomic rows, it is obvious that the substrate is covered by a film of different material. This film region is clearly associated with the Ce-Pt surface compound. Hence, the micrographs show that alloying of Ce deposited to a Pt(111) surface results in the formation of a well-defined film. An alternative, apparently untrue scenario would have been an alloy with a gradual decrease of Ce percentage towards deeper sample regions.

It is remarkable that the observed lateral periodicities of film and substrate agree very well. Since the film lattice is assumed to have relaxed at this thickness, this means that the strain is indeed taken by the substrate.

Structure 1 was found only once, whereas structure 2 appeared on several spots on the lamella. The schematic drawing of Structure 1 does not allow conclusions about the unit cell dimensions. Structure 2 suggests a structure with two alternating layer types. Although detailed models for the two structures cannot be provided at the present stage, important conclusions on the film

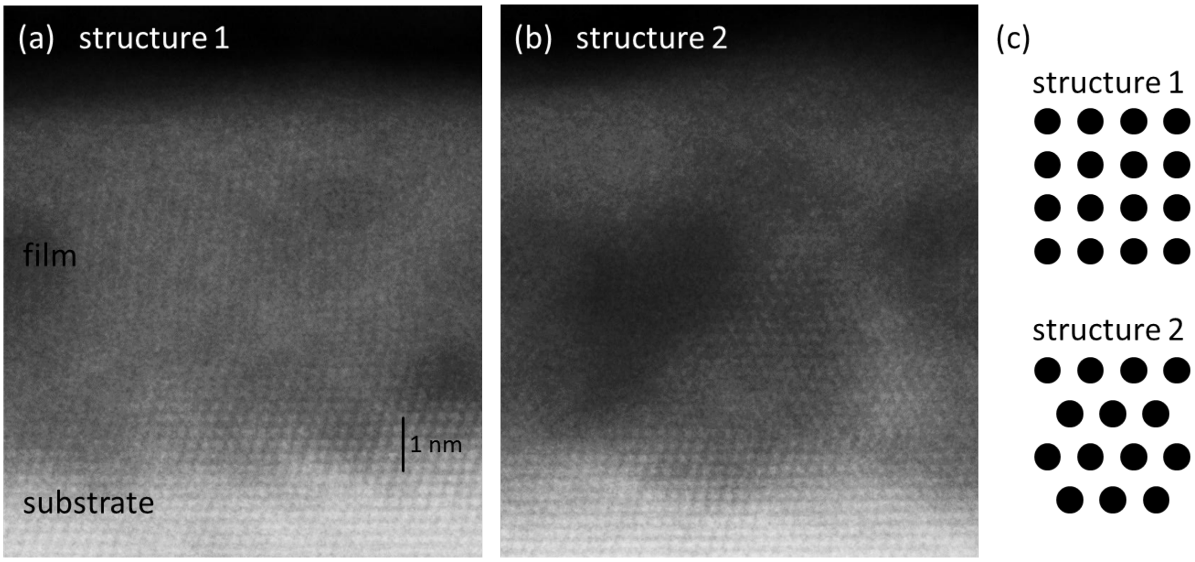

Figure 7.9: STEM images of a lamella produced from a $CePt_5$/Pt(111) sample with a nominal thickness of 10 u.c. View along the $\left[1\bar{1}0\right]$ direction. (a) minority structure 1. (b) majority structure 2. (c) Schematic drawings of the two structures.

thickness and the Ce density can be drawn.

The averaged layer spacing in the compound film was evaluated to $c = 0.216 \pm 0.008$ nm as described in section 3.5. Evaluation of the vertical unit cell dimension from this value requires the number of unit cells in the film. To get this information, the total thickness of the compound film needs to be related to the amount of Ce deposited.

In order to measure the compound film thickness from the STEM images, both interfaces have to be identified. A problem here is that the material contrast is rather low. The compound consists largely of Pt, which is the material of both the substrate and the capping layer on top of the film. Furthermore, the brightness of the images depends on the local lamella thickness, which is not necessarily homogeneous.

The compound film thickness was measured at 30 different positions in different images. The averaged result amounts to $t = 5.21 \pm 0.73$ nm. Together with the layer spacing evaluated from the images, this translates to 24 ± 3 layers or 12 ± 1.5 double layers. The nominal deposit was 10 Ce atoms per 2×2 surface unit cell. Hence, the observed thickness can be obtained only if one Ce atom per surface unit cell induces a structure that is two layers thick.

The measured film thickness then exceeds the nominal one by 20 %. However, this deviation might to large parts be caused by the errors of the STEM evaluation. With the availability of a dataset for a single sample only, this evaluation is regarded as less reliable than the microbalance measurement. In order to achieve definite conclusions regarding the calibration of the microbalance, systematic experiments should be performed. With the knowledge of the compound thickness per Ce atom obtained from the present STEM experiment, diffraction methods that directly access the film thickness should be employed. For the interpretation of the following results, the uncertainty that remains at the present stage has only minor impact and is regarded as acceptable. Hence, no corrections were applied to the nominal microbalance results.

In any case, the STEM results show that the film thickness is an appropriate quantity to characterize the Ce-Pt(111) surface compounds. The approximate confirmation of the film thickness as calculated from the quartz microbalance measurements allowed assignment of a thickness range to each of the LEED phases, which was anticipated in section 7.2.

This procedure can be reversed, which means that the thickness of a sample can be determined from its LEED pattern. Especially at thicknesses around 2 . . . 5 u.c., this can be done with very high precision, since the LEED pattern seems to be sensitive to addition or removal of single atomic layers. Based on this calibration, important structural information about a sample can be obtained with nearly atomic precision by a relatively simple method, and without further sophisticated evaluation.

7.4 Stoichiometry and TEY electron escape depth

The next step towards the identification of the crystal structure of the Ce-Pt(111) compounds is the determination of the stoichiometry. The only direct stoichiometry determination reported so far can be found in the work by Tang *et al.* [79]. By evaluation of X-ray photoemission spectra, these authors found a thickness-dependent composition of the compounds under assumption of a homogeneous stoichiometry within the probing depth. Their results lie in between $CePt_3$ and $CePt_{2.23}$, with higher Pt percentage for thin samples. Hence, the films would belong to the homogeneity domain in the binary Ce-Pt phase diagram (see section 2.2.1).

The results of the preceding sections show that the Ce-Pt(111) compounds form well-defined, homogeneous films at the surface. Hence, a homogeneous stoichiometry can be assumed within the film thickness t. However, t can be much smaller than the PES probing depth, which amounts to $\lambda_{\mathrm{IMF}} = 1 \ldots 2$ nm for the energies used by Tang *et al.* [105].

Hence, the increasing Pt percentage for their thin samples most likely arises from the fact that a considerable part of the substrate was probed by Tang *et al.* as well. The only result that can thus be regarded as valid for the film stoichiometry is $CePt_{2.23}$. It was obtained for the thickest samples, where t is significantly larger than the probing depth.

This result is contradicted by the proposal of Baddeley *et al.* [83], who concluded towards a $CePt_5$ structure of the films. While this assumption is well in line with the lattice constants seen in their STM data, these authors did not directly address the stoichiometry in their experiments. The conclusion was rather made from LEED, arguing that the sixfold symmetry of the diffraction spots indicates a hexagonal crystal structure. As already discussed in section 2.2.2, the LEED observations can also be explained by rotational domains of a structure with threefold symmetry, as would be expected for the cubic symmetry of homogeneity phase proposed by Tang *et al.* (compare tab. 2.2).

In order to resolve the discrepancy between these contradictory results, attempts were made in the present work to determine the film stoichiometry from thickness-dependent Ce $M_{4,5}$ XAS data. An adequate model for this purpose is presented in section 5.5, the result is given in eq. 5.26 by additional use of eq. 5.3. The model is based on the assumption of a homogeneously mixed film with well-defined thickness on top of a substrate. The parameters of the model are the TEY electron escape depths λ_{e} of film and substrate, atomic absorption cross-sections $\sigma(E)$ of all elements in the sample at two different photon energies and the atomic densities ρ^{at} of the constituents in both parts of the sample.

The electron escape depths of film and substrate are in general unknown and have to be determined experimentally. As argued in section 5.5, a direct determination for the substrate crystal was not possible. A value of $\lambda_{\mathrm{e}}^{\mathrm{s}} = 2$ nm is assumed, motivated by results for Au [180]. The escape depth of the film is left as a free fit parameter. The result depends on the vertical lattice parameter, which determines the thickness of a unit cell. It was set to $a_3 = 0.432$ nm as derived from the evaluation of the STEM images in section 7.3.

Values for the atomic absorption cross-sections $\sigma(E)$ can be taken from literature. The photon energies that were used in the experiments are the one of the Ce M_4 maximum at $E_1 = 900$ eV, which yields a maximal signal in the Ce $M_{4,5}$ spectrum, and $E_2 = 870$ eV, which represents the pre-edge region where the continuum background was measured for normalization.

For Pt, no resonant absorption is present for both photon energies, as is the case for Ce at E_2. Hence, the three respective values for $\sigma(E)$ can be taken from Henke *et al.* [160] (see fig. 5.2). For Ce at the peak energy, $\sigma(E)$ was calculated from the transmission data shown by Fernández-Perea *et al.* [178]. Tab. 7.1 gives a summary of the relevant parameters for the two elements at the two photon energies.

Concerning the atomic densities in the model, the value for the Pt substrate is given in tab. 7.1. The Pt density of the film is unknown, but the considerations made for the STEM results in section 7.3 together with the surface lattice constant determination of section 7.2 allow calculation

Element	E (eV)	ρ (kg/m^3)	m^{at} (u)	ρ^{at} (at/nm^3)	μ_{x} (μm^{-1})	σ (nm^2)
Pt	870	21450	195.1	66.2	13.31	$2.01 \cdot 10^{-4}$
Pt	900	21450	195.1	66.2	12.52	$1.89 \cdot 10^{-4}$
Ce	870	6771	140.1	29.1	1.40	$4.81 \cdot 10^{-5}$
Ce	900	6771	140.1	29.1	36.50	$1.25 \cdot 10^{-3}$

Table 7.1: Summary of the relevant parameters for X-ray absorption on pure Ce and Pt at the Ce M$_4$ resonance ($E_1 = 900$ eV) and in the pre-edge region $E_2 = 870$ eV. The mass density ρ at room temperature [104] and the atomic mass m^{at} [37] are given, which allows calculation of the atomic density ρ^{at}. This quantity connects the linear absorption coefficient $\mu_{\mathrm{x}}(E)$ [160, 178] with the atomic absorption cross-section $\sigma(E)$ via eq. 5.3.

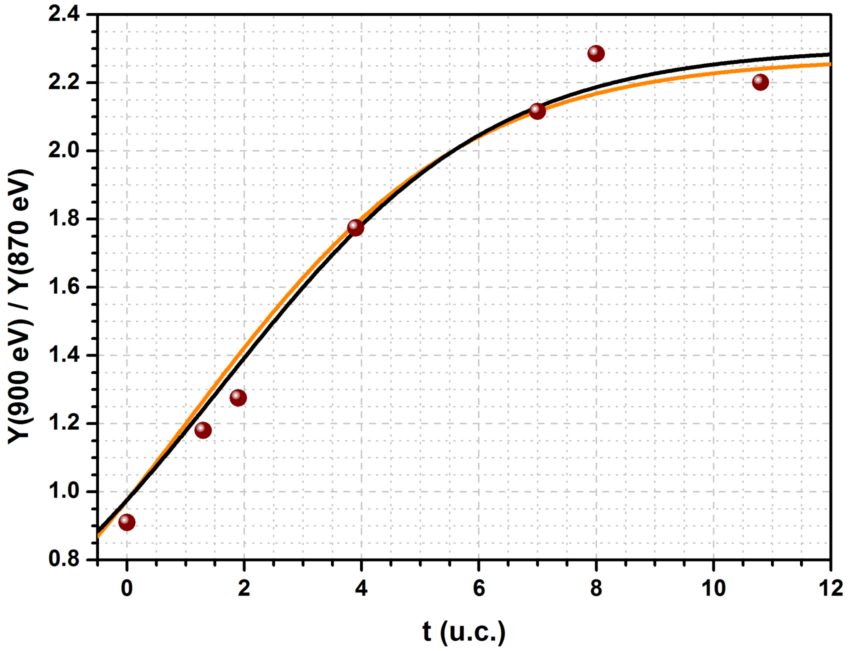

Figure 7.10: Ratio of TEY signals $Y(E_1)/Y(E_2)$ for the Ce M$_4$ peak at $E_1 = 900$ eV and the pre-edge region at $E_2 = 870$ eV in dependence of the compound film thickness t. Symbols: Experimental data. Solid lines: Least square fits of eq. 5.26 for different parameter sets, as given in the text.

of the Ce density based on experimental findings.

Under neglect of a possible thickness-dependence of the unit cell volume in the film, which should only affect the thinnest films (see fig. 7.7), and taking the lattice constant of $a = 0.534$ nm as obtained from LEED images at $t \approx 3$ u.c. as representative, the Ce density amounts to 9.4 at/nm^3. Determination of the Pt density from the model fit then allows calculation of the stoichiometry.

For evaluation of the experimental values, nearly isotropic spectra taken at $\theta = 60°$ were used to avoid influences of the crystal field (see section 5.2). The spectral shape is thus independent of the sample temperature, and the peak height can be taken as a measure of the spectral weight. Only data taken at BESSY were used, since the higher energy resolution at SOLEIL prohibits a direct comparison of peak heights. Normalization of the measured TEY signal to the storage ring current instead of I$_0$ was chosen due to technical problems with the gold grid during some of the beamtimes.

The data are shown as the symbols in fig. 7.10). The value for $t = 0$ u.c. was obtained from a spectrum of the clean Pt(111) crystal. Its deviation from unity reflects the general decrease of $\sigma(E)$ with energy (compare section 5.1.2, in particular fig. 5.2). The progression of $Y(E_1)/Y(E_2)$ with t reflects that the peak height increases with increasing Ce content, while the background absorption decreases since it is smaller for Ce than for Pt.

The black line represents a fit of eq. 5.26 with the electron escape depth and the atomic Pt density of the compound film as free parameters. Obviously, the model is capable to reproduce the characteristics of the experimental data, the agreement is good. The fit results are $\lambda_e^f = 1.01 \pm 0.25$ nm and $\rho^{at}_{Pt,f} = 39.9 \pm 3.3$ at/nm^3. The resulting stoichiometry of the compound is CePt$_{4.3}$.

The value of the M$_4$ absorption taken from Fernández-Perea *et al.* suffers from several uncertainties. While the reading accuracy is a minor problem, the height of the peak strongly depends on the experimental energy resolution. A comparison of the general shape of the transmission data with spectra obtained in the present work (see, e.g., fig. 6.1) clearly shows that the multiplet substructure is much less resolved in the spectrum of Fernández-Perea *et al.* Indeed, the experimental energy resolution, which is specified as $\Delta E \approx 0.5$ eV for the Ce M$_{4,5}$ edges, is considerably worse than $\Delta E \approx 100$ meV as achieved in the present thesis. Consequently, the assumed atomic cross-section for the peak is most likely underestimated. Successively increasing it in the model leads to an increase of the atomic Pt density. Hence, the stoichiometry result of CePt$_{4.3}$ can be regarded as a lower limit for the Pt percentage.

The orange line in fig. 7.10 represents a fit result with the stoichiometry fixed to CePt$_5$ and the Ce absorption cross-section at the M$_4$ maximum along with the film escape depth as free parameters. The results amount to $\lambda_e^f = 1.04 \pm 0.48$ nm and $\sigma_{Ce}(E_1) = 1.42 \pm 0.1710^{-3}$ nm^2. In this case, $\sigma(E_1)$ would be underestimated by 13 % by Fernández-Perea *et al.* In order to test this assumption, an exemplary spectrum of the present thesis was convoluted with Gauss peaks of variable FWHM Γ. A reduction of the peak by 13 % was obtained for $\Gamma \approx 1$ eV, which is considerably larger than ΔE as indicated by Fernández-Perea *et al.* However, a convolution with $\Gamma = 0.5$ eV largely conserved the visible multiplet structure, which is not present in the transmission data. It is possible that these data were recorded with a worse energy resolution than specified and that the fit result for $\sigma_{Ce}(900\text{ eV})$ is correct.

In conclusion, the stoichiometry as obtained from the present evaluation ranges in between CePt$_4$ and CePt$_5$. This disagrees with the evaluation of Tang *et al.* [79]. It rather supports the assumption of CePt$_5$ as proposed by Baddeley *et al.* [83].

The TEY electron escape depth is evaluated to be of the order of $\lambda_e^f \approx 1$ nm. For further considerations, it is set to this value. Uncertainties arise from the vertical lattice parameter a_3 of the compound, and from the imprecision in knowing λ_e^s of the substrate. The error is estimated to amount to $\Delta\lambda_e = 0.3$ nm.

An escape depth of $\lambda_e = 1 \pm 0.3$ nm compares well to experimentally determined values for other rare earth compounds that are given in the literature [184, 255, 256]. Due to the smallness of the probing depth, the results that can be obtained with XAS and XMCD are dominated by the sample surface. This surface-sensitivity has been misjudged in the past [205] (see section 6.1.4), although the debate about small TEY escape depths has been going on for quite some time [257].

7.5 Discussion of the crystal structure

The experimental results of the preceding sections regarding unit cell dimensions and stoichiometry of Ce-Pt(111) surface compounds provide a solid basis for a discussion of the possible crystal structures. The most promising candidates for the crystal structure of the intermetallic films are the binary Ce-Pt phases that are known in the bulk (see section 2.2.1).

In principle, also a phase which does not exist as bulk material could be stabilized at the Pt(111) surface. A possible scenario would be the formation of a true surface alloy, with Ce on substitutional positions of the Pt surface lattice. This could even happen in an ordered manner leading to the observed (2×2)-like superstructure. However, the observation of lattice relaxation with increasing sample thickness and the appearance of rotated superstructures suggests that the alloyed films possess a distinct crystal structure. For thick films, the structure becomes independent of the substrate or even forces the substrate to adapt to its lattice parameters. In this thickness regime, the films do not behave as a surface system, but rather show bulk-like characteristics. The observation of equivalent $I(E)$ curves in LEED allows transfer of this

Compound	$V_{\text{u.c.}}$ (nm^3)	$N_{\text{Ce}}^{\text{u.c.}}$	$\rho_{\text{Ce}}^{\text{at}}$ (at/nm^3)
$CePt_2$	0.4639	8	17.2
$CePt_3$	0.4477	6	13.4
$CePt_5$	0.1095	1	9.1

Table 7.2: Unit cell volume $V_{\text{u.c.}}$, number of Ce atoms per unit cell $N_{\text{Ce}}^{\text{u.c.}}$ and atomic Ce density $\rho_{\text{Ce}}^{\text{at}}$ for selected Ce-Pt bulk phases.

argument to the complete thickness range of the present experiments.

Most phases listed in tab. 2.2 can be excluded for the surface compound due to their lattice constants. The orthorhombic and tetragonal structures can hardly adapt to the hexagonal lattice of the Pt(111) surface. While this is in principle possible for the hexagonal structures, all but the $CePt_5$ phase possess lattice constants too large to be compatible with a superstructure close to (2×2), as observed in LEED. In contrast, the $CePt_3$ phase in the $AuCu_3$ structure would rather lead to a (1×1) reconstruction. For the $CePt_{x\approx4.5}$ phase, nothing but the existence and the approximate stoichiometry are known. However, the unit cell is supposed to be rather large, since it has to host at least 2 Ce and 9 Pt atoms. It is therefore unlikely that it will be able to adapt to a (2×2) superstructure.

Based on these arguments, only the $CePt_5$ phase and the $CePt_{2+x}$ homogeneity domain come into consideration for the surface compound, as was already concluded by other authors [70, 83]. The hexagonal $CePt_5$ structure would align with its (001) plane parallel to the Pt(111) surface with $a_{\text{surf}} = 0.5367$ nm, whereas the interfaces of a cubic $CePt_{2+x}$ film would be its (111) planes, and $a_{\text{surf}} = a_{\text{cub}}/\sqrt{2} = 0.5409\ldots0.5474$ nm (compare fig. 3.1). In order to explain the sixfold symmetry observed in LEED patterns, $CePt_{2+x}$ needs to form rotated domains, which can be expected for the present preparation routine.

Both structures possess Pt Kagome nets as building elements, which represents a possibility for Pt termination as concluded from different experiments (see section 2.2.2). In between these pure Pt layers, both structures feature Ce-containing layers with different composition, which are slightly buckled for the $MgCu_2$ structure of $CePt_{2+x}$. The finding of alternating Ce-containing and pure Pt layers by Baddeley *et al.* could thus be explained by both structures [83].

While the PES-based stoichiometry analysis by Tang *et al.* indicates $CePt_{2+x}$ [79], the lattice constants as determined from STM images by Baddeley *et al.* support the assumption of $CePt_5$ as the film structure. The present interpretation of the LEED pattern at $t \approx 3$ u.c. (phase IV in section 7.2) as resulting from a combination of substrate and film allowed determination of $a = 0.534$ nm, which is slightly below and thus closer to the smaller lattice constant of $CePt_5$.

From the combined STEM and quartz microbalance analysis presented in section 7.3, the atomic Ce density of the compound film can be calculated. It amounts to $\rho_{\text{Ce}}^{\text{at}} = 9.4$ at/nm^3. This number can be compared to respective values for the bulk structures under consideration, which are given in tab. 7.2. The atomic Ce density increases with decreasing Pt percentage, and the experimentally obtained value for the surface compound is well in line with the one of $CePt_5$.

Finally, the XAS-based stoichiometry analysis, which is presented in section 7.4, clearly favors $CePt_5$. However, it is not possible to distinguish between this and a $CePt_{x\approx4.5}$ phase. In addition to the considerations about unit cell size given above, another aspect should be taken into account: $CePt_5$ is the most Pt-rich intermetallic phase in the bulk phase diagram. When alloying a thin Ce film deposited onto a Pt substrate, certainly much more Pt than Ce is available for compound formation. It is therefore very likely that a Pt-rich phase is formed, especially if the lattice constant is so well in line with the one of the substrate. Hence, the present discussion is concluded with the result that the crystal structure of the intermetallic surface compounds is most likely $CePt_5$.

7.6 Structure confirmation with LEED IV

As a final step of structure determination for the surface intermetallics, a full LEED IV analysis was performed by application of the CLEED software. The principles of this procedure are treated in section 4.2.

The probing depth of LEED is of the same order as the one of XMCD. Hence, both methods are sensitive to the same sample region and LEED provides the crystallographic information that is relevant for the interpretation of XMCD results.

As a result of the considerations concerning lattice constant, Ce density and stoichiometry presented in section 7.5, only the $CePt_5$ structure is regarded as plausible. The $CePt_{x\approx4.5}$ phase could not completely be excluded, but without a structure model as a basis for the calculations, this phase disqualifies for a LEED IV study. This also applies for any further possible Ce-Pt phase that is unknown to date.

Hence, the structure search was restricted to $CePt_5$. The aim of the study was to optimize the R-factor by adjustment of model parameters and then to judge whether the quality of agreement convincingly confirms the assumed structure. Furthermore, an important degree of freedom for model construction is the surface termination. Three different assumptions were tested, which are described in the following section. The results are presented and discussed afterwards.

7.6.1 Structure models

$CePt_5$ crystallizes in the $CaCu_5$ structure, which consists of alternating layers of $CePt_2$ and pure Pt (see fig. 2.7). Since the surface-nearest layers yield the largest contribution to the LEED signal, the question of termination is of crucial importance for modeling of LEED IV data.

Concerning the surface layer of the intermetallic films, all publications on the topic agree that it largely consists of Pt, at least for samples prepared by the method applied in the present work. The exact structure of the terminating layer has not been investigated experimentally in detail yet, although a number of accounts can be found in the literature. Most authors argue on the basis of bulk truncation with a Pt Kagome layer. Baddeley *et al.* interpret features that are visible in their STM images as resulting from the hexagonal holes in the Kagome layer [83]. Vermang *et al.* discuss their adsorption experiments against the background of this finding [91]. The STM image shown by Berner and Schierbaum lacks a clear signature of the Kagome holes [86], which makes the authors search for an explanation by referring to the density of states of the underlying Ce atoms.

A theoretical study of six different surface terminations for $CePt_5$/Pt(111) with $t = 1$ u.c. in terms of LDA+U is reported in the PhD thesis of M. Klein [92], and has been published independently in the meantime by Tereshchuk *et al.* [93]. In the geometry with lowest energy that was found in this study, every fourth Pt atom is removed in the topmost substrate layer, which thus forms the first Kagome net of the $CePt_5$ structure. This is followed by a $CePt_2$ layer and a terminating Pt layer. The latter is a Kagome net with additional Pt atoms inside the hexagonal holes. Apparently, the Pt atoms in top of the Ce atoms slightly protrude out of the surface.

Based on this level of information, three different models for the termination were tested in the LEED IV analysis of the present work: bulk truncation with $CePt_2$ and Pt Kagome layers as well as a closed Pt surface layer. In the following, these models are referred to as models C, K and P, respectively.

The sample that was chosen for the structural analysis had a nominal thickness of $t \approx 4$ u.c. It displayed a LEED pattern that was classified as phase V[4]. Hence, no distinct satellite spots were visible, which are interpreted as a signature of scattering on the substrate. Furthermore, preliminary tests showed that the coordinates of atoms below the second $CePt_2$ layer were subject to significant statistical noise, if they were set as free search parameters. It is therefore concluded that the measured signal primarily results from the first two unit cells, which means

---

[4] In fact, the image shown for phase V in fig. 7.3 belongs to the energy series of this sample.

that the Pt substrate does not contribute. This allows neglecting it in the structure models, which were therefore constructed purely of $CePt_5$.

The $CePt_5$ structure is highly symmetric, which should be reflected by the structure models. The sixfold rotational symmetry is of highest importance, since the symmetry regarding mirror planes parallel to the layers is broken at the surface. The atoms in the structure can be divided into three groups of equivalent symmetry: the Ce atoms, the Pt atoms in the $CePt_2$ layers and the Pt atoms in the Kagome layers. Defining the coordinate system in a way that the z direction is perpendicular to the layers, the rotational symmetry of the structure is broken if any atom is displaced in the x-y plane or if equivalent atoms in the same layer are unequally displaced in the z-direction.

In order to account for this, the collective z coordinates of the groups of equivalent atoms are the only set of free parameters that conserves the rotational symmetry. Furthermore, the overall lateral lattice constant meets this demand, but it is fixed for a particular optimization cycle in CLEED. The additional Pt atoms in model P represent another group of equivalent atoms and can be given a distinct z-coordinate, which yields an additional parameter.

The structure models that were used for the final study were constructed as shown in fig. 7.11. The bulk part was terminated with a Pt Kagome layer. For model C, the overlayer consisted of two $CePt_2$ layers with a Pt Kagome layer in between. Another Pt Kagome layer was placed on top for model K, which was further amended by additional Pt atoms in the hexagonal holes for model P.

The maximum number of free parameters that conserve the rotational symmetry was reduced by one by equalization of the z-coordinates of the Ce and Pt atoms in the second $CePt_2$ layer. The remaining 4, 5 and 6 geometric parameters for the models C, K and P, respectively, were independently set as free for the structure optimization to account for the influence of the surface. In the following, the parameters are expressed by the distances d_n of the Pt atoms in the different layers and deviations Δd_n thereof for the Ce and optional additional Pt atoms. Those quantities are defined in Fig. 7.11, positive values for Δd_1 and Δd_2 correspond to the depicted arrangement.

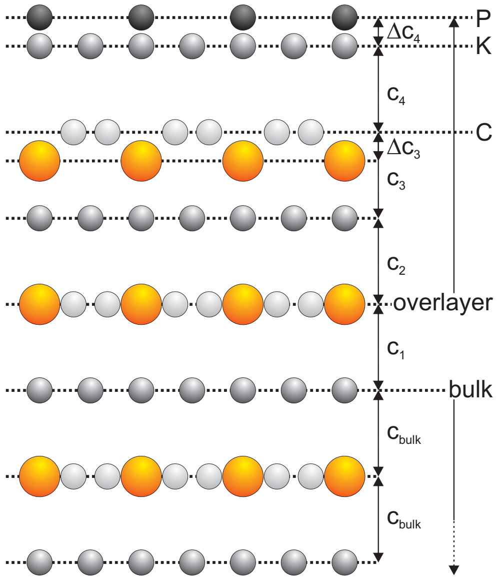

Figure 7.11: Sketch of the structure models that were tested in the LEED IV analysis. The $CePt_5$ structure is viewed along the [100] direction. Large yellow circles represent Ce atoms. Small gray circles represent Pt atoms in $CePt_2$ layers, Pt Kagome layers and additional surface positions (from bright to dark). C, K and P mark the terminating layer of the respective model.

7.6.2 The LEED IV study

The optimization of each of the three models was started from equivalent, well-defined geometries. The non-geometric parameters were set to $V_{o,i} = 4$ eV and $\Delta r = 0.005$ nm for both Ce and Pt. As start values for the angles of incidence, $\vartheta_i = 1°$ and $\varphi_i = 60°$ were chosen, which were the results of a rough preliminary evaluation. The lateral lattice constant was set to $a = 0.533$ nm, which was the most reliable result of LEED pattern evaluation of phase IV at that time[5]. The deviations of z-coordinates of Ce and additional Pt atoms from the ones of the other atoms in their respective layers were started from zero, $\Delta c_3 = \Delta c_4$[6] $= 0$ nm. The layer distances were set to equal values, $c_{bulk} = c_1 = c_2 = c_3 = c_4$[7]. On this basis, a first series of optimization

---

[5] The LEED IV study was performed before the STM results of [1] were available, which allowed identification of the strict $\mathcal{S} = 3\sqrt{3}$ relation between film and satellite superstructures.

[6] only for model P

[7] not for model C

Model	R_P	R_R	ϑ_i (°)	φ_i (°)	$V_{o,i}$ (eV)	Δr_{Ce} (nm)	Δr_{Pt} (nm)
P	0.2593	0.1312	1.22 ± 0.12	66.47 ± 0.50	2.4	0.005	0.007
K	0.3509	0.1312	0.38 ± 0.14	65.59 ± 2.73	2.4	0.004	0.002

Table 7.3: Results of the LEED IV analysis: Optimized R-factors, angles of incidence and non-geometrical parameters for the tested structure models.

Model	a	c_{bulk}	c_1	c_2
P	0.535	0.207	0.2334 ± 0.0177	0.2126 ± 0.0313
K	0.535	0.216	0.2363 ± 0.0120	0.1776 ± 0.0265

Model	c_3	Δc_3	c_4	Δc_4
P	0.2300 ± 0.0244	0.0229 ± 0.0170	0.2277 ± 0.0166	0.0220 ± 0.0139
K	0.2721 ± 0.0211	0.0177 ± 0.0147	0.1913 ± 0.0137	—

Table 7.4: Results of the LEED IV analysis: Optimized geometrical parameters as defined in fig. 7.11 for the tested structure models. All values are given in nanometer.

cycles was calculated for each model under variation of the start value of the layer distance in the range $c = 0.205 \ldots 0.23$ nm.

The best R-factor results that were obtained in these series amounted to $R_P^C = 0.5612$, $R_P^K = 0.4228$ and $R_P^P = 0.2901$ for the three models, with a double reliability factor near $R_R = 0.17$. The qualitative picture of the resulting structures, i.e., the relative arrangement of the atomic layers, corresponded to the schematic shown in fig. 7.11 for all three models. Both the R-factor results of models C and K do not fulfill the reliability criterion given in eq. 4.22. Model C was excluded at this point, whereas for model K the optimization procedure was nevertheless performed.

For models P and K, the parameters were optimized by the procedure described in section 4.2.7. In this course, neither the hierarchy of the R-factors nor the qualitative picture of the structures changed any more. However, the R_P results could significantly be improved. The results of these efforts are summarized in tabs. 7.3 and 7.4, whereas the full sets of $I(E)$ curves of the optimized structures are shown in figs. 7.12 and 7.13.

The error bars given with the results were calculated as described in section 4.2.6. CLEED provides uncertainties for its actual free search parameters, which are the z-coordinates of atomic layers in addition to the angles of incidence in the present structure model. The layer distances given in the tables are obtained as differences of the z-coordinates. A maximum uncertainty is assumed by adding the individual errors of the subtracted coordinates.

The relative errors of the angles and main layer distances are reasonably small. For the small layer displacements Δc_3 and Δc_4, the relative errors naturally become large. Nevertheless, both errors bars are smaller than the parameter results, which means that the direction of the deviations and thus the qualitative picture as drawn in fig. 7.11 is not questionable.

A somewhat striking result is the optimized value for $V_{o,i}$, which turns out to be very low compared to typical values of $V_{o,i} = 4 \ldots 5$ eV [113, 114]. This means that the inelastic mean free path must be rather large, which contradicts the assumption that this quantity is largely material-independent. The $V_{o,i}$ results for both models are equal, which reflects that it is directly connected to the peakwidth of the experimental $I(E)$ curves. An interpretation of the small value for $V_{o,i}$ cannot be offered at the present stage, since neither systematic studies of $V_{o,i}$ nor any other optimized results for materials with rare earth atoms are presently known to the author.

The low value of $V_{o,i}$ affects the double reliability factor via eq.4.21 and thus the error bars. Those were calculated assuming the CLEED default value of $V_{o,i} = 4$ eV, and are thus overestimated.

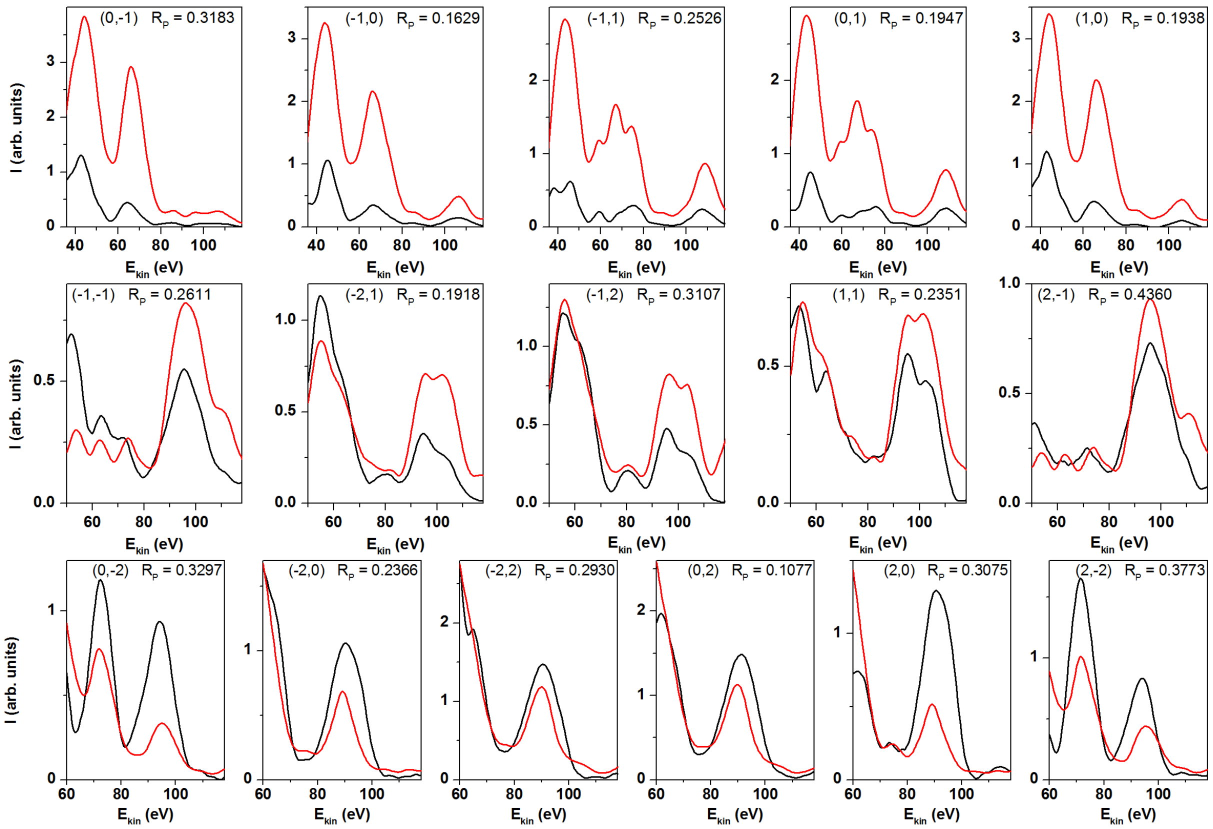

Figure 7.12: Full set of experimental (black) and calculated (red) $I(E)$ curves, result of the optimization for model P. Spot indices are given along with individual R_P values.

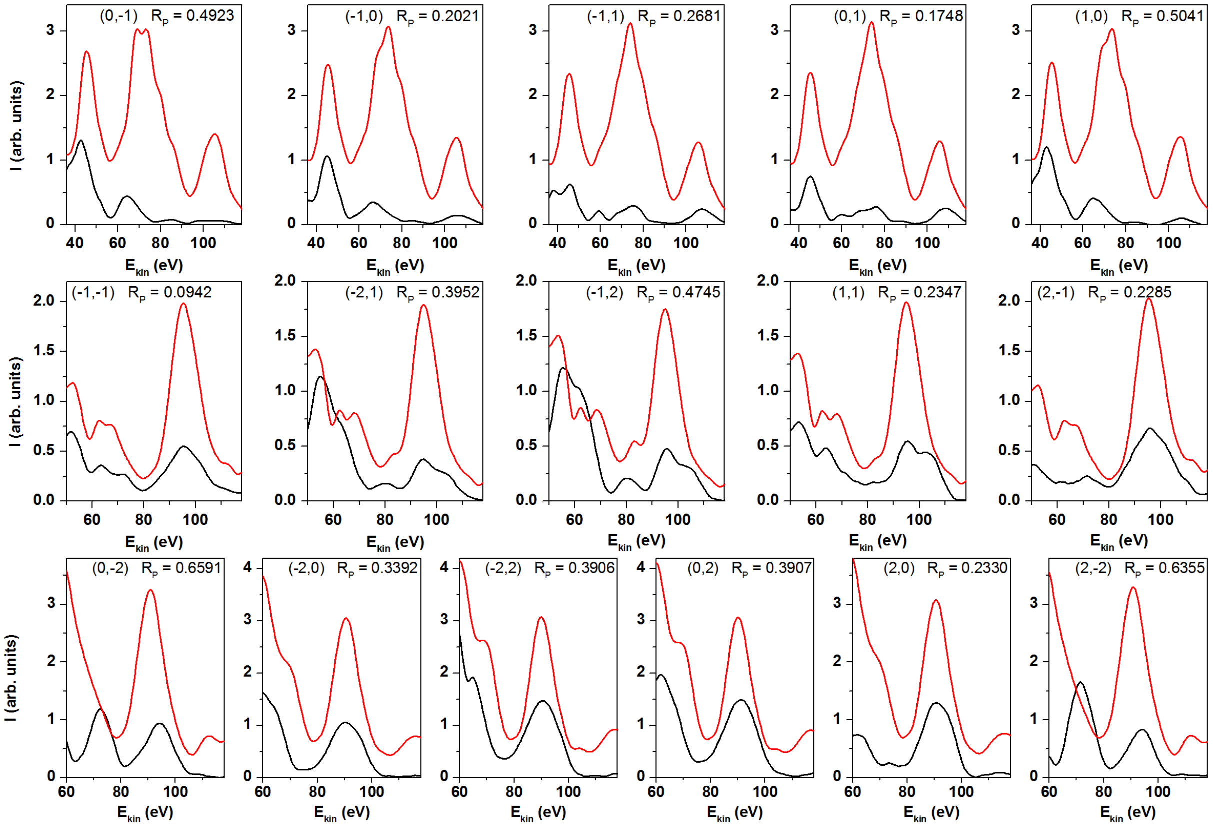

Figure 7.13: Full set of experimental (black) and calculated (red) $I(E)$ curves, result of the optimization for model K. Spot indices are given along with individual R_P values.

In turn, R_{R} also depends on the total energy range, which was assumed as $\Delta E^{\mathrm{tot}} = 1111$ eV. This large range relies on the assumption that the symmetrically equivalent spots used for the study provide inequivalent curves due to a significant tilt of the sample surface with respect to the incident electron beam (compare section 4.1.3). This assumption is not fully justified regarding the small value of $\vartheta_i \approx 1°$. The overestimation of $V_{\mathrm{o,i}}$ in the calculation of R_{R} can be seen as a compensation for the overestimation of ΔE^{tot}.

The R-factor results given in tab. 7.3 are clearly in favor of model P, which is supported by visual comparison of the $I(E)$ curves. Furthermore, the plausibility of the solution found for model K suffers from the fact that the polar angle of incidence ϑ_i is nearly zero. Consequently, the $I(E)$ curves calculated for symmetrically equivalent spots exhibit only minor differences, which contradicts the experimental results. The curves calculated for model P reproduce the observed azimuthal angle dependence.

The low absolute value of $R_{\mathrm{P}} = 0.2593$ for model P encourages the assumption that this model is an appropriate description of the surface structure. In the literature, even lower R-factor results were reported for other intermetallic compounds [258]. However, studies involving rare earth atoms with f electrons frequently yield optimized R-factors of this order or larger [259–262].

Lower R-factor results might by prevented by deficiencies in the dynamical scattering formalism regarding the properties of rare-earth atoms. As already stated in section 4.2.5, an independent LEED IV study involving Ce in a well-known structure is currently missing. Unfortunately, the required experiments are complicated by the high reactivity of pure Ce surfaces.

In any case, the structure models represent approximations to the real structure. While the influence of the surface is explicitly addressed by the different terminations, the effect of the interface to the substrate is only reflected by the strained lattice constants. Together with the approximations that are used in dynamical calculations and with the experimental uncertainties, the approximative character of the model prevents the calculations to perfectly reproduce the experimental data.

The main drawback of the models certainly is the assumption of a single-domain surface termination. The large-scale STM images of $CePt_5/Pt(111)$ samples shown by Baddeley *et al.* [83] and Kemmer *et al.* [1] indicate a coexistence of several surface phases, some of which are interpreted as terminated with a $CePt_2$ layer. A technical realization of coexisting surface structures is currently not implemented in CLEED, and such modeling bears the risk of over-parametrization. The model with the best agreement can therefore only be assumed to represent the largest part of the surface, whereas contributions from minority phases downgrade the agreement of experiment and calculation.

Against this background, the obtained R-factor result is regarded as satisfactory low. It is very likely that the intermetallic films have the $CePt_5$ structure. Most of the surface terminates at a Pt Kagome layer, where additional Pt atoms are situated in the hexagonal holes. Those additional surface atoms slightly protrude out of the surface, whereas the Ce atoms directly underneath are displaced away from the surface, probably by the presence of the additional atoms.

Hence, the LEED IV study reproduces the LDA+U result of Tereshchuk *et al.* [93]. The existence of a closed Pt surface layer can explain the absence of Kagome holes in the STM data of Berner and Schierbaum [86]. The different experimental settings of Baddeley *et al.* may have made their instrument more sensitive to the corrugation of the top layer, which they interpreted as signatures of the Kagome holes [83].

The optimized values for the atomic displacement, Δr_{Ce} and Δr_{Pt}, are in the range of typical values. Furthermore, the dependence of R_{P} on Δr was not strong near the optimized values. At an intermediate step of the model optimization, a distinct displacement was assigned to the additional surface atoms, in contrast to the other Pt atoms. However, the differences in the two optimized values and the improvement of R_{P} were insignificant, which is why this over-sophistication of the model was dismissed in the final optimization.

The optimized lateral lattice constant $a = 0.535$ nm is intermediate to the value that was evaluated from the LEED pattern of phase IV and the one of bulk $CePt_5$. This finding is

consistent with the scenario of lattice relaxation developed in conjunction with fig. 7.7.
The vertical lattice constant is represented by the layer spacings. The value obtained for c_{bulk} appears rather small, which might be an effect of the interface to the substrate. However, the contribution of the deeper bulk layers to the signal is small, which was one of the reasons to construct the overlayer from two unit cells only. Hence, c_{bulk} should be regarded as an approximate model parameter, its determination is not very accurate.
Averaging of the Pt layer distances that were obtained for the overlayer yields $c_{\text{ave}} = 0.2259$ nm. This value is beyond the error bars of the layer spacing that was evaluated from the STEM images, and it exceeds the value of bulk CePt_5 by nearly 3 %. However, the STEM experiment was performed on a much thicker sample, where the lateral lattice constant is supposed to have relaxed to the bulk value. In the thickness regime of the sample used for LEED IV, the lattice is laterally compressed. Hence, a vertical dilation can be explained by transverse deformation. In addition, a relaxation of layer spacings is often induced by the presence of a surface.
For a more profound interpretation of these findings, thickness-dependent LEED IV studies would be necessary. However, this level of accuracy is not required in the present work. The aim of the present LEED IV study was to clarify the crystal structure and stoichiometry of the CePt_5/Pt(111) surface intermetallics. This was successfully done for a representative sample. The general results can be transferred to samples from the complete thickness range, as already concluded from the data shown in fig. 7.6. Furthermore, with the additional Pt atoms in the surface layer, an important modification of the surface structure compared to the bulk was discovered.

7.7 Conclusions to the chapter

The results of the structural charactertization of Ce-Pt(111) surface compounds indicate that the applied sample preparation procedure produces well-ordered intermetallic films of CePt_5 on top of the Pt(111) substrate. Although six different LEED phases were identified, all seem to share the same crystal structure, as is shown by comparison of LEED IV data. The rotational alignment of the film lattice with respect to the substrate as well as the lateral lattice constant vary with the film thickness, which can be explained by subsequent lattice relaxation. While analysis of the LEED patterns particularly allowed tracking relative lattice constant changes, an accurate determination of the lateral lattice parameter was made possible for a reference phase by a refined interpretation of the diffraction pattern with the support of STM data [1], which revealed that the LEED pattern has contributions from a well-defined moiré lattice, which represents a combination of the film and the substrate lattices.
A combination of quartz microbalance measurements and a STEM cross-section allowed addressing the film profile as well as the vertical lattice parameter. The film forms with well-defined interfaces. The film thickness, which can be calculated from the initial Ce deposit, represents a meaningful parameter to characterize the samples. After this calibration, the analysis of the LEED pattern of a given preparation allows determination of the film thickness with precision up to single unit cells.
The stoichiometry of the films was evaluated from thickness-dependent Ce $M_{4,5}$ XAS data, which yielded a result in favor of CePt_5. Hence, the CaCu_5 structure can be assumed for the films. In order to confirm this assumption and to determine the surface termination, a LEED-IV study was performed in a last step. Apparently, the surface is terminated by a Pt Kagome layer. The hexagonal holes of this final layer enclose additional Pt atoms, which slightly protrude out of the surface. This result is in line with theoretical modeling of the surface and consistent with the observed robustness of the surface intermetallics against contamination.
The symmetry of the CePt_5 structure is hexagonal, which is also the local symmetry of the Ce atoms. This result provides a sound basis for modeling of crystal field effects, which is required for the interpretation of data on the electronic and magnetic properties of the films. Such data, which were obtained by Ce $M_{4,5}$ XAS and XMCD, are presented in the following chapters.

Chapter 8

The spectral shape of Ce $M_{4,5}$ XAS and XMCD

Contents

With the structural characterization of $CePt_5$/Pt(111) accomplished in chapter 7, the stage is set for the spectroscopic investigations of the present thesis. These were performed at the Ce $M_{4,5}$ absorption edges, which represent the resonant transition $3d^{10}4f^n \rightarrow 3d^9 4f^{n+1}$. In many cases, interpretation of such spectra in terms of electronic and magnetic sample properties can be done without detailed knowledge of the spectral shape, prominent examples being the XMCD sum rules (see section 5.3). However, in the case of Ce $M_{4,5}$ absorption, the spectral details bear valuable information about the $4f$ state, as is summarized in the following. In order to extract these information, the present chapter provides a detailed study of the Ce $M_{4,5}$ XAS and XMCD line shape including the attempt to theoretically reproduce the spectra.

Exemplary Ce $M_{4,5}$ XA and XMCD spectra with the typical rich multiplet structure are shown in fig. 6.1, where also a nomenclature for the substructure of the spectra is introduced. The description of spectra in the following relies on this information, which is why the reader is advised to have them ready at hand.

Following the argumentation presented in section 6.1.1, contributions from an $f^0 \rightarrow f^1$ transitions can be identified in XA spectra of most Ce compounds (features F and K in fig. 6.1 (a)) in addition to the dominant $f^1 \rightarrow f^2$ spectrum. Since the final states of the two contributions are well separated in energy, the spectrum can be described as their incoherent sum. The $f^0 \rightarrow f^1$ contribution does not display XMCD, since the initial state without $4f$ electron cannot be polarized magnetically (see the two-step model described in 5.3).

The relative weight of the $f^1 \rightarrow f^2$ and $f^0 \rightarrow f^1$ contributions is indicative of the occupancy of the $4f$ level n_f, which is a measure of hybridization with conduction states (see section 2.1.5). As is shown in fig. 1.1 (a), the Kondo energy scale is closely connected to n_f.

Ce $M_{4,5}$ XAS shows considerable dependence on the polarization state of the light, if the $4f$ level is subject to a non-spherical environment. Hence, analysis of the linear dichroism can give insights to the crystal field scheme of the material under investigation (see section 6.1.2).

As is reviewed in section 6.1.3, it has been reported in the literature that an increase of the $f^0 \rightarrow f^1$ weight is accompanied by considerable changes in the $f^1 \rightarrow f^2$ line shape. It is commonly assumed that the variations are induced by admixture of $j = 7/2$ character to the ground state and that they can be taken as a measure of this admixture, as was first proposed by van der Laan *et al.* [189]. Since a significant admixture would compromise the simple picture of a localized $j = 5/2$ state for the interpretation of magnetic results (see section 2.1), an estimate of this quantity is highly desirable.

As a consequence of the high degree of localization of the $4f$ level, the Ce $M_{4,5}$ spectrum is excellently reproduced by atomic multiplet calculations (see sections 6.1.2 and 6.3). Such calculations provide an ideal basis for quantitative evaluation of n_f, the degree of $j = 7/2$ admixture and the CF-induced linear dichroism.

Simulation of experimental spectra requires high-quality data free of experimental artifacts. In general, experimental XA spectra taken in TEY mode are subject to saturation effects that can falsify the evaluation of quantitative results (see section 5.5). Hence, the magnitude of this effect is estimated as a first step in section 8.1. This is followed by a detailed analysis of the experimentally observed line shape in section 8.2. Section 8.3 is devoted to the calculation of spectra. Finally, section 8.4 addresses remaining discrepancies between the experimental and theoretical data and provides scenarios for their explanation.

Based on the results of the present chapter, quantitative evaluations of both the $f^0 \rightarrow f^1$ weight as a function of temperature and sample thickness as well as of the CF-induced LD of $CePt_5$/Pt(111) intermetallic films are presented in chapter 9.

8.1 Analysis of TEY saturation

The effect of TEY saturation is introduced in section 5.5. As discussed for eq. 5.22, this deviation from proportionality between measured TEY signal $Y(E)$ and absorption coefficient $\mu_x(E)$ depends on the ratio of the X-ray penetration depth $\lambda_x(E) = \cos\theta/\mu_x(E)$ and the electron escape depth λ_e. The interpretation of experimental XA spectra and derived XMCD data, in particular the simulation with full multiplet calculations (see section 6.3) and the application of the XMCD sum rules (see sections 5.3 and 6.4), presupposes that the detected signal is linearly related to $\mu_x(E)$.

In order to decide whether or not TEY saturation represents a problem for a given experiment, the saturation-induced deviations have to be quantified. If the effect is serious, a correction procedure has to be developed and applied to the data. An analysis of the present Ce $M_{4,5}$ experiments on $CePt_5$/Pt(111) surface intermetallics is described in the following. The discussion is based on the model description for $Y(E)$ that is presented in section 5.5, and on the results of its application to thickness-dependent XAS data in section 7.4.

A rough estimate of the relevance of saturation can be done by comparison of λ_e and the smallest occurring value for $\lambda_x(E, \theta)$, which is usually found at the maxima of resonant peaks and for large θ. With the results for the atomic densities of Pt and Ce in the intermetallic film and the obtained values for the absorption cross-section of the isotropic spectrum at the M_4 maximum ($E_1 = 900$ eV) and in the pre-edge region ($E_2 = 870$ eV), values for the absorption coefficient can be calculated using eq. 5.3. For the assumption of $CePt_5$ stoichiometry, this yields $\mu_x(E_1) = 22.2\ \mu\text{m}^{-1}$ and $\mu_x(E_2) = 9.9\ \mu\text{m}^{-1}$, whereas the TEY electron escape depth is evaluated to $\lambda_e \approx 1$ nm. The angle of incidence was set to no higher value than $\theta = 60°$ in the present experiments, which means that $\lambda_x(E, \theta) \geq \lambda_x(E_1, 60°) = 22.5$ nm. This comparably large value is mostly due to the rather low Ce density in the film.

Hence, the influence of saturation in XAS might not be critical in the present experiments. However, when evaluating the magnetic moment via the sum rules from XMCD data for magnetized samples, things get more complicated. For one of the polarization directions, $\lambda_x(E, \theta)$ can be

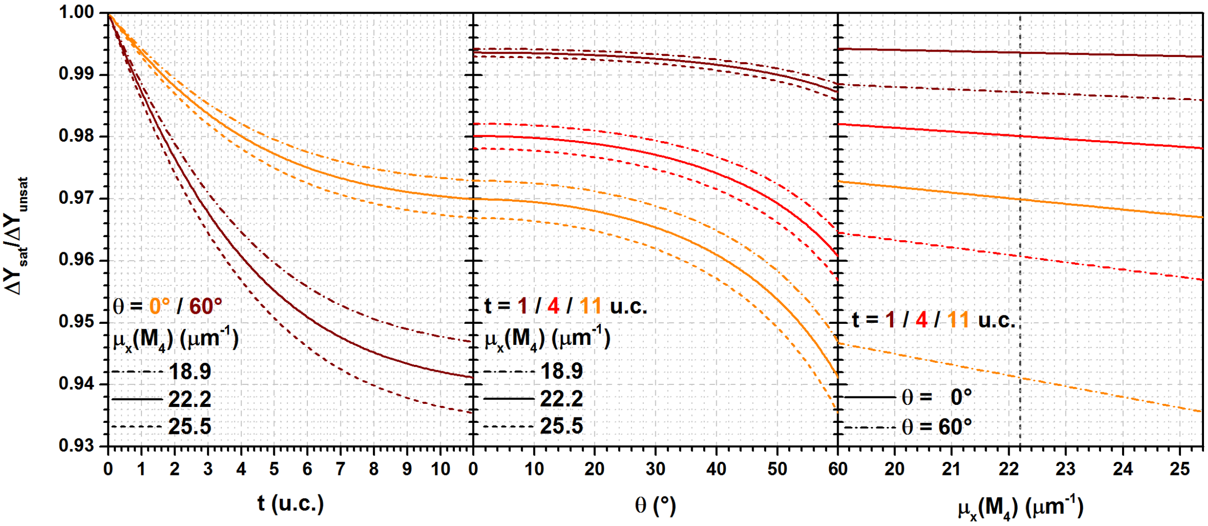

Figure 8.1: Calculated results for the deviation of the saturated TEY signal relative to a hypothetical unsaturated one according to eq. 8.1 in dependence of (a) film thickness, (b) angle of incidence and (c) absorption coefficient. Representative parameter values were chosen for the simulations, which includes the most extreme that are encountered in the present experiments.

considerably reduced compared to the non-magnetic spectrum and especially compared to the other direction. The maximum enhancement of the Ce M_4 peak over background for a sample in a magnetic field relative to the non-magnetic spectrum that was observed in the present thesis amounts to approximately 15 % (see fig. 6.1 (b)). This asymmetry, the subtraction to obtain the XMCD signal and the integration of the same to obtain the magnetic moment can lead to an error propagation that is hard to control.

Therefore, simulations of the magnitude of saturation effects were performed for the given length scales in $CePt_5/Pt(111)$ to obtain a more quantitative estimation. The relevant parameter for quantitative analysis of resonant spectra is the oscillator strength, which can be represented by the peak height over background for a given transition and energy resolution. The continuum background has to be subtracted for experimental data, it is usually approximated by a straight line.

In order to quantify the influence of saturation, the signal at the peak minus the signal at the pre-edge in presence of saturation according to eq. 5.22 is related to the same quantity for a hypothetical, unsaturated case. For the latter, $Y(E) \propto \mu_x(E)$ according to eq. 5.23. The prefactors are eliminated by the division. The full model reads

$$\frac{\Delta Y_{\mathrm{sat}}}{\Delta Y_{\mathrm{unsat}}} = \frac{\overbrace{\frac{\mu_x(E_1)}{\frac{\mu_x(E_1)}{\cos\theta}+\frac{1}{\lambda_e}}\left(1-e^{-\left(\frac{\mu_x(E_1)}{\cos\theta}+\frac{1}{\lambda_e}\right)t}\right)}^{\text{saturated, peak}} - \overbrace{\frac{\mu_x(E_2)}{\frac{\mu_x(E_2)}{\cos\theta}+\frac{1}{\lambda_e}}\left(1-e^{-\left(\frac{\mu_x(E_2)}{\cos\theta}+\frac{1}{\lambda_e}\right)t}\right)}^{\text{saturated, pre-edge}}}{\underbrace{\mu_x(E_1)\lambda_e\left(1-e^{-t/\lambda_e}\right)}_{\text{unsaturated, peak}} - \underbrace{\mu_x(E_2)\lambda_e\left(1-e^{-t/\lambda_e}\right)}_{\text{unsaturated, pre-edge}}} \tag{8.1}$$

Results of this model are shown for representative parameter values and as a function of film thickness t, angle of incidence θ and absorption coefficient μ_x in fig. 8.1. The most extreme values for each of the three parameters that were encountered in the present experiments are included. These are $t \approx 11$ u.c., $\theta = 60°$ and an XMCD-induced deviation from the isotropic spectrum[1] of $\Delta\mu_x/(\mu_x) \approx 0.15$. The simulation shows that the reduction of the relative peak height due to saturation is never larger than 7 %, and much smaller in most cases.

---

[1] compare fig. 6.1 (b) and note that the continuum background is subtracted in the present analysis of μ_x

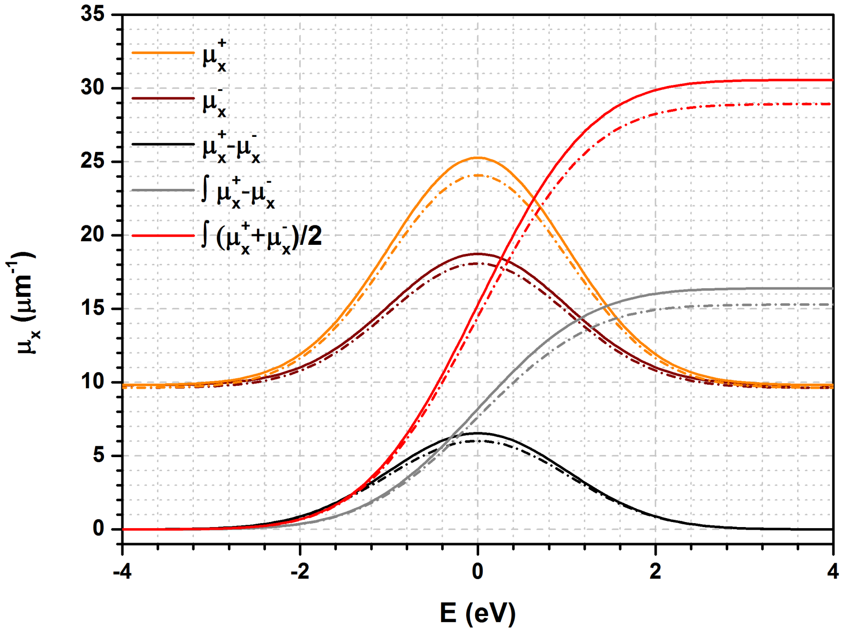

Figure 8.2: Simulated XA and XMCD spectra as well as their integrals used to estimate the impact of saturation on the XMCD sum rule evaluation for extreme experimental conditions. Solid and dash-dotted lines represent the situation without and with saturation, respectively. Note that the unit of the integrated intensity is eV/μm.

In the present thesis, quantitative evaluation of spectral information is primarily done in the application of the XMCD sum rule of the orbital moment (eq. 5.17). This involves integration of the XMCD signal as well as the non-magnetic spectrum and division of the two values. A simulation for this procedure is shown in fig. 8.2. The Ce M_4 edge is modeled as a single Gauss peak, the peak height scales with the magnetization. The difference of the spectra for the two magnetization directions reflects the maximum XMCD signal that was observed in the present thesis.

Unsaturated spectra were obtained by application of eq. 5.23. For both magnetization directions, saturated spectra were separately calculated by application of eq. 5.22. For reasons of presentation, all spectra were divided by $\lambda_e/\cos\theta$, the prefactors C^Y and I_0 were set to unity. For the saturation, the most extreme conditions of $t = 11$ u.c. and $\theta = 60°$ were assumed. The simulation thus represents a situation which was not encountered in the present work, since no such thick samples were measured at the high magnetic fields and low temperatures necessary to obtain an XMCD signal that large.

For both the unsaturated and saturated case, XMCD signals were calculated by subtraction of the two magnetization directions. The numerical integral functions are shown for these XMCD signals as well as for the non-magnetic XA spectra. The latter are not shown, they were calculated by averaging of the magnetic spectra and subtraction of the individual baseline.

The orbital magnetic moment obtained for the saturated spectra by this procedure amounts to more than 98 % of the non-saturated case. This relative error is even smaller than the estimated maximum deviation of 7 % for the peak height in XAS.

Due to the assumptions of extreme conditions in the model, the small deviations for both peak height and magnetic moment can be regarded as an upper limit for the real effect. In principle, TEY data can be corrected for saturation effects [177, 179]. However, these procedures are complex and require additional assumptions, which introduce further uncertainties to the evaluation. In the case of deviations as small as shown by the simulations presented here, these uncertainties are most likely larger than the effect that is to be corrected. Hence, TEY saturation is neglected in the following and the TEY data are regarded as proportional to $\mu_x(E)$.

8.2 Line shape analysis of the experimental spectra

Based on the results of section 8.1, artifacts in the present experimental spectra due to saturation effects are neglected. The next step towards a detailed understanding and an optimized theoretical description of the data is a thorough analysis of the experimentally observed line shape.

For this purpose, both Ce $M_{4,5}$ XAS (section 8.2.1) and XMCD (section 8.2.2) spectra are studied as a function of several experimentally accessible parameters: The angle of incidence θ with respect to the surface normal, the temperature T and the sample thickness t. For the XMCD data, the magnetic field strength B is additionally considered.

Another degree of variability is provided by the detection method for the XA signal (see section 5.4.2). A comparison of TEY and TFY data allowed drawing important conclusions concerning the continuum background and the peak shape of the recorded Ce $M_{4,5}$ spectra. These results are presented in sections 8.2.3 and 8.2.4.

8.2.1 Parameter-dependence of the XAS line shape

As is described in section 5.2, the variation of θ with circularly polarized light allows control of the relative portions of light that is polarized parallel and perpendicular to the hexagonal c-axis of the present samples. In the presence of a spatially anisotropic initial state, as induced by a crystal field (see section 2.1.2), the two polarization directions produce different spectra. Consequently, a linear dichroism can be observed in their comparison.

Fig. 8.3 (a) shows Ce $M_{4,5}$ spectra of an exemplary $CePt_5/Pt(111)$ sample for $\theta = 0°$ and $60°$ at both ends of the accessible temperature range. Both pairs of spectra clearly exhibit LD in the $f^1 \rightarrow f^2$ part. Since the initial state of the $f^0 \rightarrow f^1$ transition has no f electron and is thus not subject to CF splitting, this part of the spectrum exhibits no LD.

The LD is larger for low temperature. This result is consistent with the assumption of a CF split $4f^1$ state, since increasing population of the higher lying states with increasing temperature reduces the LD. The observation of a significant LD near room temperature indicates that the overall CF splitting of this sample is at least of the order of $\Delta E \approx 20$ meV.

The example shows that the CF can have a relevant influence in $CePt_5/Pt(111)$. This has to be considered for the interpretation of properties related to the $4f^1$ level, like the paramagnetic susceptibility. Since the LD shows significant variation in the accessible temperature range, a detailed analysis of its temperature dependence is a promising approach to determine the character and ordering of the CF split $4f$ level as well as the splitting energies. Such an analysis is presented in section 9.2. For the following discussion of the spectral shape, only isotropic spectra are considered. As introduced in section 5.2, the isotropic spectrum is characterized by equal contributions from light that is polarized along the three Cartesian coordinate directions and is thus independent of CF effects. In the present experimental setup, this is approximately achieved for $\theta = 60°$.

The isotropic $f^1 \rightarrow f^2$ spectrum should be independent of temperature. The two spectra taken at $\theta = 60°$ that are shown in fig. 8.3 (a) exhibit only small differences in the $f^1 \rightarrow f^2$ part. These reflect that the spectra are not perfectly isotropic ones, which requires $\theta = 54.7°$.

The temperature-dependence of the $f^0 \rightarrow f^1$ contribution is more clearly visible for another sample in fig. 8.3 (b). The two spectra clearly indicate that n_f is smaller at low T. This behavior is predicted by NCA results by Bickers *et al.* [27] (see section 1.1). As is reproduced in fig. 1.1 (a), the T-dependence of n_f is directly connected to the Kondo temperature in these calculations. A detailed analysis of the relative weight of $f^1 \rightarrow f^2$ and $f^0 \rightarrow f^1$ contributions as a function of temperature with the aim to estimate T_K is presented in section 9.1.2.

Comparison of the spectra in figs. 8.3 (a) and (b) reveals a significant influence of the sample thickness on the spectral shape. The relative weight of the $f^0 \rightarrow f^1$ contribution is affected as well as details of the $f^1 \rightarrow f^2$ multiplet. A representative collection of spectra from the whole thickness range that was investigated in the present work is shown in fig. 8.3 (c). As can be seen in the inset, the relative $f^0 \rightarrow f^1$ weight varies non-monotonously with t. Of all the

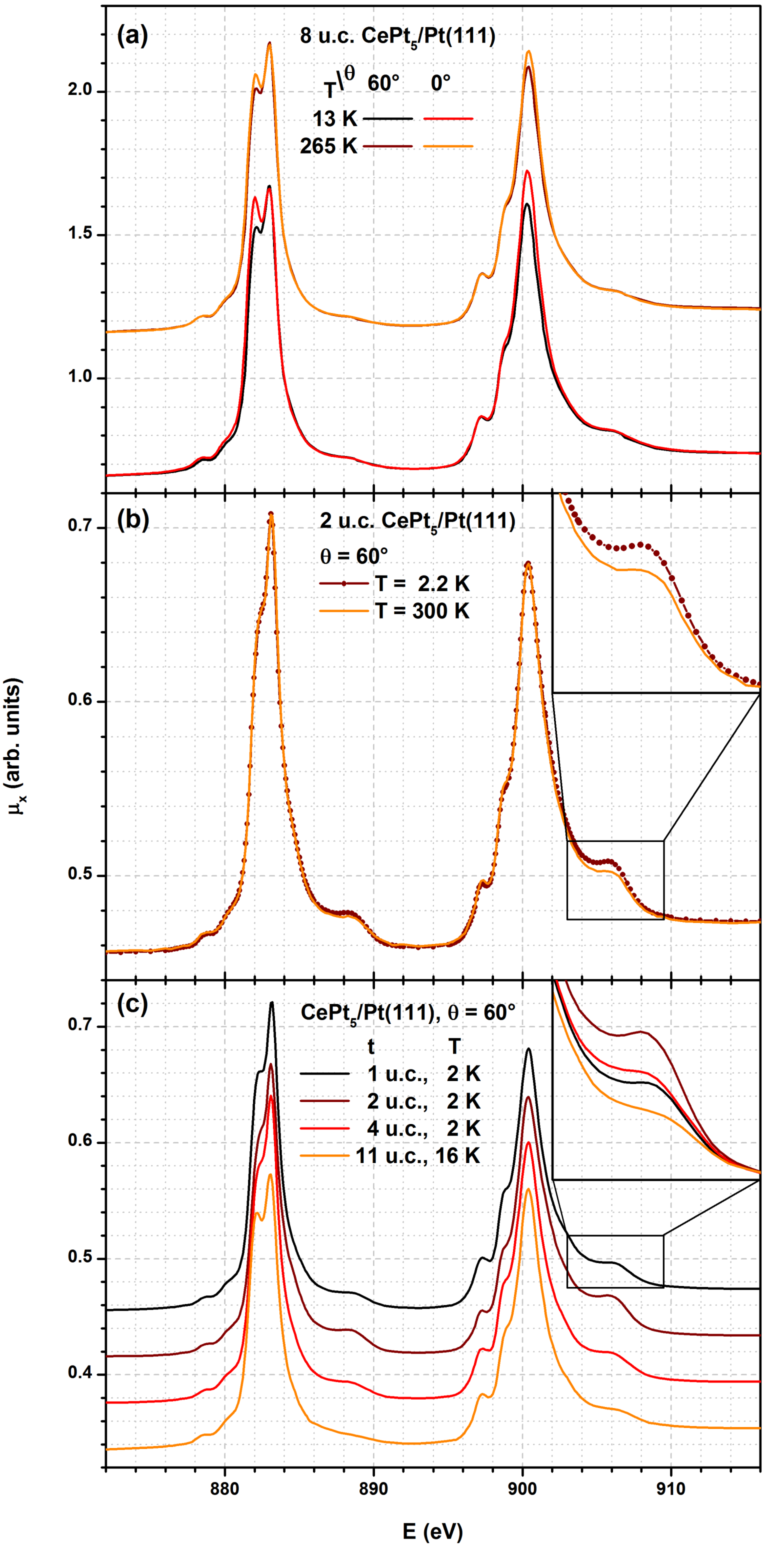

Figure 8.3: Ce $M_{4,5}$ XA spectra of $CePt_5/Pt(111)$ samples with different combinations of θ, T and t. (a) Spectra for $t = 8$ u.c. measured at BESSY and adjusted to equal heights of the M_5 maxima. The spectra taken at different θ show T-dependent linear dichroism. (b) Spectra for $t = 2$ u.c. taken at $\theta = 60°$. The data were measured at SOLEIL and adjusted to equal $f^1 \to f^2$ weight. The inset is a blow-up of the $f^0 \to f^1$ contribution at the M_4 edge, which shows variation with T. (c) Spectra of samples with various thicknesses measured at $\theta = 60°$ and at the lowest temperature available. The $t = 11$ u.c. spectrum was taken at BESSY, the others at SOLEIL. The spectra were adjusted to equal height of the M_4 peak and are displayed with a constant offset. The inset shows the $f^0 \to f^1$ contributions at the M_4 line without offset, indicating the variations of this feature. The inset has the same size and scale as the one of panel (b), the dark red curves in both insets are equal.

data recorded in the present work, the spectra for $t = 2$ u.c. and 11 u.c. exhibit the largest and smallest relative $f^0 \rightarrow f^1$ weight, respectively. A comparison of the insets of panels (b) and (c) shows that the magnitude of the observed variation of the relative $f^0 \rightarrow f^1$ weight as a function of thickness is larger than the temperature-dependent one.

As is introduced in section 2.1.5, the $f^0 \rightarrow f^1$ weight is connected to the hopping matrix element between the $4f$ level and conduction states, which represents a measure of the hybridization strength. Hence, the degree of hybridization in $\mathrm{CePt_5}$/Pt(111) can be tuned by variation of the intermetallic film thickness t. This is a highly interesting feature of the material, since it allows experimental control of one of the most important parameters for the study of Kondo and heavy fermion physics.

The progression of the relative $f^0 \rightarrow f^1$ weight with t is analyzed in more detail in section 9.1.1, where also a model scenario for the observations is presented. In the context of the present spectral shape analysis, the focus is laid on the line shape variations in the $f^1 \rightarrow f^2$ part that accompany the variation of the relative $f^0 \rightarrow f^1$ weight.

Observation of such line shape variations has been reported in several previous studies. This is reviewed in section 6.1.3, where a list with four key observations is presented. The following discussion refers to the items in this list.

The data of the present work confirm the often made observation that the multiplet structure is smeared out (1) [187–192]. For the $\mathrm{M_5/M_4}$ weight ratio (2), values in the range $w(M_5)/w(M_4) \approx 0.814 \ldots 0.850$ were found, with systematically smaller values for higher $f^0 \rightarrow f^1$ weight. This qualitatively and quantitatively reproduces earlier results [189, 191, 192].

A systematic increase of the energy separation of the two lines with increasing hybridization (3), as reported by Finazzi *et al.* [191, 192], was not observed in the present work. However, the maximum shift in these works amounts to $\Delta E \approx 0.15$ eV, and their investigation includes a considerably larger range of $f^0 \rightarrow f^1$ weights. The effect in the present $\mathrm{CePt_5}$/Pt(111) samples would certainly be much smaller. No dedicated measurement series was performed to identify the effect in $\mathrm{CePt_5}$/Pt(111) with appropriate sensitivity. The detection threshold for the effect is limited by a lack of comparability of the monochromator settings between different beamtimes and thermal instabilities in the beamline optics during the experiments (see sections 5.4.1 and 5.4.5).

The observation of van der Laan *et al.* regarding additional intensity at the high-energy side of the $\mathrm{M_4}$ line (4) [189] is systematically confirmed by the present data and can be extended to the $\mathrm{M_5}$ line as well. At both edges, the flank at the high-energy side of the main peak gets broader with increasing $f^0 \rightarrow f^1$ weight (features E and J in fig. 6.1).

It should be noted at this point that the observed increase in intensity at the high-energy flanks is not due to oxidation of the sample. This suspicion arises from the fact that the spectrum of $\mathrm{CeO_2}$ has its main peak at a slightly higher photon energy than metallic Ce and common Ce compounds [188]. Indeed, signatures of gradual oxidation at these photon energies were observed for individual $\mathrm{CePt_5}$/Pt(111) samples, which is presented in appendix A.3.

The systematic connection of an increasing $f^0 \rightarrow f^1$ weight and broadening high-energy flanks for several different preparations indicates that the preparation conditions are not responsible for this feature. Furthermore, this effect is also visible in many published spectra of various materials [61, 188, 190, 192], albeit only van der Laan *et al.* explicitly mention it [189].

Further support that the broadening does not occur due to oxidation is provided by fig. A.3 (b). It shows spectra of a $t = 2$ u.c. sample directly after preparation *in situ* and after the sample was removed from the UHV environment and stored under ambient conditions *ex situ* for several months. The *in situ* spectrum clearly features the large $f^0 \rightarrow f^1$ weight typical for this film thickness, as well as the accompanying characteristics in the line shape of the $f^1 \rightarrow f^2$ contribution. In contrast, the *ex situ* spectrum exhibits a very small $f^0 \rightarrow f^1$ part, a sharp $f^1 \rightarrow f^2$ multiplet substructure and less broad high-energy flanks at both edges. If the broad flanks were induced by oxidation, the sample would be less oxidized after contact to ambient air. Since this is very unlikely, the observed $f^1 \rightarrow f^2$ line shape variations are fully attributed to variations in the hybridization strength.

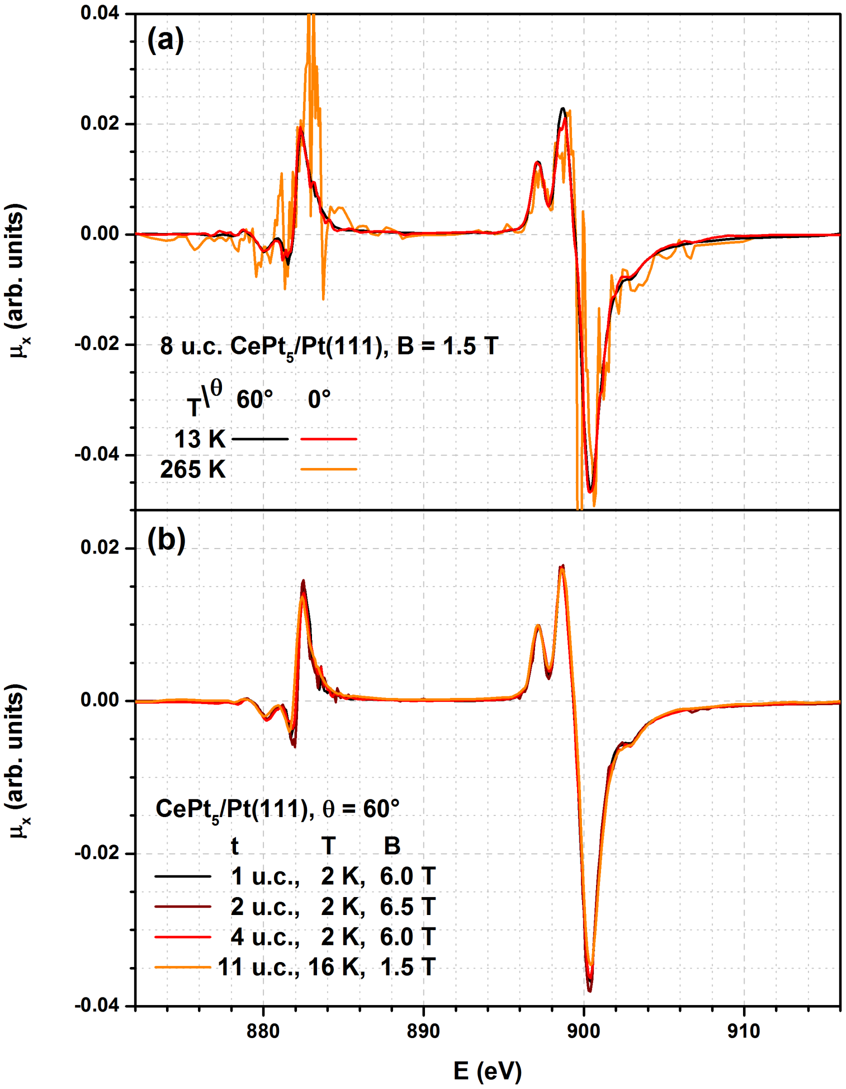

Figure 8.4: Ce $M_{4,5}$ XMCD spectra of $CePt_5$/Pt(111) samples with different combinations of θ, T, t and B. In each panel, the spectra are adjusted to equal magnitude. (a) XMCD of a sample with $t = 8$ u.c. measured at BESSY, corresponding to fig. 8.3 (a). (b) XMCD of samples with various thicknesses measured at $\theta = 60°$ and at the lowest temperature available, corresponding to fig. 8.3 (c). The $t \approx 11$ u.c. spectrum was taken at BESSY, the others at SOLEIL. Note the different temperatures and magnetic field strengths, as given in the legend.

8.2.2 Constancy of the XMCD line shape

The XAS data of $CePt_5$/Pt(111) that are shown in fig. 8.3 reveal a strong dependence of spectral details on the angle of incidence θ, the sample temperature T and the intermetallic film thickness t. This gives rise to the question to what extent the line shape of the XMCD spectra, which are derived from the XAS data, also depends on these parameters. This allows important conclusions regarding the possible admixture of $j = 7/2$ character to the ground state.

Fig. 8.4 (a) shows exemplary Ce $M_{4,5}$ XMCD data corresponding to three of the four XA spectra in fig. 8.3 (a), which have been adjusted to equal magnitude. The two low-T spectra coincide within the given uncertainties. Those are primarily introduced by the larger noise in the $\theta = 0°$ spectrum, which arises from the smaller absolute XMCD magnitude in the raw data.

Since the paramagnetic polarization strongly decreases with increasing temperature, the noise is drastically enhanced at $T = 265$ K. This strongly reduces the reliability of conclusions regarding possible changes in the line shape with T. Nevertheless, it can be said that the characteristic features of the XMCD are conserved regarding both their energy position and magnitude. The presentation of the high-T spectrum at $\theta = 60^\circ$ in analogy to fig. 8.3 (a), which is also very noisy, is omitted for reasons of clarity.

The results of fig. 8.4 (a) suggest that the XMCD line shape is constant under variation of the angle of incidence and the temperature. In panel (b), XMCD of samples with varying film thickness t are shown in correspondence to fig. 8.3 (c). The spectra coincide very well, in particular regarding the fact that they were recorded on different samples and at different beamtimes. The $t \approx 11$ u.c. spectrum was measured at BESSY with worse energy resolution compared to the others, which were all taken at SOLEIL. Among those, the $t = 2$ u.c. spectrum was recorded at a different beamtime with slightly better energy resolution.

The differences in the resolution can explain the observed small degree of disagreement in the four spectra. The spectral shape is also qualitatively well in line with all published data for materials with moderate hybridization that are known to the author (see section 6.1.4 for references).

Apparently, the variations in the $f^1 \to f^2$ XAS line shape as a function of sample thickness do not affect the XMCD line shape. If these were induced by an admixture of $j = 7/2$ states, this should also affect the XMCD [191, 192]. If such admixture is not responsible for the observed variations in XAS, an alternative explanation is needed. This is of particular importance if a theoretical simulation of spectra with varying degree of hybridization is aimed as, as in the present work. This issue is further addressed in section 8.3.2.

8.2.3 Continuum absorption in Ce $M_{4,5}$ XAS

The continuum absorption (see section 5.1.2) is usually not considered explicitly in calculated XA spectra. However, it contributes to the experimental data, which means that the stepped continuum background either has to be subtracted from the experimental signal or it has to be added to the theoretical simulation. The former is also required for quantitative evaluation of oscillator strengths from experimental spectra, like for the XMCD sum rules. Since both procedures require a conception of the spectral signature of continuum absorption, the present section is devoted to the analysis of the continuum background of Ce $M_{4,5}$ XA spectra.

As is apparent in fig. 6.1, continuum steps in the Ce $M_{4,5}$ spectrum are rather unobtrusive compared to the resonant absorption lines. The difference in the background before and behind the resonant lines amounts to only 8 % of the maximum peak height.

For pure Ce metal, this has been explained by the fact that the valence states that are available for the excitation of an electron from the $3d$ shell are reduced to mainly $6p$ states by the dipole selection rules (see section 5.1.1). This excitation has a small transition matrix element M_{if} compared to the resonant excitation to the $4f$ shell due to the small DOS $\rho^{6p}_{\mathrm{DOS}}(\epsilon_{\mathrm{F}})$ of the $6p$ states at the Fermi edge [61, 184]. For Ce compounds, the step height is reported to increase with the amplitude of the $f^0 \to f^1$ peak [61]. While this might hint at an increasing $\rho^{6p}_{\mathrm{DOS}}(\epsilon_{\mathrm{F}})$ with increasing hybridization, the observation of a comparably small step remains true for all Ce $M_{4,5}$ spectra that are presently known to the author (see section 6.1 for references).

While the total edge jump in the spectrum can be identified rather easily, the question of the number of steps and their positions is more challenging. As with the oscillator strength of the resonant lines, one could expect that each edge exhibits a step the height of which is proportional to the number of states that are available for core-hole formation. However, the strong configuration interaction that is present in Ce disallows application of this simple picture, as noted in chapter 6.

Furthermore, the resonant lines are expected to be “exciton-like” due to the strong $3d$-$4f$ Coulomb interaction, which means that they appear at considerably lower energies than the corresponding continuum steps. Fuggle *et al.* mention an energy separation of $\Delta E \approx 10\,\mathrm{eV}$ [61]. Consequently, the M_5 line should not be superimposed by a step, while the M_4 line, which extends over a broader energy range, could be superimposed by both the M_5 and M_4 continuum steps.

All published spectra that are presently known to the author indicate the presence of an edge jump somewhere below M_4. Fuggle *et al.* also identified a smaller step below M_5, which they describe as puzzling. Thole *et al.* associate a very broad feature in the spectra of the heavier

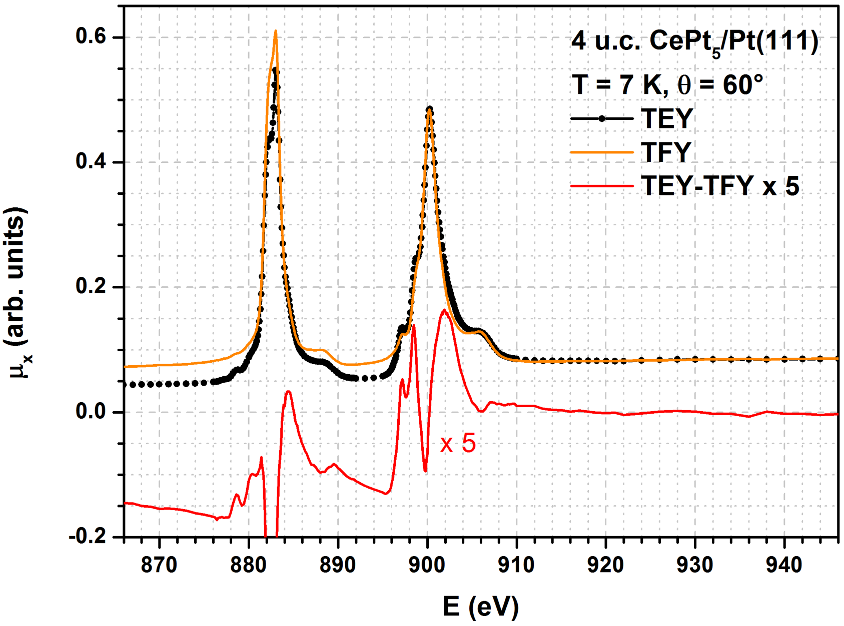

Figure 8.5: Comparison of simultaneously measured TEY and TFY Ce $M_{4,5}$ spectra of a CePt$_5$/Pt(111) sample with $t = 4$ u.c. at $T = 7$ K and $\theta = 60°$ measured at SOLEIL. The difference of the spectra gives access to the continuum background that is contained in the TEY spectrum only.

rare earths with the M_5 continuum step [184]. This suggests that the step is not very sharp for Ce as well.

Regarding the data of the present thesis, an approach to visualize the continuum steps is presented in fig. 8.5. Here, simultaneously measured TEY and TFY Ce $M_{4,5}$ spectra of a $t = 4$ u.c. CePt$_5$/Pt(111) sample are compared (black and orange lines, respectively). The spectra were offset and multiplied by constants to match in the post-edge region and at the M_4 peak. The resonant lines in the two datasets show certain distinctions, but the most striking difference is the fact that the TFY data lack a continuum step at all. Apparently, the excitation associated with the continuum absorption seems to have a negligible probability for radiant relaxation (compare section 5.4.2).

As a consequence, the difference of the two spectra (red line in fig. 8.5) is indicative of the continuum step. The significant edge jump at the M_4 line is clearly visible, although no conclusions can be drawn about the number of steps or their exact position. This is due to artifacts arising from different relative peak heights and a different peak shape at M_4 in the two spectra. These issues are further addressed in section 8.2.4.

Concerning the M_5 edge, the presence of a step cannot completely be excluded. The maximum step height is estimated to amount to 25 % of the total jump, which translates to 2 % of the maximum resonant peak height. The main problem is to identify where the baselines before and in between the edges have to be positioned. The TFY peaks seem to have a more Lorentzian-like shape (see fig. 6.3) with broader tails compared to the TEY data, which contributes to the difference in a wide energy range to both sides of the lines. For the pre-edge region, this could be solved by a further extension of the measurement range to lower energies.

An extended pre-edge range would generally be desirable, since it facilitates the identification of the background slope. The spectra shown here already have an extended range compared to the data shown by Fuggle *et al.* [61]. Their short measurement range might be the main reason for their finding of a significant step superimposed to the M_5 line.

In any case, the possible step at M_5 is small enough to neglect its impact on the quantitative evaluation of oscillator strengths. In the following, a single step is assumed below the M_4 edge. Furthermore, quantitative analysis of XA spectra often necessitates to assign absolute $\mu_x(E)$ values to the measured signal. A common practice is to adjust the total edge jump of an experimental spectrum to the corresponding step in the data by Henke *et al.* [160] (compare fig. 5.2).

For Ce $M_{4,5}$ spectra, this might be misleading. In their transmission study of Ce, Fernández-Perea *et al.* compare measured Ce $M_{4,5}$ transmission data to the Henke values [178], which reveals a significant discrepancy behind the edge. The use of post-edge data for quantitative conclusions is therefore avoided in the present thesis.

8.2.4 Autoionization effects in Ce $M_{4,5}$ XAS

If different final states of an atom can be produced for a certain excitation energy, these final states can interact. This requires that the different final states can be converted to each other by second-order processes, which means that the final states can be produced via different paths. Quantum mechanically, the result is a mixed final state, which possesses some of the properties of each participating state [44].

The coincidence of transition energies is highly unlikely for two otherwise independent resonant final states. However, excitations involving continuum states are usually superimposed to resonant transitions in absorption spectra. This is reflected by the sum in eq. 5.5. If the resonant and the continuum final states interact, the absorption cross-section cannot be described by a simple sum of the two contributions, since interference effects have to be taken into account.

The interaction of a resonant and a continuum state is usually very small, but becomes significant near the ionization threshold of the the continuum state [44]. Hence, interference effects in absorption can only be observed if the resonance energy is close to, but larger than the energy of a continuum step.

The admixture of continuum state character to the discrete, resonant state has two main consequences: First, the excited atom can autoionize by spontaneous emission of an electron. A special case of autoionization is the Auger-Meitner effect. It is of importance for AES (see section 3.4) and for TEY detection of XAS (see section 5.4.2).

Second, the resonant absorption profile becomes asymmetric, which can be regarded as a combination of the symmetric isolated resonant profile and the asymmetric continuum step. This asymmetric peak shape is called a Fano-profile, since it was shown by Fano in 1961 that it can be expressed by a rather simple function [248] (see eq. 6.5). Since the transition profile has to be known for the simulation of experimental data, it is important to analyze their occurrence in the present data.

The possibility of autoionization effects in $M_{4,5}$ XA spectra of rare earths was pointed out by Karnatak *et al.* in 1981 [263], who observed an asymmetric line shape for La. La is particularly suited for such studies, since it does not exhibit the rich multiplet structure arising from multiple f-electrons, but features single, well-isolated lines in the $M_{4,5}$ spectrum. In the same year, Motais *et al.* [264] gave an alternative explanation for the appearance of an asymmetric line shape in La, but this idea was refuted by Thole *et al.* in 1985 [184]. De Groot and Kotani treat autoionization in La XAS in terms of many-body charge transfer [59].

Thole *et al.* convoluted the M_4 line of their calculated spectra for the whole Lanthanide series with a Fano profile instead of a Lorentz profile in order to reproduce the experimental data. While this approach was not continued in more recent studies of calculated Ce $M_{4,5}$ spectra [167, 194, 195, 197, 215–217], the data of the present thesis are strongly indicative of asymmetry at the Ce M_4 edge. This is best seen in the comparison of TEY and TFY data in fig. 8.5. In the region between the two main lines, the TFY spectrum has a distinct positive slope, while the TEY spectrum is more or less constant over a considerable energy range. The difference curve clearly reflects this observation.

The positive slope in the TFY data corresponds to the extended tail of a Lorentz profile at the M_4 line. During modeling of the experimental spectra, it became obvious that the steep low-energy flank of the M_4 line in TEY cannot be reproduced by Lorentz convolution of the calculated transitions. Convolution with a Fano profile solves this issue. The exemplary profiles that are shown in fig. 6.3 illustrate this argument.

The considerations concerning the positions of the continuum step that were made in section 8.2.3 allow construction of a consistent scenario for the interaction of resonant and continuum excitation. The M_5 edge is not located in the direct vicinity of a continuum step. Hence, no

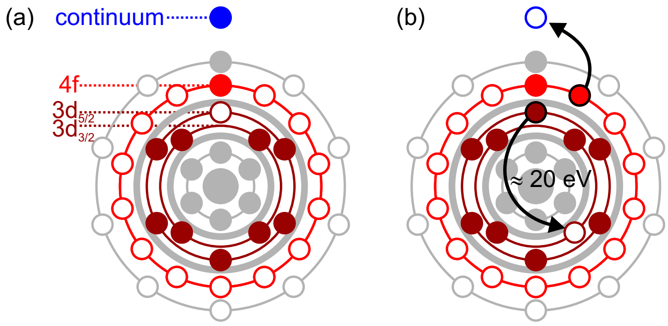

Figure 8.6: (a) Final state of Ce M_5 continuum absorption (compare fig. 5.1). (b) Final state of M_4 resonant absorption. The black arrows indicate a subsequent autoionization process that leads to the same final state as in (a).

asymmetry is induced by interaction with continuum states. The M_4 edge is superimposed to stepped background, which is at least in part produced by the M_5 continuum step. If the M_5 threshold is located at a slightly lower photon energy than the M_4 resonance, the requirements for interference and an asymmetric line shape in absorption are met.

In fig. 8.6, the two relevant processes are schematically drawn. Panel (a) shows the final state of continuum excitation of a $3d_{5/2}$ electron in analogy to fig. 5.1 (c). Panel (b) shows the final state of resonant $3d_{3/2} \rightarrow 4f$ excitation. This excitation can be followed by the autoionization process that is indicated by the black arrows. A $3d_{5/2}$ electron relaxes to the $3d_{3/2}$ shell. The gained energy of $\Delta E^{3d}_{\mathrm{SOC}} \approx 20$ eV is transferred to one of the $4f$ electrons, which is thus excited to the continuum. This results in a final state that is identical to panel (a). Hence, the two processes can interfere with each other.

The presence and absence of autoionization effects can be an explanation for the different line shapes in TEY and TFY, respectively, as shown in fig. 8.5. This observation is consistent with the presence respectively absence of a continuum step. The continuum excitation channel does not exist in TFY, but it does in TEY, where it also seems to affect the line shape of the resonance. It should be noted that the only other comparison of Ce $M_{4,5}$ TEY and TFY spectra that is known to the author does not show this effect. The data shown by Dallera *et al.* do not show a continuum step at all [65], even for TEY, which suggests that corrections have been made to the spectra for the presentation.

Furthermore, it is remarkable how well the general shape of the spectra of Dallera *et al.* agrees compared to the data shown in fig. 8.5. There are two likely sources for differences in TEY and TFY data. First, the different information depth makes the two methods differently sensitive to possibly altered surface properties. Second, both methods can be subject to distortions in the spectrum. These effects are called saturation for TEY and self-absorption for TFY and are introduced in section 5.4.2.

Compared to the bulk samples of Dallera *et al.*, the influence of altered surface properties should be of lesser importance for the thin films investigated in the present work, where the TEY information depth still covers most of the sample thickness. The same is true for self-absorption effects. In analogy to TEY saturation, those depend on the sample thickness and the Ce density, which are both much smaller for the intermetallic films. Hence, the good agreement of the spectra of Dallera *et al.* is puzzling compared to the deviations that are observed in the present work.

Whether or not Dallera *et al.* applied correction procedures to their data is not commented on in their publication. Since the mentioned effects are not controlled in the present work and the amount and quality of available data is rather low, the TFY spectra were not used for further quantitative evaluation.

8.3 Theoretical description of isotropic spectra

The isotropic spectrum of a certain transition is the average of nonmagnetic spectra for all polarization directions. It can be produced by averaging the spectra for the three Cartesian polarization directions as defined by eq. 5.16. This corresponds to the average of the spectra for all possible, potentially anisotropic initial states in the given j subspace (see section 2.1). For circularly polarized light in the presence of magnetization, both directions of CPL must additionally be averaged to obtain a nonmagnetic spectrum. This usually equals the average of the spectra for opposite magnetization directions (compare section 5.3).

The isotropic spectrum is insensitive to spatial anisotropy and magnetization of the initial state. In the present context, this means that it is not affected by the relative population of crystal field split initial states and is thus independent of the CF energies and the temperature. Therefore, isotropic data are used for the analysis of XA spectra in the present work regarding every other effect than the CF induced linear dichroism (compare fig. 8.3).

The isotropic spectrum is the point to start from for the theoretical simulation of XAS data, which can be done based on the full multiplet calculations that are introduced in section 6.3. Its independence of the CF scheme keeps the parameter space manageable. The remaining parameters, including the HF reduction values and parameters for the broadening (see section 6.3.2), are determined by the simulation of isotropic experimental data. These parameters can then be adapted for simulations of non-isotropic data.

In addition to the determination of simulation parameters, there are further reasons to investigate the isotropic spectrum theoretically: As introduced in section 6.1.3, the $f^1 \rightarrow f^2$ line shape can bear signatures of the j character of the initial state under investigation. The presence and magnitude of an admixture of $j = 7/2$ states has consequences, e.g., for the interpretation of magnetic data, since the g factor is different (see section 2.1.1). Furthermore, the relative weight of the $f^0 \rightarrow f^1$ and $f^1 \rightarrow f^2$ transitions can only be adequately quantified if all contributions are well characterized (see section 6.2).

8.3.1 The pure $j = 5/2$ initial state

The starting point for the full multiplet calculations of Ce $M_{4,5}$ XA spectra is the pure atomic $j = 5/2$ Hund's rule ground state with a single $4f$ electron (see section 2.1.1). It characterizes the $f^1 \rightarrow f^2$ transition if two conditions are fulfilled:

First, the total crystal field splitting has to be small compared to the spin-orbit splitting. Otherwise, the CF can significantly mix states from the $j = 5/2$ and $j = 7/2$ subspaces, since the respective off-diagonal elements cannot be considered small compared to the energetic separation of the states[2].

Second, the hybridization strength, which is connected to the Kondo temperature (see chapter 1 and section 2.1.5), should be small. It is known that Ce compounds with high hybridization exhibit characteristic changes in their Ce $M_{4,5}$ XAS and XMCD line shape, which can be attributed to admixture of $j = 7/2$ character to the initial state (see section 6.1.3).

The two conditions are related to each other, in the same sense as ionic and ligand crystal field effects are (see section 2.1.2). Nevertheless, they are treated separately here with reference to the terms as used in the literature.

Both conditions are well fulfilled for many Ce compounds. The ionic approach, which means to analyze Ce $M_{4,5}$ spectra and particularly the CF-induced LD in terms of a pure $f^1 \rightarrow f^2$ transition from the $j = 5/2$ ground state, has been successfully applied to a considerable number of materials by the group of Tjeng [47, 167, 194, 195, 197, 214–217].

For $CePt_5$/Pt(111) surface intermetallics, the applicability of this approach first has to be verified. Regarding the crystal field, Lueken *et al.* found a total splitting of $\Delta E_{\mathrm{CF}} \approx 76$ meV for

---

[2] An example for a material where the $j = 5/2$ assumption breaks down due to a large CF splitting is $CeRh_2B_3$, which is characterized by a total CF splitting of $\Delta E_{CF} \approx 500$ meV. Experimental XAS data of this unusual material along with calculated spectra can by found in [47].

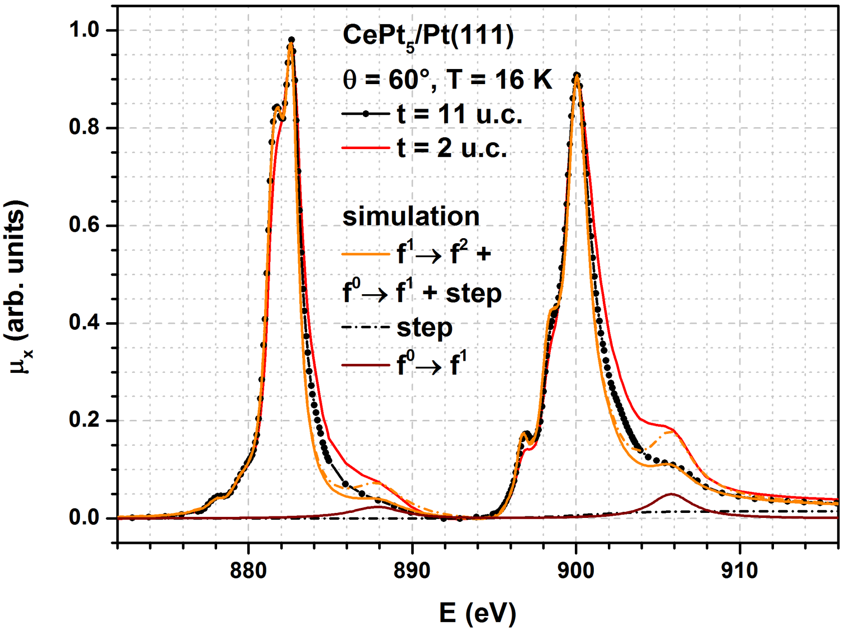

Figure 8.7: Theoretical simulation of the experimental Ce $M_{4,5}$ spectrum of a CePt$_5$/Pt(111) sample with $t \approx 11$ u.c. at $T = 16$ K and $\theta = 60°$. Details of the calculation are given in the text. The experimental spectrum of a sample with $t \approx 2$ u.c. that was taken under comparable conditions is also shown. The dashed orange line represents an adjustment of the calculated $f^0 \rightarrow f^1$ contribution to this spectrum. The experimental data were obtained at BESSY.

CePt$_5$ bulk material. This is a rather large value compared to many Ce compounds[3], but still considerably smaller than $\Delta E^{4f}_{\mathrm{SOC}} \approx 300$ meV. The effect of the CF in the thin films might be different from bulk material due to lattice strain and the breaking of the symmetry at the interfaces. Since no respective data for the surface intermetallics are available in the literature, the bulk value is taken as a first reference point. The results of the present thesis indicate that the total splitting is considerably smaller in the surface compounds (see sections 9.2 and 10.4). The condition for the hybridization strength is more critical. As is discussed in section 8.2.1, it varies with the sample thickness. The maximum weight of the $f^0 \rightarrow f^1$ contribution at $t = 2$ u.c. (see fig. 8.3 (c)) is significantly larger than for all of the materials that were investigated by Tjeng *et al.*, and the accompanying changes in the $f^1 \rightarrow f^2$ spectral shape might indicate that the ionic approach already breaks down.

While the investigation of this transition is one of the points of interest here, the first approach to the calculations is best done for a sample with small $f^0 \rightarrow f^1$ weight, where the ionic picture is applicable. Since the $f^0 \rightarrow f^1$ weight decreases with t for $t > 2$ u.c., the data of the thickest film available were taken for these simulations. This is the spectrum for $t \approx 11$ u.c. shown in fig. 8.3 (c). The $f^0 \rightarrow f^1$ contribution in this spectrum is still more distinct than for most of the compounds that were analyzed by Tjeng *et al.* However, it represents the best dataset for this purpose that has been obtained on CePt$_5$/Pt(111) in the present work.

For the simulation, the $f^1 \rightarrow f^2$ and $f^0 \rightarrow f^1$ spectra were calculated independently and added incoherently (see sections 2.1.5 and 6.3). The same reduction factors for the HF parameters were applied to both calculations. In order to resemble the experimental data, the calculated spectrum was treated as described in section 6.3.2. The isotropic spectrum was produced by averaging spectra with linear light polarization parallel to the three Cartesian directions.

Fig. 8.7 shows the experimental spectrum (black) along with the best simulation that was found (solid orange). The agreement between experiment and simulation is exceptionally high. Remarkable differences only occur at the high-energy flanks of both edges (features E and J in fig. 6.1) and at the smaller low-energy features of the M_4 line (G,H). This will be discussed

---

[3] see, e.g., the collection of materials that are analyzed in [47]

$\beta_{\mathrm{SI}}^{4f\text{-}4f}$	$\beta_{\mathrm{SI}}^{3d\text{-}4f}$	$\beta_{\mathrm{SOC}}^{3d}$	$\beta_{\mathrm{SOC}}^{4f}$
0.6	0.8	0.98	1.0

$\Gamma_B^{\mathrm{M}_5}$ (eV)	$\Gamma_A^{\mathrm{M}_5}$	$\Gamma_B^{\mathrm{M}_4}$ (eV)	$\Gamma_A^{\mathrm{M}_4}$	q^{M_4}	$\Gamma_{f^0\to f^1}^{\mathrm{M}_5}$ (eV)	$\Gamma_{f^0\to f^1}^{\mathrm{M}_4}$ (eV)
0.993	0.049	1.501	0.199	10.5	4.0	3.1

$\mathcal{A}$ (arb. units)	ΔE (eV)	$\mathcal{A}_{f^0\to f^1}$	$\Delta E_{f^0\to f^1}$ (eV)	E_{st} (eV)	Γ_{st} (eV)
2.96	891.5	0.066	3	900.5	2

Table 8.1: Parameters of the simulation shown in fig. 8.7 (solid orange line) as introduced in section 6.3.2. Top: Reduction factors of the HF parameters. Middle: Parameters of the lifetime broadening. Bottom: Amplitudes, energy shifts and parameters of the continuum step.

below.

While the high reproducibility of experimental rare earth $M_{4,5}$ spectra by atomic calculations was already noticed in 1985 by Thole *et al.* [184], two additions to their approach were made here that further improved the agreement: The assignment of different reduction factors to the $4f$-$4f$ and $3d$-$4f$ SIs and the use of energy-dependent lifetime broadening. Both aspects were adopted from the works of the Tjeng group. However, these authors ignored the presence of autoionization effects at the M_4 edge, which especially concerns the adjustment of the low-energy features (G,H).

A possible point of criticism for the present approach is the resulting large number of parameters in the model. This is counterweighted by the large amount of information that is contained in the rich multiplet structure of the spectrum. Furthermore, the parameters are physically motivated and they have distinguishable effects on the spectrum (see section 6.3.2), so there is practically no ambiguity in the fitting procedure.

The parameter values of the optimized simulation are given in tab. 8.1. The reduction factors for the HF values (top section) are well in line with the results of the Tjeng group, $\beta_{\mathrm{SI}}^{3d\text{-}4f}$ also equals the value of Thole *et al.*

For the lifetime parameters (middle section), no details have been published by Tjeng *et al.* The Γ_B values at the main peaks of both edges are significantly larger than values published by Thole *et al.* [184, 189], but a direct comparison is difficult due to the different approaches. The asymmetry parameter q is in the range 8 to 12 that is spanned in the publications by Thole *et al.* A comparison of the present results for the lifetime widths to calculated individual transition widths with the t-matrix approach would be desirable, but the only publication on this approach for Ce $M_{4,5}$ spectra that is currently known to the author gives no detailed values [249].

The results for the lifetime widths of the $f^0 \to f^1$ contribution at the two edges are surprising, since the width is larger at the M_5 edge with lower energy. Taking each edge separately, the margin for the optimization of the widths is certainly rather large. This is due to the fact that only the high-energy flank of the peak can be clearly identified. Furthermore, the $f^0 \to f^1$ contribution is rather small in the chosen spectrum, especially at the M_5 edge, where additionally the data point density is very low. To address this problem, the given width parameters were chosen in accordance with a spectrum of a sample with $t \approx 2$ u.c., which has the largest $f^0 \to f^1$ contribution obtained in the present work. The experimental spectrum and a calculation with the parameters of tab. 8.1 but an altered relative $f^0 \to f^1$ amplitude of $\mathcal{A}_{f^0\to f^1} = 0.156$ are shown in fig. 8.7 as the solid red and dashed orange curves, respectively.

The need for a broader $f^0 \to f^1$ peak at the M_5 edge is a consequence of the fact that the peaks at both edges in the calculated spectrum have to be adjusted to the experiment simultaneously. The problem does not occur without this restriction, as can be seen in the analysis by Okane *et al.* [196]. Furthermore, the discrepancy might well be connected to the inability of the calculations to reproduce the broadened high-energy flanks at both edges. This broadness is strongly enhanced

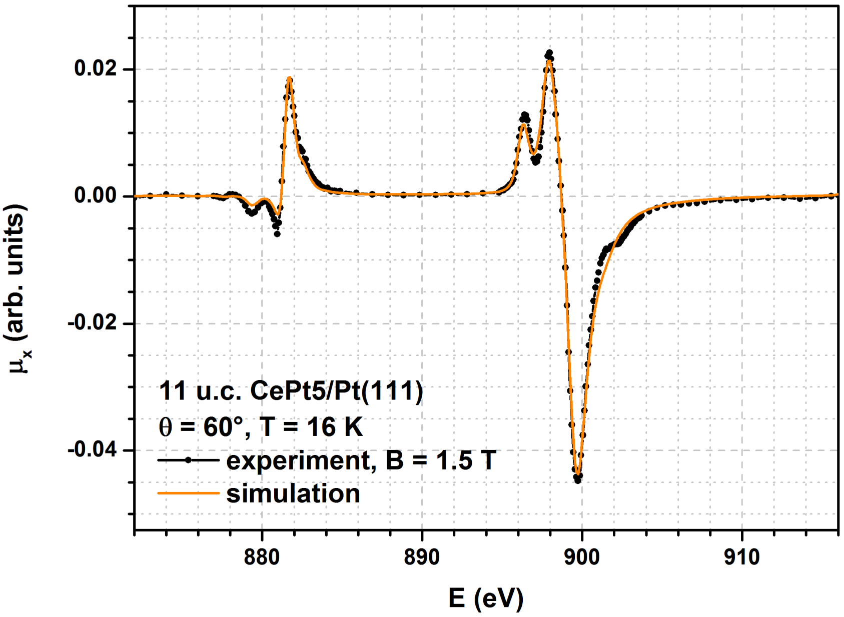

Figure 8.8: Comparison of experimental and calculated XMCD line shape. The experimental data correspond to the spectrum for $t \approx 11$ u.c. that is shown in fig. 8.7. The theoretical curve was calculated with the model parameters that were obtained by simulation of this isotropic spectrum (see tab. 8.1).

for the $t \approx 2$ u.c. spectrum. For an unambiguous quantification of the $f^0 \to f^1$ weight and width, the source of this additional weight has to be identified and included in the calculations. The bottom section of tab. 8.1 contains a number of parameters that concern the representation of the spectrum but are of lesser physical interest, with the exception of the relative amplitude of the $f^0 \to f^1$ contribution. It directly gives the ratio of the spectral weights of $f^0 \to f^1$ and $f^1 \to f^2$ contribution $w_{\text{rel}}^{0\to1}$. The same value is obtained from integration of the two spectral contributions. The validity of this value might be questionable due to the implausible lifetime widths and the unclear additional weight at the high-energy flanks. Taking it seriously, the f-occupancy of the calculated spectrum is evaluated to $n_f = 0.942$ according to eq. 6.2 under neglect of the GS-model corrections.

With the optimized parameters given in tab. 8.1, it is straightforward to calculate spectra for left and right circularly polarized light. Their difference yields the XMCD signal. Its line shape is equal for each $\pm m_j$ doublet, which reflects the Wigner-Eckhart[4] theorem [44].

The such calculated XMCD signal is compared to an experimental one in fig. 8.8. The latter was produced from the same left- and right-circularly polarized spectra as the isotropic XA spectrum that was used to obtain the model parameters (black curve in fig. 8.7).

The agreement between theory and experiment is very high, especially since the simulation was not optimized to fit the experimental XMCD spectrum. The occurring differences, which are most striking at the high-energy flank of the M_4 edge (feature S in fig. 6.1), seem to arise from the broadening procedure. This region is also not well reproduced by the model in XAS.

The good agreement of the XMCD in addition to the XA spectra generates further confidence in the assumptions that were made in constructing the model. Despite the small deviations from the experiment, the calculated XMCD shown in fig. 8.8 represents the best theoretical description of Ce $M_{4,5}$ XMCD that is known to the author. In the literature, data calculated by Goedkoop *et al.* in 1988 are frequently used [191, 192, 196, 208]. These data show a negative feature at the high-energy side of the M_5 edge, which is not found in the experimental spectra presented here and in all published data that are known to the author. The only exception are spectra of highly hybridized materials shown by Finazzi *et al.* [191, 192], were the negative feature is explained by significant admixture of $j = 7/2$ character to the ground state. The calculations by

---

[4] Carl Eckhart, American physicist and oceanographer, 1902-1973 [144]

Goedkoop *et al.* were performed with different SI reduction factors and broadening parameters than the results presented here.

The fact that the experimental XMCD data are well reproduced by calculations for a pure $j = 5/2$ ground state together with the invariance of the XMCD spectral shape despite considerable line shape variations in XAS, as already mentioned in section 8.2.2, again raises the question if there is significant admixture of $j = 7/2$ states to the ground state. If there is not, the question remains what the mechanism behind the hybridization-dependent XAS line shape is. These issues are addressed in the following sections.

8.3.2 Admixture of $j = 7/2$ character to the initial state

Van der Laan *et al.* proposed that the hybridization-induced line shape changes are indicative of an increasing admixture of $j = 7/2$ character to the f^1 contribution of the initial state [189], which thus can be written as

$$|i\rangle = \cos\phi\,|j = 5/2\rangle + \sin\phi\,|j = 7/2\rangle\,. \tag{8.2}$$

In this representation, the mixing coefficients are expressed by a hypothetical angle ϕ. In their study, van der Laan *et al.* present calculated Ce $\mathrm{M}_{4,5}$ spectra. They point out the importance of an interference term, which causes the spectrum to differ from the simple, incoherent sum of the spectra for the pure j initial states. As is discussed in section 6.1.3, the presence of this term in the isotropic case has been doubted in the literature.

In order to clarify this issue, isotropic Ce $\mathrm{M}_{4,5}$ spectra for mixed initial states were calculated. As a first approach, the initial state was written as in eq. 8.2 with

$$|j\rangle = \sum_{m_j=-j}^{j} \frac{1}{\sqrt{2j+1}}\,|j, m_j\rangle\,. \tag{8.3}$$

The such obtained spectra in dependence of ϕ resemble incoherent sums of the pure j spectra, no effects of interference were found.

The homogeneously mixed state as described by eq. 8.3 considers all participating $|j, m_j\rangle$ states equally, but does not reflect the physical mechanism of mixing. In analogy to the crystal field theory (see section 2.1.2), this mixing occurs symmetry-adapted. In terms of spherical harmonics, this means that only states with certain m_j can be combined.

As a more general approach, the contributions to the spectrum from off-diagonal transition matrix elements in eq. 5.4 were investigated in detail, with the result that the interference terms cancel out in the isotropic case [265]. Furthermore, calculations with consideration of a ligand level that introduces the mixing were performed. This also lead to spectra free of interference effects [266].

Hence, for the description of the isotropic spectrum in terms of an initial state with admixed $j = 7/2$ character, no interference term has to be considered and the spectrum can be produced as a weighted sum of the isotropic spectra of the pure j states,

$$\mu_{\mathrm{x}}^{\mathrm{mix}} = \cos^2\phi\;\mu_{\mathrm{x}}^{5/2} + \sin^2\phi\;\mu_{\mathrm{x}}^{7/2}. \tag{8.4}$$

Respective incoherently added XAS and XMCD spectra for representative values of ϕ are shown in fig. 8.9. The parameter values as given in tab. 8.1 were used for the calculations. It should be noted that for a progressive admixture of $j = 7/2$ states to the $j = 5/2$ ground state, the mixing should never exceed $\phi = 45°$. Nevertheless, the spectra for larger values are shown here to illustrate the complete crossover between the pure j states.

These results can now be used to interpret the spectral shape of the experimental data that are shown in figs. 8.3 and 8.4. As presented there, the XAS line shape significantly varies with increasing hybridization, while the XMCD spectrum is remarkably invariant. The calculated data for progressive $j = 7/2$ admixture show a reverse behavior: The differences between the pure j spectra are much more drastic in XMCD than in XAS. Consequently, the changes in

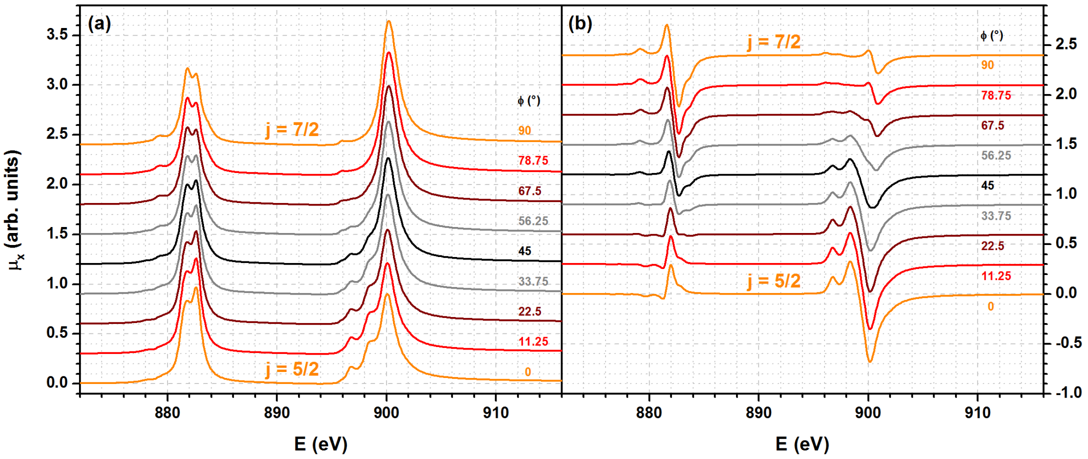

Figure 8.9: Calculated isotropic Ce $M_{4,5}$ $f^1 \rightarrow f^2$ (a) XAS and (b) XMCD spectra for different mixing coefficients of the $j = 5/2$ and $j = 7/2$ states in the initial state according to eq. 8.2. The spectra are incoherent sums of the pure j spectra according to eq. 8.4.

XMCD are more significant.

The most prominent qualitative changes that are introduced to the XMCD line shape by the $j = 7/2$ admixture are visible at the M_5 edge. The small negative features at the low-energy side (L and M in fig. 6.1) are gradually reduced and replaced by a positive feature. In parallel, the positive shoulder at the high-energy side (O) is reduced and converted into a negative feature. All of the experimental XMCD spectra clearly show negative features at low, and a positive shoulder at high energies in the M_5 multiplet. While the red curve for $\phi = 11.25°$ in fig. 8.9 is still consistent with the data, the dark red curve for $\phi = 22.5°$ is not. This allows estimating that the admixed $j = 7/2$ weight to the ground state in $CePt_5$/Pt(111) is not larger than $5 \ldots 10$ % for the complete range of hybridization strength that was observed. It should be noted that the simulated XMCD data nicely reproduce the experimental data for highly hybridized systems shown by Finazzi *et al.* [191, 192].

While the XMCD data thus allow a very definite statement, the XAS data are less conclusive. Regarding the list in section 6.1.3, only some of the points can be explained by $j = 7/2$ admixture. The smearing out of the multiplet substructure (1) is to some extent observed at the M_4 edge. At the M_5 edge, the theoretical data behave in contrast to the experimental ones. The left apex of the double-peak structure (feature C in fig. 6.1) increases in the calculated spectra, whereas it decreases and adapts to the low-energy flank of the main peak in the experimental data. Hence, this most prominent line shape variation is not reproduced by a mixed ground state.

The M_5/M_4 weight ratio of the calculated $j = 7/2$ spectrum amounts to $w(M_5)/w(M_4) = 0.641$ compared to 0.864 for the calculated $j = 5/2$ spectrum. Hence, a decrease of this quantity with increasing hybridization (2) is well explained by a mixed ground state. However, in the experimental data of the present thesis the determination of the weights was done including the $f^0 \rightarrow f^1$ weight, since an independent treatment is complicated by the need to unambiguously separate the two contributions. Analysis of the calculated $f^0 \rightarrow f^1$ spectrum yields a weight ratio of $w(M_5)/w(M_4) = 0.608$. This means that the M_5/M_4 weight ratio of the complete spectrum is automatically reduced with increasing hybridization strength, since the growing $f^0 \rightarrow f^1$ contribution produces a redistribution of weight between the two edges.

Regarding the present data and the relative $f^0 \rightarrow f^1$ weight values obtained from the simulations in fig. 8.7, this effect might be able to explain half of the maximum reduction, which amounts to $4 \ldots 5$ %. The remaining reduction could be explained by an admixed $j = 7/2$ weight of the order of 10 %, which is in line with the XMCD analysis.

The calculated spectra in fig. 8.9 do not show a change in the energy separation of the two main peaks (3). This effect, which is reported in literature for highly hybridized materials, is thus not reproduced by the model. Finally, the $j = 7/2$ spectrum does not exhibit additional weight at the high-energy flank of the main peaks (4). Hence, admixture does not explain this observation either.

In summary, the comparison of calculated Ce $\mathrm{M}_{4,5}$ spectra with admixed $j = 7/2$ character to the experimental data allowed estimation of the upper limit for the admixed weight to a maximum of $5 \ldots 10$ %. This small admixture does not explain the significant line shape variations that are observed in XAS. In particular, the increasing width of the high-energy flanks of both edges with increasing hybridization remains a nuisance, since it complicates the unambiguous separation of $f^0 \to f^1$ and $f^1 \to f^2$ contributions. Hence, alternative explanations have to be searched for, which is attempted at in the following.

8.4 Alternative approaches to the line shape variations in XAS

In section 8.2.1, experimentally observed Ce $\mathrm{M}_{4,5}$ XAS line shape variation in dependence of the hybridization in CePt_5/Pt(111) are described (see fig. 8.3 (c)). Simulations of the experimental data with full multiplet calculations yielded very good results for the case with low hybridization (see section 8.3.1), but failed to reproduce the line shape of highly hybridized samples by considering an admixture of $j = 7/2$ character to the ground state (see section 8.3.2).

In comparison of the two extreme experimental spectra that are shown in fig. 8.7, two characteristics of the line shape difference can be named apart from the understandable change in the $f^0 \to f^1$ weight: At both edges, smaller features at the low-energy sides (features A,B,C, G and H in fig. 6.1) are reduced and smeared out, while the weight at the high-energy sides (E and J), the transition region to the $f^0 \to f^1$ part, increases.

Regarding the model that was used to calculate and represent the theoretical spectra (see section 6.3), one could expect that the considerable number of parameters should allow producing the observed line shape variations. As can be seen in fig. 6.4, the details of the calculated spectral shape are indeed strongly influenced by the choice of the reduction factors of the HF parameters. Since the motivation of this reduction is to account for the altered spatial and electronic environment in a solid compared to the free ion, it is possible that the spectral signatures of hybridization can be produced by a further modification of these parameters.

A closer inspection of the exemplary spectra in fig. 6.4 reveals that most of the individual characteristics of increasing hybridization can indeed be produced by variation of the HF parameters. The sharpness of the low-energy features at both edges can be modified, as well as the $\mathrm{M}_5/\mathrm{M}_4$ weight ratio. However, it is not possible to find a solution that covers all effects simultaneously. An increase of $\beta_{\mathrm{SI}}^{4f\text{-}4f}$ gives the right trend for the double-peak structure at the M_5 edge, but increases the sharpness of the low-energy features at the M_4 edge.

A reduction of $\beta_{\mathrm{SI}}^{3d\text{-}4f}$ could be applied to represent the compression of the multiplet as described by Jo and Kotani [185, 186]. However, if this reduction is made strong enough to produce line shape changes as distinct as the experimentally observed ones, it also changes the width of the multiplet groups in a way that is not compatible to the data. Furthermore, the produced line shapes do not match the experimental ones either.

Hence, a variation of the HF parameters does not explain the observations. No combination was found that fits the data of CePt_5/Pt(111) films with $t \approx 2$ u.c. In particular, the increase in intensity at the high-energy flank of both edges cannot be produced by altered HF parameters. As is addressed in section 8.2.1, the line shape variations are not a signature of sample contamination. Many experimental spectra of various materials show the effect, but no calculations are known to the author that reproduce it, especially regarding the broadness of the high-energy flanks (compare section 6.1.3). Furthermore, interference effects between the $f^0 \to f^1$ and $f^1 \to f^2$ contributions are also refuted as an explanation, since no interference is expected in isotropic geometry (compare section 8.3.2).

In the following sections, different scenarios that could explain these line shape variations are presented. The discussion is divided into the interpretation as additional spectral weight and the interpretation as a variation of the profiles of the individual transition lines that generate

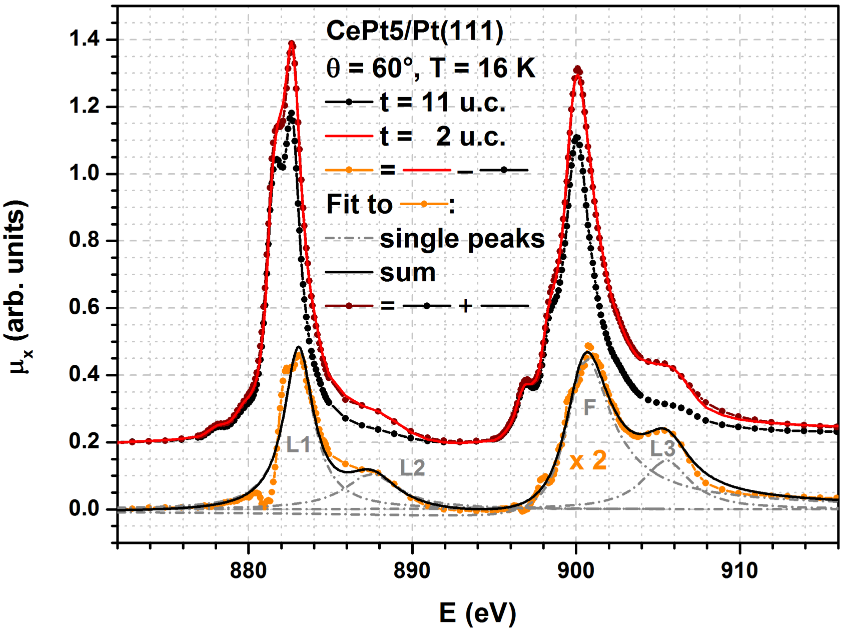

Figure 8.10: Alternative scaling of the experimental curves shown in fig. 8.7 and reproduction of the obtained difference by a fit with three Lorentz (L plus number) and one Fano (F) profile according to eqs. 6.4 and 6.5, respectively.

the complete spectrum.

8.4.1 Interpretation as additional spectral weight

Fig. 8.10 illustrates the idea that the line shape variations might be the consequence of an additional contribution to the highly hybridized spectrum. It makes use of the fact that the two experimental spectra that are shown in fig. 8.7 were arbitrarily scaled to equal heights of the M_5 maximum.

The figure shows an alternative relative scaling of these spectra of samples with low and high hybridization (black symbols and red curve, respectively), with equal heights of the smallest low-energy peak at the M_4 edge (feature G in fig. 6.1). The difference of the such scaled spectra is shown as the orange symbols. It exhibits two peaks at each edge, which can be reproduced by three Lorentz and one Fano profile with $q = 5$, as indicated in the figure. The dark red curve represents the sum of the two black curves and agrees well with the highly hybridized spectrum. The difference peaks at higher energies reflect the difference in $f^0 \rightarrow f^1$ weight. The peaks at lower energies could represent an additional contribution that is present in the highly hybridized spectrum.

Possibly, the additional weight arises from dipole-forbidden transitions. The dipole description of XAS is only an approximation (see section 5.1.1), which might become less valid in the presence of hybridization. In order to provide a basis for such arguments, Thole *et al.* included dipole-forbidden transitions to their calculation of the $M_{4,5}$ spectra of the rare-earth series [184]. Van der Laan *et al.* [189] already pointed out that the forbidden lines are generally located at lower photon energies than the allowed ones. However, the suspected additional weight is identified at the high-energy side of the main peak. A breakdown of the dipole approximation is thus ruled out as the source of the line shape variation.

Within the dipole approximation, transition to electronic shells with higher n are allowed and could represent the additional weight. However, these contributions are expected to be negligibly small (see section 5.1.1). Furthermore, in order to seriously consider this scenario, a consistent explanation for the strong correlation of the transition weight and the degree of hybridization is required.

This correlation gave rise to the idea that the additional weight could represent the contribution

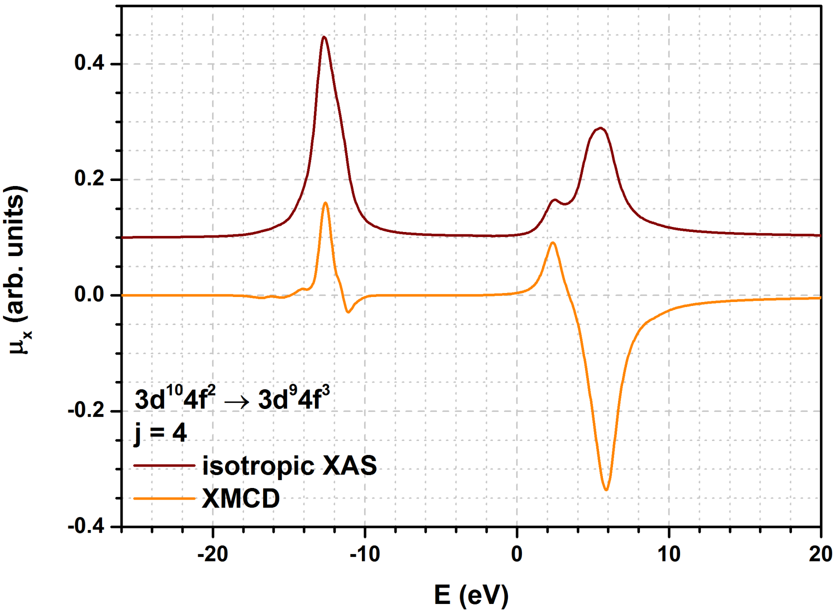

Figure 8.11: Calculated Ce $M_{4,5}$ XAS and XMCD for the transition $3d^{10}4f^2 \rightarrow 3d^94f^3$. The model parameters are given in the text.

of the $3d^{10}4f^2 \rightarrow 3d^94f^3$ transition. In general, threefold occupation of the Ce $4f$ level is usually neglected due to the strong Coulomb repulsion, but this argument is only applicable to the ground state. For an excited state in the presence of a core-hole, the energetic order of the states with different f occupation changes drastically, as can be seen in fig. 2.6. Regrettably, the $3d^94f^3$ configuration is not included in the calculations of Gunnarsson and Schönhammer, where the data of the figure were taken from [39].

The $f^2 \rightarrow f^3$ contribution to the spectrum is not considered in any publication that is known to the author. The only account is given in an early study of the applicability of the GS theory to Ce $M_{4,5}$ XAS by Fuggle *et al.* [61]. These authors mention that the $f^2 \rightarrow f^3$ contribution should be located at higher photon energy than the $f^1 \rightarrow f^2$ part and that it is expected to be small. It could not be identified in the spectrum, and was therefore neglected in the analysis.

However, spectral signatures related to a $4f^2$ configuration in the ground state are frequently found in PES and $L_{2,3}$ XAS [26, 64, 65]. The existence of this configuration requires a hopping matrix element V^{ic}, as does the $4f^0$ configuration. While the details of the distribution of spectral weight to the different f occupancies in the framework of the GS theory depend on several parameters like the hybridization strength Δ [26, 43], it is reasonable to assume that a stronger interaction between f level and conduction states can lead to an increase of both the $4f^0$ and $4f^2$ fractions.

In order to test this idea, the Ce $M_{4,5}$ spectrum for a $4f^2$ initial state was calculated. The required HF parameters are given in tab. 6.1, and the same reduction factors as for the $f^1 \rightarrow f^2$ simulation were used (see tab. 8.1). A simple energy-independent Lorentz lifetime broadening with widths of $\Gamma^{M_5} = 1$ eV and $\Gamma^{M_4} = 1.5$ eV was applied to the M_5 and M_4 edges, respectively, in accordance with the widths that were obtained for the main peaks of the calculated $f^1 \rightarrow f^2$ contributions.

The ground state of the $4f^2$ configuration is characterized by $j = 4$. The isotropic spectrum of this 9-fold degenerate manifold is shown in fig. 8.11 as the black line. As could be expected, the spectral shape resembles the $f^2 \rightarrow f^3$ spectrum of Pr [184, 208].

In general, the XAS shape is consistent with the additional spectral weight as identified in fig. 8.10. It is indeed possible to remove the discrepancies at the high-energy flanks in the simulation of the $t = 11$ u.c. spectrum shown in fig. 8.7 by incoherent addition of the calculated $f^2 \rightarrow f^3$ spectrum and slight readjustment of the model parameters.

However, there are two important concerns which can be raised over the interpretation of the line shape variations as arising from the $f^2 \rightarrow f^3$ contribution. First, in contrast to the $f^0 \rightarrow f^1$ transition, the $f^2 \rightarrow f^3$ transition exhibits XMCD. The calculated signal is also shown in fig. 8.11. The magnitude of this XMCD in relation to the weight in XAS depends on the crystal field scheme of the $4f^2$ multiplet, which is unknown. However, a variation of the $f^2 \rightarrow f^3$ contribution to the spectrum should become manifest in a visible variation of the total XMCD line shape if the $f^2 \rightarrow f^3$ contribution to the spectrum is as large as indicated in fig. 8.10. Such a variation is not observed.

Second, the additional weight exceeds the identified $f^0 \rightarrow f^1$ contribution by a factor of $2 \ldots 3$. While it is difficult to imagine an additional spectral contribution of the indicated magnitude at all, this is especially true for the weight of the $f^2 \rightarrow f^3$ transition. As is known from PES experiments, it should be considerably smaller than the $f^0 \rightarrow f^1$ contribution [61].

This discrepancy can be resolved if the roles of the two contributions that are not $f^1 \rightarrow f^2$ are reversed in the interpretation of the spectrum. In this scenario, the peaks that are commonly interpreted as the $f^0 \rightarrow f^1$ contribution (features F and K and in fig. 6.1) would represent the $f^2 \rightarrow f^3$ transition, whereas the $f^0 \rightarrow f^1$ weight is distributed between this and the $f^1 \rightarrow f^2$ part and cannot easily be separated from the latter. In that case, the $f^2 \rightarrow f^3$ XMCD might be too small to make a significant difference for the range of hybridization as observed in the present thesis.

The identification of the $f^0 \rightarrow f^1$ part by Fuggle *et al.* was based on the expectation that it is located some electronvolts above the $f^1 \rightarrow f^2$ part and should vary for different materials in analogy to the respective contributions in PES, which had been identified before [61]. The $f^2 \rightarrow f^3$ contribution to Ce $M_{4,5}$ XAS is also expected some electronvolts above the $f^1 \rightarrow f^2$ part, and the respective contributions in PES also depend on the hybridization.

Hence, the proposed scenario is not in conflict with the expectations formulated by Fuggle *et al.* If proven to be true, it would significantly affect the interpretation of Ce $M_{4,5}$ XAS as frequently found in literature, including the present thesis. A test of the scenario could be done by analyzing thickness-dependent PES data on $CePt_5$/Pt(111) films in comparison to the present XAS data. Such PES data were recorded by H. Schwab in the course of his PhD thesis [242], but a respective analysis could not be performed in the scope of the present work.

8.4.2 Interpretation as altered transition line profiles

An alternative to the interpretation of the hybridization-induced line shape variations as arising from additional spectral weight is an interpretation as a redistribution of spectral weight. In the relative scaling of the data as shown in fig. 8.7, it seems that features at low energies are reduced, while the high-energy flanks are broadened at both edges when increasing the hybridization. This observations could be explained by a mechanism that transfers weight from low to high energies. Asymmetries in line shape are already included to the model by the Fano profile, which is used as the transition line profile at the M_4 edge instead of the common Lorentz profile. This is motivated by the presence of autoionization effects, as discussed in section 8.2.4. The hybridization-dependent asymmetry would be an additional effect, since it also occurs at the M_5 edge. Furthermore, the stronger asymmetry at the M_4 at high hybridization edge cannot be reproduced by a simple readjustment of the Fano asymmetry parameter q, since this causes a negative dip at the low-energy side in the continuum-subtracted spectrum (compare fig. 6.3). The hybridization-induced asymmetry apparently lacks this feature.

In order to test this proposed scenario, an asymmetric Lorentz profile was constructed according to

$$f_{\mathrm{L}}^{\mathrm{asy}}(E, \Gamma^-, \Gamma^+) = \frac{2}{\Gamma^- + \Gamma^+} \cdot \begin{cases} \Gamma^- \cdot f_{\mathrm{L}}(E, \Gamma^-) & \mathrm{for} E \leq 0 \\ \Gamma^+ \cdot f_{\mathrm{L}}(E, \Gamma^+) & \mathrm{for} E > 0 \end{cases}, \tag{8.5}$$

which simplifies to eq. 6.4 in the symmetric case $\Gamma^- = \Gamma^+$. An example for $\Gamma^- = 1.0$ eV, $\Gamma^+ = 1.7$ eV is shown in fig. 8.12 (a) (orange) together with a symmetric profile for $\Gamma = 1.0$ eV (dark red). These two profiles were used for the lifetime broadening of the calculated spectra

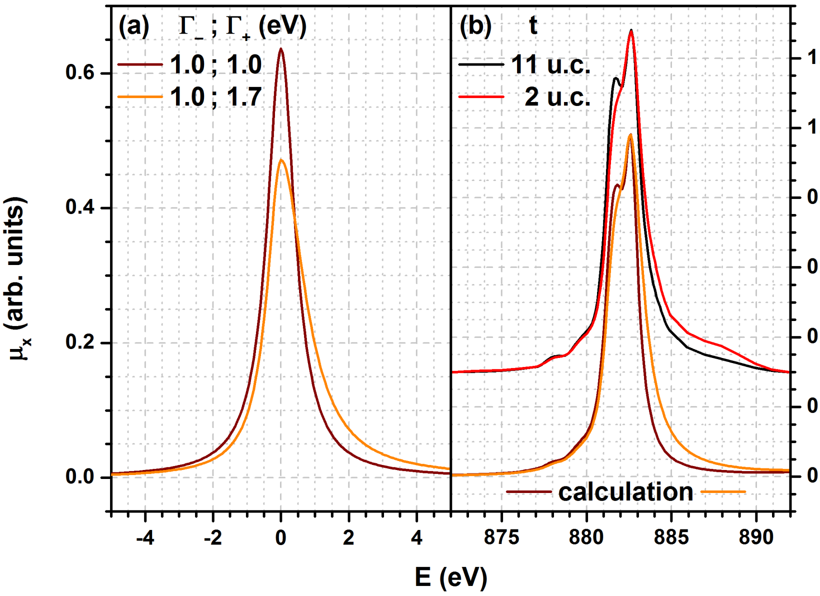

Figure 8.12: (a) Comparison of a symmetric and an asymmetric Lorentz profile according to eq. 8.5. (b) M_5 edge of a calculated spectrum. The dark red and orange curves refer to the two profiles in panel (a), which were used for the lifetime broadening. The HF reduction parameters were used as given in tab. 8.1. Energy shift and amplitude of the two calculated spectra were adjusted in order to reproduce the appearance of the experimental data for $t \approx 11$ u.c. and 2 u.c. (black and red line, respectively).

that are shown with respective coloring in panel (b). No energy-dependent lifetime width and no $f^0 \rightarrow f^1$ or continuum contributions were considered in this simulation. The HF parameters were adopted from the simulation presented in section 8.3.1, amplitudes and energy shifts were adjusted to match the representation of the experimental spectra.

The simulation of the lowly-hybridized spectrum for $t \approx 11$ u.c. in fig. 8.7 yielded only weak energy-dependence of the M_5 lifetime width. Hence, the $f^1 \rightarrow f^2$ part of the M_5 edge is also well reproduced by the dark red curve in fig. 8.12 (b). The orange curve, which was produced with the asymmetric Lorentz profile, strongly resembles the highly-hybridized spectrum for $t \approx 2$ u.c. Fig. 8.12 shows that an asymmetric peak profile for the lifetime broadening is a promising candidate to reproduce the hybridization-dependent lifetime changes. However, no model for the occurrence of this asymmetry, which increases with increasing hybridization, can be presented at the current stage. One could think of a connection to the Mahan-Nozières-de Dominicis model [267, 268], which is known to lead to the asymmetric Doniach-Šunjić (DS) profile in PES [269]. It treats dynamical screening of a deep core-hole, as present in the final state of the XA process, by the conduction electrons and represents a many-body theory with analogies to the description of the Kondo effect (see chapter 1).

The $3d$ core-hole is certainly more effectively screened by the localized $4f$ electrons than by the conduction electron sea. However, screening by conduction electrons is required for dynamical many-body effects. Increasing hybridization between the $4f$ level and conduction states might lead to an increasingly efficient dynamical core-hole screening with increasing hybridization, which might explain the increasingly asymmetric line shape.

The DS profile resembles the asymmetric Lorentzian as provided by eq. 8.5 for the case with the larger width at the low-energy side. The reverse scenario with large width at the high-energy side requires a negative asymmetry index and is accompanied by a negative feature at low energies. The profile then resembles the Fano profile.

However, the DS profile was derived for PES, where the energy axis usually represents the electron binding energy with deeper lying states at larger negative energies. In contrast, a larger photon energy is required to reach a deeper lying state in XAS. Hence, it might well be that a theoretical treatment of dynamical core-hole screening in XAS leads to a DS profile with reverse sign of the energy axis. Some attempts to include dynamical core-hole screening in calculations of XA spectra can be found in the literature, especially regarding K edge spectra [270]. However, no discussion of the line shape in terms of an analytical function is known to the author.

Such a theoretical study would be highly desirable in order to clarify to what extend dynamical core-hole screening can explain the apparent hybridization-dependent asymmetry in Ce $M_{4,5}$ XAS. If proven to be true, an analytical expression for the asymmetric line shape is essential in order to reliably separate the $f^1 \rightarrow f^2$ and $f^0 \rightarrow f^1$ contributions in the simulation of experimental data.

The presence of asymmetric transition line profiles might sensitively affect the quantitative analysis of Ce $M_{4,5}$ spectra. Many evaluations in the present thesis rely on the assumption that the line shape is invariant under variation of the thickness. In particular, this concerns the stoichiometry analysis in section 7.3 and the results presented in chapter 9, where the peak height is taken as a measure of the spectral weight.

Hence, it is instructive to investigate the error that is introduced by the asymmetric line profile. The two spectra in fig. 8.12 (b) are scaled to equal M_5 main peak heights. The scaling factor for the asymmetric profile amounts to $A \approx 1.15$. Hence, the introduction of asymmetry in the lifetime broadening reduces the peak height by 15 %, which is thus a realistic estimate for the induced uncertainty. This value is smaller than the respective factor for the normalized line profiles as shown in panel (a), since in the complete spectrum, some of the intensity at the main peak that is lost to the high-energy side is compensated by asymmetric contributions from lower-lying transitions.

8.5 Conclusions to the chapter

As presented in the preceding sections, The detailed study of the Ce $M_{4,5}$ line shape of both XAS and XMCD for $CePt_5/Pt(111)$ surface intermetallics over a wide thickness range gave access to the rich information that is contained in the spectra. The analysis of the experimental data (see section 8.2) revealed the presence of spectral signatures of both crystal field splitting and Kondo interaction in the accessible temperature range. Furthermore, it is shown that the intermetallic film thickness t provides a parameter to sensitively tune the hybridization between the localized $4f$ level and conduction states.

This tunability makes $CePt_5/Pt(111)$ an ideal model system, since it allows study of the effects of hybridization strength variations on various physical properties. Regarding the Ce $M_{4,5}$ spectral shape, this is shown in section 8.3. Simulations of experimental data based on full multiplet calculations yielded excellent results for lowly-hybridized samples. The ingredients of the applied model, like, e.g., the details of the continuum background and the consideration of autoionization effects at the M_4 edge, were carefully selected and supported by experimental findings. Both XAS and XMCD are reproduced with high agreement. The XMCD spectrum that was derived from simulated XA spectra is by far the most realistic calculated one that is known to the author.

Nevertheless, the model reached its limits in the reproduction of highly-hybridized spectra. A generally accepted scenario in the literature, the admixture of $j = 7/2$ character to the ground state, was studied in detail. It was found that no interference term of the two configurations is present in the isotropic case. Based on this finding and on the experimental XAS and XMCD data, a mixed ground state is refuted as the explanation of the experimentally observed, hybridization-dependent line shape variations in the present samples.

Two alternative scenarios are proposed that are capable to explain the variations. The first, the interpretation as additional weight, is a reinterpretation of the spectral signature that is commonly assigned to the $f^0 \rightarrow f^1$ weight as arising from a $f^2 \rightarrow f^3$ contribution. The $f^0 \rightarrow f^1$ weight is then suspected to produce the additional intensity at the high-energy flank of the $f^1 \rightarrow f^2$ part.

In this scenario, drastic consequences arise for the interpretation of Ce $M_{4,5}$ XAS data. On one hand, the separation of the $f^1 \rightarrow f^2$ and $f^0 \rightarrow f^1$ contributions is even more complicated than in the traditional interpretation. On the other hand, the clear identification of the $f^2 \rightarrow f^3$ contribution highly increases the informative value of XA spectra compared to PES data, since the presence of all contributions that are relevant in the GS model would allow obtaining all model parameters, like the hybridization strength Δ, from XAS alone.

The second approach is the introduction of an asymmetric peak profile for the lifetime broadening of the individual transitions that compose the spectrum. A motivation for this assumption might be dynamical core-hole screening, which is known to produce asymmetric line profiles in other core-level spectroscopies.

Both scenarios were shown to reproduce the experimental observations. The additional weight-scenario might appear more unlikely, since it contrasts the traditional interpretation. A more scientifically sound argument can be formulated with respect to the observed constancy of the XMCD signal, as presented in section 8.2.2. A significant contribution of $f^2 \rightarrow f^3$ character should affect the XMCD signal, which is not observed.

In any case, further studies are required to clarify this issue. The additional weight-scenario could be tested by comparison of the thickness-dependent XAS data to respective PES data. The asymmetric profile-scenario requires a theoretical treatment of the XAS line shape in presence of dynamical screening, or another model for the apparent asymmetry.

A decision in favor of one of the two scenarios could be made if it was possible to determine absolute values for the spectral weight from the XAS data. For samples with different thickness, this is complicated by the variation in the amount of probed material. Ideally, such an experiment requires a material that changes its degree of hybridization in dependence of an easily accessible parameter without drastic changes of further sample characteristics. A promising candidate is metallic Ce, which exhibits the archetypical α-γ valence transition in dependence of temperature (see section 2.1.5). Regrettably, the only published Ce $M_{4,5}$ XAS data of this transition that are known to the author are presented in arbitrary scaling [65].

While the described analyses, simulations and discussions should give valuable impact to the understanding of the Ce $M_{4,5}$ line shape, one of the main goals of the study could not be achieved. Due to the ambiguities regarding the hybridization-dependent spectral weight at the high-energy flanks of both edges, it was not possible to clearly separate the contributions of the $f^0 \rightarrow f^1$ and $f^1 \rightarrow f^2$ transitions. In fact, with the additional weight-scenario additional uncertainty was introduced to the discussion of the $f^0 \rightarrow f^1$ weight.

As th e best compromise against the background of the current state of knowledge, the traditional assignment of the $f^0 \rightarrow f^1$ weight is kept throughout the present thesis. This has the advantage that the results are comparable to previous works. Since the ambiguities are smallest for low hybridization, the spectrum for $t \approx 11$ u.c., as simulated in fig. 8.7, is used as a reference for the $f^0 \rightarrow f^1$ weight in chapter 9. The simulated value amounts to $w^{0\rightarrow 1}_{\mathrm{rel,ref}} = 0.066$. In any case, the discussion of relative weight changes of the different contributions in dependence of the hybridization strength is unaffected by each of the two scenarios and does not rely on exact numbers.

Chapter 9

Hybridization and CF splitting of the Ce 4*f* level probed by XAS

Contents

The delicate balance of localization and itinerancy of the $4f$ electrons is the guiding theme in the description of Ce compounds. Two approaches to this interplay are the crystal field (see section 2.1.2) and the Ce valence (see section 2.1.5). The former represents the electron reconfiguration of the Ce $4f$ level in order to adapt to the anisotropic point charge potential of the crystalline environment. The latter is introduced by a hopping matrix element between $4f$ and conduction states and thus gives access to Kondo interaction. In both cases, the consequent coupling of the $4f$ states occurs symmetry-adapted. Hence, a unified theoretical description in terms of an “ionic” and a “covalent” part of the crystal field is possible.

As is discussed in chapter 6, the Ce $M_{4,5}$ XAS line shape bears signatures of both aspects. The degree of hybridization is contained in the relative magnitude of the $f^0 \rightarrow f^1$ weight, whereas the anisotropy of the CF-adapted ground state can be addressed as linear dichroism in polarization-dependent experiments. In chapter 8, it is shown that both effects are accessible by the XAS experiments that were performed on $CePt_5$/Pt(111) surface intermetallics in the present thesis. Since the primary aim of these experiments was the investigation of $4f$ magnetism by XMCD, the XAS data were to most part not recorded under ideal conditions for their analysis regarding hybridization and crystal field. However, the information that can be accessed is highly valuable: Both the Kondo interaction as well as the crystal field strongly influence the interpretation of the XMCD data shown in chapter 10. Hence, the analysis was nevertheless attempted and conclusive results were obtained by application of dedicated evaluation routines.

This is shown in the following. The $f^0 \rightarrow f^1$ weight as a function of thickness and temperature is addressed in section 9.1. In section 9.2 the results for the analysis of the linear dichroism are presented.

9.1 Variations of the $f^0 \to f^1$ weight in Ce $M_{4,5}$ XAS

The $f^0 \to f^1$ weight in Ce $M_{4,5}$ XA spectra of $CePt_5$/Pt(111) surface intermetallics varies as a function of film thickness and sample temperature, as is shown in fig. 8.3. In the following, these variations in the spectrum are quantified and analyzed in detail. While the tunability of the $f^0 \to f^1$ weight and thus the hybridization strength provides the option to study its effect on the $4f$ magnetism, the temperature-dependence gives access to the single-impurity Kondo energy scale (see section 1.1), an important parameter in the description of Kondo materials.

The evaluation of the relative $f^0 \to f^1$ weight in a certain Ce $M_{4,5}$ spectrum requires to disentangle this contribution from the dominant $f^1 \to f^2$ part. In order to derive a procedure for this separation, the isotropic line shape of Ce $M_{4,5}$ XAS for $CePt_5$/Pt(111) films with different degrees of hybridization were studied in detail. Spectra of both contributions were calculated in full multiplet theory, including the admixture of $j = 7/2$ character to the ground state. The spectrum of a lowly-hybridized sample could be reproduced with high agreement, but significant discrepancies remained for high hybridization.

These discrepancies prevented an unambiguous separation of the two contributions and might even hint at an additional contribution from the $f^2 \to f^3$ transition. While this complicates the quantification of the $f^0 \to f^1$ weight, relative trends can still be evaluated. This is done in the following according to the procedure described in section 6.2.

The quantification of these trends is based on the assumption that the traditional interpretation of the spectra regarding the position of the $f^0 \to f^1$ contribution is valid. The hybridization-induced line shape changes are ignored. Since these mainly affect the highly-hybridized samples, the simulation of a lowly-hybridized spectrum for $t \approx 11$ u.c. is used to quantify the $f^0 \to f^1$ weight. This simulation, which is shown in fig. 8.7, yielded $w^{0\to1}_{\mathrm{rel,ref}} = 0.066$.

Starting from this value, the comparison of reference spectra for each sample allows determination of their $w^{0\to1}_{\mathrm{rel}}$ values according to eq. 6.1. The such obtained thickness-dependence of the $f^0 \to f^1$ weight is treated in section 9.1.1. These values are in turn used as references for the temperature-dependence of $w^{0\to1}_{\mathrm{rel}}$ of the individual samples, which is presented in section 9.1.2.

9.1.1 Thickness dependence of the $f^0 \to f^1$ weight

The procedure that is described in section 6.2 allows quantification of the observed changes in the relative $f^0 \to f^1$ weight (see fig. 8.3 (c)). Results for $w^{0\to1}_{\mathrm{rel}}(t)$ for the complete dataset of the present thesis were calculated according to eq. 6.1 and are shown as the dark red symbols in fig. 9.1.

The analysis was done for nearly isotropic spectra taken at $\theta = 60°$. The lowest temperatures available were chosen. This means that the SOLEIL data were all taken at $T = 2$ K, while the BESSY data cover a range of $T = 12 \ldots 22$ K, depending on the state of the cryostat and the exact measurement program in the different beamtimes. As is shown in section 9.1.2, the $f^0 \to f^1$ weight does not significantly change in this temperature range. This is not the case for spectra taken at higher temperatures, where $w^{0\to1}_{\mathrm{rel}}(T)$ exhibits a considerable slope for most of the samples. This is why low-T data were used, although the deviations of the $\theta = 60°$ spectra from the true isotropic case are smaller at higher temperatures.

The basis for the quantification of $w^{0\to1}_{\mathrm{rel}}$ is the simulation of the $t \approx 11$ u.c. spectrum shown in fig. 8.7. The relative spectral weight of the $f^0 \to f^1$ contribution with respect to the simulated $f^1 \to f^2$ spectrum is obtained by integration of the calculated parts. It amounts to $w^{0\to1}_{\mathrm{ref}}/w^{1\to2}_{\mathrm{ref}} \approx 0.066$, which equals the relative amplitude of the $f^0 \to f^1$ part in the simulation. The chosen reference spectrum is indicative of a comparably small $f^0 \to f^1$ contribution, which can lead to large relative errors in the determination of its magnitude. However, the rest of the spectrum is better understood than for highly-hybridized samples at the present stage.

The data in fig. 9.1 clearly demonstrate the non-monotonousness of $w^{0\to1}_{\mathrm{rel}}(t)$ (compare fig. 8.3 (c)). At $t \approx 2$ u.c., a maximum is observed. There is one data point ($t = 3.9$ u.c.) that deviates from the other data in the vicinity. The rather high $f^0 \to f^1$ weight is characteristic for all spectra of this sample. This finding is addressed in section 9.1.2.

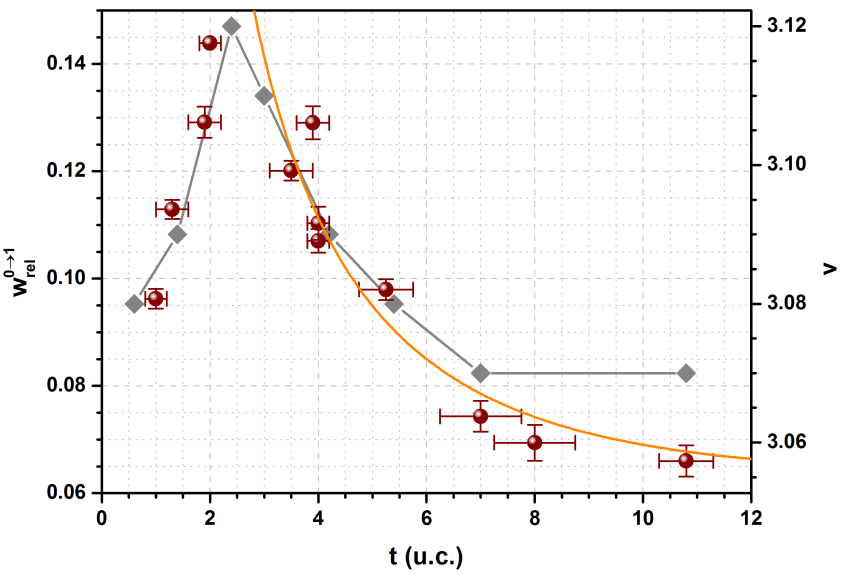

Figure 9.1: Dependence of $w_{\text{rel}}^{0\to1}$ on the film thickness in CePt$_5$/Pt(111) surface intermetallics for $T \lesssim 22$ K (dark red symbols). Data were obtained from Ce M$_{4,5}$ XAS according to eq. 6.1, including the spectra that are shown in fig. 8.3 (c). The error bars reflect the errors of the fitting routine as described in section 6.2. The orange line represents a fit to the data for $t > 2$ u.c. with eq. 9.1. For comparison, results of the room-temperature valence by Tang *et al.* are shown (gray symbols) [79]. Thickness values were assigned to their data according to the considerations that are presented in section 7.3. The two y-axes are connected according to eq. 6.2.

The f-occupancy of CePt$_5$/Pt(111) surface compounds was already studied by Tang *et al.* [79], who extracted data of the valence for various initial Ce coverage from core-level PES measurements at room temperature. These results are also displayed in fig. 9.1 for comparison. The initial coverage as given by Tang *et al.* was calculated to a film thickness following the considerations that are presented in section 7.3. The valence values of the right y-axis are connected to the left $w_{\text{rel}}^{0\to1}$ axis according to eq. 6.2.

The observed trend of $w_{\text{rel}}^{0\to1}(t)$ is also clearly visible in the data of Tang *et al.* The quantitative agreement is striking, especially regarding the uncertainties that are accepted in the evaluation. The errors that are made due to the ignorance of the thickness-dependent line shape are hard to quantify without knowing the exact mechanism. For the scenario with asymmetric transition line profiles, the $f^0 \to f^1$ weight for high hybridization is overestimated in a twofold manner. The $f^1 \to f^2$ weight, which is transferred to higher energies, is missed in the normalization, but additionally considered in the determination of the $f^0 \to f^1$ weight. The relative error in the normalization is estimated to 15 % in section 8.4.2.

Furthermore, the connection of the two ordinates is done under neglect of the GS correction, which is required to calculate the valence from $w_{\text{rel}}^{0\to1}$ (see section 6.2). It is known that the $f^0 \to f^1$ weight in XAS underestimates the coefficient c_{f^0} in eq. 2.40. This means that the valence is underestimated as well.

The good agreement between the XAS and PES data might indicate that the uncertainties that are induced due to the ignorance of the line shape variations and the ones due to the neglect of the GS correction compensate to some extent.

For a discussion of the progression of $w_{\text{rel}}^{0\to1}(t)$, it is instructive to recall some of the results on the CePt$_5$/Pt(111) crystal structure that are presented in chapter 7. As is shown there, the crystal structure of the intermetallic films is independent of the film thickness. Apart from some surface modification, it is the CePt$_5$ structure shown in fig. 2.7. However, the lattice constants of the films vary with the thickness. As is shown in fig. 7.7, this dependence is strongest for $t < 2$ u.c., where the lateral lattice parameters decrease with increasing t. Above $t \gtrsim 4$ u.c., no strong variation is observed.

The lattice constant variation at low t is explained by successive release of epitaxial strain. This effect is very similar to the application of pressure. It is well known that the Ce valence can be influenced by external pressure, with the tendency for higher valence at higher pressure [41]. This is readily explained by the increasing overlap of the localized f orbitals and the orbitals that form the conduction bands, if the next-neighbor distance is reduced via the lattice parameters. This scenario is a reasonable explanation for the observed increase of the $f^0 \rightarrow f^1$ weight with thickness for $t \leq 2$ u.c.

For $t \gtrsim 4$ u.c., the lattice parameter variations are too small to explain the observed negative slope of $w_{\text{rel}}^{0\rightarrow 1}(t)$. The structure of the film seems to be very robust in this thickness range, the only variation that is observed is the gradually changing preference of the rotational alignments on the substrate. Hence, it can be assumed that the hybridization in the film does not vary. A possible explanation for the observed progression can then be given by the consideration of interface effects.

Both interfaces of the film, namely the one to the substrate and the one to the vacuum, represent a breaking of the structural symmetry. The LEED IV study that is presented in section 7.6 clearly confirms that the surface is Pt terminated and reveals a surface modification. The topmost layer is not a Pt Kagome net, as would be the regular building block in the bulk structure, but is characterized by additional Pt atoms in the Kagome holes.

Regarding the interface to the substrate, no such detailed information are available. However, the most logical scenarios only leave the question whether the last Ce-containing layer is followed by another Kagome net or by the first closed hexagonal Pt layer of the substrate. In both cases, the Ce atoms of the last layer are adjacent to fewer Ce atoms but more Pt atoms than in the bulk. Hence, the local environment of surface and interface are different from the bulk, but similar to each other.

A realistic model for the observed $w_{\text{rel}}^{0\rightarrow 1}(t)$ behavior at higher thicknesses can be constructed by assuming that the valence of Ce atoms in the interface-nearest layers is larger than in the rest of the film. In this case, the interplay of the finite information depth of XAS in the TEY mode and the increasing film thickness lead to a decrease of the depth-averaged $f^0 \rightarrow f^1$ weight. An equivalent scenario is also proposed by Rothman *et al.* in order to explain their results on epitaxial γ-Ce films [200]. The reverse scenario was found by Mulazzi *et al.* in their study of CePd$_7$/Pd(001) surface alloys [241].

In analogy to eq. 5.25 but with neglect of saturation effects and under the assumption that the total weight $w^{\text{tot}} = w^{1\rightarrow 2} + w^{0\rightarrow 1}$ of the spectrum is constant, a model for this scenario can be written as

$$w_{\text{rel}}^{0\rightarrow 1}(t) = \frac{w^{0\rightarrow 1}(t)}{w^{1\rightarrow 2}(t)} = \frac{\frac{w_{\text{s}}^{0\rightarrow 1}}{w^{\text{tot}}}\,\mathcal{F}(0,t_{\text{s}}) + \frac{w_{\text{b}}^{0\rightarrow 1}}{w^{\text{tot}}}\,\mathcal{F}(t_{\text{s}},t-t_{\text{i}}) + \frac{w_{\text{i}}^{0\rightarrow 1}}{w^{\text{tot}}}\,\mathcal{F}(t-t_{\text{i}},t)}{\left(1-\frac{w_{\text{s}}^{0\rightarrow 1}}{w^{\text{tot}}}\right)\mathcal{F}(0,t_{\text{s}}) + \left(1-\frac{w_{\text{b}}^{0\rightarrow 1}}{w^{\text{tot}}}\right)\mathcal{F}(t_{\text{s}},t-t_{\text{i}}) + \left(1-\frac{w_{\text{i}}^{0\rightarrow 1}}{w^{\text{tot}}}\right)\mathcal{F}(t-t_{\text{i}},t)} \tag{9.1}$$

with the depth-dependent contributions to the TEY signal

$$\mathcal{F}(t_1,t_2) = e^{-t_1/\lambda_{\text{e}}} - e^{-t_2/\lambda_{\text{e}}}. \tag{9.2}$$

The indices s,b,i denote surface, bulk and interface, respectively, t_{s} and t_{i} are the thicknesses of the surface and interface region, respectively, and λ_{e} is the TEY electron escape depth. The latter is evaluated to $\lambda_{\text{e}} \approx 1$ nm ≈ 2.3 u.c. in section 7.4.

The model has three free parameters $w^{0\rightarrow 1}/w_{\text{tot}}$, which can be reduced to two if the similarity of surface and interface layer is accounted for by setting $w_{\text{s}}^{0\rightarrow 1} = w_{\text{i}}^{0\rightarrow 1}$. The parameters can be transferred to the relative $f^0 \rightarrow f^1$ weight as used throughout the present thesis via $w_{\text{rel}}^{0\rightarrow 1} = 1/(w_{\text{tot}}/w^{0\rightarrow 1} - 1)$.

A satisfactory agreement between the model and the experimental data with reasonable parameter values is obtained for $t_{\text{s}} = t_{\text{i}} = 1$ u.c., $w_{\text{rel,s,i}}^{0\rightarrow 1} = 0.173$ and $w_{\text{rel,b}}^{0\rightarrow 1} = 0.021$. The TEY electron escape depth is chosen to $\lambda_{\text{e}} = 1.5$ nm. This yields a better result than for the smaller value evaluated in section 7.4 and is done in analogy to section 9.2.3. The fit in section 7.4, which

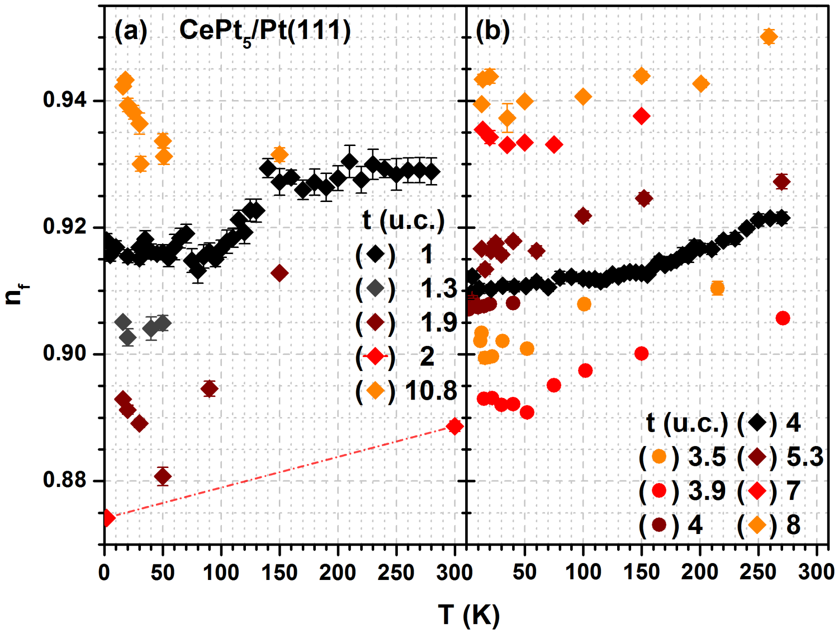

Figure 9.2: Temperature dependence of the $4f$ occupancy for CePt$_5$/Pt(111) intermetallic films with varying thickness. The data were calculated from the relative $f^0 \rightarrow f^1$ weight of Ce M$_{4,5}$ XA spectra according to eq. 6.2. Nearly isotropic spectra taken at $\theta = 60°$ were used, with the exception of the two datasets shown in black. The data for $t = 1$ u.c. and 4 u.c. were taken at $\theta = 0°$ and 54.7°, respectively. The red line highlights the data for $t = 2$ u.c. The error bars reflect the errors of the fitting routine as described in section 6.2.

allowed determination of λ_e in the first place, also yields a respectable result for the larger value of λ_e without to significantly alter the interpretation given there. In particular, λ_e is still very small, although the adjusted value is larger by 50 %.

The resulting curve is shown as the orange line in fig. 9.1. It shows that the consideration of interface effects provides an adequate scenario for the description of the experimental data. While the electron escape depth is slightly adjusted in this fit compared to section 7.4, the general agreement is encouraging. The finding underlines the importance of surface effects when discussing XAS data taken in TEY mode.

Regrettably, the present dataset lacks points in the thickness range $t \approx 3$ u.c. It would be interesting to complete the data in this region, since it is adjacent to the observed maximum of $w_{\mathrm{rel}}^{0\rightarrow 1}(t)$.

9.1.2 Temperature dependence of the $f^0 \rightarrow f^1$ weight

The NCA solution to the single-impurity Kondo problem that was presented by Bickers *et al.* in 1987 [27] allowed connecting the temperature-dependence of the $4f$ occupancy n_f to a universal temperature scale T_{K} (see section 1.1). As is reproduced in fig. 1.1 (a), $n_f(T)$ is constant in both the low- and high-temperature limits and exhibits a maximum of the slope at $T = T_{\mathrm{K}}$.

Experimental observations of the predicted behavior of $n_f(T)$ with different spectroscopic techniques and for several Ce compounds are reported in the literature (see section 6.1.1). As is shown in fig. 8.3 (b), Ce M$_{4,5}$ spectra of CePt$_5$/Pt(111) intermetallics exhibit a smaller weight of the $f^0 \rightarrow f^1$ contribution at room temperature compared to low temperatures, which is qualitatively in line with the expectations.

Results of a more detailed evaluation for the CePt$_5$/Pt(111) samples of the present thesis are shown in fig. 9.2. Those were obtained by evaluation of relative changes in $w_{\mathrm{rel}}^{0\rightarrow 1}$ as presented in section 6.2. Absolute values for $w_{\mathrm{rel}}^{0\rightarrow 1}$ were obtained from the simulations shown in fig. 8.7 via the evaluation of $w_{\mathrm{rel}}^{0\rightarrow 1}(t)$ as shown in fig. 9.1. For each sample, the spectrum that was used for the evaluation of the t-dependence was also used as the reference for the evaluation of its temperature-dependence. In order to provide comparability to the calculated results by Bickers *et al.*, the $4f$ occupancy was calculated from the $f^0 \rightarrow f^1$ weight according to eq. 6.2.

In analogy to the data in fig. 9.1, nearly isotropic spectra were used for the evaluation of the data in fig. 9.2. This assures that no line shape changes that are induced by the crystal field splitting affect the evaluation. The only exception from this rule is the dataset for $t = 1$ u.c., which was recorded at $\theta = 0°$. However, the variations of the peak heights with temperature are comparably small in the thin samples (compare fig. 9.5). If an effect of the crystal field is present in the data, it is significantly smaller than the distinct step at $T \approx 100 \ldots 150$ K

Most of the datasets show a T-dependence that is in line with the NCA results. The most prominent exception is the sample with $t = 10.8$ u.c.that is represented by the orange symbols in fig. 9.2 (a). It shows a strong decrease of $n_f(T)$ at low temperatures. This effect can unambiguously be identified as a time-dependent change of the spectra. There are three data points at $T = 30, 50, 150$ K, which are characterized by low n_f. The other points points, which display the distinct negative slope in $n_f(T)$, were measured monotonously in time starting from low temperatures within the first 24 h after preparation of the sample. The aforementioned three spectra were also recorded monotonously in the given order in a time interval of $\Delta\tau = 6$ h, but after another 15 h.

Apparently, there is a change of the spectrum towards lower $f^0 \rightarrow f^1$ weight during the first day of measurement, which then saturates. A probable source of this change is the influence of residual gas molecules that are successively adsorbed on the surface. Their influence certainly increases with increasing coverage, but might saturate when the adsorbate overlayer is thick enough to prevent further adsorbates from interacting with the surface. This requires at least one completely closed monolayer of adsorbates. The monolayer formation time at the given pressures is of the order of several hours (see section 3.2), a time scale that is consistent with the observation.

Changes in the Ce $M_{4,5}$ spectrum were also observed for samples that were brought in contact to air, as is addressed in appendix. A.3. However, contact to air seems to reduce $w_{\mathrm{rel}}^{0\rightarrow 1}$, which contrasts the time-dependent changes *in situ*. This observation might arise from the fact that the type of expected adsorbates is different in the two cases. After contact to air, the sample surface is most likely largely covered with water, whereas the residual gas in the UHV systems mainly consisted of hydrogen. Water is strongly polar and could have a larger and especially different influence on the electronic structure of a Ce compound it is adsorbed on compared to hydrogen.

Of all the samples that were investigated, the $t = 10.8$ u.c. sample shows the most drastic time-dependence of n_f. This might hint to substandard vacuum conditions during these experiments. This suspicion is supported by the dataset for $t = 1.9$ u.c. (dark red symbols in fig. 9.2 (a)), which was recorded during the same beamtime. The earliest $\theta = 60°$ spectrum in this series is the one for $T = 150$ K, the others were recorded monotonously from low to high temperatures. In analogy to the $t = 10.8$ u.c. data, n_f decreases with time, with the exception of the spectra at $T = 50$ K and 90 K. The increase in n_f here seems to reflect a true temperature-dependence. The time-dependent increase of $f^0 \rightarrow f^1$ weight amounts to 15 % for the $t = 10.8$ u.c. sample, which equals 1 % of the total weight. For the $t = 1.9$ u.c. sample, the change between $T = 16$ K and 50 K amounts to 12 %, which is 1.5 % of the total weight. While these numbers illustrate the high sensitivity of the evaluation method, it is not known at the present stage to what extent these changes influence other quantities like the magnetic susceptibility addressed in chapter 10. It should be noted that the change in $w_{\mathrm{rel}}^{0\rightarrow 1}$ is accompanied by the characteristic line shape changes in the $f^1 \rightarrow f^2$ part as discussed in section 8.2.1. Hence, it represents an increase in the hybridization, and no additional line shape effect. If the interpretation in terms of adsorbates is true, this should mainly affect the surface-nearest Ce layer. For a comparison of magnitudes, it can be said that the change in the most drastic cases is of the order of the temperature-dependent changes, but considerably smaller than the full range of $f^0 \rightarrow f^1$ weight variation that is observed by varying the thickness of $\mathrm{CePt_5/Pt(111)}$ films.

Less noticeable time-dependent changes in $w_{\mathrm{rel}}^{0\rightarrow 1}$ are also visible for other samples than the two that were already discussed. In these cases, the variation mainly produces some scatter of the data at low temperatures. However, this effect can also explain the apparently too high $f^0 \to f^1$ weight of the $t = 3.9$ u.c. sample. During recording of this dataset, the first spectrum at $\theta = 60°$ was measured 30 h after preparation. Indeed, the previously measured spectra at $\theta = 0°$ also show an increase in $w_{\mathrm{rel}}^{0\to1}$ with time. Hence, the $n_f(T)$ dataset of this sample was completely recorded in the "saturated" state with enhanced $f^0 \to f^1$ weight.

With the exception of the dataset for $t = 10.8$ u.c. and the ones that only consist of low-temperature data, all samples show $n_f(T)$ behavior that can be interpreted in terms of the NCA results by Bickers *et al.* However, an exact determination of T_{K} is complicated by the low point density for most samples, especially at high temperatures. This prevents an unambiguous identification of a region with constant n_f in the high-T limit, which might also be caused by the fact that this regime is not reached in the accessible temperature range.

The best datasets are the results of two "$n_f(T)$ fast scan mode" measurements (see section 6.2), which are represented by the black symbols in fig. 9.2. The data for $t = 1$ u.c. exhibits artificial jumps at $T = 70$ K and 130 K, which are consequences of reconfigurations of the experimental setup (see section 6.2). Nevertheless, the dataset can readily be interpreted to indicate $T_{\mathrm{K}} \approx 120$ K. For $t = 4$ u.c., high-T saturation might just be reached at the highest temperatures measured, which leads to $T_{\mathrm{K}} \approx 200$ K.

Regarding the other samples, T_{K} would also be estimated in this range. There is no apparent connection between the magnitude of n_f and T_{K}, as the two fast scan samples with similar $n_f(T \to 0)$ already show. In a simple picture, one could expect that a large $f^0 \to f^1$ weight represents strong Kondo interaction and is thus accompanied by a large Kondo temperature. Such behavior has been observed in comparable experiments [203]. In contrast to this, the increase in n_f with temperature seems to start at lower temperatures for samples with low $n_f(T \to 0)$. This is most apparent for the $t = 3.9$ u.c. and 1.9 u.c. samples.

In this discussion, it has to be considered that variation of the film thickness does not only change $n_f(T \to 0)$, but also the sample volume that is probed. This could give rise to interface effects, as proposed in section 9.1.1. The data then represent the average $4f$ occupancy, and $n_f(T)$ might have different contributions from different layers.

A more detailed analysis of these aspects requires a larger amount of data. At the present stage, it can be said that the Kondo temperature in CePt$_5$/Pt(111) surface intermetallics is of the order of $T_{\mathrm{K}} \approx 100 \ldots 200$ K and it seems to depend on the film thickness. The obtained value for T_{K} is quite high, but this is not unusual for Ce compounds [64, 198, 203]. It is in line with the observation of a Kondo resonance in PES at $T \approx 120$ K [80].

9.2 Crystal field-induced linear dichroism in Ce M$_{4,5}$ XAS

The Hund's rule ground state of the $4f$ electron in a Ce^{3+} ion is characterized by $j = 5/2$. This assignment is also valid in CePt$_5$/Pt(111), as is shown in the detailed analysis of the Ce M$_{4,5}$ XAS line shape in chapter 8. The confrontation of the Ce $4f$ wave function with a non-spherical crystalline environment leads to the energetic splitting of the $j = 5/2$ sextuplet into three Kramers doublets, which is described by crystal field theory (see section 2.1.2).

The total crystal field splitting in Ce compounds is typically of the order of some ten millielectronvolts. According to Boltzmann's law (see eq. 2.11), this means that the three doublets are unequally populated at room temperature and lower. This has major consequences for many physical properties of the material, like the magnetic response (see section 2.1.3). Knowledge of the CF scheme is of crucial importance for the interpretation of such data.

The spatial anisotropy of the CF ground state leads to linear dichroism in Ce M$_{4,5}$ XAS (see section 5.2). It was shown by Hansmann *et al.* that the comparison of experimentally observed LD and respective calculations in full multiplet theory can allow determination of the crystal field scheme [167] (see section 6.1.2). For this purpose, spectra have to be calculated for each of the three doublets in a given CF scheme and for different alignments of the light polarization and crystal axes according to the experiment. The temperature dependent spectrum is then

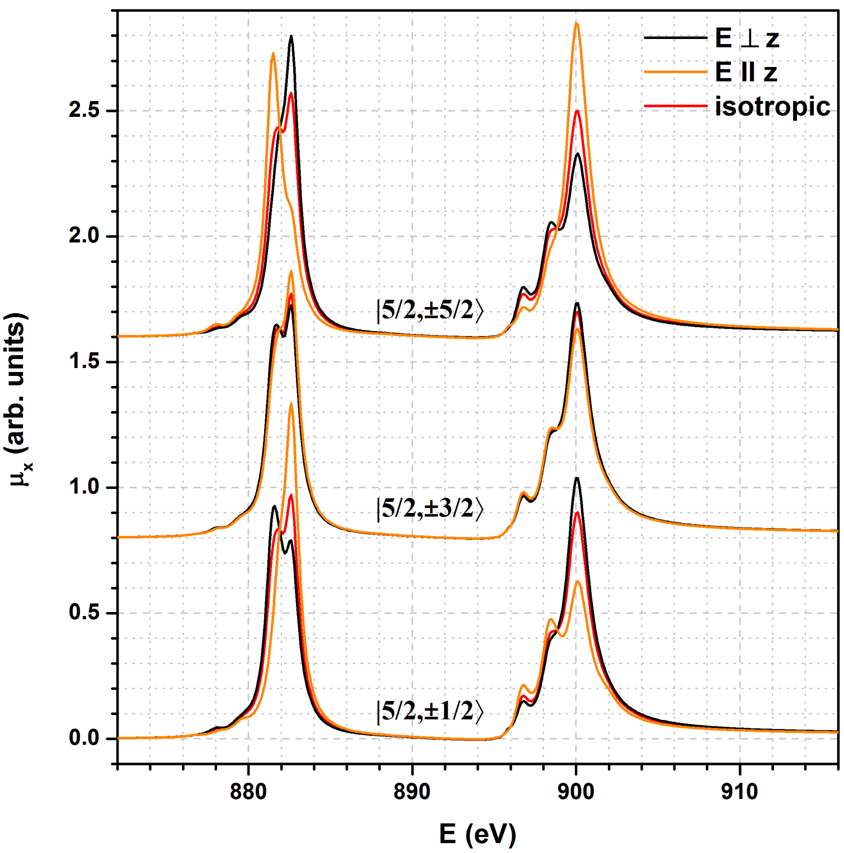

Figure 9.3: Calculated Ce $M_{4,5}$ $f^1 \rightarrow f^2$ spectra for linearly polarized light with $\vec{E}$ perpendicular and parallel to the quantization (z) axis, as well as the resulting isotropic spectra according to eq. 5.16, for the three different $|j = 5/2, \pm m_j\rangle$ initial states. The parameters that are given in tab. 8.1 were used for the simulation. The spectra are vertically offset by $\Delta\mu_x = 0.8(|m_j| - 1/2)$.

obtained by summation of these spectra with respective Boltzmann weighting factors according to the energy position of the doublet. This is done for all crystal field schemes that come into consideration, the one with best agreement between theory and experiment is taken as the result. It is self-evident that this procedure benefits from all information that can be used to reduce the number of possible level schemes[1]. The most important information is the local symmetry of the Ce ions. It determines which combinations of $|j, m_j\rangle$ states generate the new eigenstates. For the $CePt_5$/Pt(111) surface intermetallics that are studied in the present thesis, the local symmetry is hexagonal. This result was obtained in the detailed structural characterization that is described in chapter 7. For a $j = 5/2$ sextuplet in a hexagonal symmetry, the $|j, m_j\rangle$ states remain the eigensystem. In the following, these states are addressed as $||m_j|\rangle$.

With the eigenstates known, the only free parameters in the model are two energy splittings, the relative magnitude and sign of which determine the ordering of the three doublets. In the present thesis, the energy differences of the $|3/2\rangle$ and $|5/2\rangle$ doublets with respect to the $|1/2\rangle$ doublet are used to parametrize the crystal field.

No further information on the crystal field scheme of the surface intermetallics were available prior to the present thesis. $CePt_5$ bulk material has been characterized in 1979 by Lueken *et al.* [55]. These authors analyzed susceptibility measurements and obtained $\Delta E_{3/2} = 26$ meV and $\Delta E_{5/2} = 76$ meV. These values can be used as a starting point for the investigation, but it has to be considered that thin films can behave different from bulk material.

9.2.1 Simulation of the linear dichroism

Based on the simulation of the isotropic Ce $M_{4,5}$ XA spectrum of a $CePt_5/Pt(111)$ sample with $t \approx 11$ u.c. that is presented in section 8.3.1, the spectra for the three $|j, m_j\rangle$ doublets are readily calculated for alignment of the X-ray's electric field $\vec{E}$ parallel and perpendicular to the hexagonal c axis. These spectra are shown in fig. 9.3 along with the isotropic spectrum that was calculated according to eq. 5.16 for each state.

As expected for a complete j manifold, the three isotropic spectra coincide. Furthermore, the same isotropic spectrum can also be obtained as the average of the spectra of the three $\pm m_j$ substates for each of the two geometries.

The most prominent differences between the spectra for the different geometries are present in the relative height of the double-peak structure at the M_5 edge (features C, D in fig. 6.1) and in the relative height of the M_5 and M_4 main peaks (D, I). Analysis of these characteristics should allow interpretation of experimental spectra in terms of the calculated ones.

The calculated spectra for $|3/2\rangle$ in both geometries equal the sum of the spectra for $|5/2\rangle$ and $|1/2\rangle$, weighted in the ratio 1:2. This prevents the unambiguous identification of the ingredients to a measured spectrum, since the spectra for the three initial states are not linearly independent. Otherwise, it would have been possible to determine the crystal field energies in a hexagonal system from a single non-isotropic experimental spectrum taken at a certain temperature by fitting it with a Boltzmann-weighted sum of the three calculated spectra.

Nevertheless, valuable conclusions can be drawn from such an analysis. In particular, if a spectrum is taken at a temperature where the $4f$ electrons are not significantly excited above the ground state, which furthermore is not $|3/2\rangle$, an unambiguous identification of the ground state can be made. This attempt is described in the next section.

9.2.2 Analysis of selected spectra

Fig. 9.4 shows non-isotropic experimental data for the $t = 10.8$ u.c. sample at the lowest and highest temperature available. Both spectra were taken with circularly polarized light at $\theta = 0°$, which represents the case $E \perp z$.

The spectra are arbitrarily scaled to equal heights of the M_5 main peak (feature D in fig. 6.1). A representation that conserves the true linear dichroism as obtained in the calculated spectra is not possible for these data. This is mainly due to the fact that the spectra were recorded in presence of a magnetic field, which introduces an unknown angle-dependence of the TEY efficiency (see section 5.4.2).

The spectrum for $T = 14$ K (black symbols) shows significant deviations from the isotropic one. Relative to the M_5 main peak, both the secondary M_5 peak and the M_4 maximum are significantly enhanced. In comparison to the calculated spectra in fig. 9.3, the data resemble the spectrum for $m_j = \pm 1/2$ rather than $m_j = \pm 5/2$. This indicates that the $|1/2\rangle$ doublet is lower in energy than the $|5/2\rangle$ doublet.

However, the low-temperature spectrum is not reproduced by the pure $m_j = \pm 1/2$ spectrum. This indicates that the population of the $|1/2\rangle$ doublet is not 100 % at $T = 14$ K. Due to the aforementioned linear dependence of the calculated spectra, no conclusions regarding the other participating doublets are possible.

In order to quantify the degree to which the spectrum can be reproduced by the one for $m_j = \pm 1/2$, the experimental data were fitted with a linear combination of the calculated spectra shown for $E \perp z$ in fig. 9.3. Any two of the spectra can be used to produce any linear combination. Starting from the assumption of a $|1/2\rangle$ ground state, the spectrum can only get closer to the isotropic one with increasing temperature, which is obtained at high T independent of the CF scheme. Therefore, $\mu_{\mathrm{x}}^{\mathrm{iso}}$ was chosen as the second contribution. As is shown by the red line in fig. 9.4, excellent agreement between the fit and the $T = 14$ K data is obtained for a combination with 46 % contribution from the isotropic spectrum.

The dark red symbols in fig. 9.4 represent a spectrum taken at $T = 272$ K. In accordance with

---

[1] In this respect, the method resembles LEED IV studies, as described in section 4.2

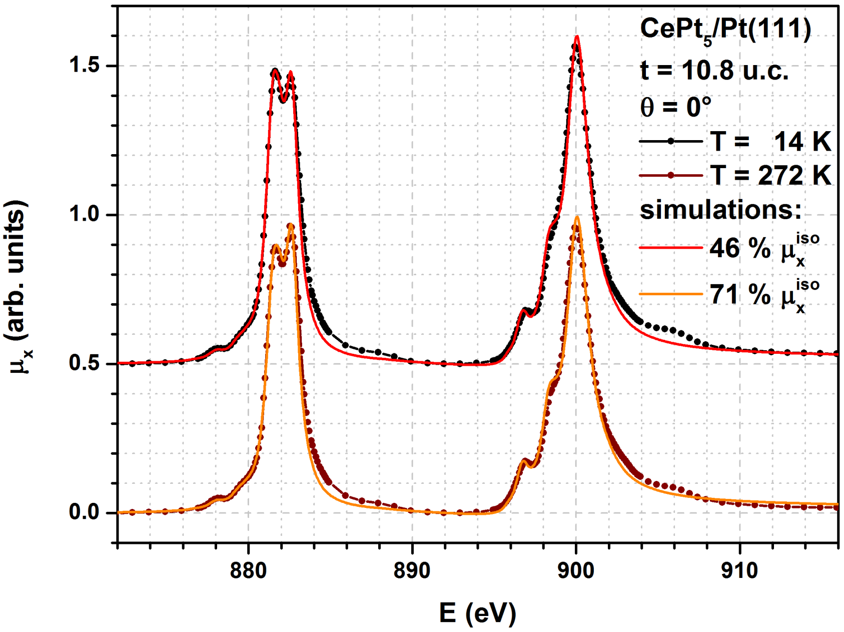

Figure 9.4: Non-isotropic spectra taken at $\theta = 0°$ on a $t = 10.8$ u.c. CePt$_5$/Pt(111) sample at low and high temperature. The solid lines represent fits to the experimental spectra under exclusion of the $f^0 \rightarrow f^1$ parts. The fit model is a linear combination of the simulation of the isotropic spectrum and the one for $m_j = \pm 1/2$, both are shown in fig. 9.3.

the expectation, the deviation from the isotropic spectrum is reduced at higher temperatures. A fit to this spectrum (orange line) yielded a relative fraction of 71 % of μ_x^{iso}.

In conclusion, the comparison of calculated spectra to selected experimental data indicates that the $|1/2\rangle$ represents the ground state in CePt$_5$/Pt(111), or it is energetically close to the ground state. In any case, it is lower in energy than the $|5/2\rangle$ doublet.

9.2.3 Temperature and thickness dependence of the linear dichroism

While the crystal field ground state of CePt$_5$/Pt(111) surface intermetallics can be narrowed down by inspection of low-T spectra, an analysis that aims at the energy splittings needs to include the progression of the linear dichroism with temperature.

For this purpose, the LD at each temperature should ideally be represented by a single number. This would allow direct fitting of the data with a model curve that includes the CF splitting energies as fit parameters.

The largest LD in a uniaxial crystal structure is observed as the difference of spectra taken for $E \parallel z$ and $E \perp z$. However, the former geometry is not achieved in the present dataset, where LD is addressed by circularly polarized light and varying the angle of incidence. Furthermore, extraction of the true LD from two spectra requires very careful alignment of the data. In particular, the relative scaling of the spectra has a major influence on the produced signal. This is difficult for the present data, since the electron yield is subject to unknown angle-dependence in the presence of a magnetic field (see section 5.4.2).

As a solution to this problem, the relative M$_5$/M$_4$ peak ratio Υ is defined. This dimensionless quantity exploits the aforementioned observation that the relative height of the two edges in the Ce M$_{4,5}$ spectrum is a good indicator of the linear dichroism. For an evaluation of $\Upsilon(T)$, the main peaks of both edges (features D and I in fig. 6.1) of a $\theta = 0°$ spectrum are independently fitted to an isotropic reference spectrum. The isotropic spectrum is required for normalization of the arbitrary units of the spectrum. In the fits, only the background before and behind the edge and some data points directly at the peak are considered. The ratio of the such obtained fit amplitudes $\mathcal{A}$ then yields

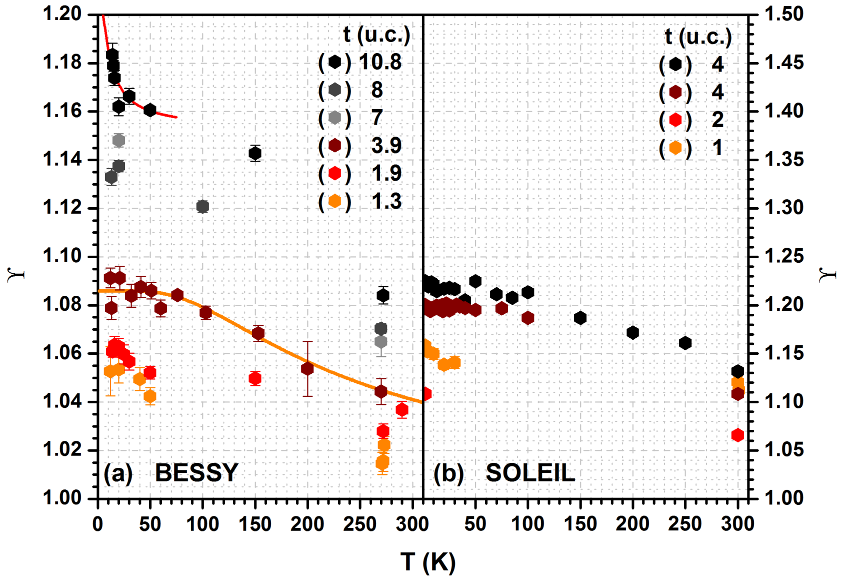

Figure 9.5: Visualization of the linear dichroism as $\Upsilon(T)$ for CePt$_5$/Pt(111) films with different thickness. The data in panels (a) and (b) were taken at BESSY and SOLEIL, respectively. The error bars reflect the errors of the fitting procedure. The solid red and orange lines represent least square fits according to eg. 9.4 to the data for $t = 10.8$ u.c. and 3.9 u.c., respectively (for details see text).

$$\Upsilon = \frac{\mathcal{A}(\mathrm{M}_5)}{\mathcal{A}(\mathrm{M}_4)}. \tag{9.3}$$

The definition of Υ is somewhat cumbersome. However, it yields a quantity that is very sensitive to the degree of LD in a $\theta = 0°$ spectrum, since the deviation from $\mu_{\mathrm{x}}^{\mathrm{iso}}$ is contrary for the two peaks. This outbalances the fact that only half of the magnitude of the LD can be addressed by experiments with CPL on thin films, since $\vec{E} \parallel c$ cannot be achieved.

The problem of relative scaling of isotropic and non-isotropic spectra is solved by the fitting procedure in the definition of Υ. In contrast to a fit of the experimental spectrum with a linear combination of two simulated spectra, Υ can be evaluated from experimental data alone. This is especially important for highly-hybridized samples, where the quality of the simulation suffers from line shape changes that are not yet understood (see section 8.4).

Results of the $\Upsilon(T)$ evaluation for the present set of samples are shown in fig. 9.5. Data for the samples that were measured at BESSY and SOLEIL are shown in panels (a) and (b), respectively. The evaluation of Υ for data of the two experimental setups yielded very different absolute values for otherwise comparable samples. This can be explained by the fact that the SOLEIL data were recorded with better experimental resolution. This influences the peak heights in the spectra and thus the Υ value that is evaluated with the given procedure.

For a comparison of the data taken at the two synchrotron facilities, their ordinates were relatively scaled in fig. 9.5. The scaling was chosen such that the results for samples with $t \approx 4$ u.c. and the positions of unity agree.

A main difference between the datasets from the two facilities is the hierarchy of samples with $t \approx 1$ u.c. and 2 u.c. For the BESSY data, $\Upsilon(2\text{ u.c.}) > \Upsilon(1\text{ u.c.})$, whereas the sequence is reversed at SOLEIL. This finding is contradictory and might hint at experimental problems in one of the two measurements, although no specific source of error could be identified. Its consequences are addressed further below.

The general progression of $\Upsilon(T)$ is very similar for all samples. At low temperatures, $\Upsilon > 1$. Upon increasing T to room temperature, Υ is reduced. According to its definition in eq. 9.3, Υ always approaches unity for high temperatures. If all CF split doublets are equally populated due to thermal excitations, the isotropic spectrum is obtained independent of the measurement geometry.

In order to quantify the energy scale that is present in the progression of $\Upsilon(T)$, the solid orange line in fig. 9.5 represents an exemplary fit to the $t = 3.9$ u.c. data with a simple Boltzmann law considering two energy levels,

$$\Upsilon(T) = \Upsilon_1 \mathcal{P}_1(T) + \Upsilon_2 \mathcal{P}_2(T). \tag{9.4}$$

The relative Boltzmann weighting factors $\mathcal{P}_n$ are defined by eq. 2.11. The energy separation of the two levels in the fit amounts to $\Delta E = 28 \pm 5$ meV.

In addition to the broad decline of Υ over the full temperature range, as indicated by the orange line, some of the datasets show a steep rise towards the lowest temperatures. This is especially visible in the data for $t = 1.9$ u.c. and 10.8 u.c. This finding can be interpreted as arising from a second energy scale, as would be expected for a three-level system. The red line represents a fit of eq. 9.4 to the low-T data for $t = 10.8$ u.c. with an energy separation of $\Delta E = 1.3 \pm 0.5$ meV. However, the observed low-T slope might also be connected to the time-dependent changes in spectral shape that are observed in the analysis of $n_f(T)$ (see section 9.1.2). Those are most prominent in the two samples showing this effect most clearly. This suspicion is supported by the fact that the $\theta = 0°$ data that were used for the evaluation of $\Upsilon(T)$ for these samples were measured directly after preparation and monotonously in time, starting from low temperatures. Further support for the interpretation as time-dependent effect is provided by the sample with $t = 3.9$ u.c., the $n_f(T)$ data of which also indicated time-dependent spectral changes. Here, the $\theta = 0°$ spectra for low temperature were also measured monotonously up to $T = 50$ K, with the exception of $T = 13$ K. This spectrum was recorded later and yields a lower Υ value compared to the earlier measurements. Hence, the negative slope that is indicated by the early low-temperature points might well be an artifact of temporal spectral changes and does not represent a second energy scale.

The datasets that are least affected by such time-dependent line shape changes are the ones for $t \approx 4$ u.c. taken at SOLEIL, which furthermore exhibit a high point density for low temperatures. These datasets indicate that $\Upsilon(T)$ is constant in the range $2\text{ K} \lesssim T \lesssim 50\text{ K}$. This observation allows the conclusion that the population of the CF split states does not significantly change in this temperature range, since all low-lying states, being it one or two of the doublets, are equally populated and the next highest level is too high in energy to contribute significantly.

Independent of the ordering of the three doublets, the finding of this plateau in $\Upsilon(T)$ allows the estimation that the energy separations of the three doublets fulfill the requirements $\Delta E \lesssim 1$ meV or $\Delta E \gtrsim 15$ meV.

While the simple model in eq. 9.4 allows rough estimation of the observed energy scales, it does not represent an appropriate model for the data. Such a model should reflect the definition of Υ and the true physical situation with three energetically separated doublets. A better description, which might also somewhat alter the estimated energy limits, especially requires an expectation for the absolute value of Υ for the different ground states that are possible. With this information, a model can be written as

$$\Upsilon(T) = \frac{\mathcal{A}(\mathrm{M}_5)(T)}{\mathcal{A}(\mathrm{M}_4)(T)} \quad \text{with}$$
$$\mathcal{A}(\mathrm{M}_n)(T) = \mathcal{A}^{\pm 1/2}(\mathrm{M}_n) + \mathcal{A}^{\pm 3/2}(\mathrm{M}_n)\, e^{-\frac{\Delta E_{3/2}}{k_\mathrm{B} T}} + \mathcal{A}^{\pm 5/2}(\mathrm{M}_n)\, e^{-\frac{\Delta E_{5/2}}{k_\mathrm{B} T}}. \tag{9.5}$$

The required reference values can be obtained from the calculated spectra that are shown in fig. 9.3 by performing a fitting routine equivalent to the evaluation of Υ from experimental data. The resulting fit amplitudes along with Υ values for all possible ground state combinations are given in tab. 9.1.

The experimental result of $\Upsilon > 1$ is not compatible with the assumption of a participation of $|5/2\rangle$ in the ground state. This is in line with the analysis of a low-T spectrum for $t = 10.8$ u.c.

ground state	$\mathcal{A}(\mathrm{M}_5)$	$\mathcal{A}(\mathrm{M}_4)$	Υ
$\|5/2\rangle$	0.823	1.237	0.665
$\|3/2\rangle$	1.046	0.964	1.085
$\|1/2\rangle$	1.208	0.869	1.390
$\|5/2\rangle + \|3/2\rangle$			0.849
$\|5/2\rangle + \|1/2\rangle$			0.964
$\|3/2\rangle + \|1/2\rangle$			1.230
$\|5/2\rangle + \|3/2\rangle + \|1/2\rangle$			1.0

Table 9.1: Theoretical reference values of Υ for the three possible ground states in a hexagonal crystal field (upper part). Values for the relative peak amplitudes $\mathcal{A}$ were obtained from least square fits of the calculated spectra for $E \perp z$ to the isotropic ones (see fig. 9.3) for both edges separately. The ratio of these values yields Υ according to eq. 9.3. In the lower part, Υ values for each possible combination with equal population of several of the three doublets are also given.

and $\theta = 0°$ in section 9.2.2. This analysis also yielded that the $|1/2\rangle$ doublet is significantly populated at low temperatures. Together with the considerations regarding the low-T plateau, this only leaves two possible configurations for the CF scheme: Either the isolated $|1/2\rangle$ doublet is the ground state or the $|1/2\rangle$ and $|3/2\rangle$ doublets with very small energy separation represent the lowest states. This is followed by a significant energy gap that produces the plateau in $\Upsilon(T)$ up to $T \approx 50$ K.

In this interpretation, the Υ value at the plateau should be well-defined by the peak amplitudes of the spectra of the low-lying states. For the present simulations, this would be $\Upsilon = 1.39$ or 1.23 for the two scenarios, as given in tab. 9.1. It has to be kept in mind that the simulations were done for a spectrum taken at BESSY. Due to the different resolutions, the absolute values obtained from this simulation cannot be transferred to the SOLEIL data.

The experimentally observed values for the BESSY samples are all considerably lower than the theoretical values for both the pure $|1/2\rangle$ and the combined $|1/2\rangle + |3/2\rangle$ ground state. Furthermore, there is a significant thickness-dependence of the low-T values, with lower Υ at lower t. Apparently, there is a mechanism that reduces Υ, and which becomes more important for thinner samples. An explanation for this observation can either be searched for in the physical properties of the sample or in the evaluation of Υ. Two approaches are presented in the following: A description in terms of a heterogeneous sample and the consideration of asymmetric transition line profiles due to strong hybridization in the thin samples.

Multilayer description of the films

A possible material-related source for the thickness-dependence of Υ is an interface effect. As is argued in section 9.1.1, the crystalline environment of the Ce ions close to the interfaces of the film is different than for the ions in the film "bulk". Hence, one could expect to observe different crystal field parameters in addition to different degrees of hybridization. The contributions of the two different regions to the Ce $\mathrm{M}_{4,5}$ spectrum recorded in TEY mode would be expected to depend on the thickness, with a larger contribution from the interfaces for thin films.

A theoretical description of the complete sample might not only require different values for the crystal field parameters at the interface and in the bulk, there might also be the need to consider additional terms due to the reduction of the local symmetry at the interface. The importance of such effects was pointed out by Welsch *et al.* in a theoretical study of hexagonal rare earth metal surfaces [271].

Ignoring such additional parameters to first order, a model for the complete film with different CF parameters at the interfaces can be constructed from eq. 9.5 analogous to eq. 9.1 by considering

$$\mathcal{A}(\mathrm{M}_n)(T) = \mathcal{A}^{\mathrm{s}}(\mathrm{M}_n)(T)\ \mathcal{F}(0, t_{\mathrm{s}}) + \mathcal{A}^{\mathrm{b}}(\mathrm{M}_n)(T)\ \mathcal{F}(t_{\mathrm{s}}, t - t_{\mathrm{i}}) + \mathcal{A}^{\mathrm{i}}(\mathrm{M}_n)(T)\ \mathcal{F}(t - t_{\mathrm{i}}, t). \quad (9.6)$$

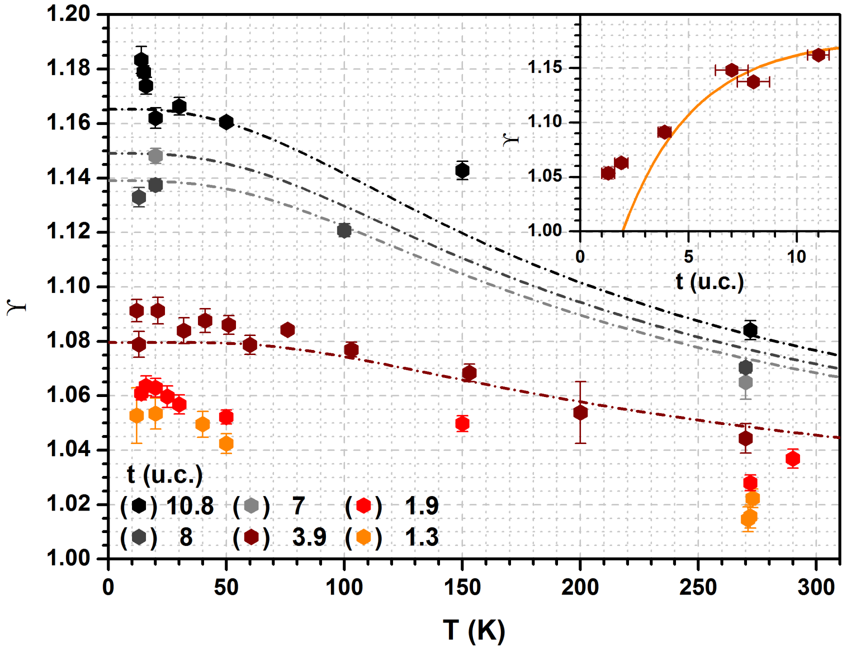

Figure 9.6: Least square fits of the model defined by eq. 9.6 to the experimental $\Upsilon(T)$ data for $t > 2$ u.c. taken at BESSY. The data are the same as in fig. 9.5 (a). Inset: Thickness dependence of Υ at $T = 20$ K along with a model curve using the same parameters as for the fits in the main panel.

If the parameters for surface and interface are set equal due to their comparable atomic arrangement (compare section 9.1.1), four different energy scales remain. For the present $\Upsilon(T)$ data, such a complexity is not observed. The conclusions that were drawn regarding the magnitude of energy splittings from the observation of a low-T plateau have to be considered for all different CF schemes that occur in the sample. Furthermore, in order to explain the reduction of Υ with decreasing thickness, one has to assume that the spectrum produced by the interface layers is closer to the isotropic one than the bulk. Hence, one has to expect that the splitting between the $|1/2\rangle$ and $|5/2\rangle$ doublets is below the lower limit that is required for the formation of the plateau.

A consistent and comparably simple description of the BESSY data can be achieved by assuming that the overall CF splitting at the interfaces is negligible. Hence, they contribute as the isotropic spectrum even at low temperature, whereas the bulk layers exhibit linear dichroism due to an excited $|5/2\rangle$ doublet. For reasons of further simplicity, the characteristics of bulk and interface layers are assumed to be independent of the thickness, which then only drives their relative mixture via the finite TEY information depth.

Least square fits of this model to the $\Upsilon(T)$ data for $t > 2$ u.c. are shown in fig. 9.6. The inset illustrates the thickness dependence at $T = 20$ K. In order to achieve agreement with the data, a higher value for the TEY electron escape depth of $\lambda_e = 1.5$ nm compared to the result of $\lambda_e \approx 1$ nm in section 7.4 has to be assumed. This is analogous to the result from modeling of $w_{\mathrm{rel}}^{0\to 1}(t)$ in section 9.1.1. Furthermore, the thickness dependence is not reproduced at all, if only the surface or the interface layer is assumed to feature different CF parameters from the rest of the film. Both interface layers need to be considered.

While the energy splittings of the interfaces were set to zero in the fits, the energy splittings in the bulk were left as free parameters. The results are $\Delta E^{\mathrm{b}}_{3/2} = 9.2 \pm 5.3$ meV and $\Delta E^{\mathrm{b}}_{5/2} = 25.6 \pm 2.0$ meV.

The agreement between model fits and data is good, at least for the thickest and thinnest sample considered. However, the model breaks down for $t \leq 2$ u.c., where the sample only consists of surface and interface layer. As can be seen in the inset of fig. 9.6, the respective data are not well described. Even if one allows for differences in surface and interface of such thin samples, samples for $t \leq 1$ u.c. should be described with one set of crystal field parameters only. Admittedly, the structural characterization that is presented in chapter 7 does not include samples with $t \leq 1$ u.c. and the results might not be conferrable to this thickness regime. Hence, there might be a completely different CF scheme due to a different, non-hexagonal local symmetry.

In the scenario provided by the fit results together with the model of fig. 9.1, the interface layers are characterized by smaller crystal field splitting but higher degree of hybridization as compared to the bulk of the film. This might reflect that the ionic and covalent contributions to the crystal field are unequally influenced by changes in the crystalline environment and that more itinerant $4f$ electrons are better capable to screen the anisotropic point charge potential of the environment.

Influence of the Ce $M_{4,5}$ line shape on Υ

As an alternative to the consideration of interface effects, the source of the thickness-dependence of Υ can also be searched for in the evaluation procedure. Different aspects come into mind that might falsify the absolute numbers obtained by the evaluation.

As was already addressed in the comparison of data taken at BESSY and SOLEIL, the experimental resolution influences the evaluation. While this affects the comparability of different experiments and the absolute numbers that are evaluated, it cannot explain the observed thickness dependence.

The spectra taken at $\theta = 60°$ are not perfectly isotropic, since this requires $\theta = 54.7°$. The comparability of spectra taken at $\theta = 60°$ to truly isotropic measurements was confirmed by exemplary measurements. The presence of unwanted LD in the isotropic spectrum would lead to an offset in Υ.

In general, concerns regarding the correct limits of the experimental $\Upsilon(T)$ data for the given procedure can be rebutted with reference to app. A.4. The $\Upsilon(T)$ results for a Ce-Ag(111) sample shown there were obtained by exactly the same procedure as for the CePt$_5$/Pt(111) intermetallics. These data approach unity for $T > 100$ K, since the total crystal field splitting in Ce-Ag(111) is much smaller.

An important aspect that needs discussion in this context is the effect of TEY saturation (see section 5.5). Even though the effect of saturation in the given material is small, it could influence the Υ evaluation, since the dichroic data and the isotropic reference spectra were taken at different angles of incidence. As can be seen in fig. 8.1 (b), saturation is much stronger for $\theta = 60°$ and the magnitude of the effect furthermore depends on the film thickness.

However, this should not play a role for the evaluation of Υ, which is mainly due to the very similar heights of the two absorption lines.The θ-induced damping of the isotropic spectrum leads to a comparable reduction of both peaks, which can be expressed by the same multiplicative factor for both fit amplitudes in eq. 9.3. Due to the quotient, this factor cancels out.

It might well be that the t dependence of Υ is connected to the t-dependence of the $f^0 \to f^1$ weight, which si shown in fig. 9.1. The theoretical values that are given in tab. 9.1 were obtained from a simulation of the spectrum of the thickest sample that was investigated in the present thesis. This sample displayed the lowest $f^0 \to f^1$ weight observed and is thus closest to a localized $4f^1$ state.

An increase of $w_{\mathrm{rel}}^{0\to 1}$ in the Ce $M_{4,5}$ spectrum should not influence the result for Υ. The transfer of weight from the $f^1 \to f^2$ to the $f^0 \to f^1$ contribution should have equal impact on the isotropic and non-isotropic geometries. However, this weight transfer is accompanied by line shape variations of the isotropic $f^1 \to f^2$ spectrum, as is discussed in chapter 8. This might well have an impact on the evaluation of Υ with the given procedure. In this scenario, time-dependent changes in n_f directly lead to a time-dependence of Υ, which is consistent with the experimental findings.

An inconsistency of this idea with respect to the experimental data is provided by the thinnest samples of the BESSY dataset. The $f^0 \to f^1$ weight and the accompanying deviations of the line shape from the fully localized case are strongest for $t \approx 2$ u.c. If this effect is responsible for the thickness-dependence of Υ, one would expect that the thickness-dependent data (best

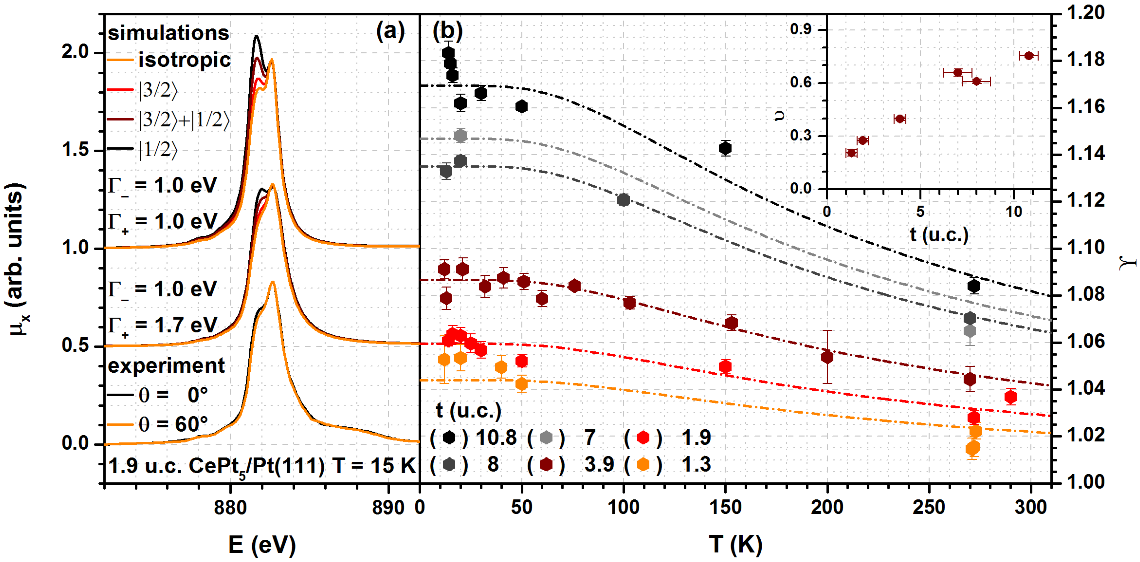

Figure 9.7: (a) Impact of asymmetric transition line profiles on the appearance of linear dichroism at the Ce M_5 edge. Calculated spectra in analogy to fig. 8.12 are shown along with experimental data for a $CePt_5/Pt(111)$ film with $t = 1.9$ u.c. (b) Least square fits to the data of fig. 9.5 (a) with a model according to eq. 9.5 and additional consideration of a correction factor υ according to eq. 9.7. The inset shows the thickness-dependence of υ.

ground state	$\mathcal{A}(M_5)$, symmetric	$\mathcal{A}(M_5)$, asymmetric	υ
$\lvert 5/2\rangle$	0.816	0.864	0.743
$\lvert 3/2\rangle$	1.049	1.033	0.687
$\lvert 1/2\rangle$	1.225	1.133	0.594

Table 9.2: Comparison of the fit amplitudes $\mathcal{A}(M_5)$ for simulated spectra with symmetric and asymmetric transition line profiles, as shown in fig. 9.7. The correction factor υ is defined by eq. 9.7.

represented by the inset of fig. 9.6) reproduce this peaking behavior. However, $\Upsilon(t)$ exhibits a monotonous incline. This finding is contrasted by the data from SOLEIL, where the low-T values of Υ resemble the progression of the $f^0 \rightarrow f^1$ weight. Hence, the SOLEIL data support the idea that the t-dependence of Υ is caused by the hybridization-induced line-shape changes. Regrettably, the mechanism of the observed hybridization-induced line shape changes could not be clarified in the present work. Nevertheless, an attempt can be made to understand their impact on the evaluation of Υ. In fig. 8.12, it is shown that an asymmetric line profile is capable to explain the observed M_5 line shape variations of the isotropic spectrum. This idea can be applied to non-isotropic spectra as well.

Examples of such simulations are shown in fig. 9.7 (a) along with corresponding experimental data for $t = 1.9$ u.c. In analogy to fig. 8.12, no energy-dependence of the lifetime width was considered. Indeed, the assumption of an asymmetric line profile reproduces the experimental observation. The differences between isotropic and non-isotropic spectrum appear strongly reduced when the two are fitted to equal height of the M_5 main peak.

The determination of alternative theoretical Υ values with respect to the ones given in tab. 9.1 requires the simulation of the full spectrum. Due to the thin knowledge base regarding the idea of an asymmetric line shape, this was not attempted at in the present thesis. Nevertheless, the simulations of the M_5 edge at least allows derivation of the fitting amplitudes $\mathcal{A}(M_5)$ for different ground state configurations. These results are given in tab. 9.2 for both the symmetric and asymmetric line profiles as shown in fig. 9.7 (a).

The quantity υ that is additionally given in the table describes the relative change in deviation of the amplitude from unity and is defined by

$$\mathcal{A}^{m_j}_{\mathrm{asym}} = 1 + \upsilon\ (\mathcal{A}^{m_j}_{\mathrm{sym}} - 1). \tag{9.7}$$

In order to consider the effect of line-shape variations on Υ, such correction factors were introduced to the model given by eq. 9.5. As an approximation, the same factor υ was used for all amplitudes, independent of the absorption edge and the m_j doublet. Fit results of this model to the BESSY data are shown in fig. 9.7 (b).

In these fits, the same crystal field splittings were used for all samples. As analyzed above, only two configurations for the ground state come into consideration: an isolated $|1/2\rangle$ doublet or nearly degenerate $|1/2\rangle$ and $|3/2\rangle$ doublets. The latter scenario was chosen for the fits by setting $\Delta E_{3/2} = 0$ meV, since υ is thus closer to unity. The temperature dependence of Υ is then only produced by the progressive population of the $|5/2\rangle$ doublet. The fit yielded $\Delta E_{5/2} = 23.6 \pm 1.1$ meV. The agreement between the experimental data and the model is good. The results for υ in dependence of the film thickness are shown in the inset of fig. 9.7 (b). It should be noted that even in the assumed CF scheme, υ is significantly smaller than unity for the thickest sample with $t = 10.8$ u.c. Since the XAS simulation that yielded the theoretical fit amplitudes of tab. 9.1 was done for this sample in the first place, one could have expected that no correction factor is needed here. In turn, the simulation that is shown in fig. 8.7 yielded good, but not perfect reproduction of the experimental data. This indicates that the $f^1 \rightarrow f^2$ line shape is already affected by the small hybridization in this sample, which has not been considered in the simulation. This could be a reason for the observed discrepancies in the non-isotropic spectra.

9.3 Conclusions to the chapter

The results of the present chapter illustrate the rich information that is contained in the line shape of Ce $M_{4,5}$ XA spectra. The analysis of the relative weight of the $f^0 \rightarrow f^1$ contribution for $CePt_5$/Pt(111) surface intermetallics with variable film thickness revealed the strong thickness-dependence of the valence in this material. A maximum of the valence at $t \approx 2$ u.c. is found in accordance with a previous PES study [79]. At lower thickness, the variation can be connected to substrate-induced lattice strain in the intermetallic films. The progression of the $f^0 \rightarrow f^1$ weight at higher thickness can consistently be explained by an interface effect in combination with the finite probing depth of XAS in the TEY mode.

The availability of temperature-dependent Ce $M_{4,5}$ XAS data allows addressing the Kondo temperature via the progression of the $f^0 \rightarrow f^1$ weight. The present results indicate that it is of the order of $T_K \approx 100 \ldots 200$ K and depends on the sample thickness. While the amount of currently available data does not allow definite conclusions, there seems to be no direct correlation between T_K and the absolute $f^0 \rightarrow f^1$ weight at low T.

The analysis and interpretation of $w^{0\rightarrow 1}_{\mathrm{rel}}(T)$ is complicated by the finding of time-dependent changes in the $f^0 \rightarrow f^1$ weight. Those are most likely caused by adsorbates from the residual gas in the vacuum chamber, which induce small variations of the potential that is experienced by the surface-nearest Ce ions. The induced changes in $w^{0\rightarrow 1}_{\mathrm{rel}}$ are small, but a changing degree of hybridization might also affect the Kondo temperature. There is currently no experience of the magnitude of correlation between the two quantities.

The finding of an adsorbate-controlled Ce valence could open a new direction of research on surface intermetallics, since there is a high interest in materials with tunable degree of electron correlation. However, this requires additional test experiments which are beyond the scope of the present thesis. In any case, a procedure to better control the aspect of time-dependent $w^{0\rightarrow 1}_{\mathrm{rel}}$ changes should be developed for future experiments in order to produce artifact-free results. Possible treatments are the repeated removal of adsorbates by sample annealing, the systematic saturation of the surface with a well-defined adsorbate layer or the deposition of an additional protection layer during preparation of the sample.

In order to address the temperature-dependence of crystal field induced linear dichroism in polarization-dependent XAS experiments, the relative M_5/M_4 peak ratio Υ is introduced in the

present chapter. This quantity expresses the deviation of a certain spectrum from the isotropic reference in a single number and is sensitive to the m_j character of the $j = 5/2$ ground state.
The modeling of $\Upsilon(T)$ on the basis of calculated non-isotropic spectra gives access to the crystal field splittings in the material under investigation. For CePt$_5$/Pt(111), Υ exhibits a strong thickness-dependence in addition to the T-dependence. This finding can be explained either by an interface effect in analogy to the interpretation of $w_{\text{rel}}^{0\to 1}(t)$, or as a consequence of the hybridization-induced line shape changes and the thickness dependence of the $f^0 \to f^1$ weight. Modeling of the data using a heterogeneous sample with distinct CF schemes at the interfaces yields good results for thick samples, but breaks down for the thinner ones. In order to reproduce the data, the CF splitting at the interfaces has to be assumed to be very low.
As is discussed in chapter 8, the line shape variations are not fully understood yet. This complicates their correct treatment regarding the evaluation of linear dichroism. At the present stage, the most plausible scenario is that the progressive delocalization of the $4f$ level leads to an asymmetric profile of the individual transitions lines. This can explain the observed variations in the isotropic spectrum as well as the apparently less-pronounced linear dichroism. In this interpretation, the observed reduction of Υ does not reflect a weaker linear dichroism, but simply means that the given evaluation procedure is less sensitive to the presence of LD for spectra of highly hybridized samples.
Regarding the modeling of $\Upsilon(T)$, the line shape variations can be approximately considered by a single correction factor for the fit amplitudes, which then depends on the degree of hybridization. For CePt$_5$/Pt(111), convincing results can be achieved by assuming that the $4f$ ground state is a quasi-quartet consisting of the $|1/2\rangle$ and $|3/2\rangle$ doublets, whereas the $|5/2\rangle$ doublet is excited by $\Delta E_{5/2} \approx 20 \ldots 25$ meV. This level scheme can explain data from the complete range of film thicknesses that was investigated in the present work.
At the present stage, this scenario is favored over alternative approaches due to its capability to describe most of the data together with its simplicity and the small number of free parameters. For definite conclusions, additional information is required. Such information are provided by measurements of the paramagnetic susceptibility, which are presented in chapter 10. It is shown there that a consistent interpretation of both XMCD and XAS data can be achieved within the scenario of asymmetric transition line profiles. The scenario of a heterogeneous sample with zero CF splitting at the interfaces is refuted. Furthermore, the larger amount of data allows to consider a thickness-dependence of $\Delta E_{5/2}$, which is shown to be in line with the lattice relaxation.

Chapter 10

Local $4f$ magnetism probed by XMCD

Contents

The results of the previous chapters represent a detailed characterization of CePt$_5$/Pt(111) surface intermetallics. The crystal structure (chapter 7) is illuminated as well as the degree of hybridization (section 8.3) and its tunability by the film thickness (section 9.1.1), the Kondo energy scale (section 9.1.2) and the crystal field scheme (section 9.2). This provides a solid basis for the application of XMCD to this model heavy fermion material.

Magnetism in Ce compounds is governed by the Ce $4f$ electrons, which are localized at the atomic Ce sites (see section 2.1). XMCD at the Ce M$_{4,5}$ edges probes this magnetic moment element and orbital specifically, which gives access to the local magnetic properties (see section 5.3). The present chapter aims at characterization of the magnetic behavior of CePt$_5$/Pt(111) in dependence on temperature T and external magnetic field strength B, as well as on the film thickness t.

Representative $\mu(B)$ curves for a CePt$_5$/Pt(111) sample with $t = 4$ u.c. are shown for several sample temperatures in fig. 10.1. In each measurement, scans with the two possible field sweeping directions produced coinciding curves. The curves displayed in the figure represent their average, which is furthermore symmetrized according to $-\mu(-B) = \mu(B)$.

The absence of hysteresis as well as the high field and low temperature that are required to obtain significant deviations from a linear $\mu(B)$ relation confirm that the samples are paramagnetic down to $T = 2$ K, the lowest temperature achieved in the present experiments. Hence, the paramagnetic susceptibility (see eq. 2.22) is a well-defined and meaningful quantity to characterize the magnetic behavior in dependence of the temperature.

The main part of the present chapter is devoted to $\chi^{-1}(T)$ data of CePt$_5$/Pt(111) intermetallics, starting with representative datasets for $t \approx 4$ u.c. (section 10.1). In the discussion, the crystal field is considered as well as RKKY interaction, screening of the effective magnetic moment due to Kondo interaction and magnetic signatures of the transition to a coherent heavy fermion state. The analysis is then extended to samples with varying film thickness (section 10.2),

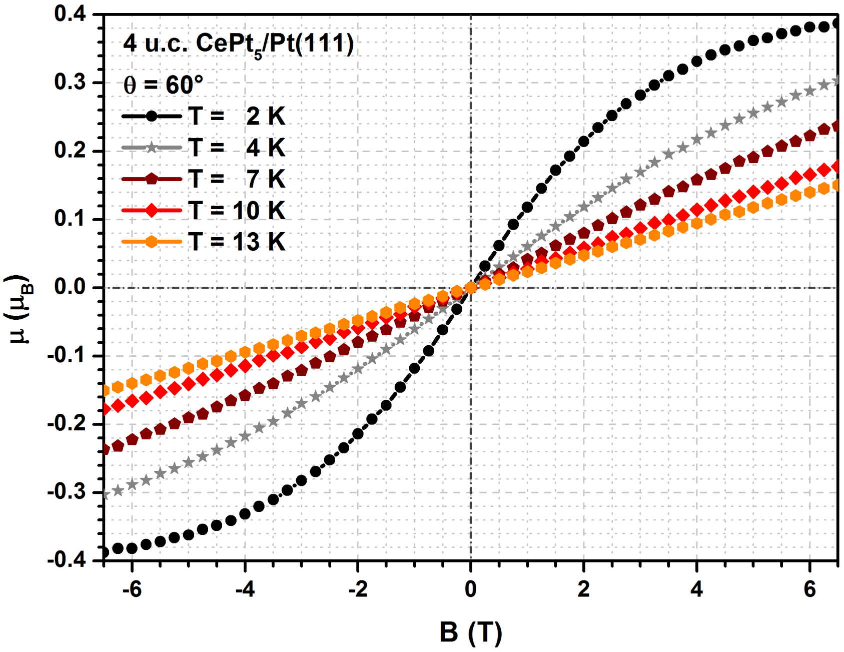

Figure 10.1: Dependence of the magnetic moment on the magnetic field for a $\mathrm{CePt_5/Pt(111)}$ sample with $t = 4$ u.c. taken at $\theta = 60°$ and various temperatures. The curves are symmetrized averages of the curves taken for both field sweeping directions.

which leads to the development of a consistent model that is capable to describe the complete dataset (section 10.3). Results are presented in section 10.4. While this treatment disregards the presence of coherent band effects at low temperatures, this regime is analyzed in detail in section 10.5. In addition to the low-T susceptibility, $\mu(B)$ curves are discussed in terms of a renormalized band structure.

10.1 The inverse susceptibility for $t = 4$ u.c.

The identification of $\mathrm{CePt_5/Pt(111)}$ as a heavy fermion material with PES by Klein *et al.* was reported for a sample with $t \approx 4$ u.c., judged by the LEED pattern (see section 7.2) [94]. Hence, comparable samples received special attention in the present experiments. A Curie-Weiss plot for two $\mathrm{CePt_5/Pt(111)}$ specimen with $t \approx 4$ u.c. is shown in fig. 10.2, including data for $\theta = 0°$ and 60°.

One of the datasets was recorded at BESSY, the other at SOLEIL. The experiments are complementary regarding the accessible temperature range. The setup at SOLEIL allowed reaching significantly lower temperatures down to $T \approx 2$ K, but it was not possible to reliably detect the XMCD signal for $T \gtrsim 50$ K (see section 5.4). A third dataset of another sample with $t = 4$ u.c., also measured at SOLEIL, is not shown here due to much worse data quality.These data reproduce the ones presented here within the given uncertainties.

The susceptibility data were obtained from XMCD measurements as described in section 6.4. The agreement of the two datasets is very good. Two dominant features can be identified in the large-scale overview of panel (a). First, the susceptibility is anisotropic regarding the direction of the magnetic field, with larger inverse susceptibility obtained at $\theta = 0°$. Second, the $\theta = 0°$ data exhibit a pronounced change of slope at $T \approx 50$ K. The slope at higher temperatures is smaller, which means that the effective moment is larger according to eq. 2.24. Below the kink, the slope appears to be constant.

These findings are consistent with the influence of a hexagonal crystal field, as is expected for the given crystal symmetry (see section 2.1.3 and chapter 7). The uniaxial CF causes the paramagnetic response to be anisotropic with respect to the relative alignment of magnetic field and hexagonal c axis. The measurement geometry with $\theta = 0°$ represents the case $B \parallel c$.

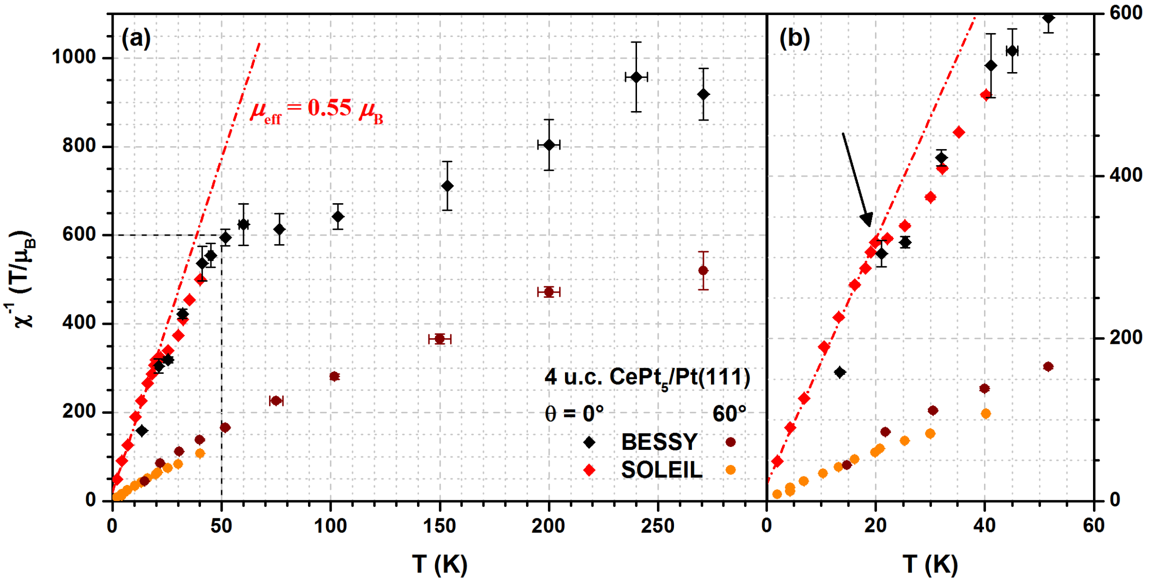

Figure 10.2: (a) Temperature-dependence of the inverse susceptibility for two CePt$_5$/Pt(111) specimen with $t \approx 4$ u.c. for $\theta = 0°$ and $60°$. Complementary temperature ranges were addressed by experiments at SOLEIL and BESSY. The dash-dotted line represents a linear least square fit to the data with $T \lesssim 20$ K of the SOLEIL sample and allows determination of an effective moment according to eq. 2.24. The scaling of the plot equals the one of fig. 2.4 (b) Zoom-in of the low-temperature region as indicated by the rectangle in panel (a). The arrow indicates an anomaly in the otherwise observed Curie-Weiss behavior.

For $\theta = 60°$, the signal is dominated by the orthogonal situation $B \perp c$, whereas $B \parallel c$ only contributes to 25 % (see eq. 6.13).

The hexagonal CF conserves the j, m_j quantum numbers of the $4f$ electron and splits the $j = 5/2$ multiplet into three Kramers doublets, which are characterized by their $\pm m_j$ values. In the following, they are referred to as $|m_j\rangle$ for short.

As can be seen from simulations of $\chi^{-1}(T)$, examples of which are shown in fig. 2.5, the character of the observed anisotropy clearly indicates that the $|1/2\rangle$ doublet is largely populated at the lowest temperatures available, which makes it a good candidate for the ground state. The $|3/2\rangle$ doublet could also be low in energy, but not more than $\Delta E_{3/2} \approx -2$ meV below the $|1/2\rangle$ doublet. Otherwise, a crossing of the curves for the two field directions would occur in the accessible temperature range, which is not observed. Contribution of $|5/2\rangle$ to the low-T behavior is excluded, since then $\chi^{-1}_{0°}(T)$ would be smaller than $\chi^{-1}_{60°}(T)$.

The constant slope of $\chi^{-1}_{0°}(T)$ for $T \lesssim 50$ K indicates that that a significant energy gap exists between the electron level that govern the low-T behavior and the next excited state. The position of the kink suggests that this gap is of the order of $\Delta E \approx 15 - 25$ meV by comparison to simulations. In order to produce an increase of the effective moment to higher temperatures, the upper level is required to possess higher m_j character than the ground level.

Concrete simulations of the $\chi^{-1}(T)$ data and a more exact determination of the CF parameters are attempted at in section 10.3. Before proceeding on this route, a closer look at the low-temperature data shall be taken. This should allow conclusions regarding the ground state, which can, e.g., be a nonmagnetic Kondo state, display magnetic order or show signatures of coherent band formation in a heavy fermion material (see chapter 1).

Fig. 10.2 (b) shows a zoom-in to the low-T region corresponding to the rectangle in panel (a). The most striking feature is an anomaly in the $\theta = 0°$ data at $T \approx 20$ K, as indicated by the arrow. It is present in both datasets, but much more clearly visible in the SOLEIL data due to the higher point density. At this point, the data deviate from Curie-Weiss behavior. It seems that the $\chi^{-1}_{0°}(T)$ curve gets displaced by some kelvin. Since the slope and thus the effective moment does not change significantly, a crystal field effect can be ruled out as an explanation for this finding. This is further supported by the absence of a signature in the analysis of LD in

XAS (see section 9.2).

Due to the linearity, the displacement of the curve is not necessarily in the direction of the T axis, but can also be considered along the χ^{-1} axis. In that case, it corresponds to a change in the mean field coupling constant, as introduced in section 2.1.4. Linear least square fits to the SOLEIL data below and above the anomaly yield axis intercepts of $\chi_<^{-1} = 21.2\ \mathrm{T}/\mu_\mathrm{B}$, $T_< = -1.4$ K and $\chi_>^{-1} = -83.2\ \mathrm{T}/\mu_\mathrm{B}$, $T_> = 5.5$ K. Hence, the coupling seems to change from ferromagnetic at high T to weakly antiferromagnetic at low T.

The finding of ferromagnetic correlations at high temperature in CePt$_5$/Pt(111) surface intermetallics is in contrast to results on CePt$_5$ bulk samples [55, 75], and untypical for a Kondo system. It might be a consequence of the reduced dimensionality of the thin film samples.

The fit for $T \lesssim 20$ K is shown as the dash-dotted line in fig. 10.2. The slope allows determination of the effective moment according to eq. 2.24, which yields $\mu_\mathrm{eff} = 0.544 \pm 0.004\ \mu_\mathrm{B}$. This value amounts to 74 % of the smallest effective moment that is possible in a localized $4f^1$, $j = 5/2$ system with hexagonal symmetry, as evaluated in section 2.1.3. Such a prominent reduction cannot be an artifact of the XMCD evaluation routine, as is shown in app. A.4. It is rather interpreted as a direct consequence of Kondo interaction. In Kondo systems, the impurity moment is screened by Kondo singlet formation (see fig. 1.1 (b)).

The analysis of the BESSY data in fig. 10.2 (b) suffers from the low point density. The available information seem to contrast the results of the SOLEIL data. While the $\chi_{0^\circ}^{-1}(T)$ curves and slopes coincide above the anomaly, the slope is much steeper below, with the consequence of an apparent enhancement of ferromagnetic coupling at low T.

However, the low-T analysis is based on two data points only. In general, the sum rule evaluation is most reliable at low T due to the large XMCD signal, and the small error bars reflect that the relative fitting procedure that was applied to obtain the $\chi^{-1}(T)$ values was free of larger uncertainties. Nevertheless, a measurement error cannot be excluded for the single measurements.

Another explanation for the apparent discrepancy would be that the temperature value of the lowest BESSY data point, which has been measured to $T = 13.4$ K, is overestimated by some kelvin. This suspicion is supported by the $\theta = 60^\circ$ data, where the same trend can be observed in comparison to the SOLEIL data. This would mean that the sample was at a lower temperature than the temperature sensor, which is rather unlikely regarding the design of the experimental setup. A miscalibration of the temperature sensor is also possible, but this should not produce a deviation of several kelvin.

Reversely, the temperature values of the SOLEIL data might also be uncertain in the low-T regime. In this setup, the temperature sensor is placed between the sample and the cryostat, which means that the sample is likely at a slightly higher temperature than measured by the sensor. A discrepancy of $\Delta T \approx 1.5$ K between the both is probable at the lowest temperatures [272]. Hence, it the SOLEIL data might be somewhat shifted to lower T, whereas the temperature of the BESSY data point seems to be slightly overestimated. This could explain the observed discrepancy of the two datasets.

The change of RKKY interaction as indicated by the anomaly at $T = 20$ K indicates a significant change of the Fermi vector at this temperature (see eq. 1.2). As depicted in fig. 1.2, a change of the Fermi surface is expected for the transition to the heavy fermion state. Hence, the anomaly is interpreted as a signature of emerging coherence and heavy fermion band formation. This interpretation is in line with the detection of a hybridization gap with PES on a comparable sample at $T = 13$ K [94]. Similar anomalies in $\chi^{-1}(T)$ data have been interpreted as signatures of coherence in CePb$_3$ [273] and CeAl$_3$ [14].

The low-T phase is investigated in more detail in section 10.5. In the following, modeling of $\chi^{-1}(T)$ and disentanglement of crystal field effects and Kondo interaction is attempted at for the single-impurity regime.

10.2 Thickness-dependent screening of the effective moment

Regarding the main characteristics, the $\chi^{-1}(T)$ data of the $t = 4$ u.c. samples are representative for the complete set of CePt$_5$/Pt(111) samples that were investigated by XMCD in the present thesis. The inverse susceptibility is always anisotropic and largest for $\theta = 0°$. Furthermore, $\chi_{0°}^{-1}(T)$ is always characterized by a linear region at low T and, where the respective data are available, by a sudden decrease in slope at $T \approx 50$ K. The linear regions coincide with plateaus in the $\Upsilon(T)$ data of fig. 9.5, which reflect the linear dichroism in XAS.
The analysis of the linear region in $\chi_{0°}^{-1}(T)$ for the $t = 4$ u.c. SOLEIL sample in fig. 10.2 revealed that the effective moment is significantly screened with respect to the smallest possible value of a Ce^{3+} ion in a hexagonal crystal field. The results of analogous evaluations for the complete set of samples are shown in fig. 10.3.
Panels (a) and (b) show $\chi_{0°}^{-1}(T)$ data and the linear least square fits for all but the $t = 4$ u.c. sample for which it is shown in fig. 10.2. Data for $T \lesssim 40$ K were used for the fits. The effective moments are calculated from the fit results of the slope according to eq. 2.24 and are shown in dependence of the intermetallic film thickness in panel (c). The error bars for μ_{eff} were calculated via error propagation from the fit errors. The impact of the uncertainties in χ^{-1} on the slope result was considered by using the error bar of each data point for its weighting in the linear fit. The error bars do not reflect the uncertainties in the sample temperature. As discussed in section 10.1, those are perceptible in the low-T region and might sensitively affect the evaluated slope. Furthermore, the possible existence of an anomaly, as is clearly visible in the SOLEIL data in fig. 10.2 (b), was not considered in the fits. This might lead to further uncertainties, but none but the named dataset was measured with the necessary high point density to unambiguously identify such an anomaly. Hence, the evaluation is certainly influenced by larger uncertainties than indicated by the error bars. The applied method represents the best compromise for the given dataset.
The left ordinate in fig. 10.3 (c) presents the absolute value of μ_{eff} in units of μ_{B}. On the right, the ratio to $\mu_{\text{eff}}(|1/2\rangle) = 0.74\ \mu_{\text{B}}$ is given, which represents the theoretical value for a pure $|1/2\rangle$ ground state (see section 2.1.3).
The $\mu_{\text{eff}}(t)$ data can roughly be divided intro three groups. At low thickness ($t < 2$ u.c.), the effective moment is highest and even exceeds $\mu_{\text{eff}}(|1/2\rangle)$ by 20 %. No mechanism is known to the author that can explain the enlargement of the effective moment of a single Kramers doublet. Hence, the result indicates that not only the $|1/2\rangle$ doublet contributes to the susceptibility of these samples in the addressed temperature range.
For intermediate thickness ($t = 2 \ldots 4$ u.c.), μ_{eff} is significantly smaller than $\mu_{\text{eff}}(|1/2\rangle)$. As already pointed out in section 10.1, this reduction is interpreted as a consequence of Kondo interaction. The smallest effective moment $\mu_{\text{eff}} = 0.52 \pm 0.02\ \mu_{\text{B}}$ is observed for a sample with $t = 1.9$ u.c.
Upon further increasing the thickness, the effective moment again increases and approaches the value of $\mu_{\text{eff}}(|1/2\rangle)$ at $t = 8$ u.c. Then, at $t = 10.8$ u.c., the evaluation again yields a significantly reduced moment.
The latter finding appears to be out of place. Ignoring it, the general appearance of the data in fig. 10.3 (c) strongly resembles the t-dependence of the $f^0 \rightarrow f^1$ weight in the XA spectra, as shown in fig. 9.1. A large $f^0 \rightarrow f^1$ weight seems to be connected to a small effective moment. This result is fully in line with the expectation for a Kondo system: The $f^0 \rightarrow f^1$ weight reflects the magnitude of the hybridization matrix element, which also governs the Kondo interaction between the localized $4f$ level and conduction states. This interaction results in an effective screening of the magnetic impurity moment, which thus is present in the $\chi^{-1}(T)$ data.
In this interpretation, the effective moment of the thickest sample seems to be underestimated, which means that the slope in the linear fit is overestimated. Regrettably, only one sample in this high-thickness range has been investigated by Ce M$_{4,5}$ XMCD in the present work. The reliability of all other data points is supported by the fact that several similar samples were measured that show a consistent behavior.
A close look at the data in fig. 10.3 (b) (orange symbols) reveals two aspects: First, there

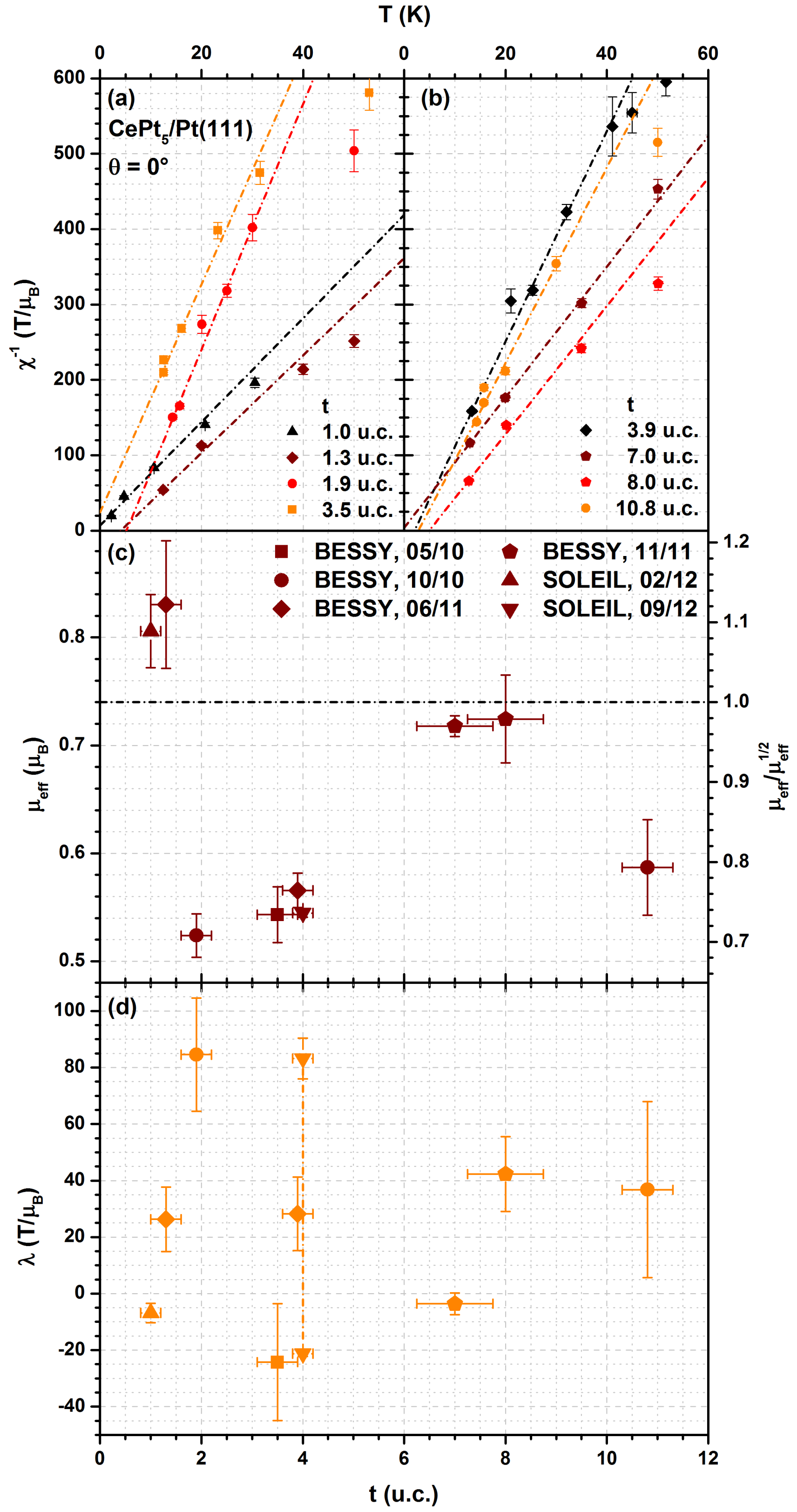

Figure 10.3: Evaluation of the effective moment at low temperature from $\chi_{0^\circ}^{-1}(T)$ data in dependence of the film thickness. (a) and (b) Linear least square fits to the low-T data for low and high t, respectively. (c) Thickness dependence of the effective moments as evaluated from the slopes of the fits in (a), (b) and fig. 10.2 according to eq. 2.24. The symbol type indicates the beamtime in which the samples were investigated, as given by the legend. The right ordinate gives the effective moment relative to the value of an isolated $|1/2\rangle$ doublet, the dash-dotted line marks unity on this scale. (d) Coupling constant λ, obtained as the ordinate intercept of the fits. The symbol types refer to panel (c). The dash-dotted line connects the low- and high-T results for the $t = 4$ u.c. data of fig. 10.2.

are two data points at $T \approx 16$ K, which were evaluated from independent measurements and which deviate by approximately 10 %. This discrepancy does not sensitively affect the linear fit, since there are more data points in the direct vicinity. However, it demonstrates the magnitude of uncertainties one can encounter in these data. Second, the distribution of the data on the temperature axis with four points in the range $T = 10 \ldots 20$ K and only one additional, isolated point at $T = 30$ K, makes the evaluation of the slope very sensitive to the latter single point. Assuming that the given value is overestimated by 10 % leads to a reduced slope and to an increase in μ_{eff} by 5 % compared to the result shown.

While this assumption alone does not bring the data point to complete consistency with the proposed scenario, it gives the right trend. Another difficulty with the $t = 10.8$ u.c. sample is that the temperature sensor was not perfectly calibrated during the beamtime it was measured in. While it is not possible to reconstruct the magnitude of the deviation completely, it could amount to some kelvin at the low temperatures. This uncertainty only affects the evaluated effective moment if the deviation is not constant in T, since μ_{eff} is derived from the slope of the curve.

Since different temperature calibration were already discussed in the comparison of BESSY and SOLEIL data in fig. 10.2, the data points in fig. 10.3 (c) are given different symbol types that indicate the beamtimes during which they were obtained. One could expect deviating results for the two setups as well as for different beamtimes. Variations in the quality of the thermal contact could also lead to temperature deviations for individual samples.

The data points at $t \approx 1$ u.c. and $t \approx 4$ u.c. show that absolute and relative results for BESSY and SOLEIL generally are in good agreement, which encourages to trust in the evaluated values. Furthermore, if the effective moment of the thickest sample was underestimated due to the temperature calibration, this should also affect the $t = 1.9$ u.c. sample, which was investigated during the same beamtime. Since the value of the latter sample meets the expectations that the thick sample doesn't, the beamtime-specific temperature calibration might not be responsible for the discrepancy. Hence, only a repetition of the experiment for a sample with high thickness could clarify this issue.

The second parameter of the linear fits, the ordinate intercept, represents the mean field coupling constant λ as introduced in section 2.1.4. Its thickness dependence is shown in fig. 10.3 (d). The data show considerable scatter, including both signs, which prohibits unambiguous conclusions on the systematics. Only the significantly low value at $t = 1.9$ u.c. allows a connection to the $\mu_{\text{eff}}(t)$ and $w_{\text{rel}}^{0\to1}(t)$ data. The ordinate intercept results are probably even more sensitive to the aforementioned uncertainties in the sample temperature than the slope, since, especially for the BESSY data, an extrapolation over a considerable range is made. Furthermore, a constant offset between sample temperature and sensor reading is directly visible. This could arise due to a deficiency in the mounting of an individual sample and the resulting substandard thermal contact between sample and cryostat. The scatter of the data might just reflect these experimental difficulties.

Moreover, the presence of an anomaly as discussed in section 10.1 can have a large effect on λ. This becomes apparent by the two values for the $t = 4$ u.c. dataset, which are obtained for a fit above and below the anomaly. These values are connected by the dash-dotted line in fig. 10.3 (c). A fit to the complete dataset ignoring the anomaly yields $\lambda = 26.1\ \text{T}/\mu_{\text{B}} > \chi_{<}^{-1}$. A fit ignoring the anomaly if it is located in the range of the available data will always yield a larger result than a fit to the low-T data. However, large differences in λ are obtained for the cases where the anomaly is above or below the investigated temperature range. This causes a significant uncertainty in the results if the position of the anomaly is unknown, as is the case for most of the present samples.

The comparison of thickness-dependent XMCD results taken at $\theta = 60°$ should be less sensitive to such uncertainties. In the $\chi_{60°}^{-1}(T)$ data shown in fig 10.2, the anomaly is, if present at all, much less pronounced compared to $\theta = 0°$. Furthermore, the slope of the data is much smaller, which reflects the larger effective moment due to the crystal field-induced anisotropy. This reduces the impact of a possible constant temperature offset.

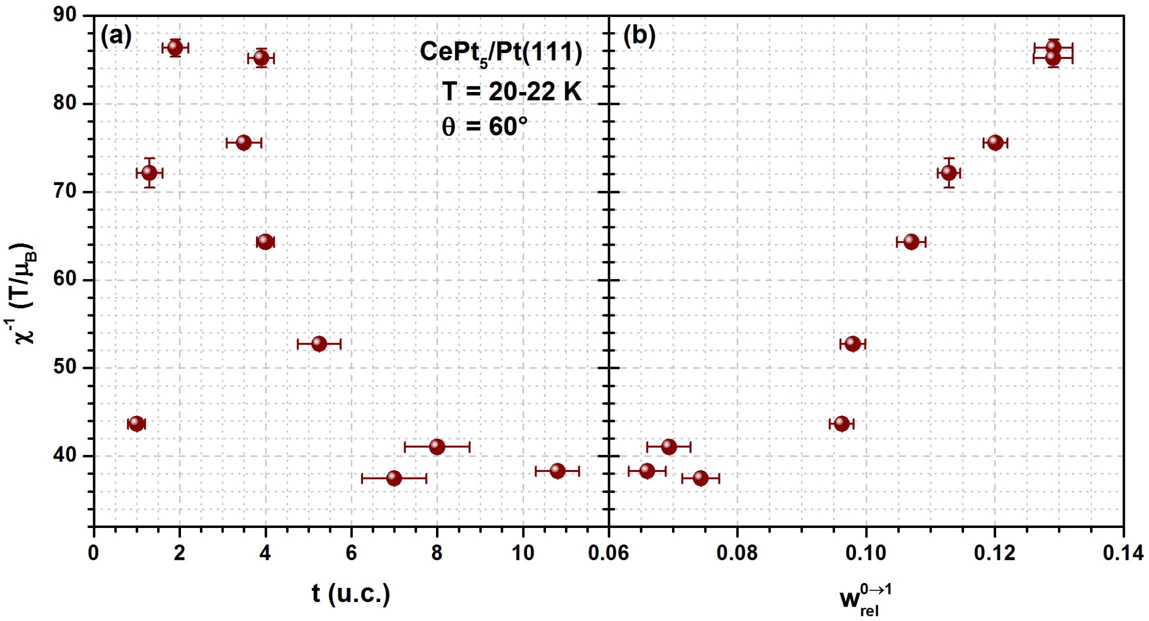

Figure 10.4: (a) Thickness-dependence of the inverse paramagnetic susceptibility of CePt$_5$/Pt(111) intermetallic films. The data were taken at $\theta = 60°$ in the temperature range $T \approx 20 \ldots 22$ K. (b) The same data plotted versus the corresponding relative $f^0 \to f^1$ weight obtained from low-T XAS, as presented in fig. 9.1.

However, the analysis of $\mu_{\text{eff}}(t)$ obtained from $\chi^{-1}_{60°}(T)$ data is complicated by the lack of a distinct linear region in a temperature range where data for a sufficient number of samples are available. The observed curvature is in line with simulations of the paramagnetic susceptibility in a hexagonal crystal field for $B \parallel c$, as shown in fig. 2.5. Nevertheless, in order to visualize the t-dependence of the experimental data, the inverse susceptibility at a certain temperature can be used.

Data for $T \approx 20 \ldots 22$ K are shown in fig. 10.4 (a). The results strongly resemble the t-dependence of the relative $f^0 \to f^1$ weight, as shown in fig. 9.1. There is a maximum at $t \approx 2$ u.c., while the sample with $t = 3.9$ u.c. apparently exhibits an enlarged value. The resemblance to the $w^{0\to1}_{\text{rel}}$ data is closer than for μ_{eff} obtained from $\chi^{-1}_{0°}(T)$, as shown in fig. 10.3 (c), which might be due to the aforementioned insensitivity of the $\theta = 60°$ data to experimental problems.

Fig. 10.4 (b) shows a plot of $\chi^{-1}_{60°}$ versus $w^{0\to1}_{\text{rel}}$. This presentation clearly reflects that there is a strong correlation between the two quantities. Again, a possible interpretation is that the paramagnetic response is reduced by the presence of hybridization, which might be a direct signature of Kondo screening.

This finding supports the interpretation of the thickness-dependence of the effective moment at $\theta = 0°$ as reflecting a Kondo-screened moment. While some uncertainty in its evaluation remain, the similarity of the evaluated values to the $w^{0\to1}_{\text{rel}}(t)$ data is indisputable. A better access to the quantity can only be achieved by more detailed measurements in analogy to the SOLEIL data shown in fig. 10.2. The higher point density and the knowledge of the presence and position of the anomaly then would allow a more reliable determination of μ_{eff} and would significantly increase the soundness of the values obtained for λ. Furthermore, a possible thickness dependence of the anomaly temperature might give insights to the connection of hybridization, the $f^0 \to f^1$ weight in XAS and the coherence temperature. It would be highly interesting to record such data in future experiments.

10.3 A model description for the inverse susceptibility

As is shown in the previous sections, the experimental $\chi^{-1}(T)$ data of CePt$_5$/Pt(111) surface intermetallics indicate the presence of crystal field effects, Kondo interaction, ferromagnetic correlations and coherent band formation. While the inverse susceptibility in a hexagonal crystal field can be described analytically in second order perturbation theory (see section 2.1.3), application of this model to the experimental data requires to disentangle the different effects. In particular, the observed reduction of the effective moment can only be quantified if the ordering of the CF split $j = 5/2$ levels is known. Hence, a starting point for modeling of the $\chi^{-1}(T)$ data is the determination of the CF scheme.

The hexagonal CF only leaves two free parameters, which can be expressed as the energy splittings of the three Kramers doublets (see section 2.1.2). In the present thesis, the differences in energy between the $|3/2\rangle$ and $|5/2\rangle$ doublets with respect to the $|1/2\rangle$ doublet are chosen for parametrization and denoted as $\Delta E_{3/2}$ and $\Delta E_{5/2}$, respectively. The magnitude and sign of these energy differences determine which states contribute to the signal at the temperatures of the experiment via the Boltzman law (see eq. 2.11), and thus determine the theoretical effective moment to which the experimental result has to be compared to (see section 2.1.3).

As discussed in section 10.1, the character of the measured anisotropy in $\chi^{-1}(T)$ indicates that the $|1/2\rangle$ doublet definitely contributes to the susceptibility at low temperatures. The $|3/2\rangle$ doublet might also contribute, but only if the energy separation between the two levels is small. The $|5/2\rangle$ doublet must be found at higher energy. The kink in $\chi^{-1}_{0^\circ}(T)$ suggests that a doublet with larger effective moment than the low-lying level is located at $\Delta E_{\text{kink}} \approx 15 \ldots 25$ meV.

For samples with $t \approx 1$ u.c., the measured effective moment exceeds $\mu_{\text{eff}}(|1/2\rangle)$ (see section 10.2). This indicates that states with $m_j > 1/2$ contribute to the susceptibility at low temperatures. As is shown in chapter 7, films with low thickness exhibit a different rotational alignment than thicker films and their lattice constants are strained due to the influence of the substrate. It could well be that the CF parameters in these samples differ from the ones for thicker films. In contrast, the interpretation of the thickness dependence of μ_{eff} in relation to the thickness dependence of $w^{0\to 1}_{\text{rel}}$ is based on an unaltered CF scheme and provides a consistent scenario. In the following, it is assumed that the sequence of the doublets does not change with the sample thickness, while the values of the energy splittings might depend on t.

These considerations leave two possibilities for the CF scheme:

1. The $|1/2\rangle$ doublet represents the isolated ground state. One of the other two doublets follows at $\Delta E \approx \Delta E_{\text{kink}}$, the last is located nearby or at higher energy.
2. The $|1/2\rangle$ and $|3/2\rangle$ doublets are degenerate or separated by some meV only, while the $|5/2\rangle$ doublet is offset by $\Delta E \approx \Delta E_{\text{kink}}$.

These two scenarios coincide with the conclusions that can be drawn from the analysis of the linear dichroism in XAS (see section 9.2.3). Both cases are consistent with a CF level scheme where the doublets are ordered in the sequence $|1/2\rangle, |3/2\rangle, |5/2\rangle$, with $\Delta E_{3/2}$ being much smaller than or equal to ΔE_{kink} in case 1 or 2, respectively. This level sequence was found by Lueken *et al.* for powdered bulk CePt$_5$ by simulation of experimental $\chi^{-1}(T)$ data [55]. Their results for the splitting energies amount to $\Delta E_{3/2} \approx 26$ meV and $\Delta E_{5/2} \approx 76$ meV.

In analogy to this work, a more detailed determination of the CF parameters in the present samples can only be done by simulation of the experimental data. Analytical expressions of the susceptibility for a hexagonal crystal field with the magnetic field applied parallel and perpendicular to the c axis are provided by eqs. 2.26 and 2.34, respectively. For arbitrary angles, the two expressions are connected in eq. 6.13, where also a mean field coupling constant λ is considered.

The assumption of nearly degenerate $|1/2\rangle$ and $|3/2\rangle$ doublets in scenario 2 might lead to a breakdown of the perturbation treatment applied for derivation of the analytical expression for $\chi_\perp$. This quasi-degeneracy is simulated by assumption of $\Delta E_{3/2} = 0.1$ eV in the following. For this case and with $\Delta E_{5/2} = 15$ eV as a lower boundary, and $B = 1.5$ T as applied in the BESSY

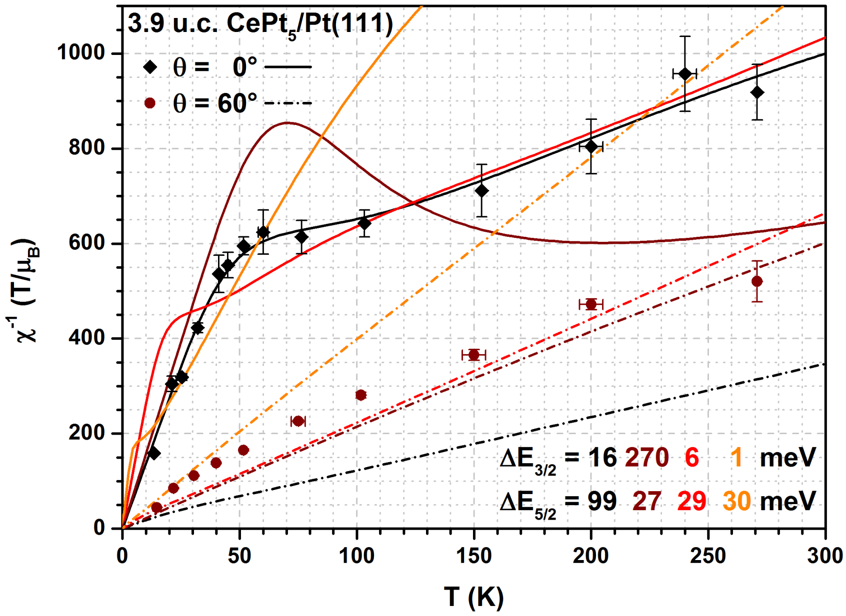

Figure 10.5: Attempts to reproduce the $\chi^{-1}(T)$ data of a CePt$_5$/Pt(111) sample with $t = 3.9$ u.c. by a model constructed from eqs. 6.13, 2.26 and 2.34 under consideration of a multiplicative screening factor and without mean field coupling. For details on the choice of parameters, see text.

experiments, the relative deviation of the perturbational expression from exact calculations by numerical diagonalization of the Hamiltonian is analyzed in appendix A.5. The error is below $\Delta\chi/\chi = 5$ % in the most relevant temperature range of $T = 10 \ldots 100$ K, which is regarded as a reasonable accuracy for the present study.

As an addition to the model, the observed reduction of the effective moment has to be considered. The simplest assumption is a temperature-independent and isotropic screening factor $C^2 \leq 1$, which is multiplied to eq. 6.13. The square reflects the connection between μ_{eff} and χ according to eq. 2.24 and assures that $\mu_{\text{eff}} = C \cdot \mu_{\text{eff}}^{\text{free}}$.

From the experimental side, the simulation requires a $\chi^{-1}(T)$ dataset with high point density over a large temperature range. Furthermore, the simultaneous simulations of data for more than one alignment of B and the c axis highly increases the credibility of the results. These criteria are best met by the $t = 3.9$ u.c. dataset measured at BESSY, which is shown in fig. 10.2. Attempts to reproduce these data by least square fits of the model described above are presented in fig. 10.5. Curves with equal color represent results with equal fit parameters but different angles of incidence. Solid and dash-dotted lines distinguish the results for $\theta = 0°$ and $60°$, respectively. The resulting CF energy splittings are given in the figure using the color code of the curves.

The solid black curve represents a fit on $\chi_{0°}^{-1}(T)$ only. It yields very good agreement with the experimental data. The resulting level sequence corresponds to the one found by Lueken *et al.* [55], and the energy splittings are comparable to their results. However, simulation of the $\chi_{60°}^{-1}(T)$ curve with the same parameters, as shown by the black dash-dotted line, significantly disagrees with the experimental data. Hence, this approach has to be dismissed.

This example underlines the importance of simultaneous fitting of data from different geometries, since both the progression of the individual curves and their relative position influence the resulting CF parameters. For all other fits that are presented in the following, both geometries were fitted simultaneously.

The red and dark red curves in fig. 10.5 represent fit results for the level sequence of Lueken *et al.* and with reversed $|3/2\rangle$ and $|5/2\rangle$ levels, respectively. In both cases, neither the kink in $\chi_{0°}^{-1}(T)$ nor the anisotropy is well reproduced. The fitting procedure rather produces unsatisfactory compromises. An aspect in favor of the red curve is the apparently better agreement at high temperatures. Nevertheless, it seems that the given model is not capable to yield a solution that correctly reproduces both the kink and the anisotropy.

A set of parameters that reproduces the kink only is already present in the black curves. The reverse approach is to focus on the anisotropy. The best fit result that reproduces the anisotropy at low temperatures is shown as the orange curves in fig. 10.5, which represents an example for scenario 2. $\Delta E_{3/2}$ is very small, such that the produced kink in $\chi_{0^\circ}^{-1}(T)$ is located at temperatures more or less below the measurement range. The prominent kink in the data is then attributed to $\Delta E_{5/2}$. However, the result demonstrates that the such produced change in effective moment is not sufficient to reproduce the pronounced change in slope that is observed in the experimental data.

In order to address the deficiency of the model to reproduce both the kink and the anisotropy, different working directions can be considered: Either one starts with the black curve in fig. 10.5 and introduces additional parameters that modify the anisotropy. Alternatively, starting from the orange curve, some mechanism could be introduced to the model that allows control of the slope of $\chi^{-1}(T)$ in dependence of the temperature and thus to amplify the strength of the kink. Both approaches are discussed in the following.

10.3.1 Modeling of a modified anisotropy

The simplest way to control the anisotropy in the model for $\chi^{-1}(T)$ is to introduce anisotropic parameters. More precisely, one could assume that either the screening factor C for the effective moment or the mean field coupling parameter λ are different for $\chi_{\parallel}$ and $\chi_{\perp}$ in eq. 6.13. As is shown in fig. 10.6 (a) and (b), these modifications allow reproduction of the data with a CF scheme similar to the one found for CePt_5 bulk material [55].

The uniaxial symmetry of CePt_5 can certainly motivate the assumption of anisotropic magnetic coupling between Ce ions along the c axis in contrast to the coupling in the ab plane. However, such anisotropic coupling does not affect the description of the susceptibility in terms of an average mean field coupling. The assumption of different coupling constants for the different alignments of B and c axis rather implies that the coupling strength depends on the crystallographic direction along which the magnetic moments are aligned. The same has to be considered for the assumption of alignment-dependent screening factors. While it is reasonable to assume that the degree of hybridization between $4f$ level and conduction states is spatially anisotropic, it should not depend on the alignment of the magnetic moment.

Hence, the assumption of field direction-dependent coupling constants and screening factors is dismissed for the description of the susceptibility. A more profound approach to consider anisotropic Kondo interaction in terms of the CF-induced anisotropy of the ground state is presented in section 10.3.2.

The anisotropic susceptibility is a direct consequence of the CF splitting of the three m_j doublets. Hence, a contribution to the signal from a region in the sample without CF splitting would reduce the observed anisotropy. In analogy to the considerations in section 9.2.3, this scenario can be introduced to the model for $\chi^{-1}(T)$ by the assumption of an altered CF scheme for the interface-nearest Ce ions.

For the degenerate $j = 5/2$ multiplet, $\chi^{-1}(T)$ is described by the Curie-law as shown in fig. 2.4. The addition of such an interface contribution to a bulk susceptibility as represented by the black curves in fig. 10.5 has further consequences apart from the reduction of the anisotropy. The effective moment as obtained from the low-T $\chi_{0^\circ}^{-1}(T)$ data has to be compared to a value larger than $\mu_{\text{eff}}(|1/2\rangle)$, and the reduction is more drastic than indicated by the right-hand ordinate in fig. 10.3 (b).

The change of slope at the kink is reduced as well. Simulations showed that a readjustment of the parameters of the bulk part alone is not sufficient to make up for this effect. Furthermore, the assumption of a completely degenerate multiplet at both interface layers for a film with $t = 4$ u.c. means that approximately 50 % of the XMCD signal are isotropic and linear. This leads to a reduction of the anisotropy that is much stronger than observed.

Hence, at least one of the crystal field energies of the interface layers has to differ from zero in order to reproduce the data. This introduces additional freedom to the model. In order to conserve the linear region in $\chi_{0^\circ}^{-1}(T)$ and the plateau in $\Upsilon(T)$, the splitting energies should not

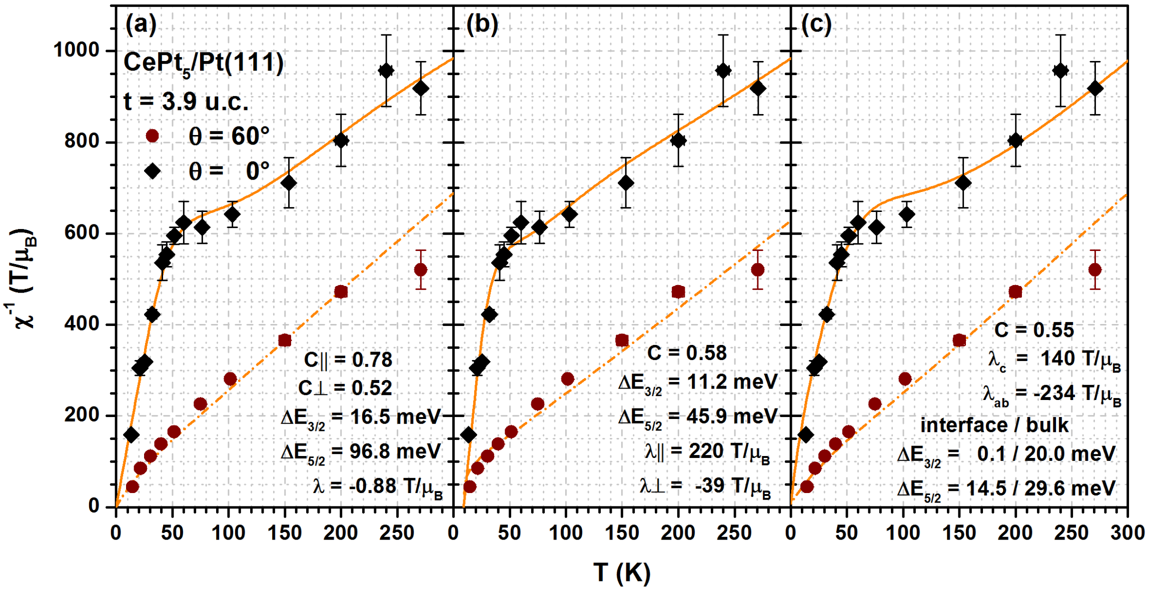

Figure 10.6: Inverse susceptibility of a $t = 3.9$ u.c. CePt$_5$/Pt(111) film measured at BESSY along with least square fits of the model for hexagonal crystal field with different modifications: (a) Anisotropic screening factor, (b) anisotropic mean field coupling, (c) interface layers with distinct CF splittings.

be in the range $1\text{ meV} \lesssim \Delta E \lesssim 15\text{ meV}$. A possible scenario is then a bulk region with a pure $|1/2\rangle$ ground state and both other doublets above the observed gap, whereas the ground state of the interface region is a quasi-quartet, presumably composed of the $|1/2\rangle$ and $|3/2\rangle$ levels.

The consideration of RKKY interaction in terms of a mean-field parameter λ has to be rethought in a multilayer description. In the standard formulation given by eq. 2.36, the molecular field is a consequence of the average magnetization that is experienced by each magnetic moment. A multilayer sample with different magnetic properties in different layers represents a highly anisotropic environment, and the average magnetization at the site of a certain magnetic moment is not well described by the total XMCD signal measured. The simplest way to consider the layered geometry is to introduce independent coupling constants for the molecular field produced by the moments in each layer (λ_{ab}) compared to the coupling of adjacent layers (λ_{c}). The susceptibility of a sample with N layers is then described by a set of N coupled equations,

$$\mu_i^n = \chi_i^n \left(B\, e_{\theta,i} + \lambda_{\mathrm{ab}} \mu_i^n + \lambda_{\mathrm{c}} \mu_i^{n-1} + \lambda_{\mathrm{c}} \mu_i^{n+1} \right) \tag{10.1}$$

with the convention $\mu_i^0 = \mu_i^{N+1} = 0$. These equations can be solved analytically. The measured, layer-averaged susceptibility is then obtained by summation of the weighted results for each layer according to eq. 9.2.

A fit result with two sets of CF splittings and the described coupling parameters to the $t = 3.9$ u.c. data is shown in fig. 10.6 (c). The data are well reproduced.

The starting point for the consideration of interface effects was the thickness-dependence of the $f^0 \to f^1$ weight in XAS (see section 9.1.1). Accordingly, the screening factors for the effective moments of bulk and interface could also be allowed different. The introduction of this additional complexity was omitted since the model already has six free parameters, considering that $\Delta E_{3/2}$ of the interface is fixed to a very small value.

As is already argued in section 9.2.3 regarding the analysis of $\Upsilon(T)$, the experimental data do not exhibit a sufficient variety of features that allows definite identification of the number of crystal field energies. While the multilayer model has the potential to reproduce the experimental data, it is rather complex. This motivates the search for an alternative, simpler description of the data.

10.3.2 Doublet-specific screening factors

As is shown by the simulations of $\chi^{-1}(T)$ for a $t = 3.9$ u.c. CePt$_5$/Pt(111) film in fig. 10.5, the magnitude of the anisotropy at low T indicates that $\Delta E_{3/2}$ is close to zero (orange curve). However, this assumption fails to reproduce the progression of the experimental data towards high temperature, where the slope of the simulated curve strongly overestimates the experimental finding.

The slope of $\chi^{-1}(T)$ is directly connected to the effective moment according to eq. 2.24. The observed reduction of the latter is expressed by the screening factor C in the applied model, which is assumed to be an isotropic and temperature-independent constant. Both assumptions are not necessarily true.

In the single-impurity picture, the NCA results of Bickers *et al.* for the susceptibility show significant temperature variation of the effective moment on the same temperature scale as for the $4f$ occupancy [27] (see fig. 1.1). For the latter, evaluation of Ce M$_{4,5}$ XAS yielded a scaling temperature of $T_K \approx 100 \ldots 200$K for CePt$_5$/Pt(111) (see section 9.1.2). Hence, it is reasonable to assume that a simple temperature-independent screening factor is not an adequate description of the $\chi^{-1}(T)$ data.

In order to introduce temperature-dependence of C to the model, two aspects have to be considered: First, the experimental data do not indicate that the fully screened state is reached down to the lowest temperatures available, which would be characterized by a constant susceptibility and zero effective moment. In this limit, the screening factor would approach zero. Second, the data indicate a linear Curie-Weiss behavior at low temperature. Any significant deviation from temperature-independence in C directly leads to a deviation from linearity in $\chi_{0^\circ}^{-1}(T)$.

The modification to the model that is required to reproduce the experimental data starting from the orange curve in fig. 10.5 is rather characterized by a constant screening factor at low temperature, which drastically increases as the temperature approaches the distinct kink in $\chi_{0^\circ}^{-1}(T)$. In the crystal field scheme under discussion, the kink is connected to the significant population of the $|5/2\rangle$ doublet.

The screening factor reflects the reduction of the effective moment due to Kondo interaction between the $4f$ level and conduction states. In the SIAM, this interaction is expressed by a hopping matrix element in analogy to hybridization (see eq. 1.1). As is discussed in section 2.1.2, such hybridization can only occur symmetry-adapted, which is expressed by the covalent part of the crystal field.

A significant crystal field-splitting, as is unambiguously indicated by the present $\Upsilon(T)$ and $\chi^{-1}(T)$ data in CePt$_5$/Pt(111), reflects a strongly non-spheric crystalline environment of the Ce ions. Consequently, a ground state with an anisotropic spatial charge distribution is formed in order to adapt to the environment. Naturally, the conduction states exhibit non-spherical symmetry as well. It is very likely that the hybridization strength between the different CF split $4f$ levels and their respective conduction state counterparts, which can be expressed by Wannier[1] functions, is different for the three doublets.

This idea has repeatedly been studied theoretically [274, 275]. It has been applied to explain experimental susceptibility data of different Kondo compounds [276–279] in the framework of a simplified NCA scheme of the SIAM that was developed by Zwicknagl *et al.* in 1990 [280]. Attempts to improve the description of the present CePt$_5$/Pt(111) data by application of this many-body approach were not successful yet [281]. In the scope of the present thesis, a simpler *ad hoc* approach is pursued by consideration of doublet-specific screening factors C_{m_j}.

Those are introduced to the current model as derived in section 2.1.3 by modification of the first identity of eq. 2.18 according to

$$\mu(B,T) = \sum_{n=1}^{2j+1} C_n^2 \mu_n \mathcal{P}_n = \sum_{n=1}^{2j+1} -C_n^2 \, \frac{dE_n}{dB} \mathcal{P}_n. \tag{10.2}$$

For $B \parallel c$, $E_n = g_j \mu_\mathrm{B} m_j B$ with the association of n and m_j in analogy to the basis vector

---

[1] Gregory Hugh Wannier, Swiss physicist, 1911-1983

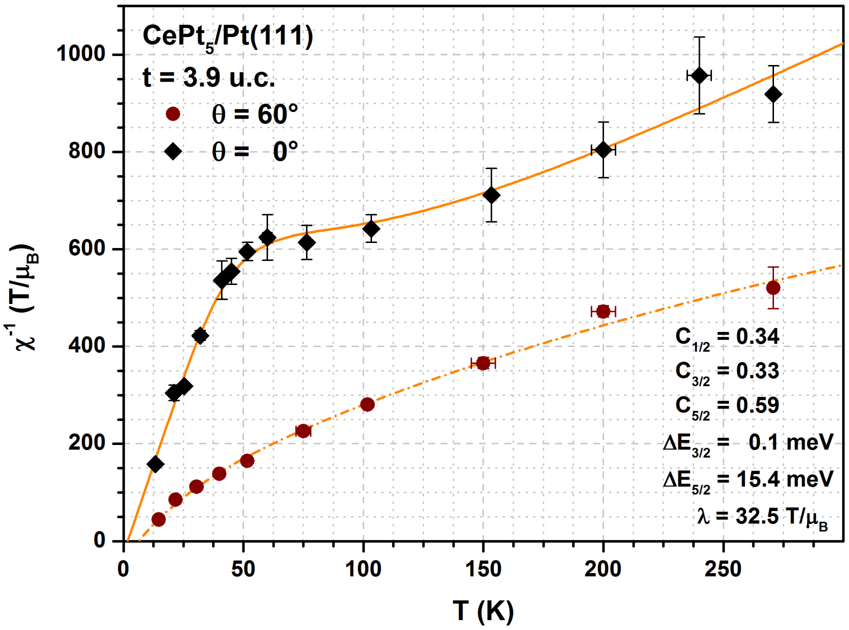

Figure 10.7: $\chi^{-1}(T)$ of a $t = 3.9$ u.c. CePt$_5$/Pt(111) film measured at BESSY along with a least square fit of the model for hexagonal crystal field with doublet-specific screening factors according to eq.10.3.

given in eq. 2.28. For $B \perp c$, the energies are given in eq. 2.33. In this representation, the basis is transformed according to eq. 2.31, but the value of m_j, which defines the affiliation to one of the three CF split doublets in hexagonal symmetry, is conserved. The expressions for the susceptibility in the two geometries then read

$$\chi_{\|}(T) = \frac{\frac{g_j^2 \mu_B^2}{4k_B T}}{1 + e^{-\frac{\Delta E_{3/2}}{k_B T}} + e^{-\frac{\Delta E_{5/2}}{k_B T}}} \left(C_{1/2}^2 + C_{3/2}^2 9\, e^{-\frac{\Delta E_{3/2}}{k_B T}} + C_{5/2}^2 25\, e^{-\frac{\Delta E_{5/2}}{k_B T}} \right)$$

$$\begin{aligned}\chi_{\perp}(T) = {}& \frac{\frac{g_j^2 \mu_B^2}{4k_B T}}{1 + e^{-\frac{\Delta E_{3/2}}{k_B T}} + e^{-\frac{\Delta E_{5/2}}{k_B T}}} \left(C_{1/2}^2 \left(9 + \frac{16 k_B T}{\Delta E_{3/2}} \right) - \right.\\ & \left. - C_{3/2}^2 \left(\frac{16 k_B T}{\Delta E_{3/2}} - \frac{10 k_B T}{\Delta E_{5/2} - \Delta E_{3/2}} \right) e^{-\frac{\Delta E_{3/2}}{k_B T}} - C_{5/2}^2 \frac{10 k_B T}{\Delta E_{5/2} - \Delta E_{3/2}}\, e^{-\frac{\Delta E_{5/2}}{k_B T}} \right).\end{aligned} \tag{10.3}$$

The doublet-specific screening factors are again assumed to be constant. Nevertheless, the resulting total screening is temperature-dependent due to the progressive population of the CF split states. In the simulation of experimental data, a possible T-dependence of the individual C_{m_j} might thus be partially covered. Furthermore, the idea of spatially anisotropic hybridization is also adequately reflected in this model. As can be seen from the electron distributions that are shown in fig. 2.3, the three doublets display very different directional dependencies. Hence, a stronger screening of the effective moment of the $|1/2\rangle$ doublet compared to $|5/2\rangle$ can be interpreted as resulting from a larger hopping matrix element along the c axis as compared to the ab plane.

The capability of this approach to excellently describe the experimental data is demonstrated by the least square fits to the $t = 3.9$ u.c. data that are shown in fig. 10.7 (a). In particular, the observed curvature of the $\chi_{60°}^{-1}(T)$ data is much better reproduced than by all previous attempts. The details of this curvature in the model sensitively depend on the difference of $C_{1/2}$ and $C_{3/2}$. The fit does not yield a good result if both are set equal.

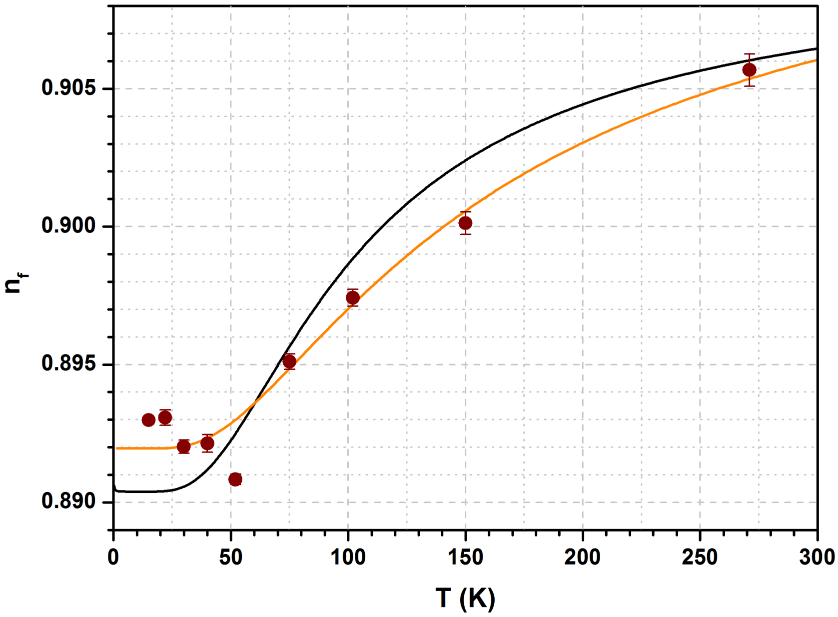

Figure 10.8: Ratio of two simulated $\chi_{0^\circ}^{-1}(T)$ curves with the CF parameters as obtained by the fit in fig. 10.7 (black curve). Data without screening of the effective moment are divided by data with the doublet-specific screening factors obtained in the fit. The curve is arbitrarily scaled to the $n_f(T)$ data of this sample (red symbols, compare fig.9.2). The orange line is a fit of eq. 10.4 to the $n_f(T)$ data with the CF parameters given in panel (a).

In summary, both the introduction of doublet-specific screening factors as well as the multilayer description have the potential to reproduce the inverse susceptibility of CePt$_5$/Pt(111) on a sound basis, as demonstrated for the $t = 3.9$ u.c. dataset in figs. 10.6 (c) and 10.7 (a). In both descriptions, the crystal field scheme of a considerable part of the sample is characterized by a ground state consisting of the nearly degenerate $|1/2\rangle$ and $|3/2\rangle$ doublets. This configuration represents a rather special case of the ionic crystal potential, which might raise concerns against this result. However, this scheme seems to be unavoidable in order to reproduce the experimental data in the framework of the present model.

Attempts to reproduce the data with a combination of both approaches were also made in the course of the present thesis. However, this model is overparametrized and cannot be handled adequately. Hence, one of the two approaches has to be chosen for the analysis of thickness-dependent $\chi^{-1}(T)$ data, which is presented in the following. The description of the samples as homogeneous films with doublet-specific screening factors is favored over the multilayer description, since it provides better fit results with fewer parameters.

10.3.3 Temperature-dependence of Kondo screening

The model fit of fig. 10.7 including doublet-specific screening factors is well capable to reproduce the experimental data. The screening factors in the model are constant with temperature, but an effective T-dependence is introduced by the progressive population of the CF split doublets. This temperature-dependence is visualized in fig. 10.8. The black line represents the ratio of two calculated $\chi_{0^\circ}^{-1}(T)$ curves with the CF energies as obtained from the fit in fig. 10.7 in arbitrary scaling. A curve with all screening factors set to unity is divided by a curve calculated with the fit results for the doublet-specific screening factors.

The progression of the resulting curve compares very well to the $n_f(T)$ data of this sample (compare fig. 9.2), which are also shown in the figure (red symbols). As is discussed in section 9.1.2, the progression of $n_f(T)$ can be interpreted as a signature of the single-impurity Kondo temperature by comparison to calculations by Bickers *et al.* [27], which is thus evaluated to $T_K \approx 100 \dots 200$ K.

The apparent coincidence of the two datasets stimulates a different conclusions: Possibly, the observed temperature-dependence of the $f^0 \to f^1$ weight is not a signature of the single-impurity Kondo temperature. It could rather reflect the progressive population of the CF split doublets, which exhibit individual hopping matrix elements and thus different degrees of screening of the effective moment.

In this scenario, one might assume that each doublet has its individual Kondo temperature and its individual $n_f(T)$ function. In order to test this scenario, a simple model can be formulated under the assumption of temperature-independent, doublet-specific $4f$ occupancies $n_f^{m_j}$ according to

$$n_f(T) = \frac{n_f^{1/2} + n_f^{3/2}\, e^{-\frac{\Delta E_{3/2}}{k_\mathrm{B}T}} + n_f^{5/2}\, e^{-\frac{\Delta E_{5/2}}{k_\mathrm{B}T}}}{1 + e^{-\frac{\Delta E_{3/2}}{k_\mathrm{B}T}} + e^{-\frac{\Delta E_{5/2}}{k_\mathrm{B}T}}}. \tag{10.4}$$

The orange line in fig. 10.7 (b) is a fit of this model to the experimental data with the CF splitting parameters set to the results of the fit in panel (a). In order to account for ambiguities caused by the quasi-degeneracy of the lower doublets, their $n_f^{m_j}$ were set equal. The results of the fit are $n_f^{1/2} = n_f^{3/2} = 0.892$ and $n_f^{5/2} = 0.957$. The experimental data are very well reproduced, considering the experimental explanation for the low-T slope given in section 9.1.2.

With this result, the proposed scenario of doublet-specific $4f$ occupancies appears reasonable. Contrariwise, one could also argue that the CF-parameter results of the $\chi^{-1}(T)$ fit do not represent the crystal field splitting but were adjusted by the fitting algorithm to reproduce the T-dependence of the Kondo interaction, which is also found in $n_f(T)$. As is shown in fig.1.1, the NCA results indicate that both screening of the moment and $4f$ occupancy vary on a universal temperature scale.

The CF scheme evaluated from the XAS experiments in section 9.2 is well in line with the one obtained from the fit to the $\chi^{-1}(T)$ data. Hence, this result is apparently no artifact of the model for $\chi^{-1}(T)$. In turn, a connection of CF scheme and Kondo interaction is not unexpected considering that hybridization acts as a covalent contribution to the CF potential (see section 2.1.2). It might well be that the two aspects thus cannot be disentangled completely.

Returning to the discussion of $n_f(T)$ as a signature of single-impurity interaction, the proposed interpretation would mean that the increase of $n_f(T)$ is a mere consequence of the crystal field splitting and has no connection to T_K. Nevertheless, the presence of this energy scale and the connected behavior of $n_f(T)$ still has to be expected. A constant value of $n_f^{m_j}$ would indicate that $T_\mathrm{K}^{m_j}$ is either much smaller or much larger than the limits of the temperature range under investigation.

The assumption of $T_\mathrm{K} \ll 12$ K must be doubted. Andrews *et al.* reported on the observation of a Kondo resonance in PES at $T = 120$ K. Furthermore, the observed low $4f$ occupancies down to $n_f = 0.88$ indicate a comparably large Kondo energy scale.

Hence, the value of $T_\mathrm{K} = 100 \ldots 200$ K obtained by XAS should be regarded as a lower limit for the Kondo temperature. It might well be that both the population of the CF split doublets and the Kondo energy scale contribute to the observed increase in $n_f(T)$. As a way to include the ambiguities of CF- and single-impurity-induced effects to the model, T-dependent screening factors could be introduced. However, this would lead to overparametrization of the model and is thus omitted.

10.4 Results of thickness-dependent modeling

The results of the analysis of paramagnetic susceptibility (see section 10.3) and the crystal-field induced linear dichroism in Ce $M_{4,5}$ XAS (see section 9.2.3) provide a solid basis for the description of the interplay of crystal field splitting, RKKY coupling and Kondo interaction in CePt$_5$/Pt(111) intermetallics. The aim of the present section is to disentangle these effects by a consistent modeling of the available $\Upsilon(T)$ and $\chi^{-1}(T)$ data for a wide range of film thickness. The most convincing scenario for the crystal field scheme of CePt$_5$/Pt(111) is a $|1/2\rangle$, $|3/2\rangle$ quasi-quartet ground state followed by an energy gap of $\Delta E_{5/2} \approx 20$ meV to the $|5/2\rangle$ doublet.

The films can be assumed to be homogeneous regarding their CF energies. Furthermore, the effective moment as measured by XMCD is significantly reduced with respect to the free Ce^{3+} ion. Apparently, the reduction is thickness-dependent and doublet-specific. Finally, the $\chi^{-1}(T)$ data indicate a small mean field coupling, at least above a transition temperature of $T \approx 20$ K that can be interpreted as a signature of emerging coherence.

Fig. 10.9 shows the experimental $\chi^{-1}(T)$ and, where available, $\Upsilon(T)$ data for nine samples with different film thicknesses along with model curves computed for the described scenario. The model for the $\Upsilon(T)$ data is provided by eq. 9.5 with the extension given by eq. 9.7. The θ-dependent $\chi^{-1}(T)$ data are described by eq. 10.3 in combination with 6.13.

In order to simulate the quasi-degeneracy of the $|1/2\rangle$ and $|3/2\rangle$ doublets, $\Delta E_{3/2}$ was set to 0.1 meV. This value is an estimate, it might as well be smaller and even negative. A complete degeneracy could of course also be the case, but this would be a highly unlikely coincidence. The assumed energetic closeness of the two doublets is already hard to explain and there is no reason why they should have exactly the same energy. True degeneracy would cause the model to break down, since the perturbation treatment for $\chi^{-1}_{60°}(T)$ fails (see section 2.1.3). As already discussed in section 10.3, the validity of the perturbation treatment for the present set of parameters is confirmed in appendix A.5.

With $\Delta E_{3/2}$ fixed, six parameters remain for the model. These are the second crystal field splitting $\Delta E_{5/2}$, the correction factor υ for the linear dichroism data, three doublet-specific screening factors C_{m_j} and the mean field coupling constant λ. The results of the modeling for these parameters are given as a function of the film thickness in fig. 10.10.

The magnitude of the energy gap to the $|5/2\rangle$ doublet was manually adjusted for each sample individually as a compromise for the $\Upsilon(T)$ and $\chi^{-1}(T)$ data. For three of the samples, which are represented by the bottom panels of fig. 10.9, $\Delta E_{5/2}$ as well as the connected quantity $C_{5/2}$ were chosen in accordance with the results for the other samples since the available data allow no individual determination. This is indicated by open symbols in fig. 10.10. The remaining parameters were determined by least square fitting to the experimental data.

As expected from the independent modeling of $\Upsilon(T)$ shown in fig. 9.7 (b) and from the excellent reproduction of the $\chi^{-1}(T)$ data for the $t = 3.9$ u.c. sample shown in fig. 10.7 (a), the agreement between the model and the data is high for $t > 2$ u.c. However, the model fails to reproduce the $\chi^{-1}_{60°}(T)$ data for the samples with $t = 1.3$ and 1.9 u.c., which exhibit a very strong curvature. This aspect is not met by the model, even though the doublet-specific screening factors were introduced to explicitly account for the temperature-dependence of the slope of $\chi^{-1}(T)$.

Since the observed discrepancy is largest for $\chi^{-1}_{60°}(T)$, it might indicate that the prerequisites for the perturbation treatment are not well met. This could be caused by a smaller value of $\Delta E_{3/2}$ for the thin samples, which would agree with the observed thickness dependence of $\Delta E_{5/2}$ (see fig. 10.10 (a)).

Alternatively, the discrepancy might be caused by the strong hybridization that is present at $t \approx 2$ u.c. (compare fig. 9.1). The description of Ce compounds with such high correlation might require dedicated many-body theory. In the framework of the present simple model, the introduction of an additional temperature-dependence of the doublet-specific screening factors might suit to explain the observation. However, such an extension of the model significantly reduces its controllability.

Despite these discrepancies, the thickness-dependence of the model parameters as shown in fig. 10.10 provides a consistent picture. The CF splitting energies (panel (a)) decrease with increasing thickness. This is consistent with the progression of the lateral lattice constant, which is largest at low thickness (see fig. 7.7). This corresponds to a weaker influence of the environment on the $4f$ states and can thus explain the smaller CF splitting.

The correction factor υ (panel (b)) is mainly governed by the low-T value of Υ and thus independent of the CF splitting energies. Hence, the results of the simultaneous modeling equal the ones shown in fig. 9.7.

The doublet-specific screening factors (panel (c)) show the same hierarchy for all samples. As already observed in the independent modeling for $t = 3.9$ u.c. shown in fig. 10.7 (a), $C_{5/2} >$

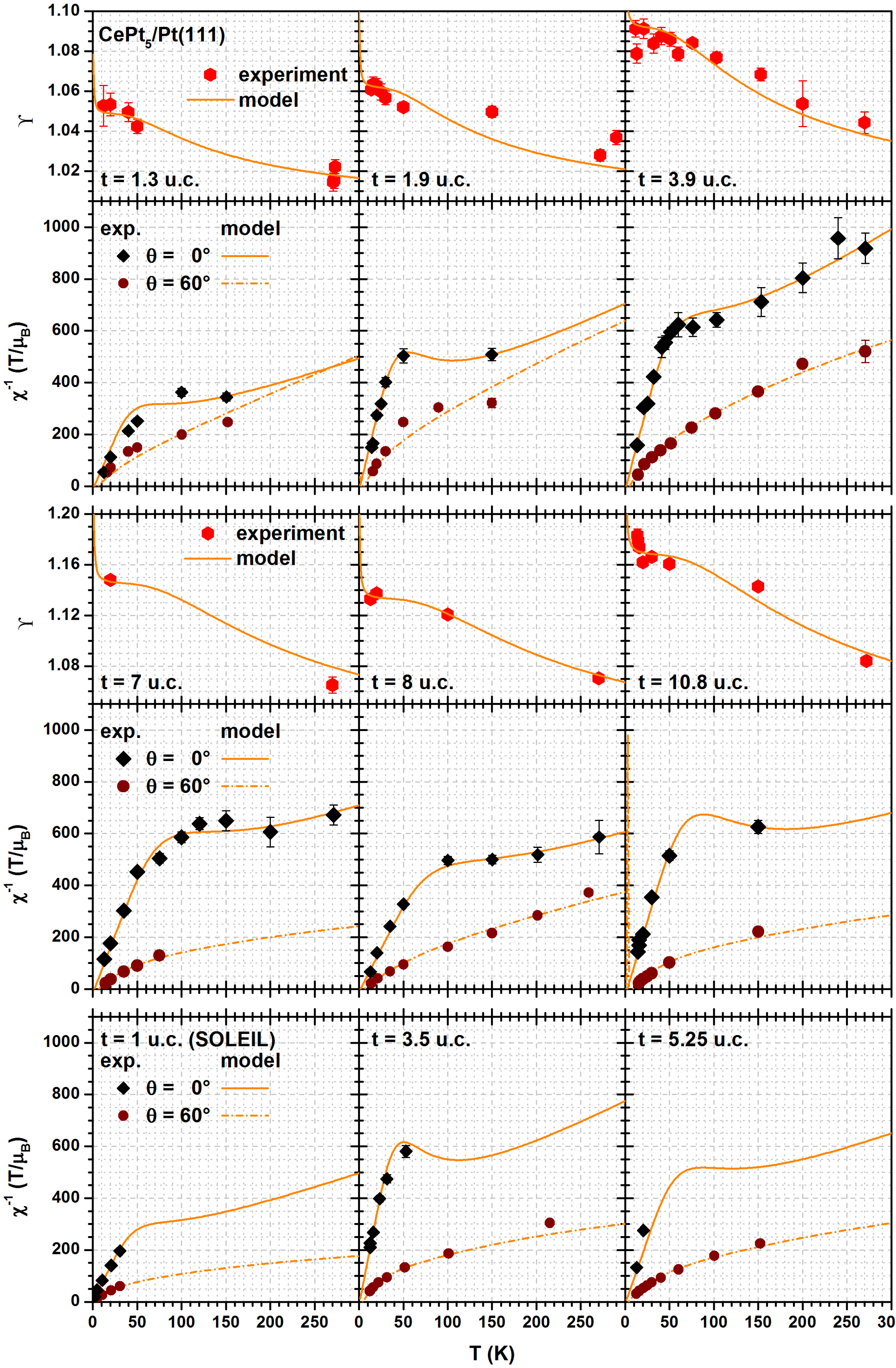

Figure 10.9: Fit results for $\chi^{-1}(T)$ and, where available, $\Upsilon(T)$ for the available set of CePt$_5$/Pt(111) samples. All but the $t = 1$ u.c. dataset were measured at BESSY. The procedure of the modeling is described in the text. The model parameter results are presented in dependence of the intermetallic film thickness in fig. 10.10.

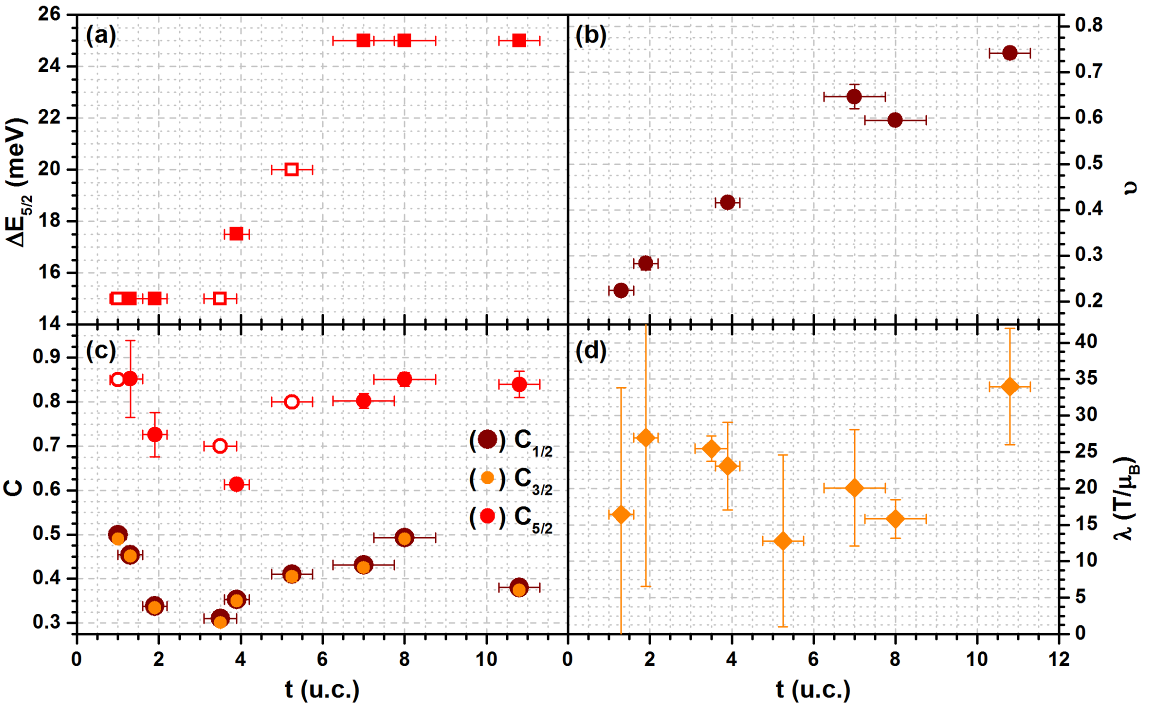

Figure 10.10: Parameter values of the model curves of fig. 10.9 in dependence of the film thickness. (a) Crystal field splitting $\Delta E_{5/2}$ between the $|5/2\rangle$ and $|1/2\rangle$ doublets. (b) correction factor υ applied for the modeling of $\Upsilon(T)$ (compare inset to fig. 9.7 (b)). (c) Doublet-specific screening factors C_{m_j} and (d) mean field coupling constant λ for modeling of $\chi^{-1}(T)$. Open symbols in panels (a) and (c) correspond to the bottom panels of fig. 10.9. These values were not obtained from the fits but estimated in accordance with the results of the other samples due to a lack of high-T measurements and $\Upsilon(T)$ data.

$C_{1/2} \gtrsim C_{3/2}$. The first inequality is required to produces the distinct kink in $\chi^{-1}_{0°}(T)$, whereas the second mainly influences the curvature of $\chi^{-1}_{60°}(T)$. This qualitative picture is not affected by uncertainties of the perturbation treatment for $\chi^{-1}_{60°}(T)$ at high temperatures, as is argued in appendix A.5.

The thickness-dependence of all three parameters strongly resembles the progression of the low-T effective moment evaluated from $\chi^{-1}_{0°}(T)$, as shown in fig. 10.3 (c). Hence, it also agrees with the progression of the relative $f^0 \rightarrow f^1$ weight evaluated from Ce $M_{4,5}$ XAS, as shown in fig. 9.1. This finding once again indicates that there is a close connection between hybridization strength and reduction of the magnetic moment in $CePt_5$/Pt(111). This behavior is expected for a Kondo system. The absolute values of the screening for the $|1/2\rangle$ doublet are in between 0.3 and 0.5, which corresponds to a reduction of the susceptibility of the order of 0.1 to 0.25.

This result can be compared to the single-impurity NCA results of Bickers *et al.* [27] (see fig. 1.1 (b)). In these calculations, a reduction of the susceptibility of this order of magnitude is obtained at $T \approx 0.1 \ldots 0.3\ \mathrm{T_K}$. Assigning the experimental result of the screening factor to an average temperature of $T = 20$ K, this translates to a Kondo temperature of $T_\mathrm{K} \approx 70 \ldots 200$ K. This is well in line with the value obtained from the analysis of the temperature-dependent $f^0 \rightarrow f^1$ weight in Ce $M_{4,5}$ XAS, as presented in section 9.1.2.

The significant reduction of the screening factor with respect to the values given by the right abscissa of fig. 10.3 (c) is due to the different reference effective moment. While the comparison given there is made with respect to a pure $|1/2\rangle$ ground state, the screening factors in fig. 10.10 (c) are related to the $|1/2\rangle$,$|3/2\rangle$ quasi-quartet, which exhibits a larger effective moment (see fig. 2.4).

Finally, the results for λ (panel (d)) allow no definite conclusions on a possible thickness-dependence due to the large uncertainties. In any case, positive values were obtained. This contrasts the results in fig. 10.3 (d), but this might just reflect the larger amount of data and the more adequate model that was applied in the present section.

In summary, the assumptions that were made for the CF scheme together with the applied model, the doublet-specificity of the screening factors in particular, allow a consistent description of most of the available data. The effects of crystal field, Kondo screening and RKKY interaction can be addressed and quantified separately in this treatment. The thickness-dependence of the hybridization strength in $CePt_5/Pt(111)$ allows uniquely studying the connections between this quantity and the paramagnetic response in a Kondo system by means of soft X-ray spectroscopy.

10.5 The heavy fermion state at low temperature

In sections 10.3 and 10.4, a model is developed that is capable of reproducing the experimental $\chi^{-1}(T)$ data. The model is based on paramagnetic ions in a hexagonal crystal field. RKKY interaction and Kondo screening are treated phenomenologically.

As reported by Klein *et al.* for $t \approx 4$ u.c. [94], $CePt_5/Pt(111)$ undergoes a transition to a coherent heavy fermion state at low temperature. Consistent with their results, the present $\chi^{-1}(T)$ data indicate a transition temperature of $T \approx 20$ K. Since the heavy fermion state is characterized by a $4f$ band rather than atomic Kondo singlet states for each impurity (see section 1.3), the ionic model for $\chi^{-1}(T)$ is not appropriate below the transition temperature. It is the aim of the present section to continue the XMCD study of $CePt_5/Pt(111)$ into the regime of heavy fermion bands.

The transition becomes manifest in the $\chi_{0^\circ}^{-1}(T)$ data of fig. 10.2 as a deviation from a linear Curie-Weiss law, which cannot be explained by crystal field effects. The observation is consistent with a loss of RKKY interaction. Non-Curie behavior is limited to a rather small temperature range of $\Delta T \approx 5$ K. Towards lower temperatures, a linear slope is reestablished that apparently matches the one above the transition temperature. A crossover to a temperature-independent Pauli susceptibility, as expected for band-induced paramagnetism, is not observed down to $T = 2$ K.

This is in line with other heavy fermion materials like the well-characterized compound $CeAl_3$. This material is treated in detail by Fazekas [14] under consideration of different experimental probes. The susceptibility of $CeAl_3$ deviates from Curie-behavior for $T \lesssim 35$ K, but $T \lesssim 0.1$ K is required to reach a regime where χ is T-independent. The temperature range in between these limits is understood as a cross-over regime where coherence is already present, but the electron system is too hot to be described by Fermi-liquid theory. This reflects the narrowness of the heavy fermion band, which leads to a low Fermi temperature T_F.

The assumption of $T \gg T_F$ can also explain the observation of Curie-Weiss behavior below the transition temperature. In this limit, a finite bandwidth can be neglected with respect to the width of the Fermi distribution. Consequently, the band thermodynamically acts as a localized level, which leads to a linear $\chi^{-1}(T)$ relationship. The observation of such linearity down to $T = 2$ K allows estimation of this temperature as an upper border for T_F.

As introduced in section 1.3, further signatures of the renormalized band structure in the heavy fermion state can be addressed by measurement of the magnetic moment μ as a function of the external field B. As is shown in fig. 10.1, significant deviations from a linear $\mu(B)$ relation are observed in $CePt_5/Pt(111)$ at the low temperature and high magnetic field available at SOLEIL. Data for samples with thicknesses $t = 1, 2, 4$ u.c. taken at $T = 2$ K and $\theta = 60^\circ$ are shown in fig. 10.11.

All three curves are non-linear and seem to approach a constant value towards $B = 6$ T. This is a surprisingly small saturation field for a band-induced paramagnet, but it is readily explained in the picture of renormalized bands according to fig. 1.2. The model used for the underlying calculations by Beach and Assaad is based on a quadratic Kondo lattice and an electron-like conduction band [33], whereas $CePt_5/Pt(111)$ possesses a hexagonal crystal structure and the PES data by Klein *et al.* indicate a hole-like conduction band [94]. Despite these differences, the qualitative picture of the integrated density of states in fig. 1.2 (e)-(g) should be applicable to $CePt_5/Pt(111)$, since its hybridization gap is located above the Fermi level.

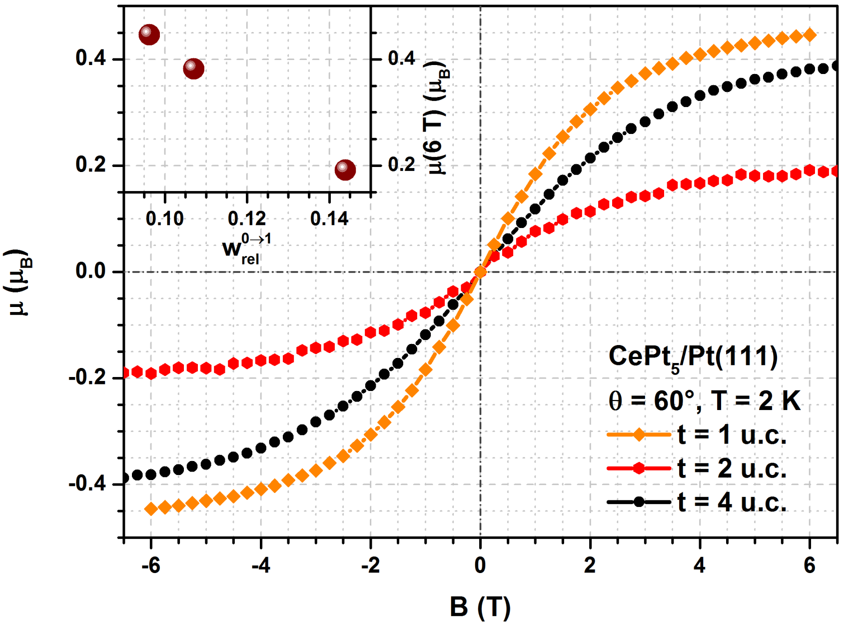

Figure 10.11: Magnetic moment as a function of the magnetic field strength for CePt$_5$/Pt(111) samples with different thickness. The data were taken at $\theta = 60°$ and $T = 2$ K at SOLEIL. The curves are symmetrized averages of the curves taken for both field sweeping directions. The black curve is the same as shown in fig. 10.1. The inset shows the moment at $B = 6$ T in dependence of the $f^0 \to f^1$ weight as evaluated from XAS (compare fig. 9.1).

This allows interpretation of the $\mu(B)$ data in terms of a metamagnetic Lifshitz transition as proposed by Beach and Assaad. This transition is caused by the presence of the hybridization gap close to the Fermi level when the momentum-resolved density of states is shifted due to Zeeman splitting (fig. 1.2 (e)). Main signature of the transition is a plateau in $\mu(B)$ at intermediate field strength (region II in fig. 1.2 (f),(g)). It might well be that the experimentally observed trend towards a constant $\mu(B)$ relation above $B = 6$ T marks such a plateau.

In this interpretation, the field strength of saturation corresponds to the headroom in the renormalized band structure. The data in fig. 10.11 indicate that this quantity does not vary significantly with the film thickness. Thus, it is independent of the thickness-dependent degree of hybridization, which is reflected by the $f^0 \to f^1$ weight in XAS (compare section 8.2.1).

In contrast, the magnetic moment at $B = 6$ T correlates with the $f^0 \to f^1$ weight, which is illustrated in the inset to fig. 10.11. Apparently, there is a linear relation of the two quantities, with smaller $\mu(6\text{ T})$ for samples with higher $w_{\text{rel}}^{0\to 1}$.

A quantitative discussion of the absolute value of $\mu(6\text{ T})$ can be done based on the assumption that the heavy fermion quasiparticles inherit the magnetic characteristics, like the g-factor, of the impurity states. Under this premise, the values for μ given in fig. 10.11, which were evaluated as described in section 6.4 and correspond to the magnetic moment per impurity atom, reflect the moment per quasiparticle band state.

In this framework, the absolute values of $\mu(6\text{ T})$ are significantly smaller than the expected saturation moment. For the given hexagonal crystal field and $\theta = 60°$, the results of sections 2.1.3 and 6.4.5 allow calculation of the paramagnetic saturation moment for an isolated $|1/2\rangle$ doublet as $\mu_{\text{sat}}^{1/2}(\theta = 60°) = 1.14\,\mu_{\text{B}}$. For other CF schemes, this quantity cannot be calculated within the perturbation treatment for $B \perp c$ applied in the present thesis. However, it can be assumed that the value for a $|1/2\rangle$ ground state is the smallest possible, in analogy to the value of the effective moment (see fig. 2.4). The observed reduction of $\mu(6\text{ T})$ supports the interpretation as an intermediate plateau at this field strength.

In the metamagnetic scenario, the plateau moment is connected to the fraction of the Brillouin zone that is occupied by the headroom. The XMCD results then give access to this basic characteristic of the renormalized band structure. The observed correlation of the plateau moment with the $f^0 \to f^1$ weight in XAS indicates a variation of the Fermi surface as a function of the hybridization strength. This could be cross-checked with high-resolution PES measurements of the Fermi surface of $\mathrm{CePt_5/Pt(111)}$ samples with different thicknesses.

Another promising experiment is to continue the XMCD measurements to higher magnetic field strength, where $\mu(B)$ should increase again due to the passing of the band gap in the momentum-resolved density of states (region III in fig. 1.2 (f),(g)). In recent experiments, no such effect was found for samples with $t = 2$ and 4 u.c. at $T = 2$ K and up to $B = 13$ T [282]. A change of slope was observed for a $t = 1$ u.c. sample at $B \approx 9$ T, but this sample showed traces of $\mathrm{CeO_2}$ contamination in LEED (compare fig. A.3 (c)), which complicates an unambiguous interpretation of the data. Further experiments are planned.

10.6 Conclusions to the chapter

The results of the present chapter show that the attempt to apply Ce $\mathrm{M_{4,5}}$ XMCD to probe local $4f$ magnetism of the model heavy fermion system $\mathrm{CePt_5/Pt(111)}$ can be regarded as successful. The experiments combine a surface-sensitive, element and orbital specific technique with a single-crystalline heavy fermion surface intermetallic. The intermetallic film thickness of $\mathrm{CePt_5/Pt(111)}$ provides the notable opportunity to tune the magnitude of hybridization between the local $4f$ level and conduction states, which becomes manifest in a variation of the $f^0 \to f^1$ weight in XAS (see section 9.1.1).

Based on the characterization of crystal structure (chapter 7), XAS line shape (chapter 8) and the thickness- and temperature-dependence of both hybridization and crystal field effects (chapter 9), a consistent interpretation of the magnetic results could be developed. A major source of complexity in Ce-based heavy fermion compounds is the coexistence of different energy scales (compare section 2.1). In the present case, these are the crystal field splittings, RKKY interaction, the single impurity Kondo scale and the coherence scale. One of the main achievements of the present study is that these different effects on the paramagnetic susceptibility could be disentangled. This was done by development of a model description for $\chi^{-1}(T)$ in the single-impurity regime, which covers the first three energy scales, and a separate analysis of the low-T coherence regime.

The hexagonal crystal field is included to the $\chi^{-1}(T)$ model in an ionic picture, the case of non-parallel alignment of magnetic field and c axis is treated perturbatively (see section 2.1.3). A combined analysis of the linear dichroism in XAS and the anisotropic paramagnetic susceptibility allowed identification of a level scheme that is most likely representative for the intermetallic films. It is assumed that the $|1/2\rangle$ and $|3/2\rangle$ doublets are almost degenerate, whereas the $|5/2\rangle$ doublet is separated by $\Delta E_{5/2} = 15 \ldots 25$ meV. The splitting depends on the thickness, the observed trend is in line with the t-dependent lateral lattice constant relaxation as observed by LEED.

The proposed CF scheme could be supported by independent determination of the CF splitting energies. The standard technique for this task is inelastic neutron scattering, which, however, requires considerably more sample volume than is provided by thin films. An alternative approach is Raman[2] spectroscopy. Such experiments were most recently performed by M. Zinner *et al.* [283], the results are well in line with the present scenario.

RKKY interaction leads to ferromagnetic correlations in $\mathrm{CePt_5/Pt(111)}$ films, which is reflected by a positive Curie temperature seen in $\chi^{-1}(T)$. However, an ordered ferromagnetic state was not found. Instead, $\chi^{-1}(T)$ curves measured with sufficiently high point density feature an anomaly at $T \approx 20$ K. It indicates a deviation from Curie-Weiss behavior that is not explained by the crystal field and is thus interpreted as marking the onset of a coherent heavy fermion state.

Quantitative evaluation of the paramagnetic susceptibility allowed identification of a signature of single-impurity Kondo interaction, since the effective moment in $\chi_{0^\circ}^{-1}(T)$ was found to be significantly reduced compared to the expected value for a free $\mathrm{Ce^{3+}}$ ion. This is interpreted as a result of Kondo screening of the $4f$ moment, which is supported by the fact that the magnitude

---

[2] Chandrasekhara Venkata Raman, Indian physicist, 1888-1970

of reduction correlates with the tunable $f^0 \to f^1$ weight in XAS.

Reproduction of the experimental $\chi^{-1}(T)$ data required introduction of doublet-specific screening factors to the model. This accounts for the spatial anisotropy of the three $|m_j\rangle$ doublets. Doublet-specific Kondo interaction should also lead to a doublet-specific $4f$ occupancy, an idea that was brought forward by comparison of the T-dependence of the screening to $n_f(T)$ data obtained by XAS. This scenario obscures the interpretation of $n_f(T)$ as indicating the single-impurity Kondo temperature to some extent. Nevertheless, it is concluded that the Kondo energy scale, be it in form of three different scales, contributes to the observed increase in $n_f(T)$, such that the estimate of $T_K \approx 100 \ldots 200$ K remains valid.

The aforementioned anomaly in $\chi^{-1}(T)$ gives access to the temperature scale of coherent band formation. Both the susceptibility as well as the field-dependence of the magnetic moment are consistently described in terms of a renormalized band structure, as observed in previous PES experiments. In this interpretation, the $\mu(B)$ data indicate a metamagnetic Lifshitz-transition and thus give access to key features of the band structure and Fermi surface. The tunability of the $f^0 \to f^1$ weight with the film thickness allows studying these features as a function of hybridization strength.

Although restricted to a specific material, the present XMCD results and their interpretation demonstrate the high potential of XMCD studies of Kondo and heavy fermion compounds. The choice of $\mathrm{CePt_5/Pt(111)}$ as a model material for these pioneering experiments allowed addressing the different energy scales, which made a consistent interpretation possible. The present results are well-suited as references for future experiments on other materials.

Summary, conclusions and outlook

The intriguing physical properties of strongly correlated electron systems are caused by large Coulomb interaction in many-body states. For Kondo and heavy fermion materials, the relevant states derive from partially filled but localized atomic orbitals of magnetic impurities, which are represented by the $4f$ multiplet in the case of Ce compounds. A local probe of $4f$ magnetism is offered by Ce $M_{4,5}$ XMCD. Hence, this technique provides direct access to the source of interesting correlation effects without the need to extract the desired information from a complex signal.
The primary object of the present thesis was the application of Ce $M_{4,5}$ XAS and XMCD to the heavy fermion surface intermetallic $CePt_5$/Pt(111) in order to investigate the interaction of localized $4f$ electrons and itinerant conduction electrons. The material was chosen for its benefits regarding the application of spectroscopy: The surface character suits the small probing depth of TEY experiments, and the opportunity to prepare single-crystalline samples allows direction-dependent experiments giving information about symmetry-related effects. Furthermore, the film thickness t provides a parameter that can be tuned during preparation.
As the central experimental result, XMCD data for thirteen samples with $t = 1 \dots 11$ u.c. were evaluated by application of the sum rules to yield the inverse paramagnetic $4f$ susceptibility $\chi_\theta^{-1}(T)$ as a function of temperature and angle θ between sample magnetization direction and sample surface normal. The temperature range $T = 2 \dots 300$ K was covered, whereas the angle was adjusted to either normal incidence or $\theta = 60°$. These data are presented in chapter 10.
Regarding the interpretation of these data, the simplest picture of $4f$ magnetism in Ce^{3+} ions relies on the spin-orbit split Hund's rule ground state, which is characterized by $j = 5/2$. A detailed analysis of $\chi_\theta^{-1}(T)$ for a $t \approx 4$ u.c. sample allowed identification of the additional presence of four relevant energy scales in $CePt_5$/Pt(111) in the accessible temperature range:

The **crystal field** induces deviations from linear Curie behavior and leads to a strong anisotropy of the signal as a function of θ.

Single-impurity Kondo interaction becomes manifest in a significant reduction of the effective paramagnetic moment.

RKKY interaction leads to a positive Curie-Weiss temperature Θ_{CW} of the inverse paramagnetic susceptibility, indicative of ferromagnetic correlations.

Heavy fermion band formation produces an anomaly in $\chi_{0°}^{-1}(T)$ at $T \approx 20$ K, which indicates a change of the Fermi surface.

Interpretation of the results on a sound basis and development of a model description for $\chi^{-1}(T)$ required to disentangle the effects of these energy scales. This was made possible by additional experiments and supporting calculations.

Adequate treatment of **crystal field** effects requires knowledge of the crystal structure. Due to contrary results in the literature, a detailed structural characterization of $CePt_5$/Pt(111) was performed as the first step. The results of this study are presented in chapter 7.
Analysis of six different LEED patterns that were obtained when varying the initial Ce coverage allowed tracking the relative changes in the surface lattice constant, which indicate lattice relaxation. Accurate determination of the lattice constant for a reference phase (denoted IV) was made possible by a refined interpretation of the pattern as a combination of diffraction on

the substrate and the film lattices.

The vertical lattice constant was investigated by a combination of quartz microbalance measurements and analysis of a STEM cross-section, which also confirmed that the intermetallic forms as a well-defined film on top of the substrate. The film thickness t can be controlled by the initial Ce deposit. Since it describes the material in its final state, t is introduced as the primary parameter to characterize a specimen. Once the different LEED phases are calibrated, inspection of the diffraction pattern for a given sample allows specification of its thickness within an uncertainty of $\Delta t = 1 \dots 2$ u.c.

The stoichiometry of the surface intermetallic was addressed by analysis of the peak-to-background ratio in XAS; the result is indicative of $\mathrm{CePt_5}$. For confirmation of the associated structure, a LEED-IV study was performed on a sample with $t \approx 4$ u.c. Comparison of experimental $I(E)$ curves from samples with different thicknesses confirmed that the crystal structure is robust over the complete thickness range that was investigated. The LEED-IV analysis produced satisfactory agreement between experimental and calculated curves for the assumption of Pt-terminated $\mathrm{CePt_5}$ in the $\mathrm{CaCu_5}$ structure with additional Pt atoms in the Kagome holes. This is in perfect agreement with theoretical modeling of the surface [93].

The local symmetry of the Ce ions in the determined crystal structure is hexagonal, which facilitates the model description of $\chi^{-1}(T)$: A hexagonal crystal field only lifts the degeneracy of the three $|5/2, m_j\rangle$ doublets without mixing them, as is the general case. Furthermore, an analytic expression for $\chi_\theta^{-1}(T)$ can be derived in second order perturbation theory, which allows fast numerical fitting of experimental data without the need to diagonalize the Hamiltonian. With the energy splittings, the hexagonal CF only introduces two free parameters to the $\chi^{-1}(T)$ model. However, in order to reliably extract the information about Kondo physics, a reduction of the free parameters turned out to be necessary.

In addition to the susceptibility data obtained at the Ce $\mathrm{M}_{4,5}$ edges, the crystal field also affects the absorption spectra that are recorded for the calculation of the XMCD. Unequal population of the CF split states, which exhibit spatial anisotropy, leads to the occurrence of linear dichroism in Ce $\mathrm{M}_{4,5}$ XAS: Differences in spectra recorded for different alignments of crystallographic axes and light polarization vector occur. The LD can be simulated by use of full multiplet theory, which allows calculation of realistic spectra. In combination with such calculations, which are presented in chapter 8, analysis of the LD as a function of temperature allows conclusions on the CF ground state and the splitting energies.

In order to concentrate the characteristics of the measured polarization-dependent spectra in a single number, the relative $\mathrm{M}_5/\mathrm{M}_4$ peak ratio Υ is introduced in chapter 9. This quantity is sensitive to the m_j character of the initial state and can be modeled by use of simulated spectra. This allowed simultaneous fitting of $\Upsilon(T)$ and anisotropic $\chi^{-1}(T)$ data with shared parameters, which lead to the proposal of a CF scheme for $\mathrm{CePt_5}$/Pt(111). It consists of nearly degenerate $|1/2\rangle$ and $|3/2\rangle$ doublets with the $|5/2\rangle$ doublet excited by $\Delta E_{5/2} \approx 15 \dots 25$ meV. The total CF splitting features thickness-dependence, which is consistent with expectations based on the lattice relaxation observed in LEED.

The access to the crystal field parameters provided by the linear dichroism in Ce $\mathrm{M}_{4,5}$ XAS is not completely independent of **single-impurity Kondo interaction**, in analogy to the susceptibility. This is due to the fact that the line shape of the $f^1 \to f^2$ contribution shows characteristic variations as a function of the $4f$ occupancy n_f, which is reflected by the magnitude of the $f^0 \to f^1$ contribution to the Ce $\mathrm{M}_{4,5}$ spectrum [61]. The $f^0 \to f^1$ contribution in $\mathrm{CePt_5}$/Pt(111) non-monotonically varies with the film thickness t, which is in line with results of a previous PES study [79]. Due to the observed robustness of the crystal structure with varying t, this provides the unique opportunity to tune an important parameter during sample preparation. The observation of a peaking behavior at $t \approx 2$ u.c. could be explained with respect to the lattice relaxation at low t and possible interface effects at high t.

The resulting line shape variations had to be considered for the calculated spectra, which were applied to quantitatively evaluate Υ and the $f^0 \to f^1$ weight from experimental data. Hence, it was attempted to identify their origin, which is described in chapter 8.

Simulations showed that the assumption of an admixture of $j = 7/2$ character to the ground state, which is frequently found in the literature [189], cannot explain the observations. Two alternative scenarios are presented that allow reproduction of the experimental XAS data: Either an additional spectral contribution emerges with increasing hybridization, which might be a transition of $f^2 \rightarrow f^3$ character, or the transition line profile becomes asymmetric. This might be caused by dynamical core-hole screening and thus represents the signature of another many-body effect.

It was not possible to clarify the nature of the n_f-induced line shape variations within the scope of the present thesis. From the information available, the scenario of asymmetric line profiles is favored over the assumption of an additional contribution; The latter should lead to a variation of the XMCD line shape, which is not observed. For the evaluation of Υ in chapter 9, the XAS line shape variations were accounted for by an empirical correction factor, whereas the variations were ignored for the determination of the $f^0 \rightarrow f^1$ weight. However, this neglect should not affect qualitative conclusions drawn from the data, and the values obtained for n_f compare well to previous PES results [79].

In addition to the XAS line shape characteristics induced by the sample thickness, similar but much smaller variations of the Ce $M_{4,5}$ line shape were observed as a function of time after preparation of a sample. These changes are attributed to adsorbates from the residual gas in the vacuum recipient, which alter the electronic environment of the $4f$ level near the surface.

Another parameter that causes spectral variation is the sample temperature, which allows determination of the single-impurity Kondo temperature T_K. As is known from NCA calculations [27], the $4f$ occupancy and thus the $f^0 \rightarrow f^1$ weight in Ce $M_{4,5}$ XAS increase with temperature and feature a maximum in its slope at $T = T_\mathrm{K}$. Based on respective measurements, the single-impurity Kondo temperature in CePt$_5$/Pt(111) is estimated to $T_\mathrm{K} \gtrsim 100 \ldots 200$ K. Apparently, the progression of $n_f(T)$ depends on the film thickness, but no conclusive correlation between T_K and the low-temperature value of n_f was found.

The T_K result is regarded as a lower limit for the Kondo energy scale, since the assignment might be complicated by a possible m_j-specificity of the $4f$ occupancy in conjunction with the crystal field splitting. Due to their very different angular momentum character and the resulting spatial anisotropy, it is reasonable to expect that each $|m_j\rangle$ doublet features a specific hybridization matrix element and thus $4f$ occupancy.

With the Kondo temperature being located in the midst or above the accessible temperature range, the effective paramagnetic moment in the XMCD data is expected to be subject to Kondo screening. Indeed, a reduction of μ_eff is observed in $\chi_{0^\circ}^{-1}(T)$, which is considered in the model description of chapter 10 by phenomenological screening factors. Introduction of a single, T-independent screening factor did not allow satisfactory reproduction of the experimental data. This was achieved by assumption of doublet-specific screening factors C_{m_j} that reflect the possibility of doublet-specific Kondo interaction.

The modeling of $\chi^{-1}(T)$ data as a function of film thickness yielded screening factors of $C_{1/2,3/2} = 0.3 \ldots 0.5$ and $C_{5/2} = 0.6 \ldots 0.85$. The magnitude of screening correlates with the $f^0 \rightarrow f^1$ weight in XAS, which supports the interpretation of the observed moment reduction as arising from Kondo interaction.

The ferromagnetic **RKKY** interaction is reflected by the positive Curie-Weiss temperature in the single-impurity Kondo regime and included to the $\chi^{-1}(T)$ model in terms of mean field coupling. However, a magnetically ordered state is not observed down to $T = 2$ K. Instead, Θ_CW is drastically reduced at the observed anomaly at $T \approx 20$ K. This indicates a change of the Fermi surface, which is assigned to the onset of **heavy fermion band formation**.

Consequently, the experimental results below the transition temperature have to be interpreted in terms of bandstructure rather than localized atomic levels. In addition to the $\chi^{-1}(T)$ data, which show Curie behavior, the measurement of XMCD magnetization curves $\mu(B)$ up to $B = 6.5$ T gives information about the heavy fermion state. The $\mu(B)$ data at $T = 2$ K indicate saturation towards a rather low magnetic moment, which correlates with the $f^0 \rightarrow f^1$ weight in XAS.

These observations can be understood in terms of a renormalized bandstructure with a narrow $4f$ band and a hybridization gap slightly above the Fermi level, as observed in previous PES experiments [94]. This leads to the following scenario: Due to the narrowness of the band, the Fermi temperature is much smaller than $T = 2$ K, the lowest sample temperature accessible. Consequently, a linear $\chi^{-1}(T)$ relationship is observed rather than a transition to a T-independent Pauli susceptibility, which is expected to occur at even lower temperature. The presence of the hybridization gap induces a metamagnetic Lifshitz transition in $\mu(B)$ [33], the onset of which leads to the observed saturation. The saturation moment then corresponds to the energy headroom between Fermi level and the band gap.

In conclusion, it can be said that the aim of the thesis was successfully accomplished. It is shown that Ce $M_{4,5}$ XAS and XMCD provide important insights into the magnetic properties of Ce-based heavy fermion materials. A route is presented to interpret these experiments by thorough consideration of all relevant energy scales that are addressed by the methods. In $CePt_5$/Pt(111), these are the crystal field, Kondo interaction, RKKY interaction and heavy fermion formation. It is regarded as the major success that it was possible to disentangle the effects of these different energy scales on the paramagnetic susceptibility, which lead to a model description for $\chi^{-1}(T)$. This allowed both investigation of each effect separately and of their complex interplay.
Probably the most important by-product of the present work is the calculation of highly realistic Ce $M_{4,5}$ spectra. In particular, the XMCD shown in fig. 8.8 represents the best theoretical reproduction of experimental spectra that is known to the author.
The choice of $CePt_5$/Pt(111) was a fortunate one, since this material proved to be a true model system. Preparation reproducibly yields single-crystalline thin-film samples. The film thickness, which ideally meets the requirements of surface-sensitive TEY spectroscopy, is adjustable. While the crystal structure is robust over the complete thickness range investigated, t allows tuning of an important model parameter: the hybridization between $4f$ level and conduction states. This provides the unique opportunity to study the effect of this key feature of Kondo physics on characteristics like the screening of the effective moment or the headroom of the renormalized band structure in the heavy fermion state, in one and the same material. Furthermore, many relevant energy scales were shown to be accessible in $CePt_5$/Pt(111) with the available experimental equipment, and the hexagonal symmetry of the crystal structure facilitates the theoretical treatment of the crystal field.
While the present thesis provides a thorough characterization of $CePt_5$/Pt(111), the performed elaboration of the immense potential offered by Ce $M_{4,5}$ XAS and XMCD on Kondo and heavy fermion materials are of general value. It might well serve as a road-map for future experiments on further Ce compounds. Such experiments can also benefit from the methodology developed, like the sum rule evaluation (see section 6.4), the $n_f(T)$ fast scan mode (section 6.2) and the possibility to record linear dichroism in XAS by use of circularly polarized light (appendix A.2).

Future experiments could involve the cross-over from single-impurity to heavy fermion behavior by partially substituting La into $CePt_5$/Pt(111). In the ideal case, this leads to the formation of homogeneously mixed $Ce_xLa_{1-x}Pt_5$ intermetallics, which requires verification by structural characterization. In such samples, only the Ce sites carry a magnetic moment. Hence, the inter-impurity interaction could be controlled by the Ce fraction x.
Another promising experiment is to investigate the influence of adsorbed molecules on the electronic and magnetic properties of the surface intermetallics. The observed time-dependent changes in the Ce $M_{4,5}$ line shape (section 9.1.2) as well as the variations occurring after contact to air (appendix A.3) indicate that adsorbates influence the $4f$-level occupancy at the surface. A verification of this interpretation would involve the systematic deposition of different molecules. In particular, polar species are expected to influence the electronic environment of the Ce ions. If the adsorption of molecules allows control of the degree of hybridization, it would provide a novel tool to tune the magnitude of Kondo interaction and thus to study its consequences.
An altered environment of the Ce ions is of course also produced by changing the host material. The techniques that were developed in the present thesis can of course be transferred to other Ce-based surface intermetallics. Results on Ce-Ag(111) are presented in appendix A.4. Another

candidate is $\mathrm{CePd}_7/\mathrm{Pd}(001)$, which shows interesting behavior in PES [241].

The modeling of the $\chi^{-1}(T)$ data as performed in the present work is done with major simplifications, especially regarding the *ad hoc* treatment of doublet- specific Kondo screening. A more sophisticated approach to this problem was provided by Zwicknagl *et al.* in a simplified NCA scheme [280]. Application of this formalism would certainly allow a refined interpretation of the data.

An open issue is the studied hybridization-dependent line shape variation. Two scenarios are proposed in chapter 8. If proven to be true, both would provide a more detailed understanding of the electronic structure of Ce compounds and of the mechanisms of core-level spectroscopy of such materials. Furthermore, clarification of this issue would improve the quantitative evaluation of experimental data regarding the $4f$ occupancy as well as the linear dichroism. Input to this question, in particular from the theoretical side, would be appreciated.

Acknowledgment

The experiments, calculations, evaluations and interpretations, as well as the writing of the present thesis would not have been possible without the support of many people and institutions, to whom the author wishes to express his gratitude.

Fundamental research often appears to be far from most humans' daily life needs, and it is luxurious for a society to afford. I am grateful that the work on my thesis was to large parts financed from tax revenue via the Deutsche Forschungsgemeinschaft (DFG). Experimental stays at synchrotron facilities were additionally funded by the Bundesministerium für Bildung und Forschung under contract no. 05ES3XBA/5, the European Community's Seventh Framework Programme (FP7/2007-2013) under CALIPSO project (grant agreement no. 226716) and the synchrotron operating institutions HZB (BESSY) and SOLEIL. Furthermore, participation on DPG spring meetings was supported by the Wilhelm und Else Heraeus Stiftung.

The thesis was embedded into the DFG research group FOR1162 in subproject P7. I want to thank the principal investigators of the research group, represented by spokesman R. Claessen, for their engagement to provide the funding in Würzburg and thus giving me the opportunity to contribute to the project. Furthermore, the various scientific activities in the research group, the workshops, seminars and conferences, stimulated a productive climate of joint research that I really appreciated.

A very special thank goes to K. Fauth, principal investigator of P7, group leader, provider of funding and equipment, thesis supervisor, advisor, interlocutor, guide and partner in the laboratory and at synchrotron facilities, supplier with dedicated computer codes and inexhaustible source of ideas.

Further gratitude is owed to:

- Björn, Martin Z., Hauke, Sebastian B., Thomas, Rafael, Annemarie K., Jens-Uwe, Sebastian G., Peter, Stephan, Alex G., Adham, Tobias, Lukas, Philipp E., Annemarie I., Ingo, Sascha, Rostand and Matthias for being workgroup colleagues, office neighbors, lab fellows and great supporters during synchrotron experiments.

- R. Claessen and M. Bode for hosting my office at their chairs and, together with all chair members, providing a pleasant working atmosphere.

- M. Kamp for performing the STEM sample preparation and measurements and the Wilhelm Conrad Röntgen-Center for Complex Material Systems for providing the experimental facilities.

- P. Hansmann for the collaboration on the full multiplet calculations, M. W. Haverkort for providing and supporting the SSPMP software and for valuable input, and T. Willers for readily sharing experience.

- G. Held for providing the CLEED package for LEED IV analysis and for support, shared knowledge and helpful discussion, as well as K. Fauth and R. Fradczyk for providing auxiliary computer programs for LEED IV data evaluation.

- J. Kemmer and M. Bode for contributing their STM data to a joint publication and for well-structured and target-oriented scientific teamwork.
- H. Schwab as well as M. Bercx and F. F. Assaad for valuable communication and discussion.
- P. Coleman for his inspiring talk at the FOR1162 Fall School 2011 in Würzburg.
- The technical staff in Würzburg, in particular R. Brauner and T. Grünebaum from the mechanical workshop for accepting every challenge my blueprints posed on them.
- The persons who made successful synchrotron experiments possible with their technical support and proficiency, namely T. Kachel, R. Follath and H. Pfau at BESSY and P. Ohresser, F. Choueikani and E. Otero at SOLEIL.
- B. Gottschlich from SPECS Surface Nano Analysis GmbH for fast and competent help with LEED problems, especially during beamtimes when time was short.
- The administrative staff that organized all these things a scientist does not want to occupy his mind with. In particular, M. Seifer for being the heart and soul of EP4 and the best secretary I ever met, C. Kosemund for always finding a vacant room in the BESSY guest house, the SOLEIL travel office for successful accommodation in the back country despite my modest French proficiency and M. Scheller from the central administration in Würzburg for his company when putting the Bundeselterngeld- und Elternzeitgesetz in conjunction with the Wissenschaftszeitvetragsgesetz into practice.
- All persons who share their expertise free of charge in the worldwide web, be it at wikipedia, in various support boards or in the form of software like TexWorks, ImageJ or Firefox.
- Don, Raffi, Sebastian M., Alex P., Martin B. and Philipp H. for proofreading, corrections and constructive criticism regarding the thesis.

Last but not least I wish to thank my family: In particular, my parents for providing me with both roots and wings and my sister for constant company and trust. A very special thank goes to my wife, who supported me not only during work on the thesis with time, motivation and love, and to our children for just being wonderful.

Appendix

Contents

A.1 Calculation of pattern distortion in LEED

In section 4.1.5, a number of possible sources for pattern distortion in LEED are discussed: Angular misalignment, translational misplacement and projection of the screen curvature. In this appendix, the calculations needed to quantitatively model these distortions are presented.

A.1.1 Angular misalignment

In the following, the relative displacement $\Delta d/d$ of a projected LEED spot caused by a finite angle ϑ_p between sample surface and projection plane is determined in dependence of the diffraction angle ϑ_n. The relevant geometry is shown in fig. A.1.
The distance d between the projection of a spot and the projection of the intersection of surface normal and the screen (K) is readily written as

$$d(\vartheta_\mathrm{p}) = R\left(\sin(\vartheta_n + \vartheta_\mathrm{p}) - \sin\vartheta_\mathrm{p}\right). \tag{A.5}$$

Hence, the relative displacement reads

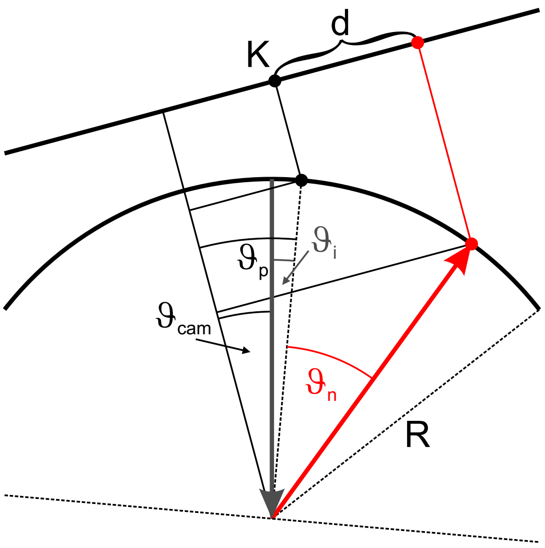

Figure A.1: Relevant geometry for pattern distortion due to non-parallel projection plane and sample surface.

$$\begin{aligned}
\frac{\Delta d}{d} = \frac{d(\vartheta_\mathrm{p}) - d(0)}{d(0)} &= \frac{\sin(\vartheta_n + \vartheta_\mathrm{p}) - \sin\vartheta_\mathrm{p} - \sin\vartheta_n}{\sin\vartheta_n} \\
&= \frac{\sin\vartheta_n\cos\vartheta_\mathrm{p} + \cos\vartheta_n\sin\vartheta_\mathrm{p} - \sin\vartheta_\mathrm{p} - \sin\vartheta_n}{\sin\vartheta_n} \\
&\approx \frac{\sin\vartheta_n + \cos\vartheta_n\vartheta'_\mathrm{p} - \vartheta'_\mathrm{p} - \sin\vartheta_n}{\sin\vartheta_n} \quad \text{for small } \vartheta_\mathrm{p} \text{ and } \vartheta'_\mathrm{p} = \frac{2\pi\ \vartheta_\mathrm{p}}{360°} \\
&= \frac{\cos\vartheta_n - 1}{\sin\vartheta_n}\ \vartheta'_\mathrm{p}. \qquad \text{(A.6)}
\end{aligned}$$

A.1.2 Translational sample misplacement

The aim of this section is to determine the relative displacement $\Delta d/d$ of a projected LEED spot due to a sample displacement Δz in dependence of the diffraction angle ϑ_n and the screen sphere radius R. Fig. A.2 defines the quantities and the coordinate system in analogy to fig. 4.3 (b). In order to purely address the problem of translational misplacement, the projection plane is assumed to be parallel to the sample surface, i.e., $\vartheta_\mathrm{p} = 0°$.
The intersection point (x, z) of a diffracted beam and the screen sphere is defined by the following two conditions:

$$\tan\vartheta_n = \frac{x}{z} \qquad \text{(A.7)}$$

$$x^2 + (z - \Delta z)^2 = R^2. \qquad \text{(A.8)}$$

Equivalently, $x = R\sin\vartheta_n$ for $\Delta z = 0$ To obtain $x(\Delta z)$, the quadratic equation

$$x^2\left(1 + \frac{1}{\tan^2\vartheta_n}\right) - x\ \frac{2\ \Delta z}{\tan\vartheta_n} + \Delta z^2 - R^2 = 0 \qquad \text{(A.9)}$$

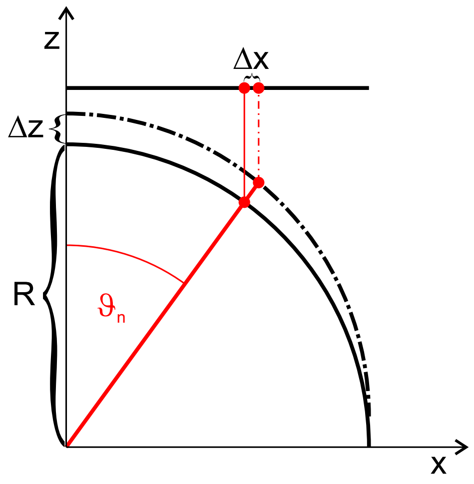

Figure A.2: Definition of quantities and coordinate system.

has to be solved. Restricting to $x > 0$, this is readily done by

$$\begin{aligned} x &= \frac{\Delta z}{\tan\vartheta_n + \cot\vartheta_n} + \sqrt{\frac{\Delta z^2}{(\tan\vartheta_n + \cot\vartheta)^2} - \frac{\Delta z^2 - R^2}{1 + \cot^2\vartheta_n}} \\ &= \frac{1}{\tan\vartheta_n + \cot\vartheta_n}\left(\Delta z + \sqrt{\Delta z^2 \ \tan^2\vartheta_n + R^2\left(1 + \tan^2\vartheta_n\right)}\right) \\ &= (\sin\vartheta_n \cos\vartheta_n)\left(\Delta z + \frac{R}{\cos\vartheta_n}\sqrt{\frac{\Delta z^2 \sin^2\vartheta_n}{R^2} + 1}\right). \end{aligned} \tag{A.10}$$

For small sample displacement, more exactly for

$$\frac{\Delta z^2 \sin^2\vartheta_n}{R^2} \ll 1, \tag{A.11}$$

the last square root can be approximated by 1. Consequently,

$$x(\Delta z) \approx \Delta z \ \sin\vartheta_n \cos\vartheta_n + R \sin\vartheta_n, \tag{A.12}$$

$$\Delta x = x(\Delta z) - x(0) \approx \Delta z \ \sin\vartheta_n \cos\vartheta_n = \Delta z \ \frac{\sin(2\vartheta_n)}{2} \tag{A.13}$$

and

$$\frac{\Delta d}{d} = \frac{\Delta x}{x(0)} \approx \frac{\Delta z \ \cos\vartheta_n}{R}. \tag{A.14}$$

A.1.3 Projection of the screen curvature

A photographic image of a LEED screen only represents a projection to a plane if the screen curvature can be neglected against the distance d_{OS} between screen and camera objective. Otherwise, the pattern photograph is subject to distortion, as is illustrated in fig. 4.4. The relative spot displacement between real and ideal image depends on the diffraction angle ϑ_n. Applying the intercept theorem it can be calculated as

$$\begin{aligned}\frac{\Delta d}{d} &= \frac{d_\mathrm{r} - d_\mathrm{i}}{d_\mathrm{i}} = \frac{d_\mathrm{r}}{d_\mathrm{i}} - 1 = \frac{\tan\alpha_\mathrm{r}}{\tan\alpha_\mathrm{i}} - 1 = \frac{x_r}{x_i} - 1 \\ &= \frac{d_\mathrm{OS}}{d_\mathrm{OS} + d_\mathrm{ref}} - 1 = \frac{d_\mathrm{OS}}{d_\mathrm{OS} + R\left(1 - \cos\vartheta_n\right)} - 1 \\ &= \frac{1}{\frac{d_\mathrm{OS}}{R(\cos\vartheta_n - 1)} - 1} \qquad \text{(A.15)}\end{aligned}$$

A.2 Addressing linear dichroism in XAS with circularly polarized light

For uniaxial crystal symmetry, linear dichroism can exist in XAS due to different transition strengths for linear light polarization parallel and perpendicular to the symmetry axis. This LD can also be addressed by circularly polarized light, if the angle of incidence θ between the symmetry axis (z) and the propagation direction of the light is varied.
By arbitrary choice of the surface coordinates as the xy-plane, the θ-dependence of the electric field vector $\vec{E}^{\pm}(\tau)$ for CPL can be written as

$$\vec{E}^{\pm}(\tau,\theta) \propto \begin{pmatrix} \cos\theta & 0 & -\sin\theta \\ 0 & 1 & 0 \\ \sin\theta & 0 & \cos\theta \end{pmatrix} \begin{pmatrix} \cos\omega\tau \\ \cos(\omega\tau \pm \pi/2) \\ 0 \end{pmatrix} = \begin{pmatrix} \cos\theta\cos\omega\tau \\ \cos(\omega\tau \pm \pi/2) \\ \sin\theta\cos\omega\tau \end{pmatrix} \qquad \text{(A.16)}$$

Hence, $\vec{E}^{\pm}(\tau,\theta)$ can be regarded as a coherent superposition of electric fields that are polarized along the three Cartesian directions. The time-dependence and the phase relation are not important in the present context. Hence, the light polarization can be written in terms of polarization vectors as

$$\vec{\epsilon}(\theta) = \vec{\epsilon}_x \cos\theta + \vec{\epsilon}_y + \vec{\epsilon}_z \sin\theta. \qquad \text{(A.17)}$$

In order to obtain the XA spectrum from eq. 5.4, this polarization vector can be substituted into the dipole transition matrix element in eq. 5.13. The absorption coefficient is then described by

$$\mu_x(\theta) \propto \left|\langle f|\, \vec{\epsilon}(\theta) e\hat{\vec{x}}\, |i\rangle\right|^2 = \cos^2\theta \left|\langle f|\, \vec{\epsilon}_x e\hat{\vec{x}}\, |i\rangle\right|^2 + \left|\langle f|\, \vec{\epsilon}_y e\hat{\vec{x}}\, |i\rangle\right|^2 + \sin^2\theta \left|\langle f|\, \vec{\epsilon}_z e\hat{\vec{x}}\, |i\rangle\right|^2. \qquad \text{(A.18)}$$

The interference terms can be neglected under normal conditions, since the unit polarization vectors are orthogonal [156]. Hence, the spectrum is composed of a superposition of the spectra that are obtained for LPL parallel and perpendicular to the symmetry axis,

$$\mu_x(\theta) = (\cos^2\theta + 1)\ \mu_x^{\perp} + \sin^2\theta\ \mu_x^{\parallel}. \qquad \text{(A.19)}$$

A.3 Signatures of sample contamination in CePt$_5$/Pt(111)

In order to judge the success of a sample preparation (see section 7.1), knowledge about unsuccessful preparations is required. In the present context, a lack of success is particularly judged by the presence of contaminations. Such samples produce certain signatures in the characteri-

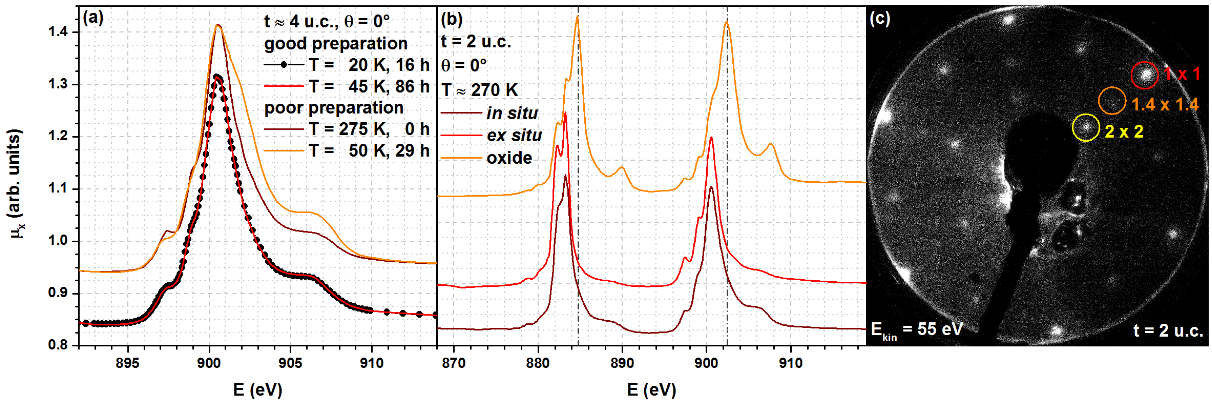

Figure A.3: Signatures of presence or absence of Cerium oxide in $CePt_5$/Pt(111) surface alloys. (a) Ce M_4 XAS of two different samples with nominal thickness $t \approx 4$ u.c. The first sample shows no changes in spectral shape after more than 3 days in UHV, the other one exhibits a growing shoulder in the spectrum after one day. The spectra were measured at BESSY (b) Comparison of Ce $M_{4,5}$ XAS of a sample directly after preparation *in situ* (taken at SOLEIL) and after two months in ambient air *ex situ* (taken at BESSY). Additionally, the spectrum of a Ce oxide reference that was measured simultaneously with the *ex situ* spectrum is shown. (c) LEED image (primary energy $E_{\text{kin}} = 55$ eV) of a $t = 2$ u.c. preparation that exhibits the expected (2×2) superstructure and additional (1.4×1.4) spots.

zation procedure, which are discussed in the following. Furthermore, the role of adsorbants on a successfully prepared sample surface is addressed.

The information given here might be helpful in the identification of such poor preparations in future experiments. Furthermore, it also allows conclusions about properties of samples that were regarded as successfully prepared.

In LEED, two different characteristics were observed that were identified as resulting from improper sample preparation: High background intensity and additional (1.4×1.4) superstructure reflexes, which were sometimes accompanied by more complicated patterns. Those superstructures were usually superimposed to one of the patterns shown in fig. 7.3, an example is shown in fig. A.3 (c). The observed additional patterns are consistent with LEED patterns of ordered CeO_2 films that are reported in the literature [84, 87, 88, 254, 284].

Samples with (1.4×1.4) spots in LEED also showed distinct oxygen peaks in AES. Furthermore, the Ce:Pt intensity ratio was larger than in the spectra of successfully prepared samples, as the ones shown in fig. 7.2. Both findings support the assumption of CeO_2 on the surface. The creation of ordered CeO_2 during alloying can either result from an oxidized evaporant, which means that CeO_2 is deposited to the surface, or the pure Ce deposit was oxidized at the surface after deposition. This could happen due to an already contaminated substrate or by reaction with residual gas. The latter is fostered by high background pressure and by extended standby times, which could occur during evaporation or between deposition and alloying.

A high LEED background indicates disorder on the surface, which can result from unalloyed, disordered Cerium. One such sample was investigated with XAS and showed a distinct change of spectral shape after one day in UHV. This is shown for the M_4 edge in fig. A.3 (a), where a shoulder evolves at high photon energy. An equivalent observation was made by A. Köhl in her preceding work [96]. In comparison, spectra of a similar but successful preparation are shown in the figure, which were not subject to such changes during long measurement time. These spectra are representative the samples that were used for the results presented in part II. The XA spectra of the sensitive sample also exhibit a higher ratio of the M4 peak and the pre-edge region (compare section 7.4). This points towards a larger amount of Ce at the surface. Hence, the change in spectral shape is most probably caused by gradual oxidation of Ce residing at the surface.

Indeed, the observed shoulder can be attributed to Cerium oxide. This can be seen in fig. A.3 (b), where spectra of a successful preparation are shown along with a reference measurement of oxidized Cerium, which was in first place used for calibration of the energy axis. The latter exhibits its major M_4 peak at a photon energy where the shoulder is observed. The spectra of the successful preparation do not exhibit spectral weight that could be distinguished from the rest of the multiplet at this energy.

This is highly interesting, since one of the spectra was taken after two months in ambient air. This spectrum exhibits distinct changes concerning the $f^0 \rightarrow f^1$ contribution and the details of the $f^1 \rightarrow f^2$ multiplet (compare section 8.2.1), but no significant trace of the oxide-related peak. This allows the conclusion that surface alloys that are very robust against further oxidation can be obtained if the preparation is accurately performed with great caution regarding possible sources of contamination. The finding of an altered spectral shape after exposition to ambient conditions underlines that for surface sensitive experiments an ultrahigh vacuum environment is crucial. Additionally, the finding of a possibly adsorbate-dependent hybridization could motivate further systematic work in this direction.

A.4 The reference material Ce-Ag(111)

The XMCD sum rules (see section 5.3) provide a powerful tool for quantitative evaluation of magnetic ground state properties from X-ray absorption experiments. However, their application to experimental data is accompanied by considerable uncertainties. For the Ce $M_{4,5}$ edges, this is discussed in section 6.4, where the evaluation procedure applied in the present work is introduced. It is highly desirable to independently calibrate such an evaluation procedure. For this purpose, a sample with well-defined characteristics is required. For this purpose, a Ce-Ag(111) surface intermetallic is used in the present work. The first study of the Ce-Ag(111) system was reported by Schwab *et al.* [95], who obtained a LEED pattern indicative of an ordered intermetallic film. Furthermore, PES measurements are presented and compared to results on $CePt_5$/Pt(111). It is concluded that the Kondo energy scale of Ce-Ag(111) is much smaller than in $CePt_5$/Pt(111). This qualifies this material as a reference system, since negligible Kondo interaction in a Ce compound means high localization of the $4f$ electrons and thus an f occupancy close to unity. Hence, the system can well be approximated in terms of Ce^{3+} ions, and the description given in section 2.1.1 applies.

The ground state is then the $j = 5/2$ multiplet. In the presence of a significant crystal field, the multiplet can be modified with respect to the free ion by mixing and energetic separation of the six m_j states. This can have considerable influence on the magnetic behavior, as is outlined in section 2.1.2. Hence, in order to calibrate the XMCD evaluation procedure by Ce-Ag(111) data, the crystal field scheme has to be known.

In analogy to the considerations on $CePt_5$/Pt(111) that are presented in section 9.2, the effect of the CF can be addressed by measurements of the linear dichroism in Ce $M_{4,5}$ XAS. A respective series of spectra is shown in fig. A.4 (a). The data were taken by M. Zinner in the course of his diploma thesis [98], where details on the sample preparation are given. In this work, the stoichiometry of the Ce-Ag(111) intermetallic is determined to $CeAg_2$. Based on this result and on the analysis of thickness-dependent LEED patterns, a thickness of $t = 1.5$ u.c. was assigned to the sample shown here.

The XAS line shape confirms the localized character of the $4f$ level. Regarding the isotropic spectrum (black line and symbols), there is barely no detectable $f^0 \rightarrow f^1$ contribution and the $f^1 \rightarrow f^2$ multiplet structure strongly resembles the calculated isotropic $j = 5/2$ spectrum of fig. 8.9 (a).

At low temperatures, the spectrum for $\theta = 0°$ deviates from the isotropic one taken at $\theta = 60°$. This linear dichroism is best visible at the double-peak structure of the M_5 edge (features C and D in fig. 6.1 (a)). The normal incidence spectrum corresponds to the case $E \parallel c$ and resembles the spectrum of the $m_j = 1/2$ state (compare fig. 9.3). The LD gets smaller with increasing temperature and is lost at $T = 100$ K, where the normal incidence and isotropic data coincide. This observation is reflected by the $\Upsilon(T)$ data that are shown in fig. A.4 (b) (compare section 9.2).

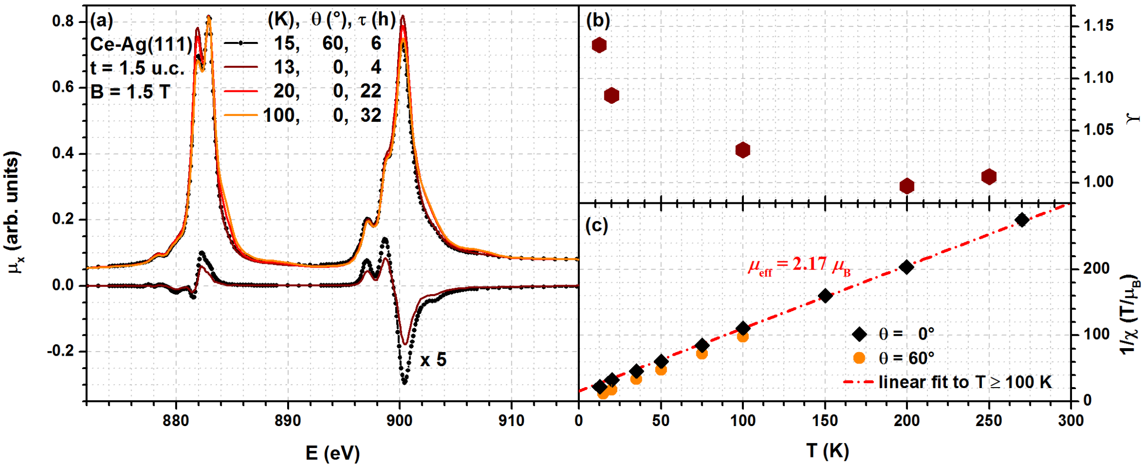

Figure A.4: XAS and XMCD results for a Ce-Ag(111) sample with $t = 1.5$ u.c. (a) Isotropic XA spectrum (black lines and symbol) and a selection of spectra taken at $\theta = 0°$ for different temperatures and at different times. Furthermore, XMCD spectra for the two geometries at the lowest temperatures are shown. (b) Temperature-dependence of the relative anisotropic M_5/M_4 peak amplitude ratio Υ. (c) Temperature-dependence of the inverse local susceptibility (Curie-Weiss plot) as evaluated from XMCD measurements. The red line represents a linear fit to the $\theta = 0°$ data for $T \geq 100$ K and allows the evaluation of the effective paramagnetic moment. The data were taken at BESSY.

This means that the crystal field in this sample induces a splitting of the $j = 5/2$ states. The character of the ground state seems to be dominated by $m_j = 1/2$, but the three doublets are equally populated at already $T = 100$ K. Hence, the overall CF splitting can only be of the order of some millielectronvolt.

Furthermore, there is a change at the high-energy flanks of both edges (features E and J in fig. 6.1 (a)). These changes can unambiguously be identified as time-dependent by comparison of subsequently taken spectra at otherwise equal conditions [98]. While this result indicates that the Ce $4f$ level in Ce-Ag(111) is much more susceptible to influences of the residual gas than $CePt_5$/Pt(111) (compare app. A.3), the effect is small enough to be neglected in the dataset presented here.

Fig. A.4 (a) also shows XMCD spectra for the two low-temperature measurements. The line shape strongly resembles the one recorded for $CePt_5$/Pt(111) samples as shown in fig. 8.4, and hence the calculated $j = 5/2$ XMCD in fig. 8.9 (b). Small differences can be identified at the high-energy flanks of both edges (features O and S in fig. 6.1) [98], which might be connected to the additional, hybridization-induced spectral weight in the $CePt_5$/Pt(111) data (see section 8.4).

The magnitude of the XMCD is anisotropic, with a somewhat larger signal at $\theta = 60°$. This finding translates to an anisotropy in the temperature-dependent local susceptibility, which is shown as a Curie-Weiss plot in fig. A.4 (c). These data were evaluated from XMCD measurements according to the procedure described in section 6.4.3. For the absolute sum rule evaluation, the $CePt_5$/Pt(111) reference spectrum was also used.

The $1/\chi(T)$ curves are nearly linear in both geometries, with small deviations at low temperatures. Together with the relatively small anisotropy, this supports the assumption of a comparably small CF effect in this Ce-Ag(111) sample, in addition to the clear indications found in XAS. This allows the assumption that the $1/\chi(T)$ curve for $T \geq 100$ K represents the magnetic response of the six equally occupied $j = 5/2$ states. Hence, the effective magnetic moment is expected to amount to $\mu_{\text{eff}}^{\text{free}} = 2.54\ \mu_{\text{B}}$ (see section 2.1.3).

The experimental result for the effective moment can be evaluated from the slope of $1/\chi(T)$ according to eq. 2.24. A linear fit to the data for $\theta = 0°$ and $T \geq 100$ K yields $\mu_{\text{eff}} = 2.17\ \mu_{\text{B}} = 0.85\ \mu_{\text{eff}}^{\text{free}}$.

Hence, the effective moment of the Ce-Ag(111) seems to be slightly reduced with respect to the

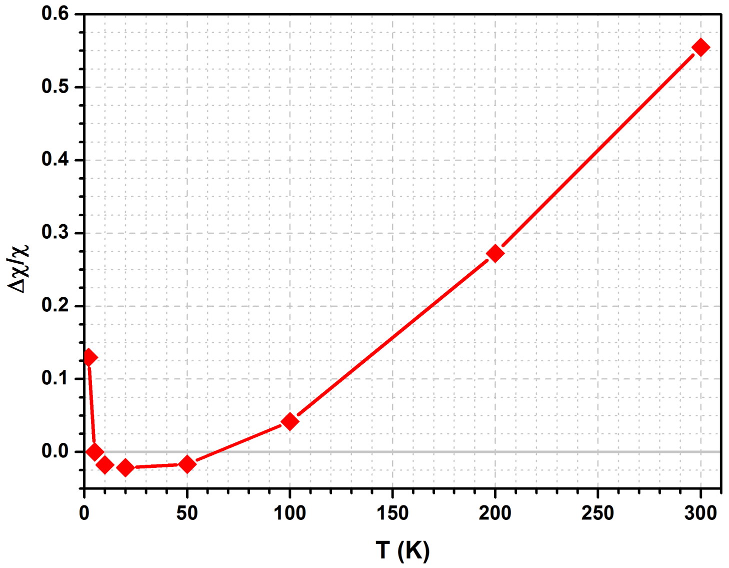

Figure A.5: Relative error of the perturbation treatment for the susceptibility of a Ce^{3+} ion in a hexagonal crystal field for the parameter values obtained in chapter 10, $B = 1.5$ T, $\Delta E_{3/2} = 0.1$ meV and $\Delta E_{5/2} = 15$ meV. The relative deviation of χ as obtained by second order perturbation theory (eq. 2.34) from the value obtained by exact treatment with numerical diagonalization of the Hamiltonian is shown versus temperature.

free moment. This result is not unrealistic, since a small screening of the magnetic moment can be expected in Kondo systems, even at temperatures well above the Kondo temperature (see fig. 1.1 (b)).

For CePt_5/Pt(111), the experimental results indicate that the reduction is considerably larger than in Ce-Ag(111) (see section 10.2). Independent of a possible Kondo screening in Ce-Ag(111), the reduction of 15 % obtained here represents an upper limit for the underestimation of μ_{eff} by the applied evaluation procedure. This is the case since the effective moment of a $j = 5/2$ system with equal population of the m_j states, as present in Ce-Ag(111), can never be larger than $\mu_{\mathrm{eff}}^{\mathrm{free}} = 2.54\,\mu_{\mathrm{B}}$. Hence, the reduction of the effective moment that is found in CePt_5/Pt(111) by application of the same procedure is significant.

A.5 Validity of the perturbation treatment for the in-plane susceptibility

In section 2.1.3, expressions for the paramagnetic susceptibility of a Ce ion in a hexagonal crystal field are derived. For the case of perpendicular magnetic field direction and hexagonal c-axis, the Hamiltonian is non-diagonal (see eq. 2.29). Hence, a perturbation approach is chosen, since it yields the analytical expression given in eq. 2.34. This expression is used in sections 10.3 and 10.4 for fitting of experimental $\chi^{-1}(T)$ data. A reproduction of the data is achieved for choice of the crystal field splittings according to $\Delta E_{3/2} = 0.1$ meV and $\Delta E_{5/2} = 15\ldots25$ meV, with higher $\Delta E_{5/2}$ at higher t (compare fig. 10.10 (a)).

The perturbation treatment of $\chi_{\perp}(T)$ is justified as long as the Zeeman splitting is small compared to the energy separation of the crystal field split levels. The Zeeman splitting (see eq. 2.15) within each $|m_j\rangle$ doublet amounts to $\Delta E^{\mathrm{Z}} \approx m_j \cdot 150$ µeV at a magnetic field of $B = 1.5$ T, as applied in the majority of experiments used for the fit. While the approximation appears save for $\Delta E_{5/2}$ and $\Delta E_{5/2} - \Delta E_{3/2}$, the small value for $\Delta E_{3/2}$ might provide a problem.

In order to estimate the impact of the small CF splitting, results for the perturbation treatment can be compared to results of numerical diagonalization of the Hamiltonian. The numeric results were provided by courtesy of K. Fauth. Magnetic moments were obtained by applying a small modulation (1 %) to the magnetic field and accounting for the resulting variation in the energy.

Fig. A.5 shows the relative deviation of the susceptibilities obtained by the two methods, $\Delta\chi = (\chi_{\mathrm{pert}} - \chi_{\mathrm{diag}})/\chi_{\mathrm{diag}}$ with parameters $B = 1.5$ T, $\Delta E_{3/2} = 0.1$ meV and $\Delta E_{5/2} = 15$ meV for eight temperature values in the range $T = 2 \ldots 300$ K.

In the temperature range $T = 5 \ldots 100$ K, the obtained relative errors are below $\Delta\chi/\chi = 5$ %. This is regarded as a reasonable accuracy for the present study. Temperatures down to the lowest value, $T = 2$ K, were reached at SOLEIL. However, apart from a single exception, the measurements used for fitting of $\chi^{-1}(T)$ were done at BESSY with $T \gtrsim 12$ K. Hence, the large error at low temperature is not relevant for the present study.

The relative error drastically increases for $T > 100$ K. While direct conclusions regarding the accuracy of the resulting fit parameters are not easily drawn, the high-T regime particularly affects the results for $\Delta E_{5/2}$ and $C_{5/2}$ in fig. 10.10. Since the results for $\Delta E_{5/2}$ are additionally supported by the independent simulation of the $\Upsilon(T)$ data, the uncertainty induced by the erroneous perturbational expression should by limited. This is not the case for $C_{5/2}$. The perturbational model tends to overestimate χ at high T, which is counterbalanced by the fitting procedure by underestimation of C, i.e., assumption of stronger screening of the effective moment.

Assuming that the relative error for the susceptibility in the high-T regime, which amounts to $\Delta\chi/\chi \approx 0.3$ in average, can directly be transferred to a negative error of the screening parameter, this leads to $\Delta C_{5/2}/C_{5/2} = -0.16$ considering that $\chi \propto C^2$ (see eq. 2.24 and section 10.3). This should be considered when interpreting the absolute values, but it does not change the qualitative picture.

A.6 Overview of samples

sample	t (u.c.)	Δt (u.c.)	prep. unit	XAS/ XMCD	LEED	AES/ STEM
SCPMZP0212_CePt084	1.0	0.1	C	x		
SCPB0611_CePt053	1.3	0.3	A	x		
SCPB1010_CePt021	1.9	0.3	A	x		
SCPP0912_CePt097	2.0	0.2	C	x		
SCPB1010_CePt015	3.3	0.4	A	x		
SCPB0510_CePt005	3.5	0.4	A	x		
SCPB0611_CePt041	3.9	0.3	A	x		
SCPMZP0212_CePt082	4.0	0.2	C	x		
SCPKFP0912_CePt095	4.0	0.2	C	x		
SCPB0510_CePt006	5.3	0.5	A	x		
SCPMZB1211_CePt071	7.0	0.8	A	x		
SCPMZB1111_CePt070	8.0	0.8	A	x		
SCPB1010_CePt018	10.8	0.5	A	x	x	
SCPW1110_CePt023	1.7	0.3	A		x	
SCPW0511_CePt034b	2.2	0.3	A		x	
SCPW1110_CePt024	2.4	0.3	A		x	
SCPW0811_CePt054	2.4	0.3	B		x	
SCPW1110_CePt026	4.1	0.4	A		x	
SCPW1110_CePt027	6.0	1.0	A		x	
SCPW0811_CePt065	6.9	0.4	B		x	
SCPW1210_CePt028	7.5	1.0	A		x	
SCPW0811_CePt066	8.0	0.4	B		x	
SCPW0811_CePt067	10.1	0.4	B		x	x
SMZB1211_CeAg001	1.5	0.3	A	x		

Table A.1: Overview of surface intermetallic samples that contributed to the present results. For each sample, the internal sample name is given along with the nominal film thickness t and the estimated thickness error Δt. The applied preparation unit is given as introduced in section 3.2 and the experimental methods the results were obtained with are indicated.
The sample name consists of the letter S followed by one or two pairs of letters, which are the initials of the scientists involved in sample preparation (Christian Praetorius, Martin Zinner, Kai Fauth). The next letter gives the place of preparation (Würzburg (home laboratory), Berlin (BESSY), Paris (SOLEIL)) and the four numbers give the date of preparation in a MMYY scheme. After the underscore, the material combination is specified, which is followed by the internal sample number.

A.7 List of abbreviations and acronyms

AES	Auger electron spectroscopy
BESSY	Berliner Elektronenspeicherring-Gesellschaft für Synchrotronstrahlung
CF	crystal field
CPL	circularly polarized light
DEIMOS	dichroism experimental installation for magneto-optical spectroscopy
DFG	Deutsche Forschungsgemeinschaft
DOS	density of states
DS	Doniach-Šunjić (profile)
eq.	equation
FIB	focused ion beam
fig.	figure
FWHM	full width at half maximum
GS	Gunnarsson-Schönhammer (theory)
HAADF	high angle annular dark field
HF	Hartree-Fock (approximation)
IUPAC	International Union of Pure and Applied Chemistry
LD	linear dichroism
LDA	local density approximation
LEED	low-energy electron diffraction
LPL	linearly polarized light
LURE	laboratoire pour l'utilisation du rayonnement électromagnétique
ML	monolayer
NCA	non-crossing approximation
PES	photoemission spectroscopy
PSE	periodic system of elements
RKKY	Ruderman-Kittel-Kasuya-Yosida (interaction)
SI	Slater integral
SIAM	single-impurity Anderson model
SOC	spin-orbit coupling
SOLEIL	Source optimisée de lumière d'énergie intermédiaire du LURE
SQUID	superconducting quantum interference device
SSPMP	solid state physics mathematica package
STEM	scanning transmission electron microscopy
STM	scanning tunneling microscopy
tab.	table
TEY	total electron yield
TFY	total fluorescence yield
u.c.	unit cell
UHV	ultrahigh vacuum
XA(S)	X-ray absorption (spectroscopy)
XMCD	X-ray magnetic circular dichroism
XMLD	X-ray magnetic linear dichroism
XNLD	X-ray natural linear dichroism
XRD	X-ray diffraction

A.8 List of symbols

A	area
$\vec{A}$	electromagnetic vector potential
$\mathcal{A}$	amplitude
a	(surface) lattice constant
$\vec{a}_n$	unit cell vector of a Bravais lattice
$\vec{a}_n*$	reciprocal unit cell vector
a_0	Bohr radius
α	statistical exchange parameter
B	magnetic field strength
$\mathcal{B}_j$	Brillouin function to angular momentum j
b	mixing coefficient for the simulation of XA spectra
β	reduction factors for atomic HF parameters in full multiplet calculations
C	screening factor for the effective magnetic moment
C^Y	TEY conversion factor
c	distance of atomic layers in a crystal
$\hat{c}$	creation operator in second quantization
c_{f^n}	mixing coefficients in the Ce ground state
χ	paramagnetic susceptibility
d	distance
D	dimension
Δ	hybridization strength in GS theory
Δx	difference or deviation of x
δx	increment of x on a discrete mesh
$\delta(x)$	Dirac's delta-function
E	energy
$\vec{E}$	electric field vector
e	elementary charge *or* Euler's number
$\vec{e}_z$	unit vector in z-direction
$\vec{\epsilon}$	unit polarization vector of an electric field
ϵ_F	Fermi level
F_DW	Debye-Waller factor
F^n	Slater integrals
$\mathcal{F}(t_1, t_2)$	Contribution of a layer between depth coordinates t_1 and t_2 to a TEY signal
f	frequency
$\vert f\rangle$	final state in XAS
$f(x)$	function of x
Φ	electromagnetic scalar potential
Φ_0	photon flux
ϕ	hypothetical mixing angle
φ	azimuthal angle in a spherical or cylindrical coordinate system
$\hat{G}$	propagator
G^n	Slater integrals
$\vec{g}$	reciprocal lattice vector
Γ	full width at half maximum
γ	angle between vectors
$\hat{H}$	Hamiltonian
h	Planck's constant
$\hbar$	$h/2\pi$
$\Theta_\mathrm{C/N}$	paramagnetic Curie/Néel temperature
θ	angle of incidence in XAS
ϑ	polar angle in a spherical coordinate system
I	intensity

$\hat{I}$	unit matrix
$\mathcal{I}$	current
i	imaginary unit
$\lvert i\rangle$	initial state in XAS
J	exchange parameter
j	total angular momentum quantum number
$\hat{\vec{j}}$	total angular momentum vector operator
$\hat{j}_z$	z-component of the total angular momentum operator
k	momentum, wave number
k_B	Boltzmann's constant
L	Lagrange function
l	orbital angular momentum quantum number
$\hat{\vec{l}}$	orbital angular momentum vector operator
$\hat{l}_z$	z-component of the orbital angular momentum operator
l_c	LEED coherence length
l_x	X-ray penetration length
λ	wavelength *or* molecular field constant
λ_e	TEY electron escape depth
λ_IMF	inelastic mean free path of electrons in solids
λ_MF	mean free path of molecules in a gas
λ_x	X-ray penetration depth
M	magnetization density
$\vec{M}$	magnetization
m	mass
m_e	electron rest mass
m_j	magnetic total angular momentum quantum number
m_l	magnetic orbital angular momentum quantum number
m_s	magnetic spin quantum number
μ	magnetic moment per atom
μ_0	magnetic constant
μ_B	Bohr magneton
μ_x	linear X-ray absorption coefficient
N	number
n	number density textitor main quantum number *or* integer
$\hat{n}$	particle number operator in second quantization
n_f	f-level occupancy
ω	angular frequency
P	probability
$\mathcal{P}_n$	relative population of the nth energy level
p	pressure
$\vec{p}$	momentum vector
π	ratio of a circle's circumference to its diameter
q	asymmetry factor for Fano profiles *or* sign factor for the photon spin
R	radius
$\mathcal{R}$	deposition rate
R_{nl}	radial part of an atomic wave function
R_P	Pendry R-factor
R_R	double reliability factor
r	radial coordinate in a spherical or cylindrical coordinate system
ρ	density
$\mathcal{S}$	relative superstructure lattice constant
s	spin quantum number
$\hat{\vec{s}}$	spin vector operator

$\hat{s_z}$	z-component of the spin operator
σ	atomic absorption cross-section
T	temperature
$\hat{T}$	electron scattering path operator
$\hat{\mathcal{T}}$	basis transformation matrix
$\hat{T}_z$	magnetic dipole term
t	thickness
$\hat{t}$	atomic electron scattering operator
τ	time
U	Coulomb potential
Υ	relative $\mathrm{M}_5/\mathrm{M}_4$ peak ratio
υ	correction factor for Υ
V	potential, voltage
V^{ic}	hopping matrix element for impurity and conduction states
v	valence
v_{Q}	elastic wave velocity of quartz
w	oscillator strength
$w_{\mathrm{rel}}^{0\to1}$	relative oscillator strengths of $f^0 \to f^1$ and $f^1 \to f^2$ contribution in Ce $\mathrm{M}_{4,5}$ XAS
x, y, z	Cartesian coordinates
$\vec{x}$	spatial coordinate vector
ξ	auxiliary length
Y	electron yield current
Y_{lm}	spherical harmonics
ψ	wavefunction of a single state
Ψ	total wavefunction
Z	atomic number

Bibliography

Own publications related to the present work

[1] J. Kemmer, C. Praetorius, A. Krönlein, P.-J. Hsu, K. Fauth and M. Bode: Structural analysis of the intermetallic surface compound $CePt_5$/Pt(111), Phys. Rev. B **90** 195401 (2014)

[2] C. Praetorius, M. Zinner, A. Köhl, H. Kießling, S. Brück, B. Muenzing, M. Kamp, T. Kachel, F. Choeikani, P. Ohresser, F. Wilhelm, A. Rogalev and K. Fauth: Electronic tuneability of a structurally rigid surface intermetallic and Kondo lattice: $CePt_5$/Pt(111), Phys. Rev. B **92** 045116 (2015)

General literature

[3] J. of Salisbury: Metalogicon (1159), Library of Latin Texts, Brepols Publishers, Turnhout (2005)

[4] D. Gjertsen: The Newton Handbook, Routledge and Kegan Paul plc (1986)

[5] Catalogue of the German National Library (Deutsche Nationalbibliothek)

[6] W. Pfeiler: Alloy Physics, Wiley-VCH (2007)

[7] E. J. Mittemeijer: Fundamentals of Materials Science, Springer-Verlag (2010)

[8] N. G. Connelly, T. Damhus, R. M. Hartshorn and A. T. Hutton: Nomenclature of Inorganic Chemistry - IUPAC recommendations 2005, RSC publishing, Cambridge (2005)

[9] E. A. Wood: Vocabulary of Surface Crystallography, J. Appl. Phys. **35** 1306 (1964)

[10] J. Kondo: Resistance Minimum In Dilute Magnetic Alloys, Prog. Theor. Phys. **32** 37 (1964)

[11] W. de Haas, J. de Boer and G. van den Berg: The electrical resistance of gold, copper and lead at low temperatures, Physica **1** 1115 (1934)

[12] A. C. Hewson: The Kondo Problem to Heavy Fermions, Cambridge University Press (1993)

[13] P. Fulde: Electron Correlations in Molecules and Solids, Springer-Verlag (1993)

[14] P. Fazekas: Electron Correlation and Magnetism, World Scientific (1999)

[15] H. Tsunetsugu, M. Sigrist and K. Ueda: The ground-state phase diagram of the one-dimensional Kondo lattice model, Rev. Mod. Phys. **69** 809 (1997)

[16] H. von Löhneysen, A. Rosch, M. Vojta and P. Wölfle: Fermi-liquid instabilities at magnetic quantum phase transitions, Rev. Mod. Phys. **79** 1015 (2007)

[17] Ternes, A. J. Heinrich and W. Schneider: Spectroscopic manifestations of the Kondo effect on single adatoms, J. Phys. Cond. Matter **21** 053001 (2009)

[18] Q. Si and F. Steglich: Heavy Fermions and Quantum Phase Transitions, Science **329** 1161 (2010)

[19] P. W. Anderson: Localized Magnetic States in Metals, Phys. Rev. **124** 41 (1961)

[20] C. Zener: Interaction Between the d Shells in the Transition Metals, Phys. Rev. **81** 440 (1951)

[21] K. G. Wilson: The renormalization group: Critical phenomena and the Kondo problem, Rev. Mod. Phys. **47** 773 (1975)

[22] N. Andrei: Diagonalization of the Kondo Hamiltonian, Phys. Rev. Lett. **45** 379 (1980)

[23] P. B. Wiegmann: The title is not known to the author, cited after [12], Sov. Phys. JETP Lett. **31** 163 (1980)

[24] B. Coqblin and J. R. Schrieffer: Exchange Interaction In Alloys With Cerium Impurities, Physical Review **185** 847 (1969)

[25] O. Gunnarsson and K. Schönhammer: Photoemission From Ce Compounds - Exact Model Calculation In the Limit of Large Degeneracy, Phys. Rev. Lett. **50** 604 (1983)

[26] O. Gunnarsson and K. Schönhammer: Electron Spectroscopies For Ce Compounds In the Impurity Model, Phys. Rev. B **28** 4315 (1983)

[27] N. E. Bickers, D. L. Cox and J. W. Wilkins: Self-consistent large-N expansion for normal-state properties of dilute magnetic alloys, Phys. Rev. B **36** 2036 (1987)

[28] D. C. Mattis: Symmetry of Ground State in a Dilute Magnetic Metal Alloy, Phys. Rev. Lett. **19** 1478 (1967)

[29] S. Doniach: Kondo Lattice and Weak Antiferromagnetism, Physica B **91** 231 (1977)

[30] W. Nolting and A. Ramakanth: Quantum Theory of Magnetism, Springer-Verlag (2009)

[31] A. Auerbach and K. Levin: Kondo Bosons and the Kondo Lattice: Microscopic Basis for the Heavy Fermi Liquid, Phys. Rev. Lett. **57** 877 (1986)

[32] S. Burdin, A. Georges and D. R. Grempel: Coherence Scale of the Kondo Lattice, Phys. Rev. Lett. **85** 1048 (2000)

[33] K. S. D. Beach and F. F. Assaad: Coherence and metamagnetism in the two-dimensional Kondo lattice model, Phys. Rev. B **77** 205123 (2008)

[34] M. A. Weeks: The discovery of the elements. XI. Some elements isolated with the aid of Potassium and Sodium: Zirconium, Titanium, Cerium and Thorium, J. Chem. Educ. **9** 1231 (1932)

[35] IAU: 2006 General Assembly: Resolution B5 - Definition of a Planet in the Solar System (2006)

[36] E. G. Forbes: Gauss and the discovery of Ceres, Journal for the History of Astronomy **2** 195 (1971)

[37] M. E. Wieser and T. B. Coplen: Atomic weights of the elements 2009 (IUPAC Technical Report), Pure Appl. Chem. **83** 359 (2011)

[38] D. C. Koskenmaki and K. A. Gschneidner Jr.: Cerium, in Handbook on the Physics and Chemistry of Rare Earths, volume 1, chapter 4, 337, Elsevier (1978)

[39] O. Gunnarsson and K. Schönhammer: Many body formulation of spectra of mixed valence systems, in Handbook on the Physics and Chemistry of Rare Earths, volume 10, chapter 64, 103, Elsevier (1987)

[40] J. M. Lawrence, P. S. Riseborough and R. D. Parks: Valence fluctuation phenomena, Rep. Prog. Phys. **44** 1 (1981)

[41] J. Röhler, D. Wohlleben, J. P. Kappler and G. Krill: The Valence of Cerium Under High-pressure, Phys. Lett. A **103** 220 (1984)

[42] J. Röhler, J. Klug and K. Keulerz: The Valence of Cerium In CeCu2Si2 Under High-pressure, J. Magn. Magn. Mater. **76-7** 340 (1988)

[43] J. C. Fuggle, F. U. Hillebrecht, Z. Zolnierek, R. Lasser, C. Freiburg, O. Gunnarsson and K. Schönhammer: Electronic-structure of Ce and Its Intermetallic Compounds, Phys. Rev. B **27** 7330 (1983)

[44] R. D. Cowan: The Theory of Atomic Structure and Spectra, University of California Press (1981)

[45] H. Haken and H. Wolf: Atom- und Quantenphysik, Springer-Verlag, 8th edition (2004)

[46] A. P. Murani, Z. A. Bowden, A. D. Taylor, R. Osborn and W. G. Marshall: Evidence for localized $4f$ states in α-Ce, Phys. Rev. B **48** 13981 (1993)

[47] T. Willers: Spectroscopic Investigations of the Crystal Field and Kondo Effect in $4f$ Heavy-Fermion Systems, Ph.D. thesis, Universität Köln (2011)

[48] R. Aleonard, P. Boutron and D. Bloch: Anisotropie de la susceptibilité paramagnétique des monocristeaux de terres rares: Gd, Tb, Dy, Ho et Er, J. Phys. Chem. Solids **30** 2277 (1969)

[49] D. J. Newman and B. Ng: Crystal Field Handbook, Cambridge University Press (2000)

[50] K. W. H. Stevens: Matrix Elements and Operator Equivalents Connected with the Magnetic Properties of Rare Earth Ions, Proc. Phys. Soc. London, Sect. A **65** 209 (1952)

[51] M. T. Hutchings: Point Charge Calculations of Energy Levels of Magnetic Ions in Crystalline Electric Fields, Solid. State Phys. **16** 227 (1964)

[52] E. Segal and W. E. Wallace: Rare-Earth Ions in a Hexaognal [*sic*] Field I, J. Solid State Chem. **2** 347 (1970)

[53] K. H. Mader and M. W. Swift: Magnetic Characteristics of $CeAl_3$ and $CeAl_4$, J. Phys. Chem. Solids **29** 1759 (1968)

[54] E. Segal and W. E. Wallace: Rare-Earth Ions in a Hexagonal Field IV, J. Solid State Chem. **13** 201 (1975)

[55] H. Lueken, M. Meier, G. Klessen, W. Bronger and J. Fleischhauer: Magnetische Eigenschaften von $CePt_5$ zwischen 4,2 und 295 K, J. Less-Comm. Met. **63** P35 (1979)

[56] K. Kopitzki and P. Herzog: Einführung in die Festlörperphysik, Teubner Verlag, 6th edition (2007)

[57] K. Fauth: Some insights about the $CePt_x$ ($x \approx 5?$) surface alloy magnetism, internal document (2011)

[58] K. Yosida: Theory of Magnetism, Springer-Verlag (1998)

[59] F. de Groot and A. Kotani: Core level spectroscopy of solids, CRC Press (2008)

[60] J. W. Allen and R. M. Martin: Kondo Volume Collapse and the $\gamma \rightarrow \alpha$ Transition in Cerium, Phys. Rev. Lett. **49** 1106 (1982)

[61] J. C. Fuggle, F. U. Hillebrecht, J. M. Esteva, R. C. Karnatak, O. Gunnarsson and K. Schönhammer: f-count effects in x-ray-absorption spectra of the $3d$ levels in Ce and its intermetallic compounds, Phys. Rev. B **27** 4637 (1983)

[62] L. Z. Liu, J. W. Allen, O. Gunnarsson, N. E. Christensen and O. K. Andersen: α-γ transition in Ce: A detailed analysis of electron spectroscopy, Phys. Rev. B **45** 8934 (1992)

[63] O. Gunnarsson, K. Schönhammer, J. C. Fuggle, F. U. Hillebrecht, J. M. Esteva, R. C. Karnatak and B. Hillebrand: Occupancy and Hybridization of the f Level In Ce Compounds, Phys. Rev. B **28** 7330 (1983)

[64] C. Grazioli, Z. Hu, M. Knupfer, G. Graw, G. Behr, M. S. Golden, J. Fink, H. Giefers, G. Wortmann and K. Attenkofer: Characteristic temperature dependence of the $4f$ occupancy in the Kondo system CeSi2, Phys. Rev. B **63** 115107 (2001)

[65] C. Dallera, M. Grioni, A. Palenzona, M. Taguchi, E. Annese, G. Ghiringhelli, A. Tagliaferri, N. B. Brookes, T. Neisius and L. Braicovich: alpha-gamma transition in metallic Ce studied by resonant x-ray spectroscopies, Phys. Rev. B **70** 085112 (2004)

[66] H. Lueken and W. Bronger: Relations Between Structure and Magnetic Properties of $LnPt_5$ Phases, Zeitschrift für anorganische und allgemeine Chemie **395** 203 (1973)

[67] B. Predel: Ce-Pt (Cerium-Platinum), in O. Madelung (ed.), The Landolt-Börnstein Database, volume 5c, SpringerMaterials (1993)

[68] A. Janghorban, M. Lomello-Tafin, J. M. Moreau and P. Galez: The phase diagram of the Ce-Pt system, Intermetallics **18** 2208 (2010)

[69] J. L. Moriarty, J. Humphreys, R. O. Gordon and N. C. Baenziger: X-ray Examination of Some Rare-earth-containing Binary Alloy Systems, Acta Crystallographica **21** 840 (1966)

[70] J. M. Essen, C. Becker and K. Wandelt: Pt_xCe_{1-x} Surface Alloys on Pt(111): Structure and Adsorption, e-J. Surf. Sci. Nanotech. **7** 421 (2009)

[71] J. M. Lawrence, Y. C. Chen, G. H. Kwei, M. F. Hundley and J. D. Thompson: Structure and magnetism in $CePt_{2+x}$, Phys. Rev. B **56** 5 (1997)

[72] J.-L. Bobet, P. Lesportes, J.-G. Roquefere, B. Chevalier, K. Asano, K. Sakaki and E. Akiba: A preliminary study of some "pseudo-AB(2)" compounds: $RENi_4Mg$ with RE = La, Ce and Gd. Structural and hydrogen sorption properties, Int. J. Hydrogen Energy **32** 2422 (2007)

[73] C. Röhr: Lecture: Intermetallische Phasen, `http://ruby.chemie.uni-freiburg.de/Vorlesung/intermetallische_0.html` (2004)

[74] I. Syozi: Statistics of Kagomé Lattice, Prog. Theor. Phys. **VI** 306 (1951)

[75] A. Schröder, R. Vandenberg, H. von Löhneysen, W. Paul and H. Lueken: Magnetic ordering of $CePt_5$, Solid State Commun. **65** 99 (1988)

[76] E. Sagmeister, E. Bauer, E. Gratz, H. Michor and G. Hilscher: Low-temperature behaviour of $CePt_{5-x}M_x$ (M = Al,Ga), Physica B **230–232** 148 (1997)

[77] R. R. Joseph, K. A. Gschneider Jr. and R. E. Hungsberg: Low-temperature heat-capacity of $LaPt_2$ and $CePt_2$ and magnetic susceptibility of $CePt_2$, Phys. Rev. B **5** 1878 (1972)

[78] J. Larrea, M. B. Fontes, A. D. Alvarenga, E. M. Baggio-Saitovitch, T. Burghardt, A. Eichler and M. A. Continentino: Quantum critical behavior in a CePt ferromagnetic Kondo lattice, Phys. Rev. B **72** 035129 (2005)

[79] J. Tang, J. M. Lawrence and J. C. Hemminger: Structure and Valence of the Ce/Pt(111) System, Phys. Rev. B **48** 15342 (1993)

[80] A. B. Andrews, J. J. Joyce, A. J. Arko, J. D. Thompson, J. Tang, J. M. Lawrence and J. C. Hemminger: Evidence for possible $4f$ bands at $T \gg T_K$ in the heavy-fermion single-crystal CePt_{2+x}, Phys. Rev. B **51** 3277 (1995)

[81] M. Garnier, D. Purdie, K. Breuer, M. Hengsberger and Y. Baer: Momentum-resolved photoemission of the Kondo peak in an ordered Ce-containing alloy, Phys. Rev. B **56** 11399 (1997)

[82] M. Garnier, D. Purdie, K. Breuer, M. Hengsberger and Y. Baer: Comparative photoemission study of Pt(111)$(\sqrt{3} \times \sqrt{3})R30^\circ$ Ce and Pt(111)(2×2) La, Phys. Rev. B **58** 9697 (1998)

[83] C. J. Baddeley, A. W. Stephenson, C. Hardacre, M. Tikhov and R. M. Lambert: Structural and electronic properties of Ce overlayers and low-dimensional Pt-Ce alloys on Pt{111}, Phys. Rev. B **56** 12589 (1997)

[84] K. D. Schierbaum: Ordered ultra-thin Cerium oxide overlayers on Pt(111) single crystal surfaces studied by LEED and XPS, Surf. Sci. **399** 29 (1998)

[85] U. Berner and K. Schierbaum: Cerium oxide layers on Pt(111): a scanning tunneling microscopy study, Thin Solid Films **400** 46 (2001)

[86] U. Berner and K. D. Schierbaum: Cerium oxides and Cerium-Platinum surface alloys on Pt(111) single-crystal surfaces studied by scanning tunneling microscopy, Phys. Rev. B **65** 235404 (2002)

[87] D. C. Grinter, R. Ithnin, C. L. Pang and G. Thornton: Defect Structure of Ultrathin Ceria Films on Pt(111): Atomic Views from Scanning Tunnelling Microscopy, J. Phys. Chem. C **114** 17036 (2010)

[88] C. Breinlich, J. M. Essen, E. Barletta and K. Wandelt: Growth, structure and electronic properties of ultrathin Cerium oxide films grown on Pt(111), Thin Solid Films **519** 3752 (2011)

[89] T. Pillo, J. Hayoz, P. Aebi and L. Schlapbach: Ce-Pt(111) surface alloys: Electronic structure by photoemission, Physica B **259-61** 1118 (1999)

[90] A. Ramstad, S. Raaen and N. Barrett: Electronic structure of the La-Pt(111) surface alloy, Surf. Sci. **448** 179 (2000)

[91] B. Vermang, M. Juel and S. Raaen: CO adsorption on Ce-Pt(111) studied with LEED, XPS, and temperature programmed desorption, Phys. Rev. B **73** 033407 (2006)

[92] M. Klein: Starke Korrelationen in Festkörpern: von lokalisierten zu itineranten Elektronen, Ph.D. thesis, Universität Würzburg (2009)

[93] P. Tereshchuk, M. J. Piotrowski and J. L. F. Da Silva: Atomic structure of the La/Pt(111) and Ce/Pt(111) surfaces revealed by DFT+U calculations, RCS Adv. **5** 521 (2015)

[94] M. Klein, A. Nuber, H. Schwab, C. Albers, N. Tobita, M. Higashiguchi, J. Jiang, S. Fukuda, K. Tanaka, K. Shimada, M. Mulazzi, F. F. Assaad and F. Reinert: Coherent Heavy Quasiparticles in a CePt_5 Surface Alloy, Phys. Rev. Lett. **106** 186407 (2011)

[95] H. Schwab, M. Mulazzi, J. Jiang, H. Hayashi, T. Habuchi, D. Hirayama, H. Iwasawa, K. Shimada and F. Reinert: Character of valence-band states in the Kondo surface alloys $CeAg_x$/Ag(111) and $CePt_5$/Pt(111), Phys. Rev. B **85** 125130 (2012)

[96] A. Köhl: Präparation von $CePt_5$-Oberflächenlegierungen und Charakterisierung mittels LEED, XAS und XMCD, Master's thesis, Universität Würzburg (2010)

[97] S. Götz: Untersuchung der magnetischen Suszeptibilität von $CePt_5$-Oberflächenlegierungen durch XMCD, Bachelor's thesis, Universität Würzburg (2010)

[98] M. Zinner: Struktur und magnetische Eigenschaften der Oberflächenlegierungen $CeAg_2$/Ag(111) und $CePt_5$/Pt(111), Diploma thesis, Universität Würzburg (2012)

[99] C. Kittel: Introduction to Solid State Physics, Wiley John and Sons (2004)

[100] G. Ertl and J. Küppers: Low Energy Electrons and Surface Chemistry, VCH, Weinheim, 2nd edition (1985)

[101] J. F. O'Hanlon: A user's guide to vacuum technology, John Wiley and Sons, 2nd edition (1989)

[102] M. Henzler, W. Göpel and C. Ziegler: Oberflächenphysik des Festkörpers, B.G. Teubner, Stuttgart (1994)

[103] G. Sauerbrey: Verwendung von Schwingquarzen zur Wägung dünner Schichten und zur Mikrowägung, Z. Phys. **155** 206 (1959)

[104] J. W. Arblaster: Crystallographic Properties of Platinum, Platinum Metals Rev. **41** 12 (1997)

[105] P. M. Seah and W. A. Dench: Quantitative Electron Spectroscopy of Surfaces: A Standard Data Base for Electron Inelastic Mean Free Paths in Solids, Surf. Interface Anal. **1** 2 (1979)

[106] L. Meitner: Über die β-Strahl-Spektra und ihren Zusammenhang mit der γ-Strahlung, Z. Phys. **11** 35 (1922)

[107] P. Auger: Sur les rayons β secondaires produit dans un gaz par des rayons, Comp. Rend. **180** 65 (1925)

[108] Z. L. W. Weilie Zhou (ed.): Scanning Microscopy for Nanotechnology, Springer-Verlag (2007)

[109] S. J. Pennycook and P. D. Nellist (eds.): Scanning Transmission Electron Microscopy, Springer-Verlag (2011)

[110] S. J. Pennycook: Seeing the atoms more clearly: STEM imaging from the Crewe era to today, Ultramicroscopy **123** 28 (2012)

[111] L. A. Giannuzzi and F. A. Stevie (eds.): Introduction to Focused Ion Beams, Springer-Verlag (2005)

[112] M. A. van Hove, W. H. Weinberg and C. M. Chan: Low-Energy Electron Diffraction, Springer-Verlag (1986)

[113] K. Heinz: LEED and DLEED as modern tools for quantitative surface structure determination, Rep. Prog. Phys. **58** 637 (1995)

[114] G. Held: Oberflächenstrukturuntersuchung mittels Beugung langsamer Elektronen (LEED) bei geringer Probenbelastung: H, O und H_2O auf Ru(001), Ph.D. thesis, Technische Universität München (1994)

[115] T. Young: The Bakerian Lecture: Experiments and calculations relative to physical optics, Philosophical Transactions of the Royal Society of London **94** 1 (1804)

[116] L. de Broglie: XXXV. A Tentative Theory of Light Quanta, Philos. Mag. **6** 446 (1924)

[117] C. J. Davisson and L. H. Germer: Diffraction of Electrons by a Crystal of Nickel, Phys. Rev. **30** 705 (1927)

[118] C. J. Davisson and L. H. Germer: The Scattering of Electrons by a Single Crystal of Nickel, Nature **119** 558 (1927)

[119] G. P. Thomson and A. Reid: Diffraction of Cathode rays by a Thin Film, Nature **119** 890 (1927)

[120] K. Robinson and D. J. Tweet: Surface x-ray diffraction, Rep. Prog. Phys. **55** 599 (1992)

[121] SPECS GmbH: User manual for the ErLEED optics and power supplies, version 1.3 (2003)

[122] P. Sprau: Ultradünne magnetische Lagen aus seltenen Erden und Silizium, Diploma thesis, Universität Würzburg (2012)

[123] R. Fradczyk: Untersuchung struktureller Eigenschaften von Fe auf Pt(997) mittels LEED, AES und TEAS, Diploma thesis, Universität Würzburg (2013)

[124] R. J. Behm, K. Christmann, G. Ertl, M. A. van Hove, P. A. Thiel and W. H. Weinberg: Structure of CO adsorbed on Pd(100) - LEED and HREELS Analysis, Surf. Sci. **88** L59 (1979)

[125] G. Held, S. Uremovic, C. Stellwag and D. Menzel: A low-energy electron diffraction data acquisition system for very low electron doses based upon a slow scan charge coupled device camera, Rev. Sci. Instrum. **67** 378 (1996)

[126] F. Sojka, M. Meissner, C. Zwick, R. Forker and T. Fritz: Determination and correction of distortions and systematic errors in low-energy electron diffraction, Rev. Sci. Instrum. **84** 015111 (2013)

[127] M. Zinner and K. Fauth: unpublished results

[128] J. C. Slater: A Simplification of the Hartree-Fock Method, Physical Review **81** 385 (1951)

[129] K. Schwarz: Optimization of the Statistical Exchange Parameter α for the Free Atoms H through Nb, Phys. Rev. B **5** 2466 (1972)

[130] K. Schwarz: Optimized Statistical Exchange Parameters α for Atoms with Higher Z, Theoretica Chimica Acta **34** 225 (1974)

[131] P. J. Rous, J. B. Pendry, D. K. Saldin, K. Heinz, K. Müller and N. Bickel: Tensor LEED - A Technique For High-speed Surface-structure Determination, Phys. Rev. Lett. **57** 2951 (1986)

[132] S. Lundqvist and A. Magnéli: Ivar Waller 1898-1991, J. Appl. Cryst. **25** 463 (1992)

[133] G. Held: private communication

[134] A. Barbieri and M. van Hove: phase shift package, private communication

[135] N. Materer, U. Starke, A. Barbieri, R. Döll, K. Heinz, M. A. van Hove and G. Somorjai: Reliability of detailed LEED structural analyses: Pt(111) and Pt(111)-p(2×2)-O, Surf. Sci. **325** 207 (1995)

[136] J. B. Pendry: Reliability factors for LEED calculations, J. Phys. C: Solid St. Phys. **13** 937 (1980)

[137] P. J. Rous: A global approach to the search problem in surface crystallography by low-energy electron diffraction, Surf. Sci. **296** 358 (1993)

[138] G. Held, M. P. Bessent, S. Titmuss and D. A. King: Realistic molecular distortions and strong substrate buckling induced by the chemisorption of benzene on Ni{111}, J. Chem. Phys. **105** 11305 (1996)

[139] W. H. Press, S. A. Teukolsky, W. T. Vetterling and B. P. Flannery: Numerical Recipes, Cambridge University Press, third edition (2007)

[140] J. A. Nelder and R. Mead: A Simplex-method For Function Minimization, Computer Journal **7** 308 (1965)

[141] J. C. Maxwell: A Dynamical Theory of the Electromagnetic Field, Phil. Trans. R. Soc. Lond. **155** 459 (1865)

[142] A. Einstein: Über einen die Erzeugung und Verwandlung des Lichtes betreffenden heuristischen Gesichtspunkt, Ann. Phys. **322** 132 (1905)

[143] W. C. Röntgen: Über Eine neue Art von Strahlen, Sitzungsberichte der Würzburger Physik.-medic. Gesellschaft (1895)

[144] Catalogue of the Library of Congress (U.S.)

[145] H. Wende: Recent advances in x-ray absorption spectroscopy, Rep. Prog. Phys. **67** 2105 (2004)

[146] M. de Broglie: Sur un nouveau procédé permettant d'obtenir la photographie des spectres de raies des rayons Röntgen, Comp. Rend. **157** 924 (1913)

[147] J. Stöhr: NEXAFS Spectroscopy, Springer-Verlag (1992)

[148] J. L. Erskine and E. A. Stern: Calculation of M_{23} Magneto-optical Absorption-spectrum of Ferromagnetic Nickel, Phys. Rev. B **12** 5016 (1975)

[149] G. Schütz, W. Wagner, W. Wilhelm, P. Kienle, R. Zeller, R. Frahm and G. Materlik: Absorption of Circularly Polarized X-rays In Iron, Phys. Rev. Lett. **58** 737 (1987)

[150] various authors: Theo Thole Memorial Issue, J. Electron Spectrosc. Relat. Phenom. **86** 1 (1997)

[151] B. T. Thole, P. Carra, F. Sette and G. van der Laan: X-ray Circular-dichroism As A Probe of Orbital Magnetization, Phys. Rev. Lett. **68** 1943 (1992)

[152] P. Carra, B. T. Thole, M. Altarelli and X. D. Wang: X-ray Circular-dichroism and Local Magnetic-fields, Phys. Rev. Lett. **70** 694 (1993)

[153] C. T. Chen, Y. U. Idzerda, H.-J. Lin, N. V. Smith, G. Meigs, E. Chaban, G. H. Ho, E. Pellegrin and F. Sette: Experimental Confirmation of the X-Ray Magnetic Circular Dichroism Sum Rules for Iron and Cobalt, Phys. Rev. Lett. **75** 152 (1995)

[154] J. Lee, G. Lauhoff, C. Fermon, S. Hope, J. A. C. Bland, J. P. Schillé, G. van der Laan, C. Chappert and P. Beauvillain: A direct test of x-ray magnetic circular dichroism sum rules for strained Ni films using polarized neutron reflection, Journal of Physics-condensed Matter **9** L137 (1997)

[155] G. Schütz, E. Goering and H. H. Stoll: Synchrotron radiation techniques based on X-ray magnetic circular dichroism, in H. Kronmüller and S. Parkin (eds.), Handbook of Magnetism and Advanced Magnetic Materials, volume 3, 1311, Wiley (2007)

[156] J. Stöhr and H. C. Siegmann: Magnetism - From Fundamentals to Nanoscale Dynamics, Springer-Verlag (2006)

[157] P. A. M. Dirac: The Quantum Theory of the Emission and Absorption of Radiation, Proc. R. Soc. Lond. A **114** 243 (1927)

[158] L. D. Landau and E. M. Lifshitz: Lehrbuch der theoretischen Physik II - Klassische Feldtheorie, Verlag Harri Deutsch, 12th edition (1992)

[159] T. Willers, F. Strigari, N. Hiraoka, Y. Q. Cai, M. W. Haverkort, K.-D. Tsuei, Y. F. Liao, S. Seiro, C. Geibel, F. Steglich, L. H. Tjeng and A. Severing: Determining the In-Plane Orientation of the Ground-State Orbital of $CeCu_2Si_2$, Phys. Rev. Lett. **109** 046401 (2012)

[160] B. L. Henke, E. M. Gullikson and J. C. Davis: X-ray Interactions - Photoabsorption, Scattering, Transmission, and Reflection at E=50-30,000 eV, Z=1-92, Atomic Data and Nuclear Data Tables **54** 181 (1993)

[161] A. Thompson, I. Lindau, D. Attwood, Y. Liu, E. Gullikson, P. Pianetta, M. Howells, A. Robinson, K.-J. Kim, J. Scofield, J. Kirz, J. Underwood, J. Kortright, W. Gwyn and H. Winick: X-ray data booklet, Center for X-Ray Optics and Advanced Light Source, Lawrence Berkeley National Laboratory, University of California (2009)

[162] A. Cotton: Absorption inégale des rayons circulaires droit et gauche dans certains corps actifs, C. R. Acad. Sci (Paris) **120** 989 (1895)

[163] J. Goulon, C. Goulon-Ginet, A. Rogalev, G. Benayoun, C. Brouder and C. R. Natoli: X-ray natural circular dichroism and chiral-EXAFS in gyrotropic crystals, J. Synchrotron Rad. **7** 182 (2000)

[164] R. D. Peacock and B. Stewart: Natural circular dichroism in X-ray spectroscopy, J. Phys. Chem. B **105** 351 (2001)

[165] G. van der Laan, B. T. Thole, G. A. Sawatzky, J. B. Goedkoop, J. C. Fuggle, J.-M. Esteva, R. Karnatak, J. P. Remeika and H. A. Dabkowska: Experimental proof of magnetic x-ray dichroism, Phys. Rev. B **34** 6529 (1986)

[166] B. T. Thole, G. van der Laan and G. A. Sawatzky: Strong Magnetic Dichroism Predicted in the $M_{4,5}$ X-Ray Absorption Spectra of Magnetic Rare-Earth Materials, Phys. Rev. Lett. **55** 2086 (1985)

[167] P. Hansmann, A. Severing, Z. Hu, M. W. Haverkort, C. F. Chang, S. Klein, A. Tanaka, H. H. Hsieh, H. J. Lin, C. T. Chen, B. Fak, P. Lejay and L. H. Tjeng: Determining the crystal-field ground state in rare earth heavy fermion materials using soft-X-ray absorption spectroscopy, Phys. Rev. Lett. **100** 066405 (2008)

[168] A. F. Starace: Potential-Barrier Effects in Photoabsorption. I. General Theory, Phys. Rev. B **5** 1773 (1972)

[169] P. Carra: Sum rules for X-ray absorption and dichroism, J. Electron Spectrosc. Relat. Phenom. **86** 139 (1997)

[170] S. Brück, G. Schuetz, E. Goering, X. Ji and K. M. Krishnan: Uncompensated moments in the MnPd/Fe exchange bias system, Phys. Rev. Lett. **101** 126402 (2008)

[171] P. Willmott: An Introduction to Synchrotron Radiation, John Wiley and Sons (2011)

[172] H. Petersen: The plane grating and elliptical mirror: A new optical configuration for monochromators, Opt. Commun. **40** 402 (1982)

[173] E. Goering, S. Gold, A. Bayer and G. Schütz: Non symmetric influences in the total electron yield X-ray magnetic circular dichroism signal in applied magnetic fields, J. Synchrotron Rad. **8** 434 (2001)

[174] T. Kachel and F. Eggenstein: BESSY II: PM3 beamline Information sheet (2002)

[175] M. Heßler: Elektronenspektroskopie an Übergangsmetallclustern, Ph.D. thesis, Universität Würzburg (2005)

[176] B. Münzing: Synthese und Charakterisierung magnetischer 3d-4d-Übergangsmetall-Nanopartikel, Diploma thesis, Universität Würzburg (2009)

[177] R. Nakajima, J. Stöhr and Y. U. Idzerda: Electron-yield saturation effects in L-edge x-ray magnetic circular dichroism spectra of Fe, Co, and Ni, Phys. Rev. B **59** 6421 (1999)

[178] M. Fernández-Perea, J. A. Aznárez, J. I. Larruquert, J. A. Méndez, L. Poletto, D. Garoli, A. M. Malvezzi, A. Giglia and S. Nannarone: Transmittance and optical constants of Ce films in the 6-1200 eV spectral range, J. Appl. Phys. **103** 073501 (2008)

[179] E. Goering, S. Gold, M. Lafkioti and G. Schütz: Vanishing Fe 3d orbital moments in single-crystalline magnetite, Europhys. Lett. **73** 97 (2006)

[180] H. Henneken, F. Scholze and G. Ulm: Lack of proportionality of total electron yield and soft x-ray absorption coefficient, J. Appl. Phys. **87** 257 (2000)

[181] E. Lindberg: The title is unknown to the author. Cited after Thole et al., Phys. Rev. B **32**, 5107 (1985) and Ottewell et al., J. Phys. B **6**, 2184 (1973), Nova Acta Reg. Soc. Sci. Upsaliensis **7** 7 (1931)

[182] D. Ottewell, E. A. Stewardson and J. E. Wilson: The $M_{4,5}$ spectrum of ^{58}Ce and the γ-α phase transition, J. Phys. B: At., Mol. Opt. Phys. **6** 2184 (1973)

[183] C. Bonnelle, R. C. Karnatak and J. Sugar: Photoabsorption in the vicinity of 3d absorption edges of La, La_2O_3, Ce, and CeO_2, Phys. Rev. A **9** 1920 (1974)

[184] B. T. Thole, G. van der Laan, J. C. Fuggle, G. A. Sawatzky, R. C. Karnatak and J. M. Esteva: $3d$ x-ray-absorption Lines and the $3d^9 4f^{n+1}$ multiplets of the lanthanides, Phys. Rev. B **32** 5107 (1985)

[185] T. Jo and A. Kotani: Narrowing Due to Valence Mixing in the 3d Core Level Spectra for Ce Compounds, J. Phys. Soc. Jpn. **57** 2288 (1988)

[186] T. Jo and A. Kotani: Effect of valence mixing on multiplet structure in core photoabsorption spectra for Ce compounds, Phys. Rev. B **38** 830 (1988)

[187] G. Kaindl, G. Kalkowski, W. D. Brewer, B. Perscheid and F. Holtzberg: M-edge x-ray absorption spectroscopy of 4f instabilities in rare-earth systems, J. Appl. Phys. **55** 1910 (1984)

[188] G. Kaindl, G. Kalkowski, W. D. Brewer, E. V. Sampathkumaran, F. Holtzberg and A. Schach von Wittenau: 4f Occupation and Hybridization From M-shell Excitations In Rare-earth Materials, J. Magn. Magn. Mater. **47-8** 181 (1985)

[189] G. van der Laan, B. T. Thole, G. A. Sawatzky, J. C. Fuggle, R. Karnatak, J. M. Esteva and B. Lengeler: Identification of the Relative Population of Spin Orbit Split States In the Ground-state of A Solid, Journal of Physics C-solid State Physics **19** 817 (1986)

[190] J. P. Schillé, F. Bertran, M. Finazzi, C. Brouder, J. P. Kappler and G. Krill: 4f Orbital and Spin Magnetism In Cerium Intermetallic Compounds Studied By Magnetic Circular X-ray Dichroism, Phys. Rev. B **50** 2985 (1994)

[191] M. Finazzi, F. de Groot, A. M. Dias, B. Kierren, F. Bertran, P. Sainctavit, J. P. Kappler, O. Schulte, W. Felsch and G. Krill: Direct Evidence of the Role of Hybridization in the X-Ray Magnetic Circular Dichroism of α-Ce, Phys. Rev. Lett. **75** 4654 (1995)

[192] M. Finazzi, F. M. F. de Groot, A. M. Dias, J. P. Kappler, O. Schulte, W. Felsch and G. Krill: Influence of hybridization in the Magnetic Circular X-ray Dichroism at the Ce-$M_{4,5}$ absorption edges of Ce-Fe systems, J. Electron Spectrosc. Relat. Phenom. **78** 221 (1996)

[193] M. Münzenberg, W. Felsch and P. Schaaf: Tuning the 4f state occupancy of Ce in highly correlated CeSi/Fe multilayers: An x-ray absorption spectroscopy study, Phys. Rev. B **76** 014427 (2007)

[194] T. Willers, Z. Hu, N. Hollmann, P. O. Koerner, J. Gegner, T. Burnus, H. Fujiwara, A. Tanaka, D. Schmitz, H. H. Hsieh, H.-J. Lin, C. T. Chen, E. D. Bauer, J. L. Sarrao, E. Goremychkin, M. Koza, L. H. Tjeng and A. Severing: Crystal-field and Kondo-scale investigations of $\mathrm{Ce}M\mathrm{In}_5$ (M=Co, Ir, and Rh): A combined x-ray absorption and inelastic neutron scattering study, Phys. Rev. B **81** 195114 (2010)

[195] T. Willers, D. T. Adroja, B. D. Rainford, Z. Hu, N. Hollmann, P. O. Koerner, Y.-Y. Chin, D. Schmitz, H. H. Hsieh, H.-J. Lin, C. T. Chen, E. D. Bauer, J. L. Sarrao, K. J. McClellan, D. Byler, C. Geibel, F. Steglich, H. Aoki, P. Lejay, A. Tanaka, L. H. Tjeng and A. Severing: Spectroscopic determination of crystal-field levels in $\mathrm{CeRh_2Si_2}$ and $\mathrm{CeRu_2Si_2}$ and of the $4f^0$ contributions in $\mathrm{Ce}M_2\mathrm{Si}_2$ (M=Cu, Ru, Rh, Pd, and Au), Phys. Rev. B **85** 035117 (2012)

[196] T. Okane, Y. Takeda, H. Yamagami, A. Fujimori, Y. Matsumoto, N. Kimura, T. Komatsubara and H. Aoki: Magnetic behavior near the boundary of $4f$ delocalization in ferromagnetic $\mathrm{CeRu_2Ge_2}$ and paramagnetic $\mathrm{CeRu_2Si_2}$ observed by Ce $M_{4,5}$ XAS and XMCD, Phys. Rev. B **86** 125138 (2012)

[197] F. Strigari, T. Willers, Y. Muro, K. Yutani, T. Takabatake, Z. Hu, S. Agrestini, C.-Y. Kuo, Y.-Y. Chin, H.-J. Lin, T. W. Pi, C. T. Chen, E. Weschke, E. Schierle, A. Tanaka, M. W. Haverkort, L. H. Tjeng and A. Severing: Crystal field ground state of the orthorhombic Kondo semiconductors $\mathrm{CeOs_2Al_{10}}$ and $\mathrm{CeFe_2Al_{10}}$, Phys. Rev. B **87** 125119 (2013)

[198] A. Delobbe, M. Finazzi, B. Buschinger, O. Trovarelli, C. Geibel, J. P. Kappler and G. Krill: $M_{4,5}$ absorption edges in Ce-Kondo systems, Physica B **259-61** 1144 (1999)

[199] J. Rothman, C. Meyer, D. Givord, J. Vogel, M. Finazzi, A. Fontaine, J.-P. Kappler and N. B. Brookes: Magnetic and electronic properties of epitaxial γ-cerium thin films, J. Magn. Magn. Mater. **198-99** 276 (1999)

[200] J. Rothman, C. Meyer, D. Givord, J. Vogel, M. Finazzi, A. Fontaine, J.-P. Kappler and N. B. Brookes: Magnetic and electronic properties of Ce(111) thin films, Physica B: Condensed Matter **259–261** 1138 (1999)

[201] G. Liang, M. Croft, D. Johnston, N. Anbalagan and T. Mihalisin: Coexistence of strong 3d antiferromagnetism and mixed-valent Kondo regime transition in $\mathrm{Ce(Mn}_x\mathrm{Cr}_{1-x})_2\mathrm{Si}_2$, Phys. Rev. B **38** 5302 (1988)

[202] J. M. Lawrence, G. H. Kwei, P. C. Canfield, J. G. Dewitt and A. C. Lawson: L_{III} x-ray-absorption in Yb compounds: Temperature-dependence of the valence, Phys. Rev. B **49** 1627 (1994)

[203] G. Liang and M. Croft: Thermal variation of Ce valence in mixed, valence-Kondo lattice systems $\mathrm{CeT_2(Si}_{1-x}\mathrm{Ge}_x)_2$ with T = Mn and Ni, Physica B **403** 1482 (2008)

[204] B. H. Choi, R. J. Jung, S. J. Oh, E. J. Cho, T. Iwasaki, A. Sekiyama, S. Imada, S. Suga, T. Muro and Y. S. Kwon: Temperature-dependence of Kondo resonance in $\mathrm{CeSi_2}$ studied by bulk-sensitive resonant photoemission, J. Electron Spectrosc. Relat. Phenom. **136** 15 (2004)

[205] S. Nakamura, T. Yoshida, Y. Takayama, T. Miyahara, H. Ishii, H. Sugawara, H. Sato and T. Nakamura: MCD study on $\mathrm{Ce}_x\mathrm{La}_{1-x}\mathrm{Ni}$: Difference between the ”local” and ”coherent” Kondo effect, J. Phys. Soc. Jpn. **75** 044707 (2006)

[206] H. Yamaoka, N. Tsujii, K. Yamamoto, H. Oohashi, A. M. Vlaicu, K. Kunitani, K. Uotani, D. Horiguchi, T. Tochio, Y. Ito and S. Shin: Direct observation of valence transition in $\mathrm{CeNi}_{1-x}\mathrm{Co}_x\mathrm{Sn}$ alloys by x-ray and photoelectron spectroscopies, Phys. Rev. B **76** 075130 (2007)

[207] R. D. Cowan: Theoretical Calculations of Atomic Spectra Using Digital Computers, J. Opt. Soc. Am. **58** 808 (1968)

[208] J. B. Goedkoop, B. T. Thole, G. van der Laan, G. A. Sawatzky, F. M. F. de Groot and J. C. Fuggle: Calculations of magnetic x-ray dichroism in the $3d$ absorption spectra of rare-earth compounds, Phys. Rev. B **37** 2086 (1988)

[209] M. Sacchi, O. Sakho and G. Rossi: Strong Dichroism In the Dy 3d → 4f X-ray Absorption At Dy/Si(111) Interfaces, Phys. Rev. B **43** 1276 (1991)

[210] M. Sacchi, F. Sirotti and G. Rossi: Crystal-field Induced Linear Dichroism In the 3d X-ray Absorption of Rare-earths, Solid State Commun. **81** 977 (1992)

[211] T. Jo: Hybridization, Crystal Anisotropy and Magnetism in Ce Compounds and Core X-Ray Absorption, Prog. Theor. Phys. Suppl. **101** 303 (1990)

[212] S. Nakai, A. Kamata, K. Matsuda, T. D., A. H., A. Yagishita and M. Kasaya: Linear Dichroism In Ce 3d X-ray-absorption of $\mathrm{CeRh_3B_2}$, Physica B-condensed Matter **186-88** 74 (1993)

[213] S. Imada, A. Yamasaki, A. Tsunekawa, A. Higashiya, A. Sekiyama, H. Sugawara, H. Sato and S. Suga: Electronic and magnetic states of Ce 4f electrons in $\mathrm{CeRh_3B_2}$, J. Electron Spectrosc. Relat. Phenom. **156** 436 (2007)

[214] P. Hansmann: Crystal-Field ground states of rare-earth materials determined by linear dichroism: A feasibility study and its experimental proof, Master’s thesis, Universität Köln (2007)

[215] T. Willers, B. Fak, N. Hollmann, P. O. Koerner, Z. Hu, A. Tanaka, D. Schmitz, M. Enderle, G. Lapertot, L. H. Tjeng and A. Severing: Crystal-field ground state of the noncentrosymmetric superconductor $\mathrm{CePt_3Si}$: A combined polarized soft x-ray absorption and polarized neutron study, Phys. Rev. B **80** 115106 (2009)

[216] F. Strigari, T. Willers, Y. Muro, K. Yutani, T. Takabatake, Z. Hu, Y.-Y. Chin, S. Agrestini, H.-J. Lin, C. T. Chen, A. Tanaka, M. W. Haverkort, L. H. Tjeng and A. Severing: Crystal-field ground state of the orthorhombic Kondo insulator $\mathrm{CeRu_2Al_{10}}$, Phys. Rev. B **86** 081105 (2012)

[217] T. Willers, F. Strigari, Z. Hu, V. Sessi, N. B. Brookes, E. D. Bauer, J. L. Sarrao, J. D. Thompson, A. Tanaka, S. Wirth, L. H. Tjeng and A. Severing: Correlation between ground state and orbital anisotropy in heavy fermion materials, Proceedings of the National Academy of Sciences (2015)

[218] T. Jo and S. Imada: Circular dichroism in the 3d and 4d Core Photoabsorption for Ferromagnetic Ce Compounds – Interplay of Hybridization, Spin Orbit Interaction and Crystal Field, J. Phys. Soc. Jpn. **59** 1421 (1990)

[219] G. Schütz, M. Knülle, R. Wienke, W. Wilhelm, W. Wagner, P. Kienle and R. Frahm: Spin-dependent photoabsorption at the L-edges of ferromagnetic Gd and Tb metal, Z. Phys. B **73** 67 (1988)

[220] G. Schütz, R. Wienke, W. Wilhelm, W. Wagner, P. Kienle, R. Zeller and R. Frahm: Strong spin-dependent absorption at the L_2 edges of 5d-impurities in iron, Zeitschrift für Physik B Condensed Matter **75** 495 (1989)

[221] C. T. Chen, F. Sette, Y. Ma and S. Modesti: Soft-x-ray Magnetic Circular-dichroism At the $L_{2,3}$ Edges of Nickel, Phys. Rev. B **42** 7262 (1990)

[222] S. Imada and T. Jo: Magnetic Circular Dichroism in Core X-Ray Absorption Spectra of Rare-Earths, J. Phys. Soc. Jpn. **59** 3358 (1990)

[223] J. P. Schillé, I. Poinsot, C. Giorgetti, P. Sainctavit, G. Fischer, C. Brouder, F. Bertran, M. Finazzi, C. Godart, E. Dartyge, J. P. Kappler and G. Krill: Experimental-evidence of A Strongly Reduced Orbital Moment In $CeRh_3B_2$, Physica B **199** 563 (1994)

[224] A. Delobbe, A. M. Dias, M. Finazzi, L. Stichauer, J. P. Kappler and G. Krill: X-ray magnetic circular dichroism study on $CeFe_2$, Europhys. Lett. **43** 320 (1998)

[225] M. Arend, M. Finazzi, O. Schutte, M. Münzenberg, A. M. Dias, F. Baudelet, C. Giorgetti, E. Dartyge, P. Schaaf, J. P. Kappler, G. Krill and W. Felsch: 4f and 5d magnetic moments in highly correlated [Ce/La/Fe] and [La/Ce/Fe] multilayers studied by x-ray magnetic circular dichroism, Phys. Rev. B **57** 2174 (1998)

[226] M. Arend, W. Felsch, G. Krill, A. Delobbe, F. Baudelet, E. Dartyge, J. P. Kappler, M. Finazzi, A. San Miguel-Fuster, S. Pizzini and A. Fontaine: Perpendicular magnetic anisotropy and the reorientation transition of the magnetization in CeH_2/Fe multilayers probed by x-ray magnetic circular dichroism, Phys. Rev. B **59** 3707 (1999)

[227] T. Miyahara, H. Ishii, Y. Takayama, M. Hirose, K. Maruyama, K. Obu, M. Shinoda, T. Muro, Y. Saitoh, T. D. Matsuda, H. Sugawara and H. Sato: MCD study on materials without magnetic order, J. Phys. Soc. Jpn. **70** 2977 (2001)

[228] T. Miyahara, H. Ishii, K. Obu, M. Shinoda, Y. Takayama, T. Muro, T. D. Matsuda, H. Sugawara and H. Sato: Precursor nonmagnetic states of $PrFe_4P_{12}$ and $CePd_3$ detected by core excitation MCD, Surf. Rev. Lett. **9** 831 (2002)

[229] H. Shiozawa, T. Miyahara, H. Ishii, Y. Takayama, K. Obu, T. Muro, Y. Saitoh, T. D. Matsuda, H. Sugawara and H. Sato: Measurements of temperature dependence of ”localized susceptibility”, Nucl Instrum. Meth. B **199** 318 (2003)

[230] H. Shiozawa, T. Miyahara, K. Obu, Y. Takayama, H. Ishii, T. D. Matsuda, H. Sugawara, H. Sato, T. Muro and Y. Saitoh: Local magnetic susceptibility in rare-earth compounds, J. Phys. Soc. Jpn. **72** 2079 (2003)

[231] T. Miyahara and H. Shiozawa: Interpretation of difference between bulk magnetic susceptibility and ”local magnetic susceptibility” detected by core excitation magnetic circular dichroism, J. Electron Spectrosc. Relat. Phenom. **136** 117 (2004)

[232] C. L. Dong, Y. Y. Chen, C. L. Chen, J. . H. Guo and C. L. Chang: Electronic and magnetic properties of $CeAl_2$ nanoparticles, J. Magn. Magn. Mater. **304** E22 (2006)

[233] T. Tolinski, J. C. Cezar, H. Wende, A. Kowalczyk and K. Baberschke: X-Ray Magnetic Circular Dichroism Studies on CeNi$_4$B, Acta Phys. Pol. A **115** 129 (2009)

[234] J. Ishikawa, T. Miyahara, Y. Hirato, H. Ishii, T. Kodama, K. Kikuchi, T. Nakamura, K. Kodama, D. Asakura and T. Koide: MCD study on Ce@C$_8$2 and Ce$_2$@C$_8$0 in the soft-X-ray region, J. Electron Spectrosc. Relat. Phenom. **184** 284 (2011)

[235] Y. Teramura, A. Tanaka, B. T. Thole and T. Jo: Effect of Coulomb Interaction on the X-Ray Magnetic Circular Dichroism, J. Phys. Soc. Jpn. **65** 3056 (1996)

[236] T. Jo: The 3d–4f exchange interaction, X-ray second-order optical processes and the magnetic circular (MCD) spin sum rule in rare earths, J. Electron Spectrosc. Relat. Phenom. **86** 73 (1997)

[237] A. P. Murani and P. J. Brown: Comment on “X-Ray magnetic circular dichroism study on FeFe$_2$” by A. Delobbe *et al.*, Europhys. Lett. **48** 353 (1999)

[238] A. Delobbe, A. M. Dias, M. Finazzi, L. Stichauer, J. P. Kappler and G. Krill: Reply to the comment by A. P. Murani and P. J. Brown on “X-ray magnetic circular dichroism study on CeFe$_2$”, Europhys. Lett. **48** 355 (1999)

[239] J. C. Parlebas and A. Kotani: Electron correlation and surface/bulk effects in various spectra of Ce compounds, J. Electron Spectrosc. Relat. Phenom. **136** 3 (2004)

[240] S. Suga, A. Sekiyama, S. Imada, J. Yamaguchi, A. Shigemoto, A. Irizawa, K. Yoshimura, M. Yabashi, K. Tamasaku, A. Higashiya and T. Ishikawa: Unraveling Genuine First Order Bulk Valence Transition and Kondo Resonance Behaviors in YbInCu$_4$ by High Energy Photoelectron Spectroscopy, J. Phys. Soc. Jpn. **78** 074704 (2009)

[241] M. Mulazzi, K. Shimada, J. Jiang, H. Iwasawa and F. Reinert: Evidence of coexisting Kondo screening and valence fluctuations in the CePd$_7$/Pd(001) surface alloy, Phys. Rev. B **89** 205134 (2014)

[242] H. Schwab: in preparation, Ph.D. thesis, Universität Würzburg (prospective)

[243] A. Tanaka and T. Jo: Resonant 3d, 3p and 3s Photoemission in Transition Metal Oxides Predicted at 2p Threshold, J. Phys. Soc. Jpn. **63** 2788 (1994)

[244] M. W. Haverkort: Spin and orbital degrees of freedom in transition metal oxides and oxide thin films studied by soft x-ray absorption spectroscopy, Ph.D. thesis, Universität Köln (2005)

[245] M. W. Haverkort, M. Zwierzycki and O. K. Andersen: Multiplet ligand-field theory using Wannier orbitals, Phys. Rev. B **85** 165113 (2012)

[246] G. van der Laan: Hitchhiker’s Guide to Multiplet Calculations, in E. Beaurepaire, H. Bulou, F. Scheurer and J.-P. Kappler (eds.), Magnetism: A Synchrotron Radiation Approach, Springer-Verlag (2006)

[247] S. Schippers: Analytical Expression for the Convolution of a Fano Line Profile with a Gaussian, IRAMP **2** 151 (2011)

[248] U. Fano: Effects of Configuration Interaction on Intensities and Phase Shifts, Phys. Rev. **124** 1866 (1961)

[249] K. T. Moore, B. W. Chung, S. A. Morton, A. J. Schwartz, J. G. Tobin, S. Lazar, F. D. Tichelaar, H. W. Zandbergen, P. Soderlind and G. van der Laan: Changes in the electronic structure of cerium due to variations in close packing, Phys. Rev. B **69** 193104 (2004)

[250] G. van der Laan, E. Arenholz, Z. Hu, A. Bauer, E. Weschke, C. Schussler-Langeheine, E. Navas, A. Muhlig, G. Kaindl, J. B. Goedkoop and N. B. Brookes: Magnetic circular dichroism in Tb $3d \to 4f$ resonant photoemission, Phys. Rev. B **59** 8835 (1999)

[251] T. Willers: private communication

[252] E. Goering: X-ray magnetic circular dichroism sum rule correction for the light transition metals, Philos. Mag. **85** 2895 (2005)

[253] P. W. Palmberg, G. E. Riach, R. E. Weber and N. C. MacDonald: Handbook of Auger Electron Spectroscopy, Physical Electronics Industries, Inc. (1972)

[254] P. Luches, F. Pagliuca and S. Valeri: Morphology, Stoichiometry, and Interface Structure of CeO_2 Ultrathin Films on Pt(111), J. Phys. Chem. C **115** 10718 (2011)

[255] J. M. Esteva, R. C. Karnatak and J. P. Connerade: Photo-absorption and Electron Yields of La and Gd In the Vicinity of the 3d Thresholds, J. Electron Spectrosc. Relat. Phenom. **31** 1 (1983)

[256] J. Vogel and M. Sacchi: Experimental Estimate of Absorption Length and Total Electron Yield (TEY) Probing Depth In Dysprosium, J. Electron Spectrosc. Relat. Phenom. **67** 181 (1994)

[257] M. Abbate, J. B. Goedkoop, F. M. F. de Groot, M. Grioni, J. C. Fuggle, S. Hofmann, H. Petersen and M. Sacchi: Probing Depth of Soft-x-ray Absorption-spectroscopy Measured In Total-electron-yield Mode, Surf. Interface Anal. **18** 65 (1992)

[258] S. Gallego, C. Ocal, M. C. Munoz and F. Soria: Surface-layered ordered alloy (Pt/Pt_3Mn) on Pt(111), Phys. Rev. B **56** 12139 (1997)

[259] J. Quinn, Y. S. Li, F. Jona and D. Fort: Surface Relaxation On Tb(0001), Surf. Sci. **257** L647 (1991)

[260] J. Quinn, Y. S. Li, F. Jona and D. Fort: Atomic-structure of A Gd(0001) Surface, Phys. Rev. B **46** 9694 (1992)

[261] J. Giergiel, A. W. Pang, H. Hopster, X. Guo, S. Y. Tong and D. Weller: Surface-structure of Epitaxial Gd(0001) Films On W(110) Studied By Quantitative Leed Analysis, Phys. Rev. B **51** 10201 (1995)

[262] C. Bonet, D. J. Spence and S. P. Tear: Structural study of 2D dysprosium germanide and silicide by means of quantitative LEED I-V analysis, Surf. Sci. **504** PII S0039 (2002)

[263] R. C. Karnatak and J. P. Esteva, J. M.and Connerade: On the profiles and linewidths of the 3d to 4f transitions in the lanthanides, J. Phys. B: At., Mol. Opt. Phys. **14** 4747 (1981)

[264] P. Motais, E. Belin and C. Bonnelle: On the Relative Intensities of the M_{IV} and M_V Absorption and Emission-spectra of La^{3+}, Journal of Physics F-metal Physics **11** L169 (1981)

[265] M. W. Haverkort: private communication

[266] P. Hansmann: private communication

[267] G. D. Mahan: Excitons In Metals - Infinite Hole Mass, Physical Review **163** 612 (1967)

[268] P. Nozières and C. T. De Dominicis: Singularities in the X-Ray Absorption and Emission of Metals. III. One-Body Theory Exact Solution, Phys. Rev. **178** 1097 (1969)

[269] S. Doniach and M. Šunjić: Many-electron Singularity In X-ray Photoemission and X-ray Line Spectra From Metals, Journal of Physics Part C Solid State Physics **3** 285 (1970)

[270] S. Bhowmick, J. Rusz and O. Eriksson: X-ray absorption spectra: Graphene, h-BN, and their alloy, Physical Review B **87** 155108 (2013)

[271] F. Welsch, M. Fähnle and P. J. Jensen: Crystal field parameters at the (0001) surface of rare-earth metals: an ab initio study, Journal of Physics: Condensed Matter **17** 2061 (2005)

[272] P. Ohresser: private communication

[273] Y. Yang, Z. Fisk, H.-O. Lee, J. D. Thompson and D. Pines: Scaling the Kondo lattice (including supplementary material), Nature **454** 611 (2008)

[274] P. M. Levy and S. Zhang: Crystal-field Splitting In Kondo Systems, Physical Review Letters **62** 78 (1989)

[275] P. S. Riseborough: Noncrossing approximation solution of the anisotropic Anderson impurity model, Physical Review B **67** 045102 (2003)

[276] Y. Zhou, S. P. Bowen, D. D. Koelling and R. Monnier: Magnetic-susceptibility of YbN, Physical Review B **43** 11071 (1991)

[277] E. D. Bauer, S. Bobev, J. D. Thompson, M. F. Hundley, J. L. Sarrao, A. Lobos and A. A. Aligia: Intermediate valence behaviour in the new Kondo lattice compound $Yb_3Ni_5Al_{19}$, Journal of Physics-condensed Matter **16** PII S0953 (2004)

[278] N. O. Moreno, A. Lobos, A. A. Aligia, E. D. Bauer, S. Bobev, V. Fritsch, J. L. Sarrao, P. G. Pagliuso, J. D. Thompson, C. D. Batista and Z. Fisk: Crystal-field effects in the mixed-valence compounds $Yb_2M_3Ga_9$ (M=Rh,Ir), Phys. Rev. B **71** 165107 (2005)

[279] A. D. Christianson, J. M. Lawrence, A. M. Lobos, A. A. Aligia, E. D. Bauer, N. O. Moreno, E. A. Goremychkin, K. C. Littrell, J. L. Sarrao, J. D. Thompson and C. D. Batista: Anisotropic intermediate valence in $Yb_2Rh_3Ga_9$, Physica B-condensed Matter **378-80** 752 (2006)

[280] G. Zwicknagl, V. Zevin and P. Fulde: Simple Approximation Scheme For the Anderson Impurity Hamiltonian, Zeitschrift für Physik B-condensed Matter **79** 365 (1990)

[281] K. Fauth: unpublished results

[282] M. Zinner and K. Fauth: unpublished results

[283] M. Zinner, B. Halbig, U. Bass, R. Hölldobler, C. Praetorius, J. Geurts and K. Fauth: unpublished results

[284] P. Luches, F. Pagliuca, S. Valeri and F. Boscherini: Structure of Ultrathin CeO_2 Films on Pt(111) by Polarization-Dependent X-ray Absorption Fine Structure, J. Phys. Chem. C **117** 1030 (2013)